

UNIVERSITY OF BIRMINGHAM

Investigation into the grinding performance and surface integrity of advanced aerospace superalloys in creep feed grinding

By

Rakan Mohammed H Albarakati

M.Sc. Eng., B.Sc. Eng.

A thesis submitted to
The University of Birmingham
for the degree of
DOCTOR OF PHILOSOPHY

School of Mechanical Engineering
The University of Birmingham
December 2023

UNIVERSITY OF
BIRMINGHAM

University of Birmingham Research Archive

e-theses repository

This unpublished thesis/dissertation is copyright of the author and/or third parties. The intellectual property rights of the author or third parties in respect of this work are as defined by The Copyright Designs and Patents Act 1988 or as modified by any successor legislation.

Any use made of information contained in this thesis/dissertation must be in accordance with that legislation and must be properly acknowledged. Further distribution or reproduction in any format is prohibited without the permission of the copyright holder.

University of Birmingham Research Archive
e-theses repository

This unpublished thesis/dissertation is copyright of the author and/or third parties. The intellectual property rights of the author or third parties in respect of this work are as defined by The Copyright Designs and Patents Act 1988 or as modified by any successor legislation.
Any use made of information contained in this thesis/dissertation must be in accordance with that legislation and must be properly acknowledged. Further distribution or reproduction in any format is prohibited without the permission of the copyright holder.

SYNOPSIS

Titanium alloys exhibit exceptional mechanical properties, including high rigidity, favourable strength-to-weight ratio, and excellent resistance to corrosion. Such features have resulted in their widespread application across several industries, more particularly in aerospace and automotive. The increased demand for enhanced burn resistance coupled with low weight has led to the development of more advanced titanium alloys such as gamma titanium aluminide intermetallic (γ-TiAl) and burn-resistant titanium alloy (BuRTi), which are considered potential alternative materials for nickel-based superalloys in aerospace components such as compressors and turbine blades or vanes. However, machining these materials poses significant challenges to the industry in part due to their inherent features, for instance, low thermal conductivity, strong chemical reactivity, and the ability to maintain their tensile strengths at elevated temperatures. The process of grinding plays a crucial role in the manufacturing of mechanical components with high surface quality and dimensional accuracy, and compared to other machining processes, grinding has consistently exhibited improved surface quality when utilised for cutting titanium alloys. In comparison to conventional grinding, creep feed grinding achieves more efficiently in terms of stock removal rate while maintaining good surface finish and tolerances (from ±8µm to ±80µm).

The available information in the literature regarding creep feed grinding of the thermo-mechanically produced duplex latest generation gamma titanium aluminide (Ti-45Al-8Nb-0.2C), the patent burn-resistant titanium alloy (Ti-25V-15Cr-2Al-0.2C) and the alpha/beta titanium alloy (Ti-6Al-4V) is scarce and only involving limited investigated machining/grinding conditions. In addition, the existing literature on creep feed grinding of γ-TiAl (Ti–45Al–8Nb–0.2C) lacks information regarding the temperature and residual stresses that are produced during the machining operation, with extremely limited information given for burn-resistant titanium (Ti-25V-15Cr-2Al-0.2C). Moreover, the majority of published work to date has primarily focused on the evaluation of the two-dimensional average surface roughness parameter (Ra), and no details on extreme or three-dimensional surface roughness parameters were reported (Rt, Rz, Sa, St and Sz).

Following an extensive literature review on titanium alloy development, grinding fundamentals, surface integrity, experimental design, and grinding of relevant titanium alloys, the thesis details the findings from three main phases of experimental work. The first focused

on creep feed grinding of gamma titanium aluminide intermetallic alloy (Ti–45Al–8Nb–0.2C wt%), whilst the second phase provided an assessment of creep feed grinding for burn resistant titanium alloy (Ti-25V-15Cr-2Al-0.2C) and compared its grindability to γ-TiAl material. The last phase is pertinent to creep feed grinding of alpha/beta titanium alloy (Ti-6Al-4V) with benchmarking against the two previously investigated materials. Results provided in each phase/material covered information for both conventional and super-abrasive wheels. Full factorial experimental designs were utilised in each phase to investigate the impact of various operational parameters (wheel speed, depth of cut and feed rate) and their corresponding levels (20 and 30m/s, 0.3 and 1mm, and 150 and 300mm/min) on performance output measures, including the G-ratio, grinding forces, grinding power, specific energy, grinding temperature, and workpiece surface roughness. Furthermore, an assessment of the surface integrity of the machined samples is provided, which encompasses the evaluation of the produced workpiece surface, microstructure, microhardness and residual stresses.

The experimental findings demonstrate that γ-TiAl showed more favourable outcomes when compared to BuRTi and Ti-6Al-4V. This was evident from the lower values observed including, 3 times lower wheel wear, ~40% lower grinding forces and power, reduced temperature at the majority of tests and ~50% lower surface roughness. BuRTi and Ti-6Al-4V materials exhibited a moderate degree of similarity in terms of their grinding performance at lower rates of material removal. At increased depths of cuts, the former showed reduced wheel wear (~27µm compared to ~50µm), ~30% lower grinding forces and ~30-40% lower surface roughness. However, these were accompanied by the occurrence of surface burn and crack formation. In terms of grinding temperature, surface integrity, and generated residual stresses, the diamond wheel exhibited superior performance compared to the SiC wheel across all materials that were examined. The results indicate that a significant rise in the G-ratio was only evident in γ-TiAl subjected to diamond wheel machining, while no such improvement was observed in BuRTi and Ti-6Al-4V. Tensile residual stresses were predominantly present on γ-TiAl and BuRTi surfaces ground with a SiC wheel under extreme operating conditions and accompanied with fractures, burn marks, and softening layers on machined surfaces. Compressive residual stresses, on the other hand, were restricted to surfaces free of burn and microstructural deformation, particularly in samples cut with diamond wheels.

The current work provides new insights into the generated temperature, residual stresses and 3D surface roughness parameters during creep feed grinding of the thermo-mechanically produced duplex alloy γ-TiAl (Ti–45Al–8Nb–0.2C), the patent burn-resistant titanium alloy

(Ti-25V-15Cr-2Al-0.2C) as well as for alpha/beta titanium alloy (Ti-6Al-4V). The findings presented in this thesis demonstrate strong correlations between the output measures pertaining to surface integrity and the generated temperature, 3D surface roughness parameters, and induced residual stress results. These aspects are missing in published literature for investigated materials. The machinability data presented here are extremely useful for future work in understanding the analysis of the performance of grinding processes for titanium alloys including modelling activities.

ACKNOWLEDGEMENTS

I would like to express my special appreciation and thanks to my lead supervisor Dr Richard Hood for encouragement, assistance, inspiration, guidance throughout this research. In addition, I would like to thank Dr Leung Soo for his co-supervision and advise.

Special thanks are reserved for my thesis committee members, Dr Debajyoti Bhaduri from Cardiff University and Dr Raya AL-Dadah from the University of Birmingham, for reviewing this thesis and for offering their expert advice.

I also would like to acknowledge and thank the machining lab technician Andy for all the technical support during my work in laboratories. I am also grateful to all members of machining group, Ali, Ramy, Fernanda, Luis, Guojie, Yiming, Mohammed and Munshi for their advice, support and help within the lab.

I extend my heartfelt appreciation to the Saudi Arabian government represented by the Royal Embassy of Saudi Arabia Cultural Bureau for funding a studentship for this research. This research and thesis would not be possible without their financial contributions.

Lastly, I wish to express my love and deepest gratitude to my family, friends and in particular my wife, Ghadeer and children, Omar, Abdulaziz and Ali for their understanding, endless encouragement, support, patience and love throughout this work, I could never have completed my study without them.

TABLE OF CONTENTS

LIST OF FIGURES viii

LIST OF TABLES xvi

LIST OF NOMENCLATURE xix

1 INTRODUCTION 1

1.1 Background to the project 1

1.2 Aims and objectives of the project 6

1.3 Structure of thesis 8

2 LITERATURE REVIEW 9

2.1 Titanium and its alloys 9

2.1.1 Conventional titanium alloys 10

2.1.2 Gamma titanium aluminide intermetallic alloys 13

2.1.3 Burn-resistant titanium alloy 17

2.2 Grinding 19

2.2.1 Creep feed grinding 21

2.2.2 Grinding system elements 23

2.2.3 Grinding wheel 24

2.2.4 Grinding mechanics 27

2.2.5 Grinding vibration 30

2.2.6 Grinding temperature 31

2.2.7 Grinding fluid application 41

2.3 Workpiece surface topography and integrity 47

2.3.1 Surface topography 47

2.3.2 Surface integrity 51

2.4 Experimental design techniques 55

2.5 Grinding of advanced titanium alloys 57

2.6 Summary of the literature review and key areas of investigations 69

3 EXPERIMENTAL WORK 73

3.1 Workpiece materials 73

3.2 Creep feed grinding wheels 74

3.3 Machine tools 75

3.3.1 Pre-machining machine centres 75

3.3.2 Creep feed grinding machine centre 78

3.4 Analysis equipment 80

3.4.1 Grinding wheel wear and grinding ratio 80

3.4.2 Grinding forces, power and specific energy 81

3.4.3 Grinding temperature 81

3.4.4 Surface roughness and topography 83

3.4.5 Microhardness and microstructure 84

3.4.6 Optical and scanning electron microscopy 85

3.4.7 Residual stresses 86

3.4.8 Statistical analysis 88

3.5 Experimental designs and test arrays 89

3.5.1 Phase 1: Creep feed grinding of γ-titanium aluminide alloy (Ti-45Al-8Nb-0.2C) 90

3.5.2 Phase 2: Creep feed grinding of burn resistant titanium alloy (Ti-25V-15Cr-2Al-0.2C) 93

3.5.3 Phase 3: Creep feed grinding of conventional titanium alloy (Ti-6Al-4V) 95

4 RESULTS AND DISCUSSION 97

4.1 Phase 1: Creep feed grinding of γ-titanium aluminide alloy (Ti-45Al-8Nb-0.2C) 97

4.1.1 Phase 1A: The influence of operating conditions on grinding performance when creep feed grinding with conventional silicon carbide wheel (SiC) 97

4.1.2 Phase 1B: Effect of operating conditions on grinding performance when creep feed grinding with super-abrasive diamond wheel and a comparison between two different wheel systems 109

4.1.3 Phase 1C: Extended surface integrity analysis (residual stress) on γ- titanium aluminide alloy (Ti-45Al-8Nb-0.2C) 118

4.1.4 Summary of results for γ-titanium aluminide alloy (Ti-45Al-8Nb-0.2C) 120

4.2 Phase 2: Creep feed grinding of burn resistant titanium alloy (Ti-25V-15Cr-2Al-0.2C) 124

4.2.1 Phase 2A: Assessment of significant operating parameters when creep feed grinding with conventional silicon carbide wheel (SiC) and benchmark against γ-titanium aluminide alloy (Ti-45Al-8Nb-0.2C) 124

4.2.2 Phase 2B: Assessment of grinding performance when creep feed grinding with super-abrasive diamond wheel, and benchmark against γ-titanium aluminide alloy (Ti-45Al-8Nb-0.2C) 137

4.2.3 Phase 2C: Extended surface integrity analysis (residual stress) on burn-resistant titanium alloy (Ti-25V-15Cr-2Al-0.2C) 147

4.2.4 Summary of results for burn resistant titanium alloy (Ti-25V-15Cr-2Al-0.2C) 149

4.3 Phase 3: Creep feed grinding of conventional titanium alloy (Ti-6Al-4V) 154

4.3.1 Phase 3A: Benchmarking the performance against γ-titanium aluminide alloy and burn-resistant titanium alloy with SiC wheel 154

4.3.2 Phase 3B: Benchmarking the performance against γ-titanium aluminide alloy and burn-resistant titanium alloy with diamond wheel 163

4.3.3 Phase 3C: Comparison of the performance of different super-abrasive wheel specifications 175

4.3.4 Phase 3D: Extended surface integrity analysis (residual stress) on conventional titanium alloy (Ti-6Al-4V) 185

4.3.5 Summary of results for conventional titanium alloy (Ti-6Al-4V) 187

5 CONCLUSION 192

5.1 Correlations between examined machining output measures 192

5.2 Overall conclusions 194

5.3 Recommended operating conditions for CFG of investigated advanced titanium alloys 196

5.4 Contributions to knowledge 200

5.5 Recommendations for future work 201

6 REFERENCES 204

Appendix A: Assessments of the correlations between grinding inputs and outputs 219

Appendix B: Grinding wheel standard coding systems 220

Appendix C: Surface integrity evaluation techniques 221

Appendix D: OMEGA High temperature cement specification 222

Appendix E: Grinding coolant specifications 223

Appendix F: Additional experimental results 224

LIST OF FIGURES

Figure 1-1: Distribution of titanium and nickel alloys in an aero-engine 3

Figure 1-2: Materials uptake in turbine aeroengine 3

Figure 2-1: Kroll process for the production of titanium sponge 9

Figure 2-2: Titanium crystalline transformation 10

Figure 2-3: Ti-Al phase diagram 14

Figure 2-4: Ti-Al different microstructure 15

Figure 2-5: Microstructures of Ti-47Al 3.7(Nb,Cr,Mn,Si)-0.5 B (at. %) [41]: a) Coarse, nearly lamellar, b) equiaxed microstructure, T = 1,300ºC, (c) duplex microstructure, T = 1,340ºC, (d) nearly-lamellar microstructure, T = 1,360ºC. 15

Figure 2-6: γ-TiAl components 17

Figure 2-7: Burn resistance of different titanium alloys 19

Figure 2-8: Basic grinding operations 20

Figure 2-9: Surface grinding types 20

Figure 2-10: Illustration of surface grinding vs creep feed grinding 22

Figure 2-11: Grinding process inputs and outputs 23

Figure 2-12: Grinding wheel structure 24

Figure 2-13: Basic dressing tool configurations, a) Stationary single-point dressing tool, b) rotary roll dressing an external grinding wheel. 27

Figure 2-14: The effect of dressing ratio on the roughness of produced surface 27

Figure 2-15: Schematic illustration of grinding variables 28

Figure 2-16: Regenerative workpiece vibration 31

Figure 2-17: Heat flow mechanism 35

Figure 2-18: Thermal image method 37

Figure 2-19: Infra-red pyrometer with local optical fiber temperature 37

Figure 2-20: A Schematic of the PVD method of temperature measurement 38

Figure 2-21: Different methods for implementation of thermocouples 40

Figure 2-22: Thermocouples assembly by Black 40

Figure 2-23: Effects of lubrication and cooling in the machining processes 41

Figure 2-24: Coolant supply methods 44

Figure 2-25: Influence of air barrier on grinding coolant 45

Figure 2-26: Surface topography components 48

Figure 2-27: 2D surface parameters Ra, Rz and Rt 50

Figure 2-28: S-N curve for mild steel and aluminum alloy 55

Figure 2-29: Produced surfaces of γ-TiAl alloy and burn resistant titanium alloy following creep feed grinding with SiC wheels by Hood 62

Figure 2-30: SEM images of g-TiAl surfaces ground using SiC 64

Figure 2-31: Microstructures of g-TiAl samples after UACFG 64

Figure 2-32: Effect of grinding parameters on grinding temperature by Xinxin 66

Figure 2-33: Main effects plots for γ-TiAl and BuRTi by Hood et al. 68

Figure 3-1: Microstructures of tested workpieces: a) gamma titanium aluminide, b) burn-resistant titanium alloy, c) Ti-6Al-4V 73

Figure 3-2: Utilised Creep feed grinding wheel: a) SiC wheel, b) vitrified diamond wheel, c) single layer diamond wheel D252 74

Figure 3-3: As supplied blocks vs testing blocks 75

Figure 3-4: Wire electric discharge machine centre 76

Figure 3-5: Drilling centre (DMG MORI ULTRASONIC 20 linear) 77

Figure 3-6: Jones and Shipman 540AP reciprocating surface grinder unit 78

Figure 3-7: Bridgeport FGC1000 79

Figure 3-8: (a) diamond roller dresser, (b) nozzles arrangement 80

Figure 3-9: CMM Mitutoyo Euro Apex 80

Figure 3-10: Forces measurement set up: (a) amplifiers, (b) platform dynamometer 81

Figure 3-11: Blind hole thermocouple installation process: (a) grinding temperature measurement, (b) cross-section of the thermocouple blind hole, (c) BuRTi workpiece and thermocouple assembly 82

Figure 3-12: (a) FORMTRACER Avant, (b)Alicona G4 InfiniteFocus 83

Figure 3-13: (a) Buehler mounting equipment, (b) Buehler grinder-polisher 85

Figure 3-14: Mitutoyo HM-124 microhardness tester 85

Figure 3-15: (a) Keyence VHX digital microscope, (b) Hitachi TM3030 86

Figure 3-16: Strain gauge orientation and arrangement 87

Figure 3-17: The arrangement for incremental drilling 87

Figure 3-18: Experimental set-up 92

Figure 4-1: G-ratio and radial wheel wear for different grinding conditions (Phase 1A) 97

Figure 4-2: The main effect plot for G-ratio (Phase 1A) 98

Figure 4-3: Grinding forces for different operating conditions (Phase 1A) 99

Figure 4-4: Main effect plot for specific energy (Phase 1A) 101

Figure 4-5: Measured maximum temperature at different operating conditions (Phase 1A) 102
Figure 4-6: 2D surface roughness parameters for ground surfaces (Phase 1A) 104
Figure 4-7: 3D topographical parameters of ground surfaces (Phase 1A) 104
Figure 4-8: Observed ground workpiece surfaces (Phase 1A) 106
Figure 4-9: Higher magnification images of the ground surfaces (Phase 1A) 106
Figure 4-10: Cross-sectional microstructure of ground surfaces (Phase 1A) 107
Figure 4-11: Microhardness depth profiles (Phase 1A) 108
Figure 4-12: Radial wear and G-ratio for diamond wheel at different conditions (Phase 1B) 109
Figure 4-13: Grinding forces at different operating conditions (Phase 1B) 110
Figure 4-14: Recorded temperature at different operating conditions (Phase 1B) 112
Figure 4-15: 2D and 3D surface roughness parameters for ground surfaces (Phase 1B) 113
Figure 4-16: Workpiece surface images (Phase 1B) 114
Figure 4-17: SEM micrographs of ground γ-TiAl surfaces with diamond wheel (Phase 1B) 115
Figure 4-18: The microstructure of γ-TiAl ground with diamond wheel (Phase 1B) 116
Figure 4-19: Microhardness depth profiles (Phase 1B) 117
Figure 4-20: Residual stress depth profiles for γ-TiAl samples 119
Figure 4-21: G-ratio and radial wheel wear for different grinding conditions (Phase 2A) 125
Figure 4-22: Grinding forces for different operating conditions (Phase 2A) 126
Figure 4-23: Recorded temperature at different operating conditions (Phase 2A) 129
Figure 4-24: 2D surface roughness parameters for ground surfaces (Phase 2A) 131
Figure 4-25: 3D topographical parameters of ground surfaces (Phase 2A) 131
Figure 4-26: SEM micrographs of ground BuRTi surfaces with SiC wheel (Phase 2A) 134
Figure 4-27: Cross-sectional microstructure of ground surfaces (Phase 2A) 135
Figure 4-28: Microhardness depth profiles (Phase 2A) 136
Figure 4-29: G-ratio and radial wheel wear for different grinding conditions (Phase 2B) 137
Figure 4-30: Grinding forces for different operating conditions (Phase 2B) 139
Figure 4-31: Measured temperature at different operating conditions (Phase 2B) 140
Figure 4-32: 2D and 3D surface roughness parameters for ground surfaces (Phase 2A) 142
Figure 4-33: Higher magnification images of the ground surfaces (Phase 2B) 144

Figure 4-34: The microstructure of BuRTi samples ground with diamond wheel (Phase 2B) 145
Figure 4-35: Microhardness depth profiles (Phase 2B) 146
Figure 4-36: Residual stress depth profiles for BuRTi samples 148
Figure 4-37: G-ratio for different titanium alloys (Phase 3A) 154
Figure 4-38: Radial wheel wear for different titanium alloys (Phase 3A) 155
Figure 4-39: Grinding normal forces for different titanium alloys (Phase 3A) 156
Figure 4-40: Grinding tangential forces for different titanium alloys (Phase 3A) 156
Figure 4-41: Grinding power and specific energy for different titanium alloys (Phase 3A) 157
Figure 4-42: Recorded Temperature for different titanium alloys: Ti-6Al-4V, BuRTi and γ-TiAl (Phase 3A) 158
Figure 4-43: 2D surface roughness parameters for ground surfaces (Phase 3A) 159
Figure 4-44: 3D topographical parameters of ground surfaces (Phase 3A) 159
Figure 4-45: Surface observations for Ti-6Al-4V: a) Images of machined surface, b) SEM micrographs, c) 3D topographies of ground surfaces (Phase 3A) 160
Figure 4-46: The microstructure of Ti-6Al-4V samples ground with SiC wheel (Phase 3A) 161
Figure 4-47: Individual microhardness profiles (Phase 3A) 162
Figure 4-48: G-ratio and radial wheel wear for different grinding conditions (Phase 3B) 164
Figure 4-49 Grinding normal forces against volume of workpiece material removed (Phase 3B) 165
Figure 4-50: Grinding tangential forces against volume of workpiece material removed (Phase 3B) 166
Figure 4-51: Grinding power against volume of workpiece material removed (Phase 3B) 166
Figure 4-52: Grinding specific energy against volume of workpiece material removed (Phase 3B) 167
Figure 4-53: Measured temperature at different operating conditions (Phase 3B) 168
Figure 4-54: 2D and 3D surface roughness parameters for ground surfaces (Phase 3B) 170
Figure 4-55: 3D topographies of Ti-6Al-4V ground surfaces (Phase 3B) 170
Figure 4-56: SEM images of machined surface (Phase 3B) 173
Figure 4-57: Cross-sectional microstructure of ground surfaces (Phase 3B) 174
Figure 4-58: Microhardness depth profiles (Phase 3B) 175
Figure 4-59: G-ratio and radial wheel wear for different grinding conditions (Phase 3C) 176

Figure 4-60: Grinding forces for different operating conditions (Phase 3C) 177

Figure 4-61: Grinding power and specific energy for different grinding conditions (Phase 3C) 178

Figure 4-62: Recorded temperature at different operating conditions (Phase 3C) 179

Figure 4-63: 2D surface roughness parameters for Ti-6Al-4V ground surfaces (Phase 3C) 180

Figure 4-64: 3D surface roughness parameters for Ti-6Al-4V ground surfaces (Phase 3C) 181

Figure 4-65: Surface observations for Ti-6Al-4V: a) Images of machined surface, b) SEM micrographs, c) 3D topographies of ground surfaces (Phase 3C) 182

Figure 4-66: The microstructure of Ti-6Al-4V samples ground with electroplated diamond wheel (Phase 3C) 183

Figure 4-67: Individual microhardness profiles (Phase 3C) 184

Figure 4-68: Residual stress depth profiles for Ti-6Al-4V samples 186

Figure A1: The influence of inputs characteristics on grinding outputs 219

Figure B1: The standard coding system for conventional abrasive wheels 220

Figure B2: The standard coding system for super abrasive wheels 218

Figure D1: Full description of used resin epoxy powder 222

Figure E1: TRIM C270 specifications 223

Figure F1: Interaction plot for G-ratio (Phase 1A) 224

Figure F2: Grinding forces traces (Phase 1A) 225

Figure F3: Main effect plot for normal forces (Phase 1A) 225

Figure F4: Interaction plot for normal forces (Phase 1A) 226

Figure F5: Main effect plot for tangential forces (Phase 1A) 226

Figure F6: Interaction plot for tangential forces (Phase 1A) 227

Figure F7: Main effect plot for power (Phase 1A) 227

Figure F8: Interaction plot for power (Phase 1A) 228

Figure F9: Interaction plot for specific energy (Phase 1A) 228

Figure F10: Grinding temperature traces (Phase 1A) 229

Figure F11: Main effect plot for temperature (Phase 1A) 229

Figure F12: Interaction plot for temperature (Phase 1A) 230

Figure F13: Main effect plot for 2D surface roughness parameter Ra (Phase 1A) 231

Figure F14: Interaction plot for 2D surface roughness parameter Ra (Phase 1A) 231

Figure F15: Main effect plot for 2D surface roughness parameter Rt (Phase 1A) 232

Figure F16: Interaction plot for 2D surface roughness parameter Rt (Phase 1A) 232
Figure F17: Main effect plot for 2D surface roughness parameter Rz (Phase 1A) 233
Figure F18: Interaction plot for 2D surface roughness parameter Rz (Phase 1A) 233
Figure F19: Main effect plot for 3D surface roughness parameter Sa (Phase 1A) 234
Figure F20: Interaction plot for 3D surface roughness parameter Sa (Phase 1A) 234
Figure F21: Main effect plot for 3D surface roughness parameter St (Phase 1A) 235
Figure F22: Interaction plot for 3D surface roughness parameter St (Phase 1A) 235
Figure F23: Main effect plot for 3D surface roughness parameter Sz (Phase 1A) 236
Figure F24: Interaction plot for 3D surface roughness parameter Sz (Phase 1A) 236
Figure F25: 3D topographies of ground surfaces, primary mapping not filtered (Phase 1A) 237
Figure F26: 2D topography traces – Roughness profiles (Phase 1A) 238
Figure F27: Individual microhardness profiles (Phase 1A) 239
Figure F28: Main effect plot for G-ratio (Phase 1B) 240
Figure F29: Interaction plot for G-ratio (Phase 1B) 240
Figure F30: Grinding forces profiles (Phase 1B) 241
Figure F31: Main effect plot for normal force (Phase 1B) 242
Figure F32: Interaction plot for normal force (Phase 1B) 242
Figure F33: Main effect plot for tangential force (Phase 1B) 243
Figure F34: Interaction plot for tangential force (Phase 1B) 243
Figure F35: Main effect plot for power (Phase 1B) 244
Figure F36: Interaction plot for power (Phase 1B) 244
Figure F37: Main effect plot for specific energy (Phase 1B) 245
Figure F38: Interaction plot for specific energy (Phase 1B) 245
Figure F39: Grinding temperature traces (Phase 1B) 246
Figure F40: Main effect plot for temperature (Phase 1B) 247
Figure F41: Interaction plot for temperature (Phase 1B) 247
Figure F42: Main effect plot for 2D surface roughness parameter Ra (Phase 1B) 248
Figure F43: Interaction plot for 2D surface roughness parameter Ra (Phase 1B) 248
Figure F44: Main effect plot for 2D surface roughness parameter Rt (Phase 1B) 249
Figure F45: Interaction plot for 2D surface roughness parameter Rt (Phase 1B) 249
Figure F46: Main effect plot for 2D surface roughness parameter Rz (Phase 1B) 250
Figure F47: Interaction plot for 2D surface roughness parameter Rz (Phase 1B) 250

Figure F48: Main effect plot for 3D surface roughness parameter Sa (Phase 1B) 251
Figure F49: Interaction plot for 3D surface roughness parameter Sa (Phase 1B) 251
Figure F50: Main effect plot for 3D surface roughness parameter St (Phase 1B) 252
Figure F51: Interaction plot for 3D surface roughness parameter St (Phase 1B) 252
Figure F52: Main effect plot for 3D surface roughness parameter Sz (Phase 1B) 253
Figure F53: Interaction plot for 3D surface roughness parameter Sz (Phase 1B) 253
Figure F54: 3D topographies of ground surfaces, primary mapping not filtered (Phase 1B) 254
Figure F55: Individual microhardness profiles (Phase 1B) 254
Figure F56: Main effect plot for G-ratio (Phase 2A) 255
Figure F57: Interaction plot for G-ratio (Phase 2A) 255
Figure F58: Main effect plot for normal force (Phase 2A) 256
Figure F59: Interaction plot for normal force (Phase 2A) 256
Figure F60: Main effect plot for tangential force (Phase 2A) 257
Figure F61: Interaction plot for tangential force (Phase 2A) 257
Figure F62: Main effect plot for power (Phase 2A) 258
Figure F63: Interaction plot for power (Phase 2A) 258
Figure F64: Main effect plot for specific energy (Phase 2A) 259
Figure F65: Interaction plot for specific energy (Phase 2A) 259
Figure F66: Main effect plot for temperature (Phase 2A) 260
Figure F67: Interaction plot for temperature (Phase 2A) 260
Figure F68: 3D topographies of ground surfaces, primary mapping not filtered (Phase 2A) 261
Figure F69: Main effect plot for 2D surface roughness parameter Ra in µm (Phase 2A) 262
Figure F70: Interaction plot for 2D surface roughness parameter Ra (Phase 2A) 262
Figure F71: Main effect plot for 2D surface roughness parameter Rt in µm (Phase 2A) 263
Figure F72: Interaction plot for 2D surface roughness parameter Rt (Phase 2A) 263
Figure F73: Main effect plot for 2D surface roughness parameter Rz in in µm (Phase 2A) 264
Figure F74: Interaction plot for 2D surface roughness parameter Rz (Phase 2A) 264
Figure F75: Main effect plot for 3D surface roughness parameter Sa in µm (Phase 2A) 265
Figure F76: Interaction plot for 3D surface roughness parameter Sa (Phase 2A) 265
Figure F77: Main effect plot for 3D surface roughness parameter St in µm (Phase 2A) 266
Figure F78: Interaction plot for 3D surface roughness parameter St (Phase 2A) 266
Figure F79: Main effect plot for 3D surface roughness parameter Sz in µm (Phase 2A) 267

Figure F80: Interaction plot for 3D surface roughness parameter Sz (Phase 2A) 267
Figure F81: Individual microhardness profiles (Phase 2A) 268
Figure F82: Main effect plot for G-ratio (Phase 2B) 269
Figure F83: Interaction plot for G-ratio (Phase 2B) 269
Figure F84: Main effect plot for normal force (Phase 2B) 270
Figure F85: Interaction plot for normal force (Phase 2B) 270
Figure F86: Main effect plot for tangential force (Phase 2B) 271
Figure F87: Interaction plot for tangential force (Phase 2B) 271
Figure F88: Main effect plot for grinding power (Phase 2B) 272
Figure F89: Interaction plot for grinding power (Phase 2B) 272
Figure F90: Main effect plot for specific energy (Phase 2B) 273
Figure F91: Interaction plot for specific energy (Phase 2B) 273
Figure F92: Grinding temperature traces (Phase 2B) 274
Figure F93: Main effect plot for grinding temperature (Phase 2B) 275
Figure F94: Interaction plot for grinding temperature (Phase 2B) 275
Figure F95: Main effect plot for 2D surface roughness parameter Ra in µm (Phase 2B) 276
Figure F96: Interaction plot for 2D surface roughness parameter Ra in µm (Phase 2B) 276
Figure F97: Main effect plot for 2D surface roughness parameter Rt in µm (Phase 2B) 277
Figure F98: Interaction plot for 2D surface roughness parameter Rt in µm (Phase 2B) 277
Figure F99: Main effect plot for 2D surface roughness parameter Rz in µm (Phase 2B) 278
Figure F100: Interaction plot for 2D surface roughness parameter Rz in µm (Phase 2B) 278
Figure F101: Main effect plot for 3D surface roughness parameter Sa in µm (Phase 2B) 279
Figure F102: Interaction plot for 3D surface roughness parameter Sa in µm (Phase 2B) 279
Figure F103: Main effect plot for 3D surface roughness parameter St in µm (Phase 2B) 280
Figure F104: Interaction plot for 3D surface roughness parameter St in µm (Phase 2B) 280
Figure F105: Main effect plot for 3D surface roughness parameter Sz in µm (Phase 2B) 281
Figure F106: Interaction plot for 3D surface roughness parameter Sz in µm (Phase 2B) 281
Figure F107: 3D topographies of ground surfaces, primary mapping not filtered 282
Figure F108: Individual microhardness profiles (Phase 2B) 283
Figure F109: Individual microhardness profiles (Phase 3B) 284

LIST OF TABLES

Table 2-1: Typical industrial applications of titanium alloys 12

Table 2-2: Typical industrial applications of titanium alloys 12

Table 2-3: Titanium alloys properties comparison with other metals 13

Table 2-4: Properties of a range of materials compared to γ-TiAl 16

Table 2-5: Grinding processes in aerospace applications 21

Table 2-6: Grinding conditions for different grinding operations 22

Table 2-7: Melting points and purity of PVD film materials 38

Table 2-8: Standard thermocouple types 39

Table 2-9: Grinding fluid characteristics 42

Table 2-10: 2D surface roughness amplitude parameters 49

Table 2-11: 3D surface roughness parameters 51

Table 2-12: Integrity data sets description 52

Table 2-13: Fixed and variables factors and levels for conventional wheel (SiC) by Bentley 60

Table 2-14: Fixed and variables factors and levels for diamond and cBN wheels by Bentley 60

Table 2-15: Grinding wheels specification used by Hood 61

Table 2-16: List of preferred operating parameters (γ-TiAl and BuRTi, SiC wheels) 62

Table 2-17: List of preferred operating parameters (γ-TiAl and BuRTi, super-abrasive wheels) 63

Table 3-1: Drilling speeds and feeds parameters 77

Table 3-2: Paper grinding and polishing procedures 84

Table 3-3: Material properties used for strain-to-stress data reduction 87

Table 3-4: List of possible factors and levels in creep feed grinding 90

Table 3-5: Phase 1A operating factors and levels 91

Table 3-6: Phase 1B tests array 93

Table 3-7: Phase 3A tests details 95

Table 3-8: Phase 3C tests array 96

Table 4-1: ANOVA table for normal forces (Phase 1A) 100

Table 4-2: ANOVA table for tangential forces (Phase 1A) 100

Table 4-3: ANOVA table for normal force (Phase 2A) 127

Table 4-4: ANOVA table for tangential force (Phase 2A) 127

Table 4-5: ANOVA table for power (Phase 2A) 127

Table 4-6: ANOVA table for specific energy (Phase 2A) 127

Table 4-7: ANOVA table for 3D surface roughness parameter St (Phase 2A) 132

Table 4-8: Observed machined surface under different grinding conditions and temperature (Phase 2A) 133

Table 4-9: Workpiece surface images (Phase 2B) 143

Table 4-10: ANOVA table for specific energy (Phase 3B) 167

Table 4-11: Observed machined surface under different grinding conditions and temperature (Phase 3B) 172

Table 5-1: Fixed operating parameters and levels 196

Table 5-2: List of preferred operating parameters for the best achieved output measures following CFG of gamma titanium aluminide intermetallic alloy (Ti–45Al–8Nb–0.2Cwt%) 197

Table 5-3: List of preferred operating parameters for the best achieved output measures following CFG of burn resistant titanium alloy (Ti-25V-15Cr-2Al-0.2C wt.%) 198

Table 5-4: List of preferred operating parameters for the best achieved output measures following CFG of α/β titanium alloy (Ti-6Al-4V) 199

Table C1: A list of techniques used to examine surface inhomogeneity 221

Table F1: ANOVA table for G-ratio (Phase 1A) 224

Table F2: ANOVA table for power (Phase 1A) 228

Table F3: ANOVA table for specific energy (Phase 1A) 228

Table F4: ANOVA table for temperature (Phase 1A) 230

Table F5: ANOVA table for 2D surface roughness parameter Ra (Phase 1A) 231

Table F6: ANOVA table for 2D surface roughness parameter Rt (Phase 1A) 232

Table F7: ANOVA table for 2D surface roughness parameter Rz (Phase 1A) 233

Table F8: ANOVA table for 3D surface roughness parameter Sa (Phase 1A) 234

Table F9: ANOVA table for 3D surface roughness parameter St (Phase 1A) 235

Table F10: ANOVA table for 3D surface roughness parameter Sz (Phase 1A) 236

Table F11: ANOVA table for G-ratio (Phase 1B) 240

Table F12: ANOVA table for normal force (Phase 1B) 242

Table F13: ANOVA table for tangential force (Phase 1B) 243

Table F14: ANOVA table for power (Phase 1B) 244

Table F15: ANOVA table for specific energy (Phase 1B) 245

Table F16: ANOVA table for temperature (Phase 1B) 247
Table F17: ANOVA table for 2D surface roughness parameter Ra (Phase 1B) 248
Table F18: ANOVA table for 2D surface roughness parameter Rt (Phase 1B) 249
Table F19: ANOVA table for 2D surface roughness parameter Rz (Phase 1B) 250
Table F20: ANOVA table for 3D surface roughness parameter Sa (Phase 1B) 249
Table F21: ANOVA table for 3D surface roughness parameter St (Phase 1B) 250
Table F22: ANOVA table for 3D surface roughness parameter Sz (Phase 1B) 253
Table F23: ANOVA table for G-ratio (Phase 2A) 255
Table F24: ANOVA table for temperature (Phase 2A) 260
Table F25: ANOVA table for 2D surface roughness parameter Ra (Phase 2A) 262
Table F26: ANOVA table for 2D surface roughness parameter Rt (Phase 2A) 263
Table F27: ANOVA table for 2D surface roughness parameter Rz (Phase 2A) 264
Table F28: ANOVA table for 3D surface roughness parameter Sa (Phase 2A) 265
Table F29: ANOVA table for 3D surface roughness parameter Sz (Phase 2A) 267
Table F30: ANOVA table for G-ratio (Phase 2B) 269
Table F31: ANOVA table for normal force (Phase 2B) 270
Table F32: ANOVA table for tangential force (Phase 2B) 270
Table F33: ANOVA table for grinding power (Phase 2B) 272
Table F34: ANOVA table for specific energy (Phase 2B) 273
Table F35: ANOVA table for grinding temperature (Phase 2B) 275
Table F36: ANOVA table for 2D surface roughness parameter Ra (Phase 2B) 276
Table F37: ANOVA table for 2D surface roughness parameter Rt (Phase 2B) 277
Table F38: ANOVA table for 2D surface roughness parameter Rz (Phase 2B) 278
Table F39: ANOVA table for 3D surface roughness parameter Sa (Phase 2B) 279
Table F40: ANOVA table for 3D surface roughness parameter St (Phase 2B) 280
Table F41: ANOVA table for 3D surface roughness parameter Sz (Phase 2B) 281

LIST OF NOMENCLATURE

Al_2O_3	Aluminium oxide
ANOVA	Analysis of Variance
a_e	Depth of cut
%at.	Atomic percentage (%)
b	Cutting width
bcc	Body centred cubic
β_w	Material thermal property
β_f	Fluid thermal property
BuRTi	Burn resistant titanium
c	Number of cutting points per unit area of the wheel surface
C	A factor based on Peclet number and contact angle in circle arc model
CFG	Creep feed grinding
c_w	Material specific heat
D	Grinding wheel diameter
e_{ch}	Energy within the chip
emf	Electromotive force
EBM	Electron beam melting
Ft	Tangential force
Fh	Horizontal force
Fn	Normal force
Fv	Vertical force
FFG	Form finish grinding
GE	General Electric
hcp	Closed-packed hexagonal
h_w	Workpiece convection factor
h_s	Wheel convection factor
h_{ch}	Chip convection factor
h_f	Fluid convection factor
HP	High pressure
l_c	Contact length
LP	Low pressure
P	Grinding power
PAM	Plasma arc melting titanium
PVD	Physical vaper deposition
p_w	Material density
q_t	Total heat flux
q_w	Heat conducted by the workpiece
q_s	Heat conducted by wheel
q_{ch}	Heat conducted by chip/grain
q_f	Heat conducted by coolant/fluid

Q_w	Material removal rate
r	The ratio of chip width over the average chip thickness
Ra	Athematic average roughness (2D)
Rt	Maximum peak to valley height / total height (2D)
R_{ws}	Heat partition entering both workpiece and wheel
Rz	Ten-points height (2D)
SiC	Silicon carbide
Sa	Athematic average roughness (3D)
SRG	Stock removal grinding
St	Peak to peak (3D)
Sz	Ten-points average (3D)
t	Undeformed chip thickness (µm)
T_{max}	Maximum surface temperature
T_{ch}	Temperature of the chip
γ-TiAl	Gamma titanium aluminide
u	Specific energy
v_w	Feed rate/feed velocity/workpiece velocity (mm/min)
v_s	Wheel velocity (m/s)
%vol.	Volume percentage (%)
VAR	Vacuum arc remelting

1 INTRODUCTION

1.1 Background to the project

Titanium alloys are extensively used in many industry fields, including automotive, biomedical, and aerospace. They possess unique mechanical properties, such as high specific strength and excellent corrosion resistance at elevated temperatures. Titanium alloys are considerably superior to aluminium alloys, with strengths comparable with steel alloys and having only around 60% of the density of stainless steel. Over the last few decades, more development of titanium alloys has been made, particularly in the aerospace industries, as a high strength-to-weight ratio is required. Titanium alloys account for 33% of engine weight in commercial aircraft due to their preferable mechanical properties [1]. However, due to their high tendency to ignition, they are confined to moderately lower temperature parts only (less than ~350°C), such as casings, fans, and low-pressure compressor components. For example, the conventional titanium alloy Ti-6Al-4V which accounts for ~55% of total titanium alloy production and is characterised by a high tensile strength of 1100 MPa at 20°C, and a density as low as 4g/cm^3, has an operating temperature limit of ~350°C. This has led to the development of many burn-resistant titanium alloys (Ti-V-Cr), such as alloy C in the USA, alloy Ti-40 in China, and BTT-1 in Russia. The burn resistance of the Ti-V-Cr alloy system has been demonstrated in an ignition test and was compared to other titanium alloys. Titanium alloys involved in the test were subjected to typical conditions found in intermediate-pressure engine compressors with an air temperature of 300°C, air velocity of 150m/s and 0.96MPa air pressure. Test findings showed better burn resistance performance of Ti-V-Cr alloy, whereas the conventional alloy (Ti-6Al-4V) suffered heavy burn [2]. Burn-resistant titanium alloy (Alloy C) of composition Ti-35V-15Cr was developed in 1990 by Pratt and Whitney and exhibited superior burn resistance when compared to conventional titanium alloys (up to 600°C) and good mechanical properties. They also were used in critical engine applications [3]. However, the fabrication of the alloy was costly due to the large volume of heavy elements of the alloy. A more competitive and economic alternative burn-resistant titanium alloy (BuRTi) Ti-25V-15Cr-2Al-0.2C wt% was developed later in the UK by the University of Birmingham in association with Rolls-Royce Plc. This alloy has a higher thermal conductivity than conventional Ti-6Al-4V (10W/mK compared to 6.7W/mK). It can retain greater tensile

strength at higher temperatures as opposed to α/β alloy (Ti679), given that a reduction of more than 150MPa of tensile strength at a temperature of 500°C was reported in [4].

With only half the density of nickel-based superalloy (3.80g/cm^3 compared to 8.30g/cm^3) and a thermal conductivity double that of conventional titanium alloys (22W/mK compared to 6.7W/mK), gamma titanium aluminide (γ-TiAl) exhibits favourable oxidation and creep resistance as well as high strength at increased temperatures of up to 800°C [1]. Thus, it is considered a potential substitute for nickel-based superalloys in gas turbine engines and other applications where there is a need for strength at high elevated temperatures, typically found in aerospace and automotive applications. Figure 1-1 illustrates the distribution of titanium and nickel alloys in an aero-engine [5], and Figure 1-2 shows the uptake of titanium and other materials in turbine aero-engine [6]. The structural weight of high-performance gas turbine engines is predicted to be reduced by 20-30% when replacing nickel-based superalloy sections with gamma titanium aluminides. Hence, better engine performance and fuel efficiency can be achieved [2]. Titanium aluminides have been the subject of commercial interest since at least the early 1970s when General Electric (GE) and Pratt & Whitney began their respective research efforts. Rolls Royce, SNECMA, Howmet, Ford and General Motors have also shown interest in titanium aluminide and invested in the improvement of mechanical characteristics and alloy production costs. For instance, GE has primarily focused its efforts on as-cast Ti-48Al-2Nb-2Cr; Pratt & Whitney on Ti-47Al-2Mn-2Nb + 0.8 Vol% TiB_2XD, and Rolls Royce on Ti-45Al-2Mn-2Nb+0.8Vol% TiB_2XD (45-2-2+0.8). Exhaust valves, turbocharger rotors, and connecting rods for high-performance engines have all been reported to be made using TiAl alloys in the automotive sector [7], [8]. Blades and stators in high-pressure (HP) compressors, low-pressure (LP) turbine blades, exhaust components, combustor chambers, and casings are typical aerospace target applications. In 2011, General Electric reported the successful operation of their latest GEnxTM aero-engine, which has gamma titanium aluminide intermetallic γ-TiAl alloy turbine blades in the low-pressure stage. It was the first commercial use of γ-TiAl in a commercial jet engine. Pratt and Whitney also announced the design of the new geared turbofan engine for Airbus 320neo with the last stage (lower pressure turbine) made of γ-TiAl material [9].

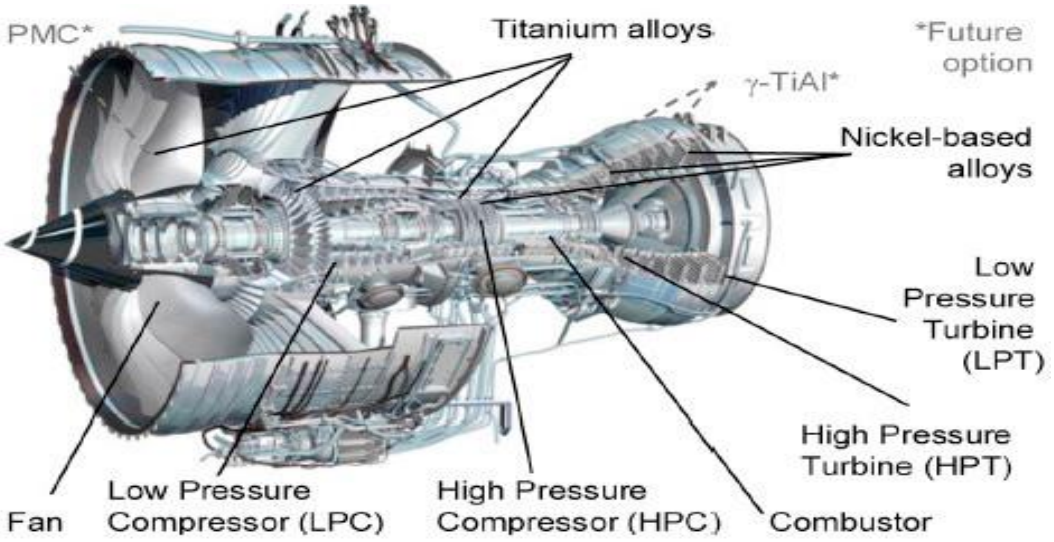


Figure 1-1: Distribution of titanium and nickel alloys in an aero-engine [5]

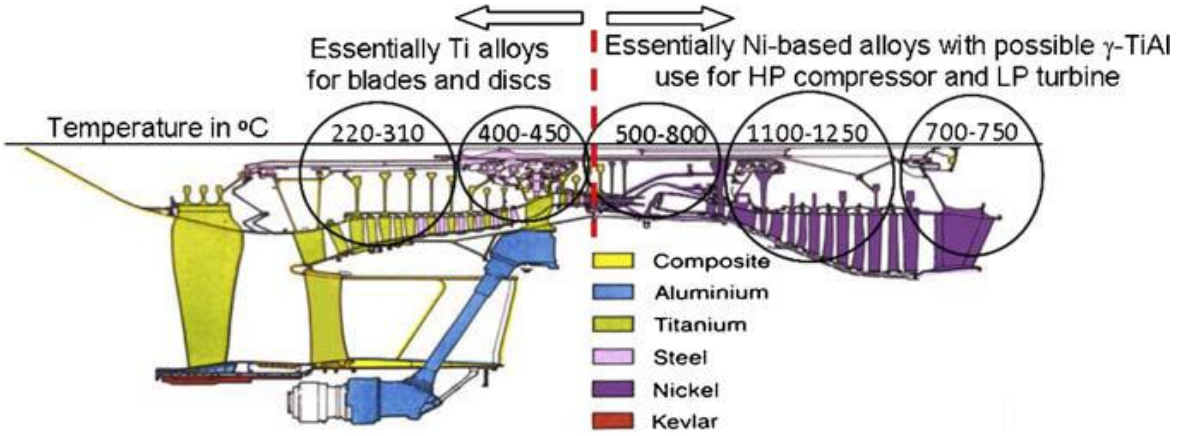


Figure 1-2: Materials uptake in turbine aeroengine [6]

Despite the preferable characteristics and mechanical properties of titanium alloys, these materials are regarded as difficult to machine materials. Several literature-review papers related to the machinability of conventional titanium alloys and titanium aluminide have highlighted the low machinability of conventional titanium alloys and titanium aluminide [8], [10], [11], [12]. Conventional titanium alloys are well known to suffer from low thermal conductivity, high chemical reactivity, and low modulus of elasticity and retain their high yield and tensile strength at elevated temperatures. Moreover, titanium aluminide, in particular, exhibits a combination of low ductility, typically less than 2%, low fracture toughness, and high crack growth rates. Some of the main reported deficiencies associated with machining titanium aluminide include microcracks formation, work-hardening tendency, and reduced tool lifetime

[12]. Numerous machining studies of gamma titanium aluminides are detailed in the literature review involving conventional processes (milling, drilling, turning, grinding) and non-conventional processes (electric discharge machining, electrochemical machining). The majority of researchers concluded that producing components with acceptable quality in terms of surface integrity and dimensional accuracy is challenging. They emphasise the importance of controlling and proper selection of machining parameters to achieve more productivity and longer tool life [8], [10], [11], [12].

Of all evaluated machining processes, only grinding has proved to produce high-quality workpiece surfaces when machining titanium alloys and titanium aluminides. Grinding is a key industrial machining process for producing final components with the desired form, size, and accuracy. In the aerospace industry, grinding is a key process for manufacturing turbine blades and vanes. Klocke et al. noted that machining a typical blade might involve up to 12 different abrasive operations, including grinding to produce features such as fir tree profile, root end profile, blade top, and trailing edge [13]. Broaching and milling were commonly used to manufacture turbine blade root profiles made from hard materials such as nickel-based alloys. However, to overcome associated poor machinability, excessive tool wear, and capital cost, creep feed grinding was introduced, which involves a greater depth of cut at lower wheel speeds and feed rates. Unlike surface grinding, this results in a higher material removal rate (MRR) in a single grinding wheel pass, thus achieving more productivity [13].

Extremely limited information on grinding temperature, 3D roughness/topography and residual stresses when creep feed grinding of γ-TiAl intermetallic and burn-resistant titanium alloy is published. Although extensive research has been carried out on understanding the grindability of both alloys, most studies have only focused on the grinding performance in terms of wheel wear, forces, 2D roughness/topography and surface integrity. Malkin [14] reported that thermal damage caused by high grinding temperature is one of the most important elements that impact workpiece surface quality and limits the production rates that can be obtained by grinding. Therefore, understanding the underlying factors that influence grinding temperatures is critical. Burning, metallurgical phase transitions, softening of the surface layer, surface hardening, undesirable residual tensile stresses, cracks, and lower fatigue strength are all examples of thermal damage to the workpiece. Furthermore, 2D topographical analysis cannot fully characterise and reflect the practical surface geometrical features and behaviour of machined parts, and given the current advancements and enhanced functionalities of surface metrology instruments, 3D topographical areal analysis is becoming widely accepted as the most

appropriate method for comprehensive surface characteristics and correlation between produced surface topography and its functional performance [15], [16].

Bentley [17] reported work including surface grinding of γ-TiAl (Ti-45Al-2Mn-2Nb+0.8 vol.%TiB_2XD). A grinding temperature of 1500°C was noted at 25µm depth of cut. Xinxin et al. [18] have recently studied surface burn behaviour in creep feed grinding of gamma titanium aluminide Ti-45Al-2Mn-2Nb-0.1B at% intermetallic using diamond and silicon carbide wheels. A maximum temperature of 1103°C was recorded when operating at a 300mm/min feed rate and 2mm depth of cut with a diamond wheel. Similarly, other most recent published research relating to creep feed grinding of γ-TiAl intermetallic alloys has only focused on Ti–45Al–2Mn–2Nb rather than the thermo-mechanically produced duplex alloy gamma titanium aluminide of composition (Ti-45Al-8Nb-0.2C). Still, however, in published literature, no information on temperature, 3D roughness/topography and residual stresses when creep feed grinding of (Ti-45Al-8Nb-0.2C) is available.

Despite extensive research into the burn-resistant alloy (Ti-25V-15Cr-2Al-0.2C) processing method, microstructure, and fracture properties in [19], [20], [21] and more recently in [22], scarce machining information is available on creep feed grinding of this alloy. First machining trials on burn-resistant titanium alloy (Ti-25V-15Cr-2Al-0.2C) were performed by Novovic et al. [23]. Their work involved investigating the impacts of workpiece surface roughness produced by high-speed milling and creep feed grinding on fatigue life. Hood et al. [24] studied the effects of different grinding conditions on grinding ratio, forces, and surface integrity when creep feed grinding the gamma titanium aluminide intermetallic alloy (Ti-45Al-8Nb-0.2C) and the burn-resistant titanium alloy (Ti-25V-15Cr-2Al-0.2C) with silicon carbide wheels. Softening of the material surface was evident at a depth of 5-15µm. Machinability of burn-resistant titanium alloy when creep feed grinding with super-abrasive wheels was carried out by Soo and his co-researchers [25]. Findings showed improvements in grinding ratio (up to 280) when utilising cubic boron nitride wheels compared to diamond wheels. Moreover, workpiece surface roughness (Ra) as low as 0.73µm was achieved. Nonetheless, no temperature, 3D roughness/topography and residual stresses data for creep feed grinding of burn-resistant titanium alloy (Ti-25V-15Cr-2Al-0.2C) were provided in [24] and [25] work. Limited information on temperature, 3D roughness/topography and residual stresses when creep feed grinding of (Ti-25V-15Cr-2Al-0.2C) was only given by Novovic [4]. Likewise, limited 3D roughness/topography data on ultrasonic creep feed grinding of Ti-45Al-2Mn-2Nb+0.8 vol.%TiB_2XD (wt%) were only detailed by Bhaduri et al. [26].

1.2 Aims and objectives of the project

Grinding conditions and parameters have significant impacts on grinding performance (wheel wear, forces, specific energy), surface topography (2D and 3D) and surface integrity (surface and sub-surface cracks, plastic deformation, residual stresses, thermal damage, etc.). Up to date, limited work relating to creep feed grinding of advanced titanium alloys (gamma titanium aluminide intermetallic alloy Ti-45Al-8Nb-0.2C, burn-resistant titanium alloy (Ti-25V-15Cr-2Al-0.2C) and the alpha/beta titanium alloyTi-6Al-4V) has been published. In addition, the available work is still lacking information on how different grinding operating parameters and conditions will affect the generated temperature, produced 3D surface topography and residual stresses. Solid knowledge is required to better understand the creep feed grinding process of the aforementioned advanced titanium alloys. Therefore, the aim of this research is to expand the existing knowledge by exploring more operating parameters and conditions as well as providing insights into their effects on grinding wheel wear, grinding forces, grinding specific energy, grinding temperature, induced residual stresses, surface topography (2D and 3D), and surface integrity when creep feed grinding the thermo-mechanically produced duplex alloy gamma titanium aluminide (Ti-45Al-8Nb-0.2C), patent burn resistant titanium alloy made by the University of Birmingham (Ti-25V-15Cr-2Al-0.2C wt%) and the conventional titanium alloy Ti-6Al-4V. The current work will also serve as baseline data for future in-depth trials by identifying the damage introduced by different operating machining conditions and relating the extent of that damage to the operating conditions, for example, linking the generated forces, temperature or residual stresses to the produced surface integrity for a given operating conditions. This will help in providing preferred/optimum operating parameters and wheel specifications for the machining of titanium-based superalloys.

The aim of this thesis will be fulfilled through the pursuit of the following objectives:

1- Conduct a comprehensive literature review on the machinability of advanced titanium alloys to identify current gaps in knowledge relating to the subject area, focusing primarily on the grinding machining process.

2- Investigate the influence of different operating conditions on grinding performance when creep feed grinding gamma titanium aluminide intermetallic alloy (Ti-45Al-8Nb-0.2C wt%), burn resistant titanium alloy (Ti-25V-15Cr-2Al-0.2C wt%) and the conventional titanium alloy Ti-6Al-4V using conventional abrasive grinding wheels

(silicon carbide), for the following assessment criteria: grinding ratio, wheel wear, grinding forces, grinding power, specific energy, temperature, workpiece surface integrity and surface topography.

3- Benchmark titanium aluminide intermetallic alloy (Ti-45Al-8Nb-0.2C wt%) against burn-resistant titanium alloy (Ti-25V-15Cr-2Al-0.2C wt.%) and the conventional titanium alloy Ti-6Al-4V when creep feed grinding with conventional abrasive grinding wheels (silicon carbide) for the following assessment criteria: grinding ratio, wheel wear, grinding forces, grinding power, specific energy, temperature, workpiece surface integrity and surface topography.

4- Investigate the impact of operating parameters on grinding performance when creep feed grinding gamma titanium aluminide intermetallic alloy (Ti-45Al-8Nb-0.2C wt%), burn resistant titanium alloy (Ti-25V-15Cr-2Al-0.2C wt%) and the conventional titanium alloy Ti-6Al-4V, using super-abrasive grinding wheels (diamond), for the following assessment criteria: grinding ratio, wheel wear, grinding forces, grinding power, specific energy, temperature, workpiece surface integrity and surface topography.

5- Benchmark titanium aluminide intermetallic alloy (Ti-45Al-8Nb-0.2C wt%) against burn-resistant titanium alloy (Ti-25V-15Cr-2Al-0.2C wt%) and the conventional titanium alloy Ti-6Al-4V when creep feed grinding with super-abrasive grinding wheels (diamond) for the following assessment criteria: grinding ratio, wheel wear, grinding forces, grinding power, specific energy, temperature, workpiece surface integrity and surface topography.

1.3 Structure of thesis

The thesis is divided into five chapters. The first chapter serves as an introduction to advanced aerospace superalloys by providing background information on the creep feed grinding of advanced titanium alloys for aerospace applications. The motivation, aims, and objectives of this study are also outlined in this chapter. Chapter 2 is designed to fulfil objective 1 of this research. It starts with a review of titanium alloy production, microstructure, properties, and industrial applications. Then, it considers important aspects of grinding technology, such as grinding system elements, grinding wheels, grinding mechanics, grinding vibration, grinding temperature, and fluid application in grinding. This is followed by an overview of workpiece surface topography and surface integrity along with their measurement techniques and statistical experimental design used to identify the significance of grinding operating conditions on the overall performance of the grinding process. The literature review chapter ends with a summary of previous research conducted in the field of interest, together with an explanation of areas that were not covered by other authors' work, and these will be the focus of the current project. The next chapter (chapter 3) was designed to meet the requirements of objectives 2-5. The methodology and experimental work are detailed in chapter 3, including workpiece materials, creep feed grinding wheels, machining centres, analysis equipment, and experimental designs. Chapter 4 covers the findings achieved throughout the experimental investigation along with a comprehensive discussion of the results. This chapter consists of three main sections in which information for both conventional and super-abrasive wheels is provided. The first one is pertinent to the creep feed grinding of gamma titanium aluminide intermetallic alloy (Ti-45Al-8Nb-0.2C wt%). The second section covers experimental findings following creep feed grinding of burn-resistant titanium alloy (Ti-25V-15Cr-2Al-0.2C), while the third section details experimental results on conventional titanium alloy Ti-6Al-4V when creep feed grinding. Finally, the main key findings of the obtained results from the study and their contributions to existing knowledge in both the academic and industrial domains are highlighted in Chapter 5, along with suggested recommendations for future work based on identified limitations.

2 LITERATURE REVIEW

2.1 Titanium and its alloys

Titanium was first discovered by W. Gregor in 1790 in the form of magnetic sand consisting of oxides iron and titanium. Four years later, the metal was first named titanium by M. Klaproth, who discovered titanium in the mineral rutile. In 1910, M. Hunter isolated the first pure titanium by the reduction of titanium tetrachloride with sodium in a steel bomb at 700-800°C. However, it was not until 1937 that titanium extraction was possible on an industrial scale through a process called the Kroll process, which was invented by W.J. Kroll [27]. A flow sheet of the production of titanium by the Kroll process is shown in Figure 2-1 [28]. The process involves three steps: chlorination of oxide ores of titanium (extracted from ilmenite), purification of the produced tetrachloride, and vacuum distillation, where a reaction between liquid magnesium and purified tetrachloride takes place to create a titanium sponge. This sponge can then be crushed, pressed, and melted to produce titanium ingots [28], [29]. Traditional methods used for melting/casting titanium are vacuum arc remelting (VAR), Plasma arc melting (PAM), and electron beam melting (EBM). They provide ingots with a high degree of homogeneity and reduced porosity [30]. More details on the chemical reactions required to extract titanium ores from ilmenite are given in [29]. The cost of titanium is significantly increased by the complexity of these multistep thermochemical procedures. New electrochemical extraction technologies are being developed in order to reduce the number of steps and energy consumption, lowering the cost of titanium production.

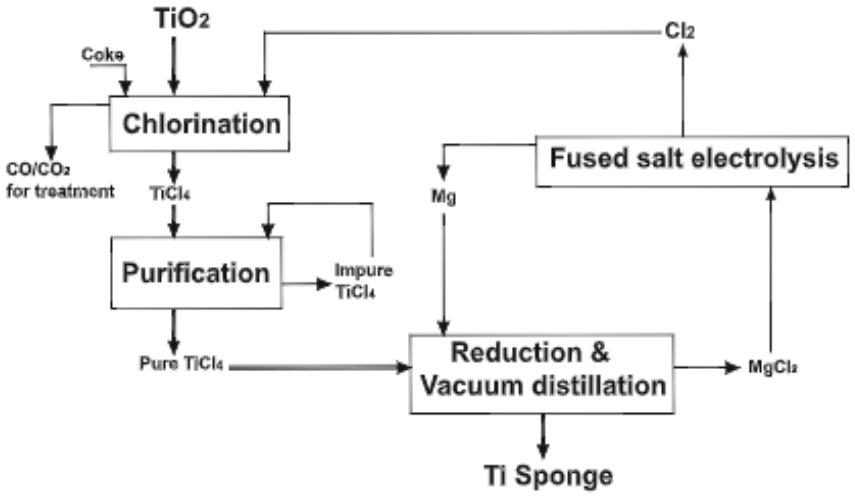


Figure 2-1: Kroll process for the production of titanium sponge [28]

Titanium has a close-packed hexagonal (hcp) structure commonly known as the alpha phase at room temperature and transforms to a body-centred cubic (bcc) structure known as the beta phase at around 885°C. This allotropic transformation is shown in Figure 2-2 [31]. The temperature of allotropic transformation can be changed by adding alloying element. Elements such as aluminium, oxygen, nitrogen and carbon increase the transformation temperature and are referred to as alpha stabilizers. On the other hand, elements that decrease the transformation temperature are called beta stabilizers, such as hydrogen, vanadium, niobium, and molybdenum. Pure unalloyed titanium has excellent corrosion resistance but relatively low strength. The addition of carbon and iron enhances the strength of titanium at the expense of ductility [31].

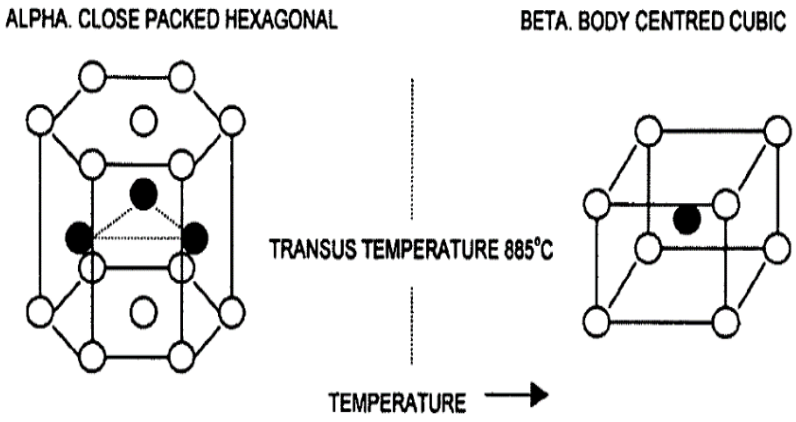


Figure 2-2: Titanium crystalline transformation [31]

2.1.1 Conventional titanium alloys

Titanium alloys are extensively used in many industry fields, including automotive, biomedical, and aerospace. They possess unique mechanical properties, such as high specific strength and excellent corrosion resistance at elevated temperatures. They are also characterised by a modulus of elasticity of around 55% of that of steel, a density of approximately 60% of that of steel, high fatigue strength (superior to steel) [32]. Many constituents of titanium alloys are available; thus, they are classified into the following microstructures: alpha alloys, near alpha alloys, alpha/beta alloys, and beta alloys [31], [32].

- Alpha alloys have a close-pack structure and only contain alpha stabilizer elements. They exhibit high creep resistance at high elevated temperatures, but unlike alpha/beta and beta alloys, they cannot undergo heat treatment.
- Near alpha alloys mainly consist of alpha stabilizers and have about 2% of beta stabilizers. These alloys possess similar properties to alpha alloys.
- Alpha/beta alloys exhibit a mixture of both alpha phase and beta phase. These alloys can be strengthened by quenching, ageing and heat solution. They are widely used in the aerospace industry. A commonly used alpha/beta alloy is Ti-6Al-4V, which contains 6% aluminium and 4% vanadium by weight and undergoes an allotropic transformation at about 1000°C.
- Beta alloys have a body-centred cubic structure and a small number of alpha stabilizers. Their density is higher than other alloys due to the properties of beta stabilizer alloying elements, and they also have high hardenability and formability.

Owing to their exceptional mechanical properties, the major application of titanium and its alloys is in the aerospace industry (engine components and frame of the aircraft). It is reported that 33% of engine weight in commercial aircraft is made of titanium alloys [1]. Titanium alloys are typically used for applications where low density, high strength, and high corrosion resistance are key requirements. However, they are restricted to applications below 600°C as above this temperature, a fast reaction with oxygen occurs, resulting in excessive oxide layer and embrittlement [33]. Moreover, when titanium alloys are subject to elevated temperatures, their creep strength, damage tolerance, and fire resistance properties start deteriorating [34]. Typical industrial applications of titanium alloys are shown in Table 2-1 and Table 2-2 [35], [36], [37], [38]. A comparison of their properties with other metals is given in Table 2-3 [17]. Of all titanium alloys, Ti-6Al-4V is the most widely used. It accounts for between 50-60% of total titanium alloy production and has played a critical role in the rapid development of the aircraft sector. Ti-6Al-4V alloy is preferred for both rotating and non-rotating aero-engine parts, such as fan blades, low-pressure (LP) compressor blades, and disks.

Table 2-1: Typical industrial applications of titanium alloys [35]

Structure	Alloy composition	Typical Uses
Alpha (commercially pure)	99.5 Ti	Used where good weldability, high corrosion resistance and ductility is needed, e.g. marine parts and chemical plant parts
Alpha alloy	Ti-5Al-2.5Sn	Has good machinability, forging and welding properties with improved strength up to 350°C. Used in aircraft engine compressor blades and steam turbine blades
Near alpha alloy	Ti-6Al-2Sn-4Zr-2Mo	Creep resistant alloy which can be used up to 475°C. Used in parts and casings for jet engine compressors and for airframe skin parts.
Alpha-beta alloy	Ti 6/4	Has good weldability and machinability. Used for blades and disks in aircraft turbines and compressors, marine components, rocket motor cases and structural forgings. It is the most widely used Ti alloy.
Beta alloy	Ti-13V-11Cr-3Al	Used for high strength fasteners, aerospace components and honeycomb panels.

Table 2-2: Typical industrial applications of titanium alloys [36], [37], [38]

Ti alloys	Applications
α-alloys/near α-alloys	
T-0.3Mo-0.8Ni	Chemical processing, desalination, hydrometallurgical extraction
Ti-3Al-2.5 V	Aircraft ducting, tubing, watches, eye glass frames
Ti-3Al-2.5 V-Pd	Offshore hydrocarbon production
Ti-5Al-2.5Sn	Gas turbine engine parts
α-β alloys	
Ti-6Al-4 V	Aircraft ducting, Airframe parts, Automotive parts, Consumer products (watches, eye glass frames, etc.)
Ti-6Al-7Nb	Medical implants, surgical instruments
Ti-6Al-6 V-2Sn	Airframe parts
Ti-6Al-2Sn-4Zr-6Mo	Gas turbine engine parts
Ti-6Al-2Sn-2Zr-2Mo-2Cr-0.15Si	Airframe parts, Space vehicles/structures
β alloys/near β- alloys	
Ti-10 V-2Fe-3Al	Airframe parts, Landing gear parts
Ti-3Al-8 V-6Cr-4Zr-4Mo	Geothermal brine energy extraction, navy ship parts, space vehicles
Ti-3Al-8 V-6Cr-4Zr-4Mo-0.05Pd	Navy ship parts, space vehicles

Table 2-3: Titanium alloys properties comparison with other metals [17]

Property	Alpha Ti (Ti-5Al-2.5Sn)	Near Alpha Ti (Ti-6Al-2Sn-4Zr-2Mo)	Alpha / Beta Ti (Ti 6/4)	Beta Ti (Ti-13V-11Cr-3Al)	Plain Carbon Steel (AISI 1045)	18-8 Stainless Steel (301)	Superalloy (Nimonic 80A)
Structure	hcp	hcp/bcc	hcp/bcc	bcc	bcc	fcc	
Melting Point (°C)			1600-60			1430	1325-1400
Density ρ (g/cm^3)	4.48	4.54	4.43	4.84	7.9	7.8	8.3
Modulus E (GPa)	110.3	113.8	113.8	101.4		207	206
Yield strength (MPa)	805	895	925-1100	1170	530	215-760	620
Tensile strength (MPa)	860	980	990-1170	1220	625	540-1450	1240
Ductility RT (%)	16	15	10-14	8	12	10-30	24
Ductility @ Op. T. (%)	18	16	14	19	-	-	18-34
Creep Limit (°C)	250-350	450-500	350-400	300	450	600	1090-1093

2.1.2 Gamma titanium aluminide intermetallic alloys

Gamma titanium aluminide (γ-TiAl) is an intermetallic alloy that consists of titanium and 45-60% (at.%) aluminium with additional alloying elements such as niobium or manganese to improve their mechanical properties. By the mid-1950s, titanium aluminides' desirable properties had been realized, and extensive research and development on their microstructure and mechanical properties have begun since then. Early development of first-generation γ-TiAl alloys, such as Ti-48Al-1V-0.3C, showed poor performance in terms of strength and creep resistance. Later in the 1980s, a second-generation γ-TiAl was developed by General Electric (GE) with a composition of Ti-48Al-2Nb-2Cr. In the mid-1990s, further development of γ-TiAl led to the production of third generations, which involved adding TiB_2 powder into the molten base alloy to prevent grain growth. Ti-45Al-2Nb-2Mn+0.8 vol% TiB_2XD made by Howmet is an example of this [39]. Figure 2-3 illustrates the phase diagram of titanium aluminide (Ti-Al) intermetallic [17]. Gamma-TiAl (γ-TiAl), α_2-Ti_3Al, and $TiAl_3$ are the major intermetallic compounds. Gamma titanium aluminide intermetallic can be divided into two groups: single-phase (γ) and two-phase (γ+α2) alloys. The single-phase with an ordered face-centred tetragonal L1o structure has a range of 49-66 at% of aluminium, while the two-phase alloy has a composition of 30-50 (at%) aluminium. It was found that the single-phase suffers

from poor ductility and fracture toughness; hence, more focus has been paid to the development of the two-phase alloy (γ+α2).

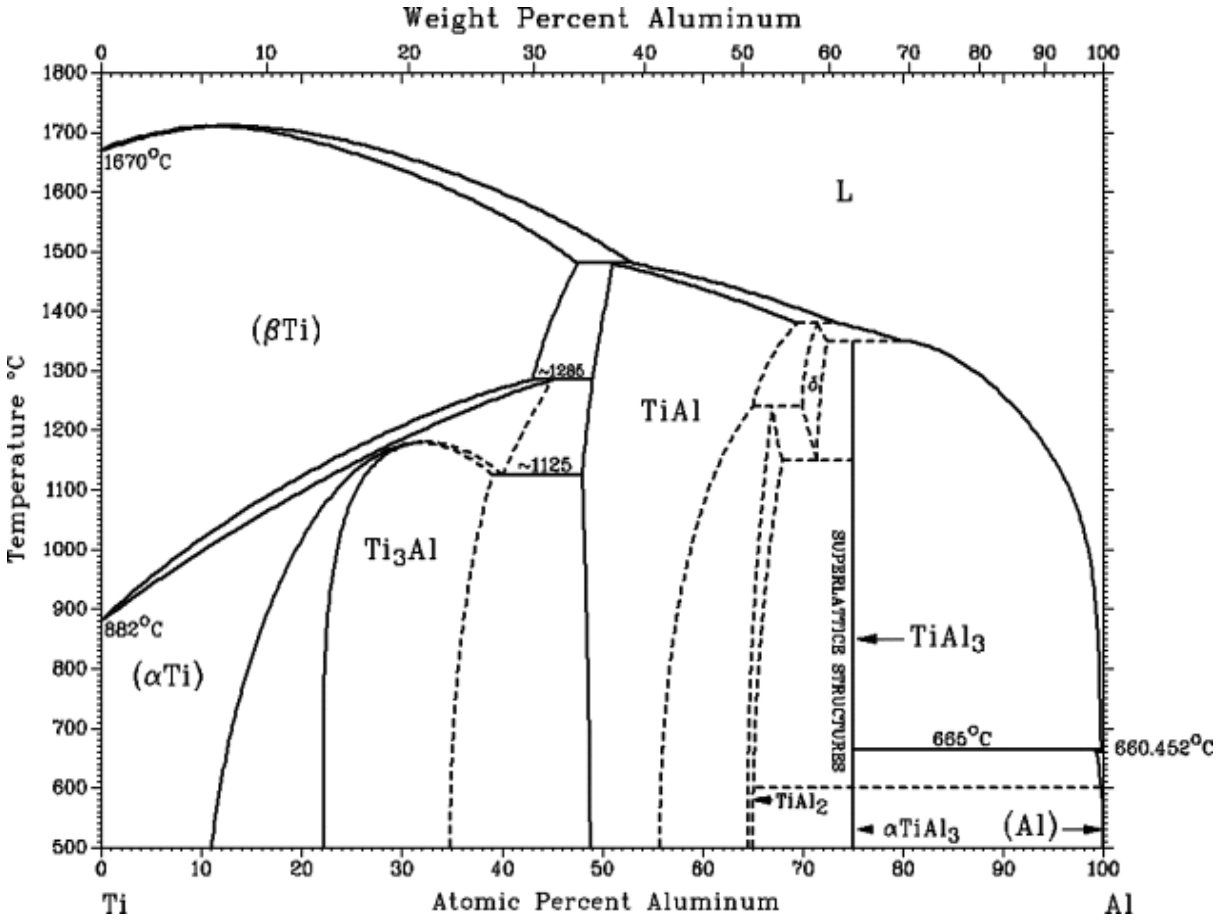


Figure 2-3: Ti-Al phase diagram [17]

A wide range of grain sizes and microstructures of titanium aluminides can be developed depending on thermal, mechanical treatment and composition as well as the aluminium content. As shown in Figure 2-4, produced microstructures involve either lamella, equiaxed, or duplex (mixture of lamella and equiaxed) [40]. These microstructures have a significant effect on the material; for example, a duplex microstructure has higher ductility than the lamella one but extremely lower fracture toughness [41]. Apple et al. [42] presented four different microstructures following heat treatment of Ti-47Al-3.7(Nb,Cr,Mn,Si)-0.5B (at.%) at different temperatures. Optical and SEM images of the microstructure are shown in Figure 2-5.

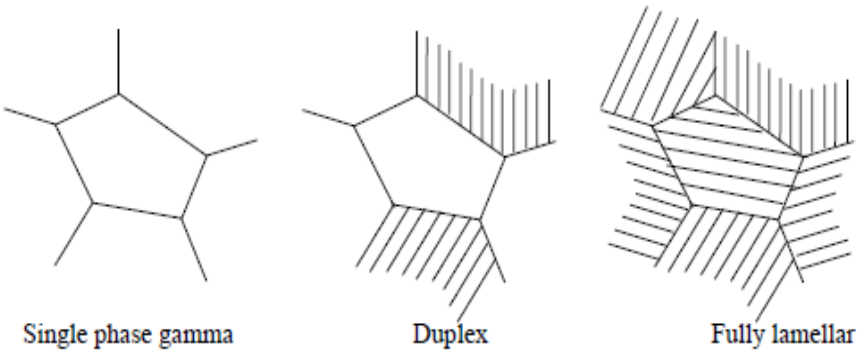


Figure 2-4: Ti-Al different microstructure [40]

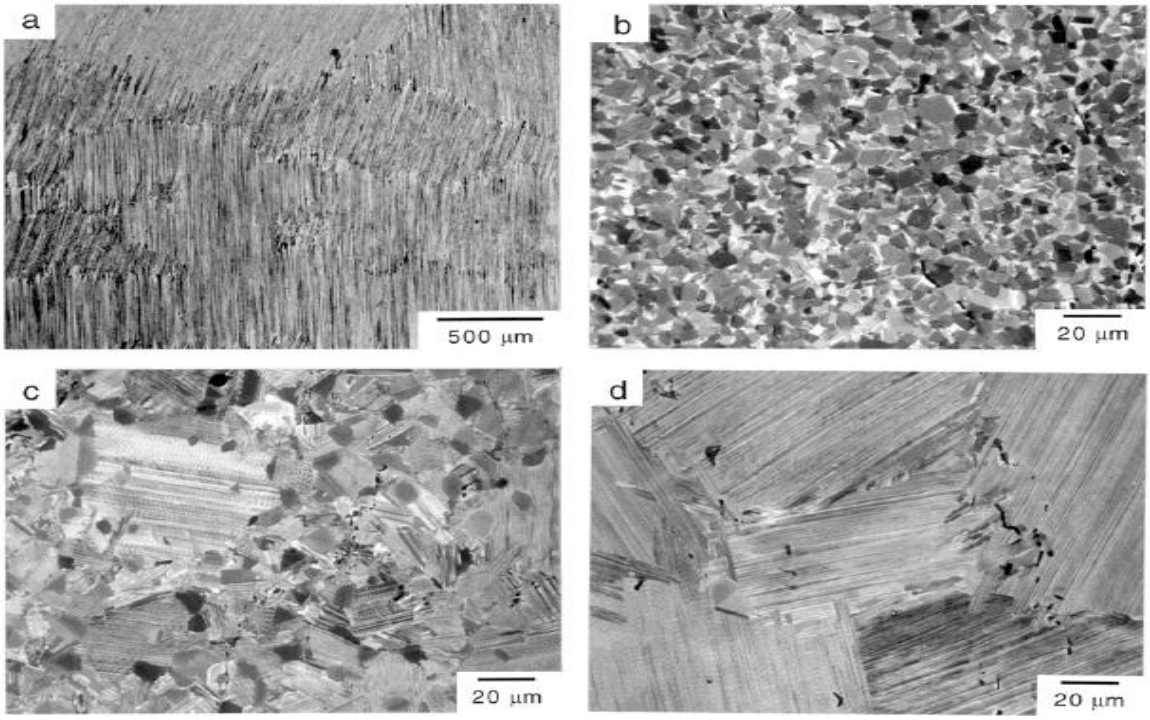


Figure 2-5: Microstructures of Ti-47Al 3.7(Nb,Cr,Mn,Si)-0.5 B (at. %) [42]: a) Coarse, nearly lamellar, b) equiaxed microstructure, T = 1,300 °C, (c) duplex microstructure, T = 1,340ºC, (d) nearly-lamellar microstructure, T = 1,360ºC.

The titanium aluminide based on gamma (γ-TiAl) has received more interest and showed more promise for replacing nickel-base superalloys than the other compounds due to its superiority. With only half the density of nickel-based superalloy (3.80g/cm³ for γ-TiAl and 8.30g/cm³ for nickel alloys) and a thermal conductivity double that of conventional titanium alloys Ti-6Al-4V (22W/mK compared to 6.7W/mK), gamma titanium aluminide exhibits favourable oxidation and creep resistance as well as high strength at increased temperatures of up to 800 °C [7], [10]. Therefore, it is considered a potential substitute for nickel-based superalloys in gas

turbine engines and other applications where there is a need for strength at high elevated temperatures, which are typically found in aerospace and automotive applications. However, its major drawback is the low room temperature ductility of around 0-4% and low fracture toughness [12]. The structural weight of high-performance gas turbine engines is predicted to be reduced by 20–30% when replacing nickel-based superalloy sections with gamma titanium aluminides. Hence, better engine performance and fuel efficiency can be achieved [43]. More properties of γ-TiAl are provided in Table 2-4.

Table 2-4: Properties of a range of materials compared to γ-TiAl [7]

	Unit	Steels	Aluminium	Nickel alloys	Ti-6Al-4V	γ-TiAl	BuRTi
Density	g/cm³	7.87	2.70	8.30	4.43	3.80	5.1
Young's modulus	GPa	195-200	69-79	180-214	110	150-175	113-126
Room temperature ductility	%	65	45	3-10	~20	2	15.4-22.6
Operating temperature ductility	%	-	-	10-20	high	5-12	
Tensile strength	N/mm²	415-1750	90-600	345-1450	895-1035	450-800	957-1125
Yield strength	N/mm²	205-1725	35-500	105-1200	825-965	400-650	895-1108
Melting point	°C	1536	660	1455	1600	1460	
Thermal conductivity	W/mK	~50	230	11.3	7,3	22	10

The advantages of gamma titanium aluminides were offset by the encountered difficulty of processing and machining due to mainly the extremely low ductility (<2%) of the material at ambient temperature. However, the ongoing improvements made in microstructure and deformation mechanisms and advancements in manufacturing methods have resulted in employing gamma titanium aluminides in many aerospace and automotive applications. γ-TiAl alloys have been adopted more quickly in automotive applications as the component safety requirements are lower than those for aerospace applications. Still, high manufacturing costs have confined their use to high-performance engines like those found in Formula 1 cars. Exhaust valves, turbocharger rotors, and connecting rods for high-performance engines have all been reported to be made using TiAl alloys in the automotive sector [3], [4]. Blades and stators in high-pressure (HP) compressors, low-pressure (LP) turbine blades, exhaust components, combustor chambers, and casings are typical aerospace target applications. Figure 2-6 shows various γ-TiAl mechanical parts for aerospace applications [44]. In 2011, General Electric (GE) reported the successful operation of their latest GEnxTM aero-engine, which has

gamma titanium aluminide intermetallic γ-TiAl alloy turbine blades in the low-pressure stage. It was the first commercial use of γ-TiAl in a commercial jet engine. Pratt and Whitney also announced the design of the new geared turbofan engine for Airbus 320neo with the last stage (lower pressure turbine) made of γ-TiAl material [9].



Figure 2-6: γ-TiAl components [44]

2.1.3 Burn-resistant titanium alloy

Titanium alloys are confined to cooler parts only (less than ~350 °C), such as casings, fans, and low-pressure compressor components due to their high tendency to ignition. Titanium fire or burn occurs in most conventional titanium alloys as they suffer from poor thermal conductivity. In order to meet aerospace industrial safety requirements, a group of titanium alloys known as burn-resistant titanium (BuRTi) alloys was developed. For instance, Alloy C in USA, alloy Ti-40 in China (Ti-25V-15Cr-0.2Si wt%), BTT-1 and BTT-3 (Ti-Cu-Al) alloys in Russia [4], [45]. Superior burn resistance properties were achievable by employing (Ti-V-Cr) systems. Adding vanadium (V) and chromium (Cr) within the alloy matrix, considerably increased the thermal

conductivity of the alloy. The difference in thermal properties between BuRTi and the conventional titanium alloy Ti-6Al-4V is shown in Section 2.1.2 (Table 2-4). High thermal conductivity is beneficial for heat transformation and uniform heat distribution, which prevents the increase in local temperature that eventually leads to burn. Burn-resistant titanium alloy (Alloy C) of composition (Ti-35V-15Cr-0.08O-0.05C wt%), developed in 1990 by Pratt and Whitney, exhibited superior burn resistance up to 600°C when compared to conventional titanium alloys and good mechanical properties, it was also used in critical engine applications such as F-119 USA Air Force engines [46]. However, producing this alloy was costly due to the large volume of heavy elements involved in the fabrication of the alloy. A more competitive economic alternative BuRTi alloy (Ti-25V-15Cr-2Al-0.2C wt%) was developed later in the UK by the University of Birmingham in association with Rolls-Royce Plc [4], [47]. This alloy has a higher thermal conductivity than conventional Ti-6Al-4V (10W/mK for the former compared to 6.7W/mK for the latter) and can retain greater tensile strength at higher temperatures as opposed to the α/β alloy (Ti679) in which a reduction of more than 300 MPa of tensile strength at a temperature of 500°C was reported [48]. The intention behind its development was to replace high-density steels and nickels used for intermediate and high-pressure compressor blades and turbine casings with an operating temperature range of 450°C-500°C.

The burn-resistant alloy microstructure is generally constructed of a disordered body-centred cubic (bcc) beta matrix and distributed carbide particles of Ti_2C and TiC. Thermomechanical processing routes, such as forging, can greatly influence the morphology of these carbides. It was found that Ti_2C and TiC carbides, which were formed by adding carbon (0.2wt%), can improve the material ductility by preventing α precipitation at the grain boundary. Aluminium is included as a master alloy to ease the melting process and reduce the cost of the materials. Oxidation studies have shown that adding chromium to the alloy matrix is crucial to improve the oxidation resistance of the alloy [4].

The burn resistance of the Ti-V-Cr alloy system has been demonstrated in an ignition test and was compared with a gamma titanium aluminide and a conventional titanium alloy, see Figure 2-7. Titanium alloys involved in the test were subject to typical conditions found in intermediate-pressure engine compressors, with an air temperature of 300°C, air velocity of 150m/s and 0.96MPa air pressure. Test findings showed better burn resistance performance of Ti-V-Cr alloy compared to the conventional alloy (Ti-6Al-4V), which suffered heavy burn [48].



Figure 2-7: Burn resistance of different titanium alloys [48]

2.2 Grinding

Grinding is a key process in manufacturing mechanical components with high surface quality and dimensional accuracy. Grinding was estimated to account for around 25% of machining technology practised in industries, and 43% of the total machinery in manufacturing industries is grinding machines [49]. Most of all manufactured components are machined with grinding at some stage during production. For components requiring smooth surfaces and fine tolerances, grinding will traditionally be applied as the last machining process in the production line of these components [50]. Nowadays, with advances in grinding technology, it is capable of bulk material removal as well. Dissimilar to other machining processes, grinding employs hard small particles called abrasive as a cutting medium instead of a cutting tool. Each abrasive operates as a cutting edge with a high negative rake angle. The abrasives have irregular shapes and are scattered randomly around the grinding wheel periphery [51]. Figure 2-8 illustrates commonly used basic grinding operations [52], [53]. Each grinding operation can have different orientations. For instance, cylindrical grinding can be further classified as external or internal. Figure 2-9 shows four surface grinding types based on wheel orientations and workpiece motions: (a) horizontal spindle with reciprocating worktable, (b) horizontal spindle with rotating worktable, (c) vertical spindle with reciprocating worktable, and (d) vertical spindle with rotating worktable. More grinding operations, specifications, and applications are detailed by Groove [54].

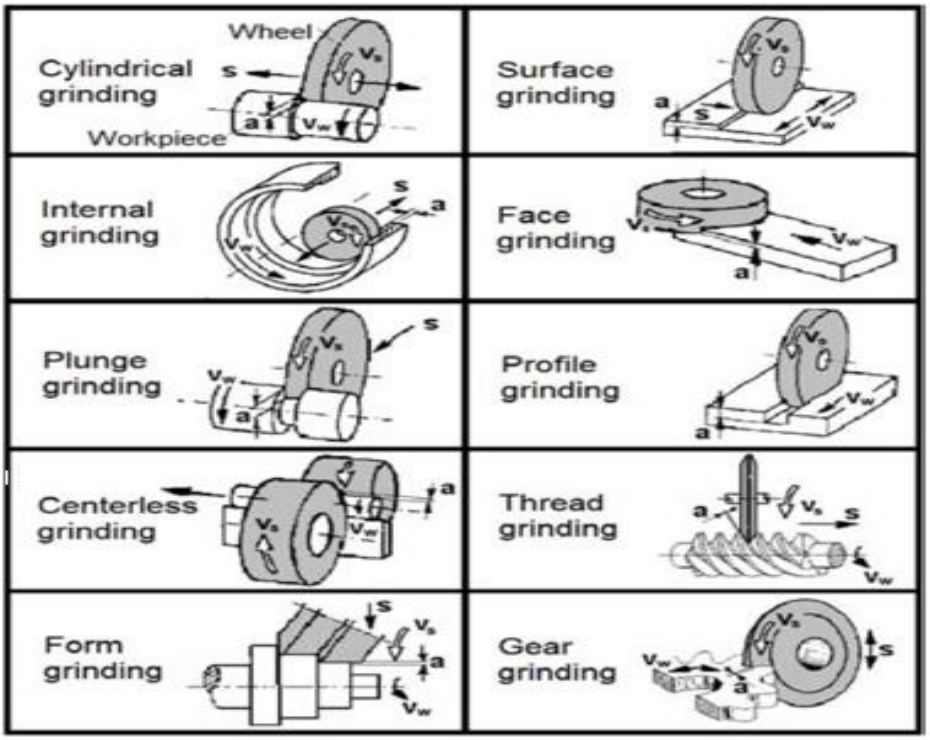


Figure 2-8: Basic grinding operations [52], [53]

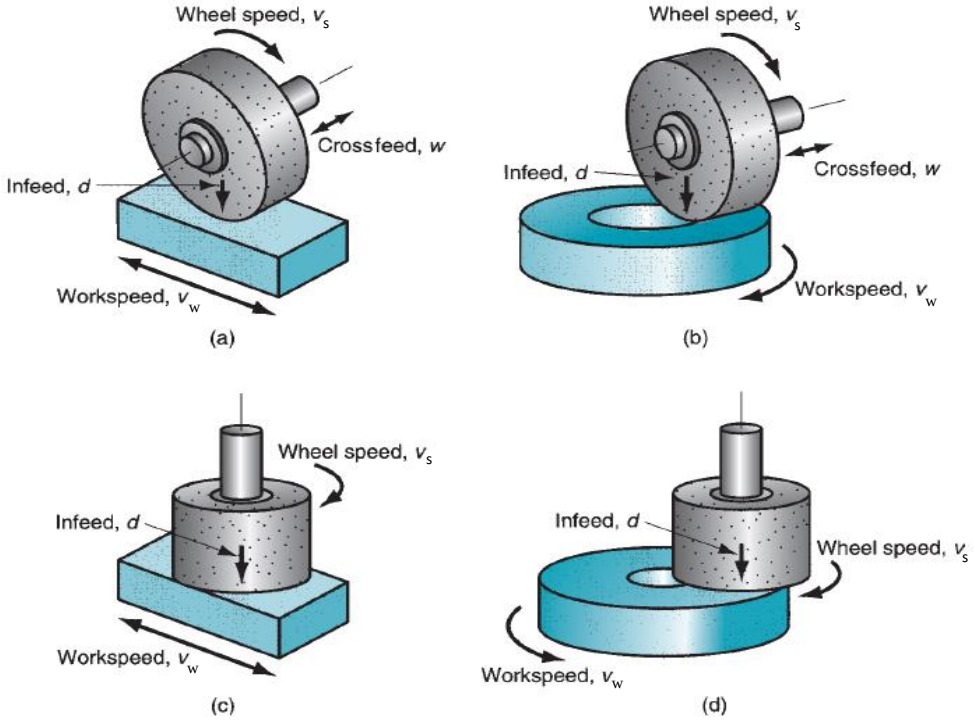


Figure 2-9: Surface grinding types [54]

Shaw reported that grinding can also be an effective removal process and classified grinding processes into two groups: form finish grinding (FFG) and stock removal grinding (SRG) [55]. In the aerospace industry, grinding is extensively used for manufacturing turbine blades and vanes. Klocke et al. noted that machining a typical blade might involve up to 12 different abrasive operations to produce features such as fir tree profile, root end profile, blade top, and trailing edge. Klocke and his co-researchers also provided a list of the most commonly employed grinding processes in aerospace applications, along with associated benefits and challenges, as detailed in Table 2-5 [13].

-

Table 2-5: Grinding processes in aerospace applications [13]

Grinding process	Specific material removal rate ($mm^3/mm.s$)	Benefits	Challenges
Surface grinding	10	Low complexity and equipment investment	Low productivity and poor wheel profile holding
Intermittent dress creep feed grinding (CFG)	20	Low complexity	Low productivity and poor wheel profile holding
Continuous dress creep feed grinding (CFG)	50	High wheel profile holding	Moderate productivity, high abrasive and dressing roll consumption
CFG with cBN wheels	20	High wheel profile holding	Low productivity, high wheel cost
Intermittent dress VIPER grinding	100	Good productivity, low wheel cost	Moderate wheel form holding
Continuous dress VIPER grinding	300	Excellent productivity, High wheel profile holding	High investment cost, high abrasive and dressing roll consumption
Speed stroke grinding	100	High wheel profile holding, low cutting forces	Equipment and lifecycle cost

2.2.1 Creep feed grinding

Creep feed grinding (CFG) overlaps the above two groups of grinding and is defined as a stock removal process that is capable of machining even the difficult-to-cut materials and simultaneously provides a good surface finish. Creep feed grinding operates at low feed rates and high depths of cut. The ‘creep’ refers to the slow movement of the workpiece (feed rate) during the cutting process, which usually ranges from 10 to 1000mm/min, and a high depth of cut in the range of 1-10mm. Table 2-6 demonstrates the grinding conditions of different grinding operations [56]. In contrast to conventional grinding (reciprocating/peripheral) processes where many successive passes are required, the stock removal in creep feed grinding is performed in a single pass of the wheel, although a second pass may be required to accomplish high dimensional accuracy and tolerance. An illustration of the distinction between

conventional surface grinding and creep feed grinding is given by Andrew [57] in Figure 2-10. Broaching and milling were commonly used to manufacture turbine blade root profiles made from hard materials such as nickel-based alloys; however, to overcome associated poor machinability, excessive tool wear, and capital cost, creep feed grinding was introduced in the late 1990s, which involves a greater depth of cut at lower wheel speeds and feed rates. This results in a higher material removal rate with only one pass of the grinding wheel, thus achieving more productivity [12]. The generated specific energy in creep feed grinding is almost 10 times higher than in surface grinding due to the heavy depths of cut employed in creep feed grinding and the larger contact area between the wheel and the workpiece surface. Therefore, it is necessary to employ an efficient level of coolant in the grinding zone to avoid thermal damage and poor tolerance as a result of the large specific energy. Moreover, continuous or intermittent dressing of the grinding wheel is of great importance to the grinding process, as dressing of the wheel will reduce the large sliding forces in creep feed grinding [50].

Table 2-6: Grinding conditions for different grinding operations [56]

Parameters	Low stress grinding	Reciprocal grinding	Creep feed grinding	High efficiency deep grinding
Depth of cut (mm)	Low 0.005-0.12	Low 0.01-0.05	High 0.1-30	High 0.1-30
Wheel speed (m/s)	Low Under 17.5	Low 20-60	Low 20-60	High 80-200
Table speed (m/min)	High 15 or up	High 1-30	Low 0.05-0.5	High 0.5-10
Specific material removal rate ($mm^3/mm.s$)	Low Up to 3	Low 0.1-10	Low 0.1-10	High 50-2000

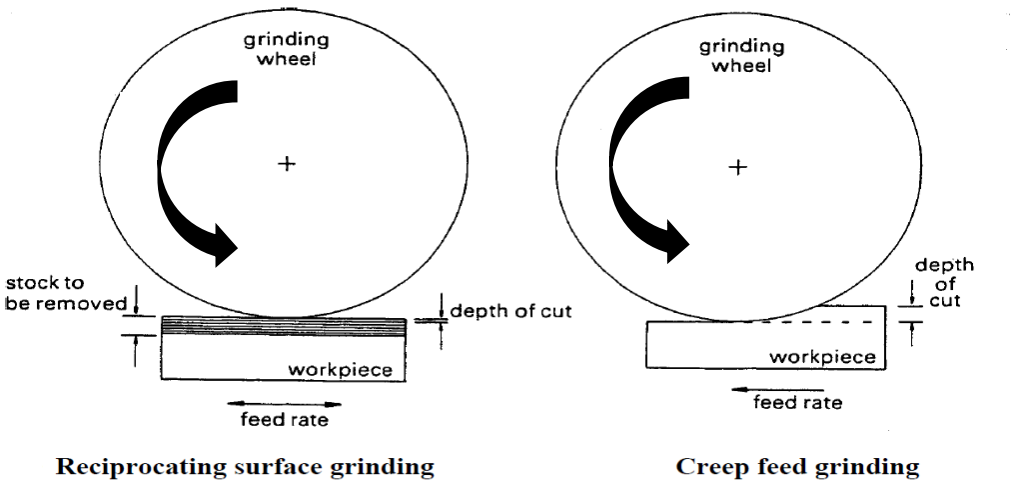


Figure 2-10: Illustration of surface grinding vs creep feed grinding [57]

2.2.2 Grinding system elements

A productive grinding process requires a deep understanding of all the elements involved in the machining process and how they interact with each other. The main basic elements for grinding systems include the grinding wheel, wheel dressing tool, workpiece, grinding fluid, and grinding machine. Attention also must be paid to each element's characteristics as they dominate the productivity of the grinding process. For the last few decades, optimization of grinding element characteristics has been a subject of intensive research. A systematic overview of the effect of machine tool and grinding wheel characteristics on grinding performance criteria are given in Appendix A. More details on how altering these characteristics improves the overall performance of grinding titanium alloys will be provided in later sections. Comprehensive descriptions of all inputs and outputs in the grinding process are presented by Rowe in Figure 2-11 [52]. Some of the characteristics are given below for the basic elements mentioned earlier:

- Grinding wheel: the abrasive, grain size, bond, structure, hardness, speed, thermal properties.
- Dressing conditions: type of tool, speeds, feeds, cooling, lubrication, and maintenance.
- Grinding machine: type, control system, accuracy, stiffness, temperature stability, vibrations.
- Grinding fluid: flow rate, velocity, pressure, physical, chemical, and thermal properties.
- Workpiece material: shape, hardness, and stiffness.

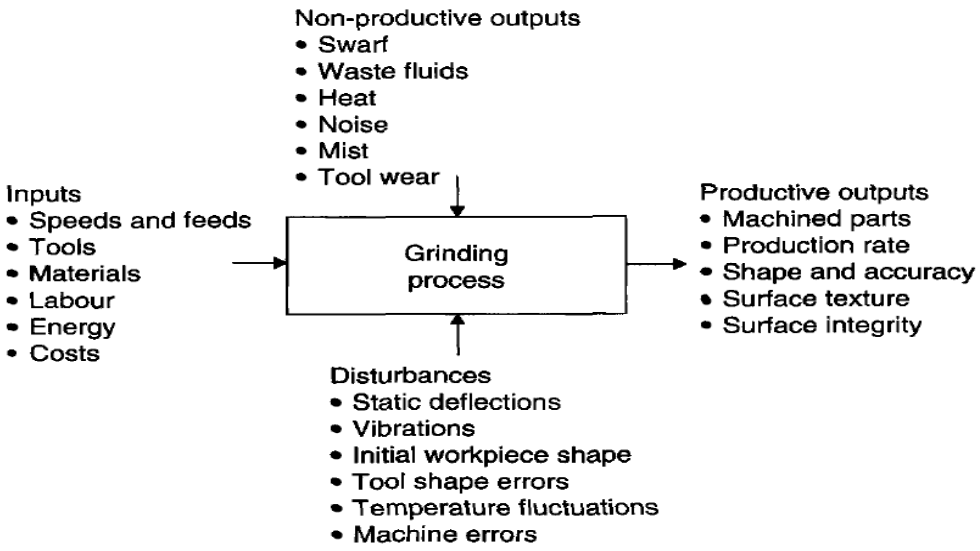


Figure 2-11: Grinding process inputs and outputs [52]

2.2.3 Grinding wheel

Grinding wheels used in creep feed grinding of titanium alloys are generally classified into two groups: conventional abrasive wheels, aluminium oxide (Al_2O_3) and silicon carbide (SiC) and super-abrasive wheels, diamond and cubic boron nitride (cBN). Each group has a standardised code. This code provides details regarding the type of abrasive, size of the grain, grit concentration, grade, structure, porosity, and bond type. The grinding wheel structure along with the wear mechanisms, are shown in Figure 2-12.

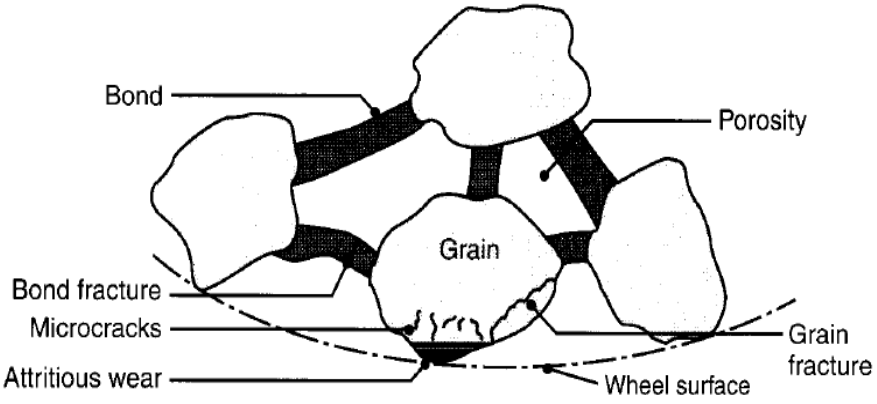


Figure 2-12: Grinding wheel structure [51]

Grinding abrasive grits are supplied in a wide range of friability (fracture cleavage resistance), and their size is expressed in terms of the average diameter in microns (μm). The wheel grade is a measure of the bond strength or wheel hardness. The structure in a conventional abrasive coding system refers to the porosity of the wheel, while in the case of a super-abrasive coding system, the structure measure is replaced by grit concentration number, which is the amount of super-abrasive grit per unit volume. The last measure is the bond type, which relates to the bond system that connects the abrasive girts [58]. The most common bond types include vitrified, resinoid, rubber, and metal. Vitrified bonds are porous, stiff, chemically resistant, and composed of feldspar and clays. Metal bonds are commonly used with super-abrasive wheels. These bonds provide more strength and enhance grit abrasion resistance. In super-abrasive wheels, multilayers of super-abrasive grits are bonded around the core of the wheel, normally up to 7mm deep, while the core of the wheel, depending on stiffness requirement, is typically made of steel, ceramic, aluminium, bronze, or even composites. The coding systems for both groups of wheels are presented in Appendix B [51].

Super-abrasive wheels possess more attractive properties than conventional wheels. Diamond and cBN wheels are characterised by sharp and smaller rake angles of grits ranging from (-60 to -70) compared to (-85 to -90) for silicon carbide and aluminium oxide. Tawakoli [59] stated that sharper grits can improve grinding performance by reducing the friction and temperature generated during grinding. When utilising super-abrasive wheels, the heat from the grinding zone between the wheel and the workpiece can be quickly dissipated, owing to the higher thermal conductivity over the conventional wheels. For example, the diamond wheel has a thermal conductivity of 2000W/mK, while the thermal conductivity of the SiC wheel is 100 W/mK. Another significant property is the substantially higher wear resistance of super-abrasive over the conventional one. It was estimated that the Knoop hardness of the former is roughly three times higher than that of the latter [55]. This will subsequently give rise to grinding efficiency and productivity by increasing the grinding ratio of the process.

There are three different types of grinding wheel wear. Attritious wear, grain fracture, and bond fracture. In attritious wear, the sharp grain's cutting edges become dull by attrition and subsequently create a wear flat area. Attritious wear can develop as a result of complex reactions between the grain and the workpiece material, such as diffusion, chemical degradation of the grain, plastic deformation, and melting. Special care must be given in selecting appropriate abrasive for a particular work material to ensure low reactivity during grinding and, hence, low attritious wear. Grain fracture occurs when abrasive particles are removed from the wheel due to fractures within the grain. This phenomenon is expected during grinding and results in continuously new cutting edges; however, at a moderate rate, or else dressing is required. During bond fracture, abrasives are expelled from the binder. In grinding operations, bond strength is a critical factor to consider. Softer bonds are generally recommended for hard materials to avoid residual stresses and heat damage to the workpiece, while softer materials and greater material removal rates require stronger bonds. If the bond is too weak, the grains may easily detach, and the wheel will wear at a fast rate, leading to poor component dimensional accuracy and precision [60].

The typical wheel wear mechanism reported by authors consists of three stages: initial wear at a low decreasing rate, then steady-state wear, where equality between the wear flats and new cutting edge is reached, and finally accelerating wheel wear, which necessitates wheel replacement (in the case of electroplated super-abrasive wheels) or wheel dressing for conventional vitrified bonded wheels [60], [61]. A good indicator of wheel wear in the grinding

process is the grinding ratio (G-ratio), it is a measure of the wheel's ability to remove material and is defined as follows:

$$G - \text{ratio} = \frac{\text{the volume of removed workpiece material}}{\text{the volume of removed wheel material}} \quad (1)\ [51]$$

In the grinding process, if the wear flat caused by attritious wear is excessive, the grain will become dull; this is followed by grain fracture at a moderate rate to develop new sharp cutting edges. However, unequal forces and stock removal during the grinding operation will eventually lead to a non-uniform wear pattern of the wheel. Resulting in an increase in sliding forces and temperatures as well as poor surface finish. In order to avoid this, dressing is required. The dressing is performed in most grinding operations to regenerate the wheel face and geometry, provide a uniform random distribution of cutting edges, and more importantly, remove loaded chips of the workpiece material from the wheel [52]. When wheels are loaded with chips, they cut inefficiently and generate excessive frictional heat, which can hinder the quality of produced surfaces. Loading of the wheel is more common when grinding soft and more ductile materials and can be minimised with an appropriate selection of operating parameters and wheel specifications [60]. The basic dressing tools are either stationary or rotary (driven by a motor). The stationary dresser involves single-point, multi-point diamond, or profile dressers. While the rotary includes a profile roller and cup wheel. A schematic illustration of different configurations of dressing tools is shown in Figure 2-13 [52]. In all different configurations, the roll dresser must be placed rigidly during the dressing operation to eliminate deflections and vibrations that might influence produced surface accuracy and roughness.

The dressing ratio, which is the ratio between dresser velocity and wheel velocity, can significantly affect the quality of produced surfaces, as shown in Figure 2-14 [58]. The dressing ratio can be either positive or negative based on the relative rotation direction of the dresser and the wheel. A positive ratio indicates that both the grinding wheel and the dresser are rotating in the same direction at the contact point, and a negative sign indicates a rotation in the opposite direction at the contact point. Positive dressing ratios close or equal to 1 provide a sharper and more open wheel, allowing for better material removal rates and more efficient cooling, thus reducing the risk of burn. However, the sharpness of the grinding wheel will result in a coarser workpiece surface finish. In contrast, a dull and less porous wheel will usually produce a finer workpiece surface quality but at the expense of higher power, forces, and likely surface burn.

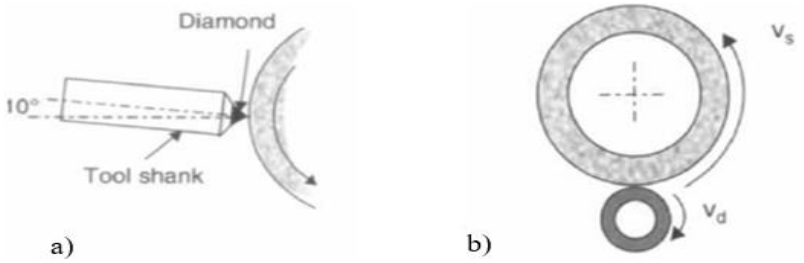


Figure 2-13: Basic dressing tool configurations [51], a) Stationary single-point dressing tool, b) rotary roll dressing an external grinding wheel.

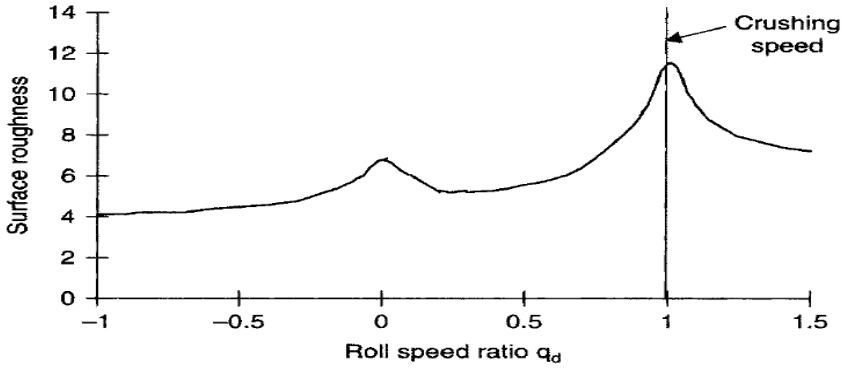


Figure 2-14: The effect of dressing ratio on the roughness of produced surface [57]

2.2.4 Grinding mechanics

In grinding operation, the material is removed from both the workpiece surface and the grinding wheel surface (abrasive surface) as a result of the relative rubbing motion of the two surfaces. Figure 2-15 [51] illustrates the main grinding process variables in surface grinding (up grinding mode), grinding wheel diameter (D) in mm, tangential velocity (v_s) in m/s, feed velocity (v_w) in mm/min depth of cut (d) in mm, undeformed chip thickness (t) in µm and contact length (l) in mm. For convenience, the following symbols are interchangeably used in this study: (a_e) for depth of cut, (h_{cu}) for undeformed chip thickness and l_c for length of contact, that can be expressed as:

$$l_c = \sqrt{Dd} \qquad (2)\ [50]$$

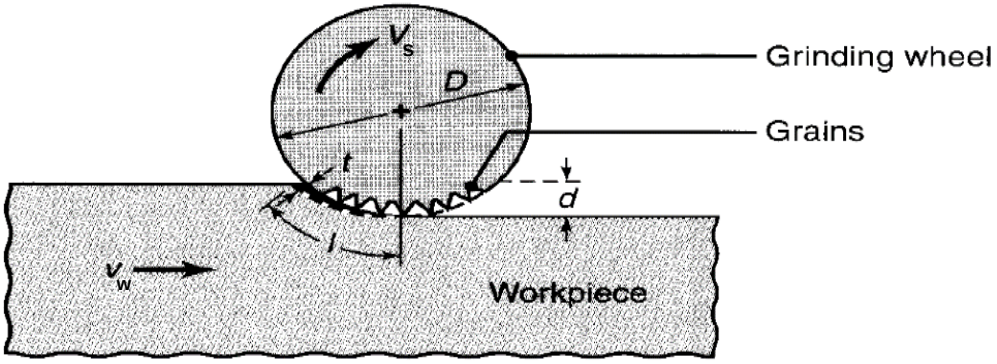


Figure 2-15: Schematic illustration of grinding variables [50]

The most basic recognized parameter to calculate the intensity of an abrasive engagement is the specific material removal rate (Q'), as shown in Equation (3). Its value can be identified with feed rate/workpiece velocity and depth of cut. It enables direct comparison of removal efficiency across a wide variety of procedures with limited operating conditions. But, when it comes to defining chip thickness, the specific material removal rate suffers from not accounting for wheel speed. Shown in Equation (4) is the equivalent chip thickness (h_{eq}), which earned more academic acceptance and has been found to be especially useful for correlating grinding parameters with removal rate characteristics for a certain grinding wheel type. It is a measure of the thickness of the layer of material removed in one pass or revolution of the grinding wheel. For their simplicity, both parameters are utilized as a basic variable in experimental experiments [62].

$$Q' = v_w \cdot a_e \quad (3)[52]$$

$$h_{eq} = a_e \cdot \left(\frac{v_w}{v_s}\right) \quad (4)[62]$$

An undeformed chip thickness (h_{cu}) is a parameter that considers the contact length and grain spacing, which were not accounted for in previous parameters. Numerous studies stated the importance of undeformed chip thickness when assessing grinding forces, workpiece surface finish, and wheel wear. Several models have been proposed to evaluate its value as the actual length of contact is proven to be difficult to predict, some of which are summarised in [62]. As opposed to grinding, the shape of the cutting edges and the distance between them are typically known in metal-cutting procedures; thus, the corresponding calculations for chip thickness are rather simple. In grinding, about two million active grits are available in a standard grinding

wheel. The spacing of the cutting points on each grit is randomly distributed, giving each grit its own distinct geometry. Moreover, dulling of the grits changes the cutting-point geometry, and grit fracture and grit pullout change the cutting-point density. During grinding, an elastic/plastic deformation takes place, resulting in changes in contact length. Assuming a constant workpiece width, Kalpakjian and Schmid state that undeformed thickness (t) or (h_{cu}) can be given for a rectangular chip by:

$$h_{cu} = \sqrt{\left(\frac{4v_w}{v_s cr}\right)\sqrt{\left(\frac{a_e}{D}\right)}} \quad (5)\ [51], [62]$$

Where c is the number of cutting points per unit area of the wheel surface, and r is the ratio of chip width over the average chip thickness or the shape factor. The value of c can be determined by several methods, including slow-rolling scratch, counting of wear flats or counting of chips, and stylus measurement [55]. Determining the value of c and r has proven to be difficult with different values reported for specific grinding operations. Badger [63] employed a dimensionless parameter in 2008 to quantify the chip thickness and to avoid estimating the values of C and r. It was recognised as the aggressiveness number, which is based solely on the process parameters: wheel diameter, feed rate, wheel speed and depth of cut, as shown in Equation 6.

$$Aggr = 10^6 \frac{v_w}{v_S}\sqrt{\frac{a_e}{D}} \quad (6)\ [63]$$

This straightforward technique allowed engineers and machine operators to simultaneously alter multiple variables to determine if the aggressiveness number increased or decreased. It helps in grinding process optimization by providing the influence of chip volume and chip thickness on the process behaviour for given operating conditions, grinding wheels, and materials. In 2020, Curtis et al. [64] used this parameter to investigate the influence of grinding wheel specification on surface integrity and residual stress when grinding Inconel 718.

Forces generated in the grinding process are divided into two components: vertical force (F_v) and horizontal force (F_h), but due to the higher depth of cut and longer length of arc associated with creep feed grinding, grinding forces are termed tangential force (F_t) and normal force (F_n) [50], and can be characterised as:

$$F_t = F_v \sin\theta + F_h \cos\theta \quad (7)\ [65]$$

$$F_n = F_v \cos\theta - F_h \sin\theta \quad (8)\ [65]$$

$$\Theta=\sqrt{(\frac{a_e}{D})} \quad (9)\ [65]$$

Grinding power is the product of the tangential force and wheel speed, as given below:

$$P= F_t \,.\, v_s \quad (10)\ [50]$$

The grinding process produces considerably higher specific energies than other conventional machining processes, typically in the range of 10-100J/mm^3. The main reasons for this rise are the highly negative angle of the grains that leads to large shear strain, the chip size effect, and the fractional energy required to wear flat [50]. In creep feed grinding, the value of specific energy is usually increased by five folds and up to 1000J/mm^3 [57] Brach et al. reported that specific energy is an imperative parameter in evaluating different grinding processes and can be an assessment criterion for grinding performance [66]. Specific energy is a measure of the efficiency of the grinding process, and it is the total sum of three components as shown in equation (11): Chip formation specific energy, ploughing specific energy, and sliding specific energy [54].

$$u = u_{chip} + u_{ploughing} + u_{sliding} \quad (11)\ [54]$$

The total specific energy is determined by equation (12) [31].

$$u = \frac{P}{Q_w} \quad (12)\ [57]$$

Where: u= specific grinding energy in (J/mm^3)

P= grinding power (J/s)

Q_w= material removal rate (mm^3/sec)

2.2.5 Grinding vibration

Grinding vibrations can result in pronounced surface waviness (chatter) on the workpiece, loss of workpiece precision, acceleration of wheel wear, and workpiece roughness deterioration. Excessive vibration can also cause material burn damage and spindle bearing failure. Identifying the source and nature of the vibration is the first step in resolving grinding vibration. The two most common types of vibration on grinding machines are force vibration and self-excited vibration [50], [52]. Force vibrations are mostly related to machine tool components. Grinding wheel unbalance, spindle unbalance, rotor dresser unbalance, faulty bearings, and

defective motors are all examples of force vibration sources. Vibration in the machine tool or/and deflections in the fixturing often result in vibration. If these machine tool factors can be minimized or eliminated, the surface roughness in grinding will be determined primarily by geometric, work material, and operating parameters. On the other hand, self-excited vibrations are only produced during the grinding process. Self-excited vibrations are closely linked to grinding parameters and natural frequencies of the machine and can cause regenerative chatter waves on both the wheel and the workpiece. Waves that form largely on the wheel are called wheel-regenerative vibrations, while waves that form primarily on the work are called work-regenerative vibrations. Control measures to reduce or eliminate vibration include adding stiffness and/or damping to the system, operating at lower speeds to avoid vibration caused by natural frequency, reducing cutting forces by lowering feeds and depths of cut or using softer grade wheels [52]. An illustration of regenerative workpiece vibration is shown in Figure 2-16 [50]. The required dimensional tolerance and surface finish of the workpiece usually determines the acceptable range of vibration level. The tighter the tolerances, the less vibration may be tolerated.

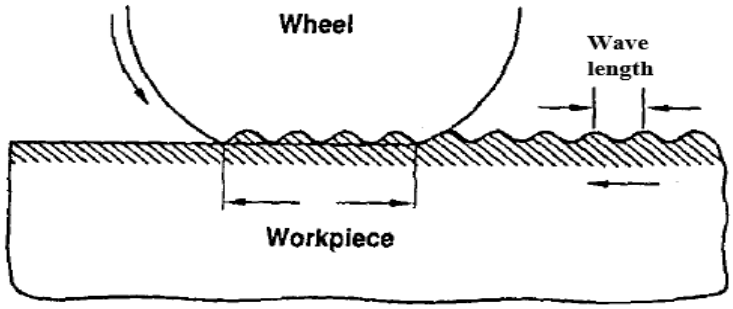


Figure 2-16: Regenerative workpiece vibration [50]

2.2.6 Grinding temperature

The grinding process is characterised by high specific energy due to the ploughing and rubbing actions of the grits against the workpiece. In machining processes, most of the generated energy is converted into the chip, but in grinding, most energy is conducted to the workpiece as heat, resulting in a very high temperature across the grinding area. This necessitates proper control of the grinding process and efficient cooling of the wheel-workpiece contact area in order to avoid thermal damage introduced by high elevated temperatures. Commonly reported deficiencies associated with high grinding temperature include surface burn, subsurface crack,

structural transformation, wheel loading, induced tensile residual stress, and wheel damage [54], [55]. Two types of transient temperatures were identified in the literature: localised temperature (spikes) and average temperature usually referred to as background temperature. The former is the result of interaction between a single active grain and the workpiece, while the latter is due to the cumulative frictions of all grains in the grinding contact area. It was argued that the short exposure of localised temperature could not cause the thermal damage observed in ground workpieces (such as burn, tempering, and phase transformation), and its damage was only limited to wear rate and attrition of the cutting grains. With respect to surface quality, it was concluded that the temperature of importance is the background temperature. Therefore, the modelling of the grinding temperature was based on background temperature rather than localised temperature to ensure high quality surface integrity of the ground workpieces. Over the last few decades, numerous studies have been published on theoretical/mathematical modelling as well as experimental measurements of temperature generated in grinding. The mathematical modelling is beyond the scope of this research, although a brief description will be provided in this paper to emphasise the importance placed on grinding temperature in the literature.

2.2.6.1 Theoretical/mathematical modelling

Maths packages and numerical software, such as finite element method-based software, are commonly applied to solve thermal models. Experimental means to measure the grinding temperature, for instance, embedded thermocouples, are often used for the validation process of the results obtained by numerical software. Shaw [55] stated that it is difficult to establish an accurate model for grinding temperature which incorporates the variations of different materials properties and grinding parameters, and he claims that the estimation of the grinding temperature is not expected to be analytically accurate. A review of analytical methods and numerical models for calculating temperature in machining processes is presented by Tay, and he concluded that Bishop's method used by Usui and Shirakashi and the FEM used by Muraka et al. give the most accurate results [67]. Examples of work made to investigate the temperature distribution in grinding and creep feed grinding via mathematical modelling are reported in [53], [68], [69], [70]. The majority of work on theoretical/mathematical modelling for temperature prediction employed the early work of Carslaw and Jaeger, which describe a moving heat source on a semi-infinite body [71], [72]. It was designed to represent shallow cut

grinding with constant feed rates, and it is assumed in this model that the majority of heat produced by the sliding heat source enters the workpiece. Subsequent investigations have led to the development of thermal models to determine workpiece surface temperature, heat flux distribution in the grinding zone, the percentage of energy entering the workpiece, and the convective heat transfer coefficient for cooling on the workpiece surface. Key findings were reported in [73], and they include the shear plane partitioning model by Outwater and Shaw [74], partition between grain and workpiece by Hahn [75], real contact length by Makino et al.[76], fluid convection by DesRuisseaux and Zerkle [77], fluid film boiling by Howes et al. [78], contact grain model by Lavine [79], and critical temperature for tensile stresses by Tonshoff et al.[80]. A circular arc model was developed later by Rowe and Jin [81] for deep depth of cuts typically found in creep feed grinding and high efficiency deep grinding. A review of the analytical methods and models used to calculate grinding thermal aspects such as heat flux, maximum surface temperature, conducted temperature, total heat flux, and energy partitions is detailed by Malkin, Guo, and Rowe [14], [82]. Malkin and Guo detailed thermal models for conventional shallow grinding, creep feed grinding and high efficiency deep grinding (HEDG). The main factors considered in their models were energy partition, cooling effect, the velocity of the heat source and arc length [14]. Energy partition (q_w) is a critical parameter in analysing grinding temperature and is defined as the fraction of total converted energy into the workpiece in the form of heat. This energy partition, as reported by Malkin, is heavily influenced by grinding conditions, operating parameters and workpiece/wheel materials. The total heat at the grinding zone must be specified in order to estimate the grinding temperature. This is determined by equation (13), where b is the width of the cut:

$$q_t = \frac{P}{l_c\, b} = \frac{F_t\, v_s}{l_c\, b} \qquad [52](13)$$

The thermal partition model assumes that the total heat is conducted by the workpiece, wheel, chip/grain, and coolant/fluid as given in Equation (14). The heat flow mechanism is presented in Figure 2-17 by Rowe [52]:

$$q_t = q_w + q_s + q_{ch} + q_f \qquad [83](14)$$

q_w represents heat conducted by the workpiece, q_s is the heat flux to the wheel, q_{ch} is the heat carried away by the chip and q_f is heat removed by the fluid. The heat partition for the workpiece, wheel, chip and fluid can be related to the maximum surface temperature by the conduction factor of each element as shown below [84]:

$$q_w = h_w \,.\, T_{max} \quad [84]\ (15)$$

$$q_s = h_s \,.\, T_{max} \quad [84]\ (16)$$

$$q_{ch} = h_{ch} \,.\, T_{max} \quad [84]\ (17)$$

$$q_f = h_f \,.\, T_{max} \quad [84]\ (18)$$

The workpiece surface maximum temperature rise during grinding (T_{max}), can be defined as:

$$T_{max} = C.\frac{q_w}{\beta_w}.\sqrt{\frac{l_c}{v_w}} \quad [83](19)$$

Where, β_w is thermal property of the workpiece material and it is based on the thermal conductivity, density, and specific heat capacity. C is a factor that can be taken from circular arc model diagrams (detailed by Rowe), depending on Peclet Number and contact angle. The convection factor for the workpiece is determined by Equation (20):

$$h_w = \frac{\beta_w}{C}\sqrt{\frac{v_w}{l_c}} \quad [84](20)$$

The convection factor for the heat entering the wheel is given by:

$$h_s = h_w\left[\frac{1}{R_{ws}} - 1\right] \quad [83]\ (21)$$

Where R_{ws} is the percentage of heat flux entering both workpiece and wheel. This value can be calculated using Hahn's model [75], where k_g is the thermal conductivity of grit and r_0 is the active radius of the grain.

$$R_{ws} = \frac{q_w}{q_w+q_s} = \frac{h_w}{h_w+h_s} = \left[1 + \frac{0.97k_g}{\beta_w\sqrt{r_0 v_s}}\right]^{-1} \quad [85]\ (22)$$

Heat flux entering the chip is calculated using Equations (23) and (24):

$$q_{ch} = e_{ch}\frac{v_w \,.\, a_e}{l_c} \quad [84]$$

(23)

$$e_{ch} = p_w.c_w.T_{ch} \quad [84]\ (24)$$

Where e_{ch} is the energy within the chip, p_w the density of the material, T_{ch} estimated temperature of the chip and this temperature is assumed to be less than the melting temperature of the workpiece [86].

In order to calculate the heat flux to the fluid, the heat convection factor must initially be estimated. Assuming an effective fluid delivery on the contact area the value of the fluid heat conduction factor can be theoretically predicted using Equation (25).

$$h_f = \frac{3\beta_f}{2} \cdot \sqrt{\frac{v_s}{l_c}} \qquad \text{[52] (25)}$$

Different values of fluid heat convention factors have been determined experimentally by several authors. Rowe and Jin [81] noted values of 290,000W/m^{2}K for water-based emulsions, for neat oil a value of 23,000 W/m^{2}K was presented by Stephenson et al. [87]. In 2008 more results of fluid convection factor were detailed by Jin and Stephenson for both neat oil and water-based coolant when grinding 51CrV4 steel with a cBN wheel [86]. The authors addressed that the value of the fluid convection factor (h_f) should be neglected and set to zero if the temperature of the fluid exceeds the boiling temperature. At this temperature, the fluid starts boiling and loses its cooling ability. As a result, the grinding process is then considered a dry grinding process rather than a wet grinding process. From Equations (14-25) the maximum surface temperature can alternatively be established as:

$$T_{max} = \frac{q_t - h_{cp} T_{ch}}{\frac{h_w}{R_{ws}} + h_f} \qquad \text{For wet grinding (fluid boiling temperature not reached) [84](26)}$$

$$T_{max} = \frac{q_t - h_{cp} T_{ch}}{\frac{h_w}{R_{ws}}} \qquad \text{For dry grinding or when boiling temperature is reached [84](27)}$$

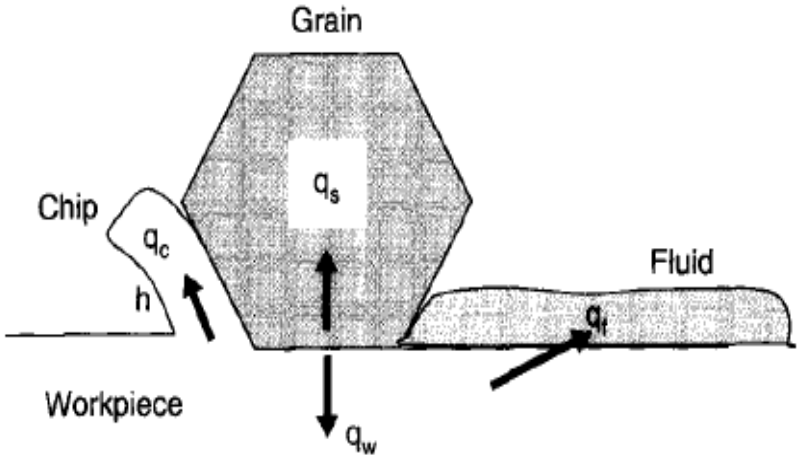


Figure 2-17: Heat flow mechanism [52]

2.2.6.2 Experimental measurements of temperature

Accurate and direct temperature measurements are essential for correlation with theories. A variety of experimental techniques has been developed for measuring grinding temperature, with each having both advantages and disadvantages. The main working principles of these techniques are based on heat conduction or heat radiation for temperature determination. Reviews of applied techniques in the literature and available for researchers are presented by Komanduri, Hou [88]; for manufacturing processes in general, Tonshoff et al. [89], and Batako et al. [85]; specifically for grinding processes. They include thermocouples, infrared photography, infrared optical pyrometers, thermal paints, and materials of known melting temperatures (PVD films). The authors noted that the selection of an appropriate method for a particular thermal situation depends largely on several factors, for example, accessibility, heat source size, situation dynamics, required precision, and instrumentation cost.

Infrared measurement techniques are non-contact measurements that detect the heat radiation emitted during grinding by either thermal imaging or an infrared pyrometer. One of the advantages offered when utilising infrared techniques is the elimination of noises caused by mechanical vibrations since there is no contact with the ground surfaces. In addition, direct measurements are provided in real-time. An example of a thermal image method for temperature measurement is given by Hwang et al. [90] in Figure 2-18. Here, the temperature distribution is displayed graphically using an array of sensors of a thermal camera. Hwang et al. [90] implied that the capacity to examine temperature measurements across a wider area than the wheel-workpiece contact zone offers a significant advantage. The main drawback of this method is the high level of uncertainty within the measurement. This is in part due to the fact that the initial radiation produced in the contact zone is greatly diminished in the mist or by direct flow of the coolant until it is detected by the camera. Furthermore, the camera captures heat radiation from a side-plane perpendicular to the contact zone. As a result, this technique finds more application in dry machining processes [85].

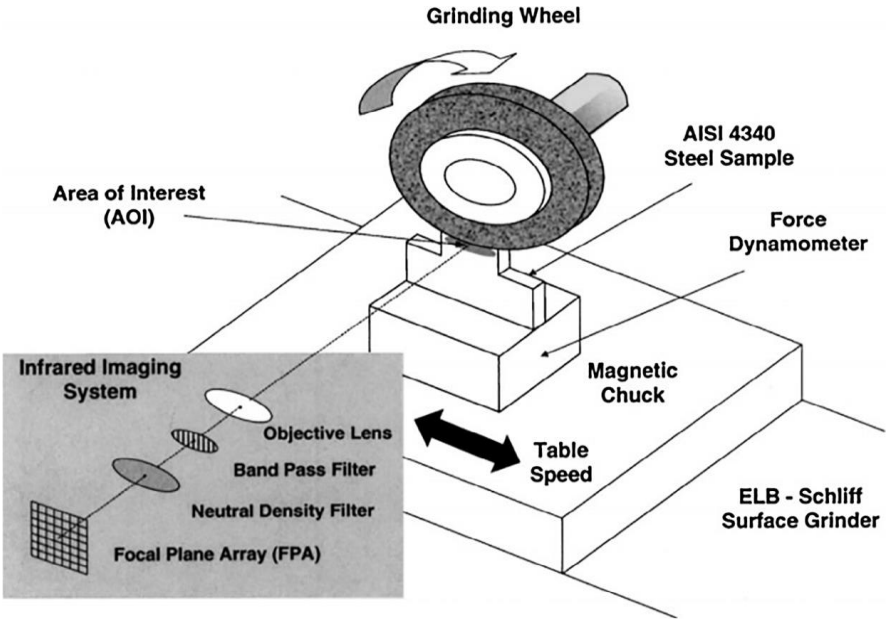


Figure 2-18: Thermal image method [90]

Work by Ueda et al. [91] gave earlier observations of the grinding temperature detected with an infrared radiation pyrometer. Figure 2-19 Illustrates the experimental arrangement in his study [91]. Temperatures at the workpiece surface are measured via an optical fibre, which transmits the information to an infrared pyrometer that is placed remotely. The authors described benefits such as fast response time and the ability to accurately determine peak temperatures. However, issues were raised in [85], [92] relating to the pyrometer technique being relatively expensive, fragile to handle, and difficult instrumentation involved in setting up.

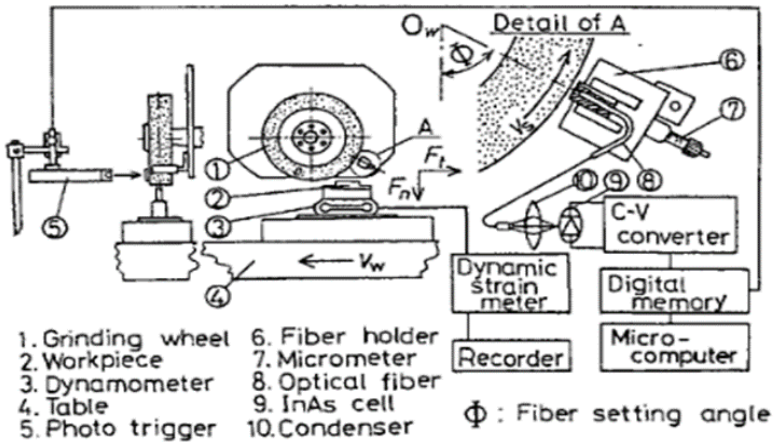


Figure 2-19: Infra-red pyrometer with local optical fiber temperature [91]

Experimental investigations of grinding temperatures employing a direct contact measurement with PVD (physical vapor deposition) film method were presented by Kato and Fujii [93], [94]. PVD film method is an improvement on earlier work involving fine powder instead of film [95]. Superior thermal responses were achieved by the former as the latter suffered from thick porous layers that prevented full contact with the split workpiece. The experimental work carried out by the authors is shown in Figure 2-20. The PVD film is used as a thermal sensor consisting of a material with a defined melting temperature sandwiched between two split workpieces. The process is capable of providing temperatures at different depths from the surface and is considered an easy and cheap method of providing insights into the temperature distribution [88]. Walton et al. [96] applied PVD film method to measure the temperature on the finished surface under aggressive grinding conditions. Theoretical temperatures derived from mathematical modelling were compared to PVD coating results. The authors concluded that the obtained findings showed good agreement between modelled and measured values of temperature and there was no detrimental effect observed on the film even with high-pressure fluid delivery. Table 2-7 provides various materials used in PVD film along with their respective melting temperatures.

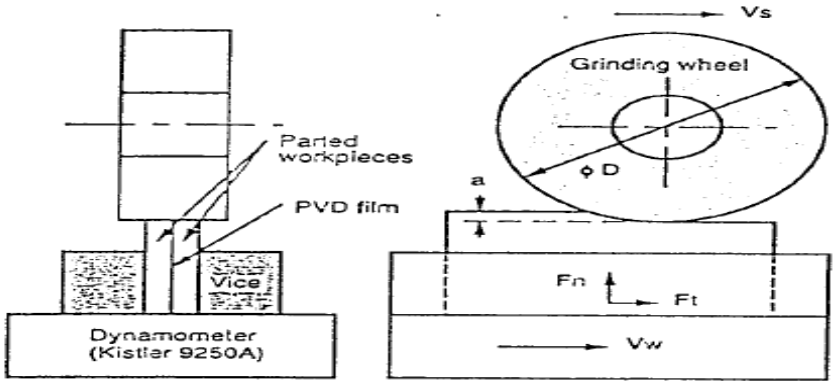


Figure 2-20: A Schematic of the PVD method of temperature measurement [94]

Table 2-7: Melting points and purity of PVD film materials [88]

PVD film material	Symbol	Melting point (K)	Purity %
Germanium	Ge	1211	99.9
Antimony	Sb	904	99.9999
Tellurium	Te	723	99.999
Lead	Pb	601	99.999
Bismuth	Bi	545	99.999
Indium	In	429	99.999

Another direct contact measurement method is thermocouples. Among previously mentioned approaches, thermocouples are the most preferred application. Advantages of implementing thermocouples include low cost, reliability, and simplicity in construction, operating, and signal processing. The working principle of a thermocouple is that when two dissimilar materials are joined together at both ends with each end subject to different temperatures (one end is a cold junction and the other end is a hot junction), then an electromotive force (emf) will generate. This emf is a function of the two materials' properties and temperature difference between the junctions. Table 2-8 provides temperature ranges for eight standard thermocouples [88]. Two main types of thermocouples are available, namely, embedded thermocouples and foil-workpiece thermocouples.

Table 2-8: Standard thermocouple types [88]

SLD[a]	Popular name	Materials (color code) (positive material appears first)	Typical temperature range
S	–	Platinum–10% rhodium vs. platinum	−50 to 1767°C
R	–	Platinum–13% rhodium vs. platinum	−50 to 1767°C
B	–	Platinum–30% rhodium vs. platinum–6% rhodium	0 to 1820°C
T	Copper–constantan	Copper (blue) vs. a copper–nickel alloy (red)	−270 to 400°C
J	Iron–constantan	Iron (white) vs. a slightly different copper–nickel alloy (red)	−210 to 760°C
E	Chromel–constantan	Nickel–chromium alloy (purple) vs. a copper–nickel alloy (red)	−270 to 1000°C
K	Chromel–Alumel	Nickel–chromium alloy (yellow) vs. nickel–aluminium alloy (red)	−270 to 1372°C
N	Nicrosil–Nisil	Nickel–chromium–silicon alloy (orange) vs. Nickel–chromium–magnesium alloy (red)	−270 to 1300°C

[a] Standard letter designation.

Tonshoff et al. [87] reviewed implementation methods for both types of thermocouples, as shown in Figure 2-21. As demonstrated by Tonshoff et al., Thermocouples can be inserted either in the workpiece or the grinding wheel using a split workpiece. In embedded thermocouples, a blind hole is drilled in the bottom of the workpiece and close to the surface, and then a double pole thermocouple is inserted or welded in the blind hole to measure the grinding temperature below the surface. The accuracy and reliability of obtained readings were proved by several authors when using this technique including [18], [97], [98], [99], [100]. In the second type, a thin foil is sandwiched between a split workpiece and the hot junction is formed during grinding in the micro-contact area between the film material and the wheel, thus allowing the direct measurement of surface temperature. Single-pole thermocouple compared

to double-poles, is easier to assemble as it utilises lower layers of mica strips and foil elements, which lead to a reduction in junction size. It also provides great reliability in signal response. Black [101] used a grindable single-pole thermocouple (K-foil RS256-130) arrangement when grinding ferrous metals, see Figure 2-22. This technique was also reported in the work of the following researchers [85], [100], [102]. A more recent study by Peng et al. [103] aimed to analytically estimate the heat partition into the workpiece when high-speed grinding of a nickel-based superalloy using a grindable K-type thermocouple (10-20μm thick) to measure the surface temperature. The thermocouple was sandwiched between two workpiece blocks in a pre-machined thin slot, insulated by thin mica films. The response time of foil-workpiece thermocouples is in the range of microseconds, while for the embedded one, the range lies in milli-seconds. Dehao [92] demonstrated that the foil-workpiece approach is susceptible to noise and that, under wet grinding conditions, its signal may not be reliable.

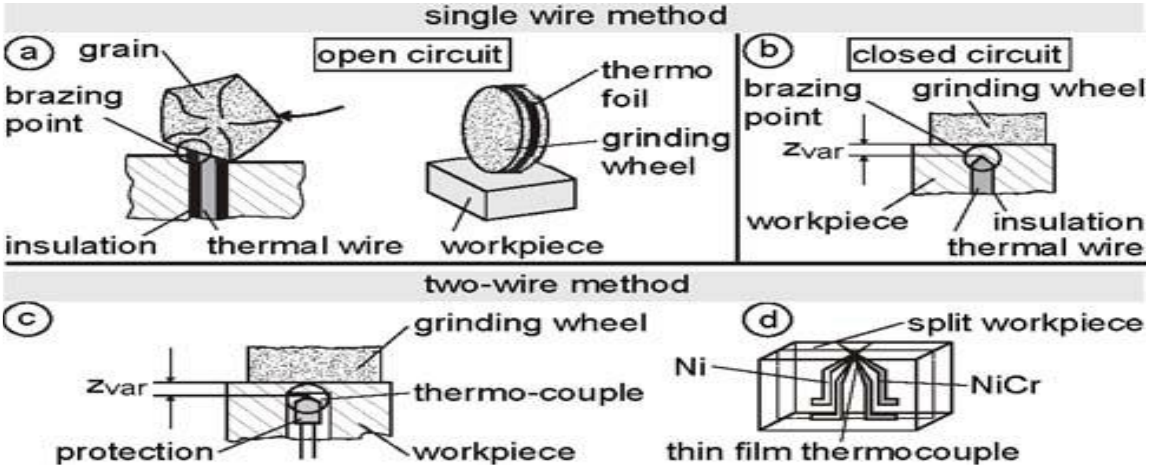


Figure 2-21: Different methods for implementation of thermocouples [89]

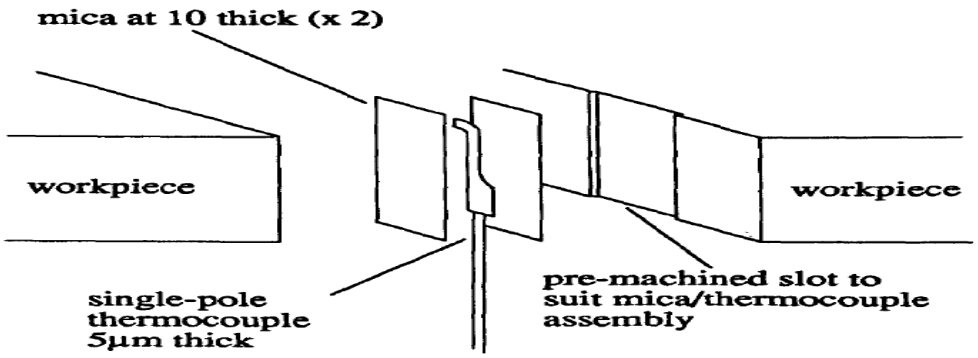


Figure 2-22: Thermocouples assembly by Black [101]

2.2.7 Grinding fluid application

Applying coolant in the grinding process is vital for surface finish and wheel life and is heavily demanded in creep feed grinding, owing to large depths of cut, long arc of contact, and very high thermal input associated with the process. Many studies concerning the application of fluid in grinding have reported that more than 90% of the generated heat during creep feed grinding can be carried out by coolant [14], [104]. Therefore, applying cutting fluid into the grinding zone is of significant importance. Cutting fluid in grinding serves four functions: cooling, lubricating, flushing and cleaning. It plays a critical role in the reduction of generated grinding energy as its lubricating properties reduce the amount of friction between the wheel and the workpiece. It also flushes away chips and abrasive particles which are responsible for wheel clogging up, leading to more rubbing and ploughing energies. According to Shaw [55], the use of coolant is the most crucial component of a successful creep feed grinding process. Coolant must be supplied in a way that provides uniform coverage of the wheel-work contact zone to ensure an effective reduction of the high contact temperatures produced in the grinding zone. Webster et al. [105] added that the application of fluid in the grinding process offers many benefits, such as lower dressing frequency, reduction of thermal damage, reduced misting and vapour problems, and reduced disturbance caused by the air barrier. Brinksmeier et al. [106] gave a demonstration of the primary effects of lubrication and cooling in the machining processes as a whole in Figure 2-23.

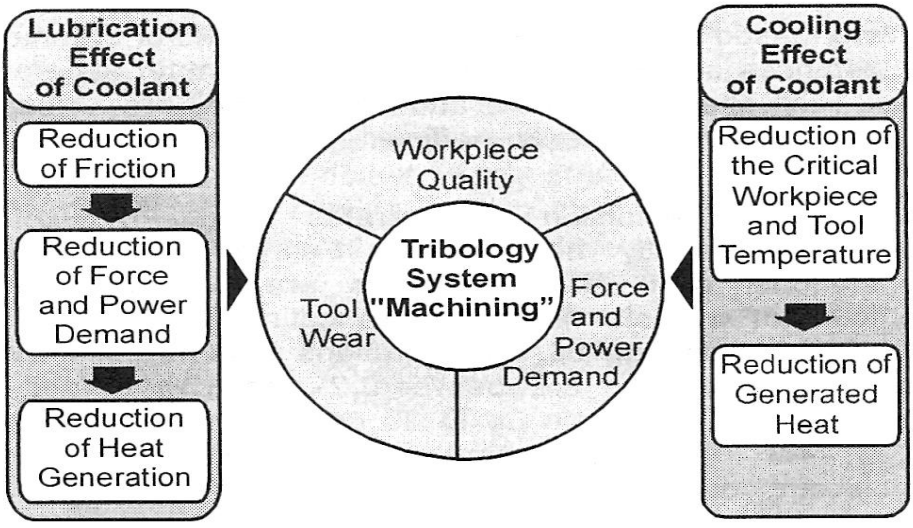


Figure 2-23: Effects of lubrication and cooling in the machining processes [106]

Cutting fluid employed in machining process can be divided into the following categories: gases, a mixture of gas and fluids, liquid fluids, and liquid fluids mixed with solid lubricants. In abrasive processes like grinding, liquid fluids are the most applied category, and these are further classified into the following groups: synthetics, semi-synthetics (2-30% petroleum oil), soluble oil (60-90% petroleum oil), and straight oil (100% petroleum oil) [107], [108]. Anti-wear, anti-corrosion or emulsifying agents are commonly combined in a base mixture of coolant to further enhance coolant properties. Synthetic fluids are oil-free lubricants that consist primarily of water-dissolved chemical lubricants and rust inhibitors (usually referred to as water-based fluid). Chemical lubricants such as amines, nitrites phosphates, glycol, and germicides are added to improve lubrication and friction reduction. Synthetics are non-flammable and offered as a concentrate that is combined with water to create the metalworking fluid. They can handle heavy-duty grinding and cutting operations on tough, hard-to-machine, and high-temperature alloys because of their wettability and superior cooling characteristics. Semi-synthetics are essentially a combination of synthetics and soluble oils, typically 2-30% oil in a water-dilutable concentrate. Semi-synthetics have similar benefits as synthetics in that they can be used in a variety of machining applications. However, adding oil molecules in a semi-synthetic mixture provides more lubricity than synthetic fluid. The main disadvantages associated with synthetics and semi-synthetic fluids are reduced lubrication compared to soluble and straight oil, misting, foaming, and dermatitis. Foam can prevent heat transfer by reducing the amount of fluid that comes into contact with the wheel and workpiece. Soluble oil and straight oil possess excellent lubricity and are generally performed in low-speed machining operations. The main limitations reported for oil-based coolants are poor heat dissipation and high fire risk [108], [109]. Characteristics rankings for the four types of liquid fluids are given by Irani et al. [109] in Table 2-9 (best is denoted by 4; worst is denoted by 1).

Table 2-9: Grinding fluid characteristics

Characteristic	Synthetics	Semi-synthetics	Soluble oil	Straight oil
Heat removal	4	3	2	1
Lubricity	1	2	3	4
Maintenance	3	2	1	4
Filterability	4	3	2	1
Environmental	4	3	2	1
Cost	4	3	2	1
Wheel life	1	2	3	4

The selection of an appropriate coolant type is important to ensure economical and high-performance operation. Moreover, operating conditions for grinding applications may largely vary from one to another, and as a result, variable cooling and lubrication need to be applied. Many authors studied the cooling effectiveness of oil and water when grinding. For instance, Ye and Pearce reported a lower wear rate for oil base coolant when creep feed grinding nickel-based alloy in comparison to water coolant, but surface burn was observed even at a low material removal rate when compared to water; they stated that oil is not suitable for creep feed grinding application due to poor heat dissipation of oil-based fluid [110]. Tsukuda and Yasui stated that burnout power flux is heavily influenced by the coolant type, as the boiling points of water and oil are extremely different (around 100°C for water; roughly more than 300°C for oil) [111]. Brinksmeier and his co-researchers reported that water-based coolant is not suitable for cBN wheels due to the chemical affinity between water and cubic boron nitride. They confirmed lower wheel wear and superior performance of oil application when grinding with cBN wheels [106]. They also noted that oil outperformed water-based fluids in terms of grinding forces, wear rate and grinding ratio, but yet no clear evidence for workpiece roughness and residual stress was observed. Better cooling effectiveness of water-based coolant over oil-based coolant was reported by Wang and Kou, they used a finite difference approach to investigate the cooling effectiveness of both oil and water coolants and suggested that water coolant is more suitable for creep feed grinding [112]. In dry grinding of mild steel by Chattopadhyay and Hinetermann [113], loading of the grinding wheel was noticed after the grinding process. The grinding wheel topography was damaged by the loaded particles, which also increased the tangential force as they rubbed against the workpiece surface. Delivering water-based grinding fluid resulted in reducing the amount of loading that was visible, and as a result, the forces were reduced. In a study by Campbell, a comparison of oil and water when creep feed grinding Ti-6Al-4V was carried out, grinding performance of both coolants was compared in terms of residual stress, specific energy, power flux, and microstructure. Campbell's major findings were that oil grinding produced the maximum compressive residual stresses while lower specific energy and power flux were observed in water grinding [114]. Regardless of the reported preferred compressive residual stresses and better surface finish of oil grinding applications in the literature, it is recently being replaced by water-based coolant due to environmental concerns, such as the high risk of fire. Although special care must be taken when operating with water-based coolant, the machine needs to be completely enclosed to prevent floor contamination and atmospheric mist. Another imperative point when using water-based fluids is the fluid film boiling temperature. This occurs at a temperature of about

120°C, causing the coolant solution to evaporate and consequently leading to a considerable reduction in the heat transfer coefficient between the workpiece and the coolant.

In order to achieve a maximum cooling effect, an appropriate injection of the fluid into the grinding area at an adequate flow rate is required. Factors to be considered for maximum cooling effectiveness are wheel speed, wheel properties, jet position, and geometry of grinding assembly. In the published literature, the maximum useful coolant flow rate in grinding is assumed to be 50% of the surface pore space of the wheel. Thus, higher porosity wheels offer a more cooling effect compared to lower porosity wheels. There is a common agreement between several authors that matching nozzle jet velocity to wheel velocity can significantly increase useful coolant flowrate [115], [116]. Nozzles and diffusers are used to supply the coolant to the contact zone with different configurations, as illustrated in Figure 2-24 [106].

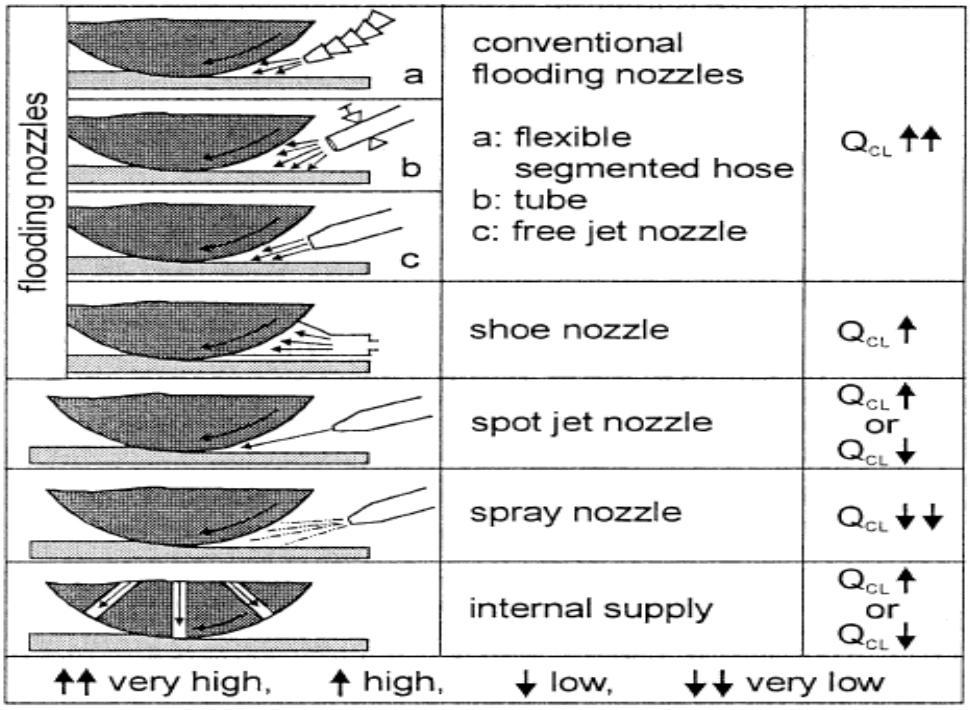


Figure 2-24: Coolant supply methods [106]

The shoe nozzle and free jet nozzle are the most commonly employed methods. The shoe nozzle delivers fluid at low pressure across a large area of contact; the main limitation of this method is the frequent adjustment of the position of the nozzle as the wheel wears. Another reported drawback of the shoe nozzle is that it is restricted to low-speed grinding applications because low-pressure fluid delivered by the shoe nozzle is not able to penetrate the air barrier

formed at the periphery of the grinding wheel. This barrier is a major problem associated with coolant application. It prevents the flow of coolant onto the contact area, resulting in less effective cooling. The influence of the air barrier is shown in Figure 2.25 [106]. This barrier is a combination of two airflows, the first is the airflow in the circumferential direction, and the second is the induced air into the wheel direction by the centrifugal force of wheel rotational speed. A scraper is a simple method to reduce the effect of the air barrier boundary and is fitted close to the wheel surface. Providing a second jet nozzle (high-pressure nozzle) close to the grinding wheel proximity can control the development of an air barrier [105]. Employing a free jet nozzle for delivering coolant can overcome the momentum of this barrier as fluid is supplied with a high velocity enough to penetrate the boundary layer of air. Free jet nozzles can provide accurate matching of fluid velocity to wheel velocity as well as cleaning the wheel and removing adhered material. Irani et al. [109] reviewed all means of cutting fluid application, the authors noted that out of the techniques presented, the coherent jet, developed by Webster and his co-researcher [105], [117] is the most practical for industry. Irani et al. [109] also addressed that the popularity of these jets has increased significantly over time due to their excellent performance in a range of circumstances.

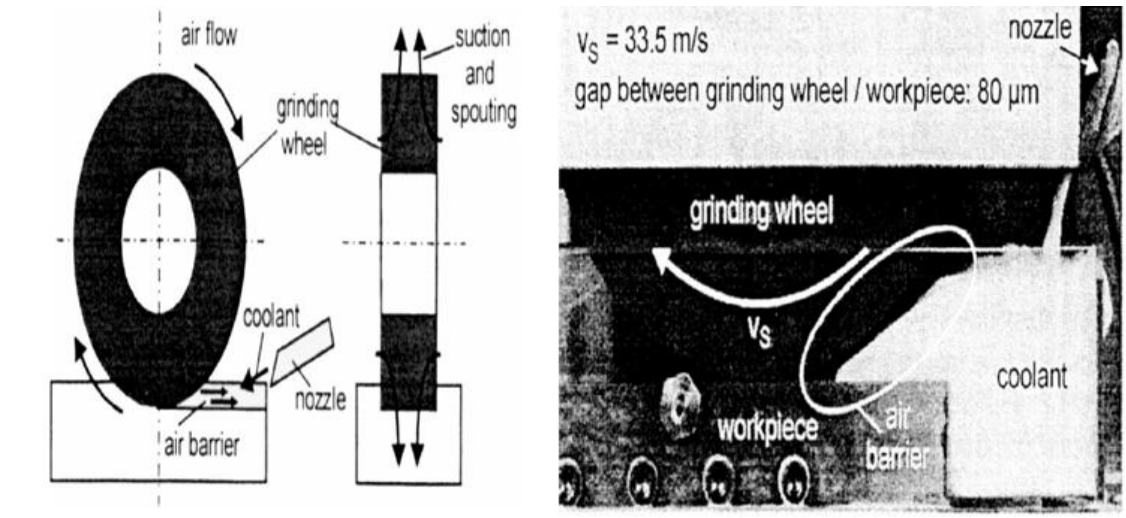


Figure 2-25: Influence of air barrier on grinding coolant [106]

Advances in cooling techniques are more recently reported in several review papers. Pimenov et al. [118] published a comprehensive review of the most recent cooling strategies used when machining titanium alloys. It describes how the type of cooling delivery affects surface

roughness, tool wear, tool life, temperature, cutting forces in milling, drilling, turning and grinding. The paper extensively reviews dry cutting, flooding cooling system, minimum quantity lubricant, high pressure coolant and finally cryogenic coolant strategies. Pervaiz et al. [119] detailed the most current numerical and experimental advancements made using the minimum quantity lubrication (MQL) and minimum quantity cooling lubrication (MQCL) supported approaches when machining titanium alloys. A thorough understanding of the main advantages, drawbacks, and mechanisms of cooling methods based on MQL and MQCL from a sustainable perspective is detailed by Sen et al. [120] and Singh et al. [108]. MQL and MQCL are the most significant spray nozzle strategies, and it has been demonstrated in some instances that they offer effective lubrication. However, it is still unclear how beneficial these techniques will be for grinding, particularly in creep feed grinding of titanium superalloys. Grinding with liquid nitrogen cryogenic cooling and minimum quantity lubrication (MQL) with oil supplied as a spot jet or spray mist are alternative methods for achieving a sustainable process with less harm to the environment and worker health. The majority of cutting fluids are non-biodegradable and serve as breeding grounds for bacteria that are dangerous to machine operators. In addition, cutting fluids have also been linked to dermatitis and respiratory problems when coming into direct contact with the operator or inhaled. Moreover, the disposal process of waste coolant in the flooding process is costly and poses huge environmental hazards. These factors have promoted the application of dry cutting, minimum quantity lubricant, and cryogenic coolant strategies.

Singh et al. [108] presented work related to applying minimum quantity lubrication in grinding for steel, titanium grade 5, Inconel-751, and carbon fibre-reinforced ceramic matrix. Although results, in some instances, showed better performance of MQL compared to dry and conventional grinding, the studies were limited to very small depths of cut (5µm-50µm). Fernandes et al. [121] evaluated MQL and conventional cooling when surface grinding AISI 4340 steels, they found that traditional cooling was superior to MQL since workpieces did not suffer thermally-induced damage. They also asserted that there was a clogging issue on the grinding wheel surface during MQL. Lopes et al. [122] compared the performance of conventional flood cooling and MQL in plunge cylindrical grinding of alumina. The lowest surface roughness was achieved by conventional flood cooling (0.60µm compared to 0.80µm for MQL). In terms of grinding quality indicators, Rodriguez et al. [123] found that flood cooling was superior to the MQL application. Despite the superior surface quality, friction coefficient, temperature, and force provided by the latter when compared to dry cutting, it is

still lagging behind the former, particularly in grinding specific materials like hardened alloys. An overview of the recent advances in the high-performance cutting of aerospace alloys was presented by M'Saoubi [124]. The performance of cooling strategies on surface integrity characteristics of difficult-to-machine materials such as nickel-based alloys, titanium, and composites was discussed. The authors assert the difficulties of implementing dry or MQL cooling strategies in many instances as a result of the high mechanical and thermal loads in the cutting of various aerospace alloys with low thermal conductivity.

2.3 Workpiece surface topography and integrity

2.3.1 Surface topography

The real surfaces of machined objects are not fully flat or smooth. They consist of numerous very little uneven peaks and valleys or a combination of different types of irregularities with different magnitudes. Figure 2-26 shows surface topography/texture components, which are roughness, waviness, and error of form. The total profile of any machined surface is the combined effect of these components, with each component having different wavelengths. Surface roughness is the term used to describe the tiny, closely spaced variations from the nominal surface. The surface is considered rough if these variations are large and smooth if they are minimal. Surface roughness is usually referred to as surface finish, and it has a significant effect on part functional performance, such as lubrication, wear, and fatigue [125].

Roughness is generally produced from the cutting action between the tool and the workpiece; hence, the effects of workpiece structure and machining processes are predominant. Waviness has longer wavelengths than roughness and generally results from the machine or cutting tool vibration, run out, deflection or chatter marks on the workpiece. Deviations from the ideal surface shape are characterized by the error form and are caused by the vibration of the machine or thermal distortions. One more evident feature on the machined surface is the lay. It represents the dominant direction of surface pattern on the machined surface and largely depends on the production method [126], [127]. All of the aforementioned topographic features are sometimes accompanied by unintended abnormalities or defects, such as deposits, cracks, scratches, and holes.

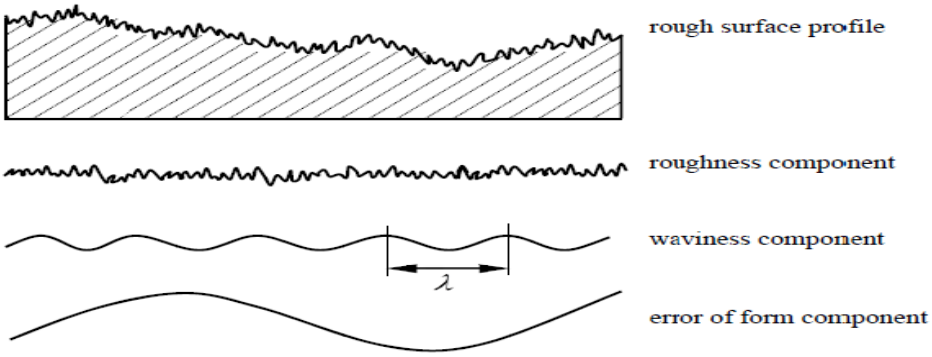


Figure 2-26: Surface topography components [126], [127], [128]

Profilometry is the oldest and most common way to describe the topography of a surface. In this contact method, a stylus is used to draw a 2D profile of the surface, which is then analysed using standard mathematical methods to get a set of parameters. Other utilised non-contact techniques for roughness measurement include optical instruments and scanning microscopes [129]. When the surface topography is quantified, it is frequently only the roughness that is analysed, with the waviness and form error or shape being removed from the recorded data electrically, mechanically, or digitally [130]. The basic technique for separating surface roughness frequency from other components' frequencies is filtering technology. The evolution of digital filters in the application of surface roughness, in addition to the benefits and limitations of their respective performances, are detailed in [131].

Numerous parameters have been developed since the early work to quantify surface topography; many countries have developed their own standards for measuring and characterising surface roughness. However, most of these national standards were based on the mean-line system adopted and proposed by ANSI/ASME B46.1-1988 [132], as a result a lot of similarities with respect to calculating surface roughness parameters were evident. This explains why they have developed into generally accepted and acknowledged parameters in the manufacturing industry and were later adopted by the International Organization for Standardization (ISO). ISO discarded some parameters, redefined others and also created a number of global standards for the measurement and assessment of 2D surface roughness, including ISO 4287, ISO 13565-2 and ISO 12085 [133], [134], [135]. Depending on specific aspects of the profile, 2D roughness parameters can be classified as either amplitude parameters, spatial parameters or hybrid parameters. Table 2-10 provides the standard definitions and numerical equations for some 2D surface roughness amplitude parameters. Ra

is one of the most widely employed measures for average surface roughness. It is defined, according to ISO, as the arithmetic mean deviation of the assessed surface profile over a sampling length. As opposed to Ra, 2D amplitude parameters Rt, Rz, Rp, and Rv measure extreme deviations rather than the average along the sampling length. R_t is defined as the total height of the profile, while R_z is defined as the average value of the five highest peaks and the five lowest valleys within the sampling length. There are also other reported amplitude parameters that can be estimated to further help in defining the surface topography. For instance, surface kurtosis Rku and surface skewness Rsk. Graphical representations of Ra, Rz and Rt are illustrated in Figure 2-27. Sampling length and evaluation length are noted by 'lr' and 'ln', respectively. The evaluation length is introduced to account for the effect of undulation of micro asperities over one sampling length; commonly, it consists of 5 consecutive sampling lengths. This ensures that the measured values of surface roughness can accurately reflect the measured surface characteristics. The recommended measurement series of sampling length in ISO standards are 0.08mm, 0.25mm, 0.8mm, 2.5mm, 8mm and 25mm. The optimal value is decided by either the accuracy of the measuring instruments or the wavelength of the surface being measured.

Table 2-10: 2D surface roughness amplitude parameters [125], [128], [133]

2D amplitude parameters		
Denotation	**Name**	**Remark**
R_a	Arithmetic average roughness	$R_a = \frac{1}{SL}\int_0^L \lvert z(x)\rvert dx = \frac{1}{N}\sum_{i=1}^{N}\lvert z(x_i)\rvert$
R_q	Root-mean-square roughness	$R_q = \sqrt{\frac{1}{SL}\int_0^L [z(x)]^2 dx} = \sqrt{\frac{1}{n}\sum_{i=1}^{n} z(x_i)^2}$
R_t	Max peak-to-valley height	$R_t = \lvert z(x_i)_{\max} - z(x_j)_{\min}\rvert$
R_z	Ten-points height	$R_z = \frac{1}{5}\left[\sum_{i=1}^{5} z(x_i)_{\max} + \sum_{j=1}^{5}\lvert z(x_j)_{\min}\rvert\right]$
R_p	Max peak height	distance from the highest peak to mean line
R_v	Max valley depth	distance from the deepest valley to mean line

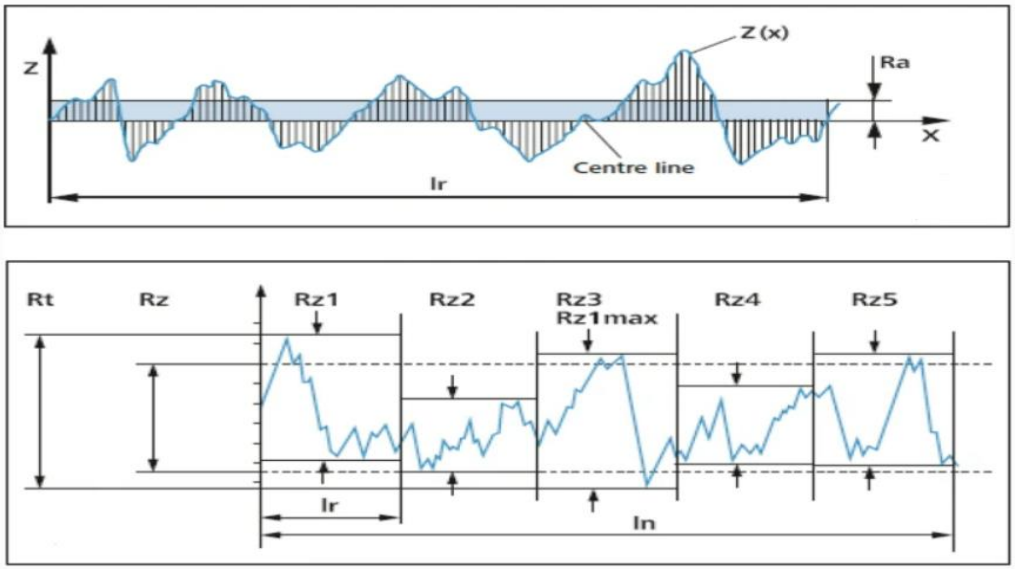


Figure 2-27: 2D surface parameters Ra, Rz and Rt [133], [136]

The 2D profilometry method of surface characterisation has proven to be highly effective in practical applications and facilitating interaction between production and quality control. But it could not fully characterise and reflect the practical surface geometrical features and behaviour of machined parts for a specific application [15], [16]. Thus, the necessity of a three-dimensional approach (3D) to surface characterization in order to fully understand the relationship between surface topography and functional performance has become increasingly apparent. In this approach, surface topography/texture parameters are measured over an area instead of one trace across the surface. One major benefit of 3D surface evaluation is that it integrates visualisation with a parameterization for defining surface texture, which allows a more realistic representation of machined surface features. The first recognised 3D characterisation standards were developed in 1993 by Prof. Stout and his research group at the University of Birmingham, then were revised later to include a set of 14 3D parameters and were called Birmingham Fourteen (B14) [137]. Most of these parameters were included and established the foundation of the new ISO 25178 standards for 3D surface topography [138]. Some 3D surface roughness parameters are presented in Table 2-11. 3D parameters are essentially the extensions of 2D parameters, denoted by S instead of R, to imply that the calculations were performed over an area. More details of 3D surface characteristic parameters and definitions can be found in [128]. Practical and effective means to implement accurate characterization and correlation of functionality-related properties with surface texture

parameters and specific characteristics of machined components were reported by Zeng et al. [139] when turning and grinding Ni-based superalloy GH4169.

Table 2-11: 3D surface roughness parameters [138], [140]

Name	Symbol	Equation
Arithmetical mean height (μm)	S_a	$\frac{1}{A}\iint_A \lvert z(x,y)\rvert dxdy$
Root mean square height (μm)	S_q	$\sqrt{\frac{1}{A}\iint_A z^2(x,y)dxdy}$
Skewness	S_{sk}	$\frac{1}{S_q^3}\frac{1}{A}\iint_A z^3(x,y)dxdy$
Kurtosis	S_{ku}	$\frac{1}{S_q^4}\frac{1}{A}\iint_A z^4(x,y)dxdy$
Maximum peak to valley height (μm)	S_z	$\max_{x,y\in A} z(x,y) - \min_{x,y\in A} z(x,y)$
Root mean square gradient	S_{dq}	$\sqrt{\frac{1}{A}\iint_A \left[\left(\frac{\partial z(x,y)}{\partial x}\right)^2 + \left(\frac{\partial z(x,y)}{\partial y}\right)^2\right] dxdy}$
Developed interfacial area ratio	S_{dr}	$\frac{1}{A}\left[\iint_A \left(\sqrt{\left[1 + \left(\frac{\partial z(x,y)}{\partial x}\right)^2 + \left(\frac{\partial z(x,y)}{\partial y}\right)^2\right]} - 1\right) dxdy\right]$

2.3.2 Surface integrity

The term surface integrity is used to characterise the inherent relationships between the machining process, surface geometrical and subsurface metallurgical properties on the resulting functional performance. This term was first introduced by Field and Kahles as “the inherent or enhanced condition produced in a machining or other surface generation operation” [141] Griffiths described it as “the topographical, mechanical, chemical and metallurgical 'worth' of a manufactured surface and its relationship to functional performance from the point of view of surface quality and machining process control” [125]. Surface integrity has become a crucial factor in order to meet the ever-increasing demands placed on the performance, reliability and durability of complex components, particularly those found in aerospace industry. Surface integrity involves the study of surface alterations produced by the machining process. These alterations, including recrystallisation, tears, laps, residual stress, and embrittlement, have proven detrimental to product functional performance (fatigue, creep, corrosion and wear resistance). High temperature generated during the machining process, plastic deformation, and chemical reactions between the workpiece material and the cutting tool are the main causes of these alterations [142].

In 1972, Field and Kahles introduced a paradigm for the characterization and assessment of surface integrity; they established three sets of integrity data based on the depth of details required, as shown in Table 2-12. The table also details typical surface integrity defects induced by machining processes. They describe the necessary tests to offer adequate information on surface integrity. Their work served as the basis for the establishment of the American National Standard of Surface Integrity (ANSI B211.1) [143]. The minimum integrity data set primarily focuses on the metallographic information and microhardness measurements. The standard integrity data set involves fatigue and residual stress tests in addition to the completion of the minimum data set. For critical application, the extended data set is performed, which involve completing the standard data sets and more mechanical test, such as stress rupture, fracture toughness, bearing performance and creep. Machinability research on titanium and nickel superalloys heavily relied on the minimum integrity data set as it is the least expensive to perform [7].

Table 2-12: Integrity data sets description [7], [141]

Minimum surface integrity data sets	Surface texture	-Roughness measurement. -Lay designation or photo. -SEM images at increasing magnifications.
	Macrostructure (10x or less)	-Macrocracks or surface imperfections -Macroetch imperfections -Chemical etchant tests
	Microstructure (at 100x)	-Microcracks -Plastic deformation -Phase transformations -Intergranular attack -Pits, tears, laps and protrusions -Built-up edge -Melted and deposited layers -Selective etching -Metallurgical transformations
	Microhardness alterations	Heat affected zones Plastic deformation or work hardened zones
Standard Surface Integrity Data Set	-Minimum surface integrity data set -Residual stress profile -Fatigue tests (screening only using full reverse bending at room -Temperature using tapered area flat specimens	
Extended Surface Integrity Data Set	Standard surface integrity data set Fatigue tests – statistical data to established design Stress corrosion tests at selected environmental conditions	
	Additional mechanical testing	-Tensile -Stress rupture -Creep -Specialised: friction, wear, sealing, -bearing performance -Fracture toughness -Low cycle fatigue -Elevated or cryogenic temperature -Crack propagation -Surface chemistry

The machined workpiece is subjected to several evaluation techniques to examine the influence of the machining process on the workpiece properties as well as the damage introduced to the workpiece surface. These techniques are categorised into destructive and non-destructive methods. A comprehensive list of techniques used to detect surface inhomogeneities is given in Appendix C. Visual inspection is the most employed method to evaluate surface defects such as cracks/macrocracks. However, some embedded imperfections like plastic deformation, tears, pits, etc., cannot be detected with this method. Consequently, it is advisable to employ dye penetrants and magnetic particles, which have proven to be superior in detecting minor defects and microcracks. In addition, some techniques provide insights into the microstructural alterations of the machined surface and subsurface but require sectioning, mounting, polishing and etching of the examined specimens. For instance, variations in microhardness and phase transformation can only be determined once the specimen is sectioned, mounted and polished.

Ulutan and Ozel provided an overview of the most prevalent machining-induced surface integrity imperfections in nickel and titanium alloys. Among them are the white layer surface, hardening layer, residual stresses and microstructural alterations. Ulutan and Ozel also summarized many researchers work in investigating the relationships between inputs and outputs parameters for different machining processes using experimental results. The review has shown that there is a general consensus that input operating parameters (cutting speed, feed, depth of cut, tool properties and workpiece properties) have a significant and direct effect on output parameters, in particular, roughness, microhardness and residual stresses [144].

The hardness/microhardness of the machined specimen can alter due to thermal, mechanical, or chemical changes, resulting in greater hardness at the surface and near the surface compared to the bulk of the material and up to 200-500µm deep into the bulk material. Microhardness values are determined by applying a load of an order of 5 to 100g to produce indentations in the range of 10-500µm. The hardness value can be given either with Knoop or Vickers diamond indenter. The former has been reported to have more accuracy than the latter due to smaller indentation depth and longer diagonal length [4].

Residual stresses are either tensile or compressive stresses that remain in the component after being machined, resulting from thermal effects, plastic deformation and chemical reactions involved in the machining process. The mechanical load tends to produce compressive residual stress and a work-hardening layer through the deformation of grains, while the thermal loads have a tendency to produce residual tensile stresses and a lower microhardness value/

softening. Tensile residual stresses have a significant impact on material fatigue, creep and fracture resistance and usually result in crack initiation. Machining post-processes, such as heat treatment, lapping, and shot peening, are often applied subsequently in order to minimise residual stresses. X-ray diffraction and hole-drilling are the most commonly used techniques to assess residual stresses [145]. Bentley used a modified version (by Rolls Royce) of the blind-hole drilling technique as a mean to measure the residual stresses on ground Ti-45Al-2Mn-2Nb+0.8 Vol% TiB_2 [17]. Xi et al. utilised the X-ray method to measure produced residual stresses when creep feed grinding gamma titanium aluminide intermetallic [18].

Fatigue failure is caused when a metal is subjected to repetitive or fluctuating stress (cyclic loads) that leads to localized damage and initiates crack and eventually failure. The material can deteriorate or degrade at stresses that are lower than its ultimate tensile stress limit. There are two main types of fatigue: low-cycle fatigue and high-cycle fatigue. Both low and high-cycle fatigue account for around 60% of the total failures in aircraft components, with the latter being the most prominent cause [146], [147].

Fatigue test is performed by applying axial loading, bending or torsion test at a number of cycles per minute. Test stress is sinusoidal with a constant amplitude, and results are presented in (S-N) curve. This curve shows the number of cycles required to failure at different magnitudes of cyclic stresses. Figure 2-28 demonstrates a typical S-N curve for mild steel and aluminium alloy. The fatigue limit indicated on the mild steel curve represents the stress limit below which material can undergo an infinite number of cycles without failure. Wang conducted a fatigue test using a tension test at a stress ratio R=0 and 25Hz wave frequency when grinding Ti-6Al-4V [56]. Bentley used a four-point bend test in order to develop a fatigue life (S-N) curve for Ti-45Al-2Mn-2Nb+0.8 Vol% TiB_2 with frequencies of 70-100Hz, stress ratio R=0.1 and 1.2×10^7 run out cycles [17]. Li et al. applied low cycle tension-compression fatigue testing with 0.1 cyclic fatigue ratio following high speed grinding of Inconel 718 and Ti-6Al-4V workpieces with cBN electroplated wheel [148]. Novovic et al. performed fatigue tests at room temperature, at a frequency of 75 Hz and a stress ratio R of 0.1 on burn-resistant titanium alloy (Ti–25V–15Cr–2Al–0.2C wt%) to study the influence of surface and subsurface conditions on fatigue life for three machining processes [149]. All aforementioned work suggested that residual stresses and metallurgical conditions of the machined surface play an important role in fatigue life.

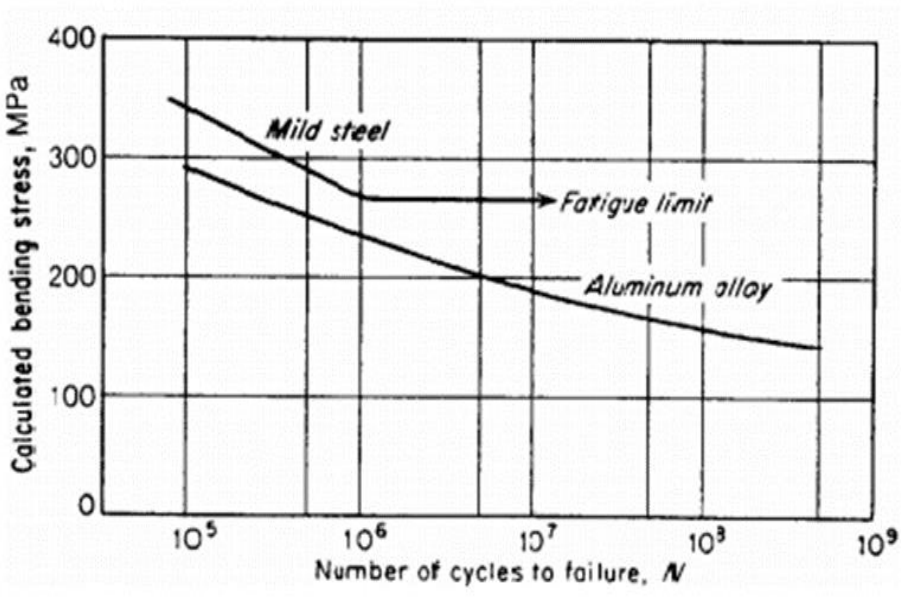


Figure 2-28: S-N curve for mild steel and aluminum alloy [17], [150]

2.4 Experimental design techniques

Experimental design is a statistical method used to investigate the effects of single or multiple variables in an experiment on the overall performance. These variables are referred to as factors. Machining/grinding processes of aerospace materials involve many factors, each at different levels. Testing of all factors will require a large volume of experiments; therefore, an experimental design is essential in order to control experiment variables, optimise cutting parameters and reduce the number of trials required in an experiment. Hence reducing the time and expense associated with conducting machinability testing. The traditional applied experimental design is the one factor at a time (OFAT); here, only one factor is changed and tested while other factors are kept constant. However, in engineering applications where many factors considerably influence the overall result, this approach is not efficient and only limited to applications with a few factors. Full factorial, fractional factorial orthogonal arrays and Taguchi experiments are commonly used techniques for experimental design [151]. According to British standards on statistical terminology, a full factorial is defined as ‘an experiment in which all possible treatments formed from two or more factors, each being studied at two or more levels, are examined so that interactions as well as main effects can be estimated’. In order to reduce the size of the experimental design, a fractional factorial is used instead and is defined as ‘a factorial experiment in which only an adequately chosen fraction of the treatments

required for the complete factorial experiment is selected to be run' [152]. It can be used to analyse systems with a greater number of factors but at the expense of reduced information on the interactions between variables. Taguchi's orthogonal array is commonly applied when a minimum number of tests is required, generally for screening tests. It has the ability to identify the key factors affecting the result; assuming the data is normally distributed and the first and second-order interactions are insignificant, then these factors can be evaluated further in larger arrays. Experimental designs for either screening tests or fully factorial arrays have three main phases: (a) planning and identifying experiments of factors and levels, (b) conducting experiments and collection of results, and (c) statistical analysis of data to identify significant factors [151].

These experimental design techniques have been extensively employed in the literature for multiple machining/grinding processes to study the correlation between operating parameters and produced cutting forces, temperature, surface integrity, etc. For instance, Bentley used L_{12} orthogonal arrays to identify significant factors when surface grinding (45-2-2+0.8). Fixed factors in his design were wheel profile, bond type, dresser type and cutting fluid application, whilst material, grit size, wheel grade, wheel porosity, wheel speed, depth of cut, feed rate and cutting fluid type are variable factors. His findings showed that grit type, grit size, and wheel grade are not statistically significant on the measured outputs in his design [17]. Hood applied L_9 Taguchi fractional factorial orthogonal array when creep feed grinding gamma titanium aluminide and burn-resistant titanium alloy with silicon carbide wheels. He evaluated the effects of different operating parameters on wheel wear, forces, specific energy, and surface roughness. Three factors each at three levels were selected. Only wheel speed was statistically significant at the 5% level when evaluating maximum normal force for burn-resistant titanium alloy, and for the titanium aluminide alloy depth of cut was proved significant in terms of maximum power with a contribution percentage ratio of 75% [24]. A full factorial experimental array comprising 18 trials was conducted by Bhaduri et al. involving three factors (wheel speed, table speed and ultrasonic vibration) to study the influence of applying ultrasonic vibration when creep feed grinding Inconel 718 with an alumina-based grinding wheel (POROS 2), reductions in vertical force and horizontal force of up to 23% and 43%, respectively were observed in his study [153].

2.5 Grinding of advanced titanium alloys

Early work on grinding of titanium alloys began in 1950s by Tarasov [154], he noted in his work that chemical affinity between titanium and abrasives caused difficulties in the grinding process. He later focused on optimising the wheel specification for alumina grit wheels, findings showed improved grinding efficiency with increasing wheel hardness. Yang and Shaw, in expanding on Tarasov's work, demonstrated that grinding titanium and titanium alloys with aluminium oxide (Al_2O_3) and silicon carbide (SiC) wheels was possible with the use of inorganic water-soluble coolants and more friability of grits gave better performance [155]. Subsequent work in the 1960s, 1970s and 1980s focused on shallow grinding of conventional titanium alloys with conventional wheels to investigate the following aspects: the effect of the coolant system on residual stress [156], optimum fatigue life operating conditions [157], Saturation of surface layer [158], and interactions between the abrasive tool and the workpiece in different atmospheres (air and argon) [159].

Sagarda [160] was the first to report the use of super-abrasives in grinding of titanium, he examined the rate of wheel wear when grinding steels and titanium alloys with diamond and cubic boron nitride (cBN) wheels, results showed that diamond wheel exhibited a substantially lower rate of wear, with grit fracture being the major wear mechanism. In a further study in the use of super-abrasive wheels, Kumagai et al. [161], [162] applied a high-pressure soluble coolant jet (2MPa) to grind Ti-6Al-4V with a resin bonded diamond wheel. Increasing the jet pressure resulted in high compressive residual stresses and improved the grinding ratio, surface roughness and grinding temperature. It was suggested that applying high jet pressure prevented wheel loading and offered better cooling efficiency. He later investigated the effect of grain size on the overall grinding performance when grinding Ti-6Al-4V with diamond wheels together with a high-pressure jet. He concluded that fine-grain wheels are not effective for high removal rates and smaller grains are more likely to produce rough surfaces [163]. Kumar studied the grinding performance and wear rates when grinding Ti-6Al-4V with different friability cBN, diamond and vitrified SiC wheels by utilising two cooling nozzles and one cleaning nozzle. Findings indicated poor performance of cBN in comparison to diamond when grinding Ti-6Al-4V, this is due to larger propensity for chemical interaction between cBN and Ti-6Al-4V. Findings also showed better performance of medium tough diamond abrasive when compared to low toughness abrasives [164].

The creep feed grinding of titanium was initially reported by Silin when operating at wheel speed 27m/s, 1.5mm depth of cut and 70mm/min feed rate to produce fir tree root in OT4 titanium alloy. Grinding forces and temperature were evaluated in his work using black and green SiC wheels in both up and down grinding. Temperature recorded in down grinding were ~50% lower than those in up grinding. Moreover, grinding a different composition titanium alloy with higher tensile strength under the same conditions increased both forces and temperature [165]. Down-mode creep feed grinding with a diamond wheel was further examined for the alpha-beta titanium alloy Ti-6Al-4V by Campbell. A fractional factorial designed experiment was used to compare the performance of surface grinding and creep feed grinding using petroleum oil. Statistical analysis results for specific energy for employed grinding conditions revealed that wheel speed was the most influential factor, followed by abrasive grit size, feed rate, and grinding mode [166]. Nosenko also ground two distinct titanium alloys in creep feed mode using SiC grinding wheels of varying grit sizes and various types of coolant, according to the findings, a burn-free surface can be achieved by using wheels with a higher porosity [167]. Most recent published work on grinding of Ti-6Al-4V paid more attention to surface grinding rather than creep feed grinding; these covered the following aspects: surface grinding with SiC [168], [169], surface grinding using nano lubrication [170], [171], surface grinding with super-abrasive wheels [172], [173], [174], [175], [176], [177]. Whilst the only published work that could be found in creep feed grinding of Ti-6Al-4V is given in [178], [179], [180]. Key findings reported in the aforementioned studies are presented later in Chapter 4 (Section 4.3).

Grinding of titanium aluminide (TiAl) alloys was first documented by Nolan. His work involved grinding of TiAl, Inconel 718 and nickel aluminides with resin-bonded diamond wheel operating at 25m/s wheel speed, 15.2m/min feed rate, and 5-50µm depth of cut. According to findings, TiAl was substantially easier to grind than 718 in terms of wheel wear and power. Out of the three ground materials, TiAl had the highest grinding ratio [181]. The feasibility of creep feed grinding XD-modified gamma TiAl with conventional abrasive wheels was evaluated in a preliminary investigation [182]. The study aimed at identifying the impact of altering dresser infeed rate, depth of cut, table speed and wheel speed on the overall performance of the grinding process; results revealed that during the continuous dressing cycle, depths of cut of 2-3mm on a 25m slot could be achieved at table speeds of 200-300mm/min and dresser infeed speeds of 0.8–1.2µm/rev. Zhang et al. used alumina, SiC, diamond, and cBN wheels to further examine the impact of creep feed grinding on the surface integrity of 45-2-

2+0.8. The main reported findings include observed hardened layers with values generally reaching 700$HV_{0.025}$ and extending to a depth of 50µm below the surface and high tensile residual stresses in all samples [183]. However, it was difficult to evaluate the performance of a given wheel or operating parameters as the work was not subjected to an experimental design and no wheel wear and other output measures data were provided.

Later research by Bentley aimed to extend the work of Zhang using statistical experimental designs for surface and creep feed grinding of gamma titanium aluminide (45-2-2+0.8) manufactured by Rolls Royce. The work also involved surface grinding of two more titanium aluminides and Ti-6Al-4V. Two L_{12} fractional factorial designs were utilised for conventional and super-abrasive wheels (one for each wheel type) to examine the effect of operating parameters on peak current, normal and tangential forces, workpiece surface roughness and surface integrity. Fixed and variable factors used in the experimental designs are illustrated in Table 2-13 and Table 2-14, respectively [17]. During super-abrasive trials, 6 out of 12 tests could not be performed successfully due to spindle stall. A lack of machine rigidity and low wheel speeds were believed to be the main causes. As a result, a further L_8 factorial design was used at the higher wheel speeds. The normal and tangential forces in the conventional abrasive testing ranged from 200 to 4500N and 100 to 1000N, respectively. Workpiece surface roughness ranged from 0.25-1.25µm. Analysis of variance indicated the dressing method as statistically significant for the output measures. Indeed, lower values were achieved when applying continuous dressing with no spindle stall as opposed to those that occurred when intermittent dressing (2 tests). Meanwhile, in super-abrasive trials, normal force ranged from 140-4500N, tangential forces from 200-900N and workpiece surface roughness from 0.5-1.2µm. Surface integrity analysis in both cases revealed cracks on burned ground surfaces, deformed lamellae to a depth of 30µm below the surface, and surface hardening extending to 100µm below the surface. Lower depth of cut, higher grit concentrations, and higher wheel speeds were found to reduce the magnitude of the hardened layer. The residual stresses were measured using the blind hole drilling method; the stresses were compressive in the longitudinal direction with values reaching 600MPa and tensile of up to 700MPa in the traverse direction. The amplitude of both stresses was much reduced when a spring back pass was applied. Bentley also states that in the case of conventional wheel creep feed grinding, a reduction in chatter was achieved by the use of jet-cutting fluid delivery in addition to continuous dressing, whilst in the case of a super-abrasive wheel, the chatter was less apparent with lower depth of cut and the use of diamond grit instead of cBN grit [17].

Table 2-13: Fixed and variables factors and levels for conventional wheel (SiC) by Bentley [17]

	Fixed factor	**Level**	
Workpiece	Material	45-2-2+0.8	
Wheel	Bond type	Vitrified	
	Profile	Plain	
	Diameter (mm)	400	
	Width (mm)	25	
Operation	Wheel direction	Down	
Dressing	Dressing type	Continuous	
	Dresser type	Diamond wheel crush	
	Dresser speed	+0.7 x speed of grinding wheel	
	Dresser feed rate ($\mu m\ rev^{-1}$)	1.5	
Cutting fluid	Type	Soluble oil	
	Flow rate (ls^{-1})	5	
	Variable factor	**Level**	
Grinding Wheel	Grit Size (mesh)	A	46 / 80
	Grade	B	F / J
	Structure	C	18 - 30
Operation	Wheel Speed (ms^{-1})	D	15 / 30
	Depth of Cut (mm)	E	1 / 4
	Workpiece feedrate ($mm\ min^{-1}$)	F	150 / 600
Dressing	Dressing method	G	Intermittent / Continuous
Cutting fluid	Cutting fluid Application	H	Jet / Shoe

Table 2-14: Fixed and variables factors and levels for diamond and cBN wheels by Bentley [17]

	Fixed factor	**Level**	
Workpiece	Material	45-2-2+0.8	
Grinding Wheel	Profile	Plain	
	Diameter (mm)	100	
	Width (mm)	25	
Operation	Wheel direction	Down	
Cutting fluid	Type	Soluble oil	
	Flow rate (ls^{-1})	5	
	Factor	**Level**	
Grinding Wheel	Grit Material	A	Diamond / CBN
	Bond type	B	Vitrified / Metal
	Grit Size (μm)	C	91 / 181
	Concentration	D	75 / 100
	Porosity (%)	E	25 / 30
Operation	Wheel Speed (ms^{-1})	F	15 / 30
	Depth of Cut (mm)	G	1 / 4
	Workpiece feedrate ($mm\ min^{-1}$)	H	150 / 600
Cutting fluid	Cutting fluid Application	I	Jet / Shoe

Creep feed grinding of the thermo-mechanically produced duplex alloy gamma titanium aluminide Ti-45Al-8Nb-0.2C was first reported by Hood et al. [7], [24], [184]. A comparison of the performance of different wheel specifications on the overall grinding performance was studied. The main goal was to find the optimum operating conditions for a given wheel that results in the best grinding performance in terms of grinding ratio, forces, specific power, and surface integrity. Six different wheels (three conventional abrasive and three super-abrasive) were examined at various operating conditions. Wheels specifications are shown in Table 2-15 [7]. Results showed that when creep feed grinding with conventional wheels, wheel A, associated with higher grit content, outperformed wheels B and C with respect to the highest achieved grinding ratio (~30), lowest obtained roughness and best surface integrity. Other conventional wheels with more open structures (higher porosity) showed a reduction in surface burn and cracking. However, this was at the expense of a very low grinding ratio (<5). Super-abrasive grinding wheels produced ~1000% higher grinding ratio than conventional abrasive wheels under the same operating parameters. This was attributed to the increased hardness and improved thermal conductivity (2000W/mK for diamond and ~1300W/mK for cBN when compared with SiC grit material ~40W/mK). In comparison to SiC wheels, wheels D and E produced ~25% and ~70% lower surface roughness values, respectively [7].

Table 2-15: Grinding wheels specification used by Hood [7]

Wheel coding	Wheel specification	Grit type	Grit mesh size/size	Grit material	Bond	Porosity
				%	%	%
A	GC 601 J 45 VKRNN#	SiC	60grit*	54.2	6	39.8
B	GC 601 J 62 VKRNN	SiC	60grit	43.7	5.9	50.5
C	GC 601 H 62 VKRNN	SiC	60grit	43.6	4.2	52.1
D		Diamond	91µm	31.25	30	38.75
E		cBN	91µm	40	37	23
F		Diamond	91µm	31.25	27.75	41

Images of the produced surface when creep feed grinding γ-TiAl alloy and burn-resistant titanium alloy with conventional wheel SiC are shown in Figure 2-29. In general, Cracking, chatter and burn on the surfaces of the workpieces did not appear to have occurred with either alloy when operating at low parameters 15m/s wheel speed, 1.25mm depth of cut and

150mm/min feed rate (T1). As the operating parameters are increased, burn, chatter mark and cracks become more noticeable.

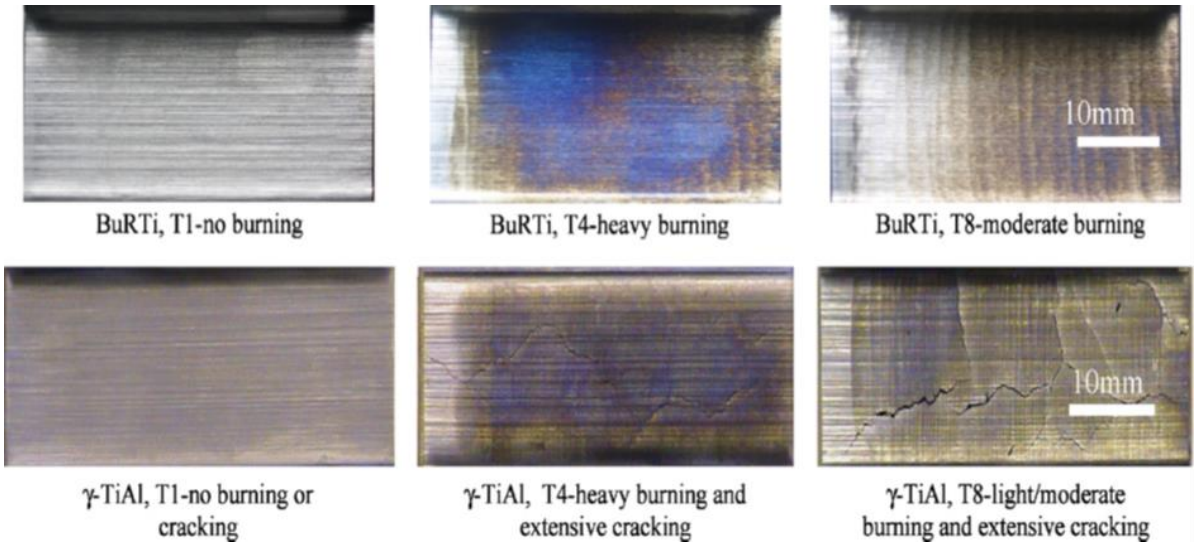


Figure 2-29: Produced surfaces of γ-TiAl alloy and burn resistant titanium alloy following creep feed grinding with SiC wheels by Hood [24]

Hood work also involved benchmarking the gamma titanium aluminide Ti-45Al-8Nb-0.2C against burn-resistant titanium alloy (Ti-25V-15Cr-2Al-0.2C wt%) and the conventional titanium alloy Ti-6Al-4V. In comparison between the three alloys, the highest grinding ratio was achieved when grinding γ-TiAl alloy; this is followed by BuRTi and Ti-6Al-4V. These results were consistent in both SiC abrasives and super-abrasive tests with grinding ratio differences as high as 70 folds between γ-TiAl alloy and conventional titanium alloys Ti-6Al-4V. Table 2-16 and Table 2-17 detail lists of recommended operating parameters by Hood for γ-TiAl alloy and burn-resistant titanium alloy for both cases of abrasive wheels stemming from his work [7].

Table 2-16: List of preferred operating parameters (γ-TiAl and BuRTi, SiC wheels) [7]

	Wheel specification	**Wheel speed**	**Depth of cut**	**Feed rate**	**Fluid type**
		(m/s)	(mm)	(mm/min)	
Highest G-ratio	Wheel A	15	γ-TiAl: 1.25 BuRTi: 5	γ-TiAl: 150 BuRTi: 600	Water
Lowest workpiece surface roughness Ra	Wheel A	15	1.25	150	Water
'Best' workpiece surface integrity	Wheel A	15	1.25	150	Water

Table 2-17: List of preferred operating parameters (γ-TiAl and BuRTi, super-abrasive wheels) [7]

	Wheel specification	Wheel speed	Depth of cut	Feed rate	Fluid type
		(m/s)	(mm)	(mm/min)	
Highest G-ratio	Wheel F	35	1.25	150	Oil
Lowest workpiece surface roughness Ra	Wheel F	50	γ-TiAl: 1.25 BuRTi: 2.5	γ-TiAl: 600 BuRTi: 150	γ-TiAl: Oil BuRTi: Water
'Best' workpiece surface integrity	Wheel D	35	1.25	150	Water

Machinability experiments involving creep feed grinding of Ti–45Al–2Mn–2Nb+0.8 vol.% TiB_2 (45-2-2+0.8) were later reported by Hood et al. [185]. Three single-layer electroplated diamond grinding wheels were investigated; the wheels had various grit sizes (D252, D126 and D46), and were operating at a wheel speed of 35m/s, feed rate of 150mm/min and 1mm depth of cut with the exception of wheel D46 which was set to 0.1mm depth of cut. Findings concluded that grinding performance in terms of surface roughness and surface integrity was satisfactory from an aero-engine components standpoint. For instance, grinding ratios as high as 100 were achieved using the D252 grit. In addition, when employing the D252 wheel, a surface roughness value of 2.94µm (Ra) was produced, whilst a value of less than 0.3µm (Ra) was accomplished with a D46 wheel. A hardened layer with a maximum value of 625HK, reaching a depth of 100µm, was evident following grinding with D252 and D126 wheels. However, the D46 wheel exhibited significantly less hardening and a nearly flat profile [185].

In 2017, research on γ-TiAl (45-2-2+0.8) by Bhaduri et al. [186] has been subsequently undertaken to assess the feasibility of ultrasonic assisted creep feed grinding (UACFG) using conventional SiC and electroplated diamond wheels. An ultrasonic transducer 20kHz linked to an ultrasonic generator rated at 1kW with a maximum amplitude of 8µm was used to deliver the ultrasonic vibration to a specially designed assembly for mounting samples of tested workpieces. In comparison between creep feed grinding (CFG) and ultrasonic assisted creep feed grinding (UACFG), around 35% reduction in grinding forces was observed in the use of ultrasonic assistance. This was claimed to be attributed to the self-sharpening of the abrasive grains promoted by the ultrasonic assistance. Operating under hybrid conditions resulted in a substitutional increase in grinding ratio (up to ~70% utilising SiC wheels and ~600% with

diamond wheels). Similarly, marginally better workpiece surface roughness was observed (~10%). High resolution SEM images of the ground surfaces are shown in Figure 2-30; surfaces produced under conventional creep grinding revealed surface fractures and redeposited material, while under hybrid conditions, no fracture was observed on the surface. However, a high degree of overlapping grit marks and ploughing were evident on the surfaces. Lateral movement of the abrasives under vibration was suggested to be the cause of these changes in surface damage [186]. Figure 2-31 details higher magnification images of workpiece cross-sectional microstructure following UACFG for three tests. Deformation and bending of the lamellae beneath the surface can be observed in both wheel systems (10µm with SiC and 20µm with diamond wheel) parallel to the feed direction. Neither the microhardness of the workpieces nor the microstructure was significantly altered by the transition from standard CFG to UACFG. Bhaduri et al. reported that the effects of UACFG were less pronounced with increasing cut depth and operating parameters, which most likely prevented the transfer of vibration amplitude to the cutting zone.

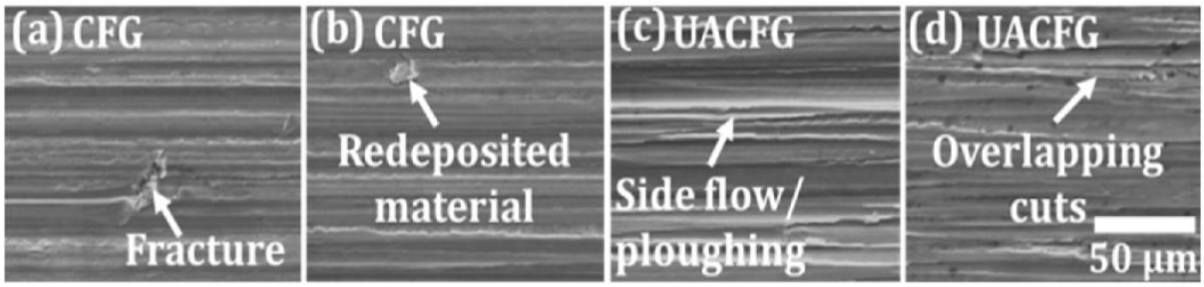


Figure 2-30: SEM images of g-TiAl surfaces ground using SiC [186]

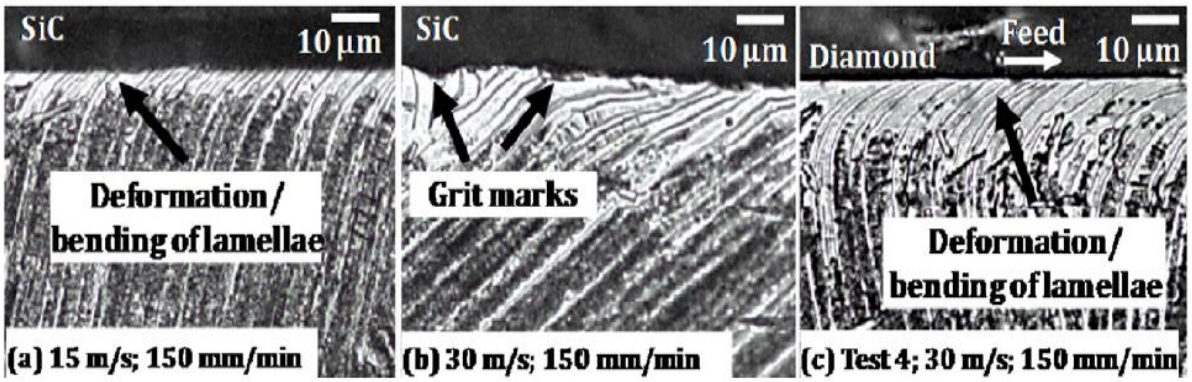


Figure 2-31: Microstructures of g-TiAl samples after UACFG [186]

More recently, a study on the surface burn behaviour of a gamma titanium aluminide intermetallic (Ti-45Al-2Mn-2Nb-0.1B) was reported in [18]. The study highlighted the impacts of grinding temperature on griding forces and surface integrity following creep feed grinding with SiC abrasive wheels and diamond abrasive wheels. Experimental testing involved variations in depth of cut, feed rate and wheel speed (two levels for each wheel). A 5 % concentration water-based emulsion delivered at 0.7MPa was used as a coolant. K-type thermocouples (OMEGA GG-K-36) were utilised to measure the grinding temperature. At a high grinding temperature up to 1000°C, a dark purple colour on the ground surfaces was observed together with severe burning, while at medium burn surfaces, a light brown colour was evident at ~800°C. The predominant chemical reaction that occurred during surface burning was the oxidation of Ti and Al, and these were found as TiO_2 and Al_2O_3 on the ground surfaces. Figure 2-32 illustrates the effect of grinding parameters on grinding temperature for both wheels. As expected, increasing the material removal rate by increasing either the feed rate or depth of cut generated more temperature [18].

Information on the use of a single-layer super-abrasive wheel when creep feed grinding γ-TiAl (Ti-45Al-2Mn-2Nb) is given in [187]. The work compared the grindability performance of electroplated cBN and diamond wheels with respect to wheel wear, surface integrity and the maximum achievable material removal rate before the onset of burn. The coolant was a Castrol Syntilo 9954 solution with a 5% concentration supplied at a pressure of 1.5MPa pressure. Wheel speed was fixed at 30m/s, and three levels of depth of cut (0.9mm, 1mm and 1.2mm) and feed rate (150mm/min, 300mm/min, 600mm/min) were selected; this allows the assessment of the wheel under various material removal rates. Two wheels of each super-abrasive were utilised in the experiments, all of which are 400mm in circumference, 10mm in width, and with a grain size of 200µm. Findings confirmed that under the tested condition, electroplated diamond wheels were far preferable to electroplated cBN, as the former exhibited lower wheel wear rates than the latter. Moreover, the diamond wheel reached a material removal rate value of 12(mm^3/mm.s) below the burn limit, which is double that obtained with cBN. All tests resulted in compressive residual stresses ranging from -125MPa to -500MPa. Also, produced surfaces revealed a hardening layer of up to ~200$HV_{0.05}$ above the bulk hardness.

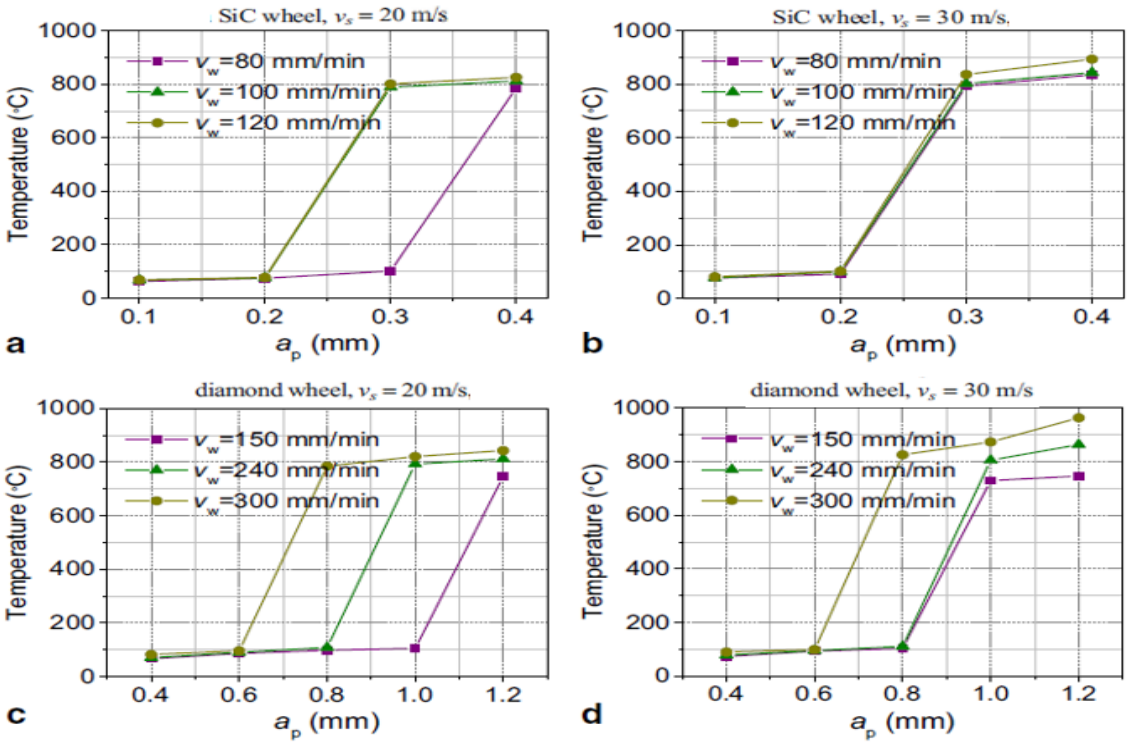


Figure 2-32: Effect of grinding parameters on grinding temperature by Xinxin [18]

Novovic et al. conducted the first machining trials on the burn-resistant titanium alloy (Ti-25V-15Cr-2Al-0.2C) [4], [149]. Their primary objective was to investigate the effect of workpiece surface roughness on fatigue life and not cutting performance. Machining processes involved reciprocating surface grinding, high speed milling, creep feed grinding, shot peening and polishing. Limited temperature measurements were undertaken under creep feed grinding. A maximum temperature of 870°C was recorded with SiC wheel at 0.2mm depth of cut. This value was reduced to 550°C when a more open structure SiC wheel (higher porosity) was used even at a higher depth (1mm depth of cut). While under the same conditions, the highest temperature recorded when using a diamond wheel was around 200°C. The work also involved comparative experiments on the standard titanium alloy (Ti-6Al-4V), and the results have shown similar trends in terms of surface temperature, wheel wear, and surface integrity between the two alloys, which further support what is suggested in [12] regarding the machineability of burn resistant titanium alloys.

The cutting performance of the burn-resistant titanium alloy (Ti-25V-15Cr-2Al-0.2C) followed by creep feed grinding with conventional and super-abrasive wheels was later reported in [7], [24], [25]. Hood et al. utilised L_9 Taguchi fractional factorial arrays with variations in wheel

speed, depth of cut and feed rate to compare the grindability of gamma titanium aluminide and burn-resistant titanium alloys. The results of the study showed that the former alloy was easier to grind than the latter alloy, given that a 10-fold increase in grinding ratio, 10% lower maximum power, 25% lower maximum specific energy, 28% lower tangential force and 15% lower average workpiece surface roughness Ra were observed when grinding with SiC. Whilst, for super-abrasive wheels, the trends were as follows: a 4-fold increase in G-ratio, 4.5% lower maximum power, 14% lower maximum specific energy, 8% lower normal force, 36% lower tangential force and 40% lower average workpiece surface roughness. According to him, the presence of Ti_2C and TiC carbides in the microstructure of the BuRTi alloy, as well as its 20-30% greater strength compared to gamma titanium aluminide, are the key contributory factors in these findings [7]. Figure 2-33 provides main effects plots for different output measures for both γ-TiAl and BuRTi when creep feed grinding with SiC wheels.

In an attempt to assess the grindability of burn-resistant titanium alloy (Ti-25V-15Cr-2Al-0.2C wt%) with super-abrasive wheel systems, L_8 fractional factorial Taguchi experimental design was employed by Soo involving two levels variations in abrasive type (diamond and cBN), wheel speed (35m/s and 50m/s), depth of cut (1.25mm and 2.50mm), feed rate (150mm/min and 600mm/min), and fluid type (water and oil). The down-grinding mode was performed in all tests. Study results revealed that cBN grits obtained the highest G-ratio and the lowest surface roughness at the feed direction, albeit at the cost of extreme burn, chatter and surface/subsurface defects. Lower grinding forces were achieved with diamond wheels but with poor wheel wear rates. Recast layers and heat-affected zones (HAZs) were present in the majority of tests. This was accompanied by workpiece softening up to ~20μm beneath the machined surface [25].

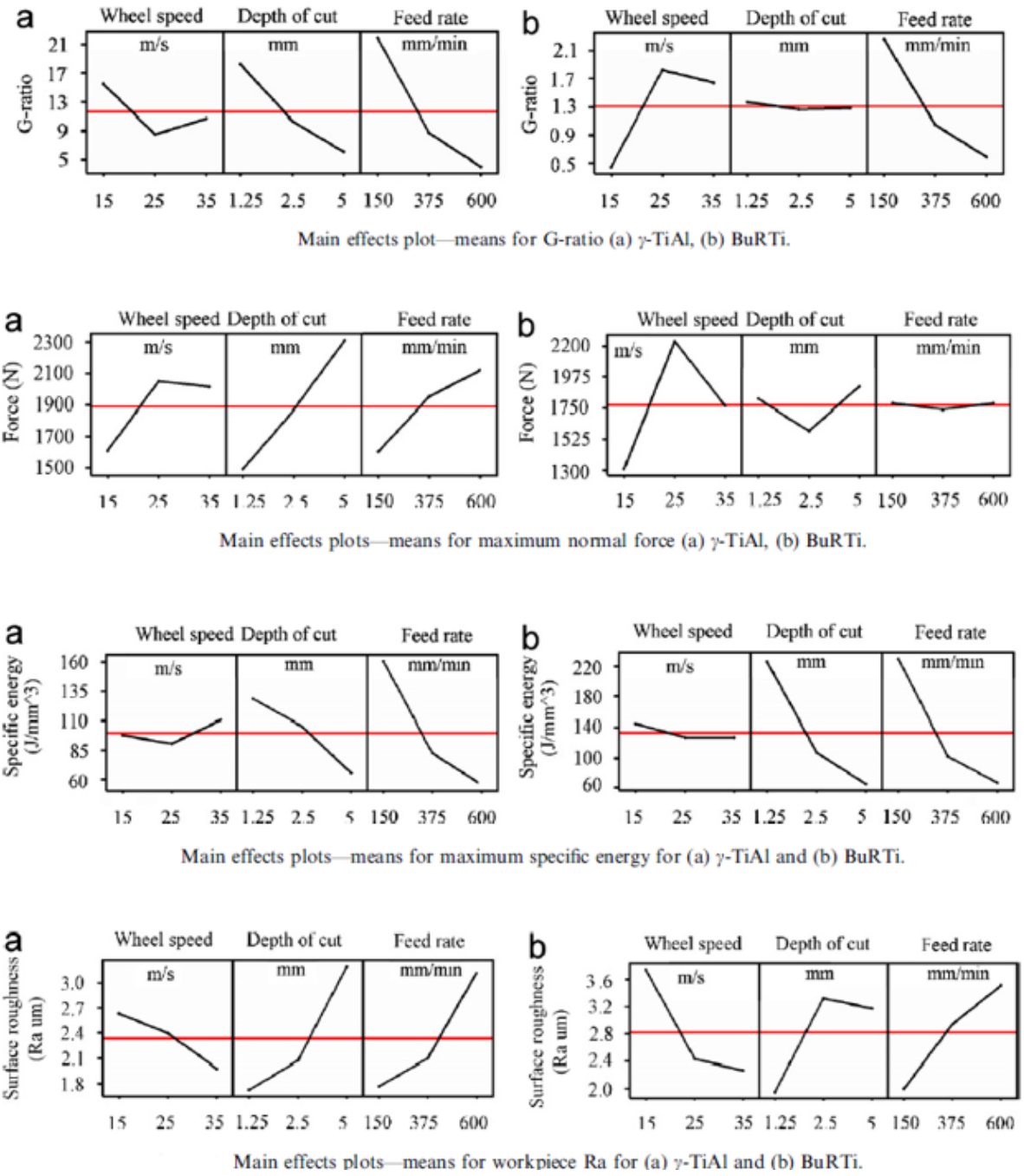


Figure 2-33: Main effects plots for γ-TiAl and BuRTi by Hood et al.[24]

2.6 Summary of the literature review and key areas of investigations

A detailed literature review on titanium alloy development, microstructure, properties, and industrial applications has been presented with more emphasis on α/β titanium alloy, titanium aluminide alloy, and burn-resistant titanium alloy. This was followed by a thorough review of grinding definitions, configurations, elements, mechanics, vibration, temperature, and fluid applications. Next, the chapter discussed workpiece surface topography and integrity along with their assessment techniques and practices. The review demonstrated that grinding performance in terms of grinding ratio, forces, power, temperature, surface integrity, etc., is extremely sensitive to process elements and operating parameters. This chapter ends with a discussion of previous work conducted in creep feed grinding on materials of interest to this research, highlighting the impacts of altering operating parameters and/or conditions on the grinding process quality. The main findings from the literature review are summarised as follows:

- Global research has been dedicated to explore the potential of γ-TiAl material for use in aerospace applications. The primary motivations are benefits arising from reduced weight, given that the density of γ-TiAl is approximately 50% that of nickel-based-superalloys.

- The patent burn-resistant titanium alloy (Ti-25V-15Cr-2Al-0.2C) developed by Interdisciplinary Research Centre and Rolls-Royce Plc has the capability to sustain favourable mechanical characteristics while also providing enhanced burn resistance up to ~500°C. This provides a larger scope for application in either aerospace or automotive industries when compared to conventional titanium alloys which are subject to temperatures <300°C.

- Titanium alloys are well acknowledged for their favourable characteristics and mechanical properties. Nevertheless, their low thermal conductivity, strong chemical reactivity, low modulus of elasticity, and ability to maintain tensile strength at increased temperatures present numerous difficulties during the machining process. In addition to these challenges encountered when machining titanium alloys, γ-TiAl alloys exhibit poor ductility at room temperature and low fracture toughness.

- The existing body of literature highlights that among various machining methods, grinding has been consistently demonstrated to yield superior surface quality when employed for cutting titanium alloys. For instance, grinding plays a crucial role within the aerospace sector in the manufacturing of turbine blades and vanes made from either nickel-based or titanium-based super-alloys.

- Creep feed grinding presents numerous advantages in comparison to surface grinding. These include the ability to achieve grinding regimes that are more efficient in terms of stock removal rate. Additionally, creep feed grinding allows for the elimination of multiple process stages, resulting in reduced process chains. Thus, this method can lead to lower manufacturing costs due to higher production rates and reduced capital investment.

- Among the available technologies to experimentally measure the temperature generated during grinding, thermocouples have emerged as the most favoured method in most published work. The utilisation of thermocouples offers several benefits, including low cost, reliability, and simplicity in construction, operating, and signal processing.

- Cooling techniques such as minimum quantity lubricant (MQL) and cryogenic coolant strategies have proven to offer a sustainable process with less harm to the environment and the operator. In addition, superior surface quality, lower levels of temperature and forces were achieved at shallow grinding by MQL when compared to dry cutting. However, the implementation of these cooling techniques in the machining of aerospace nickel or titanium alloys, which have limited thermal conductivity, presents many challenges, particularly when operating at greater depths of cut. This is primarily owing to the elevated mechanical and thermal loads generated during cutting.

- The produced surface integrity and topography are predominantly governed by the material and cutting tool/wheel characteristics as well as the cutting/operating conditions. The task of manufacturing components that meet the required standards in terms of surface integrity and dimensional accuracy is still a formidable challenge. Thus, appropriate control of machining parameters is vital in order to enhance produced components productivity.

- There is a scarcity of published work on creep feed grinding of γ-TiAl (Ti–45Al–8Nb–0.2C), burn-resistant titanium (Ti-25V-15Cr-2Al-0.2C) and Ti-6Al-4V alloys in the literature. Therefore, further research is required to enhance/increase the knowledge regarding the grindability of these materials. The optimisation of material machinability and performance can only be achieved by fully understanding the characteristics of the generated surface integrity which can be linked back to the grinding and operating conditions.

- None of the work on creep feed grinding of γ-TiAl (Ti-45Al-8Nb-0.2C) provided details about the generated temperature and residual stresses during the machining process, with extremely limited information on temperature and residual stresses given for burn-resistant titanium alloy (Ti-25V-15Cr-2Al-0.2C).

- The body of research on CFG of titanium alloys to date has placed more emphasis on the analysis of the 2D surface roughness parameter (Ra). However, no data or details were provided on 2D extreme parameters (Rt and Rz) or the 3D parameters (Sa, St, and Sz). It was asserted in the literature that information on surface conditions (such as a sharp peak, valley or crack) and surface functional performance (friction, wear, fatigue and fluid retention) can only be obtained when topographical 3D surface parameters are considered. The limitations of 2D topographical analysis in accurately representing the practical surface geometrical features and behaviour of machined parts have led to the widespread acceptance of 3D topographical areal analysis as the preferred method for comprehensively assessing surface characteristics and establishing correlations between surface topography and functional performance.

In reflection of the literature review, the points listed below summarise areas that have not been sufficiently addressed in the literature, and these are what the current study will consider:

- Extremely limited studies on creep feed grinding of the thermo-mechanically produced duplex alloy gamma titanium aluminide of composition (Ti-45Al-8Nb-0.2C) are published with few variations of levels and factors. Thus, more investigation is needed to provide more understanding of the grindability of this material. The machinability

and performance of the material can be optimised through an understanding of the grinding conditions associated with produced surface integrity.

- None of the work on (Ti-45Al-8Nb-0.2C) provided details about the generated temperature during the cutting process.

- Reported roughness data when creep feed grinding of gamma titanium aluminide (Ti–45Al–8Nb–0.2C) concentrated only on 2D amplitude roughness parameter (Ra), while no information on other 2D parameters (Rt and Rz), and 3D parameters (Sa, St and Sz) were given.

- Similarly, neither sufficient temperature data nor 3D roughness/topography data for creep feed grinding of burn-resistant titanium alloy (Ti-25V-15Cr-2Al-0.2C) are available, with limited information given in just one study [4].

- The majority of research on creep feed grinding of burn-resistant titanium alloy (Ti-25V-15Cr-2Al-0.2C) has failed to address generated residual stresses after machining process, and none can be found for γ-TiAl (Ti-45Al-8Nb-0.2C).

- Most of the recent work on grinding of Ti-6Al-4V in published literature pays particular attention to surface grinding (shallow depth of cut) rather than creep feed grinding.

3 EXPERIMENTAL WORK

This chapter provides experimental details with respect to workpiece materials, utilised machine tools, analysis equipment and employed experimental designs in this study.

3.1 Workpiece materials

Workpiece materials involved in this study are the γ-titanium aluminide (Ti-45Al- 8Nb-0.2C), burn-resistant titanium alloy (Ti-25V-15Cr-2Al-0.2C), and conventional α/β titanium alloy (Ti-6Al-4V). All materials were the remaining from previous projects reporting earlier work on creep feed grinding of Ti-45Al- 8Nb-0.2C and Ti-25V-15Cr-2Al-0.2C [4], [7]. The materials were supplied by Rolls-Royce Plc, and the γ-TiAl alloy was cast as a billet (Ø225mm and 275mm high) that was hot isostatic pressed at 1260°C and 150MPa for four hours. This resulted in a bulk hardness of ~400$HK_{0.025}$ and a grain size of ~2mm. This was delivered as two rectangular blocks with 50mm length×70mm width ×60mm height. The burn-resistant titanium alloy was produced via forging at 1050°C, followed by heat treatment for two hours at 600°C to enhance the mechanical properties of the alloy as well as the thermal stability. This provides the alloy with a microhardness of 375$HK_{0.025}$ and a grain size ranging from 30μm to 50μm. The microstructure of the alloy consisted of equiaxed grains and strings of carbide particles running generally perpendicular to the forging direction. BuRTi alloy workpieces were supplied in the form of Ø55mm circular blocks. Ti-6Al-4V was provided in the annealed condition (700°C for 1h, then cooled by air), with a bulk hardness of 320$HK_{0.025}$. The microstructure of γ-titanium aluminide alloy, burn-resistant titanium alloy and Ti-6Al-4V are shown in Figure 3-1.

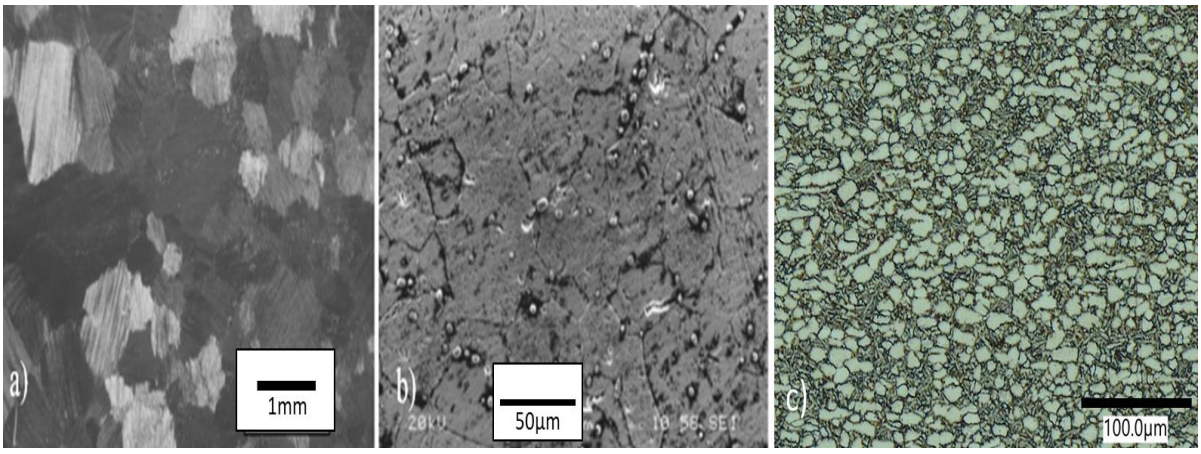


Figure 3-1: Microstructures of tested workpieces: a) gamma titanium aluminide, b) burn-resistant titanium alloy, c) Ti-6Al-4V [7]

3.2 Creep feed grinding wheels

All wheels involved in this study are supplied by Saint-Gobain Abrasives and have a plain profile. A vitrified silicon carbide (SiC) wheel was utilised for phases of experimental work involving conventional abrasives. The SiC wheel of specification GC60J45VKRNN had a diameter of 220mm, a width of 20mm, and ~40% porosity. For super-abrasive phases, a 91µm -grit size vitrified bonded diamond wheel was employed, having a 175mm diameter, wheel width of 20mm and ~38% porosity. Identical SiC and diamond wheels were involved in an initial creep feed grinding project, where their performance was proven to be superior to other similar grit wheels, however, of different specifications [7]. Three single-layer electroplated diamond wheels (D252, D126 and D46) with a diameter of 200 mm and width of 20 mm were used in the last phase of experimental work. The first wheel had a grit size of ~252µm (~60 mesh), while the second and third wheels had a grit size of ~126µm (~120 mesh) and ~46µm (~325 mesh), respectively. All wheels were involved in preliminary creep feed grinding trials in [185] thus, were not delivered in new conditions. Therefore, it was decided to perform only one test for each wheel. Figure 3-2 illustrates creep feed grinding wheels used in this study along with higher magnification images showing the grits distribution for each wheel.

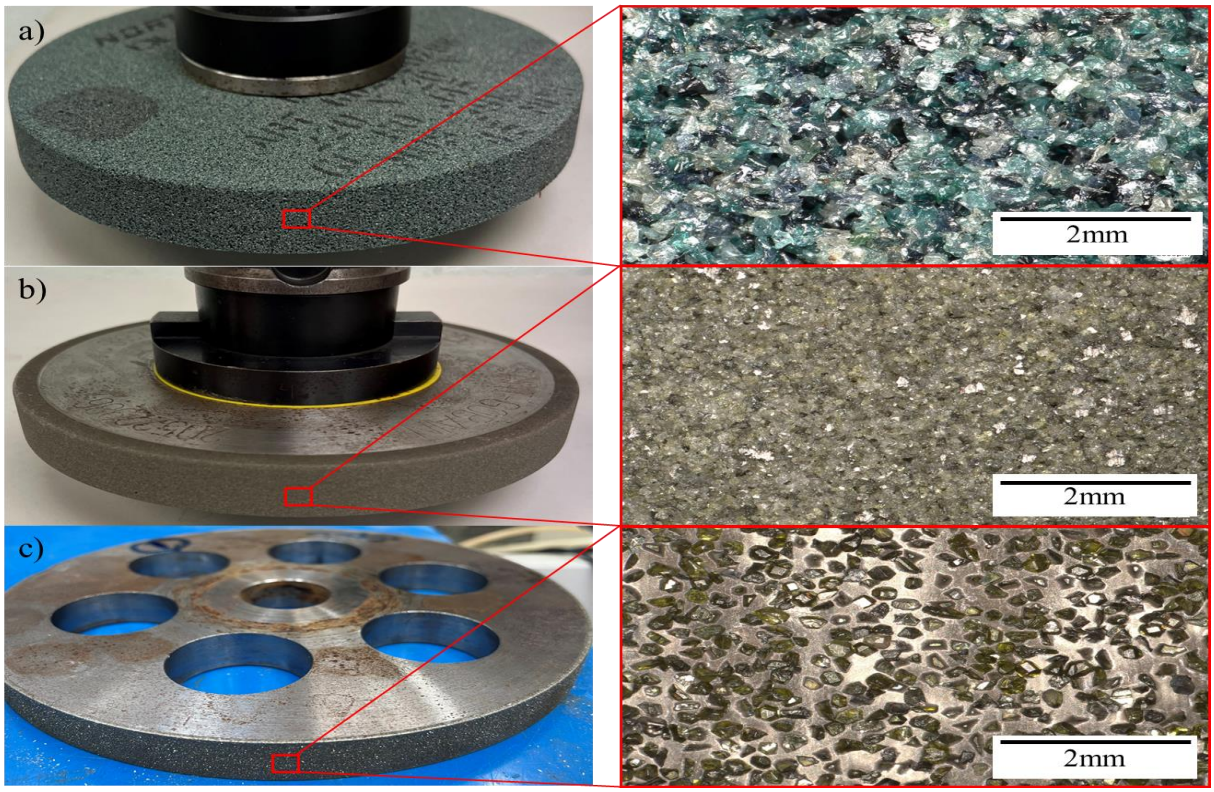


Figure 3-2: Utilised Creep feed grinding wheel: a) SiC wheel, b) vitrified diamond wheel, c) single layer diamond wheel D252

3.3 Machine tools

3.3.1 Pre-machining machine centres

All blocks were provided in different shapes and sizes, see Figure 3-3. Therefore, pre-machining prior to creep feed grinding was essential to clamp the blocks onto the mounting plate and meet the required testing dimensions. This involves three stages of machining processes: wire electric discharge machining, drilling and surface grinding. The two large blocks of γ-TiAl alloy have undergone electrical discharge machining to produce smaller blocks with the following dimensions: 77mm × 47.5mm × 15mm. Ti-6Al-4V were similarly cut from a larger block to produce smaller blocks with approximate dimensions 49mm × 45mm × 14mm. The Ø55mm circular blocks of BuRTi alloy were also electrical discharge wire machine to produce flat-sided blocks sizing 53mm × 48mm ×15mm. Then, two through holes were drilled into all workpieces to facilitate direct attachment of the block to the Kistler platform dynamometer and one blind hole for insertion of thermocouples into the blocks. Finally, all blocks were surface ground to provide equally smooth, uniform surfaces.

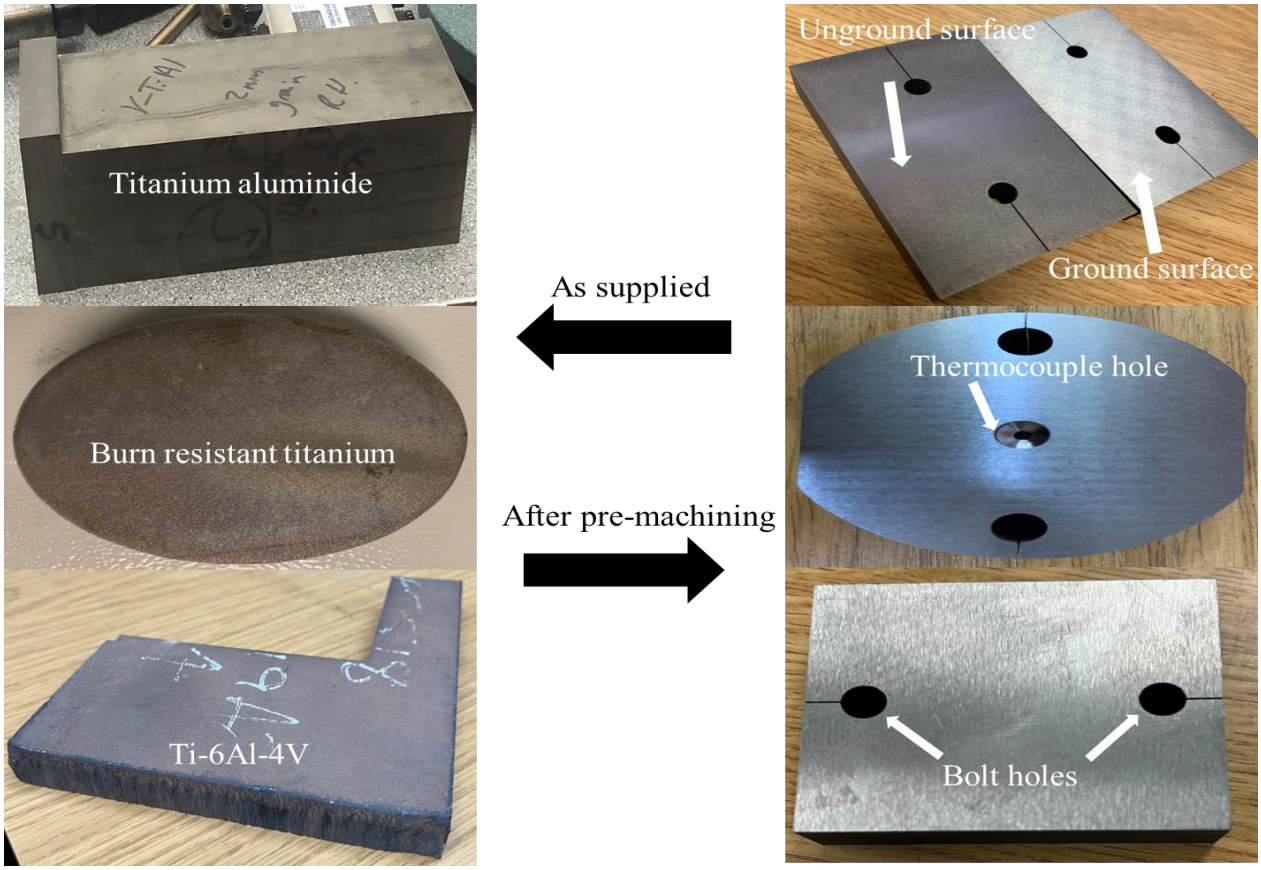


Figure 3-3: As supplied blocks vs testing blocks

3.3.1.1 Wire electric discharge machining machine centre

Electrical wire discharge machining was conducted on Agie Charmilles Robofil FI240cc wire EDM machine (computer numerical controlled), see Figure 3-4. Workpieces were submerged in deionized water dielectric with an electrical conductivity of 5S/cm, and subsequent cutting operated at 10 ignition-current (IAL), 80 open gap voltage, 44 servo voltage, 1N wire tension, 13mm/s wire speed, and a frequency of 20% for TiAl and 10% for BuRTi. Copper core-based wire (0.25mm in diameter) is used, coated with $CuZn_{50}$, providing a total tensile strength of 520MPa/75.420PSI.

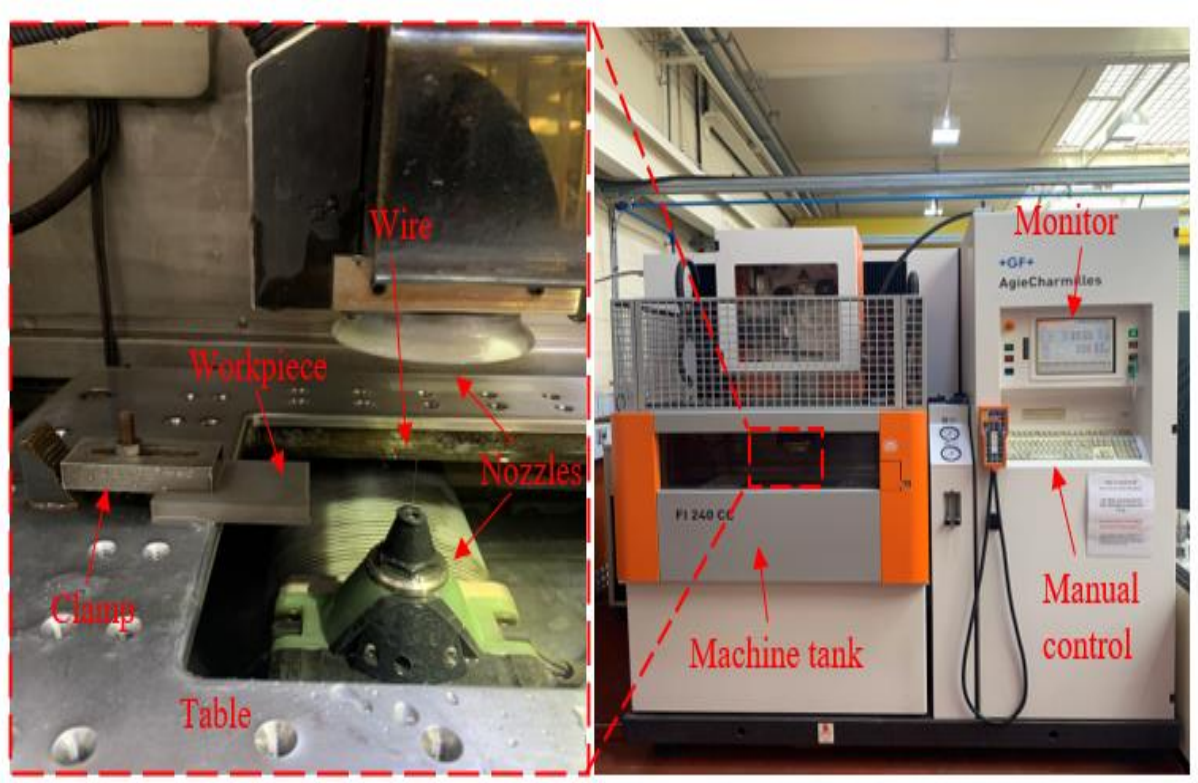


Figure 3-4: Wire electric discharge machine centre

3.3.1.2 Drilling machine centre

Drilling of workpieces was carried out on DMG MORI ULTRASONIC 20 linear (computer numerically controlled), having maximum axes strokes of 200mm, 220mm and 280mm for the X-axis, Y-axis, and Z-axis, respectively, see Figure 3-5. Two sets of PVD-coated twist drill bits (three each) were involved in the drilling process, all of which were supplied by SECO. The first set of drill bits has a 6mm cutting diameter and 21mm usable length with a designation

of (SD203A-0600-021-06R1-MS). These are mainly used to produce blind holes to accommodate the thermocouples into the workpiece. The second set includes 2mm cutting diameters and 7mm usable length drill bits, designated (SD203A-0200-007-04R1-MS), and was utilised to drill blind holes for thermocouples junctions. 10% oil-concentrated water-based emulsion (Hocut 795 B-EU) was delivered at a 17l/min flow rate and a pressure of 5.5bar by two nozzles for cooling of the drilling process. Initial drilling trials at low speeds and higher feed rates resulted in drill bits fracture/failure and high wear rate. Therefore, it was decided to set the feeds at the lowest value (in the machine controller) while increasing the speeds. Drilling operating feeds and speeds for each drill bit for the three materials under investigation are shown in Table 3-1.

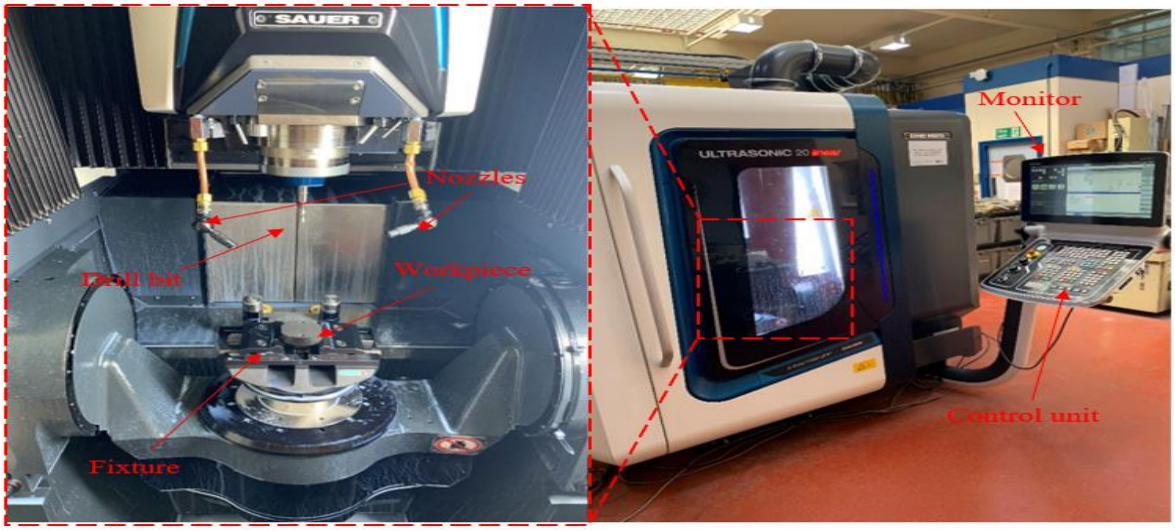


Figure 3-5: Drilling centre (DMG MORI ULTRASONIC 20 linear)

Table 3-1: Drilling speeds and feeds parameters

Material	TiAl		BuRTi		Ti-6Al-4V	
Drill bit cutting diameter (mm)	6	2	6	2	6	2
Speed (RPM)	2000	2500	2200	3000	2200	3000
Cutting speed (m/min)	37	16	41	19	41	19
Feed rate (mm/rev)	0.002	0.002	0.001	0.001	0.001	0.001

3.3.1.3 Surface grinding machine centre

Surface grinding was performed on a Jones and Shipman 540AP reciprocating surface grinder unit. The machine has a maximum longitudinal and traverse travel of 600mm and 150mm, respectively, along with a vertical wheel travel of 150mm. A plain SiC abrasive wheel was employed at a speed of 22m/s and a down feed rate of 10µm per pass. The wheel was dressed periodically using a single-point diamond dresser to provide sharp cutting edges. Table speed was set at 0.3m/s. Cooling fluid (Trim C270) was supplied through twin jet nozzles at 8l/min flow rate. Figure 3-6 demonstrates the surface grinding unit as well as the workpiece/wheel arrangement.



Figure 3-6: Jones and Shipman 540AP reciprocating surface grinder unit

3.3.2 Creep feed grinding machine centre

The Bridgeport flexible grinding centre FGC1000 (computer numerically controlled), shown in Figure 3-7, was utilised for creep feed grinding trials, with a horizontal grinding arrangement and a vertical spindle axis with a maximum speed of 6000rpm and 28KW maximum rating power. It has a maximum travel distance of 1020mm, 560mm and 600mm along the X, Y and Z axis, respectively; the rapid feed rate for the X and Y axes was set at 43m/min, while for the Z axis, the value is 30m/min. The machine is equipped with MST BT40 FMSB32-60 tool holders with associated blotters and flanges for holding the grinding wheels. The machine also facilitates a plain profile, handset sintered hydraulically driven diamond roller dresser

(Ø105mm) with an average grain size of 800µm and spacing of 1.5mm, see Figure 3-8 (a). It was used to intermittently dress the grinding wheel before each test to provide similar initial wheel conditions while operating at a dress depth of (50µm for SiC, 5µm for diamond wheel), and an infeed per revolution of 2.0µm. In order to produce a dresser/wheel speed ratio of 0.8 during the dressing process, the wheel speed was fixed at 15m/s and the dresser speed at 2910 RPM. This in turn, provides a sharp cutting edge wheel as recommended in [7], [25], [186].

Two Hydra jet G25 pumping systems were used to supply the wheel with grinding fluid for both cleaning and cooling. A water-based synthetic fluid with a concentration of 7-10% is used as the grinding fluid (TRIM C270) with a boiling point of ~100°C, see Appendix E [188]. The fluid was delivered via free jet nozzles with a rectangular cross-section. These were designed according to Webster and his co-researchers' model involving a concave surface and high contraction ratio (inlet to outlet) to produce coherent jet flow with less air entrainment [105], [117]. The cooling nozzle (20mm height × 2mm wide) was aimed at the contact area between the wheel and the workpiece at a pressure of 7bar, whilst the cleaning nozzle (20mm height × 0.5mm wide) was aimed at the back of the wheel to eliminate the effect of the air barrier and was delivered at 20bar pressure, the arrangement of both nozzles with respect to grinding wheel is illustrated in Figure 3-8 (b). The nozzles positions were periodically changed as the radius of the grinding wheel decreases over time due to wear and dressing. Identical nozzle design, orientations and conditions were detailed by [7], [25], [26] when utilising the same machine tool for initial creep feed grinding trials on titanium and nickel-based superalloys. Considerations were taken to match the cooling fluid velocity and wheel velocity as this will provide maximum effectiveness of cooling flowrate as suggested in [115], [116], [117].



Figure 3-7: Bridgeport FGC1000

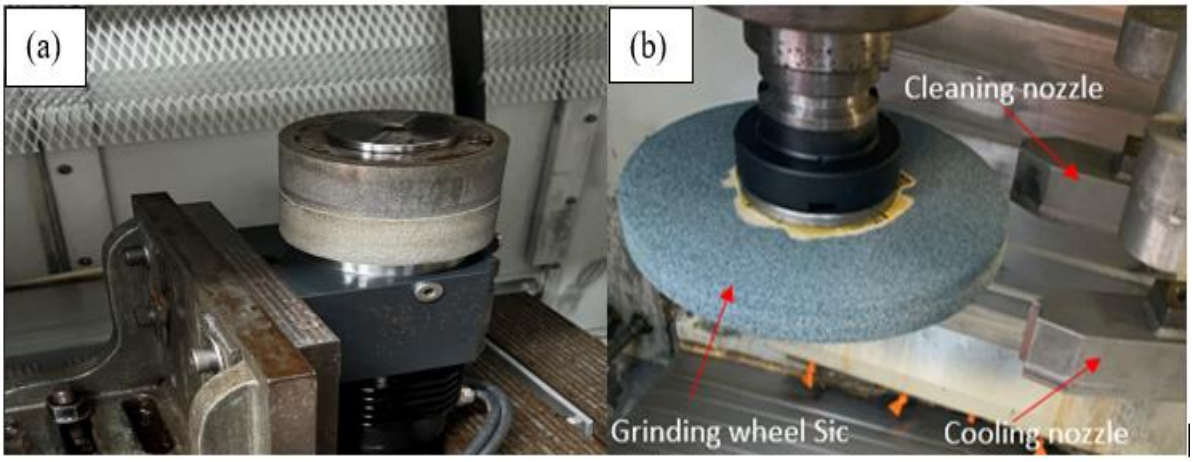


Figure 3-8: (a) diamond roller dresser, (b) nozzles arrangement

3.4 Analysis equipment

3.4.1 Grinding wheel wear and grinding ratio

In order to estimate wheel wear, wheel diameters were measured before and after each grinding pass using a Mitutoyo Euro Apex coordinate measuring machine (CMM) connected to a computer programmed with metrology software (MCOSMOS), see Figure 3-9. The wheel was measured at 16 equally distant points around the periphery, each at different levels of the wheel width, and then the average of three measurements was taken. Next, the G-ratio (the volume of removed workpiece material per the volume of removed wheel material) is determined using equation (1).



Figure 3-9: CMM Mitutoyo Euro Apex

3.4.2 Grinding forces, power and specific energy

Figure 3-10 demonstrates the experimental setup for measuring cutting forces during creep feed grinding trials. Grinding horizontal forces (parallel to feed direction) and vertical forces (radial to wheel) were recorded with a Kistler 9257A three-component piezo-electric platform dynamometer with 2.3kHz resonant frequency and <760Hz operating frequency; this was connected to charge amplifiers and a PC programmed with Dynoware software for forces analysis (120sec measuring time and 3000Hz sampling rate). Then, normal forces and tangential forces can be calculated using Equations 7, 8 and 9 described in section 2.2.4. Besse reported that in shallow grinding, both normal and tangential force components could be assumed as or equal to vertical forces and horizontal forces; however, this is not the case in creep feed grinding due to the higher depth of cut and longer length of arc associated with creep feed grinding [189]. Grinding power was estimated directly from the power monitor integrated into the machine tool controller (Heidenhain), and specific energy was calculated using Equation 12.

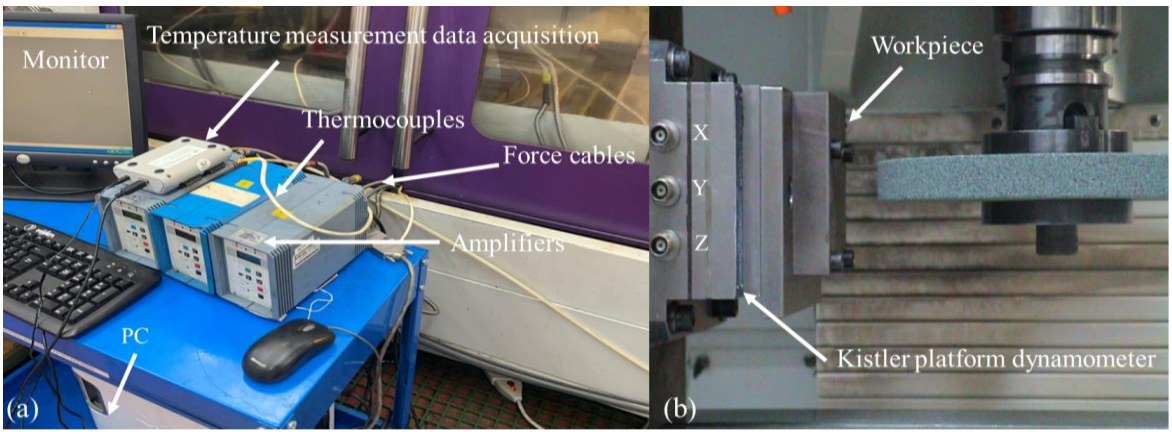


Figure 3-10: Forces measurement set up: (a) amplifiers, (b) platform dynamometer

3.4.3 Grinding temperature

A literature review on grinding temperature measurement techniques [89] suggested that an embedded split foil thermocouple would produce the most accurate results. However, the preparation of very small thickness mica layers assembly and the alignment of the thermocouple poles has proved to be difficult and time-consuming, particularly if a large number of tests is required. Therefore, from an economical point of view, temperature measurement was carried out through an embedded thermocouple. As previously mentioned in

section 2.2.6, this technique is more convenient to apply and able to obtain a good temperature signal; moreover, several researchers have demonstrated the accuracy and reliability of readings obtained using this method. Prior to grinding, thermocouples were embedded in the workpiece, and the tips of the tube of thermocouples were placed at the position of the target cutting depth beneath the grinding surface (0.5mm away from the surface) so that thermocouples are not cut during the grinding process. Temperature measurement is carried out with K-type, beaded thermocouples (XC-24-K-79), connected to a data acquisition logger (OM-DAQ-USB-2401). The data acquisition logger was connected to a PC running DAQ central software for analysis of recorded temperature signals. Each thermocouple was inserted into the blind hole in the middle of the workpiece/cutting length in order to measure the grinding temperature at a 500Hz sampling rate and a thermocouple response time of less than ~0.42s (time required to achieve 63.2% of an instantaneous temperature change) [190]. Resin epoxy powder (OMEGABOND 400 high-temperature cement) was used to bond the thermocouple junction with the workpiece blind hole, which can withstand a maximum temperature of up to 1425°C. Full specification of the cement is given in Appendix D [191]. This was supplied by OMEGA, including the thermocouples as well as the data acquisition logger. Multiple passes were performed for each test until the tip of the thermocouple was reached. An identical design schematic of the grinding temperature measurement, as well as the cross-section of the thermocouple blind hole, are described by Shen and his co-researchers [99] and shown in Figure 3-11 (a) and (b).

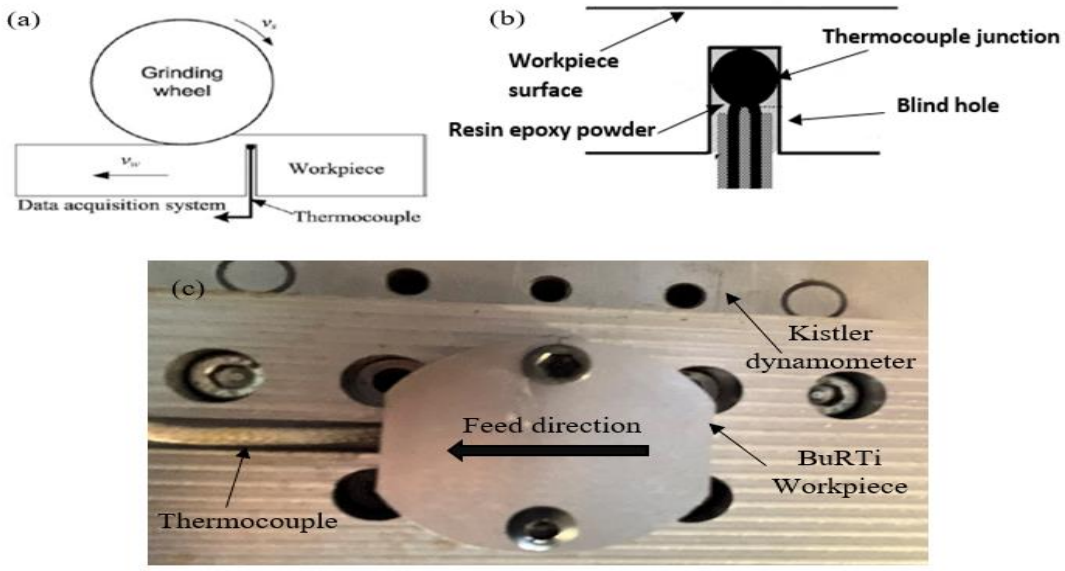


Figure 3-11: Blind hole thermocouple installation process [98]: (a) grinding temperature measurement, (b) cross-section of the thermocouple blind hole, (c) BuRTi workpiece and thermocouple assembly

3.4.4 Surface roughness and topography

Workpiece surface 2D roughness parameters (Ra, Rt and Rz) both perpendicular and parallel to feed direction, were measured by a Mitutoyo surface roughness tester (FORMTRACER Avant), which is connected to a software (FORMTRACEPAK) for efficient measurement automation, see Figure 3-12 (a). It has a travel distance of 100mm and 500mm along the X and Z axes, respectively, an inclination angle of ±45° and 0.75mN detector measuring force. The fitted stylus angle is 60° with a tip radius of 2µm. ISO 4287 [133] was set as the measurement condition standard in the software. The average of three readings recorded from different areas along the ground surface track is estimated with a 0.8mm cut-off distance and an evaluation length of 4.0mm. 3D surface roughness parameters (Sa, St and Sz) have been measured using the Alicona G4 InfiniteFocus (IF) system (Figure 3-12(b)), which is based on a rapid non-contact optical 3D measurement procedure and capable of conducting high resolution 3D surface measurements with a vertical and lateral resolution of down to 10nm and 440nm respectively. It was also used to obtain 3D topographic maps of the ground surfaces. The device applies the following standards during measuring: ISO 25178 [138] and ASME B46.1 [192]. The captured range by the optical instrument in this work is 4.432mm in length (X-direction), 2.260mm in width (Y-direction), and the height (Z-direction) ranged from 50µm-100µm. The measured area covered 13 million points at a sampling distance of 0.883µm × 0.883µm. For 2D and 3D roughness measurement, a Gaussian filter was subsequently applied on the primary profile/area of the measured surface to obtain the roughness profile/areal and their associated values. Due to time constraints, only one 3D roughness measurement was taken for each test ground surface.

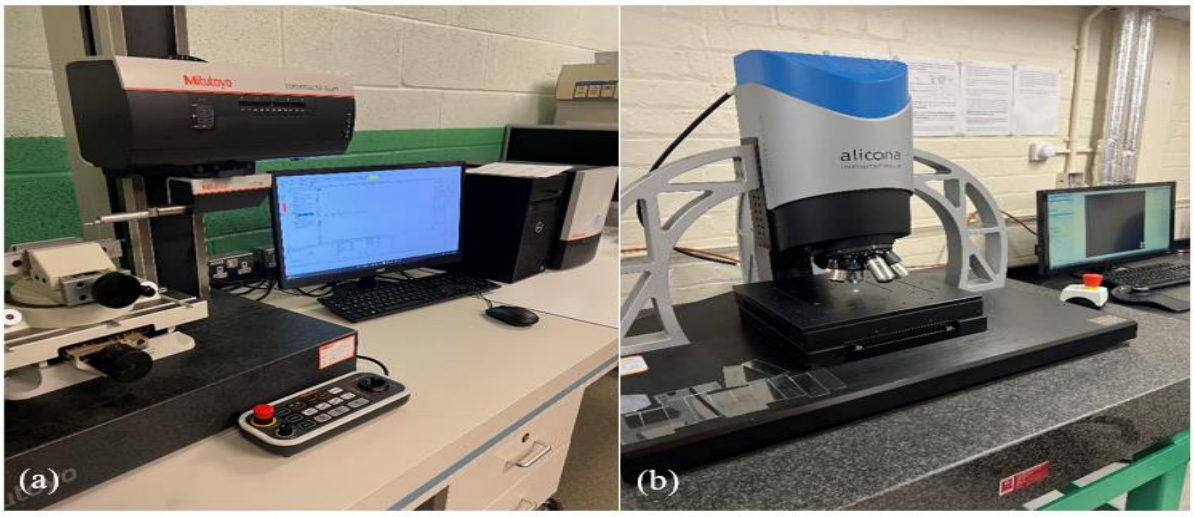


Figure 3-12: (a) FORMTRACER Avant, (b)Alicona G4 InfiniteFocus

3.4.5 Microhardness and microstructure

In order to conduct microhardness, selected samples of the machined surface were cut via electric discharge wire machining (5mm x 10mm), then mounted in hot edge retentive Bakelite using Buehler mould equipment (Figure 3-13 (a)), and finally ground with silicon carbide papers and polished in Buehler grinder-polisher (Figure 3-13 (b)), SiC papers grinding and polishing stages and regimes for the specimens are detailed in Table 3-2, which follows the work reported in [7], [26]. Drilled blind holes in the middle of workpieces made it impossible to examine samples from the centre location or the nearby surrounding areas due to the damage introduced by the drilling process. Alternatively, microstructure analysis samples were taken from the start of the cut to ensure that produced subsurface damage is primarily due to creep feed grinding process.

Table 3-2: Paper grinding and polishing procedures

Step No.	Base surface	Abrasive size	Load (Ib)	Base Speed (rpm)	Direction of rotation	Time (min)
1	CarbiMet Abrasive disc	SiC paper P240	6	240-300	Complimentary	6
2	CarbiMet Abrasive disc	SiC paper P600	6	240-300	Complimentary	6
3	CarbiMet Abrasive disc	SiC paper P1200	6	240-300	Complimentary	6
4	Ultra-Pol polishing cloth	9µm SUPREME diamond suspension	5	120-150	Complimentary	5
5	TRIDENT polishing cloth	6µm SUPREME diamond suspension	5	120-150	Complimentary	5
6	TRIDENT polishing cloth	3µm SUPREME diamond suspension	5	120-150	Complimentary	5
7	MICROCLOTH pad	0.06µm MASTERMET colloidal silica suspension	5	120-150	Complimentary	5

Microhardness variation is obtained by Mitutoyo HM-124 microhardness tester (Knoop microhardness depth profile) shown in Figure 3-14. Surface microhardness measurements were taken at the cessation of each test with a 50g load indenter and 15s indention time in both the

parallel and perpendicular directions to feed. The average of three readings along different locations from the surface of the specimen were calculated, each set at ~10μm intervals from the surface until bulk hardness is reached. Indents were kept ~30μm apart to avoid overlapping effects on the readings. For microstructural analysis, samples were immersion etched using 'Kroll etchant' (2ml HF, 6ml HNO_3, 92ml H_2O) until the microstructure was revealed. The immersion period differed depending on the alloy, as being 4 minutes for BuRTi, 40 seconds for TiAl, and 10 seconds for Ti-6Al-4V.

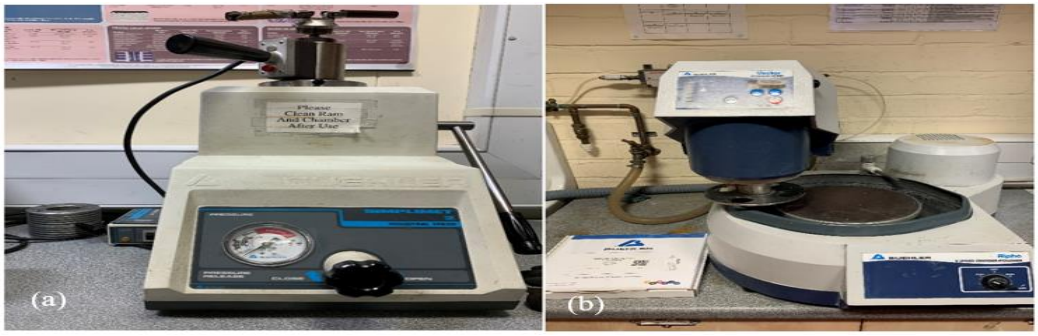


Figure 3-13: (a) Buehler mounting equipment, (b) Buehler grinder-polisher



Figure 3-14: Mitutoyo HM-124 microhardness tester

3.4.6 Optical and scanning electron microscopy

Photographs of the ground surfaces and subsurface cross-sectional microstructure were taken by Keyence VHX digital microscope (Figure 3-15(a)). It is capable of capturing high resolution images of a maximum 108 megapixels of resolution and accommodates four fully integrated head lenses with a magnification range of 20-6000x. High resolution scanning electron micrographs (SEM) were captured with tabletop Hitachi TM3030 equipped with back scattered electron detector (BSE) and Energy Dispersive X-Ray Analysis (EDX) and a maximum sample size of 70mm in diameter, 50mm in thickness (Figure 3-15(b)).



Figure 3-15: (a) Keyence VHX digital microscope, (b) Hitachi TM3030

3.4.7 Residual stresses

Residual stress measurement was determined by the hole-drilling residual stress method. The advantages of this method of measuring include its high precision and low cost of equipment. In this method, a strain gauge target is gradually drilled to a desired depth, resulting in releasing the near-surface residual stresses, which in turn deform the surrounding area. Then, the level of deformation is quantified by the strain gauges (located on the same circumference), giving the corresponding materials properties. A full description of the hole-drilling residual stress method is given by Guo et al. in [193]. Target strain gauges were applied to nine ground samples. For each sample, one EA-06-031RE-120 target gauge was installed at a position offset longitudinally 6mm from the thermocouple hole centre. The target gauge type used was Vishay Measurements Group Type EA-06-031RE-120. Target site surfaces were prepared for gauge installation by two passes of fine (400 grade) SiC paper with light hand pressure followed by thorough degreasing. In each case, gauge element 3 was aligned with the longitudinal (machining direction) and element 1 in the transverse direction. Directions 1 and 3 also refer to the directions of stresses σ1 and σ3. Typical strain gauge installations are shown in Figure 3-16. Each gauge was subjected to orbital drilling using an inverted cone T/C cutter with depth increments set at 4×16μm + 4×32μm + 8×64μm to give a final hole depth of 704μm. The arrangement for incremental drilling is shown in Figure 3-17, and the relevant material properties used for strain-to-stress data reduction are detailed in Table 3-3. Residual stress measurement was carried out by Stresscraft Ltd, Leicestershire, UK because of the unavailability of testing equipment. It was initially planned to investigate residual stresses of

all ground samples in this work, but due to time and cost restrictions, only 9 out of 32 ground samples (3 samples of each material) were tested.

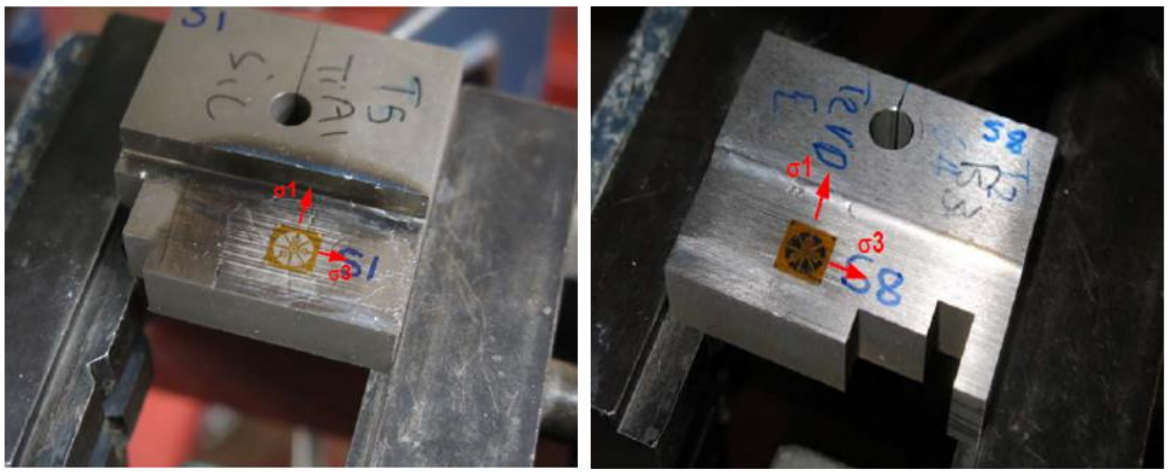


Figure 3-16: Strain gauge orientation and arrangement

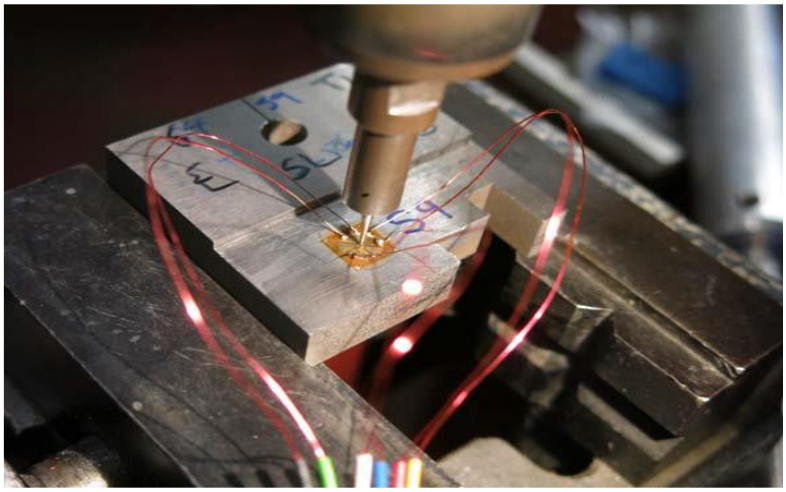


Figure 3-17: The arrangement for incremental drilling

Table 3-3: Material properties used for strain-to-stress data reduction

Material	Young's modulus of elasticity (GPa)	Poisson ratio
Gamma titanium aluminide (Ti–45Al–8Nb–0.2C)	170	0.27
Burn resistant titanium alloy (Ti-25V-15Cr-2Al-0.2C)	120	0.34
Conventional titanium alloy (Ti-6Al-4V)	115	0.32

3.4.8 Statistical analysis

Statistical analysis was carried out in MINITAB software with the production of analysis of variance (ANOVA) tables, main effects plots and interaction plots. Analysis of variance is a statistically based, objective decision-making tool performed on the obtained data to determine which of the examined factors and/or levels is statistically significant at the 95% confidence interval with respect to output response (G-ratio, grinding forces, grinding temperature, surface roughness, etc.). In ANOVA, the null hypothesis assumes that there are no significant differences between the populations means of independent factor levels for a given dependent factor or response, while the alternative hypothesis states that a difference between means does exist. In simple terms, ANOVA estimates F values (mean sum of squares between sample variations over mean sum of squares within sample variations) for each independent factor with respect to response or dependent variable. If this value lies beyond the F-critical value limit or is bigger than the F-critical value, then there is strong evidence against the null hypothesis, thus it is rejected. The 95% confidence interval indicates the p-value which is associated with the estimated F-value (critical value) from analysis of variance. If the p-value is equal to or less than 0.05, then the null hypothesis is rejected, and the alternative hypothesis is supported [151]. The purpose of the main effects plot is to graphically present the difference in levels means for one or more factors. Interaction plots are a graphical tool that demonstrates how the relationship between independent and dependent variables changes depending on the value of another independent variable or how the effect of a given variable on the response changes with respect to another variable [151].

3.5 Experimental designs and test arrays

The research involved three main phases of experimental testing. Phase 1 investigated creep feed grinding of gamma titanium aluminide alloy (Ti-45Al-8Nb-0.2C). Phase 2 covered experimental details following creep feed grinding of burn-resistant titanium alloy (Ti-25V-15Cr-2Al-0.2C), while Phase 3 evaluated conventional titanium alloy Ti-6Al-4V when creep feed grinding. Each phase is subdivided into relevant sub-phases as listed below:

Phase 1: Creep feed grinding of γ-titanium aluminide alloy (Ti-45Al-8Nb-0.2C)

- Phase 1A: The influence of operating conditions on grinding performance when creep feed grinding with conventional silicon carbide wheel (SiC).

- Phase 1B: Effect of operating conditions on grinding performance when creep feed grinding with a super-abrasive diamond wheel and a comparison between two different wheel systems.

- Phase 1C: Extended surface integrity analysis (residual stresses).

Phase 2: Creep feed grinding of burn resistant titanium alloy (Ti-25V-15Cr-2Al-0.2C)

- Phase 2A: Assessment of significant operating parameters when creep feed grinding with conventional silicon carbide wheel (SiC) and benchmark against γ-titanium aluminide alloy (Ti-45Al-8Nb-0.2C).
- Phase 2B: Assessment of grinding performance when creep feed grinding with a super-abrasive diamond wheel and benchmark against γ-titanium aluminide alloy (Ti-45Al-8Nb-0.2C).

- Phase 2B: Extended surface integrity analysis (residual stresses).

Phase 3: Creep feed grinding of conventional titanium alloy (Ti-6Al-4V)

- Phase 3A: Benchmarking the performance against γ-titanium aluminide alloy and burn-resistant titanium alloy with SiC wheel.

- Phase 3B: Benchmarking the performance against γ-titanium aluminide alloy and burn-resistant titanium alloy with a diamond wheel.

- Phase 3C: Comparison of the performance of different super-abrasive wheel specifications.

- Phase 3D: Extended surface integrity analysis (residual stresses).

These phases were developed to fulfil the objectives of this study (detailed in section 1.2) and to meet the assessment criteria (grinding ratio, wheel wear, grinding forces, grinding power, specific energy, temperature, workpiece surface integrity and surface topography) for each alloy (γ-TiAl, BuRTi and Ti-6Al-4V). Subsequent sections provide comprehensive descriptions for each phase/subphase, except for residual stresses and their associated procedures and test arrays.

3.5.1 Phase 1: Creep feed grinding of γ-titanium aluminide alloy (Ti-45Al-8Nb-0.2C)

3.5.1.1 Phase 1A: The influence of operating conditions on grinding performance when creep feed grinding with conventional silicon carbide wheel (SiC).

This phase is carried out as part of Objective 2 and was aimed to investigate the influence of operating conditions on grinding ratio, wheel wear, grinding forces, grinding power, specific energy, temperature, workpiece surface integrity and surface topography. The selection of levels and factors was largely based on earlier work by Bentley and Aspinwall, Hood and Bhaduri, which involved creep feed grinding of γ-titanium aluminide alloy with SiC wheels [184], [186], [194]. All possible factors and levels in creep feed grinding, as reported in [7], [17], are shown in Table 3-4.

Table 3-4: List of possible factors and levels in creep feed grinding [7], [17]

	Factors	Levels
Wheel	Grit material	SiC, cBN, diamond
	Grit size (conv. abrasives) Grit size (diamond and cBN)	46 - 600 mesh (508 – 8 µm) 430 – 8 µm
	Wheel grade / friability	Soft (A) – Hard (Z)
	Bond type	Resin, Metal, Vitrified, Electroplated
	Bond structure: Concentration (conv. abrasives) Concentration (diamond, cBN)	Dense – Open 1 – 30 50 – 200
	Wheel profile	Plain, Profiled
	Wheel diameter	50 – 400 mm
	Wheel width	10 – 50 mm
Operation	Surface speed	15 – 60 m/s
	Depth of cut (CFG)	0.01 – 10 mm
	Feed rate	10 – 1000 mm/min
	Wheel direction	Up, Down
Dressing	Dressing method	Intermittent, Continuous
	Dresser type	Single point diamond Diamond wheel crush Brake truer
	Dresser speed, cont. dressing	-1.5 – +1.5 x v_s
	Dresser feed rate, cont. dressing	1.5 µm/rev.
	Infeed rate, intermittent dressing	5 – 500 µm
Fluid	Fluid type	Water based, Oil, Synthetics
	Fluid application	Jet, Shoe
	Fluid flow rate and pressure	1 – 360 l/min; 0 – 100 bar

In order to limit the number of experiments and reduce the extensive time required to test all detailed factors and levels above, it is concluded to investigate the most significant factors (based on literature) with other factors kept fixed. A full factorial experimental design comprising eight tests was used, including three independent factors (wheel speed, depth of cut, and feed rate), each at two levels. Array details are given in Table 3-5. This factorial experimental design allows the evaluation of interactions between variables, which was not possible with a Taguchi design. Replications were not possible due to a lack of materials and the associated cost of testing.

Table 3-5: Phase 1A operating factors and levels

Test no.	**Factors and Levels**		
	Wheel speed (m/s)	Depth of cut (mm)	Feed rate (mm/min)
1	20	0.3	150
2	20	0.3	300
3	20	1.0	150
4	20	1.0	300
5	30	0.3	150
6	30	0.3	300
7	30	1.0	150
8	30	1.0	300

Following preparation and pre-machining of TiAl testing blocks (EDM, surface grinding and drilling), a thermocouple was placed into the blind hole of a rectangular block sized 48mm×70mm×13mm, then the resin epoxy powder was mixed with water and poured into the blind hole to bond the thermocouples junction with the workpiece. After the mixture dried and cured, the rectangular block was then screw-mounted on the Kistler platform. The mixing ratio and curing schedule are detailed in Appendix D. A plain profile vitrified bonded silicon carbide (SiC) grinding wheel (GC60J45VKRNN) with an open structure was used in all trials. Down grinding was performed in all trials involving five consecutive passes at 48 mm cut length and without spark-out, giving a maximum volume material removed of 4800 mm^3 for tests involving a 1mm depth of cut and 1440 mm^3 for a 0.3 mm depth of cut tests. The dressing ratio, infeed of the dresser per revolution and the dressing depth were kept fixed at 0.8, 2.0μm and 50μm, respectively, for all tests and performed prior to each test (intermittent dressing) to provide a sharp wheel. The cooling jet nozzle pressure was constant at 7bar and was aimed at the wheel/workpiece contact area; the nozzle was placed 100mm from the contact area, whilst the cleaning nozzle was placed 20mm from the wheel. This was aimed at the rear of the wheel

to eliminate the effect of the air barrier with a constant pressure of 20 bar. Grinding wheel wear was calculated after each grinding pass, while grinding forces, power, and temperature were measured during each pass for each test. After each grinding pass, the workpiece was left to cool to room temperature. The Minimum Surface Integrity Data Set (detailed in section 2.3.2) was performed for surface integrity assessment for surfaces produced at the end of every test. The respective experimental setup for this phase and all subsequent phases in this study is shown in Figure 3-18. Analysis of variance (ANOVA) was performed on measured data to identify significant factors and percentage contribution ratio (PCR) of each factor or interaction together with corresponding main effects plots and interaction plots.

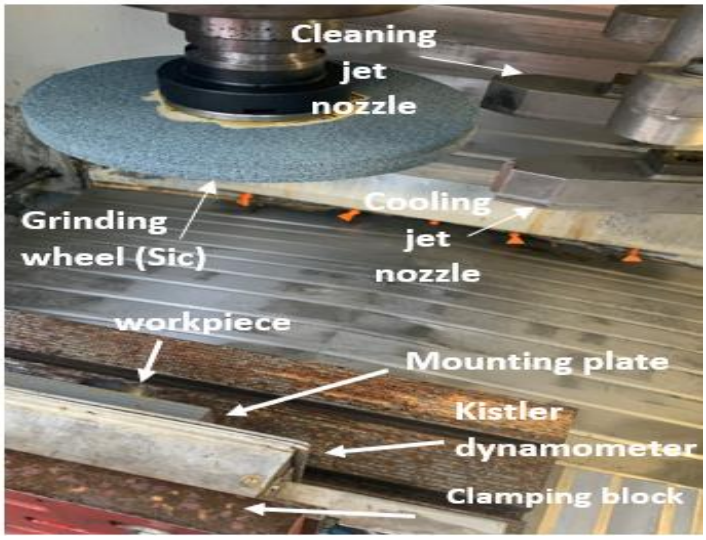


Figure 3-18: Experimental set-up

3.5.1.2 Phase 1B: Effect of operating conditions on grinding performance when creep feed grinding with super-abrasive diamond wheel and a comparison between two different wheel systems.

The work in this phase investigated the performance of super-abrasive grinding wheels on output measures (as part of Objective 4), with grinding performance evaluated identically to that of Phase 1A. A full factorial design in which two factors, each at two levels, were established. The design considered variations in depth of cut (0.3mm and 1mm) and feed rate (150mm/min and 300mm/min), while the wheel speed was kept fixed at 30m/s. Table 3-6 details the test array used in this phase. Chosen levels of depth of cut, feed rate and wheel speed allowed a direct comparison between conventional and super-abrasive wheels' performance.

Due to limitations in workpiece material, only four tests were performed for the current phase. Tests were carried out with a vitrified bonded diamond wheel characterised by 91µm grit size and 38.75% porosity. Grinding fluid application arrangements as well as dressing parameters, are similar to that of Phase 1A except for dressing depth, which was reduced to 5µm to reduce pull-out of wheel grains as recommended in earlier work.

Table 3-6: Phase 1B tests array

Test no.	Factors and Levels	
	Depth of cut (mm)	Feed rate (mm/min)
1	0.3	150
2	0.3	300
3	1.0	150
4	1.0	300

3.5.2 Phase 2: Creep feed grinding of burn resistant titanium alloy (Ti-25V-15Cr-2Al-0.2C)

3.5.2.1 Phase 2A: Assessment of significant operating parameters when creep feed grinding with conventional silicon carbide wheel (SiC) and benchmark against γ-titanium aluminide alloy (Ti-45Al-8Nb-0.2C)

The main purpose of this phase is to achieve Objectives 2 and 3 by identifying the significance of operating factors and their interactions on responses and to benchmark the performance of BuRTi alloy against γ-titanium aluminide. Discussion on whether to include both γ-titanium aluminide and BuRTi alloy in one factorial design has concluded that the results of the experiments would not be accurately assignable to one material. Therefore, it was decided to separate the two materials in order to gain exact data on both materials individually; only then more realistic comparisons can be made between the two materials. In this phase, the whole experiment design used in Phase 1A was replicated for the BuRTi material using the same experimental setup, procedures, and the same fixed parameters. The cooling nozzle pressure in this phase was set to 15bar instead of 7bar in an attempt to minimise the severity of burn marks observed in the majority of produced surfaces in earlier work at 7bar cooling fluid pressure [24], [25]. Moreover, burn-resistant titanium alloy has a considerably lower thermal

conductivity value of 10W/mK compared to γ-titanium aluminide alloy 22W/mK, which would be anticipated to result in significantly higher temperatures when grinding the former. Test 4, which operates at a moderate material removal rate with a 1mm depth of cut, 150mm/min feed rate, and 20m/s wheel speed, was conducted twice during this phase. This was because of the abnormally low recorded temperature in the first trial, which was very likely due to inappropriate setup/installation or faulty thermocouple. Replication of the test did show a significant change in temperature, while similar trends were observed in terms of grinding ratio, forces and power. The evaluation of the grinding performance was used in the same manner as Phase 1A.

3.5.2.2 Phase 2B: Assessment of grinding performance when creep feed grinding with super-abrasive diamond wheel and benchmark against γ-titanium aluminide alloy (Ti-45Al-8Nb-0.2C)

As with Phase 1B, work in this phase involved further assessment of significant operating parameters on response measures when operating with a super-abrasive wheel (as part of objectives 4 and 5). Experiments were performed in accordance with a two factors two levels full factorial design; the fixed and variable factors were the same as in Phase 1B, including varying depth of cut and feed rate, constant wheel speed, application of fluid and wheel dressing parameters. This enables a direct comparison between the two different materials. The grinding performance was assessed in identical ways to those described in Phase 1A. During the drilling of the thermocouple hole in Test 1 block, the drill broke inside the blind hole; thus, a second thermocouple blind hole was drilled on this sample (6mm from the middle site of the original blind hole).

3.5.3 Phase 3: Creep feed grinding of conventional titanium alloy (Ti-6Al-4V)

3.5.3.1 Phase 3A: Benchmarking the performance against γ-titanium aluminide alloy and burn resistant titanium alloy with SiC wheel

Phase 3A involves benchmarking trials of Ti-6Al-4V against γ-titanium aluminide alloy and burn-resistant titanium while operating with SiC wheels so as to meet Objective 3. Due to time and financial constraints, only two tests were conducted on Ti-6Al-4V materials. Tests were performed at a constant feed rate (150mm/min), wheel speed (20m/s) and varying depths of cut (0.3mm and 1mm). These were then compared with γ-titanium aluminide and burn-resistant titanium material tests machined at identical parameters. Table 3-7 details the test array. All other operational parameters were as described previously in phase 1A, including fluid application and dressing. Grinding performance is evaluated similarly to previous phases.

Table 3-7: Phase 3A tests details

Test no.	Depth of cut	Workpiece material
1	0.3	Ti-6Al-4V
2	1	Ti-6Al-4V
3*	0.3	γ- titanium aluminide
4*	1	γ- titanium aluminide
5*	0.3	BuRTi
6*	1	BuRTi

*Note: Tests 3,4,5 and 6 were carried out as part of phases 1A and 2A

3.5.3.2 Phase 3B: Benchmarking the performance against γ-titanium aluminide alloy and burn resistant titanium alloy with diamond wheel

Together with phase 2B, this phase was designed to fulfil Objectives 4 and 5. It details the performance of creep feed grinding of Ti-6Al-4V with a super-abrasive wheel. This was achieved using identical sequences of tests performed in phases 1B and 2B to allow direct comparisons between the performance of the three different materials. This meant a total of 4 tests were replicated for Ti-6Al-4V involving variation in depth of cut and feed rate, while all other parameters were fixed.

3.5.3.3 Phase 3C: Comparison of the performance of different super-abrasive wheel specifications

The main purpose of this phase is to compare the performance of a new specification super-abrasive wheel (electroplated single layer diamond wheel) against the wheel used before (vitrified diamond wheel) in phases 1B, 2B, and 3B when creep feed grinding Ti-6Al-4V. This wheel is characterised by high-hardness grit materials and good bond strength. Table 3-8 details the tests that were conducted for this phase. Tests were carried out at constant wheel speed (30m/s) and feed rate (150mm/min) with variations in depth of cuts. All other parameters were kept fixed and typical to those provided in phase 3B. Unfortunately, Test 1 was terminated after the first pass due to the risk of wheel damage resulting from grit/bond failure. The depth of cut was accidentally set to 1mm instead of 0.1mm, which is a typical value for this particular type of wheel (finish operation). This resulted in excessive grinding noise and high forces of up to 3500N. Replication was not possible as only a single wheel of each grit size was available for this phase. Due to the limited availability of workpiece material, no further benchmarking tests on γ-titanium aluminide or burn-resistant materials were possible with a single-layer electroplated diamond wheel.

Table 3-8: Phase 3C tests array

Test no.	Wheel specification	Depth of cut
1	Single layer electroplated diamond (D46)	0.1mm
2	Single layer electroplated diamond (D126)	0.3mm
3*	Vitrified diamond wheel	0.3mm
4	Single layer electroplated diamond (D252)	1mm
5*	Vitrified diamond wheel	1mm

*Note: Tests 3 and 4 were performed as part of phase 3B

4 RESULTS AND DISCUSSION

4.1 Phase 1: Creep feed grinding of γ-titanium aluminide alloy (Ti-45Al-8Nb-0.2C)

4.1.1 Phase 1A: The influence of operating conditions on grinding performance when creep feed grinding with conventional silicon carbide wheel (SiC)

4.1.1.1 Wheel wear and G-ratio

Figure 4-1 shows the effects of operating conditions on the average G-ratio and radial wear rate. Typically, results showed that as the radial wear decreases, the grinding ratio increases. A volume of 960mm^3 is removed per pass for 1mm depth of cut tests (Test 3, 4, 7, 8), and a volume of 288mm^3 is removed from 0.3mm depth of cut tests (Test 1, 2, 5, 6). The maximum G-ratio (16) was obtained at one of the passes when operating with Test 7 parameters (1mm depth of cut, 30m/s wheel speed, and 150mm/min feed rate). In general, the average G-ratio in all tests ranged from 6 to 13. These findings are consistent with previous results reported by Hood et al. [184]. When creep feed grinding gamma TiAl alloy of Ti–45Al–8Nb–0.2C wt% using SiC abrasives wheels, G-ratios between 2 and 15 were achieved. G-ratio values of 3.2 - 8 were later detailed by Bhaduri et al. [186] when ultrasonic creep feed grinding of a different γ-TiAl alloy (Ti–45Al–2Mn–2Nb + 0.8 vol.%TiB_2XD) with SiC abrasive wheels.

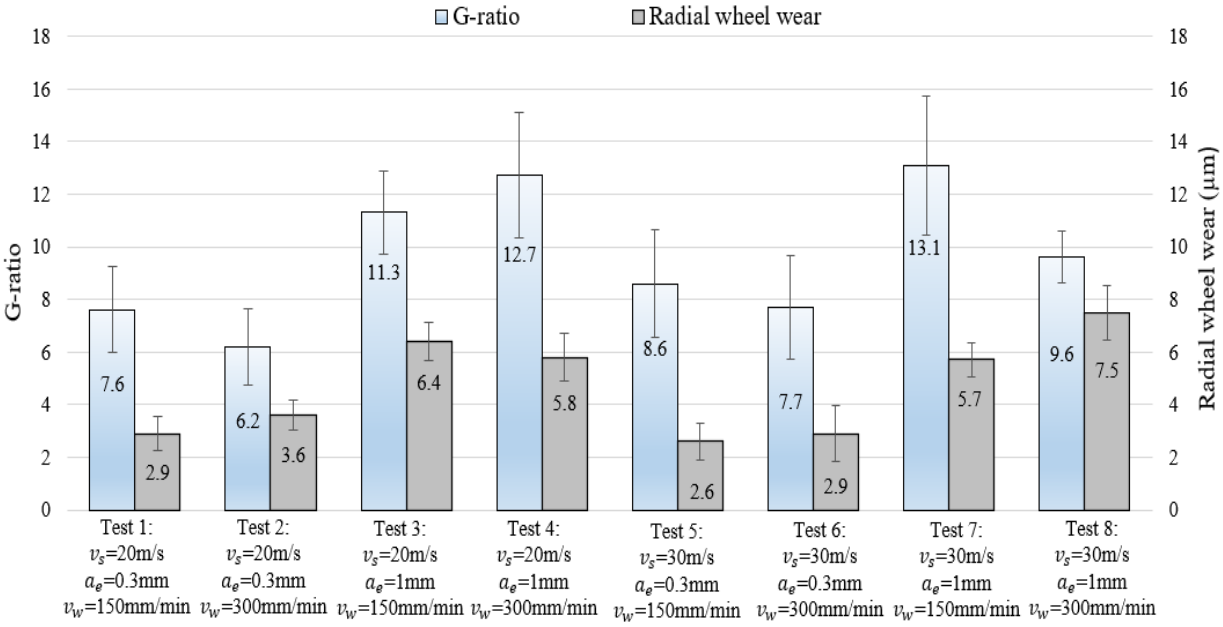


Figure 4-1: G-ratio and radial wheel wear for different grinding conditions (Phase 1A)

Grinding passes for Tests 3, 4, and 6 showed an upward trend in G-ratios up to 3840mm^3 (for Test 3 and 4) and up to 1152mm^3 (for Test 6), as increasing the volume of material removed increased the corresponding G-ratio. In contrast, other tests showed a downward trend and more wheel wear. This trend is contrary to previous studies, which have suggested that a typical wheel wear mechanism consists of three stages: initial wear, steady-state, and accelerating wear [60], [61]. This contradictory trend may reflect the differences in wheel type, porous and open nature. Also, the measurement limitations in terms of CMM accuracy (±5µm) may have caused uncertainty during wheel diameter measurement. Analysis of variance for G-ratio given in Appendix F, Tabel F1, highlights only depth of cut as a significant factor at a 95% confidence interval, with a considerably high contribution (PCR) of 76.80%. Indeed, the main effects plot for G-ratio in Figure 4-2 shows an increase by 60% in G-ratio with depth of cut rising from 0.3mm to 1mm. The associated interaction plot is provided in Appendix F, Figure F1. Interactions between factors were evident except for (feed rate × depth of cut); however, none of the interactions were significant.

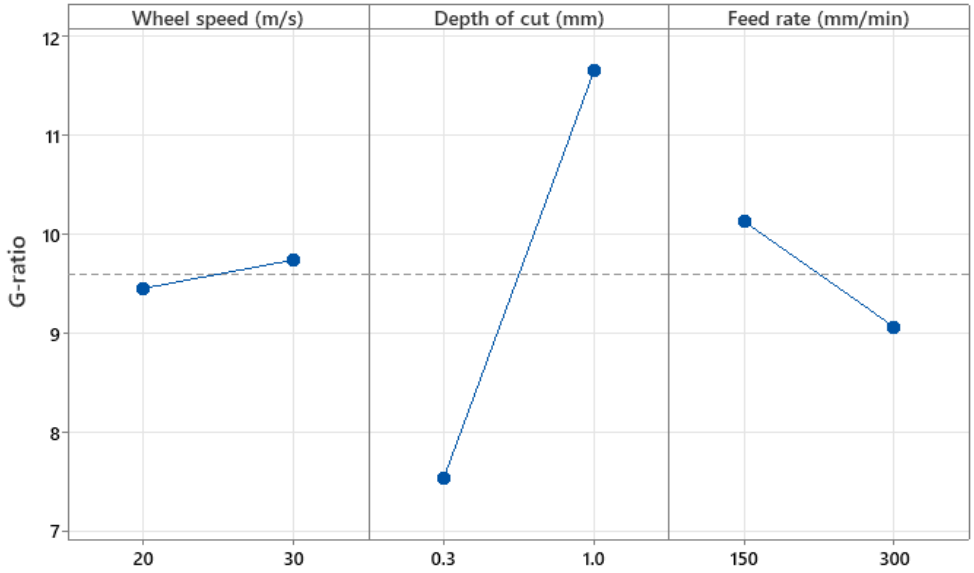


Figure 4-2: The main effect plot for G-ratio (Phase 1A)

4.1.1.2 Grinding forces, power and specific energy

Maximum tangential and normal forces for all tests are plotted in Figure 4-3. Maximum tangential forces varied from 338 to 570N, while the maximum normal forces were between 597 and 1789N. These results are comparable to those reported in [184], [186]. As expected, the lowest operating parameters (feed rate of 150mm/min, depth of cut of 0.3mm, and wheel speed of 20m/s) in Test 1 produced the lowest grinding forces (values of 338N and 597N for

tangential force and normal force, respectively). Similarly, the maximum grinding forces (533N for tangential force and 1789N for normal force) were obtained when operating with the highest operating parameters in Test 8 (feed rate of 300mm/min, depth of cut of 1mm, and wheel speed of 30m/s). Increasing the wheel speed from 20 to 30m/s whilst the depth of cut and feed rate were kept constant (Test 5 and 1) caused an increase in normal and tangential forces of ~200N and ~80N, respectively. This is likely due to increased grit wear flat area associated with increased wheel velocity, leading to more ploughing and sliding forces [50], [57]. Likewise, increasing the depth of cut while both feed rate and wheel speed remain constant (in Tests 5 and 7) produced a 700N increase in normal force component due to the longer contact area between the wheel and the workpiece and an increase in undeformed chip thickness associated with higher depth of cut.

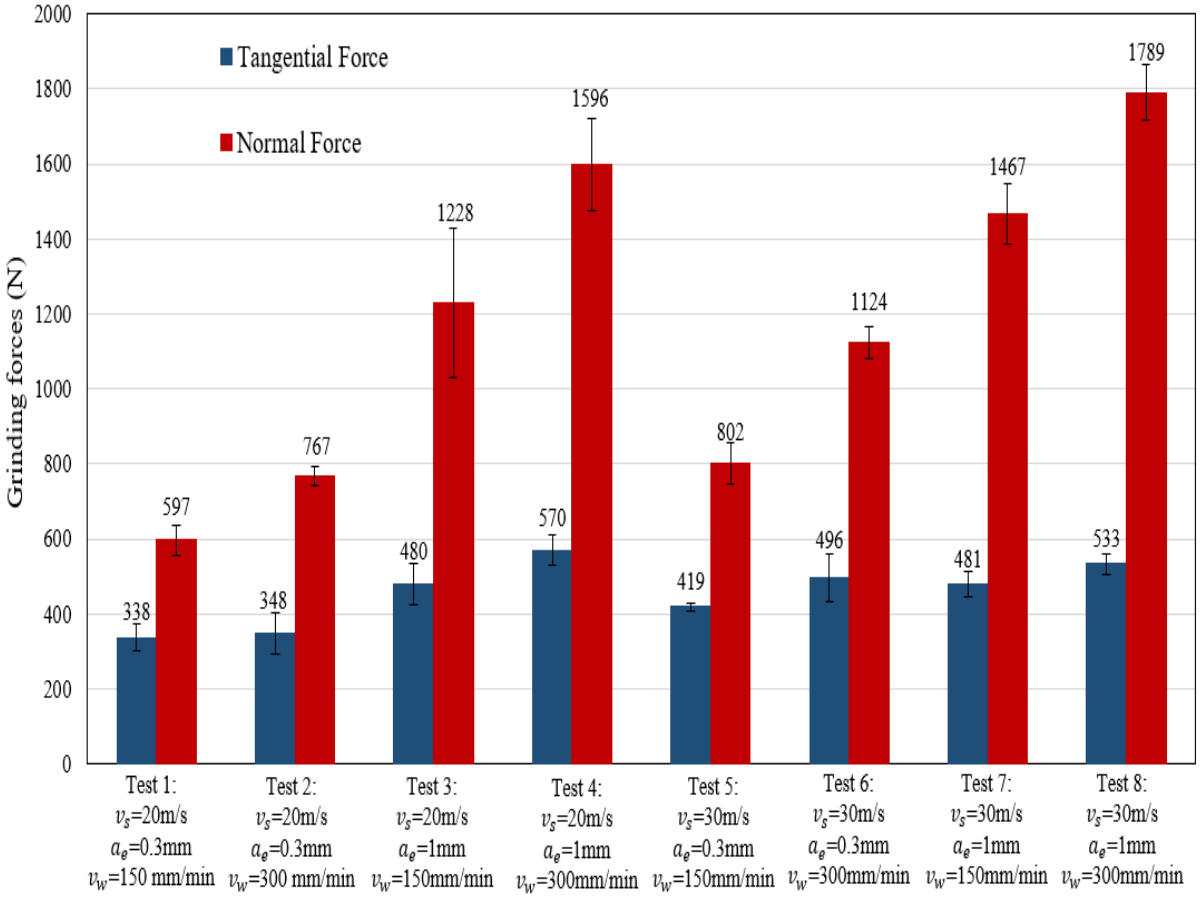


Figure 4-3: Grinding forces for different operating conditions (Phase 1A)

Analysis of variance tables for normal and tangential forces are presented in Table 4-1 and Table 4-2, respectively. Grinding force traces for all tests, along with corresponding main effects plots and interaction plots, are detailed in Appendix F, Figures F2 to F6. For normal

forces, all factors were identified as significant at the 5% level with depth of cut contributing the highest PCR of 74.68%. Whilst analysis for tangential forces revealed only the depth of cut is statistically significant with a PCR of 59.14%.

Table 4-1: ANOVA table for normal forces (Phase 1A)

Source	DF	Seq SS	Contribution	Adj SS	Adj MS	F-Value	P-Value
Wheel speed (m/s)	1	111628	8.88%	111628	111628	25.65	0.007
Depth of cut (mm)	1	939135	74.68%	939135	939135	215.78	0.000
Feed rate (mm/min)	1	189420	15.06%	189420	189420	43.52	0.003
Error	4	17410	1.38%	17410	4352	-	-
Total	7	1257593	100.00%	-	-	-	-

Table 4-2:ANOVA table for tangential forces (Phase 1A)

Source	DF	Seq SS	Contribution	Adj SS	Adj MS	F-Value	P-Value
Wheel speed (m/s)	1	5941	11.80%	5941	5941	2.52	0.188
Depth of cut (mm)	1	29768	59.14%	29768	29768	12.63	0.024
Feed rate (mm/min)	1	5202	10.33%	5202	5202	2.21	0.212
Error	4	9427	18.73%	9427	2357	-	-
Total	7	50338	100.00%	-	-	-	-

Power trends are similar to those given for normal forces. The lowest power levels (3.85KW) were obtained using the lowest operating parameters (Test 1), while the greatest power levels (18.7KW) were produced using the highest operating parameters (Test 8). This confirms the previous finding reported by Hood [184] when creep feed grinding the same material with different operating parameters. Calculated specific energy ranged from 142J/mm^3 to 370 J/mm^3. When using Test 5 operating parameters, the highest specific energy levels were recorded, whereas the lowest values were recorded when operating with Test 4 operating parameters. Main effects plots for specific energy in Figure 4-4 showed a decreasing trend with a higher depth of cut and feed rate. This reflects those trends in [7], [17], [55], [162] that reported the effect of volumetric removal rate on specific energy. Bentley created a composite graph from multiple studies demonstrating specific grinding energies for different titanium alloys ground with SiC abrasives. He demonstrated that increasing material removal rates caused lower specific energy [17]. Moreover, as defined in equation 4, specific energy is inversely proportional to feed rate and depth of cut, which further supports the trends for specific energy.

Main effects plots for power, interaction plots and analysis of variance tables for power and specific energy are provided in Appendix F, Figures F7 to F9 and Tables F2 and F3. Interestingly, analysis of variance results for grinding power and specific energy within the tested factors and levels indicated that wheel speed, feed rate, and depth of cut are all statistically significant. This is contrary to that of Hood [7] who found that no factors for both output measures were significant. Interaction plots for power and specific energy show no interaction between factors is present.

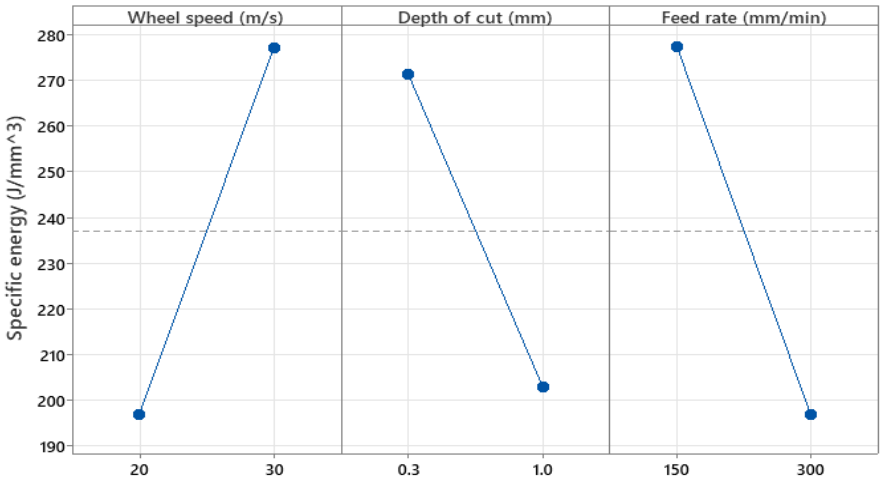


Figure 4-4: Main effect plot for specific energy (Phase 1A)

4.1.1.3 Grinding temperature

In creep feed grinding, the surface temperature results from heat generated from the relative motion between the grinding wheel abrasives and the workpiece in the contact area. This heat is a consequence of grinding energy generated during the grinding process. Malkin [50] defines grinding energy as the sum of sliding energy, ploughing energy, and chip formation energy from grains interactions. Measured temperatures at the last pass of each test are demonstrated in Figure 4-5. Surprisingly, the highest operating parameters did not produce the maximum temperature. A temperature of 582°C was recorded when operating with the highest levels of factors in Test 8 (v_s=30m/s, v_w=300mm/min, a_e=1mm), whereas operating with Test 7 parameters (both depth of cut and wheel speed are kept constant and feed rate reduced from 300mm/min to 150mm/min), produced a maximum temperature of 692°C. It may be that in the case of the former (Test 8), a faster feed rate has prevented heat build-up in the contact area due to shorter contact time between the wheel abrasives and workpiece. Temperature as high

as 1201°C was reported by Xinxin et al. when creep feed grinding a γ-TiAl alloy with silicon carbide wheel at v_s=30m/s, v_w=120mm/min, a_e=1mm [18]. In contrast to current findings, relatively lower operating parameters produced higher temperatures. A contributory factor is the changes in the γ-TiAl material composition involved in his work (Ti-45Al-2Mn-2Nb-0.1B) compared with (Ti–45Al–8Nb–0.2C) in this work, in addition to the different grinding wheel specifications employed in this study GC60J45V opposed to GC80J12. Similar trends were reported by Novovic as the results showed different magnitudes of temperature (~300°C) when two different systems of silicon carbide grinding wheels were used on Ti-6Al-4V under the same conditions [4]. The thermal conductivity is raised from about 6.7W/mK for the conventional alloy (Ti-6Al-4V) to 22W/mK for gamma alloy due to the significantly higher content of aluminium in comparison to Ti-6AI-4V. Unfortunately, this benefit of γ-TiAl is greatly diminished due to the fact that the material is far less ductile at room temperature than conventional alloys (~2% compared to ~10-15%). At higher temperatures, the ductility of γ-TiAl alloy could rise up to ~5-10% when the brittle-ductile transition is reached. For gamma-titanium aluminide, the transition commonly occurs between 600°C and 700°C, depending on grain size and microstructure [10], [12].

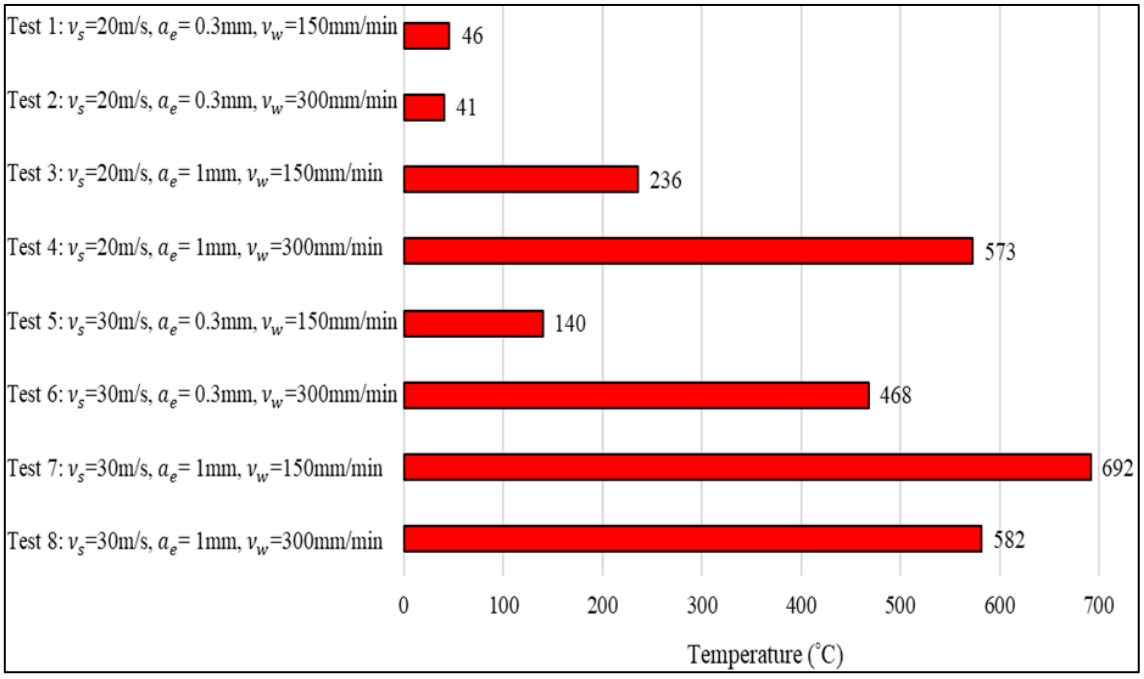


Figure 4-5: Measured maximum temperature at different operating conditions (Phase 1A)

Temperature traces, main effects plot, interaction plot and analysis of variance table for grinding temperature are shown in Appendix F, Figures F10-F12 and Table F4. Typically, the

temperature trace involves three periods. An increasing period after the grinding wheel touches the workpiece and approaches the thermocouple, then it proceeds over until it reaches the tip (peak temperature period), and finally, a cooling period as the wheel leaves the workpiece. The low level of wheel speed and depth of cut resulted in the lowest grinding temperature regardless of feed rate level. Based on the ANOVA calculations, the feed rate had a very low PCR of 7.89%. In comparison, depth of cut and wheel speed had a relatively high PCR of 50.24% and 25.35%, respectively, with only the influence of depth of cut with regard to temperature considered significant.

4.1.1.4 Surface roughness and topography

2D surface roughness parameters (Ra, Rt and Rz) taken from the start and end of grinding tracks on the produced surfaces are given in Figure 4-6, while 3D surface roughness parameters (Sa, St and Sz) are illustrated in Figure 4-7. Dagnall [195] showed that surfaces with entirely different topographies could have similar Ra value, as it only measures the average rather than extreme surface deviations obtained from Rt and Rz values. Information on surface conditions (such as a sharp peak, valley or crack) and surface functional performance (friction, wear, fatigue and fluid retention) can only be obtained when extreme amplitude parameters Rt and Rz are considered [196]. It is observed from Figure 4-6 and Figure 4-7 that 2D amplitude parameter values (Rt and Rz) are much lower than 3D amplitude values (St and Sz). This is mainly because St and Sz denote surface area information on the surface while Rt and Rz indicate one-line information. By contrast, 2D and 3D average parameters (Ra and Sa) showed slight differences in roughness values (~10%). Average surface roughness (Ra) values ranged from 0.74µm to 0.9µm, which are comparable to findings reported in [186] and relativity lower than those reported in [24] using a SiC wheel and slightly different operating conditions. The 3D roughness data shows higher values with increasing depth of cut and feed rate, likely attributed to the increase in undeformed chip thickness as suggested in previous related work. Scatter within extreme roughness parameters (Rt and Rz) was more prominent than in the average roughness parameter (Ra). The variability in topography data is very common in the machining process; significant variabilities of ~45% in extreme roughness parameters and ~15% in average roughness parameters were identified by Sharman for ground surfaces [197].

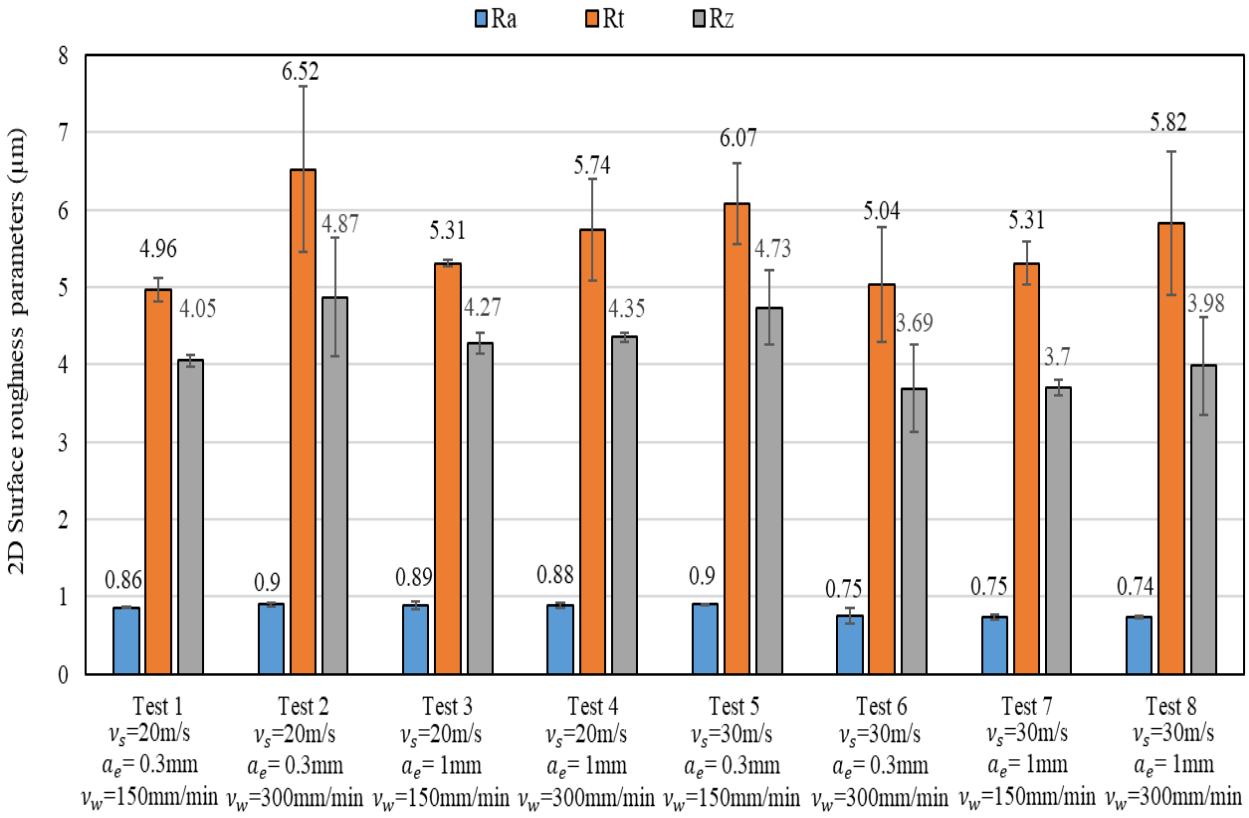


Figure 4-6: 2D surface roughness parameters for ground surfaces (Phase 1A)

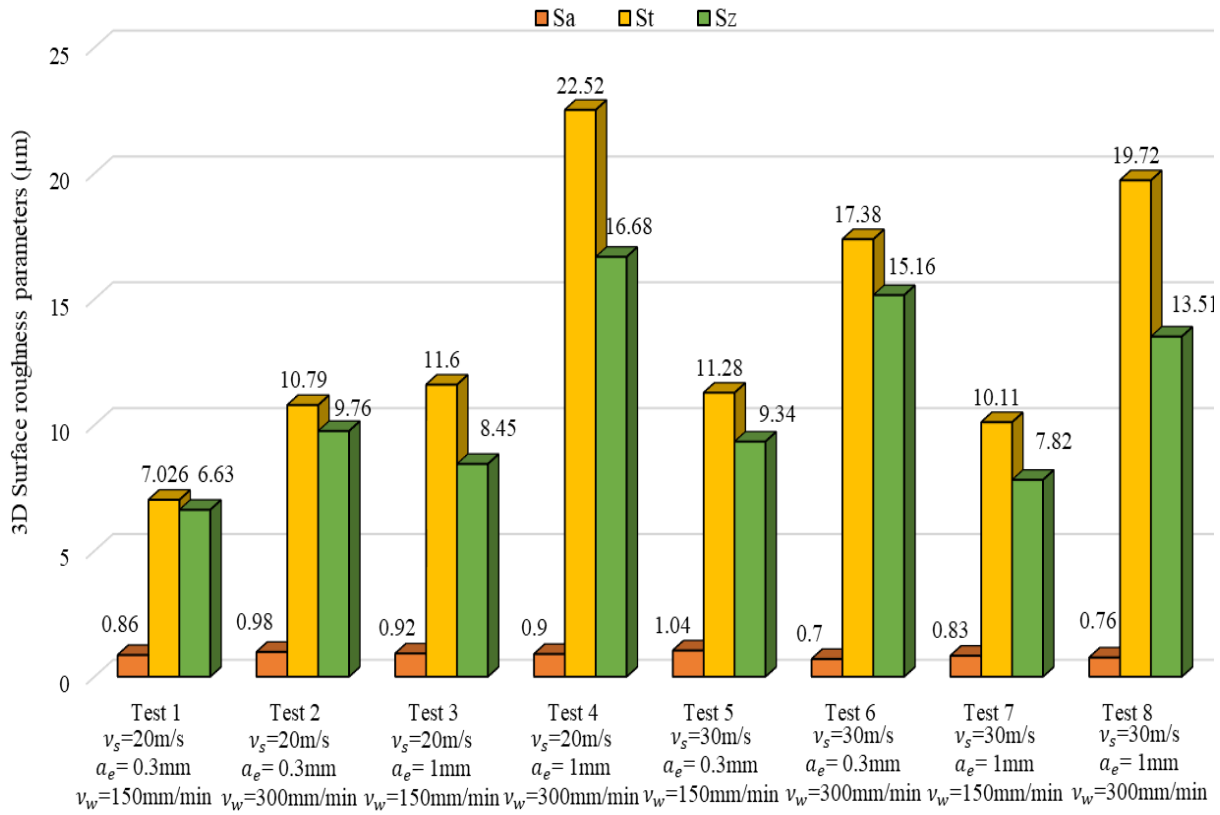


Figure 4-7: 3D topographical parameters of ground surfaces (Phase 1A)

Main effects plots, interaction plots and analysis of variance tables for 2D and 3D roughness parameters are detailed in Appendix F, Figures F13-F24 and Tables F5-F10. Representative 3D mapping of ground surfaces together with 2D roughness profiles is demonstrated in Appendix F, Figure F25 and F26, respectively. The analysis of variance for 2D and 3D roughness parameters shows that none of the factors were significant for Ra, Rt and Rz, and only feed rate was identified as significant for St and Sz with PCR as high as (58% and 68% for St and Sz, respectively). Although not significant, interactions between feed rate and wheel speed were present on most roughness parameters, which accounts for the highest percentage of contributions regarding 2D roughness parameters (PCR of 39% for Rt and 26% for Rz). Trends shown in the main effects plot for average surface roughness parameters Ra and Sa correlate well with findings reported in [186], as increasing the wheel speed resulted in a reduction of average surface roughness values, it is suggested that at higher wheel speed, lower number of grits are in contact with the workpiece surface.

4.1.1.5 Workpiece surface

Images of ground surfaces at the end of each test are presented in Figure 4-8. Of all tests, only surfaces produced with Test 1 and 2 conditions were free of crack, burn, and chatter marks. This corresponds well with the lower temperature produced in Tests 1 and 2 (~45°C). Increasing the wheel speed from 20m/s to 30m/s while keeping the feed rate and depth of cut fixed at a low level in Test 5 resulted in a surface with very slight burning and chatter. Increasing the depth of cut appeared to increase the level of surface damage. Test 4, which is performed at low wheel speed and a high combination of feed rate and depth of cut, showed limited surface burn and chatter. Extensive surface burn and a high level of cracking were evident in Tests 7 and 8, which correspond to tests involving a high level of depth of cut and wheel speed. Similar trends of high levels of cracking and workpiece burn were observed in [7], [194] when creep feed grinding gamma titanium aluminide alloys using SiC abrasive wheels. Elimination and significant reduction of the surface damage were achieved by the use of continuous dressing of the wheel instead of intermittent dressing. This prevented the generation of wear flat and maintained the grinding wheel's sharpness during grinding [194]. It has been reported that an increase in the depth of cut and wheel speed will cause more attritious wear and wear flat generation, resulting in higher sliding components and forces [198]. Higher magnification images of the ground surfaces in Figure 4-9 showed no visible

damage with the surface produced with the lowest operating parameters (Test 1). Some pull-outs, smearing, and fractures were evident with an increase in the severity of operating conditions. Deeper groove grinding marks are observed at higher depth cuts and wheel speeds.

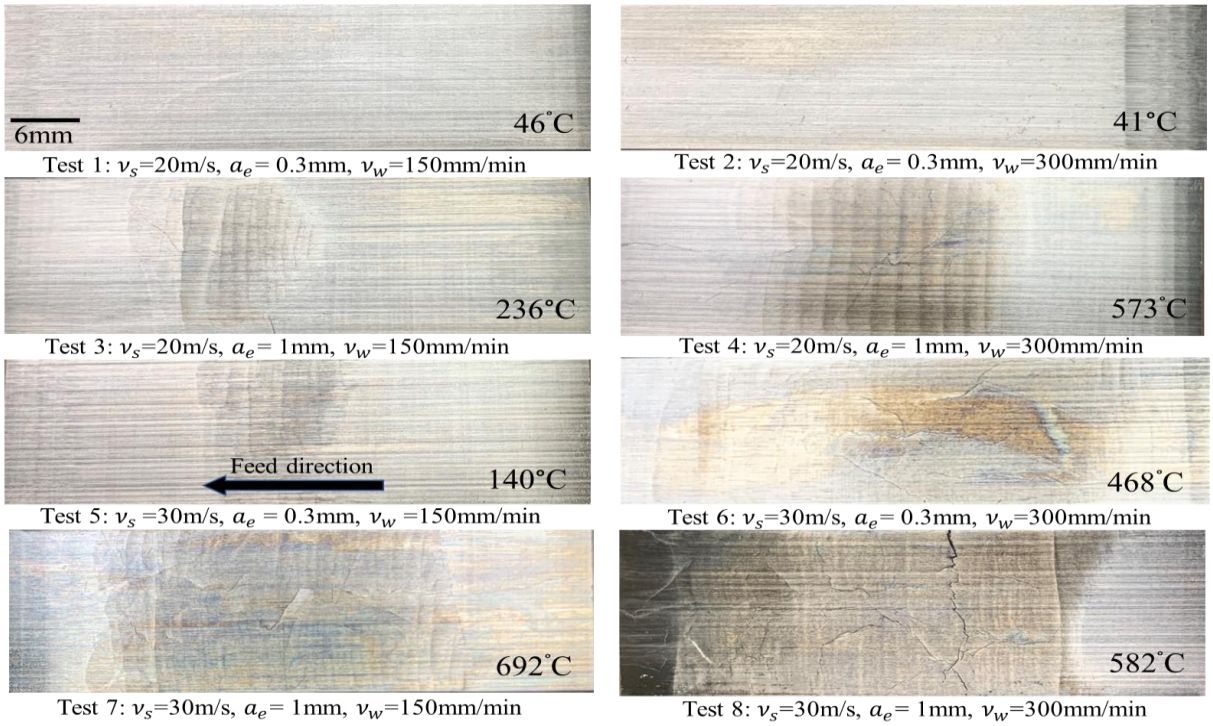


Figure 4-8: Observed ground workpiece surfaces (Phase 1A)

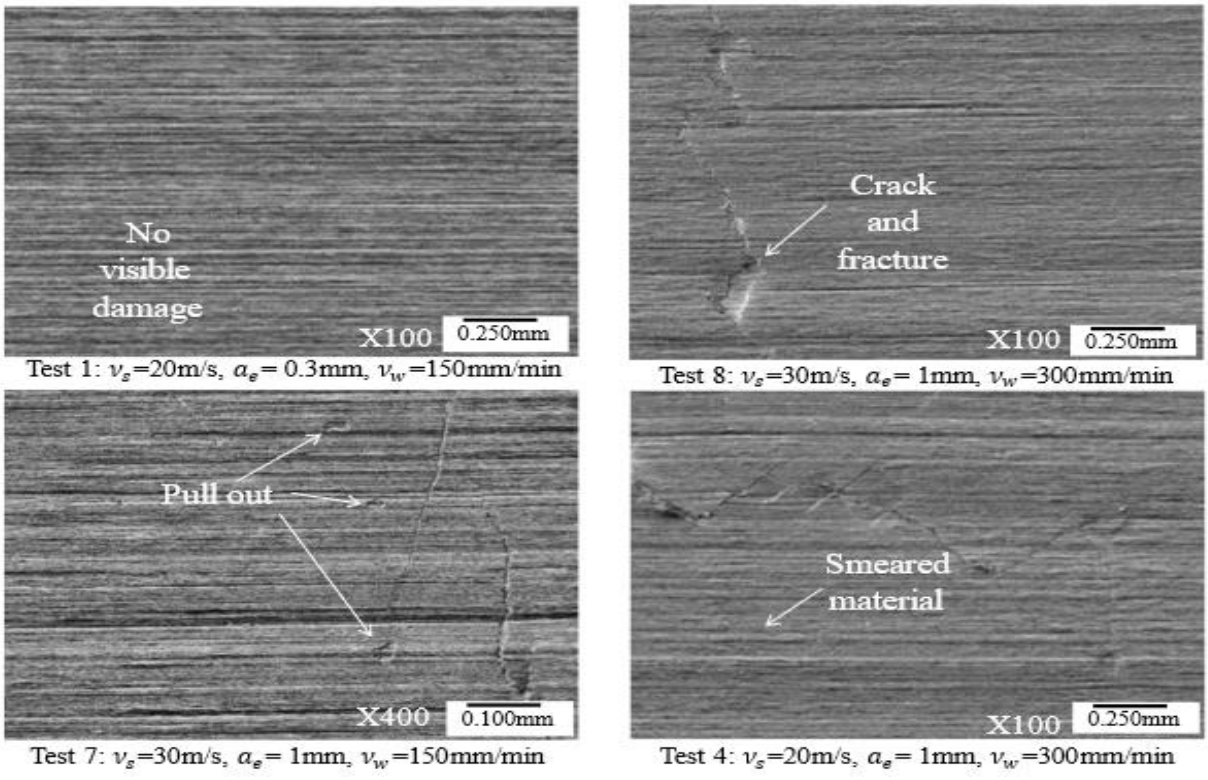


Figure 4-9: Higher magnification images of the ground surfaces (Phase 1A)

4.1.1.6 Workpiece microstructure

Figure 4-10 details visual inspections of tested workpiece sub-surfaces taken from the start of the cut. In general, for most tests, parallel sections appeared smoother than perpendicular sections; surface roughness measurements corroborate this, showing a ~50% decrease in Ra values in the direction parallel to the feed compared to the perpendicular direction. In addition, lamellae deformation was less pronounced in perpendicular sections as they are not subject to feed effect. The majority of sub-surfaces showed smooth surfaces with minimal damage consisting of bending/deformation of the lamellae to a depth of ~5µm in surfaces perpendicular and parallel to feed direction as shown in Test 4 and 8 sub-surfaces. However, no bending was observed in Test 1 and 2 sub-surfaces. The plastic deformation was only seen in tests involving higher generated temperature (exceeded or close to 600°C), which suggests the effect of brittle/ductile transition. Fracture/pull-out is visible on surfaces produced by the most severe operating parameters (Test 8); however, it is restricted to a depth of ~4µm.

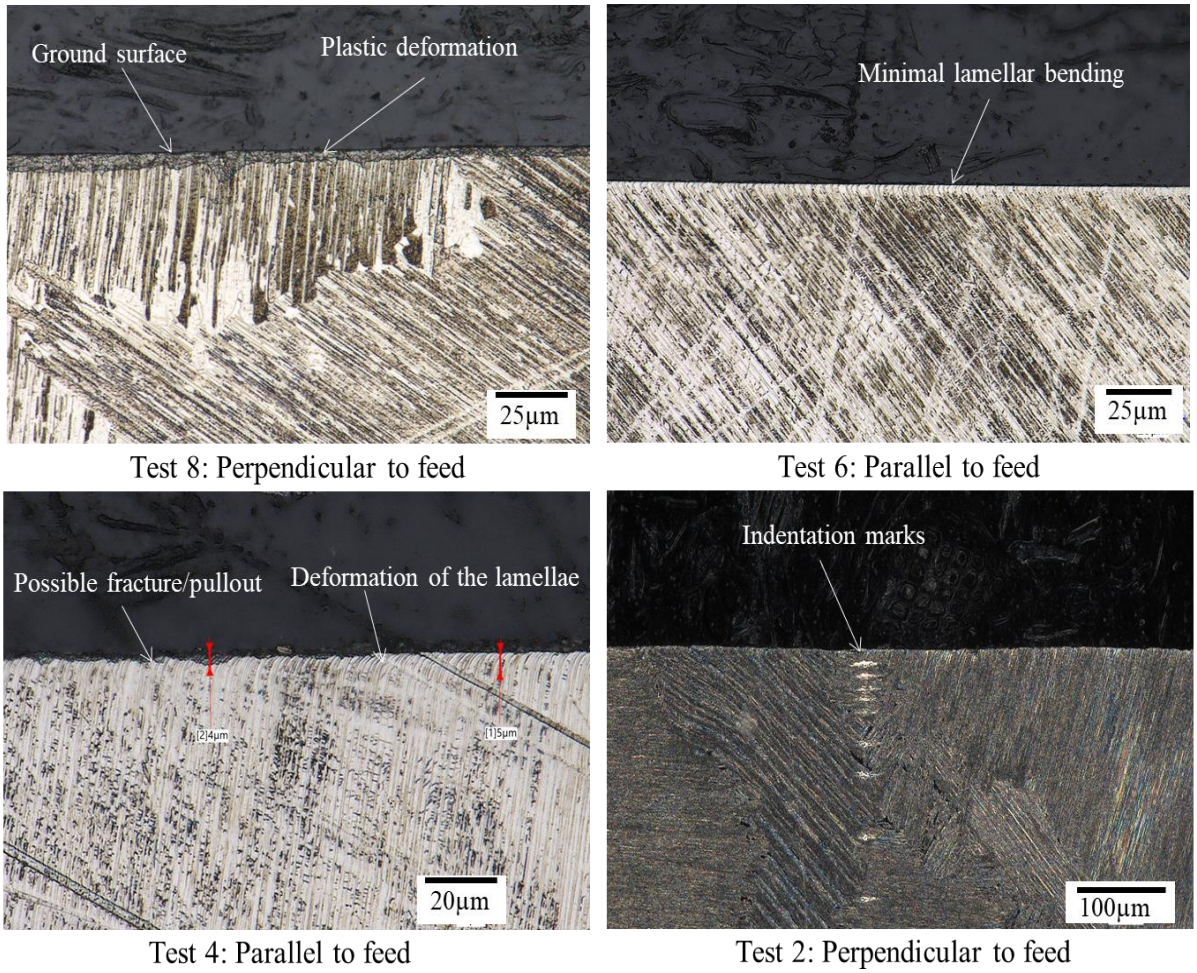


Figure 4-10: Cross-sectional microstructure of ground surfaces (Phase 1A)

4.1.1.7 Workpiece microhardness

Microhardness depth profiles measured in the parallel direction to the feed are given in Figure 4-11, with individual graphs for each test shown in Appendix F, Figure F27. A hardened layer extending to a depth of ~160µm from the workpiece surface was evident in all tests. Operating with a low feed rate and depth of cut in Tests 1 and 5, irrespective of wheel speed, produced the highest microhardness values of 465$HK_{0.050}$ and 498$HK_{0.050}$, respectively. This is in contrast to Hood's study when creep feed grinding γ-TiAl with SiC wheel, as microhardness values were shown to be lowest when operating parameter levels were increased. However, a typical trend was more pronounced with super-abrasive wheels [7]. Minimal softening within the first ~40µm below the surface is observed in Tests 3, 4, 7 and 8, all of which correspond to a 1mm depth of cut. The softening effect is probably related to the microstructural changes that occurred in the material as a result of the elevated temperature. Tests 2 and 6 showed a hardness of ~50$HK_{0.050}$ greater than the bulk value (400$HK_{0.050}$) up to ~500µm below the surface.

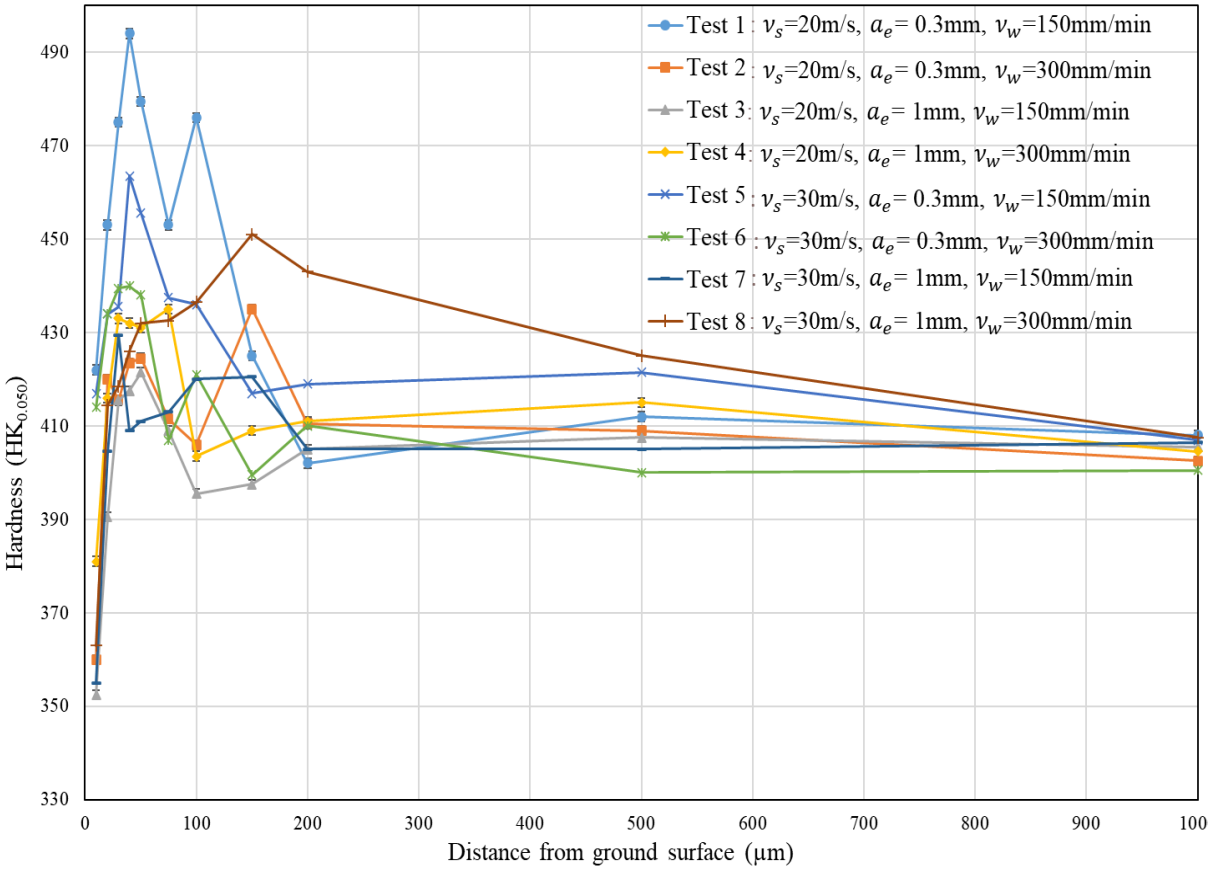


Figure 4-11: Microhardness depth profiles (Phase 1A)

4.1.2 Phase 1B: Effect of operating conditions on grinding performance when creep feed grinding with super-abrasive diamond wheel and a comparison between two different wheel systems

4.1.2.1 Wheel wear and G-ratio

In comparison to the silicon carbide wheel, the diamond wheel showed remarkably lower wear of the wheel (~1µm after 48mm length of cut). The natural hardness of the super-abrasive contributed to a slower rate of wear flat generation, keeping the wheel cutting edge sharper for longer periods. The calculated G-ratio figures also demonstrate the superior performance of the diamond wheel, given in Figure 4-12. The diamond wheel improved the G-ratio by as much as ~1,200% at identical operating conditions (Test 5 in Phase 1A compared with Test 4 in this Phase). While the G-ratio results for the silicon carbide wheel ranged from 6.2 to 13, the G-ratio for the diamond wheel ranged from 19.4 to 127, depending on the depth of cut (0.3 or 1mm). These results are consistent with Hood [7] and Bhaduri [186] findings. While comparing the performance of diamond wheels with silicon carbide wheels when creep feed grinding γ-titanium aluminide, they reported an increase of ~2000% and ~900%, respectively, in G-ratio. The main effects plot, interaction plots and ANOVA table for G-ratio are presented in Appendix F, Figures F28, F29 and Table F11. Depth of cut had a ~93% PCR on the G-ratio value, while the effect of feed rate was negligible with a PCR of ~7%. The figures are comparable to those obtained with the SiC wheel in Phase 1A.

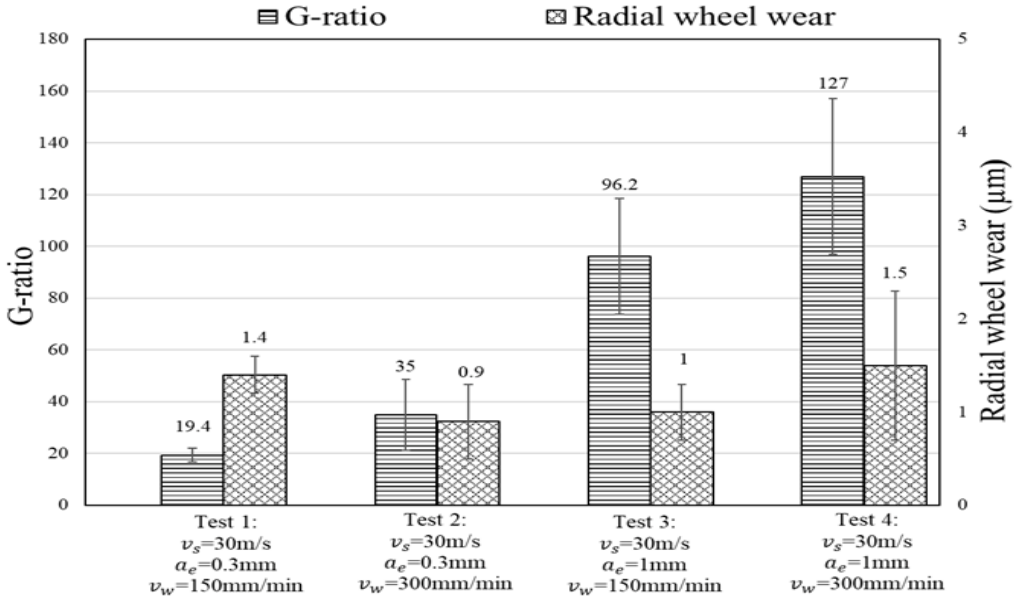


Figure 4-12: Radial wear and G-ratio for diamond wheel at different conditions (Phase 1B)

4.1.2.2 Grinding forces, power and specific energy

The normal and tangential forces component for tested super-abrasive wheels, in comparison to SiC abrasives running at the same operating parameters, exhibited a significant reduction in magnitudes (~60% in normal forces and ~40% in tangential forces) as illustrated in Figure 4-13. The observed reduction in grinding forces between SiC and the diamond wheel is attributed to the lower rubbing forces between the wheel and the workpiece due to the lower wear rate (less wear flats) associated with the latter. Increases of ~10% and ~22% in tangential and normal grinding forces, respectively, were evident with increasing depth of cut from 0.3 to 1mm, with other conditions remaining fixed. In like manner, a change in feed rate from 300 to 150mm/min resulted in ~10% reduction in grinding forces components. Operating at a higher depth of cut and feed rate increased the force per grit and subsequently led to a rise in grain fracture and attritious wear [50].

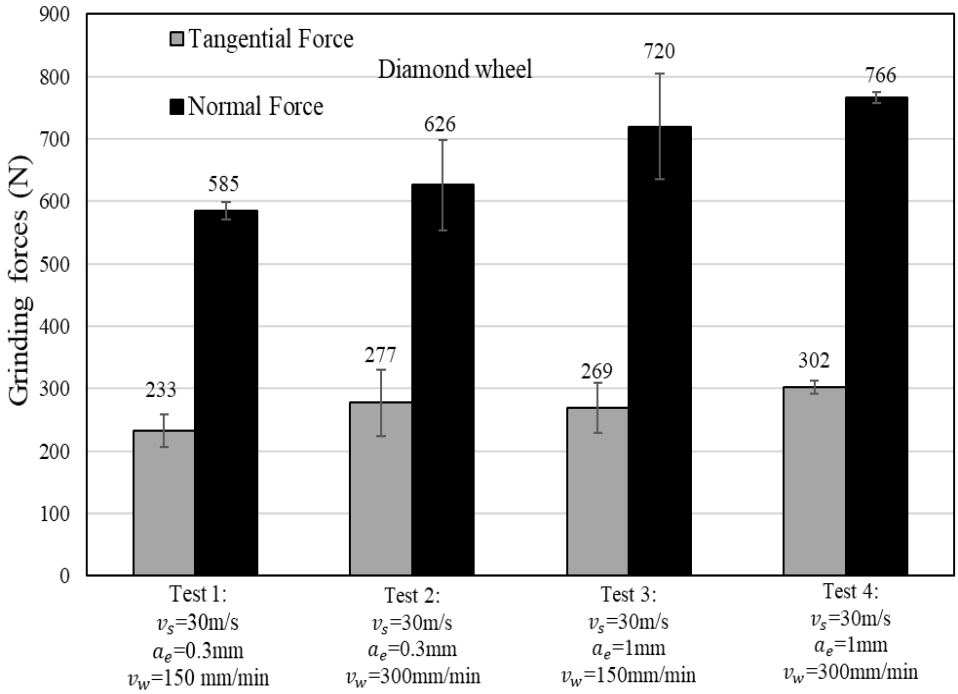


Figure 4-13: Grinding forces at different operating conditions (Phase 1B)

Recorded forces profiles for all tests together with corresponding main effects plots, interaction plots and ANOVA tables for grinding forces, power and specific energy are provided in Appendix F, Figures F30-F38, and tables F12-F15. In general, grinding force traces gradually increase until a plateau is reached due to parity between the rate of wear flats and the generation of new sharp cutting points is achieved. A sudden drop and rise of force magnitudes (spikes)

were less pronounced in the diamond wheel compared to the silicon carbide wheel, with the exception of Test 1 and 2 in (Phase 1B). Spikes observed in Phase 1A corresponded with the formation of chatter/depression marks, cracks or burning on the surfaces ground with SiC wheel at high operating conditions; however, no such damage is visible on diamond ground surfaces. As expected, power and specific energy responses mimicked grinding forces trends. In comparison to previous power values, a decrease of ~50% was achieved at identical operating conditions (18.7KW for SiC compared to 11KW for diamond wheel). As in phase 1A, trends for specific energy were inversely proportional to the depth of cut and feed rate (size of uncut chip thickness). This phenomenon was also detailed by Hwang et al. when grinding silicon nitride by a resin-bonded diamond wheel who described it as 'size effect' [199]. Analysis of variance results for forces, power and specific energy show that depth of cut and feed rate were only significant at the 5% level for normal forces and had the highest PCR in terms of tangential force output. Conversely, the feed rate had a higher PCR value when assessing power and specific energy (~61% and ~82%, respectively)

4.1.2.3 Grinding temperature

Temperature traces for all tests, together with corresponding main effects plots, interaction plots and ANOVA table, are provided in Appendix F, Figures F39-F41, and table F16. Recorded temperatures for diamond tests are shown in Figure 4-14. For involved grinding conditions, low levels of temperature were recorded, generally below 70°C. In comparison to SiC trials, variation in the wheel system used led to substantial changes in the grinding temperature. A maximum grinding temperature of 692°C was recorded when operating at 30m/s wheel speed, 1mm depth of cut and 150mm/min feed rate with the SiC wheel, this significantly reduced to 51°C when the diamond wheel was employed at the same operating conditions. Xinxin et al. reported a similar figure when creep feed grinding γ-TiAl (Ti-45Al-2Mn-2Nb-0.1B) intermetallic. Maximum cutting temperatures of 846°C and 73°C were reported for SiC and diamond wheels, respectively, at fixed grinding conditions [18]. The large difference in thermal conductivity between diamond and SiC abrasive (2000W/mK compared to 40W/mK) explains the effect, which allows a considerable amount of heat to be dissipated from the grinding area. When grinding AISI 52100 steel with aluminium oxide (Al_2O_3) and cubic boron nitride (cBN) wheels under the same conditions, a lower temperature was recorded for the latter wheel. Rowe et al. attributed the difference to the physical and thermal properties

of the used wheels, including thermal conductivity, specific heat and density [200]. The steep rise from 51°C to 692°C can be explained by the coolant heat transfer mechanism from nucleation to a film boiling when a critical temperature is exceeded (~120°C for water and ~300°C for oil-based coolant) [14]. At coolant nucleate boiling, the majority of grinding temperature is transmitted by the coolant until a critical temperature is reached, above which the coolant loses its ability to cool as the vapour film prevents the cooling fluid from penetrating into the wheel/workpiece contact area, leading to extremely high temperature, as might be expected under dry conditions.

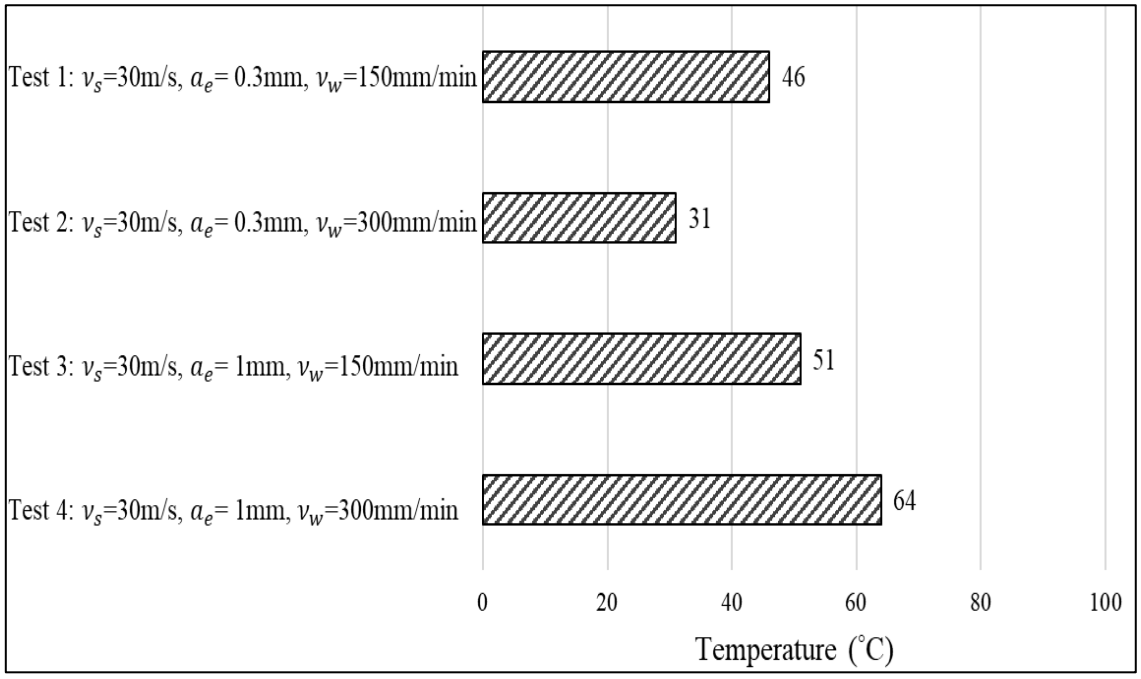


Figure 4-14: Recorded temperature at different operating conditions (Phase 1B)

4.1.2.4 Surface roughness and topography

Data for 2D and 3D topography parameters are detailed in Figure 4-15. No significant difference in 2D roughness parameters was found irrespective of operating levels, and the disparity is well within 3D roughness parameters. 3D peak to peak (St) values ranged from 8.3 to 19.4µm, and 3D 10-point average (Sz) varied between 8.1 and 17.35µm. While comparing with the surface ground with SiC wheel, minimal changes in Ra and Sa values were observed, this contradicts findings in [7] who reported a 25% decrease in roughness value with vitrified diamond wheel. However, a decrease of 30% in St and Sz 3D roughness parameters was evident only in Test 2 and 4 when compared to SiC counterpart. On the other hand, Bhaduri

and Xinxin [18], [26] noted higher Sa and Ra values, respectively with the diamond wheel than in SiC wheel when creep feed grinding γ-TiAl alloys. They claimed that the difference in grit density and average grain sizes are expected to have had an influence on their findings. 3D mapping of ground surfaces together with associated main effects plots, interaction plots and analysis of variance tables for 2D and 3D roughness parameters are detailed in Appendix F, Figures F42-F54 and Tables F17-F22. Unlike trends for SiC wheel in Phase 1A, where increasing the depth of cut and feed rate resulted in higher 3D surface roughness parameter values. Here, the feed rate and depth of cut had no effect on 2D roughness parameters results. In contrast, the tendencies for 3D roughness parameter are partially more difficult to explain as the greatest values of St and Sz were achieved when operating with a high depth of cut and a low feed rate. At the same time, changing the feed rate from 150mm/min to 300mm/min while the depth of cut is fixed resulted in the lowest values of St and Sz. ANOVA tables for roughness data show that none of the factors is statistically significant on any of the roughness parameters, although feed rate had the highest contributions on Ra and St results with PCR of 81.33% and 64.96%, respectively. In comparison, the depth of cut contributed the most to Sa and Rt values (57.92% and 20.44%, respectively). When assessing Rt, Rz, St and Sz, the interaction between depth of cut and feed rate was present with high PCR values of 51.96% for Rt, 46.80% for Rz, 34.78% for St and 41.08% for Sz. Unfortunately, assessment of interaction significance was not possible with the applied factorial.

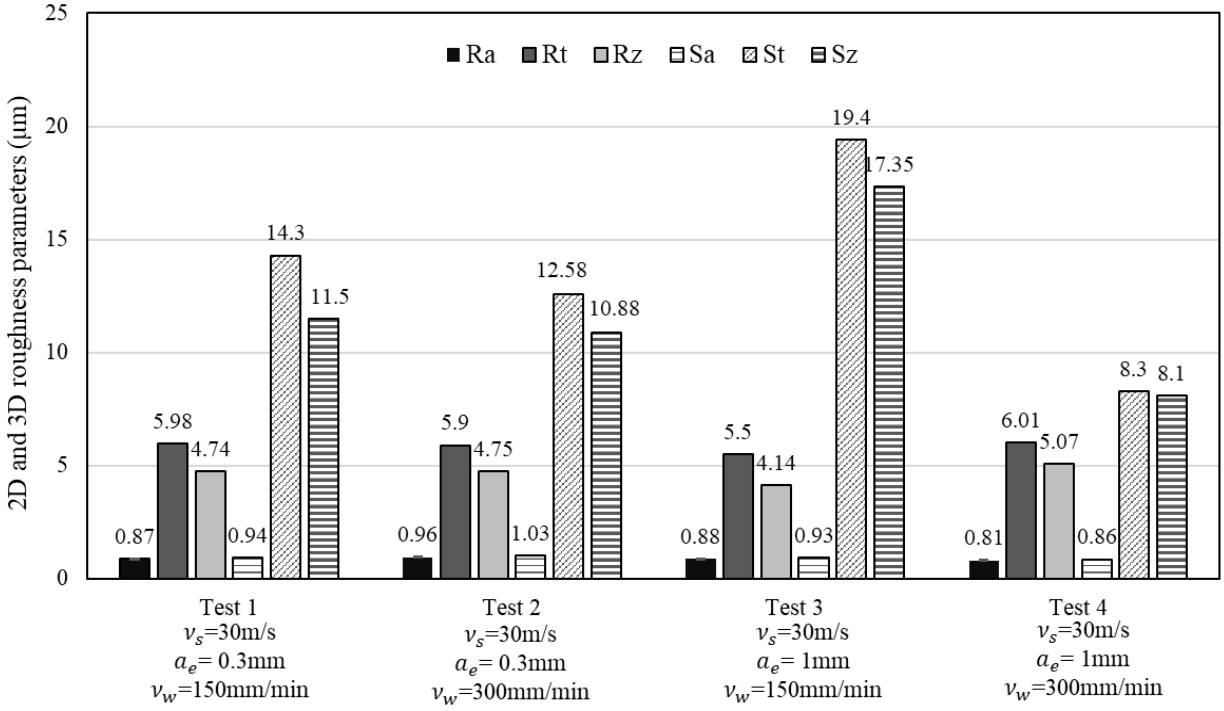


Figure 4-15: 2D and 3D surface roughness parameters for ground surfaces (Phase 1B)

4.1.2.5 Workpiece surface

Unlike surfaces produced with SiC wheels, no burn or chatter marks are observed on any of the ground workpieces with diamond wheels, as shown in Figure 4-16. Ground surfaces with SiC grits appeared free of burn only when wheel speed and depth of cut were kept to a minimum. While comparing the performance with SiC grits at identical operating conditions, a reduction by almost 10 folds in recorded temperature was achieved with diamond grits. As expected, the improved thermal conductivity of diamond abrasive allowed for greater cutting depths and feed rates to be used without causing surface burn. The corresponding SEM micrographs for ground surface in Figure 4-17 show surfaces with typical grinding grooving marks in the feed direction and are free from micro-crack, fracture and smearing. Occasional formation of minimal damage (side flow/ploughing and possible fracture/pull out) associated with higher depth of cuts was apparent in Tests 3 and 4. Operating at a lower depth of cut (0.3 instead of 1mm) produced smoother and shallower grooves as seen in Test 2 SEM image. High measured values for 3D roughness parameters St and Sz in Test 3 could be linked to the occurrence of possible fracture/pull-out and deeper grinding scratches within the surface.

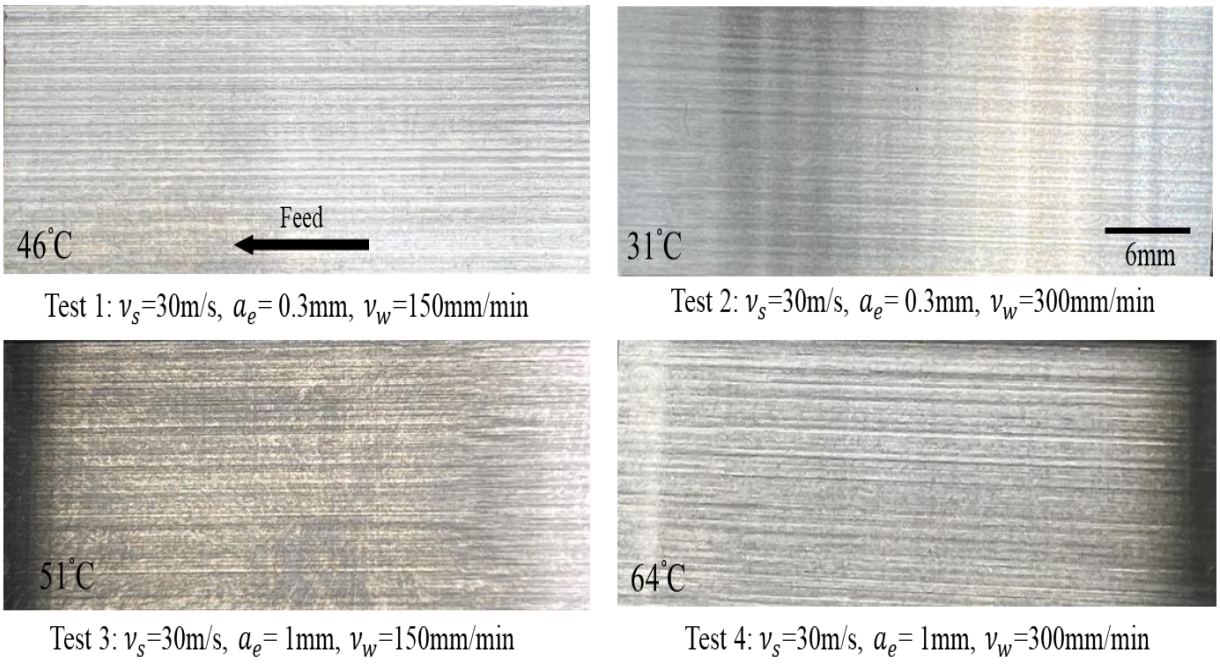


Figure 4-16: Workpiece surface images (Phase 1B)

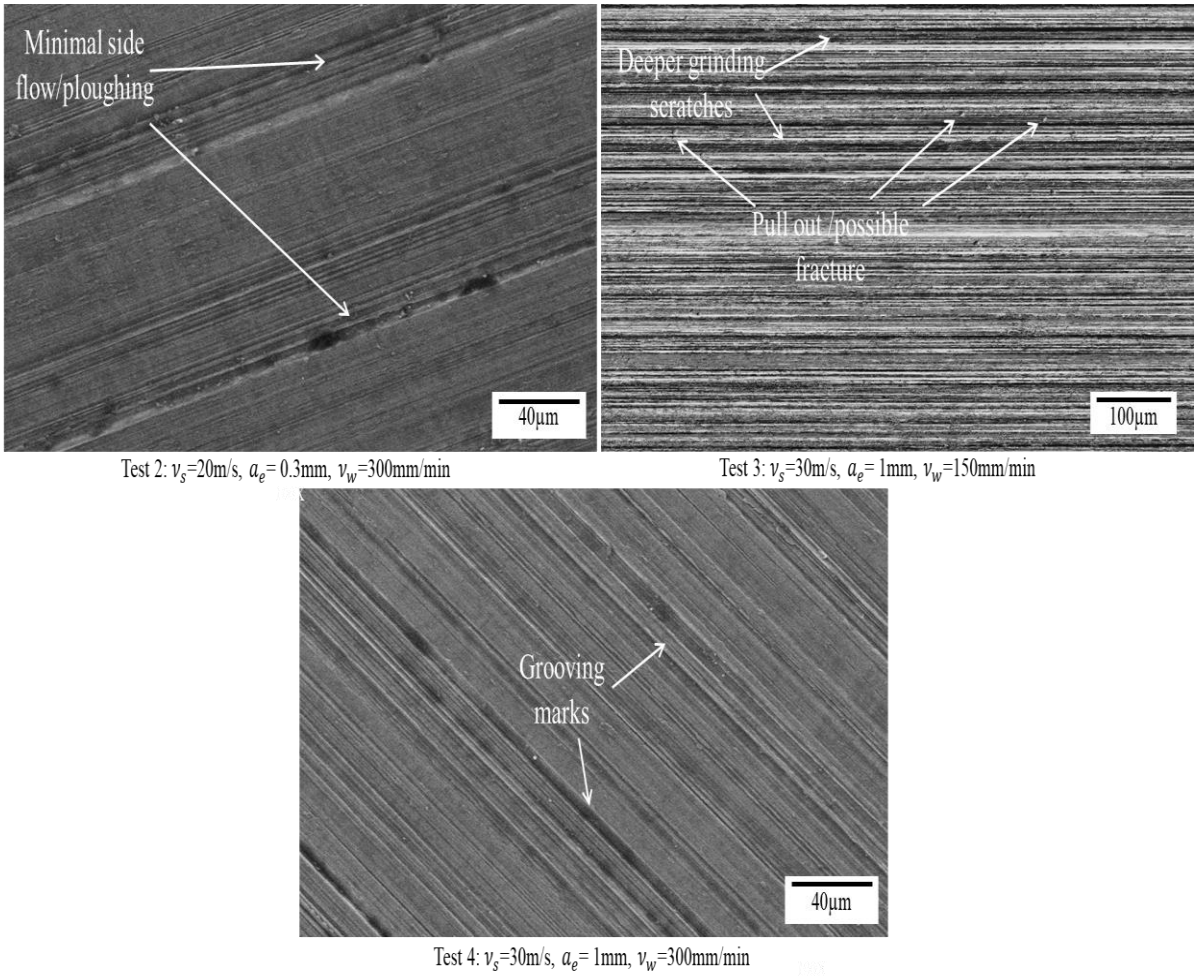


Figure 4-17: SEM micrographs of ground γ-TiAl surfaces with diamond wheel (Phase 1B)

4.1.2.6 Workpiece microstructure

Although some deformation was visible in Test 3 cross-section (parallel to feed direction), the majority of machined surfaces were generally free of damage, such as cracks, folds, and heat-affected zones, see Figure 4-18. The microstructure in the longitudinal feed plane in Test 1 and 2 (corresponds to 0.3mm depth of cut) appeared more smoother than those machined at 1mm depth of cut. This further supports the trends observed in the associated SEM images and roughness values for St and Sz. Distinctive grit marks were seen on the microstructure on transverse feed plane due to the nature of cutting process (grinding tracks). These observations are in agreement with the findings by Bhaduri [26].

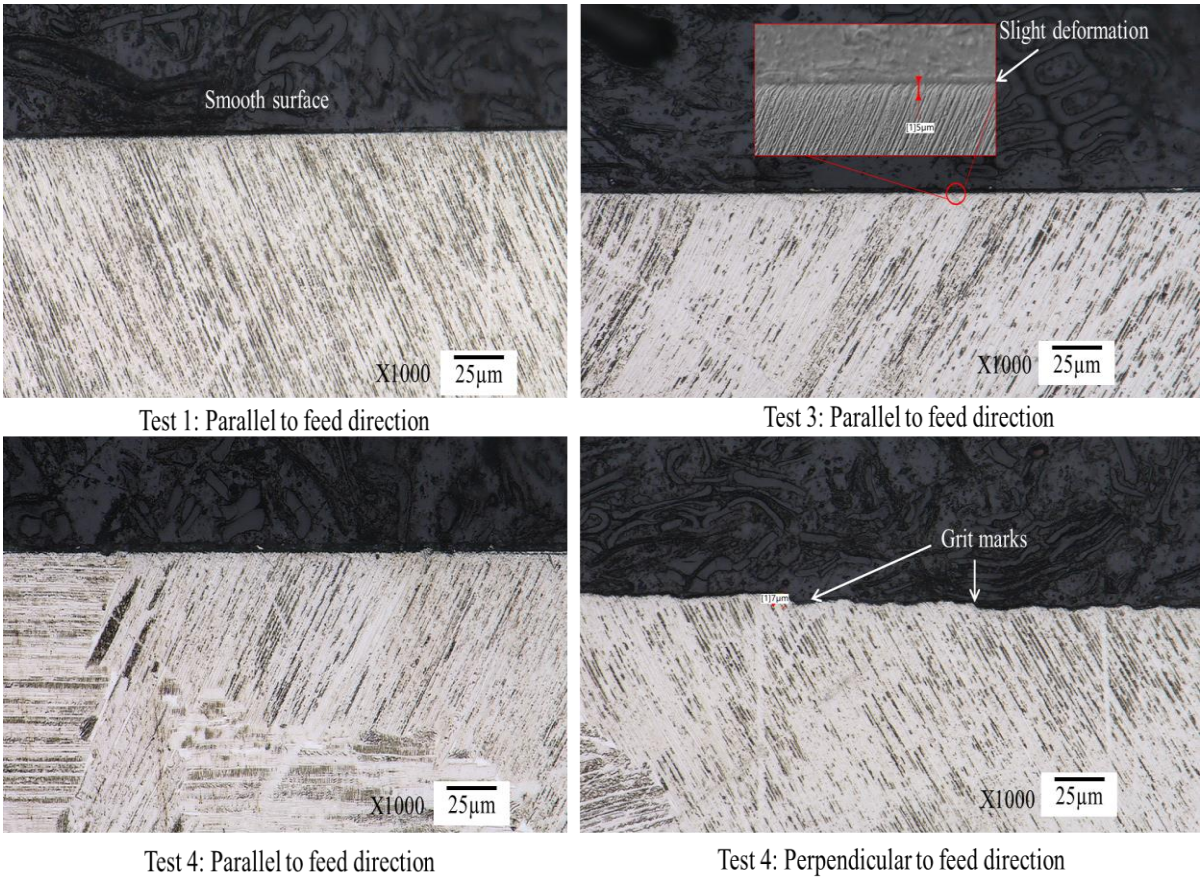


Figure 4-18: The microstructure of γ-TiAl ground with diamond wheel (Phase 1B)

4.1.2.7 Workpiece microhardness

Figure 4-19 shows microhardness depth profiles measured in the parallel direction to the feed, and separate graphs for each test are provided in Appendix F, Figure F55. Surprisingly, softening within the first 100µm below the machined surface was evident in all samples. During the machining process, deformed grains are always accompanied by an increase in microhardness, also referred to as work-hardening. Strain hardening or increase in surface hardness is typically associated with greater cutting action or mechanical working, while on the other hand, strain softening is usually caused by heat generation [144]. It was expected that the significant reduction in grinding forces and temperature in addition to the slight microstructural deformation observed on surfaces ground with diamond wheel will have a minimal increase or no effect on hardness values. As observed with surface produced with SiC wheel in Phase 1A, the majority of earlier work on γ-TiAl alloys showed that microhardness values typically increased by up to ~30% extending to a depth of ~100µm beneath the surface. However, softening within the first 30µm of γ-TiAl (having the same alloy composition) was

noted when creep feed ground with a super-abrasive wheel (cBN grit) using oil as a coolant [7]. Aspinwall et al. reported a softening layer extending to a depth of 50µm when point grinding Inconel 718 and Udemit 720, albeit with minimal plastic deformation on the machined surface microstructure [201]. It was suggested that measurement of γ-TiAl microhardness is often difficult due to the low ductility of γ-TiAl and the brittle nature of the material. Thus, the measurement of microhardness is more susceptible to error caused by fracture at the edge of the indents instead of softening. Moreover, a lack of support and poor handling of specimens (uneven surface during measurement) could largely impact indent edge shape or deformation. This in turn, could give false readings and substantially influence microhardness measurements.

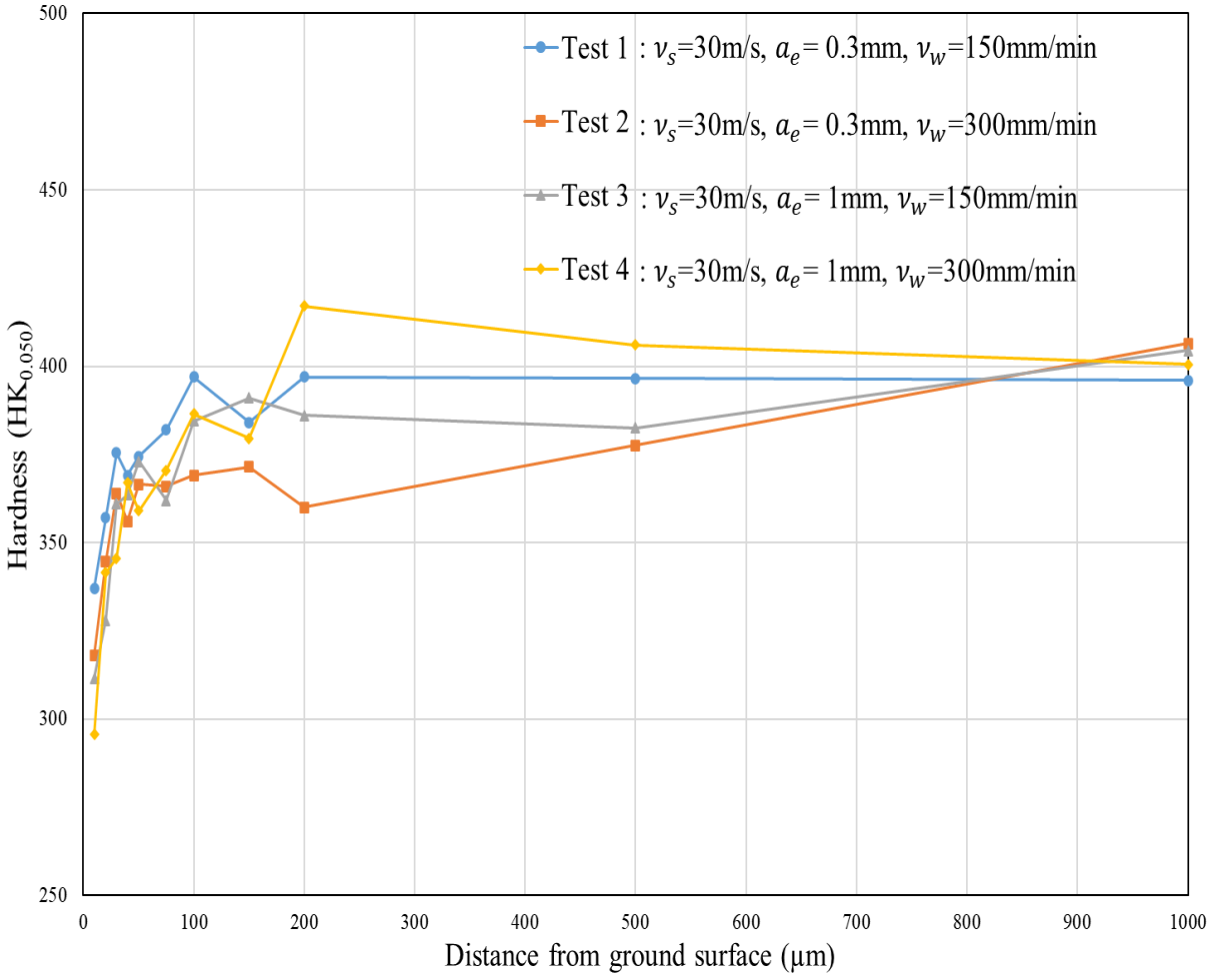


Figure 4-19: Microhardness depth profiles (Phase 1B)

4.1.3 Phase 1C: Extended surface integrity analysis (residual stress) on γ- titanium aluminide alloy (Ti-45Al-8Nb-0.2C)

The presence of residual stress has a significant impact on the structural integrity and mechanical properties of the machined materials. It can lead to various defects, including deformation and cracking, which can compromise the overall quality and performance of the workpiece. These defects ultimately influence the condition of the workpiece, affecting its life service and overall quality. Hence, it is crucial to assess the residual stress and workpiece condition in order to establish a theoretical basis for strength evaluations and predictions of machining deformation. Typically, there exists a correlation between elevated levels of hardness, mechanical deformation and the presence of compressive residual stresses. These compressive residual stresses have been seen to enhance fatigue performance, as noted in Bentley et al. work [202]. On the other hand, tensile stresses are commonly resulting from heat/thermal loads. They have the potential to negatively impact material performance or the lifespan of components and are usually correlated with reduced microhardness values [144].

Figure 4-20 presents residual depth profile data in both transverse and longitudinal directions for machined γ-TiAl samples at different conditions. Surface residual compressive stresses were present in all three tests in both assessed directions. This is in line with published work in [18], [187], [203] when CFG of γ-TiAl with SiC, vitrified diamond and electroplated diamond wheels. In their work, most surfaces exhibited compressive residual stresses ranging from -150 to -530MPa. The use of SiC wheel running at (v_s=30m/s, v_w=300mm/min, a_e=1mm) induced the highest residual stress levels (around -760MPa in the feed direction and approximately -500MPa perpendicular to the feed) with the depth of penetration extending to ~60μm, at which the residual stresses changed to tensile mode before recovering to the near neutral stress condition of the bulk with maximum value recorded at 320μm beneath the machined surface (369MPa in perpendicular direction and 210MPa in parallel direction). As suggested earlier, these tensile residual stresses can be attributed to the high recorded temperature during grinding 582°C (high heat concentration). However, it is observed from the high levels of compressive stresses at the machined surface that the mechanical load exerted had a greater influence (high levels of grinding forces) compared to temperature effects which is likely due to the larger contact area of wheel-workpiece as a result of larger depth of cut. In contrast, lower sub-surface compressive residual stresses ranging from -300 to -400MPa and extending to a depth of ~50μm below the machined surface were measured when utilizing a

vitrified diamond wheel with almost negligible tensile residual stresses. This is in agreement with the low recorded temperature for the tested samples (64°C and 46°C), suggesting the absence of thermal load or damage.

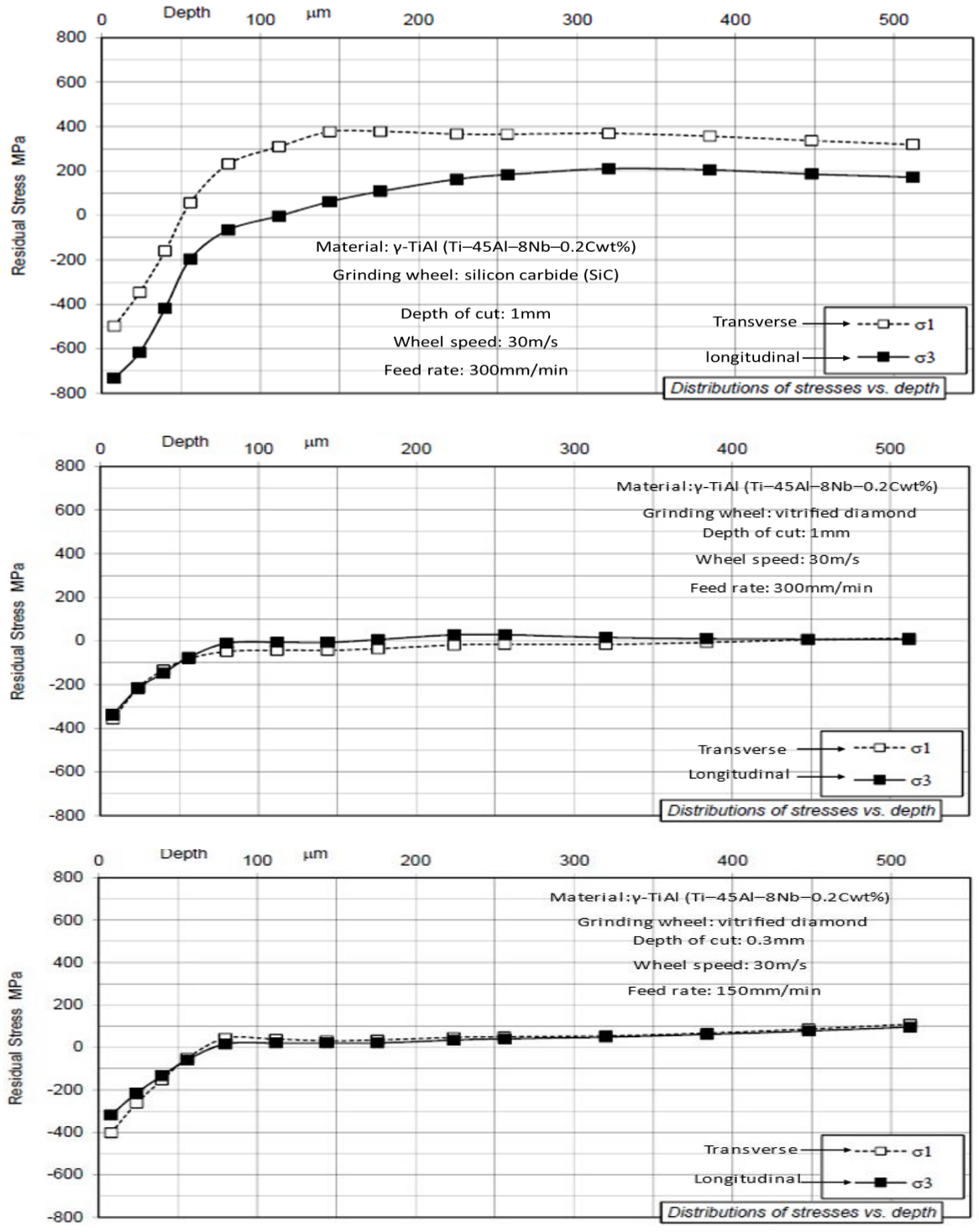


Figure 4-20: Residual stress depth profiles for γ-TiAl samples

4.1.4 Summary of results for γ-titanium aluminide alloy (Ti-45Al-8Nb-0.2C)

Phase 1A: The influence of operating conditions on grinding performance of γ-titanium aluminide alloy (Ti-45Al-8Nb-0.2C) when creep feed grinding with conventional silicon carbide wheel (SiC)

- G-ratio ranged from 6 to 16, with the maximum value achieved when running at 1mm depth of cut, 30m/s wheel speed, and 150mm/min feed rate. The analysis of variance conducted on the G-ratio reveals that only the depth of cut is a statistically significant factor at a 95% confidence interval with a percentage of contribution (PCR) of 76.80%.

- The lowest levels of normal force, tangential force and grinding power (533N,1789N and 3.85KW, respectively) were recorded when operating at the lowest levels of conditions (150mm/min feed rate, 0.3mm depth of cut, and 20m/s wheel speed). The specific energy showed otherwise, as increasing the specific material removal rate (higher depth of cut and/or feed rate) results in lower levels of specific energy. All assessed factors (wheel speed, feed rate, and depth) were highlighted as statistically significant for normal forces, power and specific energy, but for tangential forces output, only depth of cut was considered statistically significant with a PCR of 59.14%.

- The highest grinding temperature of 692°C was recorded when operating at v_s=30m/s, v_w=150mm/min, a_e=1mm, while the lowest temperatures (41°C and 46°C were measured when operating at the lowest levels of wheel speed and depth of cut (v_s=20m/s, a_e=0.3mm), irrespective of feed rate. Based on ANOVA made on temperature results, only the influence of depth of cut was significant.

- For the given operating conditions, the 2D average surface roughness (Ra) values ranged from 0.74µm to 0.9µm with slight differences in average roughness values (~10%) between Ra and Sa (3D average surface roughness). The 3D roughness data shows higher values with increasing depth of cut and feed rate. Increasing the depth of cut and/or feed rate resulted in a rise in 3D roughness parameter values. In contrast, increasing the wheel speed resulted in a reduction of average surface roughness values. None of the factors was significant for Ra, Rt and Rz, and only feed rate was identified as significant for St and Sz with PCR as high as (58% and 68% for St and Sz,

respectively). Interactions between feed rate and wheel speed were present on most examined roughness parameters.

- Cracks, burn and chatter marks were observed on the majority of ground workpieces, which were, however, absent on surfaces ground at low depth of cut (0.3mm) and wheel speed (20m/s), regardless of employed feed rate operating levels. Extensive surface burn and a high level of cracking were evident in tests involving high levels of depth of cut, wheel speed and feed rate.

- Cross-sectional microstructures of ground samples showed smooth minimal damage consisting of bending/deformation of the lamellae to a depth of ~5µm in surfaces perpendicular and parallel to feed direction, in addition, fracture/pull-out was evident on surfaces machined at high operating conditions, however is restricted to a depth of ~4µm beneath the surface.

- Sub-surface microhardness measurements revealed a hardened layer extending to a depth of ~160µm from the workpiece surface in all ground workpieces. A minimal softening effect within the first ~40µm below the surface was observed in tests corresponding to larger depth of cuts and high generated temperatures. The maximum microhardness value of ~500$HK_{0.050}$ was measured while running at (v_s=20m/s, a_e=0.3mm v_w=150mm/min) at a depth of ~50um under the machined surface.

Phase 1B: Effect of operating conditions on grinding performance when creep feed grinding of γ-titanium aluminide alloy (Ti-45Al-8Nb-0.2C) with super-abrasive diamond wheel and a comparison between two different wheel systems

- At identical operating conditions, the diamond wheel showed remarkably lower wheel wear (~1µm after 48mm length of cut) when compared to the SiC wheel, with an increase of ~1,200% in G-ratio values. The depth of cut exhibited a significant impact on the G-ratio value, with a PCR of approximately ~93%. Conversely, the influence of the feed rate was found to be negligible.

- In comparison to the SiC wheel, the vitrified diamond wheel exhibited a significant reduction by ~60%, ~40% and ~50% in normal forces, tangential forces and grinding power, respectively. Results for grinding forces revealed a rise in tangential forces by

~10% and normal forces by ~22% as the depth of cut changed from 0.3 to 1mm. Similarly, altering the feed rate from 300 to 150mm/min yielded a decrease of ~10% in the grinding force components. In terms of statistical analysis, depth of cut and feed rate were only significant at the 5% level for normal forces.

- Under the conditions investigated in the current work for both SiC and vitrified diamond wheels, extremely lower temperatures were recorded for the latter than in the former. Generated temperatures for all tested conditions were typically below 70°C, even when operating at the highest levels (10 times lower for those recorded in workpieces machined with SiC wheel).

- In terms of surface roughness, no major changes in 2D and/or 3D surface roughness parameters between the two wheels were observed, however a reduction of 30% in 3D peak-to-peak (St) and 3D 10-point average (Sz) was seen in two tests (out of four) when compared to the SiC equivalents. Interaction with high PCR values between the depth of cut and feed rate was present in the majority of examined roughness parameters.

- In contrast to surfaces produced using SiC wheels, the utilisation of vitrified diamond wheels did not result in the presence of burn or chatter marks on any of the ground workpieces. SEM micrographs displayed surfaces with typical grinding grooving marks in the feed direction and are free from micro-crack, fracture and smearing.

- Similarly, the microstructure images for γ-TiAl workpieces ground with vitrified diamond wheel exhibit surfaces generally free of damage such as cracks, folds, and heat-affected zones.

- Microhardness depth profiles showed evidence of softening within the first 100μm below the machined surface in all samples. Based on the observed lower temperature levels and the resulting compressive residual stresses, it is more likely that the observed profile trends are caused by fracture at the edge of the indents instead of the softening effect, as reported in earlier work.

Phase 1C: Extended surface integrity analysis (residual stress) on γ-titanium aluminide alloy Ti-45Al-8Nb-0.2C

- Generally, produced residual stresses at the surface in all tested samples were compressive in nature in both measurement directions (parallel and perpendicular to feed).

- The maximum compressive residual stresses of (around -760MPa in the feed direction and approximately -500MPa in the perpendicular direction) were measured for sample ground with SiC wheel operating at (v_s=30m/s, v_w=300mm/min, a_e=1mm). However, they shifted to tensile residual stresses at a depth of ~60μm below the machined surface with maximum values of 369MPa in the perpendicular direction and 210MPa in parallel direction.

- No evidence of tensile residual stresses was seen in samples that were ground using a vitrified diamond wheel at relatively identical conditions to the SiC wheel sample, even under higher operating conditions. Vitrified diamond wheel samples induced compressive residual stress levels with comparable values in both transverse and longitudinal directions, ranging from -300 to -400MPa and extending to a depth of ~50μm below the machined surface before recovering to the neutral stress condition of the bulk material.

4.2 Phase 2: Creep feed grinding of burn resistant titanium alloy (Ti-25V-15Cr-2Al-0.2C)

4.2.1 Phase 2A: Assessment of significant operating parameters when creep feed grinding with conventional silicon carbide wheel (SiC) and benchmark against γ-titanium aluminide alloy (Ti-45Al-8Nb-0.2C)

4.2.1.1 Wheel wear and G-ratio

All trials were completed successfully to the point of cessation. Figure 4-21 details the average measured G-ratio and associated wheel wear for all tests. In general, the average G-ratio ranged from 2.1 to 3.8, with the highest G-ratio (4.7) achieved when operating with Test 7 parameters (30m/s wheel speed, 1mm depth of cut and 150mm/min feed rate). The first CFG trials on this alloy produced G-ratio values ranging from 0.16 to 1.53 using two different SiC wheels [4]. Also, comparable results were reported in [24] with values of 0.5-2.1 following CFG of BuRti with SiC wheel. Although more pronounced here, trends for G-ratio and radial wheel wear between passes were similar to those in Phase 1A (CFG of γ-TiAl with SiC wheel), as they exhibited fluctuating wear rates with increasing the volume of material removed. This can be explained by the self-sharpening/dressing mechanism of the wheel, here the grits or bonds fracture to reveal fresh cutting edges (grits pullout), resulting in an increased wear rate. In addition, the trends imply that no parity (steady-state) between the wheel wear and the new cutting edge was reached. In comparison to γ-TiAl, BuRTi was more difficult to grind with 7 times lower G-ratio and 3 times higher radial wheel wear. The considerable increase in ductility of BuRTi (20% at room temperature), lower thermal conductivity and the 20-30% increase in strength over γ-TiAl are the major reasons for this. Analysis of variance table along with plots for main effects and interactions for G-ratio are provided in Appendix F, Table 23, Figures F56 and F57. As opposed to γ-TiAl results in Phase 1A, ANOVA results for G-ratio showed that none of the tested factors is significant at a 95% confidence interval, this was likely attributed to the more extreme fluctuating wear rates caused by the self-sharpening mechanism. Out of the three factors, depth of cut had the highest percentage of contribution at 44.98%.

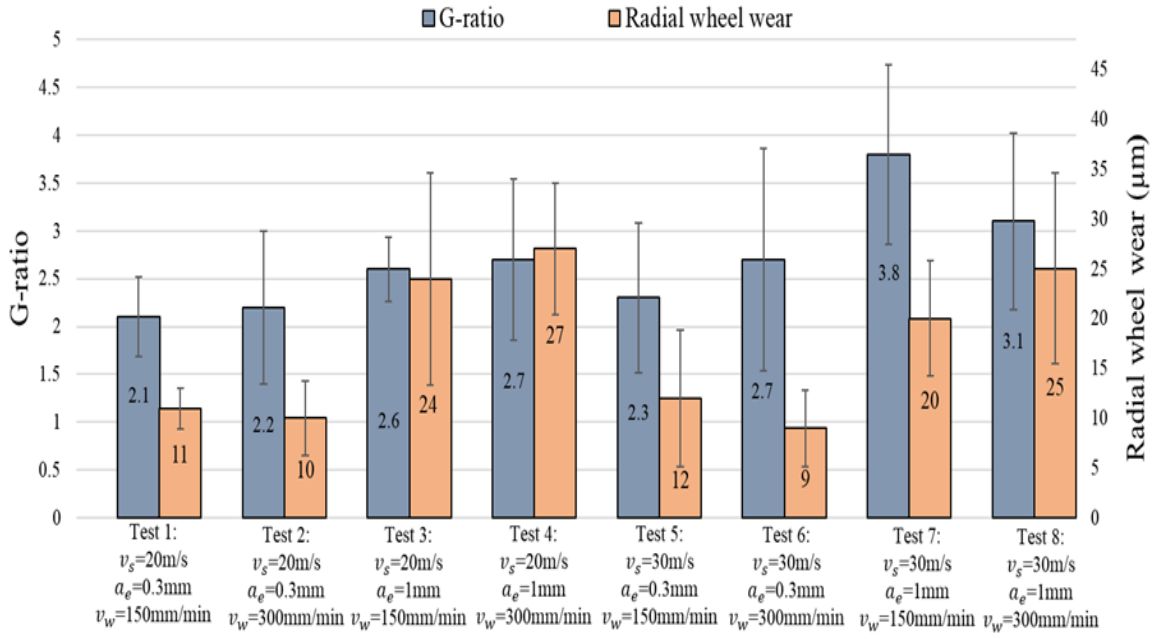


Figure 4-21: G-ratio and radial wheel wear for different grinding conditions (Phase 2A)

4.2.1.2 Grinding forces, power and specific energy

Based on applied operating conditions, normal forces ranged between 930-2314N, tangential forces 363-711N, power levels from 10 to 23KW and specific energy 231-895J/mm^3. These figures are in agreement with previous work on this alloy [7], thus providing more validation of obtained results. Unfortunately, comparison with the first work on the alloy in [4] was not possible as the work only reported force measurement for diamond wheels and no information on power or specific energy was given. Figure 4-22 shows maximum recorded normal and tangential force for each test, as observed in earlier phases, the normal force component is the highest in all tests (around three folds the tangential force). As expected, graph trends showed that increasing operating parameters resulted in increasing force components, as the highest magnitude was observed in Test 8 (2314N for normal force, 711N for tangential force). The effect of altering depth of cut (while other factors fixed) on grinding forces was very noticeable, in particular for normal forces, however, minimal change was observed for low and high levels of wheel speed and feed rate. Analysis of variance results for normal forces further supports this, as the wheel speed and feed rate were identified as insignificant in terms of normal force component with low PCR values of 12.56% and 9.85%, respectively, while the depth of cut is statistically significant. Equation (5) in section 2.2.4 shows that wheel speed is inversely proportional to the undeformed thickness squared, so it is expected that a rise in the former will

lead to a reduction in the latter, thus producing lower cutting forces and power. Contrary to expectations, higher wheel speed resulted in a rise in cutting forces and power, Hwang et al. provided a possible explanation for this phenomenon by noting that at faster wheel speeds, an increase in sliding length per unit volume of material removed will occur. This causes more wear flats to be produced, which in turn increases the power and specific energy of the rubbing and sliding force component [204]. The analysis of variance (ANOVA) for normal force, tangential force, power and specific energy are presented in Tables 4-3 to 4-6. Main effect plots and interaction plots are provided in Appendix F, Figures F58 to F65. In general, the depth of cut was significant for all assessed responses, normal and tangential forces, power and specific energy. While wheel speed for power and feed rate for specific energy. When comparing with γ-TiAl, trends for BuRTi ANOVA results were different, where both feed rate and wheel speed were significant factors for normal force, power and specific energy at the 5% level. In addition, at identical operating conditions, BuRTi cutting forces were ~40% higher for normal forces (~50% in some instances) and ~30% higher for tangential forces. The observed increase in grinding/cutting forces for BuRTi over γ-TiAl is attributed to higher tensile strength and ductility of the material and the presence of Ti_2C and TiC carbides within the material microstructure.

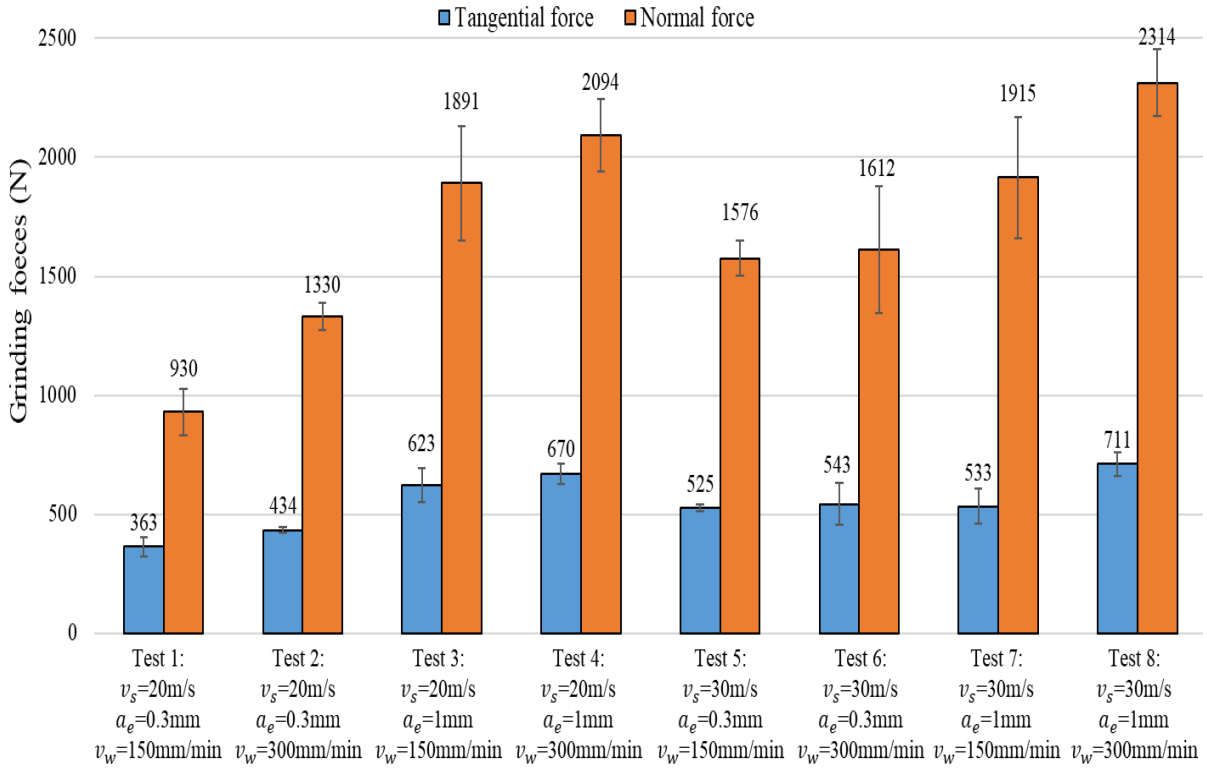


Figure 4-22: Grinding forces for different operating conditions (Phase 2A)

Table 4-3: ANOVA table for normal force (Phase 2A)

Source	DF	Seq SS	Contribution	Adj SS	Adj MS	F-Value	P-Value
Wheel speed (m/s)	1	171698	12.56%	171698	171698	6.56	0.063
Depth of cut (mm)	1	956345	69.94%	956345	956345	36.55	0.004
Feed rate (mm/min)	1	134681	9.85%	134681	134681	5.15	0.086
Error	4	104654	7.65%	104654	26164	-	-
Total	7	1367378	100.00%	-	-	-	-

Table 4-4: ANOVA table for tangential force (Phase 2A)

Source	DF	Seq SS	Contribution	Adj SS	Adj MS	F-Value	P-Value
Wheel speed (m/s)	1	6160	6.48%	6160	6160	1.23	0.330
Depth of cut (mm)	1	56448	59.40%	56448	56448	11.23	0.029
Feed rate (mm/min)	1	12325	12.97%	12325	12325	2.45	0.192
Error	4	20104	21.15%	20104	5026	-	-
Total	7	95038	100.00%	-	-	-	-

Table 4-5: ANOVA table for power (Phase 2A)

Source	DF	Seq SS	Contribution	Adj SS	Adj MS	F-Value	P-Value
Wheel speed (m/s)	1	18.000	8.91%	18.000	18.000	7.58	0.051
Depth of cut(mm)	1	162.000	80.20%	162.000	162.000	68.21	0.001
Feed rate (mm/min)	1	12.500	6.19%	12.500	12.500	5.26	0.083
Error	4	9.500	4.70%	9.500	2.375	-	-
Total	7	202.000	100.00%	-	-	-	-

Table 4-6: ANOVA table for specific energy (Phase 2A)

Source	DF	Seq SS	Contribution	Adj SS	Adj MS	F-Value	P-Value
Wheel speed (m/s)	1	20605	5.73%	20604	20604	3.14	0.151
Depth of cut (mm)	1	188498	52.39%	188498	188498	28.77	0.006
Feed rate (mm/min)	1	124500	34.60%	124500	124500	19.00	0.012
Error	4	26207	7.28%	26207	6552	-	-
Total	7	359809	100.00%	-	-	-	-

4.2.1.3 Grinding temperature

Maximum recorded grinding temperatures for burn-resistant titanium alloy with SiC wheel are shown in Figure 4-23, and associated main effects plot, interaction plots and ANOVA table are detailed in Appendix F, Figures F66, F67 and Table F24. Interestingly, the maximum generated temperatures for BuRTi were typically lower than those recorded for γ-titanium aluminide alloy. Substantially reduced thermal conductivity of the former suggested the opposite outcome (approximately 10W/mK at room temperature for the former when compared to the latter 22W/mK at room temperature). The difference between the coolant pressures employed in the current phase (15bar) and the earlier phase (7bar) may account for this. Increased coolant pressure is expected to provide more effective coolant penetration into the grinding zone. Findings here, however, are still comparable to those obtained in [4], this is the sole work that includes temperature data following creep feed grinding of (Ti-25V-15Cr-2Al-0.2C wt%). Novovic reported grinding temperature when using foil-workpiece thermocouples configuration as high as 900°C when grinding the same exact alloy with silicon carbide abrasive wheel with a depth of cut 0.2mm, the figure reduced to 450°C when a more highly porous SiC wheel was employed with a 1mm depth of cut [4]. In this phase of experimental work, the data shows that tests involving high levels of feed rate and depth of cut (Test 4 and 8), produced the highest grinding temperature, irrespective of wheel speed. ANOVA results for temperature revealed that none of the factors are statistically significant, however, the highest PCR values of 46.75% and 28.54% were contributed by depth of cut and the combined effect of depth of cut and feed rate ($a_e \times v_w$), respectively with very low PCR value for wheel speed (less than 1%). A maximum temperature of 611°C was recorded when operating with Test 4 parameters (v_s=20m/s, a_e=1mm, v_w=300mm/min), which does not correspond to the greatest operating parameters. Running with the highest operating conditions in Test 8, produced ~100°C lower temperature (476°C).

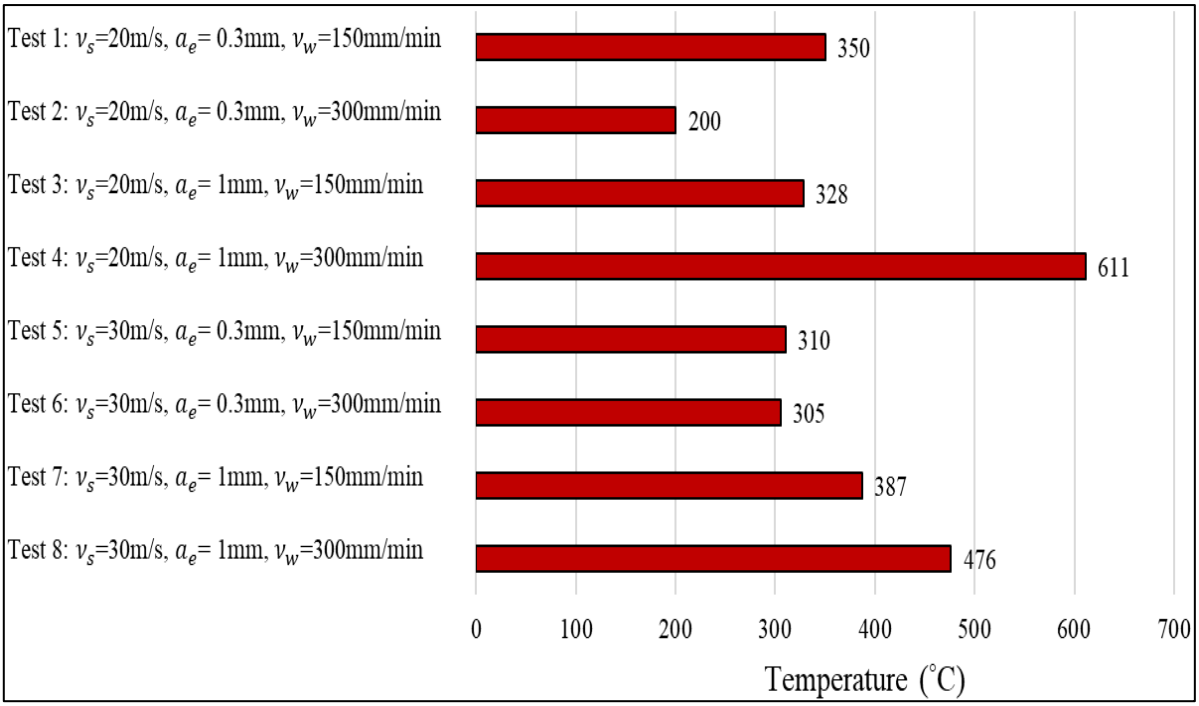


Figure 4-23: Recorded temperature at different operating conditions (Phase 2A)

4.2.1.4 Surface roughness and topography

Figures 4-24 and 4-25 show the 2D and 3D roughness parameters for burn-resistant titanium workpieces at the end of each test. For all tests with the exception of Test 6 and 8, 3D amplitude parameters (Sa) are relatively higher than their 2D equivalents. Peak-to-peak (St) and 10-point average (Sz) roughness parameters showed a substantial increase in roughness value of up to 50%. This is due to a much larger number of data points associated with 3D roughness measurement. Thus, more extreme points are expected than in the 2D equivalents, as explained by Ohlsson [205]. The roughness levels for either 2D or 3D roughness parameters were typically two times higher when compared to roughness levels in γ-titanium aluminide alloy samples ground with SiC wheels. For instance, a value of 2.02µm and 2.1µm for Ra and Sa were measured, respectively when grinding burn resistant with highest operating conditions in Test 8 here, while for γ-titanium ground samples at the same conditions (Test 8 in Phase 1A), the value reduced to 0.74µm and 0.76µm for Ra and Sa respectively. Similarly, operating at 1mm depth of cut, 20m/s wheel speed and 150mm/min (Test 3 here), produced 3D roughness values of 24.6µm and 19.73µm for peak-to-peak (St) and 10-point average (Sz), these figures reduced to 11.6µm and 8.45µm in γ-titanium aluminide samples (Test 3 in Phase 1A). The increased room temperature ductility of BuRTi and the presence of hard brittle carbides are

expected to cause higher roughness levels. In earlier work on BuRTi, the presence of fractured/lost and randomly distributed carbides is believed to cause a large variability in 2D and 3D surface topography parameters (52% for Sa and 88% for St) [4]. Unfortunately, assessment of data scatter was not possible at current work due to limited number of measurements. The lowest 2D roughness parameters were achieved when operating with Test 1 conditions (v_s=20m/s, a_e=0.3mm, v_w=150mm/min), and for 3D roughness parameters the lowest values obtained in Test 6 (v_s=30m/s, a_e=0.3mm, v_w=300mm/min). Hood noted 15% higher average 2D workpiece surface roughness for BuRTi over γ-titanium aluminide alloy under the same operating parameter levels, no information on extreme roughness parameters was given in his work [24]. Novovic produced surface roughness levels as high as 4.4µm for Ra and 29µm for Rt employing SiC abrasive on the same alloy, the variation with current work results is attributed to different chosen operating conditions [4]. Typical 3D topographical maps (unfiltered, primary map), Main effects plots, interaction plots and analysis of variance tables for 2D and 3D roughness parameters (except for 3D parameter St which is given below in Table 4-7) are detailed in Appendix F, Figures F68-F80 and Tables F25-F29. The 3D mapping of BuRTi surfaces well reflects the higher values of roughness, as opposed to γ-titanium aluminide surfaces where the height scale ranged between 9µm to -9µm on average, for BuRTi the height scale varied on average between 20µm to -10µm. Although not clear on the mapping, the reason for this is the high level of side flow/adhering material observed on ground surfaces of burn-resistant titanium. ANOVA tables results for roughness parameters showed a change in depth of cut levels significantly influenced the values of all assessed 2D parameters (Ra, Rt and Rz), and 3D roughness parameter Sa. Conversely, variation in wheel speed and feed rate levels had no significant effect on each of the examined topography parameters with low associated PCR. Interaction plots for 3D roughness parameters Sz and St show that an interaction between feed rate and depth of cut ($v_w \times a_e$) is present and was identified by ANOVA results as being statistically significant for St with high PCR of 58.47%, as detailed below in Table 4-7, and had the highest contributions on Sz (PCR of 54.45%). The interactions between wheel speed and feed rate ($v_s \times v_w$) were evident in the majority of roughness parameters, although they were not significant at the 5% level.

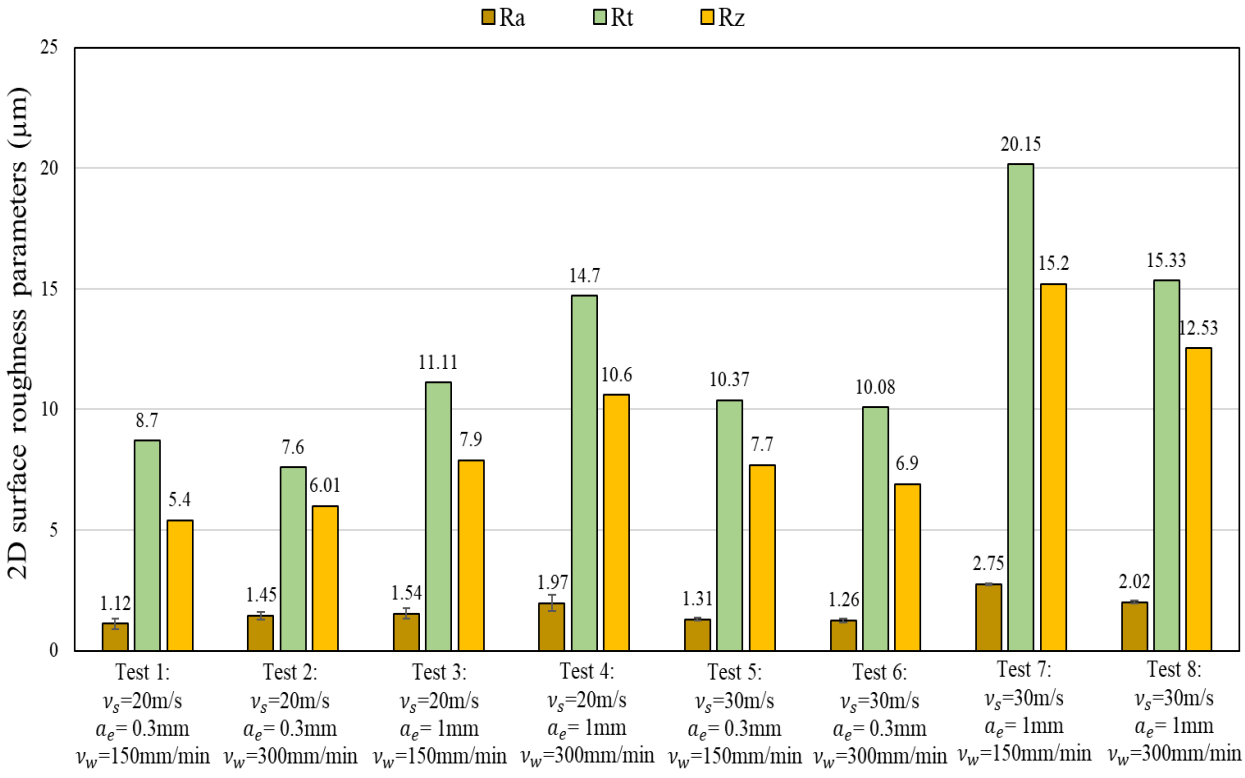


Figure 4-24: 2D surface roughness parameters for ground surfaces (Phase 2A)

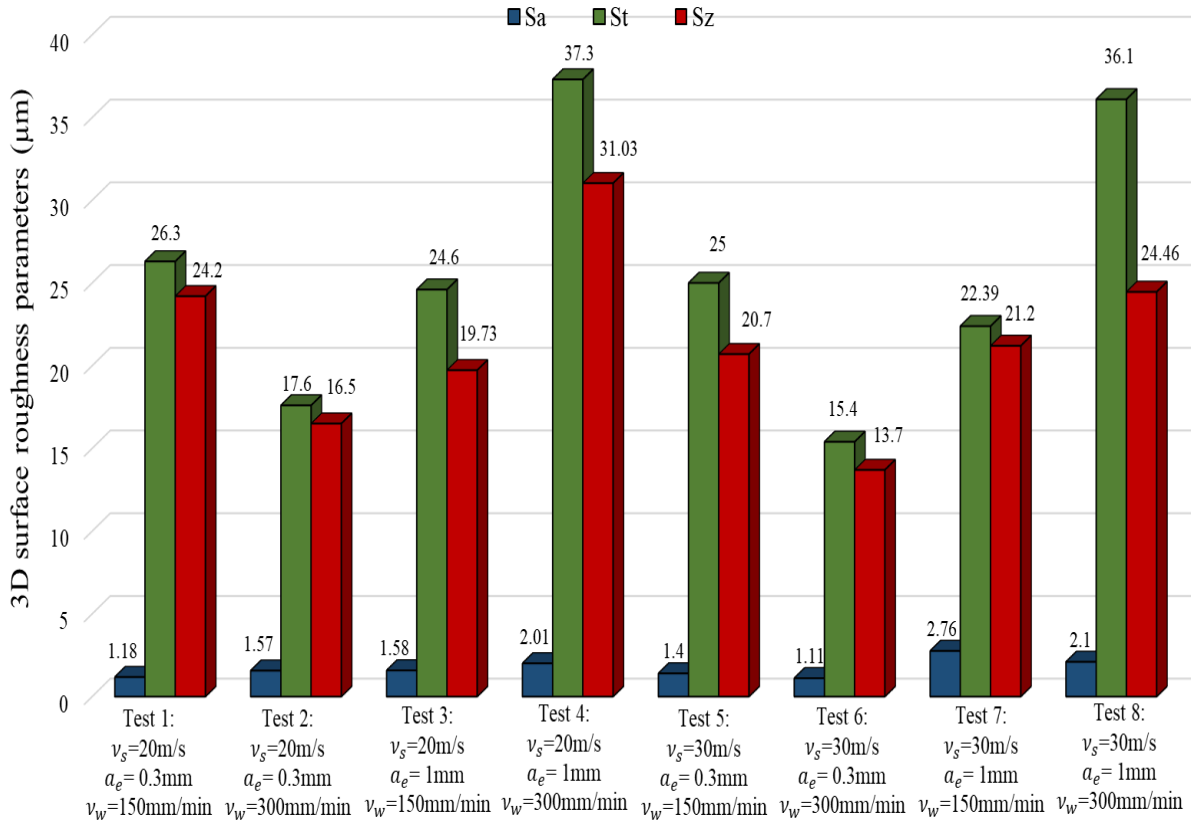


Figure 4-25: 3D topographical parameters of ground surfaces (Phase 2A)

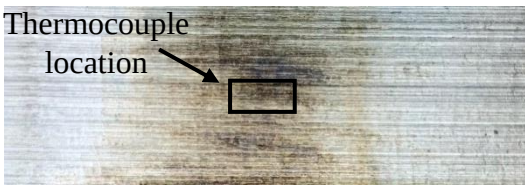
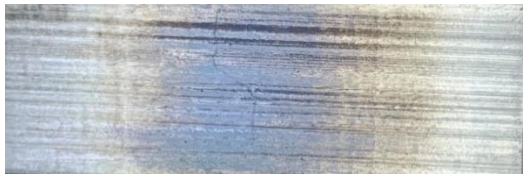
Table 4-7: ANOVA table for 3D surface roughness parameter St (Phase 2A)

Source	DF	Seq SS	Contribution	Adj SS	Adj MS	F-Value	P-Value
Wheel speed (m/s)	1	5.969	1.40%	5.969	5.969	13.09	0.172
Depth of cut (mm)	1	162.811	38.10%	162.811	162.811	357.03	0.034
Feed rate (mm/min)	1	8.222	1.92%	8.222	8.222	18.03	0.147
Wheel speed*Depth of cut	1	0.001	0.00%	0.001	0.001	0.00	0.970
Wheel speed*Feed rate	1	0.002	0.00%	0.002	0.002	0.00	0.963
Depth of cut*Feed rate	1	249.873	58.47%	249.873	249.873	547.95	0.027
Error	1	0.456	0.11%	0.456	0.456	-	-
Total	7	427.333	100.00%	-	-	-	-

4.2.1.5 Workpiece surface

Table 4-8 displays images of the machined surface at the end of each test. Workpiece surface burn and chatter are evident in all tests. Tests 4 and 8 had the most severe burns and cracks, which mirrored experiments with the most extreme operating parameters. The bulk of the surface exhibited a network of cracks when the operating parameters were increased (both parallel and perpendicular to feed direction). Surfaces produced in test 1 and 5 (involving low operating parameters) appeared free of cracks with slight burn and chatter. The poor thermal conductivity of BuRTi (about 10W/mK at room temperature), when compared to steels (roughly 45W/mK at room temperature), is responsible for the observed burn intensity on the surfaces. This means that the heat produced in the grinding zone does not dissipate rapidly. The occurrence of burning marks only in the middle of the grinding path in some samples is likely due to the effects of generation of wear flats on the wheel grains as the grinding progresses. An analysis of SEM images taken on the ground surfaces detailed in Figure 4-26 revealed high levels of smearing, cavities, side flow as a consequence of the higher ductility of the alloy. These findings are consistent with earlier work on burn-resistant titanium alloy ground with SiC wheel [4], [7].

Table 4-8: Observed machined surface under different grinding conditions and temperature (Phase 2A)

Test No.	Grinding conditions	Recorded temperature	Surface observation
1	v_s =20m/s a_e= 0.3mm v_w=150mm/min	350 °C	
2	v_s =20m/s a_e= 0.3mm v_w=300mm/min	200 °C	
3	v_s =20m/s a_e= 1mm v_w=150mm/min	328 °C	
4	v_s =20m/s a_e= 1mm v_w=300mm/min	611 °C	
5	v_s =30m/s a_e= 0.3mm v_w=150mm/min	310 °C	
6	v_s =30m/s a_e= 0.3mm v_w=300mm/min	305 °C	
7	v_s =30m/s a_e= 1mm v_w=150mm/min	387 °C	
8	v_s =30m/s a_e= 1mm v_w=300mm/min	476 °C	

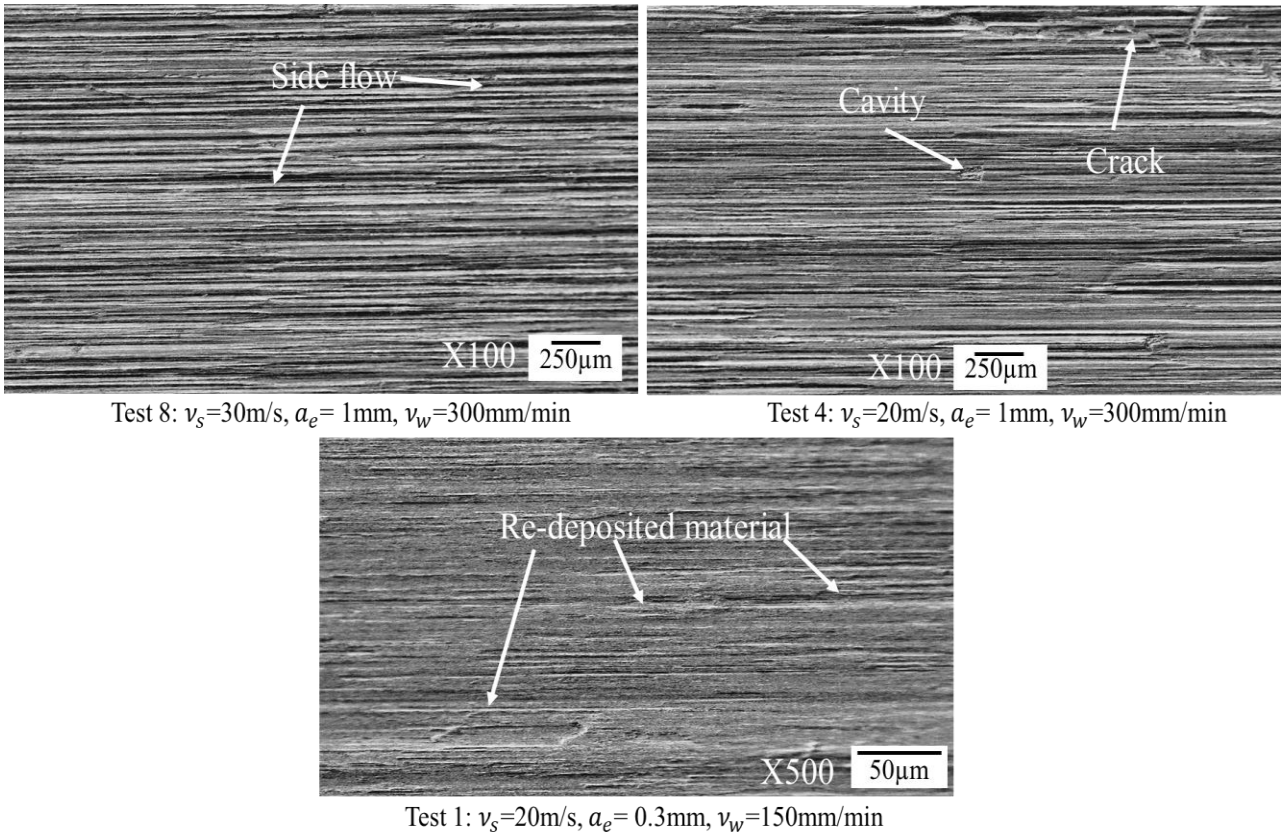
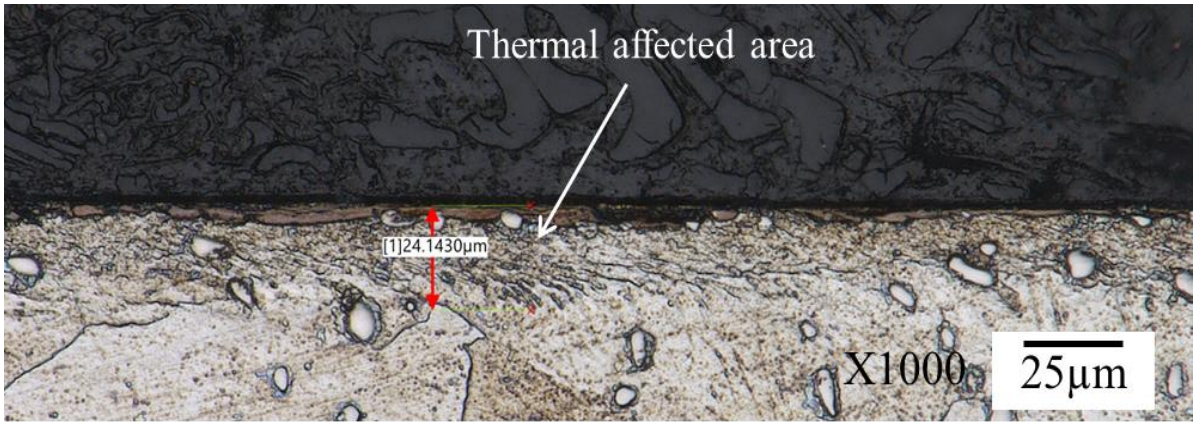


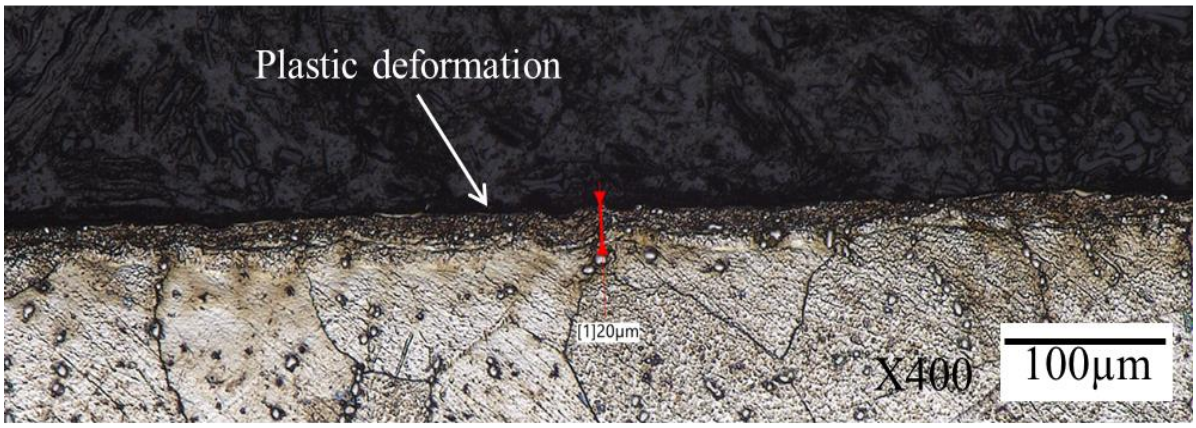
Figure 4-26: SEM micrographs of ground BuRTi surfaces with SiC wheel (Phase 2A)

4.2.1.6 Workpiece microstructure

Cross-sectional micrographs highlighting deformation of the microstructure directly beneath the machined surface and carbide precipitates are given in Figure 4-27. In contrast to γ-titanium aluminide microstructure where the bending/deformation of the lamellae was confined within only the first 5µm, extensive plastic deformation to a depth of ~20µm was visible in the majority of BuRTi tests. The plastic deformation primarily occurs as a result of the ploughing and cutting actions of the abrasive grains and the thermal load/grinding temperature. Indeed, BuRTi measured grinding forces were ~40% higher for normal forces and tangential force when compared to γ-titanium aluminide, which suggests higher levels of ploughing and cutting actions involved in the former. Although not shown here, the microstructure analysis showed that the visually appeared network of cracks on the ground surfaces extended to a depth of 1-2mm underneath the machined surface. These are likely caused by the tensile residual stresses resulted from high stress operating conditions and high generated temperatures (as in Tests 4 and 8).



Test 8: Parallel to feed



Test 6: Perpendicular to feed

Figure 4-27: Cross-sectional microstructure of ground surfaces (Phase 2A)

4.2.1.7 Workpiece microhardness

Microhardness depth profiles in the longitudinal feed direction are given in Figure 4-28, while the individual profiles for each test are given in Appendix F, Figure F81. All tests except for Tests 2 and 5, exhibited a softening layer extending to a depth of 15µm, which was then increased gradually until the bulk hardness was attained. This is in good agreement with previous work on the same material grounded with SiC wheels at comparable operating conditions [4], [24]. Typically, the slight softening observed was in conjunction with the existence of surface burn on workpiece surfaces and high generated grinding temperatures. The presence of a hardened layer extending to a depth of 100µm from the machined surface is present in Tests 4, 7, and 8, which was 12% higher than the bulk hardness value (~375$HK_{0.050}$). Test 5 produced the highest workpiece surface hardness with a peak value of ~453$HK_{0.050}$ within the first 10µm below the surface, conversely, tests involving surface with severe burning and cracking (Test 4 and 8), had a value of less than ~350$HK_{0.050}$ within the first 10µm below

the surface (softening), however, an increase in microhardness by 80HK up to a depth of 20-30µm was evident in both tests. This is possibly a result of the creation of an oxide layer or the presence of carbide particles with a diameter of up to 14µm.

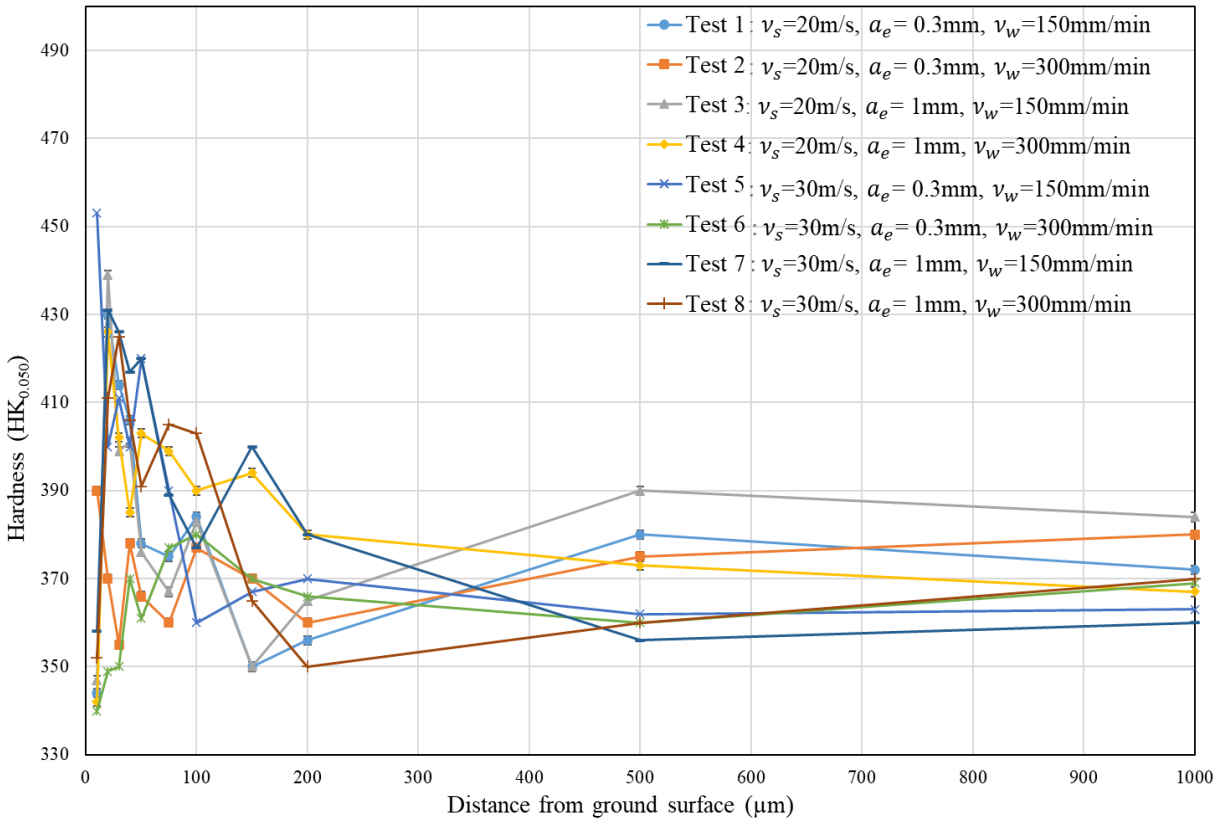


Figure 4-28: Microhardness depth profiles (Phase 2A)

4.2.2 Phase 2B: Assessment of grinding performance when creep feed grinding with super-abrasive diamond wheel, and benchmark against γ-titanium aluminide alloy (Ti-45Al-8Nb-0.2C)

4.2.2.1 Wheel wear and G-ratio

Figure 4-29 depicts the impact of operational conditions on G-ratio and radial wheel wear following CFG with diamond wheel, and the corresponding ANOVA calculations, main effects plot and interactions plot are provided in Appendix F, Table F30, Figures F82 and F83, respectively. The values for G-ratio and radial wheel wear of the diamond wheel were poor (within ~1 to 5 for G-ratio and between 8 to 27µm for wheel wear), which are comparable to SiC wheel results in previous phase (Phase 2A). This differs from those recorded for γ-TiAl in Phase 1B when employing a diamond wheel, as changing the wheel system (from SiC to Diamond) has improved the grinding ratio by up to ~1200%. Comparable G-ratio results were achieved in [25] when creep feed grinding burn-resistant titanium with a diamond wheel.

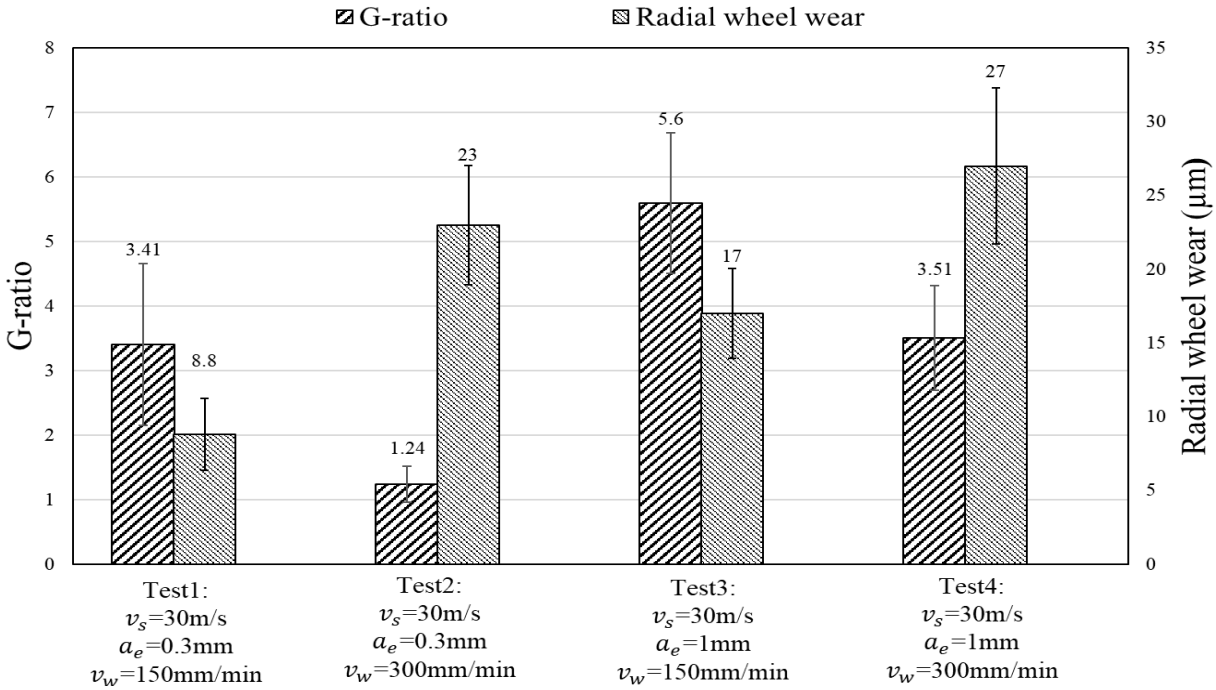


Figure 4-29: G-ratio and radial wheel wear for different grinding conditions (Phase 2B)

As was previously noted, the main effects must be taken into account in order to draw any conclusions about the impact of the operational conditions on output measure. Hence, the main effect plots for G-ratio showed that the means for grinding ratio increased by 50% with a rise

in depth of cut or feed rate from low to high levels (0.3 to 1mm for depth of cut and 150 to 300mm/min for feed rate). The associated ANOVA table further supports this highlighting both feed rate and depth of cut as significant factors affecting G-ratio with PCRs of 47.70% and 52.28%, respectively. The interaction plot for the G-ratio shows no interaction between the depth of cut and feed rate, reflecting the very low residual error percentage contribution ratio in ANOVA results (0.02%).

4.2.2.2 Grinding forces, power and specific energy

The maximum forces recorded when creep feed grinding burn-resistant titanium alloy with diamond wheel are presented in Figure 4-30. Compared with the SiC wheel, a reduction of more than 50% in normal forces along with a 30% drop in tangential forces are achieved when operating with the diamond wheel at identical operating parameters. While for grinding power and specific energy, the figures were reduced by 70% for all tests with the exception of Test 4 in this phase (only a 40% drop). For instance, running at a low depth of cut (0.3mm) and high wheel speed and feed rate (30m/s and 300mm/min) with SiC wheel in previous phase produced 1612N normal force, 543N tangential force, 15KW grinding power and 497J/mm^3 specific energy. These reduced to 739N, 354N, 5KW and 168J/mm^3 when operating with a diamond wheel here. The trends were as expected and the reasons for the results are essentially the same as those given in Phase 1B for γ-titanium aluminide alloy. The normal and tangential forces varied between 452 to 1316N and 227 to 407N, respectively when diamond CFG, which are comparable to those obtained in earlier work at comparable operating conditions [4], [7], [25]. The corresponding ANOVA calculations in Appendix F Tables F31-F34 showed that none of the factors is significant for the assessed output measures, despite relatively high PCR's (over 45% for both depth of cut and feed rate with regard to forces, power and specific energy) and low residual error contribution percentage (less than 10%). The main effects plots and interaction plots are detailed in Appendix F, Figures F84-F91.

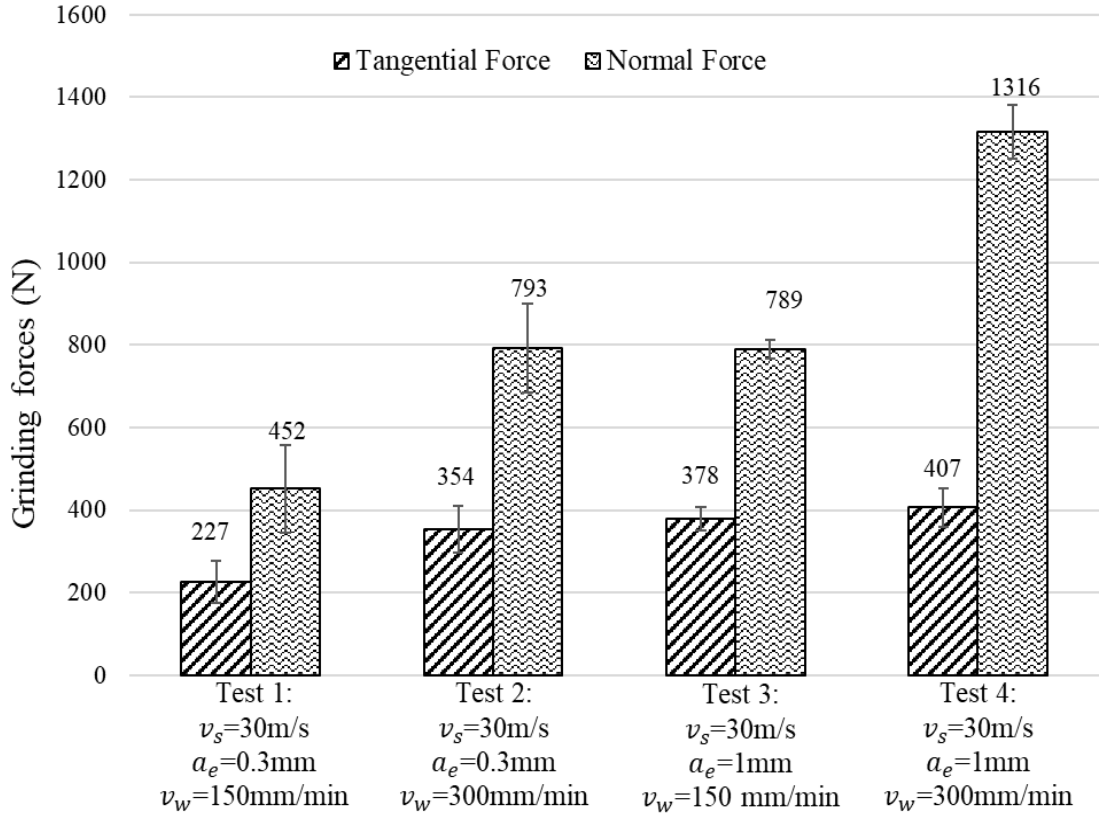


Figure 4-30: Grinding forces for different operating conditions (Phase 2B)

4.2.2.3 Grinding temperature

Maximum recorded grinding temperatures for burn-resistant titanium alloy ground with diamond wheel are shown in Figure 4-31, corresponding grinding temperature traces, main effects plot, interaction plot and ANOVA table are detailed in Appendix F, Figures F92-F94 and Table F35 respectively. In general, the trends follow those observed for γ-TiAl alloy with a significant drop in temperature for surfaces ground with diamond wheel given the superior thermal conductivity of diamond abrasives over SiC abrasives. Test 4 results, however showed otherwise, as almost identical temperature was recorded (~480°C) for both wheel systems running at fixed operating conditions (30m/s wheel speed, 300mm/min feed rate, 1mm depth of cut). It seems that the high heat concentration under high material removal rates has resulted in a coolant transition from nuclear boiling to film boiling, as a consequence of this shift, the superior thermal conductivity of the diamond wheel appears to have been mitigated. None of the tests for γ-TiAl alloy ground with diamond wheel showed such behaviour even at highest operating conditions, reflecting the higher thermal conductivity of the material itself over BuRTi (22W/mK for γ-TiAl over 10W/mK for BuRTi).

Previous work involving creep feed grinding the same alloy at 25m/s wheel speed, 500mm/min feed rate, and 1mm depth of cut produced a temperature of 500°C with SiC wheel, employing diamond wheel at the same conditions reduced the temperature to 200°C [4]. In comparison to current work, operating at a relatively lower feed rate, generated a temperature of 481°C, the difference is likely attributed to the higher coolant pressure associated with previous work (35bar compared to 7bar). Increases in contact area temperatures can be significantly influenced by the thermal and physical properties of the workpiece material and/or the grinding wheel material. Kato et al. demonstrated the findings for temperature measurement while grinding plain carbon steel and stainless steel under fixed operating conditions. There was a temperature increase of 450°C in the former and about 900°C in the latter. Differences in thermal conductivity, density, and specific heat between the two materials were cited as the main causes for changes in recorded temperature [93].

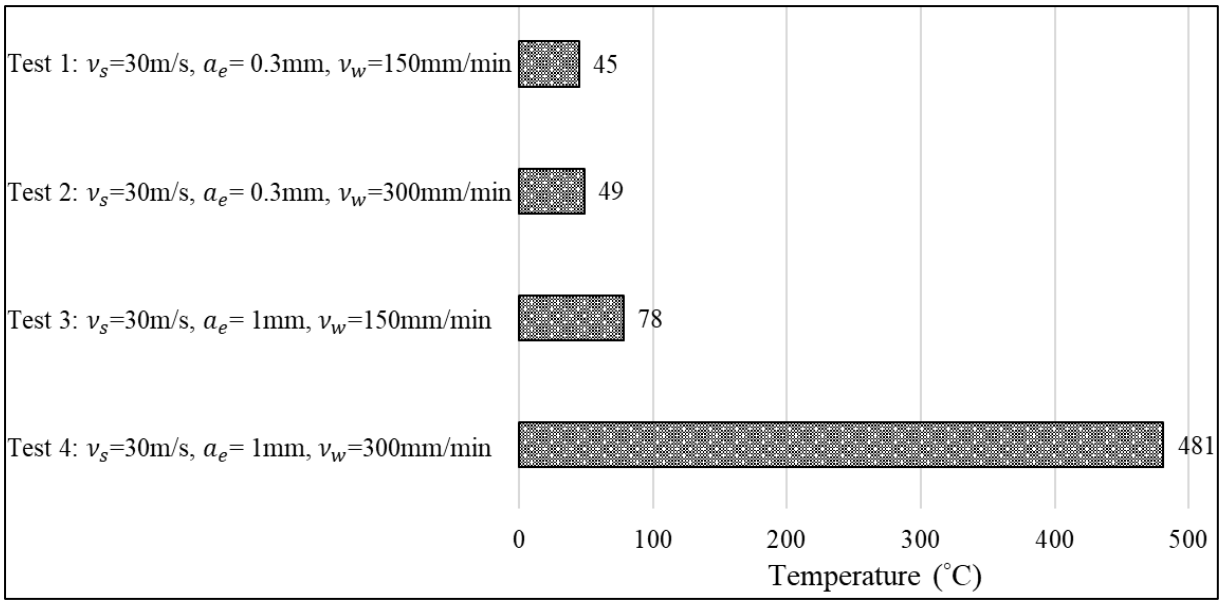


Figure 4-31: Measured temperature at different operating conditions (Phase 2B)

4.2.2.4 Surface roughness and topography

Figure 4-32 presents 2D roughness and 3D topographical parameters for burn-resistant titanium workpieces ground with diamond wheel. Typically, the tendencies shown in the previous phase continue here, compared to γ-TiAl samples ground using a diamond wheel (in Phase 1B), all 2D and 3D extreme parameters (Rt, Rz, St and Sz) for BuRTi surfaces are higher by up to 50% and by 30% for surface average parameters (Ra and Sa). These increased values

are indicative of surface carbide damage and high levels of side flow observed on the ground surface of BuRTi workpieces, giving the higher ductility of the material over γ-TiAl. The results are in agreement with Hood finding when comparing the performance of the two alloys following creep feed grinding with diamond wheel, 40% higher average 2D workpiece surface roughness (Ra) for BuRTi over γ-titanium aluminide alloy was noted under the same operating parameter levels [7]. Soo et al. reported comparable 2D average surface roughness (Ra) values, ranging from 0.97 to 1.65μm when diamond grinding the same alloy (BuRTi). Unfortunately, a comparison with other roughness parameters could not be made as no information on 2D extreme parameters or 3D roughness parameters was given [25]. In contrast to γ-TiAl findings, changing the wheel system from SiC to diamond improved the produced 2D roughness parameters and 3D average parameters (Ra, Rt, Rz and Sa) by 30-50% for the tests involving higher depth of cuts (1mm). However, no improvement was evident in 3D parameters peak to peak (St) and 10-point average (Sz). Main effects plots, interaction plots, 3D mapping of ground surfaces and analysis of variance tables for 2D and 3D roughness parameters are detailed in Appendix F, Figures F95-F107 and Tables F36-F41. Based on ANOVA calculations, depth of cut and feed rate had no significant influence on any of the roughness parameter values despite having a high percentage of contributions on their output values. Feed rate contributed the most for Ra (PCR of 40%), Rt (PCR of 73.93%), Rz (PCR of 42.55%), and Sa (PCR of 37.77%), while depth of cut had the highest PCRs value on St (32.19%) and Sz (47.77%). Interaction plots show that an interaction between feed rate and depth of cut is present at all roughness parameters, except in Sz. The ANOVA results further indicate higher residual error PCR values of over 40% for the majority of assessed roughness parameters and reaching 60% for Sa. This suggests that the interaction of feed rate and depth of cut is likely to have a significant influence on the output measures for surface roughness parameters, unfortunately, however assessment of such interaction was not possible with the used array for this experimental phase.

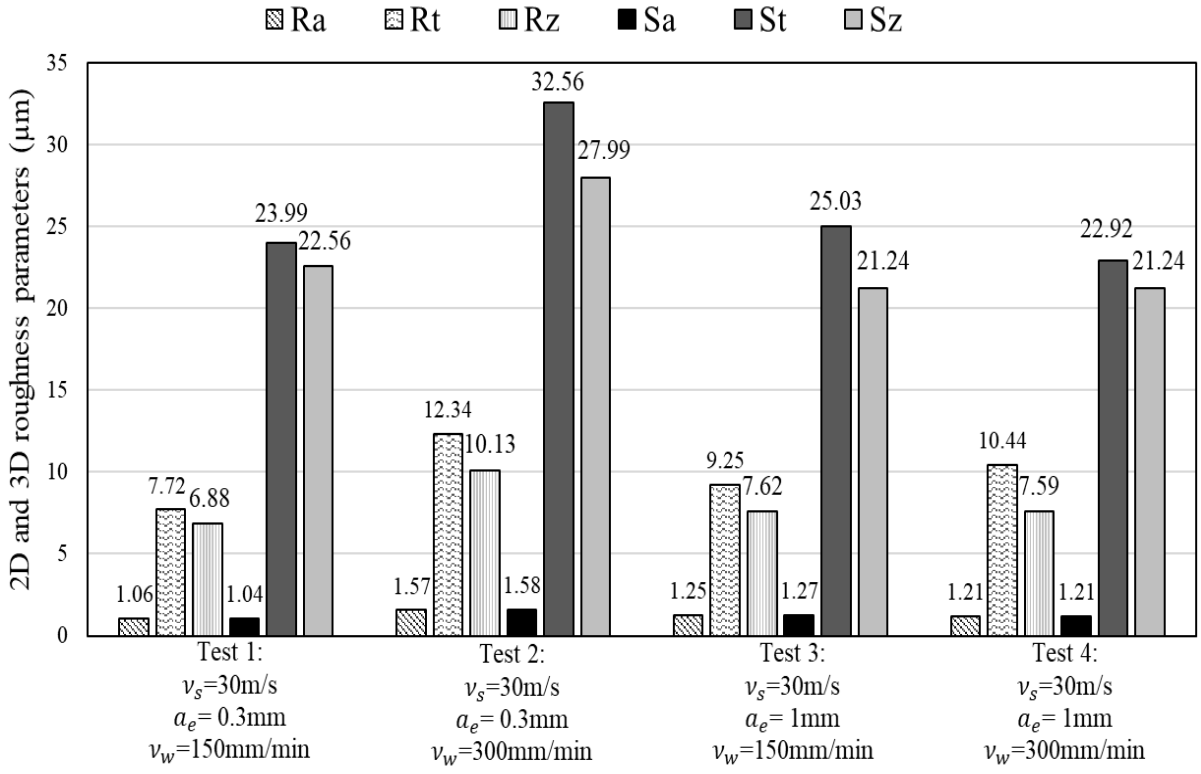


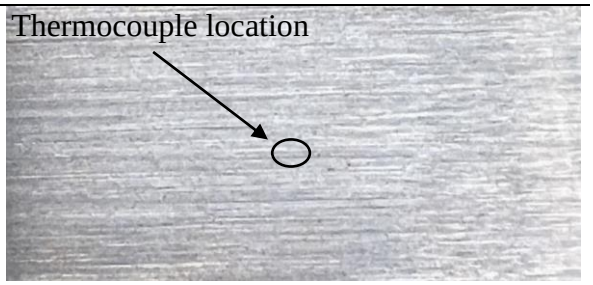
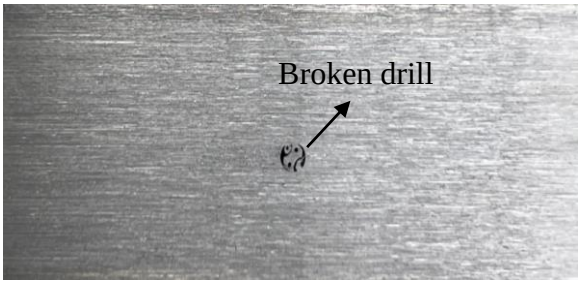
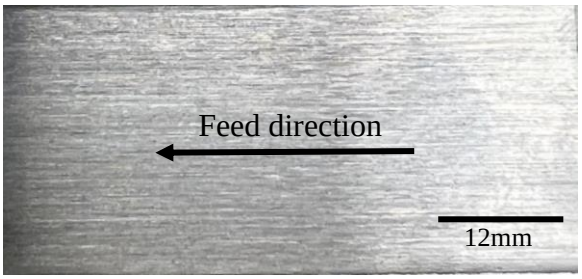
Figure 4-32: 2D and 3D surface roughness parameters for ground surfaces (Phase 2A)

4.2.2.5 Workpiece surface

The surface images for BuRTi samples ground with diamond wheel given in Table 4-9 revealed that workpiece surfaces for the first three tests (Test 1-3) appeared to be visually free of burn and chatter with slight burn marks and cracks covering over 60% of the surface area in both transverse and longitudinal directions in Test 4, which corresponded to test involving highest operating conditions. Earlier work by Hood and Soo on creep feed grinding of BuRTi with a diamond wheel at a relatively longer depth of cut (1.25mm and 2mm) and higher wheel speed (35m/s and 50m/s), showed high levels of surface burn and chatter on most ground surfaces, and only when operating at the lowest levels, the absence of burn and chatter was observed [7], [25]. The work by Novovic involved creep feed grinding BuRTi with a diamond wheel at 100mm/min feed rate, 25m/s wheel speed and varied depth of cut (1 and 2mm); subsequent surface analysis showed no evident of thermal damage or burn on any of the ground surface even at 2mm depth of cut, which is probably attributable to the increased coolant pressure used (35bar compared to 7bar in other work) [4]. Figure 4-33 shows SEM images of commonly found surface defects. As observed in the previous phase on surfaces ground with SiC wheel, surface damage was commonly present throughout all the samples inspected, consisting of

smearing materials, fracture and ploughing with cracks only occurred in Test 4. This could partially explain why the surface roughness values were so much higher than those described before for γ-TiAl ground at similar operating conditions. The higher ductility of the alloy, in addition to the presence of damaged carbide particles, might account for surface defects.

Table 4-9: Workpiece surface images (Phase 2B)

Test No.	Grinding conditions	Recorded temperature	Surface observation
1	v_s =30m/s a_e= 0.3mm v_w=150mm/min	45°C	
2	v_s =30m/s a_e= 0.3mm v_w=300mm/min	49°C	
3	v_s =30m/s a_e= 1mm v_w=150mm/min	78°C	
4	v_s =30m/s a_e= 1mm v_w=300mm/min	481°C	

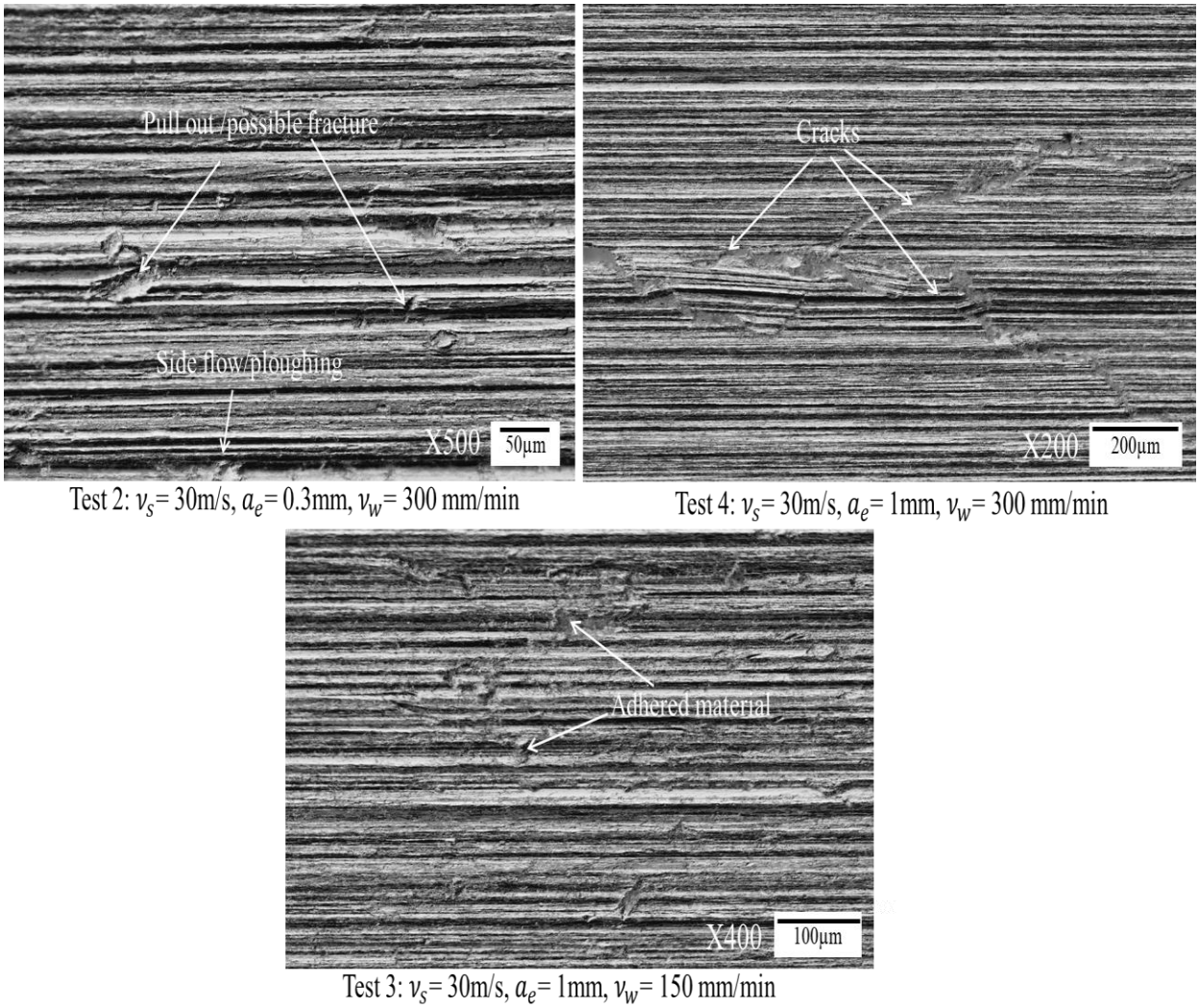


Figure 4-33: Higher magnification images of the ground surfaces (Phase 2B)

4.2.2.6 Workpiece microstructure

The optical micrographs of the microstructure for burn-resistant titanium samples ground with the diamond wheel are illustrated in Figure 4-34. The cross-sectional images of the majority of tests (Test 1-3) showed free damage surfaces with no discernible change in the microstructure. The surface showing the most damage was produced by Test 4, where the corresponding micrograph highlighted plastic deformation extending to ~17µm under the machined surface and cracks, ranging from 14-48µm in width and 600µm to 2mm in length. Similar observations were noted by Soo at most ground samples following CFG of BuRTi with diamond and cBN wheels. Nevertheless, only one out of the 8 tests used in his array displayed minimal damage [25]. This suggests that the chosen operating conditions in this work were suitable for a defect-free grinding of BuRTi. Cavities up to 6-8µm deep, laps and folds were noted by Novovic work

when CFG BuRTi with diamond wheel [4], however, these were not noticeable in this work, it could be that the degree of smearing seen makes it hard to evaluate them.

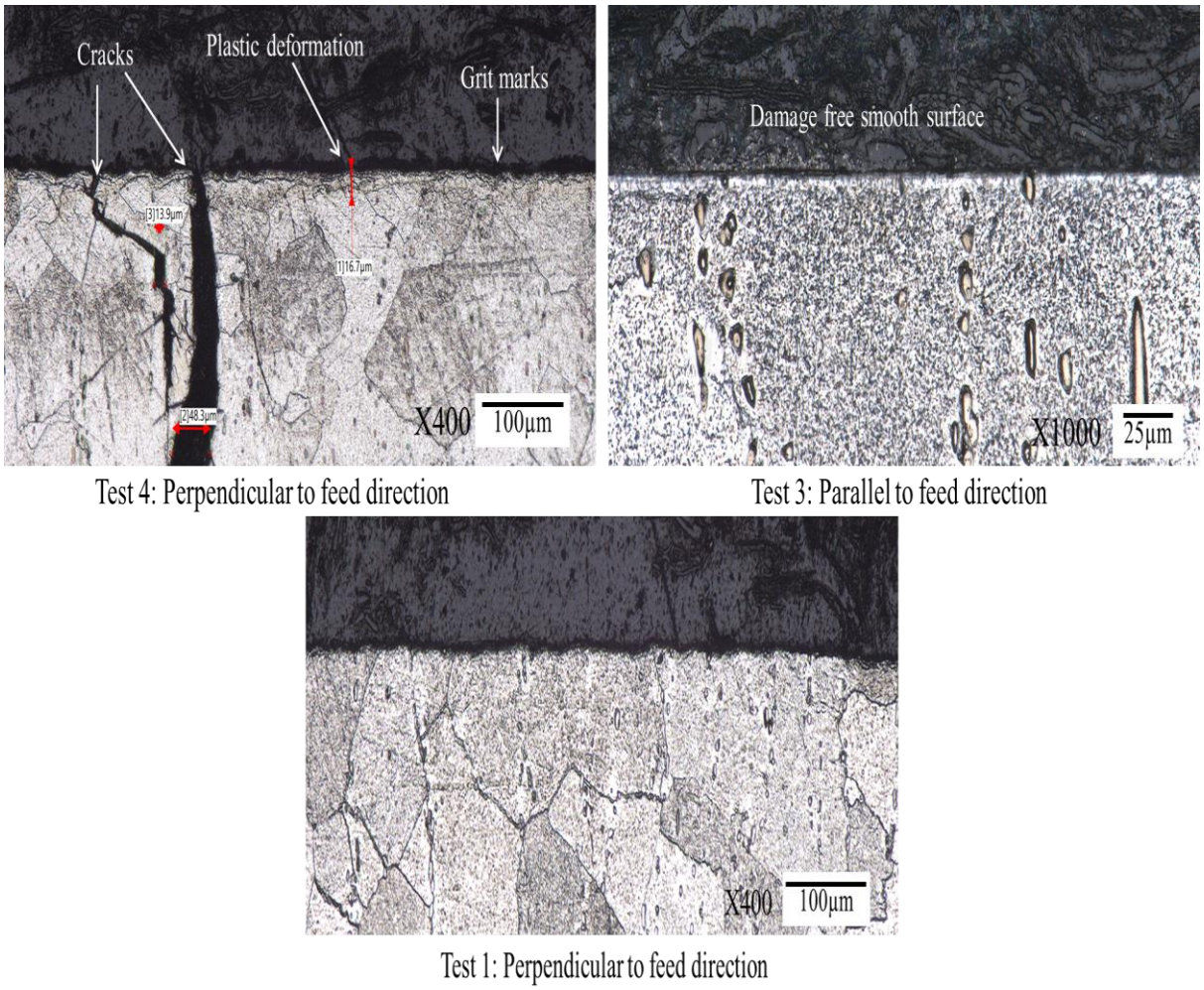


Figure 4-34: The microstructure of BuRTi samples ground with diamond wheel (Phase 2B)

4.2.2.7 Workpiece microhardness

Figure 4-35 details microhardness profiles for all BuRTi samples ground with diamond wheel, and the individual profile for each test is given in Appendix F, Figure F108. All samples exhibited soft regions (~90HK below the bulk hardness) from a depth of 10µm to 50µm beneath the machined surface and typically increased until the bulk hardness was reached ($375HK_{0.050}$) at ~500µm below the surface. The observed softening correlates well with the sub-surface microhardness results reported by Soo who also noted softening within 10-20µm below the surface of BuRTi machined with a diamond wheel [25] Soo coupled the results with the presence of surface burn and heat-affected zone on the examined surfaces and sub-surfaces. These assumptions might apply with previous phase observations (surfaces ground with SiC

wheel), however do not apply here, especially for the first three tests (Test 1-3) as no burn or heat affect zones are evident in any of their surface/sub-surfaces. Ding et al. explained that when the workpiece material is ground at high temperatures and under substantial pressure, thermal softening and work hardening occur simultaneously. The rate of thermal softening behaviour during the machining of nickel-based alloys or titanium alloys with vitrified or electroplated super-abrasive wheels is always much greater than that of the work hardening effects during the process of plastic deformation and the microstructure alteration of the sub-surface [65]. This is true for Test 4, which had the lowest microhardness value (~290$HK_{0.050}$), while only limited degrees of softening were displayed by other tests.

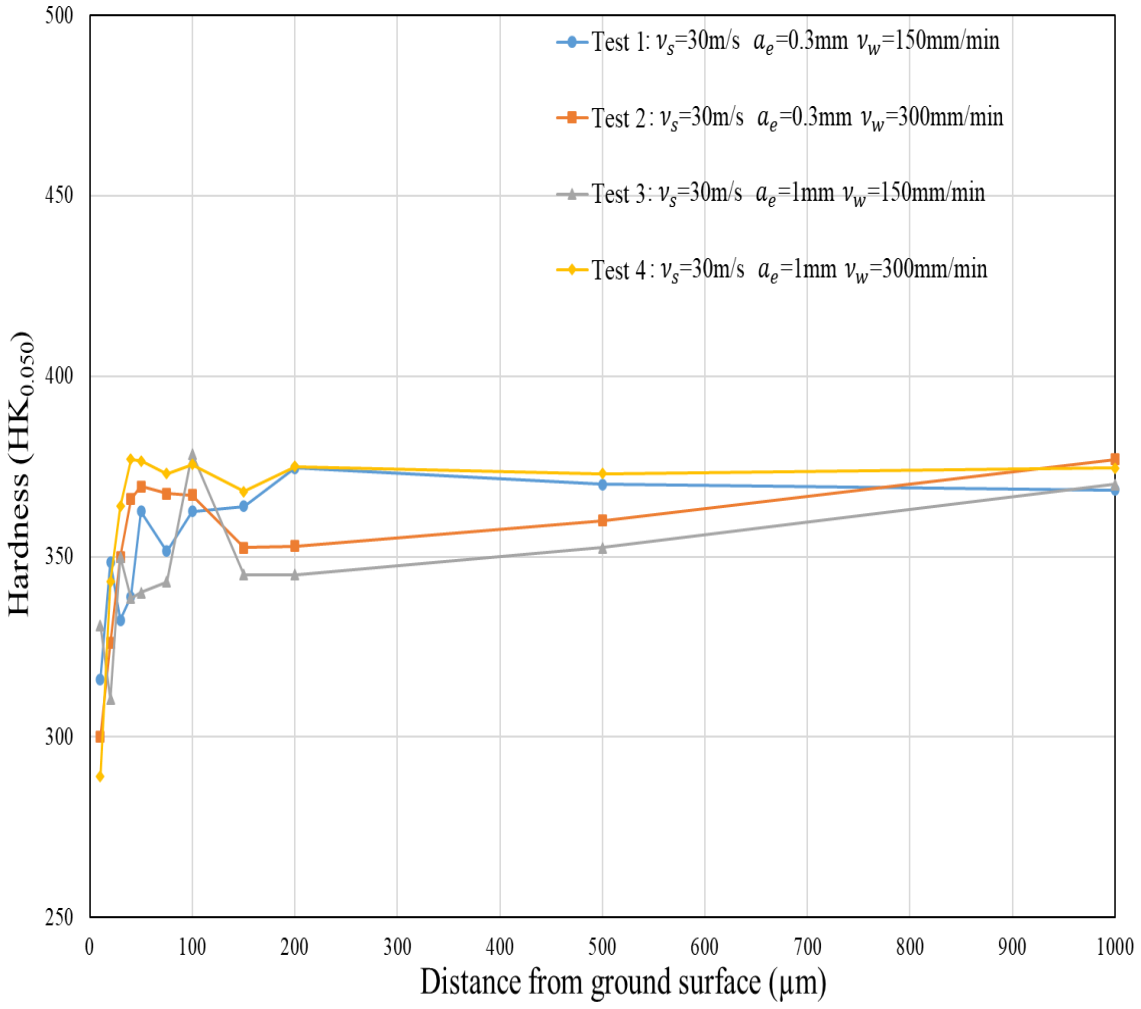


Figure 4-35: Microhardness depth profiles (Phase 2B)

4.2.3 Phase 2C: Extended surface integrity analysis (residual stress) on burn-resistant titanium alloy (Ti-25V-15Cr-2Al-0.2C)

The residual depth profile data for machined BuRTi samples under various grinding conditions, both in the transverse and longitudinal orientations, are illustrated in Figure 4-36. The highest values for surface residual stresses were observed in SiC test operated at highest levels, with values of -711MPa and -577MPa in transverse and longitudinal directions, respectively, measured at 8µm below the surface. At a depth of 100µm, they changed to tensile mode and extended to a depth of more than 500µm where the highest tensile residual stresses were recoded (596MPa in transverse direction and 317MPa in longitudinal direction). Comparable findings (around -500MPa) were given by Novovic when CFG the same alloy with SiC wheel [4]. The residual stress profile for the SiC wheel test follows the same trend as that obtained when CFG of γ-TiAl with SiC wheel at identical conditions; however, BuRTi samples exhibited higher levels of residual stresses extending beyond 500µm below the machined surface, which is attributed to the differences in thermal conductivity and plastic deformation regions between the two materials (shown earlier in cross-sectional micrographs). The presence of burn marks and a network of cracks on γ-TiAl and BuRTi samples ground with SiC wheel suggested that residual stresses are tensile in nature, however the measured residual stresses at the surfaces were compressive in both directions. This implies the occurrence of overshadowing of tensile stresses by compressive stresses due to the mechanical action between the wheel and the workpiece up to a certain depth. The utilisation of vitrified diamond, while maintaining identical grinding conditions, resulted in lower residual stress levels with similar behaviour as both samples displayed compressive stresses near the surface, which transitioned into tensile stresses at a depth of 50µm below the surface, however at a depth of 250µm underneath the surface, residual stresses for vitrified diamond wheel sample shifted again to compressive stresses reaching -205MPa at 500µm depth. This is probably because diamond grits have substantially higher thermal conductivity than SiC grits. In the case of the vitrified diamond wheel sample, there was no significant alteration in residual stresses observed in the transverse direction. However, the maximum recorded values for compressive and tensile stresses in the longitudinal direction were -108MPa (at a depth of roughly 8µm) and 260MPa (at a depth of 60µm), respectively. The presence of tensile residual stresses in the vitrified diamond wheel sample is associated with the observed occurrence of cracks and small burning marks on the ground surface at a recorded temperature of 481°C. Operating with the vitrified

diamond wheel at a lower depth of cut (0.3mm) and feed rate (150mm/min) achieved surfaces with no tensile residual stresses, no surface/surface damage, and significantly reduced the grinding temperature to 45°C, with favourable compressive stresses in both directions (-340MPa at the surface) reaching neutral state at 80µm below the surface. The existence of compressive residual stresses and the reduced levels of tensile residual stresses was not surprising given the significantly lower cutting forces, temperature, and wear rate found with the diamond wheel compared with the SiC wheel and the lack of surface/subsurface damage.

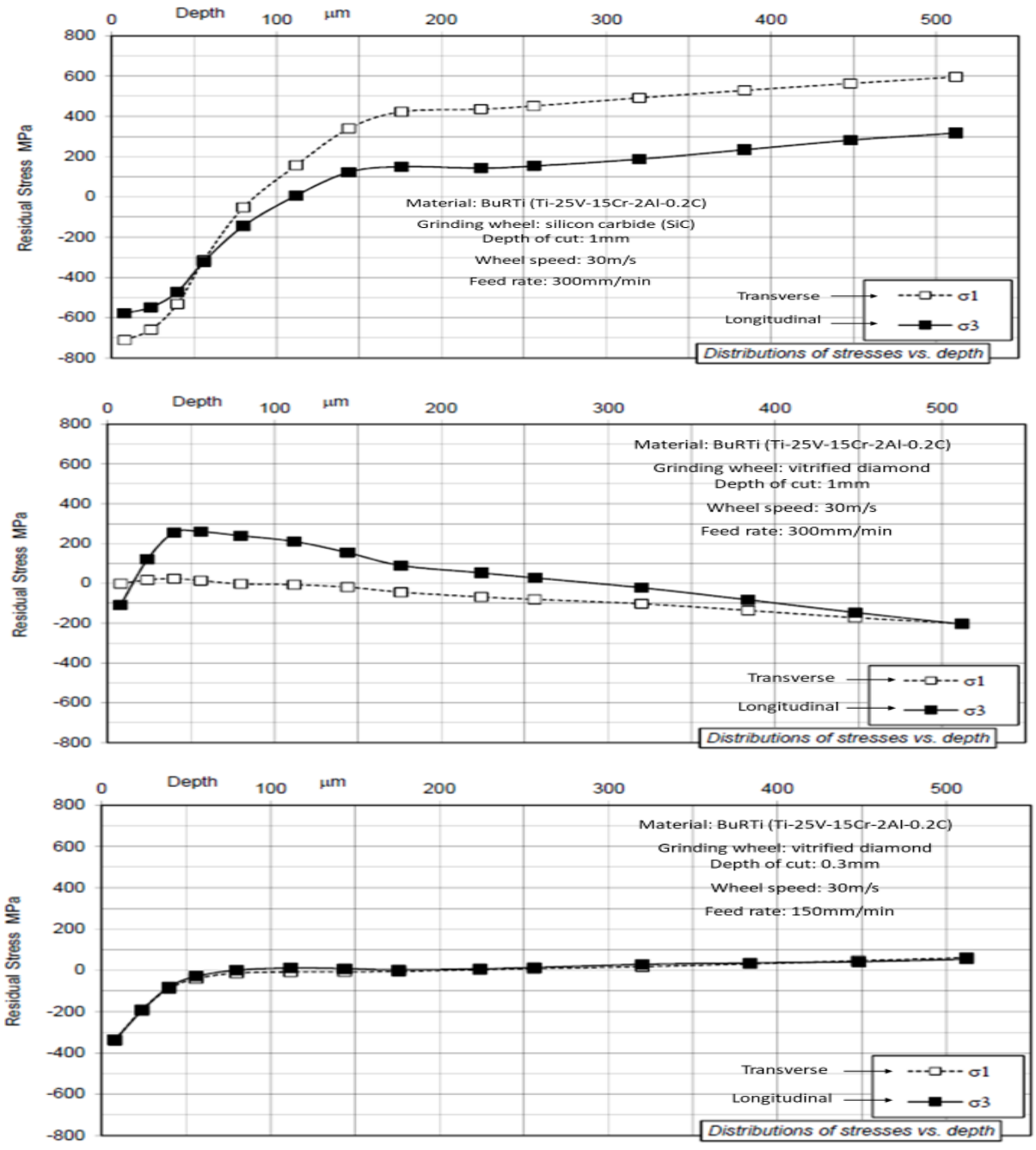


Figure 4-36: Residual stress depth profiles for BuRTi samples

4.2.4 Summary of results for burn resistant titanium alloy (Ti-25V-15Cr-2Al-0.2C)

Phase 2A: Assessment of significant operating parameters when creep feed grinding of burn resistant titanium alloy (Ti-25V-15Cr-2Al-0.2C) with conventional silicon carbide wheel (SiC) and benchmark against γ-titanium aluminide alloy (Ti-45Al-8Nb-0.2C)

- BuRTi was more difficult to grind than γ-TiAl with 7 times lower G-ratio (varied between 2.1- 3.8) and 3 times higher radial wheel wear (25µm compared to 7.5µm at similar grinding conditions). ANOVA results for G-ratio showed that none of the tested factors is significant at a 95% confidence interval.

- Cutting forces for BuRTi were 30-40% higher than in γ-TiAl with normal forces ranging between 930-2314N, tangential forces 363-711N, power levels from 10 to 23KW and specific energy 231-895J/mm^3. The effect of altering the depth of cut on grinding forces, while other factors were fixed, was very noticeable, in particular for normal forces. Conversely, minimal change was observed for low and high running levels of wheel speed and feed rate. Indeed, the depth of cut was significant for all assessed responses. Whilst wheel speed and feed rate had significant influence only on power and specific energy respectively.

- The difference in coolant pressures employed in BuRTi (15bar) and γ-TiAl (7bar) led to lower temperatures being generated in the former, despite the fact that the latter exhibits greater thermal conductivity (10W/mK for BuRTi when compared to 22W/mK for γ-TiAl). Temperature results were typically comparable ~350°C for most investigated conditions with the exception of experiments conducted with elevated levels of feed rate and depth of cut, regardless of changes in wheel speed levels (611°C and 476°C). Statistical analysis further supports this with very low PCR values identified for wheel speed (less than 1%) and relatively higher values of 46.75% and 28.54% for depth of cut and the combined effect of depth of cut and feed rate (a_e x v_w), respectively. Nonetheless, none of the factors were statistically significant for temperature response.

- In the majority of trials, the data pertaining to 2D and 3D surface roughness parameters for ground BuRTi samples were found to be twice as high as the corresponding values reported for the γ-TiAl workpiece. For instance, operating at (v_s=30m/s, a_e=1

v_w=300mm/min) resulted in 2.02µm and 2.1µm for Ra and Sa respectively, while for γ-TiAl samples machined at the same conditions, the value reduced to 0.74µm (Ra) and 0.76µm (Sa). Similarly, operating at 1mm depth of cut, 20m/s wheel speed, and 150mm/min feed rate produced 3D roughness values of 24.6µm and 19.73µm for peak-to-peak (St) and 10-point average (Sz). These were reduced to 11.6µm and 8.45µm in γ-TiAl samples. Interaction plots for 3D roughness parameters Sz and St show that an interaction between feed rate and depth of cut (v_w x a_e) is present and was identified by ANOVA calculations as being statistically significant for S_t response with a high PCR value of 58.47%.

- Burn and chatter were observed on all surfaces and were particularly more severe at tests conducted under the most extreme operating parameters. High levels of smearing, cavities, side flow were evident in SEM images.

- Associated cross-sectional micrographs of the ground surfaces highlight extensive plastic deformation to a depth of ~20µm in the majority of BuRTi samples. In addition, microstructure analysis showed that the visually appeared network of cracks on the ground surfaces extended to a depth of 1-2mm underneath the machined surface.

- With the exception of two trials, all other trials exhibited a softening layer within the first 15µm under the surface up to (~340 $HK_{0.050}$). This softening layer then gradually increased until the bulk hardness was attained.

Phase 2B: Assessment of grinding performance when creep feed grinding of burn-resistant titanium alloy (Ti-25V-15Cr-2Al-0.2C) with super-abrasive diamond wheel and benchmark against γ-titanium aluminide alloy (Ti-45Al-8Nb-0.2C)

- The G-ratio and radial wheel wear values of the diamond wheel exhibited almost similar ranges to those observed with the SiC wheel, falling within the range 1-5 for the G-ratio and from 8 to 27µm for wheel wear. This is in contrast to γ-TiAl results, where an increase of ~1200% in G-ratio was achieved with a vitrified diamond wheel. The associated ANOVA analysis showed that both feed rate and depth of cut are significant factors for G-ratio response.

- In comparison to the SiC wheel, operating with a vitrified diamond wheel under identical conditions resulted in a significant decrease of over 50% in normal forces, a 30% reduction in tangential forces and both grinding power and specific energy reduced by 70%. Such improvements were evident with γ-TiAl ground with a vitrified diamond wheel. This is mainly attributed to the lower rubbing forces (lower ploughing and sliding forces) between the workpiece and the wheel.

- Typically, the trends for temperature are consistent with those observed for γ-TiAl samples, as both surfaces ground with vitrified diamond wheel experienced a substantial decrease in temperature due to the superior thermal conductivity of diamond abrasives in comparison to SiC abrasives. However, this was not the case for the test operated at maximum conditions, as almost identical temperature (~480°C) was recorded for both wheels. It is likely that the superior thermal conductivity of the diamond wheel has been diminished as a result of the coolant transitioning from nuclear boiling to film boiling.

- As opposed to results obtained with γ-TiAl, where no significant improvement in surface roughness parameters was observed in changing the wheel system (diamond instead of SiC), findings for BuRti displayed a 30-50% improvement in 2D roughness parameters (Ra, Rt and Rz) and also in 3D average surface parameters (Sa) for experiments involving greater depths of cut (1mm). Peak-to-peak variation (St) and 10-point average (Sz) were, nevertheless, unaffected by the change. Interaction plots for roughness data show that an interaction between feed rate and depth of cut was present in all roughness parameters, except in the 3D 10-point average parameter (Sz), which indicates that the combined effect of depth of rate and feed rate is likely to have a statistically significant influence.

- In terms of surface damage, the BuRTi diamond ground surface appeared to be visually free of burn and chatter. Out of the four tests conducted, only the one utilising the most extreme operating conditions and associated with a high grinding temperature (~480°C), exhibited marginal burn marks and cracks covering more than 60% in both transverse and longitudinal directions. SEM analysis indicates the same degree of surface damage as those found in SiC ground surface, consisting of smearing, fracture and ploughing of material. This observation may explain the significantly higher

surface roughness values obtained in the BuRTi surfaces than in γ-TiAl surfaces ground under identical operating conditions.

- As expected, the optical micrographs of the microstructure for burn-resistant titanium samples ground with diamond wheel show no sub-surface damage in all machined surfaces, except in the test with extreme operating conditions. The corresponding micrograph highlighted plastic deformation extending to ~17µm under the machined surface and cracks, ranged from 14 to 48µm in width and 600µm to 2mm in length.

- No major changes in microhardness were observed for BuRTi samples machined with a vitrified diamond wheel. The examined samples displayed areas of reduced hardness ranging from a depth of 10µm to 50µm below the machined surface. The most significant softening effect was detected in the test that generated the highest temperature, with a decrease in hardness of ~90HK. These were typically increased until the bulk hardness was reached ($375HK_{0.050}$) at ~500µm below the surface.

Phase 2C: Extended surface integrity analysis (residual stress) on burn-resistant titanium alloy (Ti-25V-15Cr-2Al-0.2C)

- Compressive residual stresses in the SiC sample conducted at highest levels reached maximum values at 8µm below the surface, with values of -711MPa and -577MPa in transverse and longitudinal directions, respectively. They however, changed to tensile mode at a depth of 100µm and maintained it for over 500µm, where the greatest tensile residual stresses were recoded (596MPa transversely and 317MPa longitudinally).

- The use of a vitrified diamond wheel under identical grinding conditions led to a substantial decrease in residual stress levels. Similar to the SiC sample, the diamond workpiece exhibited compressive stresses near the surface, which then transitioned into tensile stresses at a depth of 50µm below the surface. In contrast, at a depth of 250µm beneath the surface, the residual stresses for the vitrified diamond wheel sample shifted once again to compressive stresses, reaching a magnitude of -205MPa at a depth of 500µm.

- BuRTi samples ground with the vitrified diamond wheel at the lowest depth of cut (0.3mm) and feed rate (150mm/min) produced surfaces with no tensile residual stresses, with only favourable compressive stresses in both directions (-340MPa) extending to ~50µm below the surface and then reaching neutral state at ~80µm.

4.3 Phase 3: Creep feed grinding of conventional titanium alloy (Ti-6Al-4V)

4.3.1 Phase 3A: Benchmarking the performance against γ-titanium aluminide alloy and burn-resistant titanium alloy with SiC wheel

4.3.1.1 Wheel wear and G-ratio

Comparisons between the performance of three machined titanium alloys in terms of G-ratio and radial wheal wear are presented in Figure 4-37 and Figure 4-38, respectively. At identical operating conditions, G-ratio results for Ti-6Al-4V were comparable to BuRTi results with values ranging from 1.5 to 4. A value of 1.2 was reported in earlier work relating to creep feed grinding of Ti-6Al-4V [7], [17]. Bently reported values of less than 1 for G-ratio when surface grinding the same alloy [17]. Profiles trends for BuRTi and Ti-6Al-4V in Figure 4-37 show that the G-ratio for BuRTi and Ti-6Al-4V increases as the depth of cut decreases, while for γ-TiAl, the opposite was true, as a drop in depth of cut from 1mm to 0.3mm resulted in a 40% decrease in G-ratio. The SiC wheel exhibited severe wheel wear (~50µm) when grinding Ti-6Al-4V at 1mm depth of cut, the value was reduced by ~50% when grinding BuRTi at identical conditions (~27µm). For γ-TiAl, the wheel wear was almost negligible (2.9µm) when CFG at 0.3mm depth of cut. The trends for G-ratio and wheel wear suggest that γ-TiAl was easier to grind than BuRTi and Ti-6Al-4V, owing to the lower ductility (10 times lower), and tensile strength of γ-TiAl when compared to BuRTi and Ti-6Al-4V as given in Table 2.4, section 2.1.2.

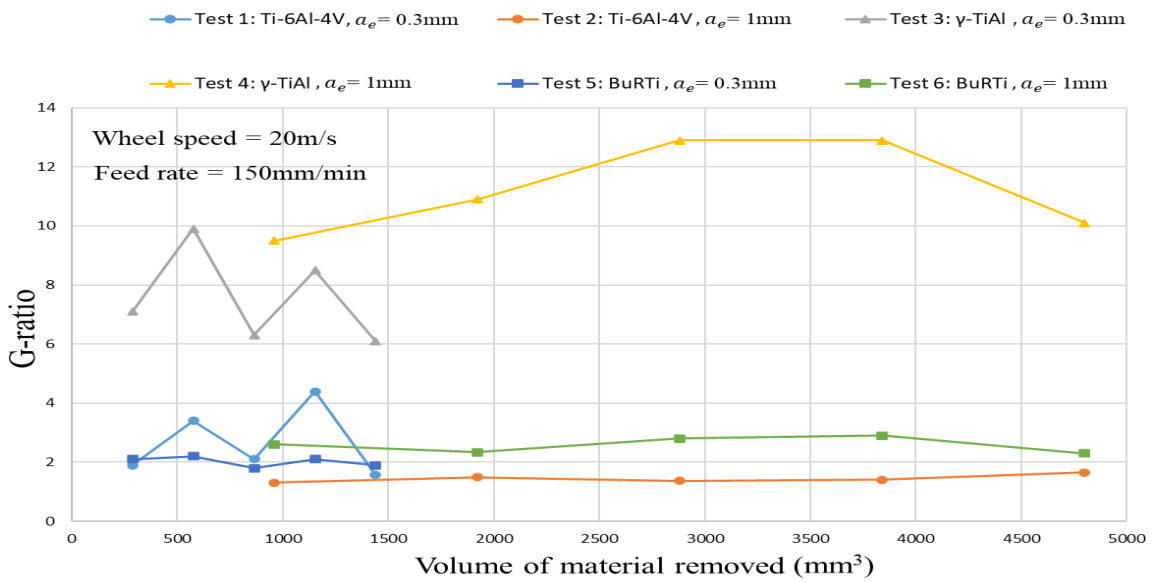


Figure 4-37: G-ratio for different titanium alloys (Phase 3A)

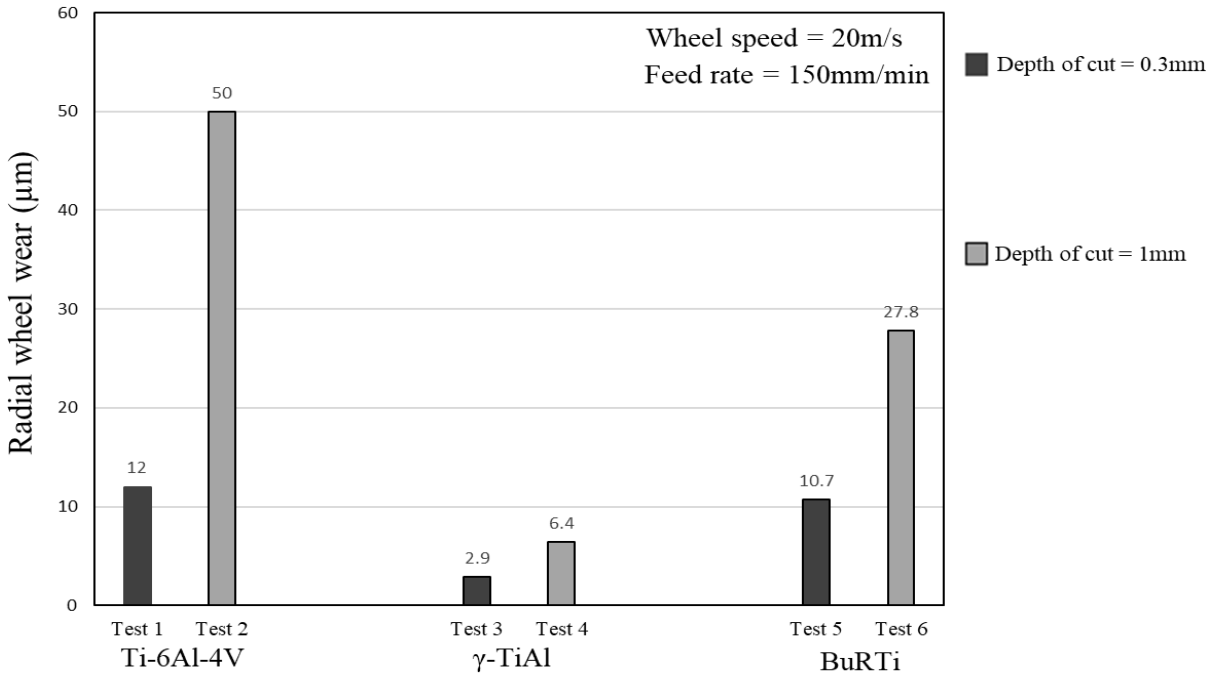


Figure 4-38: Radial wheel wear for different titanium alloys (Phase 3A)

4.3.1.2 Grinding forces, power and specific energy

Normal and tangential forces against the volume of workpiece material removed for different titanium alloys (Ti-6Al-4V, BuRTi and γ-TiAl) are plotted in Figure 4-39 and Figure 4-40, respectively. For Ti-6Al-4V, recorded normal forces were between 520 to 980N, while the tangential forces varied from 300 to 500N depending on the depth of cut used. Both normal and tangential force components for BuRTi and γ-TiAl typically increased with an increment in depth of cut from 0.3 to 1mm as a result of an increase in undeformed chip thickness as well as arc contact length. Conversely, force components when CFG Ti-6Al-4V decreased at a depth of cut of 1mm compared to those recorded at a lower depth of cut 0.3mm with marginal effect on grinding forces values. The majority of force components for the three titanium alloys showed an upward trend with an increase in the volume of material removed due to increased wear flat generation (undressed condition). The grinding forces were greatest when CFG BuRTi, followed by γ-TiAl and found to be lowest at Ti-6Al-4V. Patterns of grinding power and specific energy illustrated in Figure 4-41 are consistent with those described for grinding forces. The lowest power levels (3KW) were obtained when CFG Ti-6Al-4V at 20m/s wheel speed, 150mm/min feed rate and 0.3mm depth of cut (Test 1). On the other hand, the greatest power levels (17KW) were measured when CFG BuRTi at 20m/s wheel speed, 150mm/min feed rate and 1mm depth of cut (Test 6). Tests involving CFG of Ti-6Al-4V (Test 1 and 2)

produced almost the same value for specific energy (~196J/mm^3). Similar values were reported by Guo et al. following conventional surface grinding of Ti-6Al-4V at 3m/min feed rate and 26m/s wheel speed [168]. In addition, comparable values of specific energy (180 and 200J/mm^3) were described by Ahmed and González when surface grinding Ti-6Al-4V with different cooling conditions, including MQL, dry and flood [176].

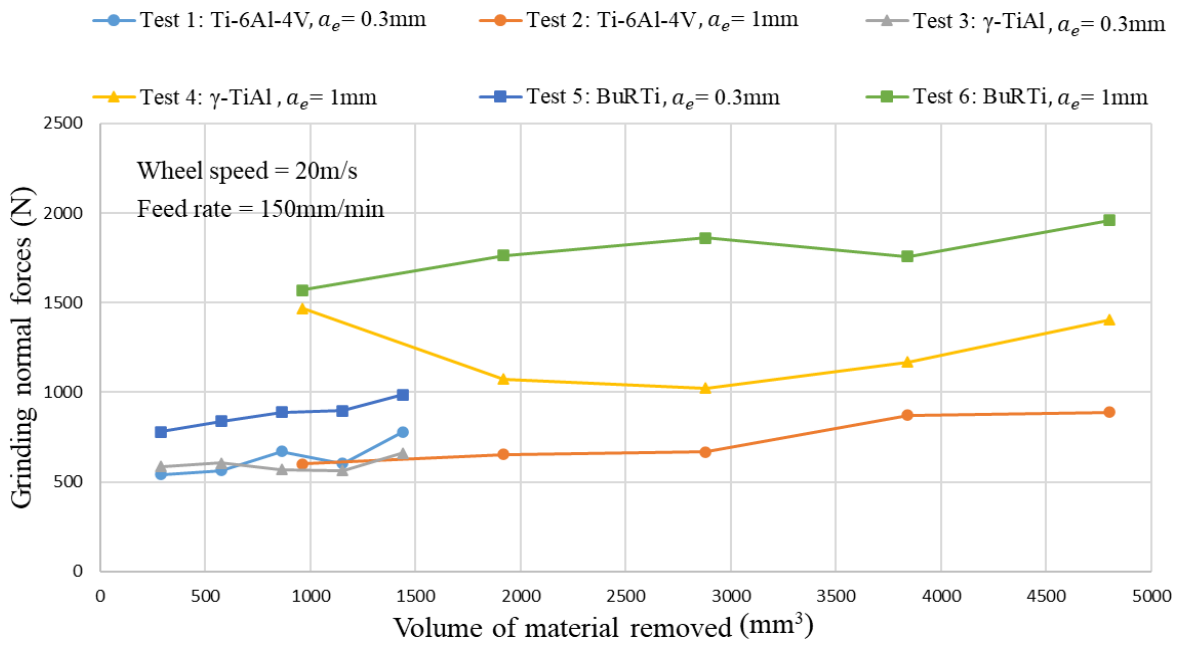


Figure 4-39: Grinding normal forces for different titanium alloys (Phase 3A)

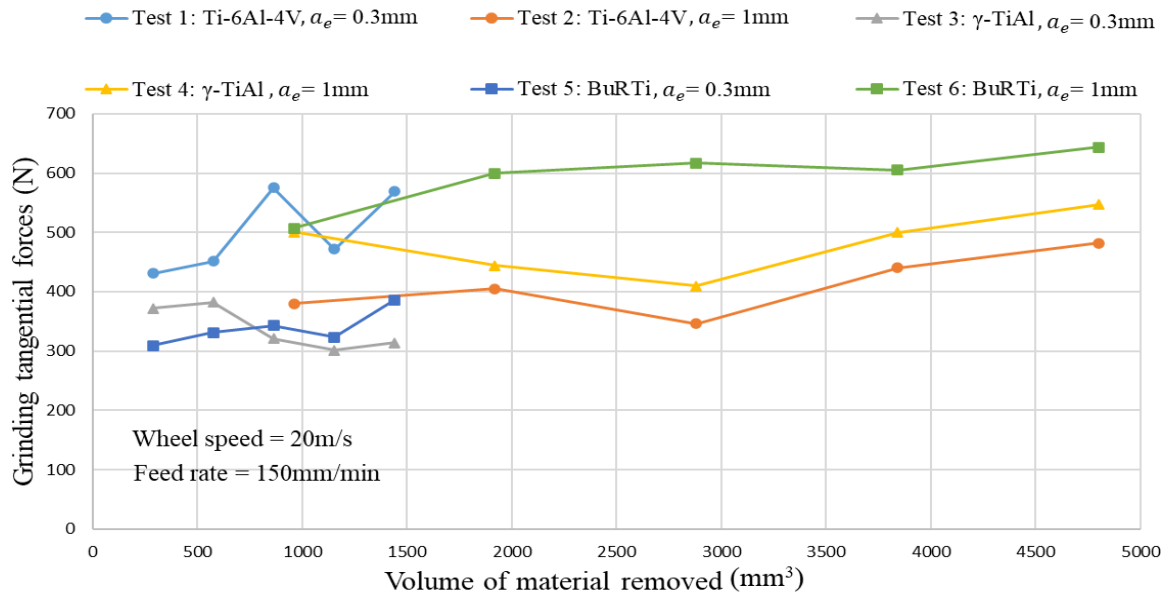


Figure 4-40: Grinding tangential forces for different titanium alloys (Phase 3A)

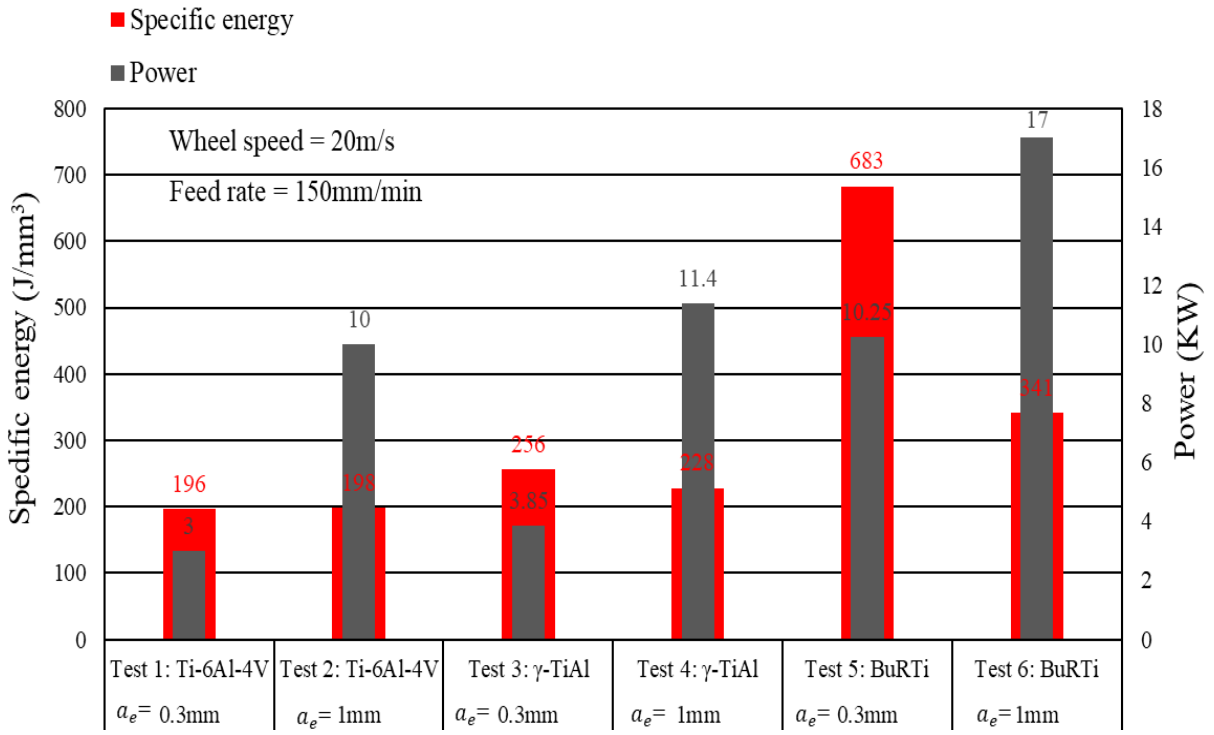


Figure 4-41: Grinding power and specific energy for different titanium alloys (Phase 3A)

4.3.1.3 Grinding temperature

Figure 4-42 shows the recorded grinding temperature for different titanium alloys machined under the same conditions (Ti-6Al-4V, BuRTi and γ-TiAl). In general, and at the given conditions, the recorded temperature range for Ti-6AI-4V lies between that of BuRTi and γ-TiAl, although more comparable to the former. A temperature of 218°C was measured for Ti-6Al-4V when operating at lowest operating levels, changes in depth of cut employed from 0.3 to 1mm resulted in a slight temperature difference (254°C). Temperatures as high as 500°C were reported in [4] when creep feed grinding Ti-6AI-4V with SiC wheels. This rise in cutting temperature can be attributed to the higher cutting speed and feed rate employed in earlier studies (ranging from 25-30m/s and 200-500mm/min), in contrast to the comparatively lower values used in the present study (20m/s and 150mm/min). In a recent study, the grinding process of Ti-6Al-4V using a SiC wheel while employing lower depths of cut and implementing two cooling methods (nano-lubricant minimum quantity lubrication and cryogenic air), resulted in comparable temperature levels. The application of these cooling techniques at a pressure of 0.6MPa yielded temperatures of 194°C and 214°C for nano-lubricant minimum quantity lubrication and cryogenic air, respectively [171].

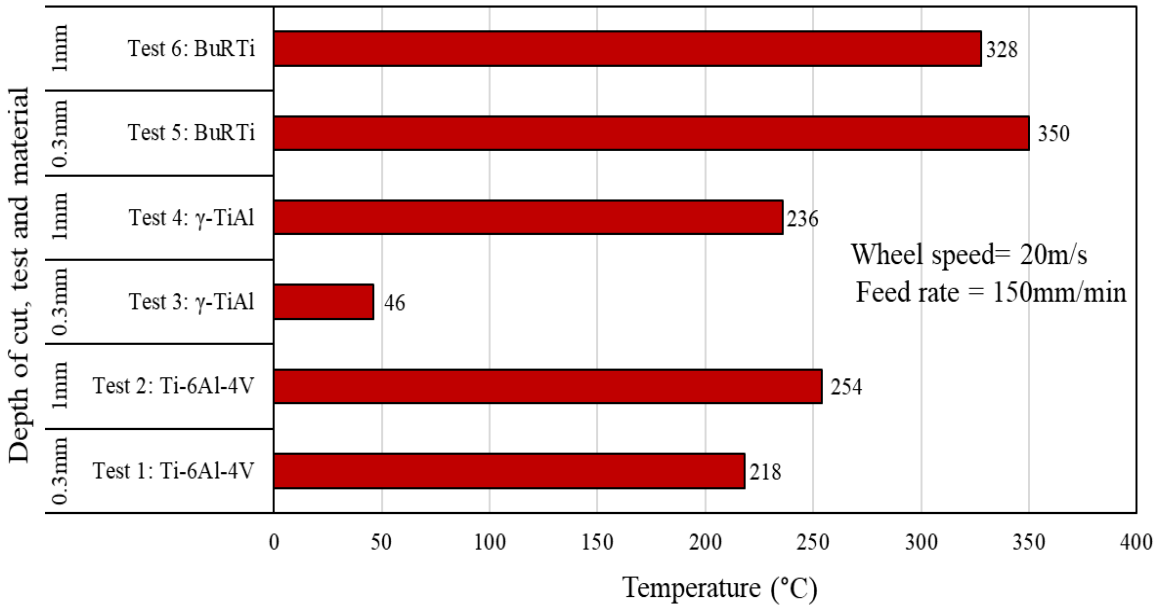


Figure 4-42: Recorded Temperature for different titanium alloys: Ti-6Al-4V, BuRTi and γ-TiAl (Phase 3A)

4.3.1.4 Surface roughness and topography

Figure 4-43 and Figure 4-44 detail the 2D and 3D surface roughness parameters of the ground track for all tested materials. Typically, 2D extreme parameters (Rt and Rz), 3D peak-to-peak (St) and 3D 10-point average (Sz) parameters increased with a rise in depth of cut. Roughness data for 2D and 3D parameters show substantial variation between tests despite being operating at identical grinding conditions, with material being the only variable. From the graphs, Ti-6Al-4V machined surfaces had the highest roughness values for both 2D and 3D parameters when compared to BuRTi (~50% higher) and γ-TiAl (3 folds higher) surfaces with the exception of St and Sz values in Test 1. It has been suggested that produced surface topography during the machining of titanium alloys is extremely sensitive to many factors, including the occurrence of chatter, tool/wheel wear, cutting tool/workpiece material and geometry, depth of cut, feed rate, thermal and mechanical deformation and microstructural transformations during machining [10], [37], [206]. The combined effect of these factors, along with the complexity of the grinding process, is thought to account for the observed disparities in 2D and 3D Roughness between materials. Nosenko et al. detailed average surface roughness (Ra) of 1.8µm when creep feed grinding Ti-6Al-4V with SiC wheel (64CF80H12V) at 1mm depth of cut, high surface roughness values were attributed to the significant adhesion found on the ground workpiece surfaces [179].

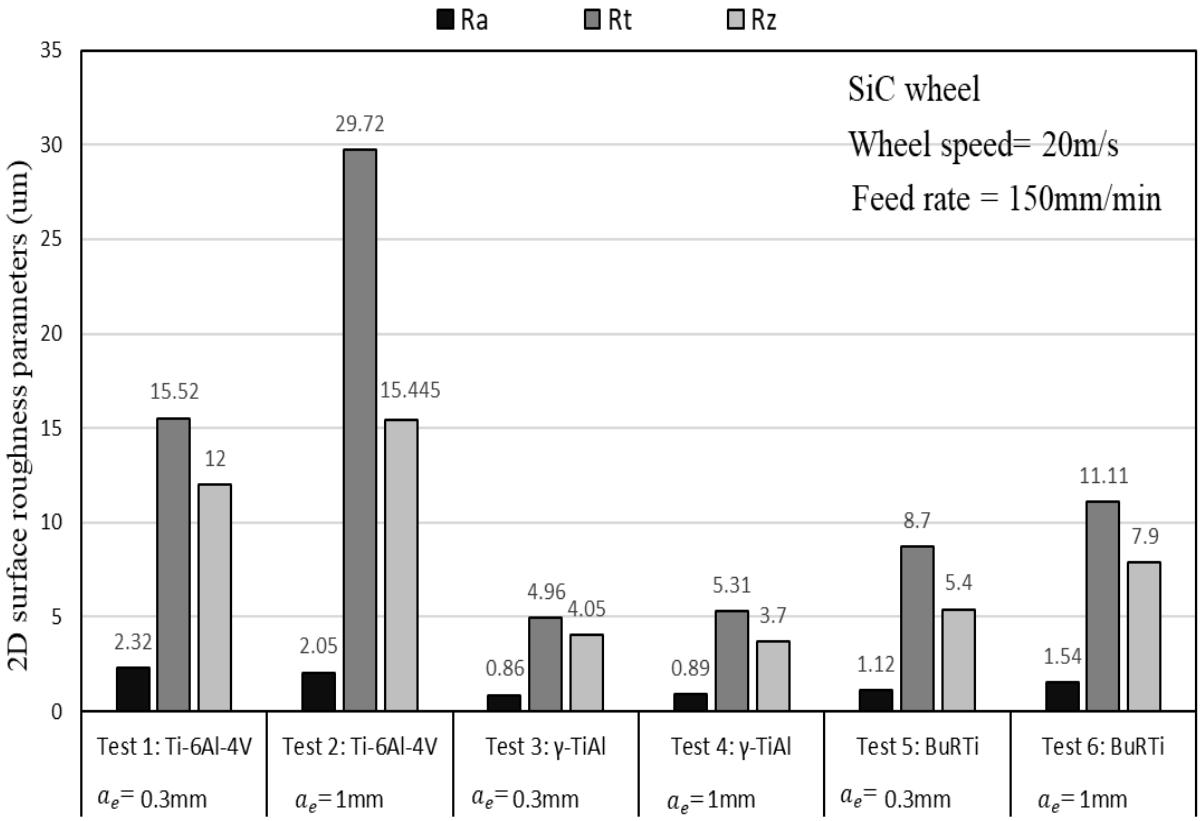


Figure 4-43: 2D surface roughness parameters for ground surfaces (Phase 3A)

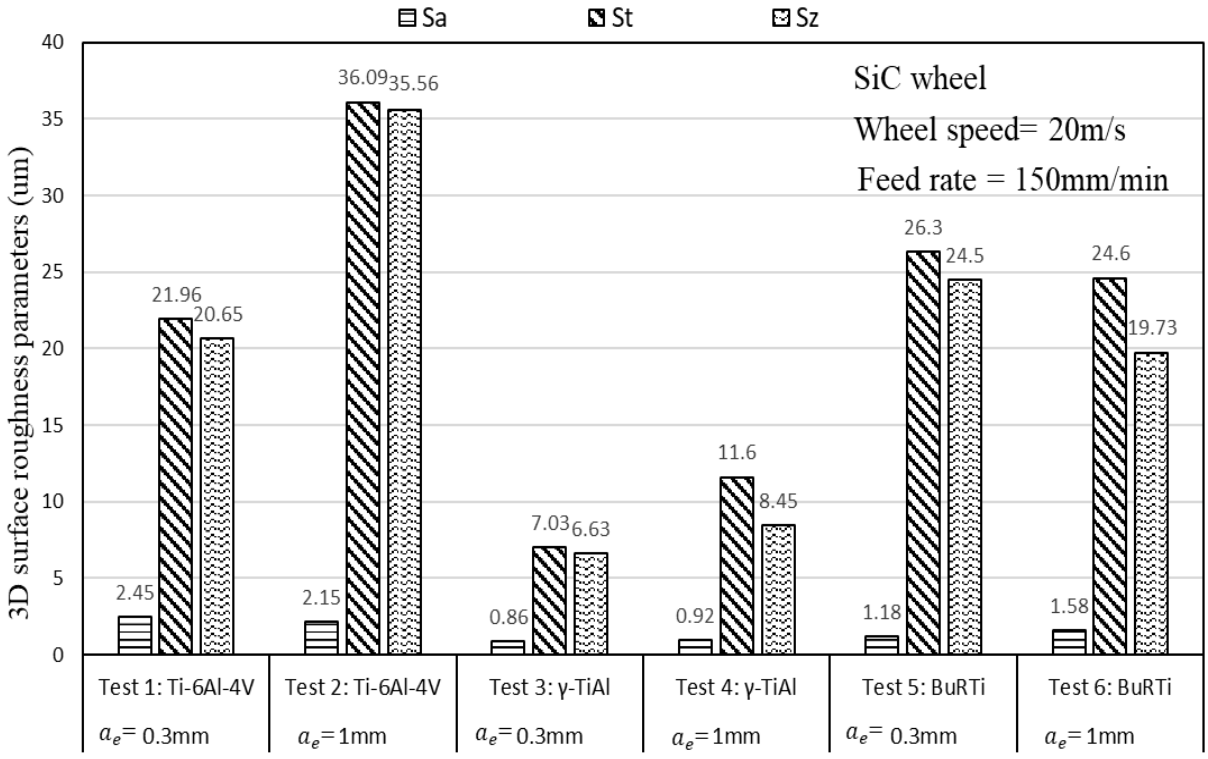


Figure 4-44: 3D topographical parameters of ground surfaces (Phase 3A)

4.3.1.5 Workpiece surface

Ti-6Al-4V sample images following CFG with SiC wheel together with SEM micrographs and 3D topographies are illustrated in Figure 4-45. Test 1 which is performed at the lowest operating conditions, showed no sign of damage. A minor burning is observed on the machined surface after increasing the depth of cut from 0.3 to 1mm while maintaining the same feed rate and wheel speed levels. SEM analysis of the ground surfaces showed surface defect consisting of significant smearing (which is visible on the 3D representations of the surface in Figure 4-45, C), as a result of the alloy's increased ductility. Previous research conducted on the grinding of Ti-6Al-4V using a SiC wheel also reported a comparable extent of damage (smearing and re-deposited material) [168], [169], [179].

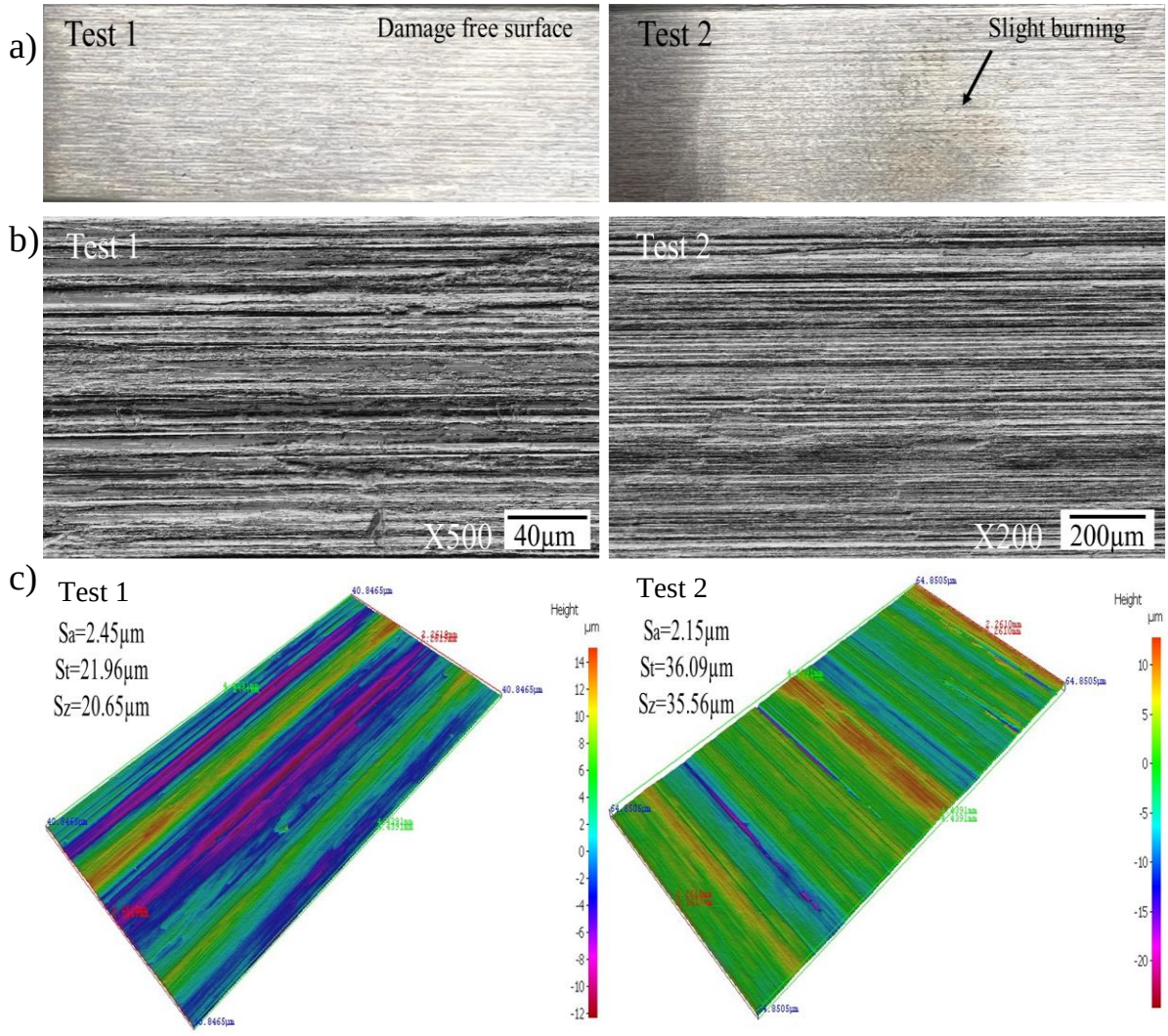


Figure 4-45: Surface observations for Ti-6Al-4V: a) Images of machined surface, b) SEM micrographs, c) 3D topographies of ground surfaces (Phase 3A)

4.3.1.6 Workpiece microstructure

Figure 4-46 shows the equiaxed microstructure of ground Ti-6Al-4V in both parallel and perpendicular directions of feed. As observed in γ-TiAl and BuRTi cross-sectional images, grit marks were only apparent on the transverse feed plane. There were no microstructural alterations in samples machined with Test 1 operating conditions, with no signs of macro/micro-cracks, tears, etc. This implies that the operating conditions employed were suitable for generating surfaces with no defects. Conversely, changes in the depth of cut from 0.3 to 1mm resulted in plastic deformation of the grain boundaries beneath the ground surface up to 15µm in parallel direction and 40µm in perpendicular direction.

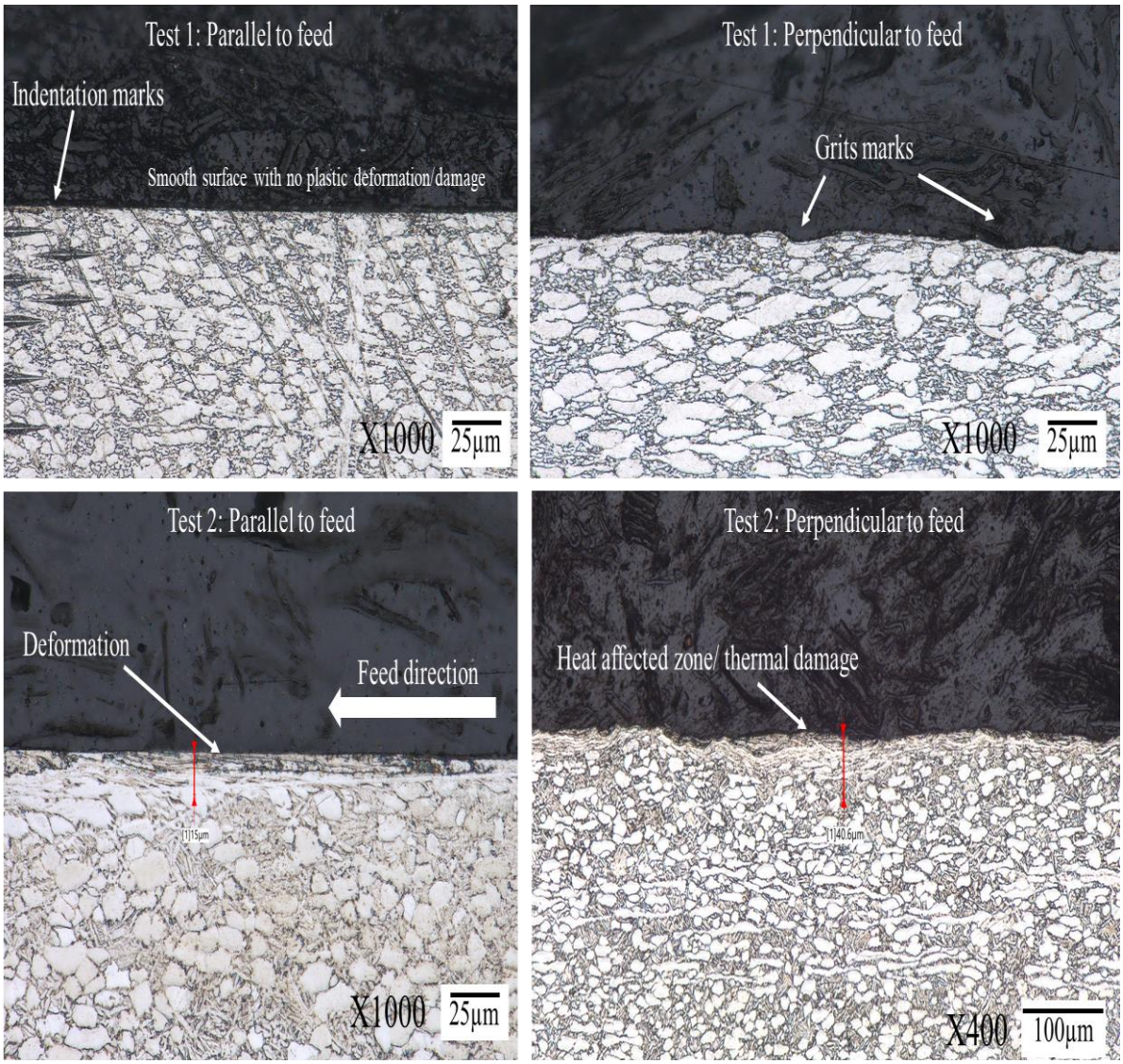


Figure 4-46: The microstructure of Ti-6Al-4V samples ground with SiC wheel (Phase 3A)

4.3.1.7 Workpiece microhardness

Individual microhardness depth profiles are given in Figure 4-47. Using a lower depth of cut in Test 1 resulted in a marginal/slightly softening layer within the first 10µm below the surface, gradually increasing to 380$HK_{0.050}$ at 80µm and then decreasing until the bulk hardness was reached (320HK). Softening of Ti-6Al-4V microstructure following the grinding process is not uncommon. When surface grinding Ti-6Al-4V with a SiC wheel, a softening by up to 100HK within the first 20µm in sub-surface was noted by Bentley [17]. Mello et al. also reported decreased microhardness values up to 80µm below the machined surface, with values reaching 100HV below the bulk hardness when surface grinding Ti-6Al-4V at different grinding conditions and cooling methods [169]. In contrast, no appreciable difference in microhardness values is observed when operating at a higher depth of cut (Test 2). Sub-surface microhardness in Test 2 was the maximum (360$HK_{0.050}$) at a depth of 10µm beneath the surface.

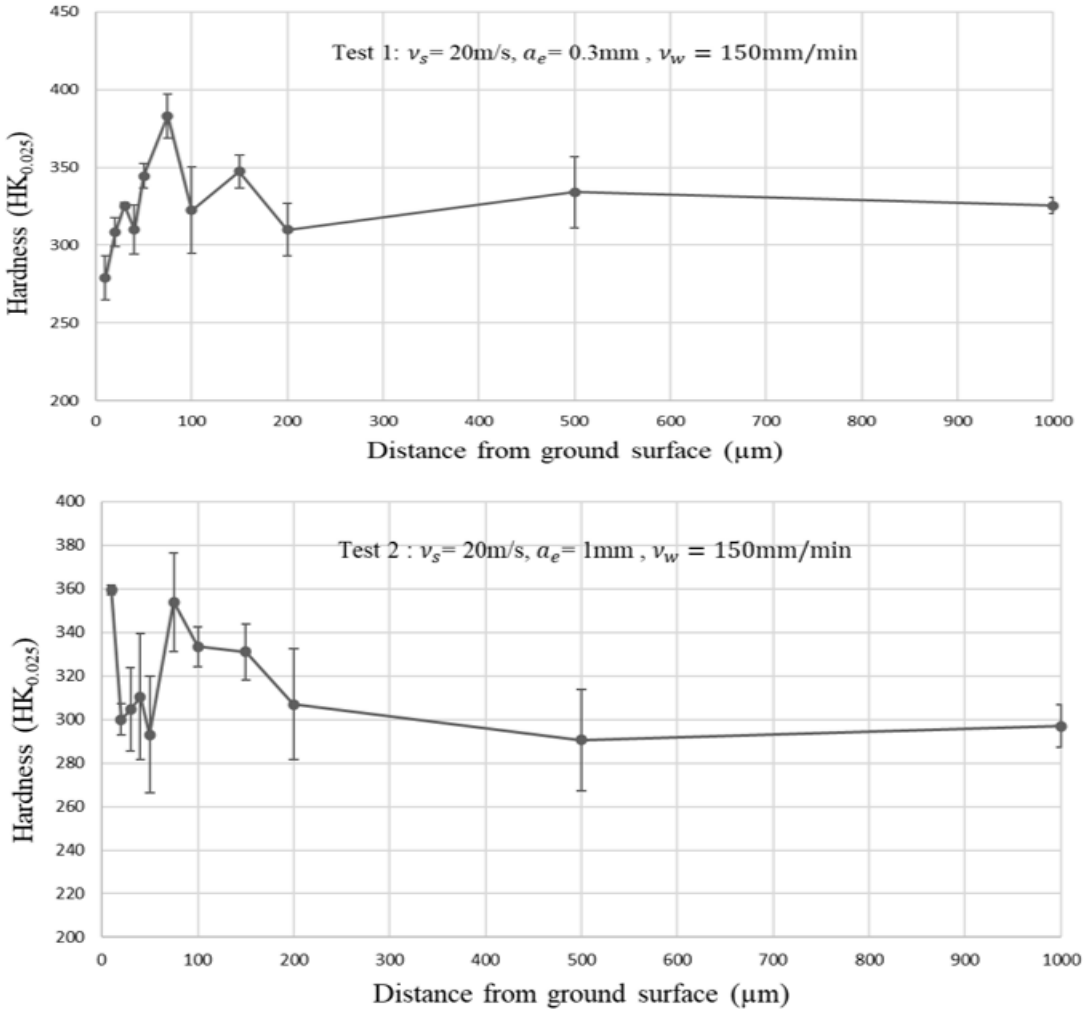


Figure 4-47: Individual microhardness profiles (Phase 3A)

4.3.2 Phase 3B: Benchmarking the performance against γ-titanium aluminide alloy and burn-resistant titanium alloy with diamond wheel

4.3.2.1 Wheel wear and G-ratio

In contrast to the preceding phases, the current phase encompasses an extended pass distance of 56mm, resulting in a cumulative removal of material amounting to 336mm^3 per pass for tests with a depth of cut of 0.3mm and 1120mm^3 per pass for tests with a depth of cut of 1mm. Figure 4.48 illustrates the influence of operational variables on the G-ratio and radial wheel wear after CFG of Ti-6Al-4V using a diamond wheel. As observed with BuRTi in Phase 2B, the substitution of the conventional wheel system (SiC) with the super-abrasive wheel system (diamond) did not yield any significant improvement in grinding performance in relation to the G-ratio and wheel wear, with G-ratio ranging from 1.5 to 5 in both wheel systems. A value of 1.5 G-ratio was noted in [7] after creep feed grinding of Ti-6Al-4V. While creep feed grinding using a diamond wheel, it was observed that when employing a low depth of cut (0.3mm), both Ti-6Al-4V and BuRTi exhibited similar G-ratios and levels of wheel wear. However, when the depth of cut was increased to 1mm, BuRTi showed much superior performance compared to Ti-6Al-4V. In comparison to BuRTi, operating at 30m/s wheel speed, 1mm depth of cut and 150mm/min feed rate resulted in higher wheel wear (65µm for Ti-6Al-4V compared to 17µm for BuRTi after one pass). Increasing the feed rate from 150 to 300mm/min resulted in a remarkably higher difference in wheel wear levels (159µm for Ti-6Al-4V compared to 27 for BuRTi after one pass). Although depth of cut displayed a high percentage of contribution of ~60%, analysis of variance findings indicates that none of the factors under examination exhibit statistical significance at a 95% confidence level. In addition, the interaction plot shows no interaction between the depth of cut and feed rate is present.

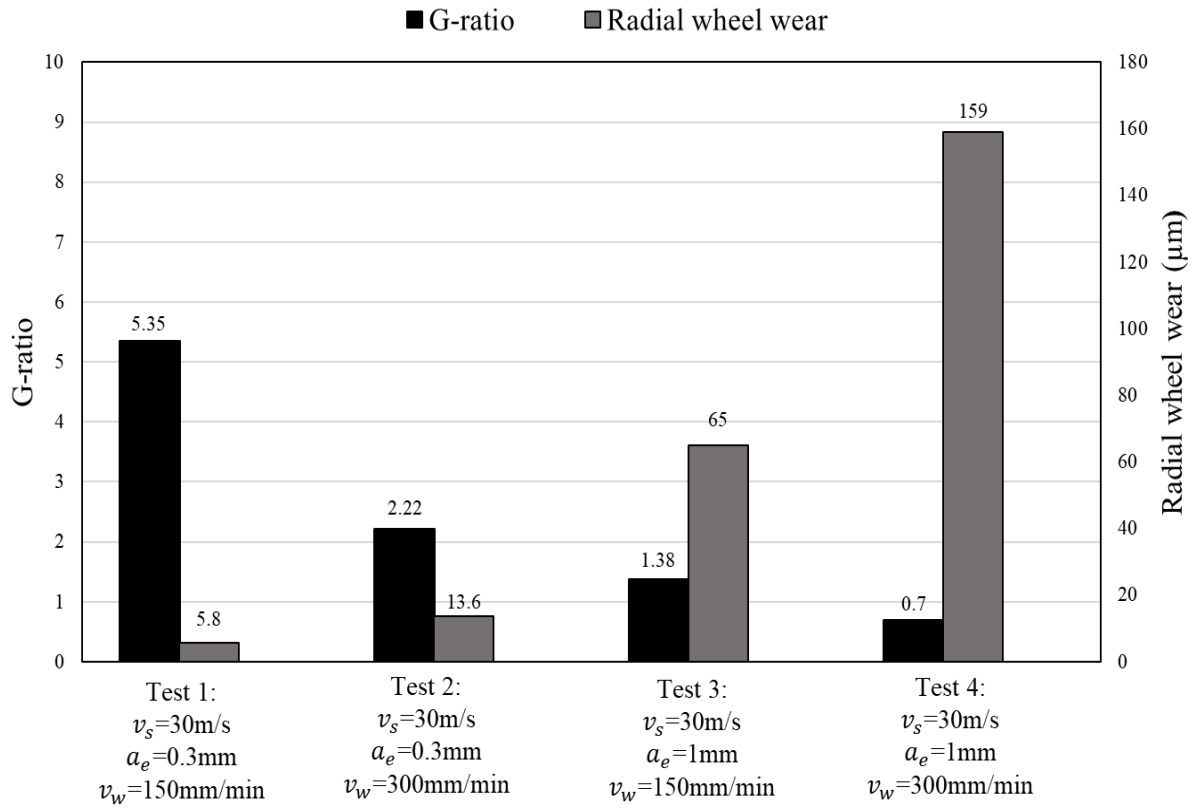


Figure 4-48: G-ratio and radial wheel wear for different grinding conditions (Phase 3B)

4.3.2.2 Grinding forces, power and specific energy

The progression of grinding normal forces, tangential forces, power and specific energy with the cumulative volume of material removed is shown in Figures 4-49 – 4-52, respectively. At a lower depth of cut (0.3mm), Ti-6Al-4V results for both normal forces and tangential forces were almost comparable (minimal difference) to those measured for γ-TiAl and BuRTi ground at identical operating conditions and diamond wheel (ranging between 400 to 700N for normal forces and from 200 to 400N for tangential forces). However, at a higher depth of cut (1mm), Ti-6Al-4V had the highest levels of grinding forces when compared to other machined alloys. In relation to normal forces, the Ti-6Al-4V material exhibited an increase of 600N and 1200N compared to BuRTi and γ-TiAl, respectively. Similarly, in terms of tangential forces, the Ti-6Al-4V material showed higher values by 600N and 700N than BuRTi and γ-TiAl, respectively. The elevated levels of force were accompanied by significant rates of wheel wear, as illustrated earlier in Figure 4-48. This indicates a significant increase in the occurrence of wheel grit pull-out and fracture as a result of greater stress per grit when employing increased depth of cuts. The grinding power and specific energy of Ti-6Al-4V exhibit intermediate values

between those of BuRTi and γ-TiAl, ranging between 2-14KW and 120-180J/mm^3, respectively. As observed earlier in other alloys, tests involving the lowest material removal rate ($a_e \times v_w$) had the highest values of specific energy (Test 1 here as illustrated in Figure 4-52). A similar observation was reported in [180] when grinding Ti-6Al-4V with a novel porous aggregated cBN wheel at multiple depths of cuts (0.2-1mm). This phenomenon was further explained by the observation that when the material removal rate is low, the interaction between the grinding wheels and the workpiece is greatly influenced by the increased sliding and ploughing effects resulting from a high grinding speed and a small undeformed chip thickness. Conversely, when the material removal rate is high, the sliding and ploughing effects are diminished as the undeformed chip thickness increases. Therefore, only the cutting process is responsible for a significant amount of the overall energy consumption, leading to a quick decrease in the specific energy value. The interaction plots revealed that there are no observed interactions between the depth of cut and feed rate for all investigated outputs. The depth of cut exhibited a PCR value exceeding 70% in relation to the grinding normal forces, tangential forces, and power. Nonetheless, based on the data obtained from the analysis of variance (ANOVA) tables, it was determined that none of the factors exhibited statistical significance on any outputs under investigation, except for the feed rate on specific energy with a high PCR of 97% as detailed in Table 4-10 below.

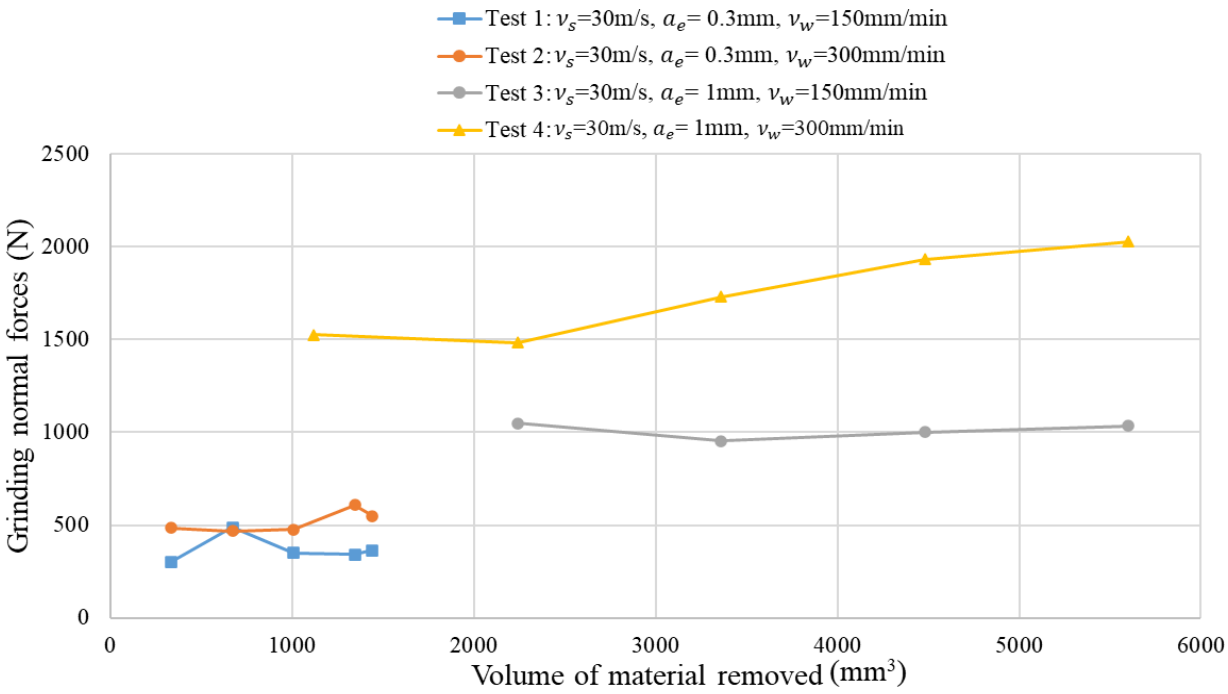


Figure 4-49: Grinding normal forces against volume of workpiece material removed (Phase 3B)

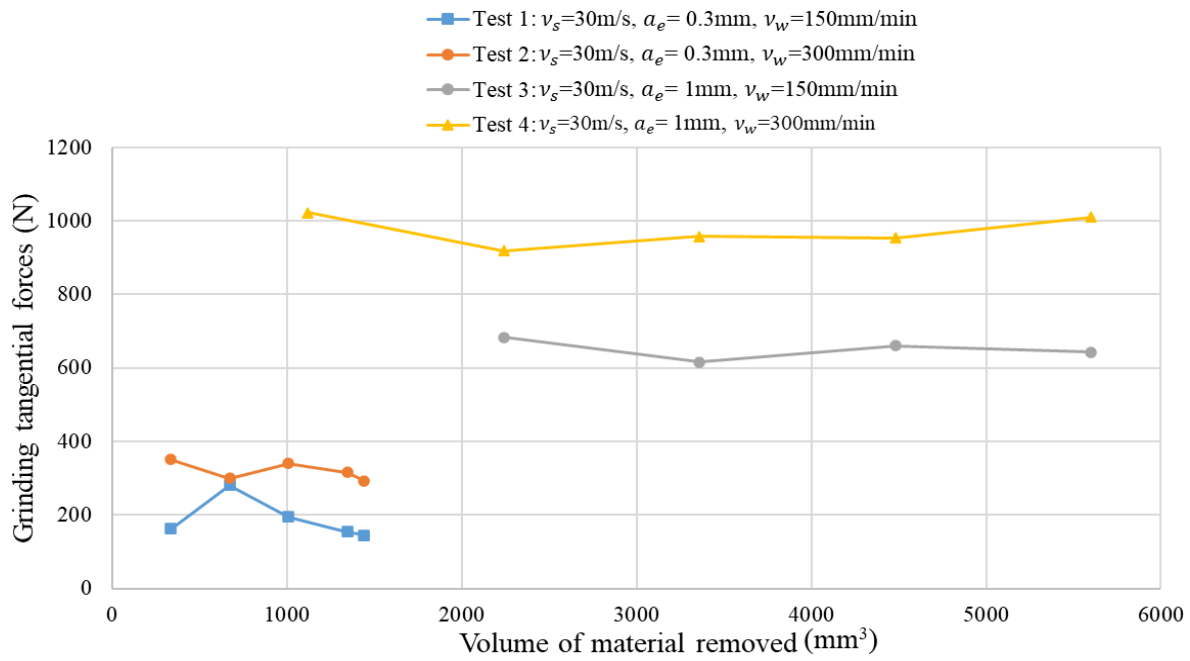


Figure 4-50: Grinding tangential forces against volume of workpiece material removed (Phase 3B)

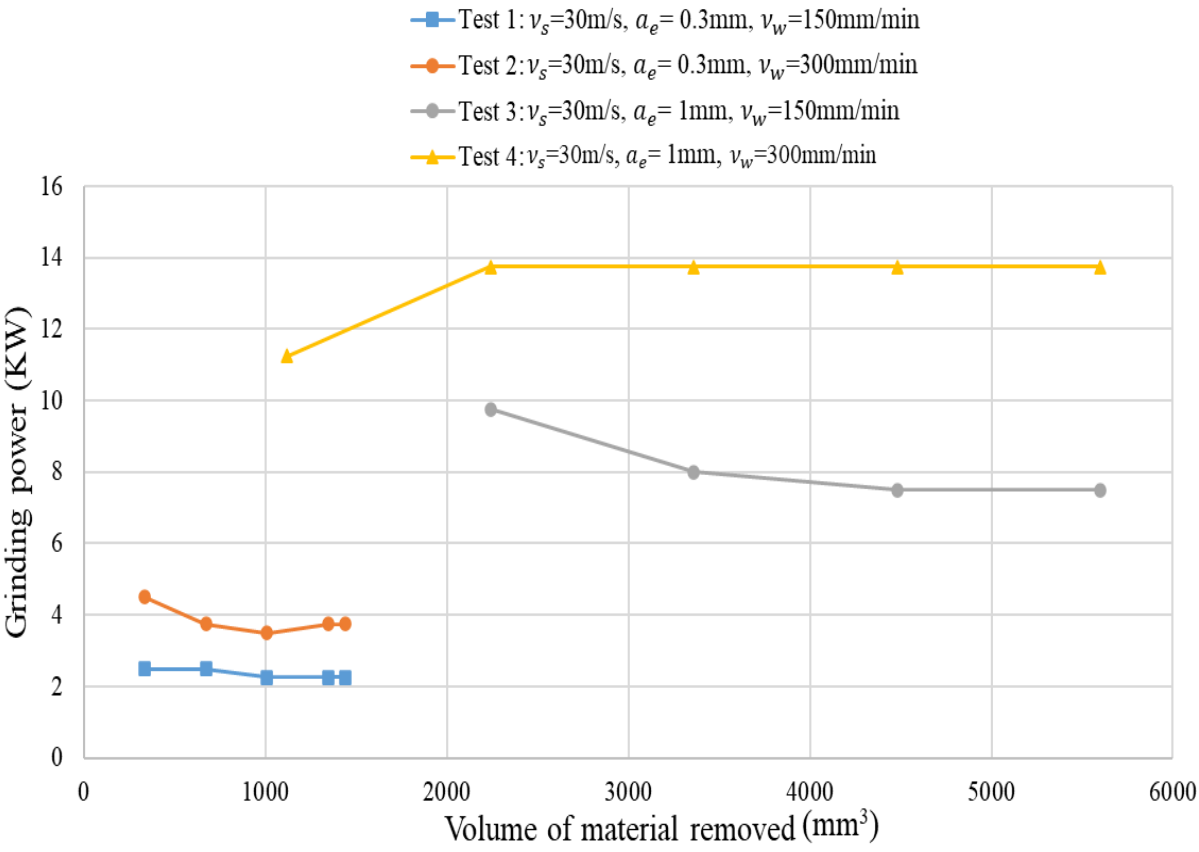


Figure 4-51: Grinding power against volume of workpiece material removed (Phase 3B)

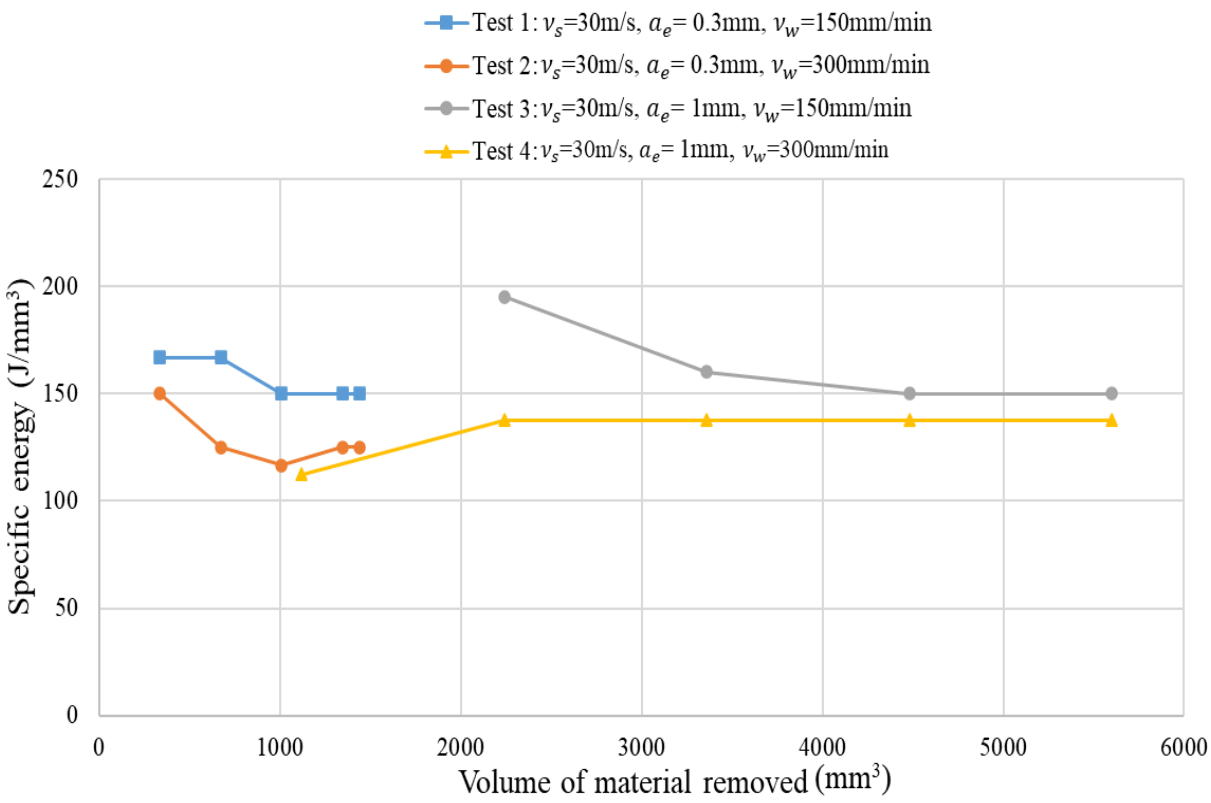


Figure 4-52: Grinding specific energy against volume of workpiece material removed (Phase 3B)

Table 4-10: ANOVA table for specific energy (Phase 3B)

Source	DF	Seq SS	Contribution	Adj SS	Adj MS	F-Value	P-Value
Depth of cut	1	20.250	2.43%	20.250	20.250	81.00	0.070
Feed rate	1	812.250	97.54%	812.250	812.250	3249.00	0.011
Error	1	0.250	0.03%	0.250	0.250	-	-
Total	3	832.750	100.00%	-	-	-	-

4.3.2.3 Grinding temperature

The temperatures recorded during the final pass of each test are illustrated in Figure 4-53. Generally, the reported trends in previous phases for γ-TiAl and BuRTi surfaces ground with a diamond wheel align with the findings here, as the greater thermal conductivity of diamond abrasives compared to SiC abrasives has led to a large decrease in temperature. When compared to SiC wheel results, temperatures for Ti-6Al-4V ground at low operating levels varied between 200-250°C, these were reduced to 32°C and 77°C while running at identical feed rates and depth of cut and even at higher wheel speeds (30m/s). However, similar temperatures to those given for the SiC wheel was recorded at Test 4 (236°C) when running

at the highest operating parameters (v_s=30m/s, v_w=300mm/min, a_e=1mm), unfortunately, direct comparison with Ti-6Al-4V ground by SiC wheel was not possible due to limited tests. It was previously shown in [4] that the temperature decreased from approximately 500°C to around 180°C during CFG of Ti-6Al-4V using both SiC and diamond wheels. These temperature reductions were observed under equal operating conditions. In comparison to γ-TiAl and BuRTi surfaces ground with a vitrified diamond wheel, Ti-6Al-4V exhibited a similar temperature range between 30°C to 70°C, only when operating at low levels of depth of cut, feed rate and wheel speed, and in some instances, at higher levels of condition. Interestingly, a lower temperature was recorded for Ti-6Al-4V than in BuRTi (236 compared to 481) when machined at highest operating parameters despite the superior thermal conductivity of the latter (10W/mK for BuRTi compared to 6.7W/mK for Ti-6Al-4V). Although not given here, the interaction plot indicates that there is no evidence of any interactions between the depth of cut and feed rate with respect to temperature values. Furthermore, the analysis of variance (ANOVA) tables revealed that none of the examined factors had statistical significance in relation to temperature results.

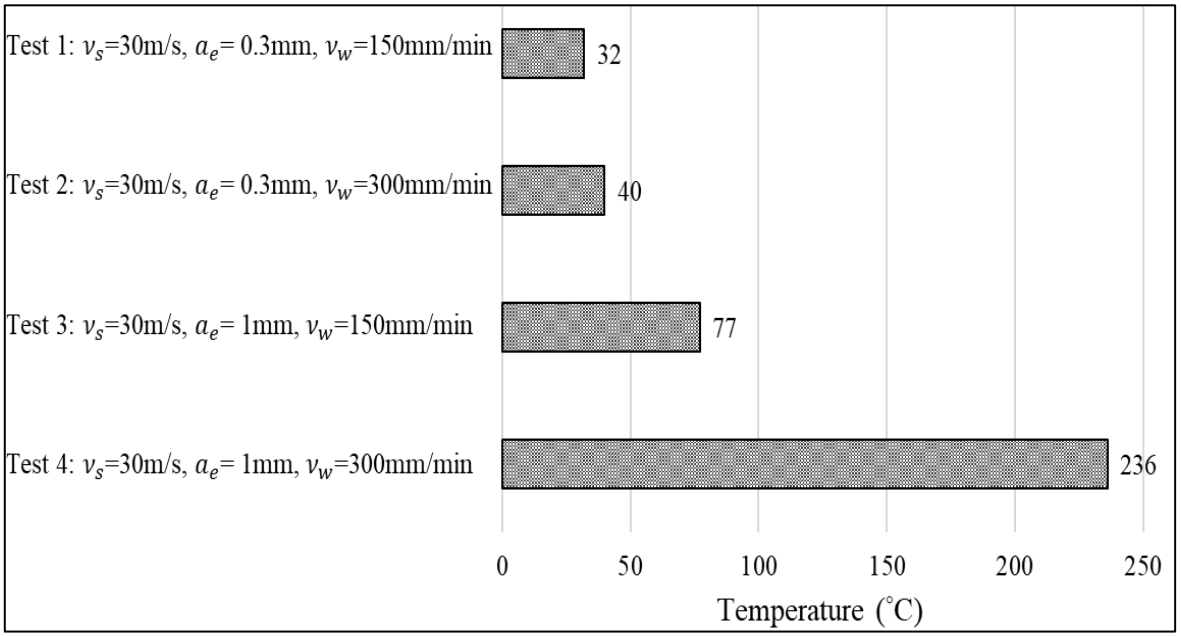


Figure 4-53: Measured temperature at different operating conditions (Phase 3B)

4.3.2.4 Surface roughness and topography

The figures labelled as Figure 4-54 and Figure 4-55 provide comprehensive information regarding the roughness parameters for both 2D profiles and 3D topographies, as well as a representative 3D mapping of ground surfaces. Changes in the wheel system from SiC to diamond significantly improved most 2D roughness parameters (Ra, Rt and Rz) as well as 3D average roughness parameters (Sa) by at least 20% even at higher wheel speed (20m/s for SiC compared with 30m/s for diamond). 2D and 3D average roughness parameters of surfaces ground with SiC wheel ranged between 2.05-2.45µm. For surfaces ground with the diamond wheel at identical depth of cut and feed rate but higher wheel speed, the average roughness results ranged between 1.43-1.59µm. When comparing the findings with those obtained for γ-TiAl surfaces, it is seen that there is a significant increase of 40-60% in roughness values for 2D parameters and the average 3D parameter (Sa). Furthermore, this rise exceeded 100% when operating at the maximum operating conditions (Rt=5.98µm for γ-TiAl in contrast to Rt=13.45µm for Ti-6Al-4V operating at similar conditions). The 3D peak-to-peak (St) and 3D 10-point average (Sz) parameters experienced a 650% rise at maximum operating conditions (St=6.01µm for γ-TiAl in contrast to St=38.28µm for Ti-6Al-4V and Sz=5.07µm for γ-TiAl in contrast to Sz=33.48µm for Ti-6Al-4V while operating at similar conditions). When comparing with BuRTi surface roughness results, Ti-6Al-4V figures exhibited an increase of 30-40% in the majority of 2D and 3D roughness parameters across most of the conducted tests. The higher roughness values observed can be attributed to the increased ductility of Ti-6Al-4V in comparison to γ-TiAl and BuRTi. This higher ductility resulted in significant smearing and material re-depositions on the ground surface, as clearly depicted in the 3D mapping of ground surfaces presented in Figure 4-55 (long height scale ranges varied on average between 15µm to -15µm). Interactions between depth of cut and feed rate were evident for St and Sz with high residual error PCR of 42.87% and 33%. The PCR of the feed rate was significantly high (~60%) for 3D peak-to-peak (St) and 3D 10-point average (Sz) outputs, while depth of cut had high PCR on Rt and Rz values. Nevertheless, none of the factors were statistically significant.

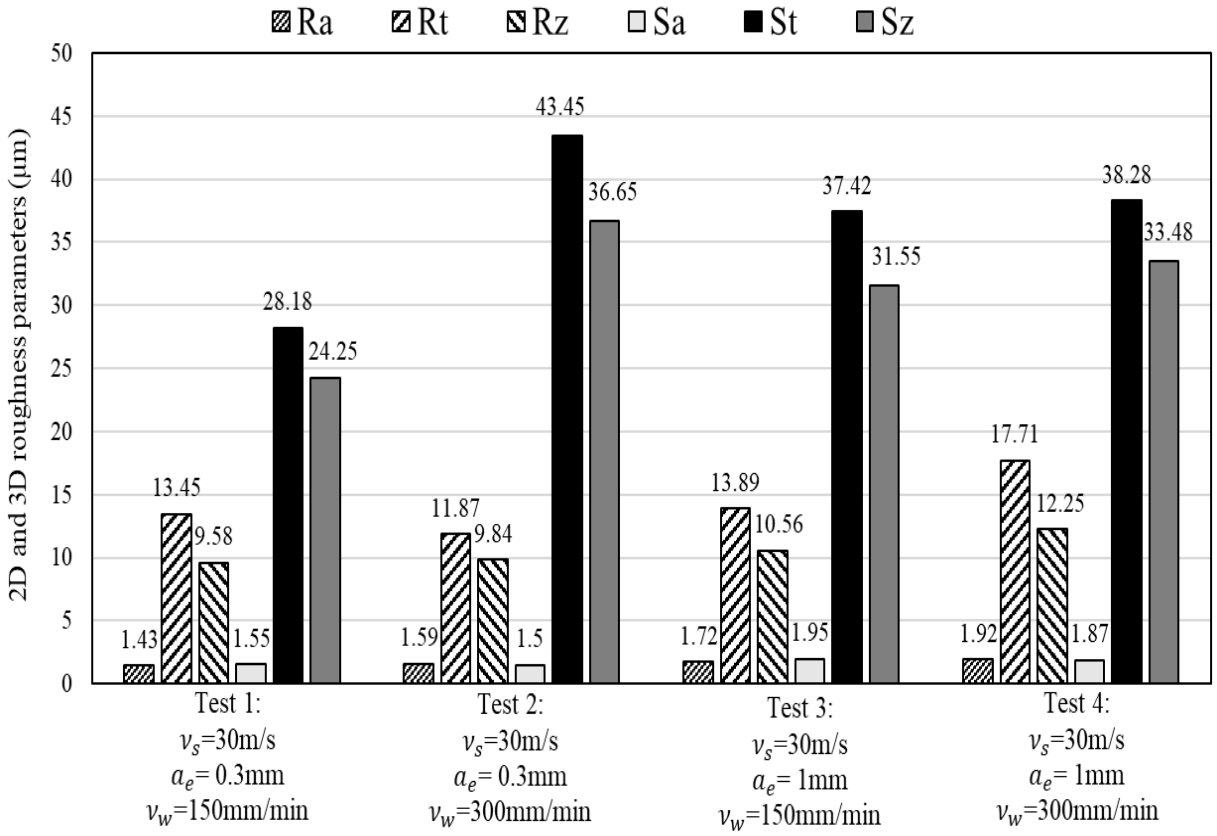


Figure 4-54: 2D and 3D surface roughness parameters for ground surfaces (Phase 3B)

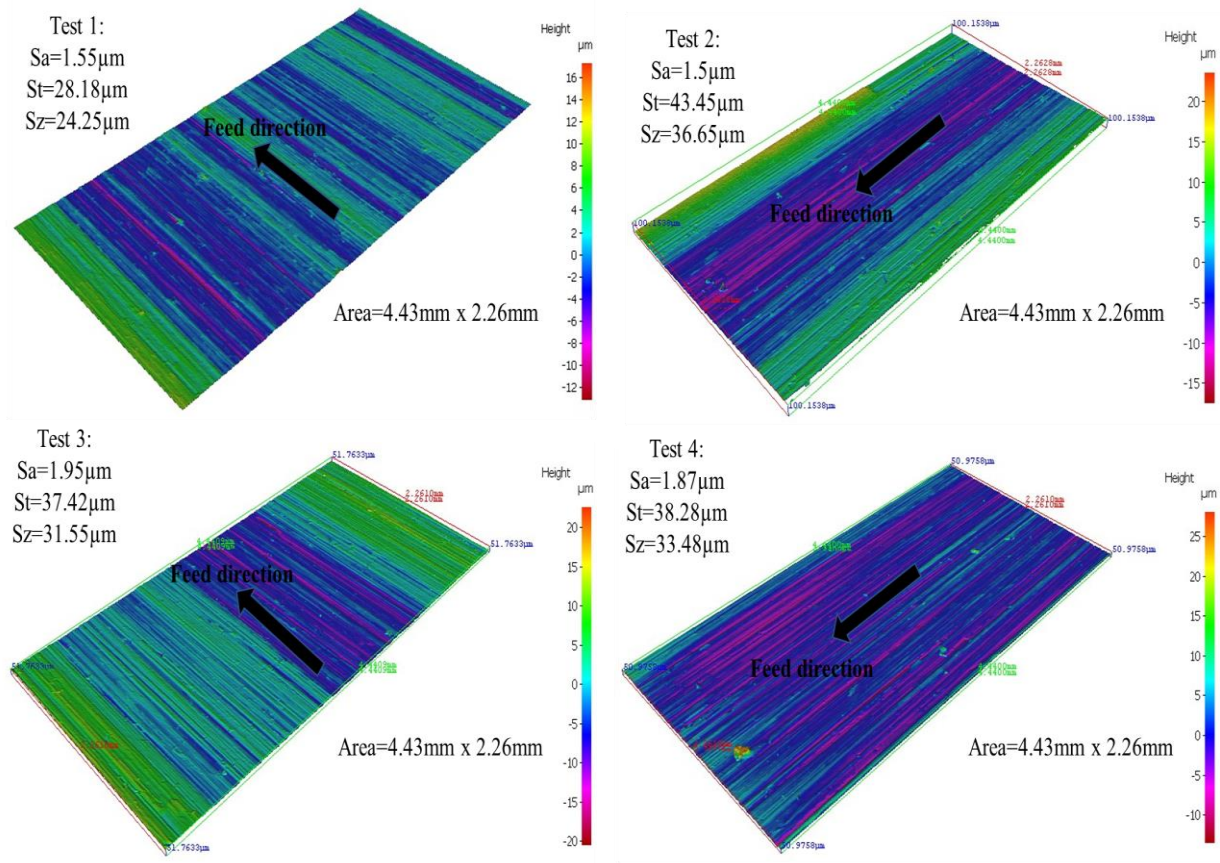
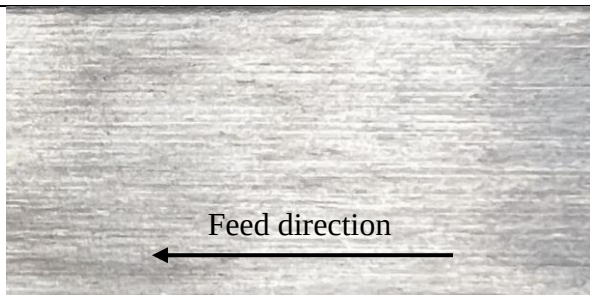
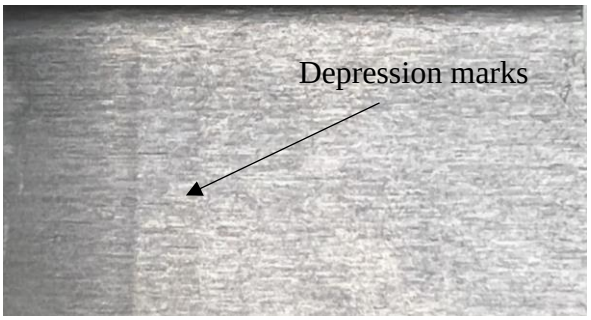
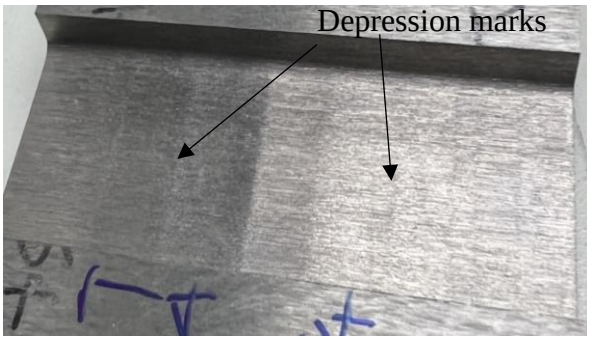


Figure 4-55: 3D topographies of Ti-6Al-4V ground surfaces (Phase 3B)

4.3.2.5 Workpiece surface

Table 4-11 presents visual observations of Ti-6Al-4V surfaces machined under different grinding conditions along with recorded temperatures. Depression marks were evident towards the end of the grinding track in Test 3, and a rise in feed rate from 150 to 300mm/min in Test 4 appeared to increase the level of depression marks (surface damage). This was likely due to the exceptionally high amount of wheel wear (65µm in Test 3 and 159µm in Test 4), which led the grinding wheel grits to rapidly lose sharpness, causing the wheel roundness to deteriorate. Depression markings of a similar nature were detected during the creep feed grinding process of Inconel 718, utilising a VORTEX 60 mesh wheel. The occurrence of these depression marks was shown to be correlated with spikes noticed in the grinding forces profiles. Subsequent reductions were achieved through the implementation of several measures, including increasing wheel speeds, decreasing the depth of cut, alterations in wheel properties, applying higher coolant pressure, and the utilisation of a dummy specimen to impede the escape of coolant [26]. Conversely, no burn, chatter marks or depression marks were observed on surfaces ground at lower depths of cuts (Test 1 and 2). In addition, no such marks were apparent on both γ-TiAl and BuRTi ground surfaces with the diamond wheel at identical grinding conditions, suggesting that Ti-6Al-4V is more difficult to grind. A thorough examination of the scanning electron microscopy (SEM) images captured on the ground surfaces depicted in Figure 4-56 reveals the presence of adherent material, material pull-out, and potential fractures. These observations were particularly prominent in Test 3 and 4 (tests associated with deeper cuts). Redeposition occurs as a result of the chip material adhering to the grit and subsequently detaching from the attached material onto the finished surface during the wheel subsequent revolution.

Table 4-11: Observed machined surface under different grinding conditions and temperatures (Phase 3B)

Test No.	Grinding conditions	Recorded temperature	Surface observation
1	v_s =30m/s a_e= 0.3mm v_w=150mm/min	32°C	
2	v_s =30m/s a_e= 0.3mm v_w=300mm/min	40°C	
3	v_s =30m/s a_e= 1mm v_w=150mm/min	77°C	
4	v_s =30m/s a_e= 1mm v_w=300mm/min	236°C	

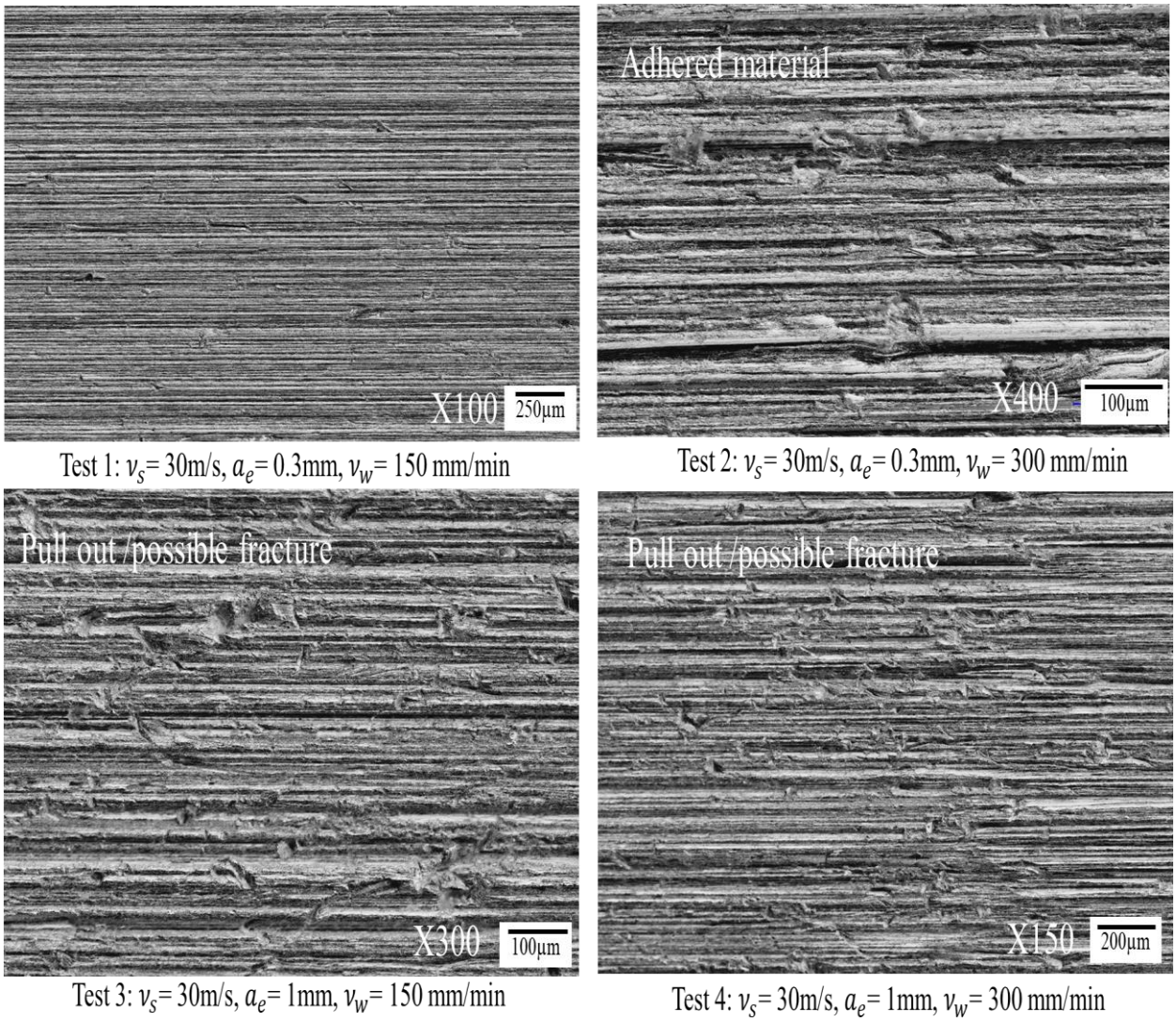


Figure 4-56: SEM images of machined surface (Phase 3B)

4.3.2.6 Workpiece microstructure

Cross-sectional micrographs illustrated in Figure 4-57 show neither discernible changes in microstructural alterations nor any plastic deformations in Ti-6Al-4V samples machined with given operating conditions, with no signs of macro/micro-cracks, tears, etc. The microstructure in the longitudinal/parallel feed plane in Test 1 and 2 (corresponds to 0.3mm depth of cut) appeared smoother than those machined at 1mm depth of cut. This confirms the extent of material re-depositions and smearing shown in the related SEM images, as well as the greater roughness values for 2D and 3D average parameters (Ra and Sa). Due to the nature of the cutting process, distinct grit marks were only observed on the transverse feed plane.

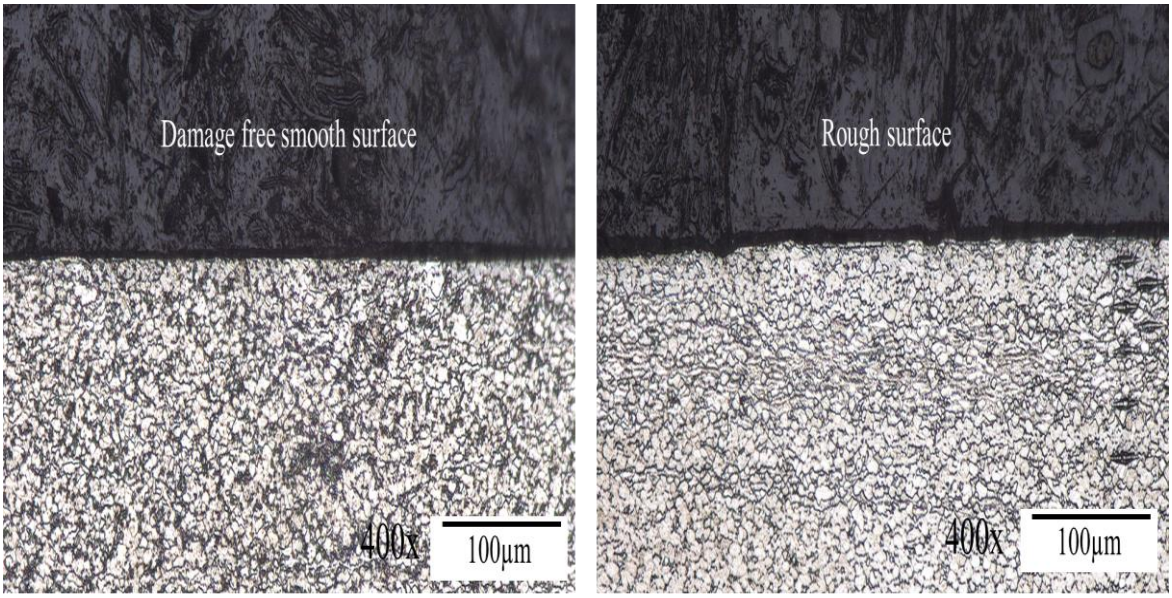


Figure 4-57: Cross-sectional microstructure of ground surfaces (Phase 3B)

4.3.2.7 Workpiece microhardness

Microhardness depth profiles measured in the parallel direction to the feed are given in Figure 4-58, with individual graphs for each test shown in Appendix F, Figure F109. There is no significant variation in microhardness value for the Ti-6Al-4V sub-surface when running at Test 2 conditions. In contrast, other tests demonstrated the presence of a layer with reduced hardness (less than ~270$HK_{0.050}$) that extended to a depth of 20-40µm into the surface, which after that exhibited a steady increase in hardness until reaching the bulk hardness of the material. A 16.9% drop in microhardness values with no evidence of microstructural alterations was reported by Ahmed and González after grinding Ti-6Al-4V with vitrified super-abrasive (cBN) wheel under different cooling conditions [176].

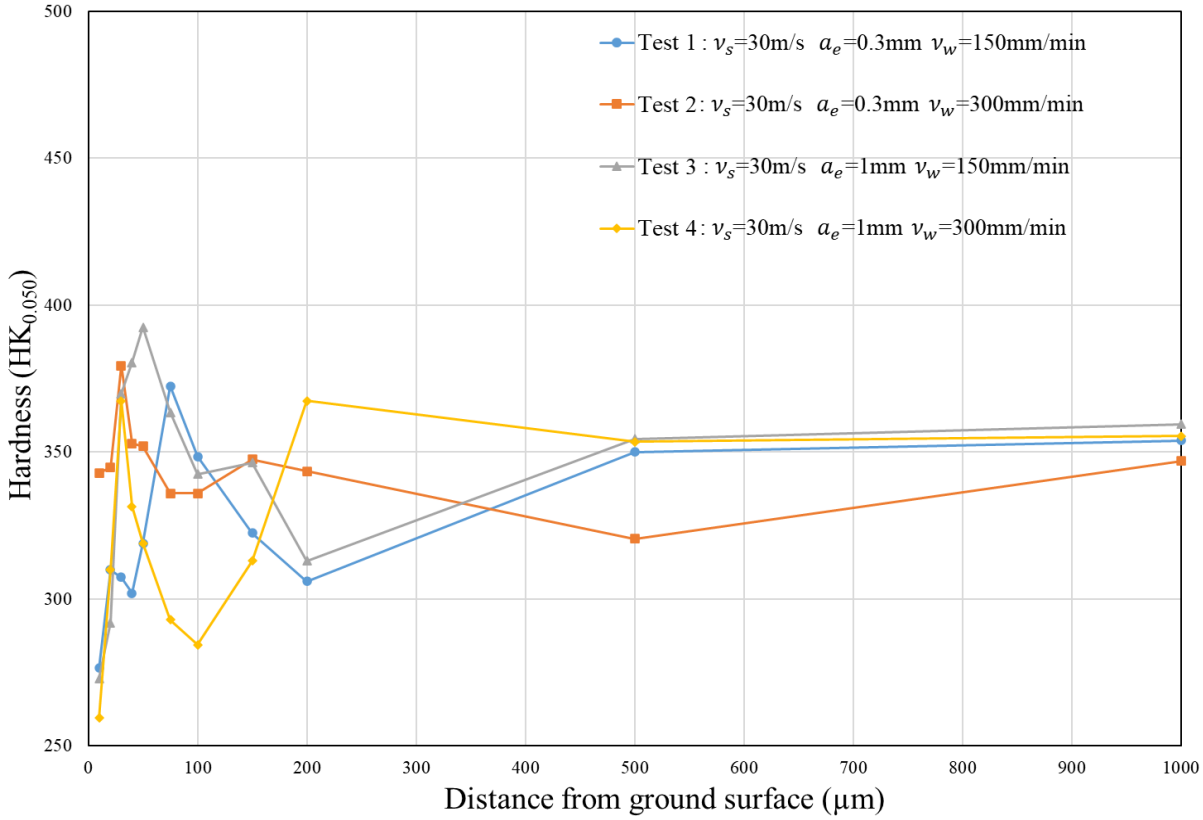


Figure 4-58: Microhardness depth profiles (Phase 3B)

4.3.3 Phase 3C: Comparison of the performance of different super-abrasive wheel specifications

As previously stated, Test 1 was concluded prematurely due to the presence of excessive grinding noise and the recording of very high forces reaching up to 3500N during the initial pass. This termination of Test 1 was made in order to mitigate the potential danger of wheel damage resulting from grit/bond failure. In this phase, only one wheel of each grain size was available, making replication impossible. The unavailability of workpiece material hindered the feasibility of conducting additional benchmarking experiments on γ-titanium aluminide or burn-resistant titanium alloy using a single-layer electroplated diamond wheel.

4.3.3.1 Wheel wear and G-ratio

Comparisons between the performance of vitrified diamond wheel and single-layer electroplated diamond wheel in terms of G-ratio and radial wheal wear are presented in Figure 4-59. Significant improvements by up to ~130% (at 0.3mm depth of cut) and ~1800% (at 1mm

depth of cut) in wheel G-ratio and radial wheel wear were seen when employing electroplated diamond wheels. Given the extremely limited availability of published machining data concerning CFG of Ti-6Al-4V when utilising single-layer electroplated wheels, the only viable option was to compare the G-ratios obtained from this study with existing data on surface grinding on the same material and/or other titanium alloys. Previous research has documented G-ratios of 50 following creep feed grinding of a Ti-45Al-2Mn-2Nb + 0.8 vol.% TiB_2 intermetallic alloy using a vitrified diamond wheel. When the identical wheel employed in this study was utilised, the G-ratios exhibited a twofold increase, exceeding a value of 100 [185]. In addition, more CFG trials with an identical wheel on the Ti-45Al-2Mn-2Nb + 0.8 vol.% TiB_2 revealed G-ratio varied within 11-80 [26]. Shi and Attia reported G-ratio as high as 296 and 944 after surface grinding of Ti-6Al-4V with electroplated diamond and cBN wheels operating at 0.05mm and 0.1mm depth of cut, respectively. Their work showed that electroplated diamond wheels exhibited lower wear rates compared to electroplated cubic boron nitride (cBN) wheels when grinding Ti-6Al-4V alloy at identical machining conditions [173]. A grinding ratio ranging from 27.2-32.2, which is comparable to the G-ratio value obtained for Test 4 (~26), was reported by Zhao et al. after grinding Ti–6Al–4V with porous metal-bonded aggregated cBN wheels running at (v_s=120m/s, v_w=3.6m/min, a_e=0.1mm) [175].

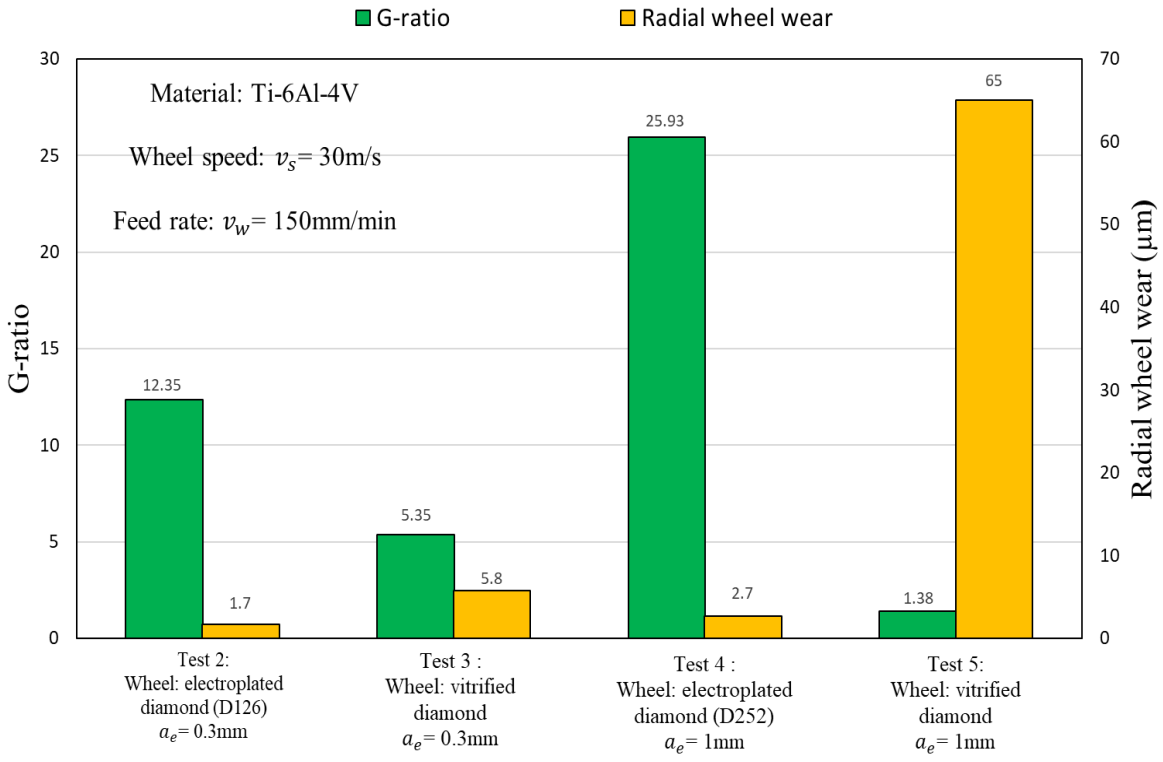


Figure 4-59: G-ratio and radial wheel wear for different grinding conditions (Phase 3C)

4.3.3.2 Grinding forces, power and specific energy

As illustrated in Figure 4-60, the evaluated electroplated diamond wheel shows a notable decrease in magnitudes for both normal and tangential forces components when compared to the vitrified diamond wheel operating at a higher removal rate (1mm). Specifically, there was an approximate reduction of ~20% in normal forces (1037N reduced to 788N) and ~46% in tangential forces (658N reduced to 300N). However, at low material removal rates (0.3mm), no significant differences were found between the two wheels. The high hardness of grit materials coupled with superior bond strength explains both the lower forces found here and the greater G-ratio (low wear rates) observed earlier when compared to vitrified diamond wheels. This is in contrast to Ti–45Al–2Mn–2Nb + 0.8 vol.% TiB_2 intermetallic trends where the opposing was found to be true, as the values obtained with single-layer electroplated diamond were reported to be almost double the values for vitrified diamond wheel [185]. This is more likely related to the differences in mechanical properties and chemical composition between the two materials. The grinding power and specific energy trends shown in Figure 4-61 mirrored the grinding forces responses. Power and specific levels were almost similar for both wheels when operating at lower removal rates, with values of 2.6KW and 170J/mm^3 for the electroplated diamond wheel and 2.35KW and 157J/mm^3 for the vitrified diamond wheel. Whilst at higher material removal rates, values for power and specific energy for the vitrified diamond wheel were ~30% and ~60% higher than the values of the electroplated diamond wheel (8KW and 161J/mm^3 compared to 5KW and 100J/mm^3).

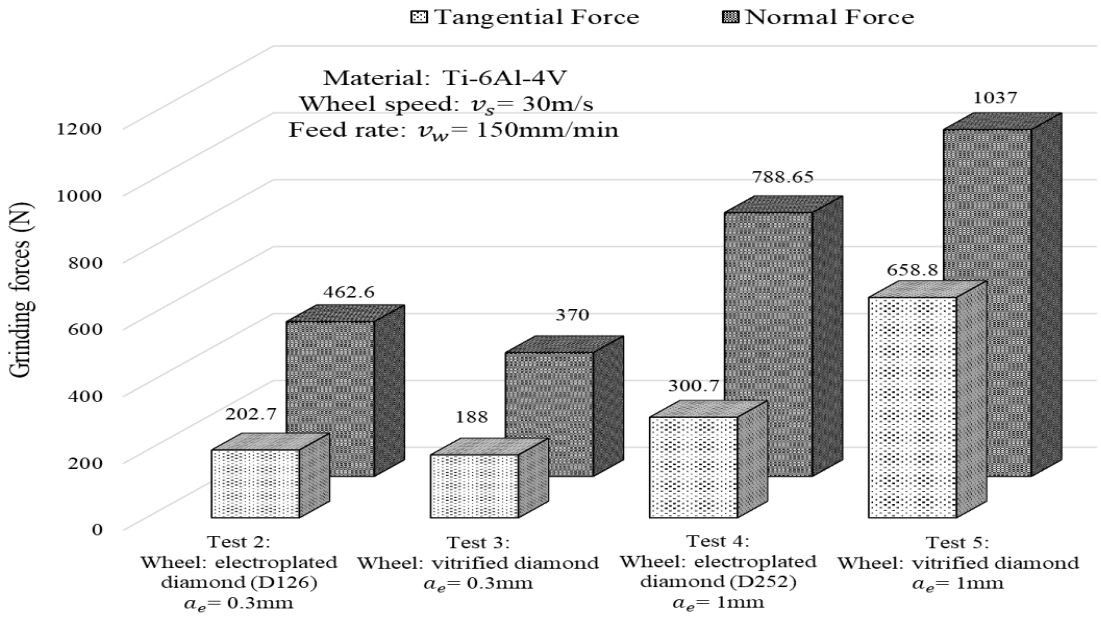


Figure 4-60: Grinding forces for different operating conditions (Phase 3C)

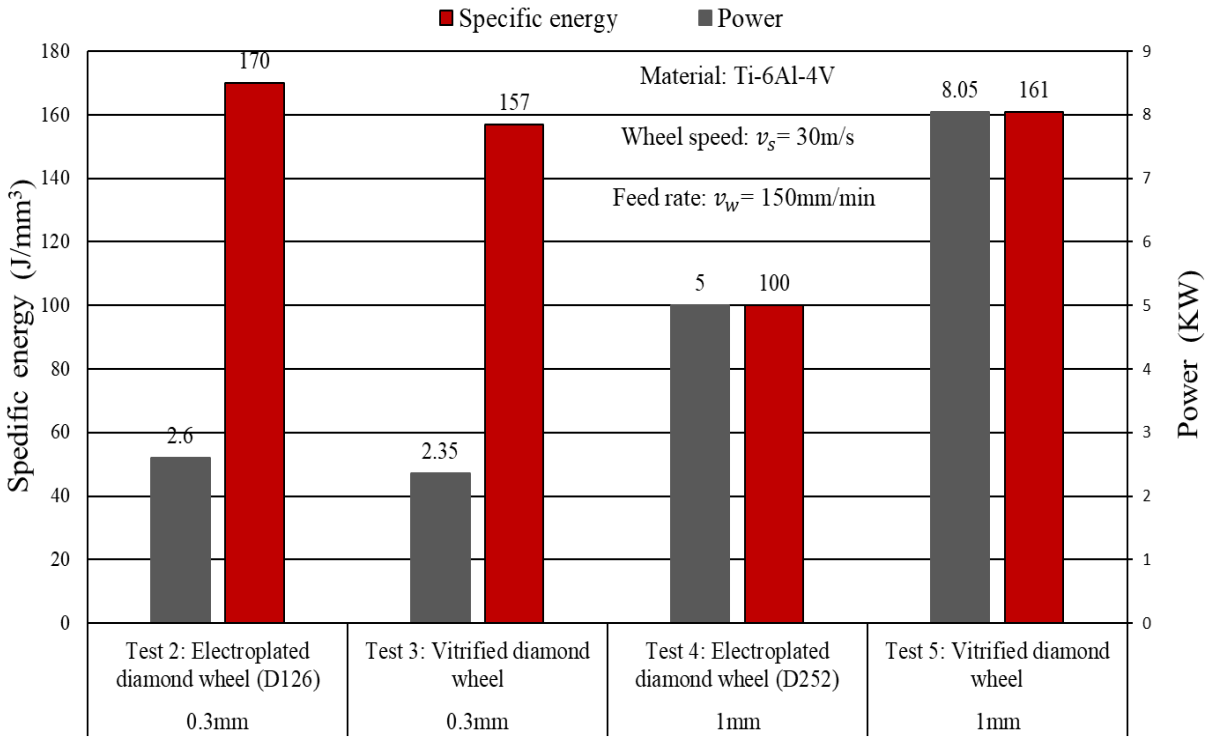


Figure 4-61: Grinding power and specific energy for different grinding conditions (Phase 3C)

4.3.3.3 Grinding temperature

Generated temperatures after CFG of Ti-6Al-4V with single-layer electroplated diamond wheel and vitrified diamond wheel are presented in Figure 4-62. Typically, the recorded temperatures for single-layer electroplated diamond wheel follow the results reported for Ti-6Al-4V and γ-TiAl ground by vitrified diamond wheel, ranging between 30°C-70°C. These are remarkably lower than those given in [180], where a temperature of ~850°C was recorded following CFG of Ti-6Al-4V with super-abrasive wheel cBN. In addition, higher temperatures (80°C-180°C) were recorded when surface grinding of the same alloy with electroplated cubic boron nitride wheel under cryogenic cooling and wet conditions in [172], suggesting the inferiority of cryogenic cooling condition to the applied cooling condition in this work for grinding process of hard materials as described in [123], [124]

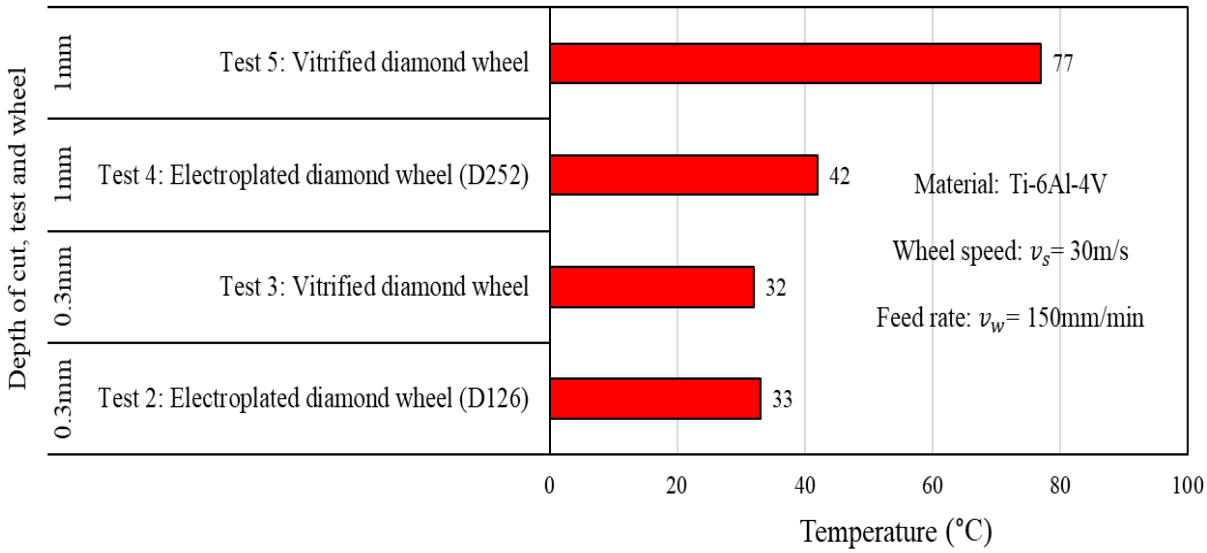


Figure 4-62: Recorded temperature at different operating conditions (Phase 3C)

4.3.3.4 Surface roughness and topography

Comparisons between the 2D and 3D surface roughness parameters for Ti-6Al-4V ground with single-layer electroplated diamond wheel and vitrified diamond wheel are shown in Figure 4-63 and Figure 4-64, respectively. For 2D roughness parameters, it was observed that there is no significant disparity between the roughness values between the two different types of wheels when the depth of cuts is low. However, when larger removal rates are employed, there is a noticeable rise of ~90% in the average roughness value (Ra) and a ~35% increase in the extreme values (Rt and Rz). The trends seen in the 3D parameters were largely consistent with those shown in the 2D parameters, except for St and Sz. In contrast to their 2D counterparts, these parameters exhibited a reduction of approximately 25% in their values. The rapid increase in average surface roughness parameters in both 2D and 3D (Ra and Sa), observed when operating at higher material removal rates, can be attributed to the significant redeposition of material. This redeposition was accompanied by minimal wear on the wheel. Redeposition during grinding Ti-6Al-4V is very common, as reported in the published literature, and usually a substantial amount of adhered material will be carried away with the grit as it pulls out from the wheel, however unlike vitrified SiC and diamond wheels where it is more commonly for grit pull-out to occur, in the single layer electroplated wheels grit pullout is rare due to the strong bonding between the grits and the electroplated layer of the wheel with grain fracture and attrition wear are being the primary mechanisms of wear [207]. Consequently, a higher accumulation of adhered material is expected on the wheel, which is then transferred back to

the machined material surface during grinding as adhered material. This results in a higher roughness value, as clearly observed in the SEM micrographs and 3D topographies of the ground surfaces in the subsequent section. For instance, in a comparison between monolayer brazed cBN wheel and vitrified cBN wheel in terms of dimension accuracy of produced surfaces of Ti-6Al-4V after creep feed grinding, Changyong et al. revealed that the average surface roughness values (Ra) when using the former wheel were as twice as those obtained with the latter [178]. Furthermore, the documented values in earlier work for the average surface roughness when CFG γ-titanium aluminides using vitrified SiC and diamond wheels ranged from 0.8 to 2.3µm. However, when an electroplated diamond wheel was utilised under similar conditions, the range of 2D average surface roughness values increased to 2.9-6µm [7], [26]. These are in agreement with current findings here for Ti-6Al-4V (R_a=3.3µm for electroplated wheel), whereas values for Ra and Sa were between 2-2.5µm and 1.5-1.9µm when vitrified SiC and diamond wheels employed respectively. Comparable results for Ra with values over 3µm following grinding Ti-6Al-4V with an electroplated cubic boron nitride wheel were given in [172].

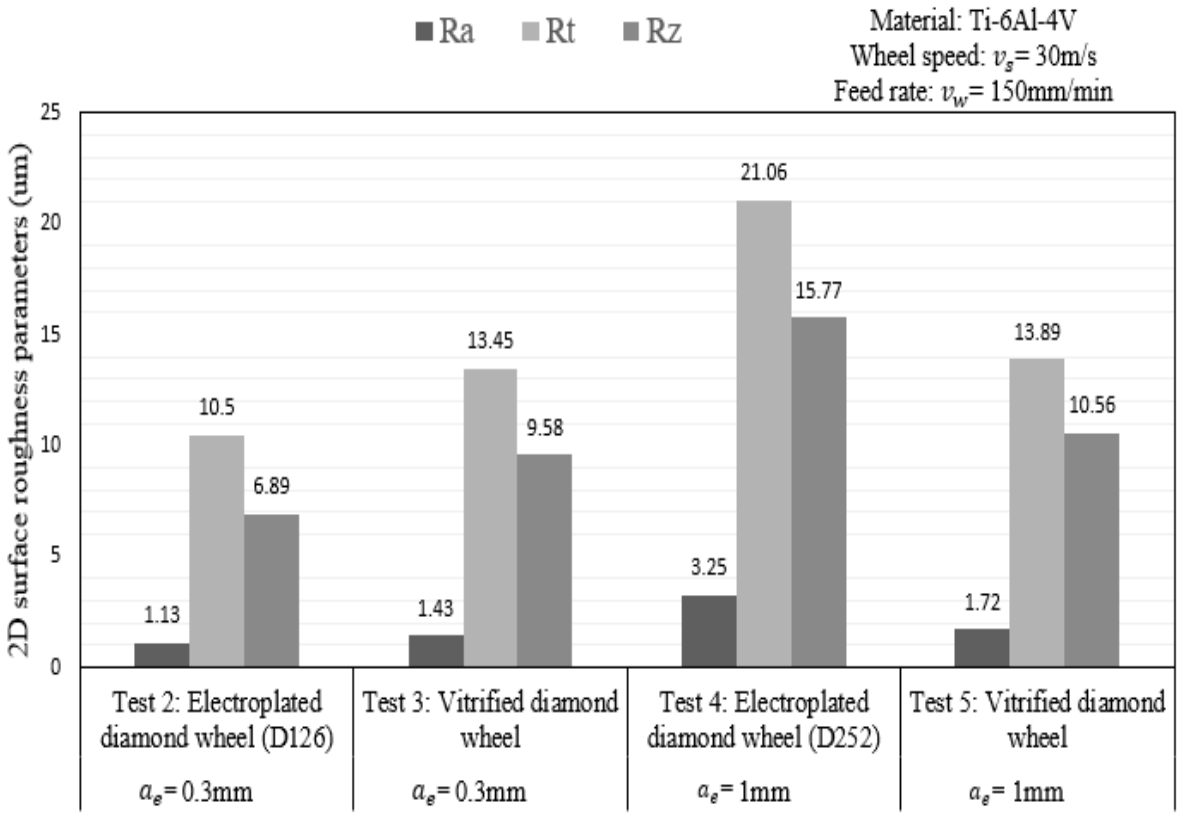


Figure 4-63: 2D surface roughness parameters for Ti-6Al-4V ground surfaces (Phase 3C)

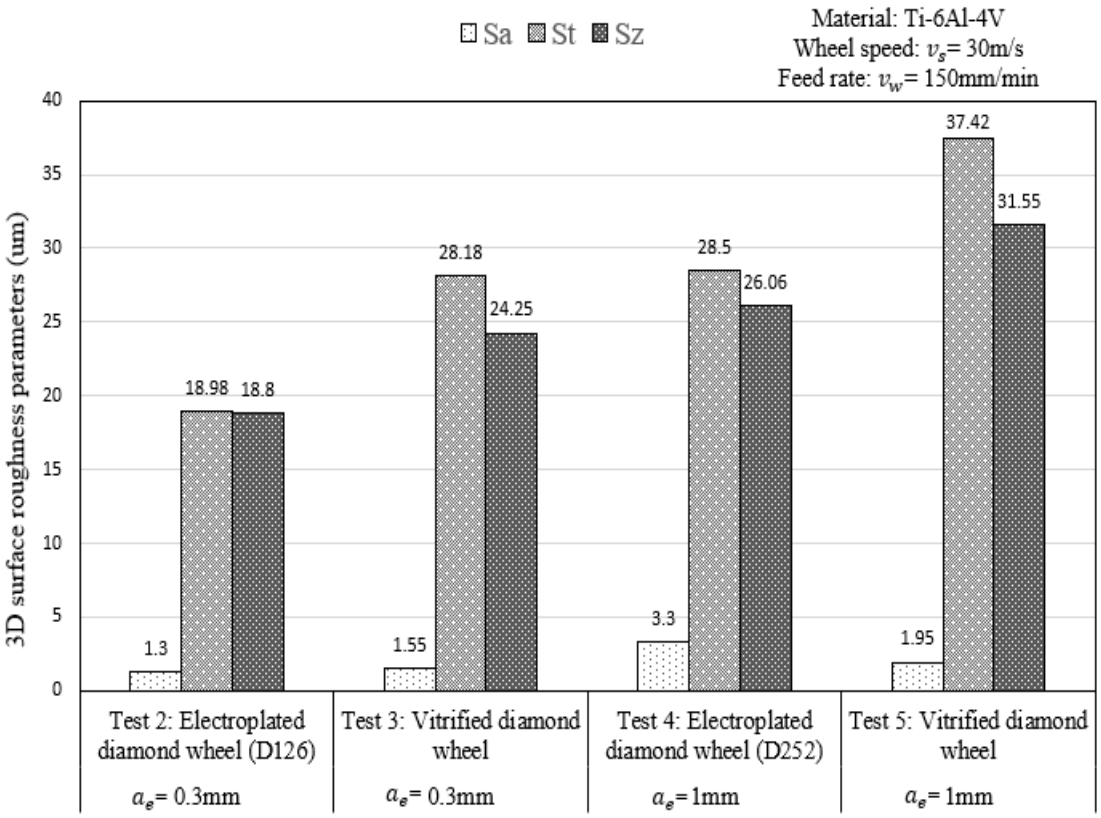


Figure 4-64: 3D surface roughness parameters for Ti-6Al-4V ground surfaces (Phase 3C)

4.3.3.5 Workpiece surface

The images of the Ti-6Al-4V workpiece surface ground with an electroplated diamond wheel, along with SEM micrographs and 3D topographies, are shown in Figure 4-65. The ground surface showed no signs of surface crack, grinding burn, chatter or fracture. However, a high level of smearing/adhered material can be seen in the associated SEM micrographs. Such strong adherence was noted by Teicher et al. when grinding Ti-6Al-4V with single-layered diamond and cBN wheels, and they also reported that the produced chips were ductile in nature. The main factors contributing to the observed phenomena were identified as the material's high chemical reactivity and ductility [177]. As opposed to γ-TiAl surfaces that were subjected to grinding with an electroplated diamond wheel, as documented in [26], [185], the SEM micrographs of the current study reveal an absence of fractures or deep grinding scratches/grooves on the surface. This discrepancy in surface characteristics can be attributed to the differing levels of ductility exhibited by the two materials.

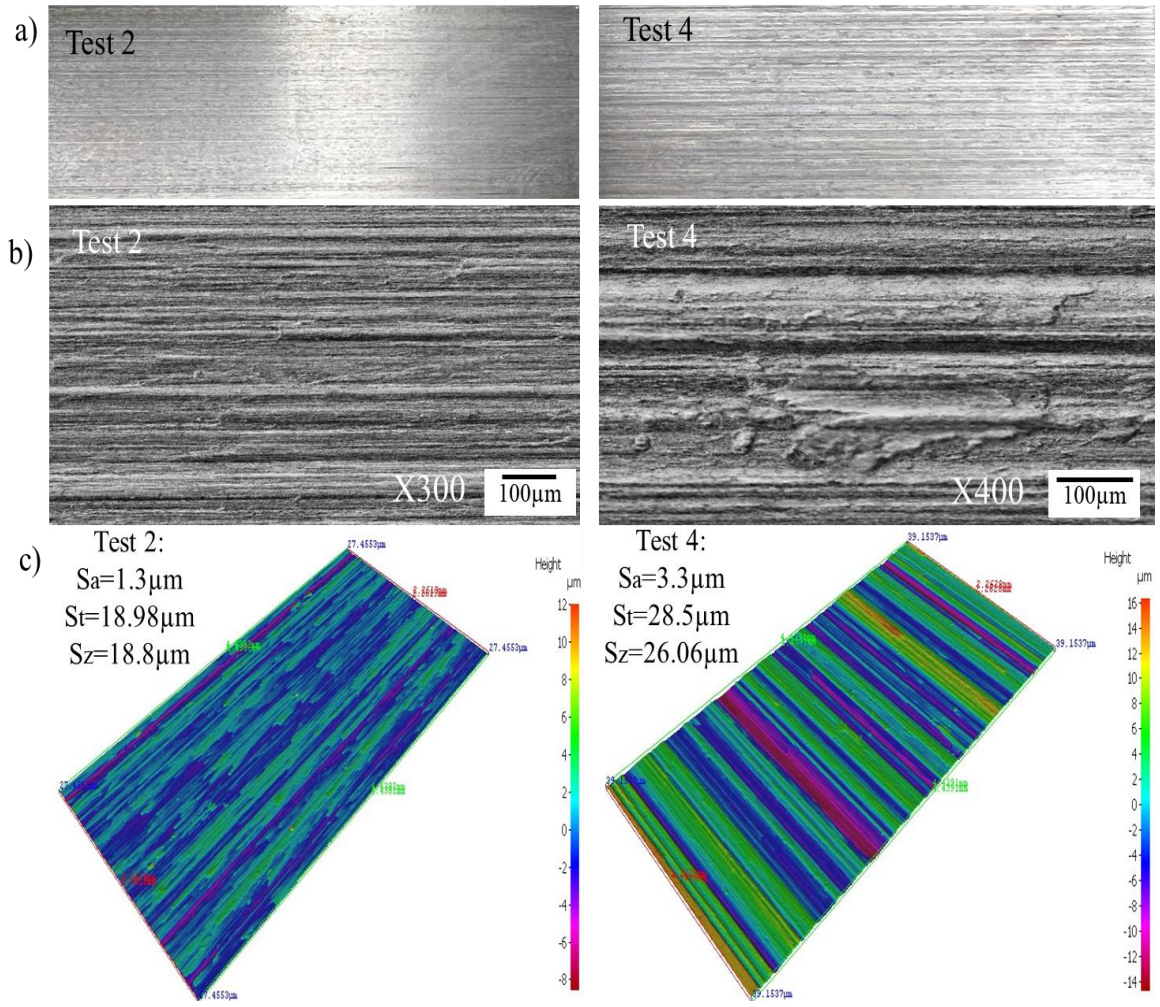


Figure 4-65: Surface observations for Ti-6Al-4V: a) Images of machined surface, b) SEM micrographs, c) 3D topographies of ground surfaces (Phase 3C)

4.3.3.6 Workpiece microstructure

Similar to surfaces ground with super-abrasive vitrified diamond wheel, the cross-sectional micrographs for surfaces machined with electroplated wheel depicted in Figure 4-66 demonstrate a lack of observable changes in the microstructure and absence of plastic deformation in Ti-6Al-4V samples subjected to the specified machining parameters. Furthermore, there are no indications of macroscopic or microscopic cracks, tears or damage like those observed when CFG γ-TiAl with the same wheel (D252) in [185]. Typically, grit marks were seen exclusively on the transverse feed plane due to the inherent characteristics of the cutting process. Test 2 microstructure in longitudinal/parallel feed plane (associated with lower material removal rate, a_e=0.3mm), exhibited a smoother surface compared to the microstructures obtained at a depth of cut of 1mm. This observation substantiates the

magnitude of material re-depositions and smearing depicted in the corresponding scanning electron microscopy (SEM) images, as well as the higher roughness values for the two-dimensional (2D) and three-dimensional (3D) average parameters, namely Ra and Sa.

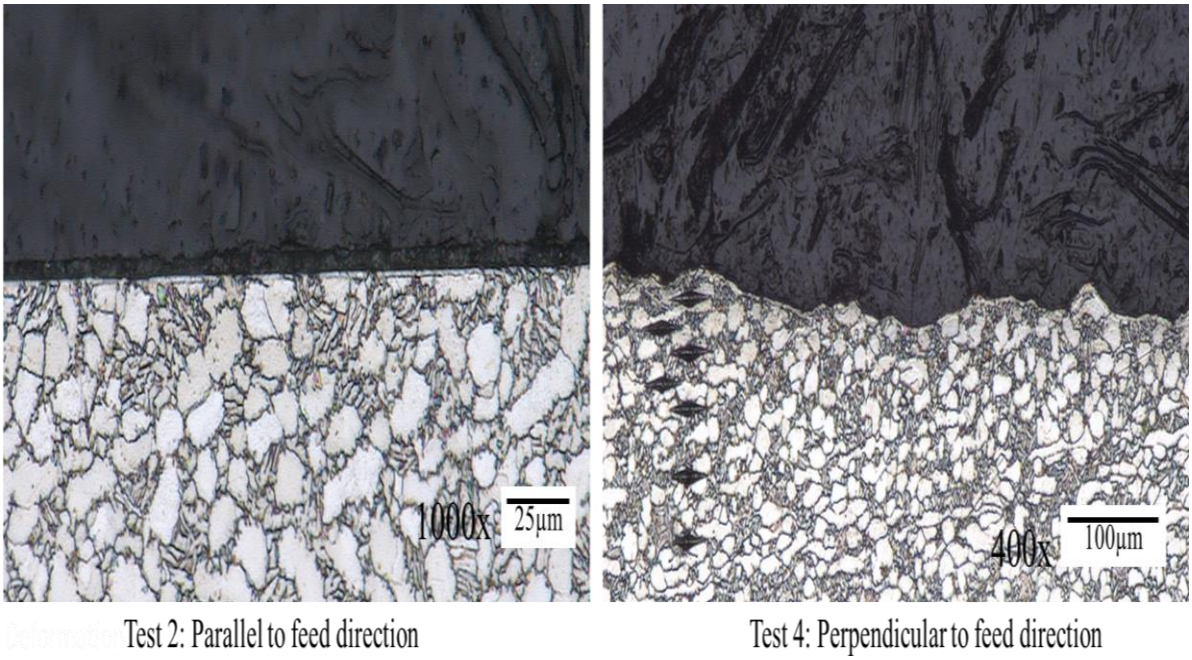


Figure 4-66: The microstructure of Ti-6Al-4V samples ground with electroplated diamond wheel (Phase 3C)

4.3.3.7 Workpiece microhardness

The microhardness profiles observed for Ti-6Al-4V in Figure 4-67 exhibit comparable patterns to the microhardness profiles obtained from surfaces that were machined using SiC and vitrified diamond wheel. These profiles exhibited a thin layer just below the surface, measuring approximately 10µm, which displays a slight softening effect. Beyond this layer, the microhardness gradually rises to a peak value of $350HK_{0.050}$ at a depth of 80-100µm. Subsequently, the microhardness decreases until it reaches the bulk hardness level of 320HK. The current findings indicate that there is no significant variation in microhardness values for Ti-6Al-4V when different wheel systems are utilised at the specified conditions. This observation presents a small contradiction to the results reported in a previous study, which documented a ~20% rise in microhardness values after CFG of Ti-6Al-4V using a monolayer brazed cubic boron nitride (cBN) wheel running at (v_s=18.5m/s, a_e=1mm, v_w=100mm/min) [178].

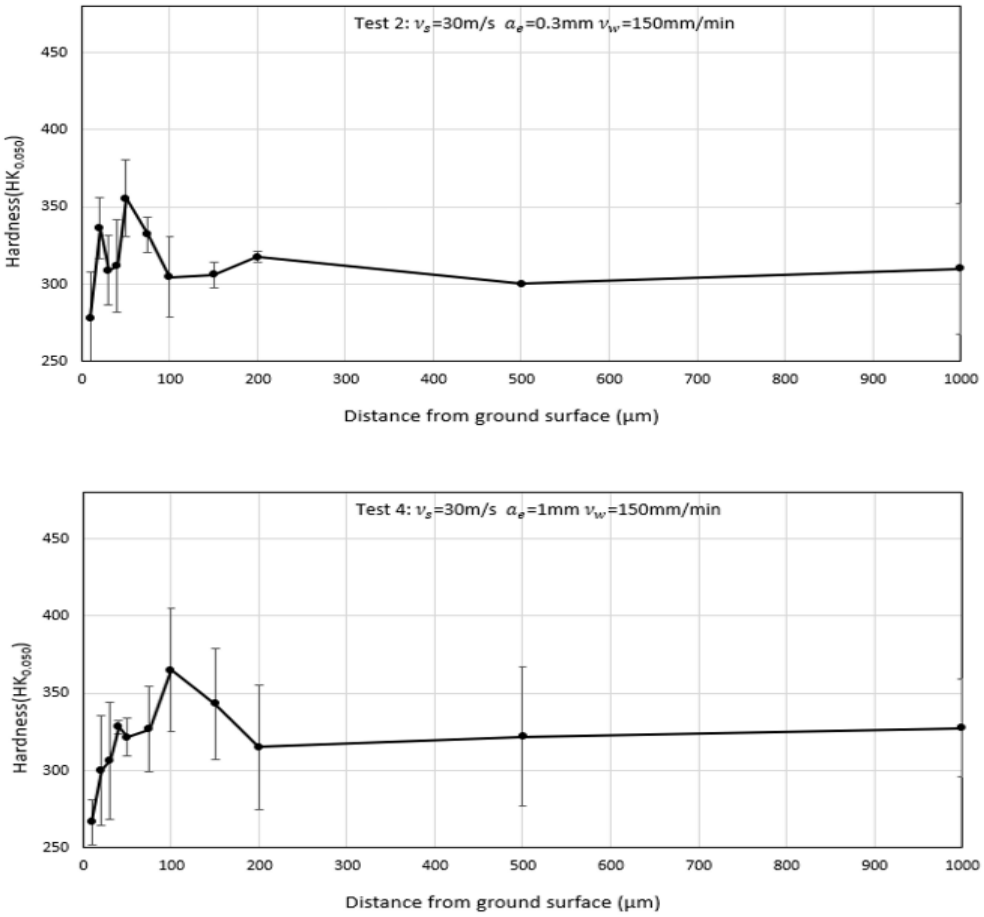


Figure 4-67: Individual microhardness profiles (Phase 3C)

4.3.4 Phase 3D: Extended surface integrity analysis (residual stress) on conventional titanium alloy (Ti-6Al-4V)

Residual stresses refer to the inherent equilibrium stresses that exist within a material after the removal of all external forces. The primary factors contributing to the generation of residual stresses in a component as a result of grinding can be attributed to three main causes: localised thermal damage, plastic deformation resulting from the mechanical load applied during grinding, and localised phase transformation [145]. Figure 4-68 shows that all residual stresses for Ti-6Al-4V samples ground with vitrified SiC, vitrified diamond and single-layer electroplated diamond wheels are compressive with no evidence of tensile stresses. Based on the findings and observations presented in the preceding sections, this was not unexpected. Low levels of temperatures and forces were measured during CFG of Ti-6Al-4V at the specified conditions. Moreover, Ti-6Al-4V produced surfaces/subsurface were free of damage or any microstructural change. Employing either SiC or vitrified diamond wheels while operating at identical depths of cut and feed rate and relatively different wheel speeds induced similar levels of compressive residual stresses, around -250MPa in the transverse direction and approximately -190MPa in the longitudinal direction in both wheel systems. Changing the wheel system from vitrified diamond to single-layer electroplated diamond generated considerably higher compressive stresses with values of -528MPa and -419MPa in traverse and longitudinal directions, respectively. Typically, these results are in agreement to those documented in [174], [178], who reported compressive stress following CFG of Ti-6Al-4V by vitrified and single-layer cBN wheels, with no signs of tensile stresses on the ground surfaces.

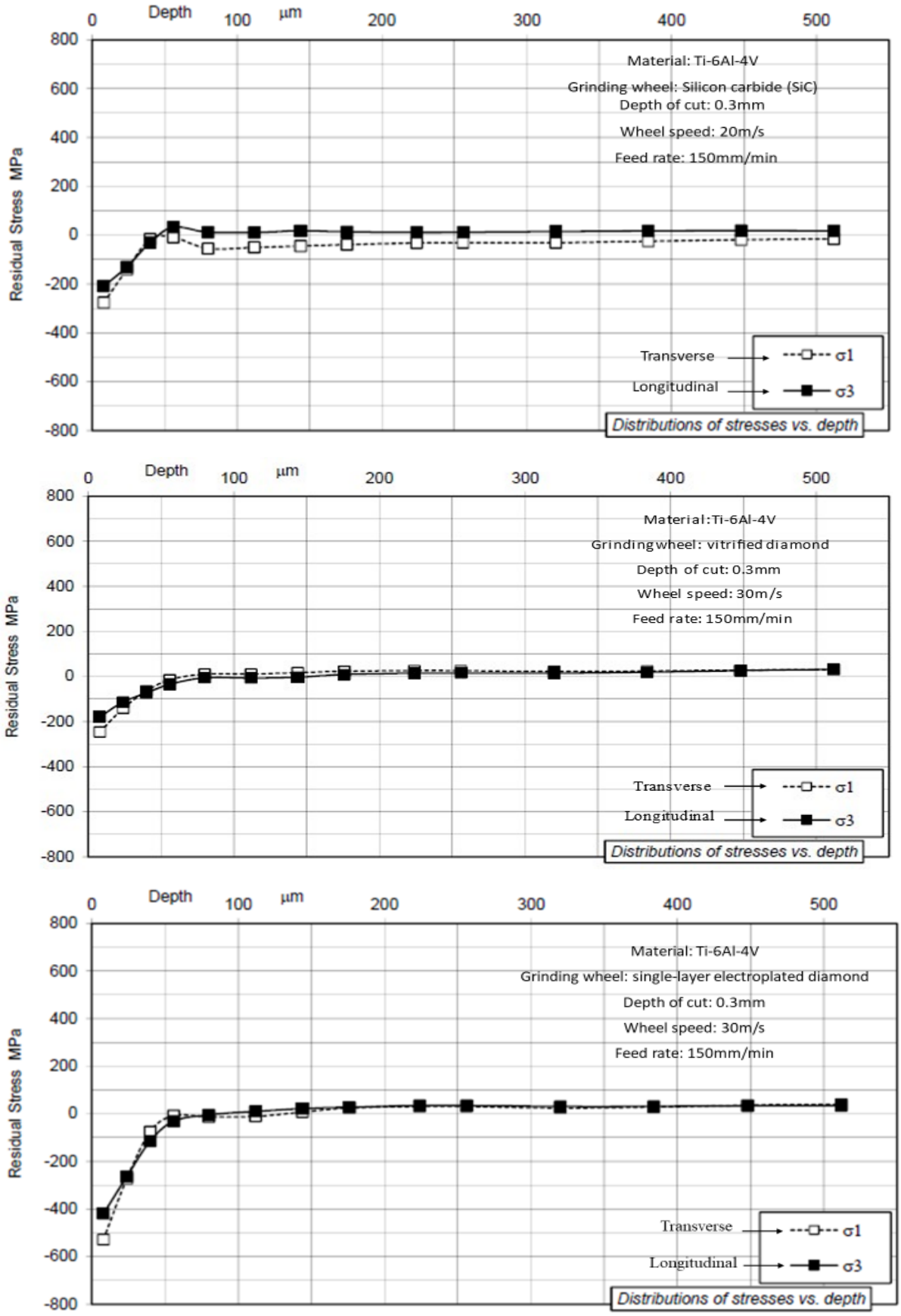


Figure 4-68: Residual stress depth profiles for Ti-6Al-4V samples

4.3.5 Summary of results for conventional titanium alloy (Ti-6Al-4V)

Phase 3A: Benchmarking the performance of conventional titanium alloy (Ti-6Al-4V) against γ-titanium aluminide alloy and burn-resistant titanium alloy with SiC wheel

- G-ratio results for Ti-6Al-4V were comparable to BuRTi values, ranging from 1.5 to 4. Nevertheless, while grinding at a depth of cut of 1mm, the SiC wheel demonstrated greater wheel wear in the former compared to the latter.

- In contrast to γ-TiAl and BuRTi measured forces, the force components in machined Ti-6Al-4V exhibited a marginal decrease when the depth of cut was increased from 0.3mm to 1mm. Furthermore, the alterations in the depth of cut yielded a nearly identical specific energy value of approximately 196J/mm^3. Compared to γ-TiAl and BuRTi, Ti-6Al-4V achieved the lowest power levels (3KW) when CFG at 20m/s wheel speed, 150mm/min feed rate and 0.3mm depth of cut.

- In general, under the specified conditions, the temperature range seen for Ti-6Al-4V falls within the range of temperatures exhibited by BuRTi and γ-TiAl. Changes in depth of cuts while other conditions are fixed, resulted in a slight difference in recorded temperature for both Ti-6Al-4V and BuRTi samples. Whereas for the γ-TiAl workpiece, a significant drop from 236°C to 46°C was observed.

- In terms of surface topography, Ti-6Al-4V machined surfaces had the greatest roughness values for both 2D and 3D parameters when compared to BuRTi (two times higher) and γ-TiAl (3 times higher) surfaces.

- Significant smearing and re-deposited material were observed over the entire ground surfaces of Ti-6Al-4V in both tests, with the extent of minor burn marks on surface machined at 1mm depth of cut.

- No sign of sub-surface damage or microstructural alteration is observed in Ti-6Al-4V surface cut at lowest operating conditions in the feed direction while grain elongation/bending up to a depth of 30μm was recorded perpendicular to the feed direction. Nonetheless, an increment in depth of cut from 0.3 to 1mm, resulted in plastic

deformation of the grain boundaries beneath the ground surface up to 15µm in parallel direction and 40µm in perpendicular direction.

- Regardless of different cutting depths and surface/subsurface conditions, no appreciable difference in workpiece strain hardening was measured, with a marginal softening layer (~265$HK_{0.050}$) within the first 10µm below the surface in test pertaining to 0.3mm depth of cut.

Phase 3B: Benchmarking the performance of conventional titanium alloy (Ti-6Al-4V) against γ-titanium aluminide alloy and burn-resistant titanium alloy with diamond wheel

- Similar to BuRti findings, replacing the wheel system from SiC to diamond, did not result in a significant improvement in grinding performances in terms of G-ratio, with the maximum G-ratios measured being 4 and 5 for SiC and diamond wheels, respectively. At 0.3mm depth of cut, Ti-6Al-4V and BuRTi showed comparable G-ratios and wheel. However, when the depth of cut was increased to 1mm, the latter exhibited much superior performance than the former.

- At a low depth of cut, grinding forces Ti-6Al-4V ranged between 400-700N for normal forces and between 200-400N for tangential forces, irrespective of wheel speed and feed rate levels. These are almost similar to γ-TiAl and BuRTi results, but at 1mm depth of cut, trends were different with the maximum level of forces recorded at Ti-6Al-4V. The Ti-6Al-4V demonstrated intermediate levels of grinding power and specific energy when compared to BuRTi and γ-TiAl. The grinding power ranged from 2 to 14KW, while the specific energy ranged from 120 to 180J/mm^3. None of the factors exhibited statistical significance on grinding forces or power, except for the feed rate on specific energy with a high PCR of 97%.

- With the exception of one test (operated at extreme levels), Ti-6Al-4V surfaces machined with a vitrified diamond wheel exhibited a similar temperature range to those obtained for γ-TiAl and BuRTi (30-70°C).

- As in Ti-6Al-4V, γ-TiAl and BuRTi samples ground with SiC wheels, the highest roughness values for both 2D and 3D roughness parameters were also measured at Ti-

6Al-4V surfaces, albeit significant improvement by at least 20% at the majority of surface roughness parameters resulted from wheel system substitution. 2D and 3D average roughness parameters for the SiC wheel ranged between 2.05-2.45µm, whilst for the diamond wheel, these were reduced to 1.43-1.59µm.

- The presence of depression marks became apparent towards the end of the grinding track in tests involving high depth of cuts (1mm) and low feed rate. An increase in feed rate from 150 to 300mm/min resulted in severe surface damage with depression marks covering most of the machined surface. In contrast, surfaces ground at lower depth of cut, were free from any burn, chatter or depression marks. Associated SEM analysis revealed the presence of adherent material, material pull-out, and potential fractures, particularly notable in tests associated with higher depth of cut and feed rate.

- There was no difference in the microstructure of Ti-6Al-4V samples machined with the vitrified diamond wheel at specified operating conditions.

- The majority of diamond ground Ti-6Al-4V samples showed the presence of a layer with lower hardness (less than $270HK_{0.050}$) extending below the surface to a depth of 20-40µm.

Phase 3C: Comparison of the performance of different super-abrasive wheel specifications when CFG conventional titanium alloy (Ti-6Al-4V)

- In comparison to vitrified diamond wheels, the G-ratio and radial wheel wear when employing an electroplated diamond wheel were observed to enhance by as much as 130% at 0.3mm depth of cut and 1800% at 1mm depth of cut.

- When operating at a higher removal rate (1mm depth of cut), the magnitudes of the normal and tangential force components for electroplated diamond wheels are significantly lower in comparison to vitrified diamond wheels. However, at a lower removal rate (0.3mm depth of cut), comparable forces were measured for both wheels. Similarly, there was no significant difference in grinding power and specific energy levels for both wheels when operating at low depth of cut with values of 2.6KW and $170J/mm^3$ for the electroplated diamond wheel and 2.35KW and $157J/mm^3$ for vitrified

diamond wheel. At 1mm depth of cut, values for the vitrified diamond wheel exceeded the electroplated diamond wheel by around ~30-60%.

- The temperatures observed on the single-layer electroplated diamond wheel ranged between 30°C to 70°C, which are consistent with those reported for the ground Ti-6Al-4V and γ-TiAl using the vitrified diamond wheel.

- The maximum average surface roughness of 3.3µm was measured for electroplated diamond wheel. While operating at low depth of cut, no significant disparity in 2D surface roughness parameters between the two wheels was observed. At higher removal rates, however, the average roughness value (Ra) increased by 90% and the extreme values (Rt and Rz) rose by 35%. With respect to 3D topographical parameters, St and Sz parameters for electroplated diamond wheel exhibited a reduction of ~25% in their values when compared to those measured for vitrified diamond wheel.

- The images of the Ti-6Al-4V workpiece surfaces ground with electroplated diamond wheel showed no evidence of surface damage including: burn, crack, chatter or depression mark. SEM micrographs of machined surfaces display high level of smearing/adhered material.

- The cross-sectional micrographs of surfaces machined with an electroplated wheel exhibit almost identical observations to surfaces ground using a vitrified diamond wheel. The microstructure of Ti-6Al-4V samples remains unchanged, with no indication of plastic deformation under the applied machining conditions.

- The trends seen in the microhardness profiles for samples ground with electroplated diamond wheel are similar to those seen in surfaces that were cut with vitrified SiC and diamond wheels, showing a slight softening effect and restricted to 10µm in depth.

Phase 3D: Extended surface integrity analysis (residual stress) on conventional titanium alloy (Ti-6Al-4V)

- Under the specified conditions, all three examined wheels (vitrified SiC, vitrified diamond and electroplated diamond wheels) produced compressive residual stresses following creep feed grinding of Ti-6Al-4V workpieces.

- Comparable levels of compressive residual stresses were induced when cutting with vitrified SiC and vitrified diamond wheels when operating at relatively different wheel speeds (-250MPa in the transverse direction and -190MPa in the longitudinal direction).

- Single layer electroplated diamond wheel generated the maximum compressive stresses with values of -528MPa and -419MPa in traverse and longitudinal directions respectively.

5 CONCLUSION

In this chapter, the key observations stemming from experimental work on creep feed grinding of advanced titanium alloys are summarised in relation to the correlation between evaluated output measures, including wheel wear, grinding forces, grinding temperature and surface integrity. This is followed by an overall conclusion and the recommended operating conditions. Then, the major contributions to knowledge of this thesis are presented, together with suggestions for future work.

5.1 Correlations between examined machining output measures

In machining processes like grinding, various output measures are crucial indicators of the efficiency and quality of the operation. Correlations between these measures can be complex and dependent on various factors such as material or wheel properties, grinding conditions and desired surface integrity. Understanding these correlations is essential for optimizing grinding processes to achieve desired outcomes effectively. The results provided in this work revealed significant relationships between the evaluated output measures such as wheel wear, grinding forces, grinding temperature, surface observations, surface roughness, microstructure, microhardness and residual stresses. For instance, higher grinding forces of 1467N and 1789N when CFG γ-titanium aluminide alloy (Ti-45Al-8Nb-0.2C) with SiC wheel, generated temperatures of 692°C and 582°C, respectively. Reduction in grinding forces (579N and 767N) resulted in a substantial decrease in grinding temperatures (41°C and 46°C) for the same material and wheel. In addition, high levels of griding forces at the majority of tests for all the investigated materials were accompanied by surface integrity defects (cracks and burn and chatter marks) but were absent at low levels of grinding forces.

High grinding temperatures across all materials were detrimental in terms of surface integrity as surface burn, softening, plastic deformation and tensile residual stresses were evident at surfaces associated with high recorded temperatures. For example, CFG of burn-resistant titanium alloy (Ti-25V-15Cr-2Al-0.2C) with SiC wheel produced high levels of temperatures (611°C and 476°C) even when ground with super-abrasive diamond wheel (481°C), these were in conjunction with the existence of tensile residual stresses with values of 596MPa and 317MPa, surface burn on workpiece surfaces, extensive plastic deformation to a depth of ~20µm and a softening layer within the first 15µm under the surface (~340 $HK_{0.050}$). With

respect to residual stresses, cracks and microhardness alterations were present at the ground surfaces of γ-TiAl and BuRTi. For γ-TiAl material ground with SiC wheel at the highest operating conditions, compressive residual surfaces near the surface (-760MPa in the feed direction and -500MPa perpendicular to the feed) promoted an increase in microhardness up to (~450 $HK_{0.050}$) at a depth extending to ~150μm below the surface.

In general, 2D and 3D surface roughness values exhibited an increasing trend with an increase in the undeformed chip thickness (increasing in feed rate and/or depth of cut) in the majority of experiments. This was supported by relevant statistical analysis results, in which higher PCR values for both feed rate and depth of cut were observed. For the materials investigated in this work, particularly BuRTi and Ti-6Al-4V, surface roughness values were greatest on surfaces with a high level of smearing, side flow, and redeposition. This is mainly caused by the ductile nature of the machined materials. Furthermore, an increment in undeformed chip thickness resulted in plastic deformation of the grain boundaries beneath the ground surfaces up to 17μm in most tests (γ-TiAl and Ti-6Al-4V samples ground with SiC wheel, and BuRTi samples ground with both SiC and diamond wheel). In contrast, the undeformed chip thickness was shown to be inversely related to specific energy, as grinding at high levels of feed rates and depth of cut produced low values for specific energy. For instance, a value of over 220J/mm^3 for specific energy was produced when CFG of BuRTi with the diamond wheel at a low level of depth of cut (0.3mm) and feed rate (150mm/min). The value dropped by ~50% (120J/mm^3) when the operating condition changed to 1mm and 300mm/min.

Identifying the correlation between the G-ratio and other output measures was found complicated and lacked both distinct trends and relationships with machining responses. However, changes in G-ratio values were primarily governed by wheel and/or workpiece material properties. For example, alternation in the wheel system from SiC to vitrified diamond wheel had a negligible effect on Ti-6Al-4V and BuRTi with comparable values ranging from 1.5 to 4. However, more than 1000% improvement in G-ratio (~13 to ~120) was achieved with γ-TiAl. In the case of Ti-6Al-4V, and when employing an electroplated diamond wheel instead of the vitrified diamond wheel, The G-ratio exhibited a fivefold rise, shifting from 1 to 4 for vitrified diamond compared to 12 to 26 for a single layer diamond wheel.

5.2 Overall conclusions

- In general, the observed lower values of G-ratio and wheel wear, grinding forces, power, temperature, and surface roughness for γ-TiAl indicate that it exhibited more promising results in creep feed grinding compared to BuRTi and Ti-6Al-4V. This can be attributed to the lower ductility of γ-TiAl and superior thermal conductivity when compared to BuRTi and Ti-6Al-4V.

- At lower material removal rates, BuRTi and Ti-6Al-4V materials showed a moderate level of similarity in grinding performance with material smearing being the major surface damage in both materials. At higher depth of cuts, however, lower grinding forces, wheel wear and better surface roughness were evident in the former, but at the expense of surface burn and crack.

- Under the specified conditions in this work, all surfaces ground with SiC wheel showed some degree of surface damage consisting of burn marks and/or crack, with the exception of γ-TiAl, Ti-6Al-4V surfaces machined at lowest cutting conditions (two tests).

- For all investigated materials, the diamond wheel significantly outperformed SiC wheel in terms of grinding temperature, produced surface integrity and induced residual stresses. A substantial increase in G-ratio was only evident in γ-TiAl machined with a diamond wheel, and no such improvement is observed in BuRTi and Ti-6Al-4V.

- Assessment of the performance of two different super-abrasive wheels when creep feed griding Ti-6Al-4V at identical operating conditions, revealed that single layer electroplated diamond wheel significantly outperformed vitrified diamond wheel, with a rise in G-ratio by up to ~1800% and a reduction in grinding forces, consumed power, specific energy by up to ~30-60%. In addition, the magnitudes of compressive residual stresses increased by three folds when operating with the electroplated diamond wheel. These improvements however, were at the expense of higher average surface roughness values caused by the high level of adhered material on the machined surfaces.

- In comparison to published work on CFG of BuRTi with SiC wheel, alterations in applied operating conditions such as coolant pressure, depth of cut, feed rate and wheel speed resulted in improved G-ratio in the majority of ground samples with maximum values of 4.7 compared to 2.5 in earlier work. Similarly, a maximum value of ~1.2 was reported in earlier work involving CFG of Ti-6Al-4V, here the value rose to 4 and 5 for samples cut with SiC and diamond wheel, respectively.

- The current research indicates good agreements between grinding temperature, residual stresses and surface/subsurface observations following creep feed grinding of γ-TiAl, BuRTi and Ti-6Al-4V. Machined surfaces exhibiting tensile residual stresses were often accompanied by cracks, burn marks, and/or softening layers (mostly observed with surfaces ground with SiC wheel at extreme operating conditions). Conversely, compressive residual stresses were only confined to surfaces free of burn and microstructural deformation (more pronounced in samples cut with diamond wheels).

5.3 Recommended operating conditions for CFG of investigated advanced titanium alloys

Table 5-1 details the fixed grinding conditions throughout the experimental testing, while Tables 5-2 to 5-4 detail the recommended/preferred operating conditions for each investigated material per wheel based on the optimal observed levels of G-ratio, surface roughness, temperature, surface integrity and residual stresses.

Table 5-1: Fixed operating parameters and levels

Operation	Wheel direction	Down
	Spark out	No
Dressing parameters	Dressing method	Intermittent
	Dresser type	Hydraulic diamond roller dresser
	Dresser speed ratio	+0.8
	Dresser feed rate	2µm/rev
	Infeed rate	Sic abrasive: 50µm Diamond abrasive: 5µm
Supplied fluid parameter	Cooling method	Free jet nozzle
	Number of nozzles	Two (cooling and cleaning)
	Coolant pressure	Cooling nozzle: 7bar and 15bar (BuRTi with SiC tests) Cleaning nozzle: 20bar

Table 5-2: List of preferred operating parameters for the best achieved output measures following CFG of gamma titanium aluminide intermetallic alloy (Ti-45Al-8Nb-0.2C wt%)

Silicon carbide wheel			
Best achieved output measure	**Depth of cut (mm)**	**Wheel speed (m/s)**	**Feed rate (mm/min)**
G-ratio	1	30	150
Temperature, 3D surface roughness parameters and surface integrity	0.3	20	150
Diamond wheel			
Best achieved output measure	**Depth of cut (mm)**	**Wheel speed (m/s)**	**Feed rate (mm/min)**
G-ratio and 3D surface roughness parameters	1	30	300
Surface integrity and residual stresses	0.3	30	150

Table 5-3: List of preferred operating parameters for the best achieved output measures following CFG of burn resistant titanium alloy (Ti-25V-15Cr-2Al-0.2C wt%)

Silicon carbide wheel			
Best achieved output measure	**Depth of cut (mm)**	**Wheel speed (m/s)**	**Feed rate (mm/min)**
G-ratio	1	30	150
Temperature and surface integrity	0.3	20	300
3D surface roughness parameters	0.3	30	300
Diamond wheel			
Best achieved output measure	**Depth of cut (mm)**	**Wheel speed (m/s)**	**Feed rate (mm/min)**
G-ratio	1	30	150
Temperature, surface roughness parameters, surface integrity and residual stresses	0.3	30	150

Table 5-4: List of preferred operating parameters for the best achieved output measures following CFG of α/β titanium alloy (Ti-6Al-4V)

Silicon carbide wheel			
Best achieved output measure	**Depth of cut (mm)**	**Wheel speed (m/s)**	**Feed rate (mm/min)**
G-ratio and surface integrity	0.3	20	150
Diamond wheel			
Best achieved output measure	**Depth of cut (mm)**	**Wheel speed (m/s)**	**Feed rate (mm/min)**
G-ratio, temperature and surface roughness parameters	0.3	30	150
Single layer electroplated diamond wheel			
Best achieved output measure	**Depth of cut (mm)**	**Wheel speed (m/s)**	**Feed rate (mm/min)**
G-ratio (D252)	1	30	150
Surface roughness parameters and residual stresses (D126)	0.3	30	150

5.4 Contributions to knowledge

- The current work provides new insights into the generated temperature, residual stresses and 3D surface roughness parameters during creep feed grinding of the thermo-mechanically produced duplex alloy gamma titanium aluminide of composition (Ti–45Al–8Nb–0.2C) as well as the patent burn-resistant titanium alloy (Ti-25V-15Cr-2Al-0.2C).

- Further machinability data for creep feed grinding of Ti-6Al-4V with SiC, vitrified and electroplated diamond wheels are presented in this work.

- This study provides additional evidence / more validations to support the limited available data on creep feed grinding of γ-TiAl intermetallic (Ti-45Al-8Nb-0.2C), burn-resistant titanium alloy (Ti-25V-15Cr-2Al-0.2C) and α/β titanium alloy (Ti-6Al-4V) by comparing and contrasting between the main findings.

- The findings of this study hold significance for the academic community as they address the existing knowledge gaps in the literature pertaining to various aspects during creep feed grinding of titanium alloys, particularly for γ-TiAl intermetallic (Ti-45Al-8Nb-0.2C), burn-resistant titanium alloy (Ti-25V-15Cr-2Al-0.2C) and conventional titanium alloy (Ti-6Al-4V). The results documented in Chapter 4 show a good link between the temperature measurement, 3D surface roughness, residual stresses results and the output measures in terms of surface integrity. These aspects are missing in published literature for investigated materials.

- This investigation achieved a comprehensive analysis of the correlations between the produced surface integrity (surface and microstructure developed during processing), mainly governed by the operating conditions, and the grinding performance outputs, including grinding ratio, forces, power, specific energy, temperature, 2D/3D surface roughness and residual stresses. These findings are beneficial to industrial sectors interested in grinding advanced titanium alloys for critical applications such as those found in the automotive and aerospace industries.

- The machinability data presented in this work is extremely useful in modelling activities and analysis of the performance of grinding processes for titanium alloys. This may benefit the future of manufacturing aerospace components by providing more validations and/or accurate simulations of the grinding processes.

- This work may serve as a valuable reference for future work exploring the grindability of titanium alloys. The comprehensive literature review on grinding fundamentals and relevant published work, the applied methodology in this work, together with findings that arose from this study are all expected to significantly reduce the time required for researchers and engineers to determine the optimal creep feed griding conditions for titanium alloys.

5.5 Recommendations for future work

As a consequence of this investigation and the conclusions made, the following additional work is advised to better understand and enhance the creep feed grinding process of advanced titanium alloys presented in this thesis:

- Conducting a number of tests using identical operating parameters to investigate the influence of continuous dressing on wheel life, grinding performance and workpiece surface integrity when creep feed grinding the same alloys. It has been reported in the literature that the elimination of surface burn and surface crack has been achieved with the application of continuous dressing.

- Further evaluation of the effect of various wheel dressing techniques/parameters and fluid application methods to determine whether wheel life and/or surface integrity can be improved.

- Performance evaluation of different super-abrasive wheel specifications, including bond type, grit size, abrasive type and grade when creep feed grinding advanced titanium alloys.

- Further in-depth assessment involving the use of Energy Dispersive X-ray Spectroscopy (EDS) and X-ray Photoelectron Spectroscopy on produced surfaces. This provides information on element distribution and content in addition to the phase transition caused by the grinding process, which then can be related back to operating conditions/ parameters and temperature.

- Further analysis in terms of surface integrity by applying Standard or Extended SI Data Set instead of Minimum Data Set, covering more residual stress measurement and fatigue performance evaluations of surfaces produced following creep feed grinding.

- It is recommended to measure the wheel surface roughness (2D and 3D) and the corresponding grit wear by means of graphite or resin replicas. This can then be linked to operational conditions/parameters and temperature.

- Future work can consider chip formation/morphology during the creep feed grinding process of titanium alloys. This will offer insights into the grinding conditions. A study of the different types of chips produced during the process can serve as a useful indicator of other features/properties and a straightforward method for monitoring the grinding operation as a whole.

- Very Impressive Performance Extreme Removal (VIPER) grinding of γ-TiAl, BuRTi and standard titanium alloys such as Ti-6Al-4V should be investigated to determine whether wheel life and workpiece surface integrity can be enhanced. This patented method by Rolls-Royce plc provides very high productivity with a specific material removal rate reaching as high as 200 (mm^3/mm.s).

- Measurement of cutting temperature when creep feed grinding of gamma titanium aluminide intermetallic alloy, burn-resistant titanium alloy and conventional titanium alloys (Ti-6Al-4V) by means of implanted split foil thermocouples and PVD coatings.

- Development of a finite element model to simulate the creep feed grinding process of gamma titanium aluminide intermetallic alloy, burn-resistant titanium alloy or conventional titanium alloys (Ti-6Al-4V) in order to predict cutting temperature based on temperature distribution models given in the literature.

- Estimations of produced grinding temperature during creep feed grinding by employing analytical grinding thermal models available in the literature together with validation tests. For example, total heat, partition between grain and workpiece, energy partition, heat fluxes and workpiece surface maximum temperature rise.

6 REFERENCES

[1] D. Rugg, “The Current Status of Titanium Alloy Use in Aero-Engines,” in *Proceedings of the 10th World Conference on Titanium,* Hamburg, 2003, pp. 2727–2735.

[2] W. E. Voice, “Burn Resistant Titanium Alloy (BuRTi).,” in *proceedings of the 10th world conference on titanium*, G. Lütjering and J. Albrecht, Eds., Hamburg, Germany, 2004, pp. 2915–2922.

[3] M. Loretto, P. Blenkinsop, W. Voice, D. Rugg, and N. Walker, “The Development of Burn-Resistant Titanium for Aeroengine Applications,” in *In Proceedings of the Rolls-Royce Conference on Advanced Engine Technology*, Tiejieng, China, 2000.

[4] D. Novovic, “The Effect of Machined Workpiece Surface Integrity and Topography on Fatigue Life,” The University of Birmingham, 2004.

[5] E. E. Ibrahim, M. Checkley, X. Chen, M. Sharp, W. Liang, S. Yuan, “Process performance of low frequency vibratory grinding of Inconel 718,” in *Procedia Manufacturing*, Elsevier B.V., 2019, pp. 530–535. doi: 10.1016/j.promfg.2019.02.075.

[6] S. L. Soo, R. Hood, D. K. Aspinwall, W. E. Voice, and C. Sage, “Machinability and surface integrity of RR1000 nickel-based superalloy,” *CIRP Ann Manuf Technol*, vol. 60, no. 1, pp. 89–92, 2011, doi: 10.1016/j.cirp.2011.03.094.

[7] R. Hood, “The Machinability of a Gamma Titanium Aluminide Intermetallic,” 2010.

[8] S. Castellanos and J. Lino Alves, “A review of milling of gamma titanium aluminides,” *U.Porto Journal of Engineering*, vol. 3, no. 2. Universidade do Porto - Faculdade de Engenharia, pp. 1–9, 2017. doi: 10.24840/2183-6493_003.002_0001.

[9] H. Clemens and S. Mayer, “Intermetallic titanium aluminides in aerospace applications – processing, microstructure and properties,” *Materials at High Temperatures*, vol. 33, no. 4–5, pp. 560–570, Jun. 2016, doi: 10.1080/09603409.2016.1163792.

[10] S. D. Castellanos, A. J. Cavaleiro, A. M. P. D. Jesus, R. Neto, and J. L. Alves, “Machinability of titanium aluminides: A review,” *Proceedings of the Institution of Mechanical Engineers, Part L: Journal of Materials: Design and Applications*, vol. 233, no. 3. SAGE Publications Ltd, pp. 426–451, Mar. 01, 2019. doi: 10.1177/1464420718809386.

[11] E. Aust and H.R. Niemann, “Machining of γ-TiAl,” *Adv Eng Mater*, vol. 1, no. 1, pp. 53–57, Sep. 1999, doi: 10.1002/(SICI)1527-2648(199909)1:1<53: AID-ADEM53>3.0.CO;2-3.

[12] D. K. Aspinwall, R. C. Dewes, and A. L. Mantle, “The Machining of γ-TiAI Intermetallic Alloys,” *CIRP Annals*, vol. 54, no. 1, pp. 99–104, 2005, doi: 10.1016/S0007-8506(07)60059-6.

[13] F. Klocke *et al.*, “Abrasive machining of advanced aerospace alloys and composites,” *CIRP Ann Manuf Technol*, vol. 64, no. 2, pp. 581–604, 2015, doi: 10.1016/j.cirp.2015.05.004.

[14] S. Malkin and C. Guo, “Thermal Analysis of Grinding,” *CIRP Ann Manuf Technol*, vol. 56, no. 2, pp. 760–782, 2007, doi: 10.1016/j.cirp.2007.10.005.

[15] W. Grzesik, “Prediction of the Functional Performance of Machined Components Based on Surface Topography: State of the Art,” *Journal of Materials Engineering and Performance*, vol. 25, no. 10. Springer New York LLC, pp. 4460–4468, Oct. 01, 2016. doi: 10.1007/s11665-016-2293-z.

[16] J. Schmidt, B. Thorenz, F. Schreiner, and F. Döpper, “Comparison of areal and profile surface measurement methods for evaluating surface properties of machined components,” in *Procedia CIRP*, Elsevier B.V., 2021, pp. 459–464. doi: 10.1016/j.procir.2021.09.078.

[17] S. A. Bentley, “Surface and creep feed grinding of gamma titanium aluminide, Doctoral Thesis, School of Manufacturing and Mechanical Engineering, The University of Birmingham.,” 2000.

[18] X. Xi, Y. Zhu, T. Chen, Z. Wu, L. Anggei, and W. Ding, “Surface burn behavior in creep-feed deep grinding of gamma titanium aluminide intermetallics: characterization, mechanism, and effects”, doi: 10.1007/s00170-021-06677-4/Published.

[19] Y. G. Li, M. H. Loretto, D. Rugg, and W. Voice, “Effect of heat treatment and exposure on microstructure and mechanical properties of Ti-25V-15Cr-2Al-0.2C (wt%),” 2001. [Online]. Available: www.elsevier.com/locate/actamat

[20] M. Roger. Wenman, “Micromechanisms of fracture in the ductile-to-brittle transition region of a MnMoNi steel weld metal and a burn resistant beta titanium alloy,” University of Birmingham, 2003.

[21] T. Udomphol, “Micromechanisms of fracture and fatigue in burn resistant Ti-25V-15Cr-2Al-0.2C alloy,” University of Birmingham, 2005.

[22] R. Ding, M. Chu, and S. Zhang, “A study of microstructure and mechanical property of a burn-resistant Ti alloy fabricated by HIPping,” *Mater Charact*, vol. 163, May 2020, doi: 10.1016/j.matchar.2020.110280.

[23] D. Novovic, D.K. Aspinwall, R.C. Dewes, W. Voice, and P. Bowen, “The surface integrity of burn resistant titanium alloy (Ti-25V-15Cr-2Al- 0.2C wt%) after high-speed milling and creep feed grinding,” in *Proceedings of the 10th World Conference on Titanium*, Hamburg, 2003, pp. 2817–2824.

[24] R. Hood, F. Lechner, D. K. Aspinwall, and W. Voice, “Creep feed grinding of gamma titanium aluminide and burn resistant titanium alloys using SiC abrasive,” *Int J Mach Tools Manuf*, vol. 47, no. 9, pp. 1486–1492, Jul. 2007, doi: 10.1016/j.ijmachtools.2006.10.008.

[25] S. L. Soo, R. Hood, M. Lannette, D. K. Aspinwall, and W. E. Voice, “Creep feed grinding of burn-resistant titanium (BuRTi) using superabrasive wheels,” *International Journal of Advanced Manufacturing Technology*, vol. 53, no. 9–12, pp. 1019–1026, Apr. 2011, doi: 10.1007/s00170-010-2876-z.

[26] D. Bhaduri, “Ultrasonic assisted creep feed grinding and dressing of advanced aerospace alloys,” University of Birmingham, 2014.

[27] H. B. Bomberger, F. H. Froes, and P. H. Morton, “Titanium - A Historical Perspective Technology, Present Status and Future Trends, The Titanium Development Association,” 1985, pp. 3–17.

[28] Ch. R. V. S. Nagesh, C. S. Ramachandran, and R. B. Subramanyam, “Methods of titanium sponge production,” *Transactions of the Indian Institute of Metals*, vol. 61, no. 5, pp. 341–348, Oct. 2008, doi: 10.1007/s12666-008-0065-7.

[29] F. Gao *et al.*, “Environmental impacts analysis of titanium sponge production using Kroll process in China,” *J Clean Prod*, vol. 174, pp. 771–779, Jan. 2018, doi: 10.1016/j.jclepro.2017.09.240.

[30] C. Cui, B. M. Hu, L. Zhao, and S. Liu, “Titanium alloy production technology, market prospects and industry development,” *Mater Des*, vol. 32, no. 3, pp. 1684–1691, Mar. 2011, doi: 10.1016/j.matdes.2010.09.011.

[31] W. F. Smith, *Structure and properties of engineering alloys*. New York: McGraw-Hill publisher, 1981.

[32] M. J. Donachie, *Titanium: a technical guide*. Metals Park, ASM International, USA, 1988.

[33] G. Lütjering and J. C. Willians, *Engineering Materials and Processes: Titanium*. Springer, Germany, 2003.

[34] ASM Committee, “Introduction To Titanium And Its Alloys,” in *Metals Handbook*, 9th ed., vol. 3, 1980, pp. 353–360.

[35] W. Bolton, *Engineering Materials*. Oxford, 1993.

[36] E. O. Ezugwu, “High Speed Machining of Aero-Engine Alloys,” *Journal of the Brazilian Society of Mechanical Sciences and Engineering*, vol. 26, no. 1. Brazilian Society of Mechanical Sciences and Engineering, pp. 1–11, 2004. doi: 10.1590/S1678-58782004000100001.

[37] E. O. Ezugwu and Z. M. Wang, “Materials Processing Technology Titanium alloys and their machinability a review,” 1997.

[38] E. O. Ezugwu, J. Bonney, and Y. Yamane, “An overview of the machinability of aeroengine alloys.”

[39] E. A. Loria, “Quo vadis gamma titanium aluminide,” *Intermetallics (Barking)*, vol. 9, no. 12, pp. 997–1001, Dec. 2001, doi: 10.1016/S0966-9795(01)00064-4.

[40] K. S. Chan and Y.-W. Kim, “Effects of lamellae spacing and colony size on the fracture resistance of a fully-lamellar TiAl alloy,” *Acta Metallurgica et Materialia*, vol. 43, no. 2, pp. 439–451, Feb. 1995, doi: 10.1016/0956-7151(94)00278-P.

[41] Y.W. Kim, “Microstructural evolution and mechanical properties of a forged gamma titanium aluminide alloy,” *Acta Metallurgica et Materialia*, vol. 40, no. 6, pp. 1121–1134, Jun. 1992, doi: 10.1016/0956-7151(92)90411-7.

[42] F. Appel *et al.*, “Recent Progress in the Development of Gamma Titanium Aluminide Alloys,” *Adv Eng Mater*, vol. 2, no. 11, pp. 699–720, Nov. 2000, doi: 10.1002/1527-2648(200011)2:11<699: AID-ADEM699>3.0.CO;2-J.

[43] K. Kothari, R. Radhakrishnan, and N. M. Wereley, “Advances in gamma titanium aluminides and their manufacturing techniques,” *Progress in Aerospace Sciences*, vol. 55. Elsevier Ltd, pp. 1–16, 2012. doi: 10.1016/j.paerosci.2012.04.001.

[44] Z. Xia, C. Shan, M. Zhang, M. Cui, and M. Luo, “Machinability of γ-TiAl: A review,” *Chinese Journal of Aeronautics*, vol. 36, no. 7. Elsevier B.V., pp. 40–75, Jul. 01, 2023. doi: 10.1016/j.cja.2023.05.029.

[45] Y. Q. Zhao *et al.*, “Microstructures of a burn resistant highly stabilized β-titanium alloy,” *Materials Science and Engineering: A*, vol. 282, no. 1–2, pp. 153–157, Apr. 2000, doi: 10.1016/S0921-5093(99)00761-3.

[46] J. O. Hansen, D. Novotnak, M. F. Welter, and J. R. Wood, “Properties and processing of a high strength beta titanium alloy. Proceedings of the Eighth World Conference on Titanium- Titanium ’95: science and technology. Eds, P.A. Blenkinsop, W.J. Evans, H.M. Flower.,” in *Proceedings of the Eighth World Conference on Titanium- Titanium ’95: science and technology. Eds, P.A. Blenkinsop, W.J. Evans, H.M. Flower.*, Birmingham, 1996.

[47] Y. G. Li, M. H. Loretto, D. Rugg, W. Voice “Effect of heat treatment and exposure on microstructure and mechanical properties of Ti–25V–15Cr–2Al–0.2C (wt%),” *Acta Mater*, vol. 49, no. 15, pp. 3011–3017, Sep. 2001, doi: 10.1016/S1359-6454(01)00206-3.

[48] W. Voice, “Burn Resistant Titanium Alloy (BuRTi),” in *Proceedings of the 10th World Conference on Titanium*, Hamburg, Germany, 2003, pp. 2915–2922.

[49] A. K. Singh, A. Kumar, V. Sharma, and P. Kala, “Sustainable techniques in grinding: State of the art review,” *Journal of Cleaner Production*, vol. 269. Elsevier Ltd, Oct. 01, 2020. doi: 10.1016/j.jclepro.2020.121876.

[50] S. Malkin and C. Guo, *Grinding technology: Theory and applications of machining with abrasives.* New York: Industrial Press., 2008.

[51] S. Kalpakjian, S. Schmid, and H. Musa, *Manufacturing Engineering and Technology*, Sixth Edition. Pearson Education, 2009.

[52] W. B. Rowe, *Principles of Modern Grinding Technology*. ISBN:978-0-8155-2018-4, 2009.

[53] M. Gostimirovic, M. Sekulic, and D. Rodic, “Thermal study of the creep feed grinding – a review,” *Journal of Production Engineering*, vol. 23, no. 1, pp. 1–10, Jun. 2020, doi: 10.24867/JPE-2020-01-001.

[54] M. P. Groover, *Fundamentals of Modern Manufacturing: Materials, Processes, and Systems*, 7th edition. ISBN: 978-1-119-47521-7, 2019.

[55] M. C. Shaw, *Principles of Abrasive Processing, Oxford University Press, ISBN 0-19-85021-0*. 1996.

[56] S. H. Wang, “Investigation into the Grinding of Titanium Alloys,” Cranfield University, 2000.

[57] C. Andrew, T. D. Howes, and T. Pearce, *Creep Feed Grinding, Industrial Press Inc*. 1985.

[58] I. D. Marinescu, M. P. Hitchiner, E. Uhlmann, W. B. Rowe, and I. Inasaki, *Handbook of Machining with Grinding Wheels*. CRC Press, 2006. doi: 10.1201/9781420017649.

[59] T. Tawakoli, *High efficiency deep grinding*. London: Mechanical engineering publication Ltd, 1993.

[60] T. W. Liao, K. Li, and S. B. Mcspadden, "Wear mechanisms of diamond abrasives during transition and steady stages in creep-feed grinding of structural ceramics," 2000. [Online]. Available: www.elsevier.comrlocaterwear

[61] Z. Shi and S. Malkin, "Wear of electroplated CBN grinding wheels," *Journal of Manufacturing Science and Engineering, Transactions of the ASME*, vol. 128, no. 1, pp. 110–118, Feb. 2006, doi: 10.1115/1.2122987.

[62] I. Marinescu, W. B. Rowe, B. Dimitrov, and I. Inaski, *Tribology of Abrasive Machining Processes*, 1st ed. William Andrew, 2004.

[63] J. Badger, R. Dražumeric, and P. Krajnik, "Application of the dimensionless Aggressiveness number in abrasive processes," in *Procedia CIRP*, Elsevier B.V., 2021, pp. 361–368. doi: 10.1016/j.procir.2021.09.062.

[64] D. Curtis, H. Krain, A. Winder, and D. Novovic, "Impact of grinding wheel specification on surface integrity and residual stress when grinding Inconel 718," *Proc Inst Mech Eng B J Eng Manuf*, vol. 235, no. 10, pp. 1668–1681, Aug. 2021, doi: 10.1177/0954405420961209.

[65] D. Wenfeng, X. Jiuhua, C. Zhenzhen, S. Honghua, and F. Yucan, "Grindability and surface integrity of cast nickel-based superalloy in creep feed grinding with brazed CBN abrasive wheels," *Chinese Journal of Aeronautics*, vol. 23, no. 4, pp. 501–510, Aug. 2010, doi: 10.1016/S1000-9361(09)60247-8.

[66] K. Brach, D. M. Pai, E. Ratterman, and M. C. Shaw, "Grinding Forces and Energy," *Journal of Engineering for Industry*, vol. 110, no. 1, pp. 25–31, Feb. 1988, doi: 10.1115/1.3187838.

[67] A. A. O. Tay, "A review of methods of calculating machining temperature," *J Mater Process Technol*, vol. 36, no. 3, pp. 225–257, Mar. 1993, doi: 10.1016/0924-0136(93)90033-3.

[68] R. J. Gu, M. Shillor, G. C. Barber, and T. Jen, "SCIENCE~DIFIECT • MATHEMATICAL AND COMPUTER MODELLING Thermal Analysis of the Grinding Process," 2004, doi: 10.1016/j.mcm2003.07.009.

[69] A. Narayan and V. Yadava, "Investigation of temperature distribution in the workpiece during creep feed surface grinding using finite element method," *Materials and Manufacturing Processes*, vol. 27, no. 10, pp. 1101–1109, Oct. 2012, doi: 10.1080/10426914.2011.654154.

[70] N. Ortega, H. Bravo, I. Pombo, J. A. Sánchez, and G. Vidal, "Thermal Analysis of Creep Feed Grinding," in *Procedia Engineering*, Elsevier Ltd, 2015, pp. 1061–1068. doi: 10.1016/j.proeng.2015.12.596.

[71] H. Carslaw and J. C. Jaeger, "Conduction of heat in solids," *J Mech Phys Solids*, vol. 7, no. 4, p. 288, Oct. 1959, doi: 10.1016/0022-5096(59)90029-8.

[72] J. C. Jaeger, “Moving Sources of Heat and the Temperature at Sliding Contacts,” in *Proceedings of the Royal Society of New South Wales*, 1942, pp. 203–224.

[73] W. B. Rowe,M N Morgan, S. C. E. Black, and B. Mills, “A Simplified Approach to Control of Thermal Damage in Grinding.”

[74] Outwater. J.O and M. C. Shaw, “Surface Temperatures in Grinding,” *Trans ASME*, pp. 73–78, 1952.

[75] R. S. Hahn, “On the Nature of the Grinding Process,” in *Proceedings of 3rd MTDR Conference*, Lodon, 1963, pp. 129–154.

[76] Makino, Suto, and Fokushima, “An Experimental Investigation of the Grinding process,” *Journal of Mech. Laboratory of Japan*, vol. 12, p. 17, 1966.

[77] N. R. DesRuisseaux and R. D. Zerkle, “Temperature in Semi-Infinite and Cylindrical Bodies Subjected to Moving Heat Sources and Surface Cooling,” *J Heat Transfer*, vol. 92, no. 3, pp. 456–464, Aug. 1970, doi: 10.1115/1.3449689.

[78] Howes. T.D, K. Neailey, and A. J. Harrison, “’Fluid Film Boiling in Shallow cut Grinding,” *Annals of the CIRP*, pp. 223–226, 1987.

[79] Lavine. A.S, “Thermal Aspects of Grinding: Heat Transfer to Workpiece, Wheel and Fluid,” *Collected Papers in Heat Transfer, ASME HTD*, vol. 123, pp. 267–274, 1989.

[80] H. K. Tonshoff, H.-G. Wobker, and G. Brunner, “CBN Grinding with Small Wheels.”

[81] W. B. Rowe and T. Jin, “Temperatures in high efficiency deep grinding (HEDG),” *CIRP Ann Manuf Technol*, vol. 50, no. 1, pp. 205–208, 2001, doi: 10.1016/S0007-8506(07)62105-2.

[82] W. B. Rowe, “Temperatures in grinding-a review,” *Journal of Manufacturing Science and Engineering, Transactions of the ASME*, vol. 139, no. 12. American Society of Mechanical Engineers (ASME), Dec. 01, 2017. doi: 10.1115/1.4036638.

[83] W. B. Rowe, “Thermal analysis of high efficiency deep grinding,” *Int J Mach Tools Manuf*, vol. 41, no. 1, pp. 1–19, Jan. 2001, doi: 10.1016/S0890-6955(00)00074-2.

[84] W. B. Rowe, M. N. Morganl, A. Batakol, and T. Jin2, “Energy and temperature analysis in grinding,” 2003. [Online]. Available: www.witpress.com,

[85] A. D. Batako, W. B. Rowe, and M. N. Morgan, “Temperature measurement in high efficiency deep grinding,” *Int J Mach Tools Manuf*, vol. 45, no. 11, pp. 1231–1245, Sep. 2005, doi: 10.1016/j.ijmachtools.2005.01.013.

[86] T. Jin and D. J. Stephenson, “A study of the convection heat transfer coefficients of grinding fluids,” *CIRP Annals*, vol. 57, no. 1, pp. 367–370, 2008, doi: 10.1016/j.cirp.2008.03.074.

[87] D. J. Stephenson, T. Jin, and J. Corbett, “High Efficiency Deep Grinding of a Low Alloy Steel with Plated CBN Wheels,” *CIRP Annals*, vol. 51, no. 1, pp. 241–244, 2002, doi: 10.1016/S0007-8506(07)61508-X.

[88] R. Komanduri and Z. B. Hou, “A review of the experimental techniques for the measurement of heat and temperatures generated in some manufacturing processes and tribology,” 2001. [Online]. Available: www.elsevier.com/locate/triboint

[89] H. K. Tonshoff, T. Friemuth, and J. C. Becker, “Process Monitoring in Grinding.”

[90] J. Hwang, S. Kompella, S. Chandrasekar, and T. N. Farris, “Measurement of Temperature Field in Surface Grinding Using Infra-Red (IR) Imaging System,” *J Tribol*, vol. 125, no. 2, pp. 377–383, Apr. 2003, doi: 10.1115/1.1537748.

[91] T. Ueda, H. Tanaka, A. Torii, and T. Matsuo, “Measurement of Grinding Temperature of Active Grains Using Infrared Radiation Pyrometer with Optical Fiber,” *CIRP Ann Manuf Technol*, vol. 42, no. 1, pp. 405–408, Jan. 1993, doi: 10.1016/S0007-8506(07)62472-X.

[92] D. Liu, G. Wang, Z. Nie, and Y. (Kevin) Rong, “An in-situ infrared temperature-measurement method with back focusing on surface for creep-feed grinding,” *Measurement (Lond)*, vol. 94, pp. 645–652, Dec. 2016, doi: 10.1016/j.measurement.2016.09.013.

[93] T. Kato and H. Fujii, “Temperature Measurement of Workpiece in Surface Grinding by PVD Film Method,” *J Manuf Sci Eng*, vol. 119, no. 4B, pp. 689–694, Nov. 1997, doi: 10.1115/1.2836810.

[94] T. Kato and H. Fujii, “Temperature Measurement of Workpieces in Conventional Surface Grinding,” *J Manuf Sci Eng*, vol. 122, no. 2, pp. 297–303, May 2000, doi: 10.1115/1.538918.

[95] S. Kato, K. Yamaguchi, Y. Watanabe, and Y. Hiraiwa, “Measurement of Temperature Distribution Within Tool Using Powders of Constant Melting Point,” *Journal of Engineering for Industry*, vol. 98, no. 2, pp. 607–613, May 1976, doi: 10.1115/1.3438946.

[96] I. M. Walton, D. J. Stephenson, and A. Baldwin, “The measurement of grinding temperatures at high specific material removal rates,” *Int J Mach Tools Manuf*, vol. 46, no. 12–13, pp. 1617–1625, Oct. 2006, doi: 10.1016/j.ijmachtools.2005.09.020.

[97] R. P. Upadhyaya and S. Malkin, “Thermal aspects of grinding with electroplated CBN wheels,” *J Manuf Sci Eng*, vol. 126, no. 1, pp. 107–114, 2004, doi: 10.1115/1.1644547.

[98] C. Guo, Y. Wu, V. Varghese, and S. Malkin, “Temperatures and Energy Partition for Grinding with Vitrified CBN Wheels.”

[99] B. Shen, G. Xiao, C. Guo, S. Malkin, and A. J. Shin, “Thermocouple fixation method for grinding temperature measurement,” *Journal of Manufacturing Science and Engineering, Transactions of the ASME*, vol. 130, no. 5, pp. 0510141–0510148, Oct. 2008, doi: 10.1115/1.2976142.

[100] X. Xu and S. Malkin, “Comparison of methods to measure grinding temperatures,” *Journal of Manufacturing Science and Engineering, Transactions of the ASME*, vol. 123, no. 2, pp. 191–195, 2001, doi: 10.1115/1.1369358.

[101] S. C. E. Black and P. D. Thesis, “THE EFFECT OF ABRASIVE PROPERTIES ON THE SURFACE INTEGRITY OF GROUND FERROUS MATERIALS,” 1996.

[102] H. Huang and X. P. Xu, “Interfacial interactions between diamond disk and granite during vertical spindle grinding,” *Wear*, vol. 256, no. 6, pp. 623–629, Mar. 2004, doi: 10.1016/j.wear.2003.10.005.

[103] K. Peng *et al.*, “Convective cooling and heat partitioning to grinding chips in high speed grinding of a nickel based superalloy,” *Journal of Mechanical Science and Technology*, vol. 35, no. 6, pp. 2755–2767, Jun. 2021, doi: 10.1007/s12206-021-0545-9.

[104] N. K. Kim’, C. Guo2, and S. Malkon2, “Heat Flux Distribution and Energy Partition in Creep-Feed Grinding.”

[105] J. A. Webster, “Improving surface integrity and economics of grinding by optimum coolant application, with consideration of abrasive tool and process regime,” *Proc Inst Mech Eng B J Eng Manuf*, vol. 221, no. 12, pp. 1665–1675, 2007, doi: 10.1243/09544054JEM804.

[106] E. Brinksmeier, C. Heinzel, and M. Wittmann, “Friction, Cooling and Lubrication in Grinding.”

[107] J. K. Steffen, A. Warkentin, R. Bauer, and C. E. Becze, “Effect of jet coherency on burn-out for non-continuous dress creep-feed grinding,” in *Transactions of the North American Manufacturing Research Institute of SME*, 2005, pp. 367–374.

[108] G. Singh *et al.*, “Progress for sustainability in the mist assisted cooling techniques: a critical review,” *The International Journal of Advanced Manufacturing Technology*, vol. 109, no. 1–2, pp. 345–376, Jul. 2020, doi: 10.1007/s00170-020-05529-x.

[109] R. A. Irani, R. J. Bauer, and A. Warkentin, “A review of cutting fluid application in the grinding process,” *Int J Mach Tools Manuf*, vol. 45, no. 15, pp. 1696–1705, 2005, doi: 10.1016/j.ijmachtools.2005.03.006.

[110] N. E. Ye, Z. Zhou, and T. R. A. Pearce, “Some observations on profile wear in creep feed grinding”, Aero-engine Factory, Hunan Prouince (chic), 1983.

[111] S. Tsukuda and H. Yasui, “Influence of fluid type on wet grinding temperature” Bulletin of the Japen society of precision engineering, vol. 17, no. 2, pp. 133–134, 1983.

[112] S.B. Wang and H.-S. Kou, “Cooling effectiveness of cutting fluid in creep feed grinding,” *International Communications in Heat and Mass Transfer*, vol. 24, no. 6, pp. 771–783, Oct. 1997, doi: 10.1016/S0735-1933(97)00064-X.

[113] A. K. Chattopadhyay and H. E. Hintermann, “On Performance of Brazed Single-Layer CBN Wheel,” *CIRP Annals*, vol. 43, no. 1, pp. 313–317, 1994, doi: 10.1016/S0007-8506(07)62221-5.

[114] J. D. Campbell, “A Comparison of Fluids used to Superabrasively Machine a Titanium Alloy,” 1991. [Online]. Available: https://asmedigitalcollection.asme.org/GT/proceedings-pdf/GT1991/78996/V002T02A021/2400637/v002t02a021-91-gt-321.pdf

[115] M. N. Morgan, A. R. Jackson, H. Wu, V. Baines-Jones, A. Batako, and W. B. Rowe, “Optimisation of Fluid Application in Grinding.”

[116] V. K. Gviniashvili, N. H. Woolley, and W. B. Rowe, “Useful coolant flowrate in grinding,” *Int J Mach Tools Manuf*, vol. 44, no. 6, pp. 629–636, May 2004, doi: 10.1016/j.ijmachtools.2003.12.005.

[117] J. A. Webster, C. Cui, and R. B. Mindek, “Grinding Fluid Application System Design,” 1995.

[118] D. Y. Pimenov *et al.*, “Improvement of machinability of Ti and its alloys using cooling-lubrication techniques: A review and future prospect,” *Journal of Materials Research and Technology*, vol. 11. Elsevier Editora Ltda, pp. 719–753, 2021. doi: 10.1016/j.jmrt.2021.01.031.

[119] S. Pervaiz, S. Anwar, I. Qureshi, and N. Ahmed, “Recent Advances in the Machining of Titanium Alloys using Minimum Quantity Lubrication (MQL) Based Techniques,” *International Journal of Precision Engineering and Manufacturing-Green Technology*, vol. 6, no. 1, pp. 133–145, Jan. 2019, doi: 10.1007/s40684-019-00033-4.

[120] B. Sen, M. Mia, G. M. Krolczyk, U. K. Mandal, and S. P. Mondal, “Eco-Friendly Cutting Fluids in Minimum Quantity Lubrication Assisted Machining: A Review on the Perception of Sustainable Manufacturing,” *International Journal of Precision Engineering and Manufacturing-Green Technology*, vol. 8, no. 1, pp. 249–280, Jan. 2021, doi: 10.1007/s40684-019-00158-6.

[121] L. de Martini Fernandes, J. Lopes, F. Ribeiro, R. Gallo, H. Razuk, L. Sanchez, P. Aguiar, H. Mello and E. Bianch, “Thermal model for surface grinding application,” *The International Journal of Advanced Manufacturing Technology*, vol. 104, no. 5–8, pp. 2783–2793, Oct. 2019, doi: 10.1007/s00170-019-04101-6.

[122] J. C. Lopes, C. Ventura, R. L. Rodriguez, A.G. Talon, R. S. Volpato, B. Sato, H. Mello, P. Aguiar and E. Bianchi, “Application of minimum quantity lubrication with addition of water in the grinding of alumina,” *The International Journal of Advanced Manufacturing Technology*, vol. 97, no. 5–8, pp. 1951–1959, Jul. 2018, doi: 10.1007/s00170-018-2085-8.

[123] R. L. Rodriguez, J. C. Lopes, R. Hildebrandt, R. Perez, A. Diniz, L. Sanchez, A. Rodrigues, H. Mello, P. Aguiar and E. Bianchi, “Evaluation of grinding process using simultaneously MQL technique and cleaning jet on grinding wheel surface,” *J Mater Process Technol*, vol. 271, pp. 357–367, Sep. 2019, doi: 10.1016/j.jmatprotec.2019.03.019.

[124] R. M’Saoubi *et al.*, “High performance cutting of advanced aerospace alloys and composite materials,” *CIRP Annals*, vol. 64, no. 2, pp. 557–580, 2015, doi: 10.1016/j.cirp.2015.05.002.

[125] B. Griffiths, *Manufacturing Surface Technology-Surface Integrity and Functional Performance*. London, 2001.

[126] British Standard, BS 1134-1, Assessment of Surface Texture. Part 1: Methods and Instrumentation, 1988.

[127] British Standard, BS 1134-2, Assessment of Surface Texture. Part 2: Guidance and General Information, 1990 (and 2010).

[128] Q. Zeng, “Surface integrity evaluation and the effect of machining-induced surface integrity characteristics on parts performance,” University of Strathclyde, Glasgow, Scotland, 2015.

[129] B. Bhushan, *Modern Tribology Handbook, Two Volume Set*. CRC Press, 2000. doi: 10.1201/9780849377877.

[130] ISO 4288:1996 Geometrical Product Specifications (GPS) — Surface texture: Profile method — Rules and procedures for the assessment of surface texture.

[131] B. He, H. Zheng, S. Ding, R. Yang, and Z. Shi, “A review of digital filtering in evaluation of surface roughness,” *Metrology and Measurement Systems*, vol. 28, no. 2. Polska Akademia Nauk, pp. 217–253, 2021. doi: 10.24425/mms.2021.136606.

[132] ANSI/ASME B46.1-1988: ‘Structure of the Surface Roughness, Surface Waviness and Processing of Grain’.

[133] International Organization for Standardization, ISO 4287, Geometrical Product Specifications—Surface Texture: Profile Method-Terms, Definitions and Surface Texture Parameters, Switzerland, 1997.

[134] International Organization for Standardization, ISO 13565-2, Surface Texture: Profile Method—Surfaces Having Stratifying Functional Properties, Part 2: Height Characterisation using the Linear Material Ratio Curve, Switzerland, 1996.

[135] International Organization for Standardization, ISO 12085, Surface Texture: Profile Method—Motif Parameters, Switzerland, 1996.

[136] M. Hamed, Y. Zedan, A. M. Samuel, H. W. Doty, and F. H. Samuel, “Milling parameters of Al-Cu and Al-Si cast alloys,” *The International Journal of Advanced Manufacturing Technology*, vol. 104, no. 9–12, pp. 3731–3743, Oct. 2019, doi: 10.1007/s00170-019-04075-5.

[137] K. Stout and L. Blunt, *Three-Dimensional Surface Topography*, 2nd Edition. 2000.

[138] ISO 25178-2: Geometrical product specifications (GPS) — Surface texture: Areal — Part 2: Terms, definitions, and surface texture parameters, 2012 (revised in 2021).

[139] Q. Zeng, Y. Qin, W. Chang, and X. Luo, “Correlating and evaluating the functionality-related properties with surface texture parameters and specific characteristics of machined components,” *Int J Mech Sci*, vol. 149, pp. 62–72, Dec. 2018, doi: 10.1016/j.ijmecsci.2018.09.044.

[140] J. F. Senge, A. H. Astaraee, P. Dłotko, S. Bagherifard, and W. A. Bosbach, “Extending conventional surface roughness ISO parameters using topological data analysis for shot peened surfaces,” *Sci Rep*, vol. 12, no. 1, p. 5538, Apr. 2022, doi: 10.1038/s41598-022-09551-9.

[141] M.Field and J.F. Kahles, (1971). Review of Surface Integrity of Machined Components, Annals of the CIRP, Vol. 20/2, pp. 153-163.

[142] Z. Liao *et al.*, “Surface integrity in metal machining - Part I: Fundamentals of surface characteristics and formation mechanisms,” *International Journal of Machine Tools and Manufacture*, vol. 162. Elsevier Ltd, Mar. 01, 2021. doi: 10.1016/j.ijmachtools.2020.103687.

[143] ANSI B211.1, American National Standards on Surface Integrity. Society of Manufacturing Engineers (SME),1986.

[144] D. Ulutan and T. Ozel, “Machining induced surface integrity in titanium and nickel alloys: A review,” *International Journal of Machine Tools and Manufacture*, vol. 51, no. 3. pp. 250–280, Mar. 2011. doi: 10.1016/j.ijmachtools.2010.11.003.

[145] W. Ding, L. Zhang, Z. Li, Y. Zhu, H. Su, and J. Xu, “Review on grinding-induced residual stresses in metallic materials,” *International Journal of Advanced Manufacturing Technology*, vol. 88, no. 9–12. Springer London, pp. 2939–2968, Feb. 01, 2017. doi: 10.1007/s00170-016-8998-1.

[146] B. A. Cowles, “High cycle fatigue in aircraft gas turbines-an industry perspective,” Kluwer Academic Publishers, 1996.

[147] S. K. Bhaumik, M. Sujata, and M. A. Venkataswamy, “Fatigue failure of aircraft components,” *Eng Fail Anal*, vol. 15, no. 6, pp. 675–694, Sep. 2008, doi: 10.1016/j.engfailanal.2007.10.001.

[148] X. Li, Y. Wang, R. Xu, S. Yang, C. Guan, and Y. Zhou, “Influence of surface integrity on fatigue behavior of Inconel 718 and Ti6Al4V workpieces with CBN electroplated wheel,” *International Journal of Advanced Manufacturing Technology*, vol. 102, no. 5–8, pp. 2345–2356, Jun. 2019, doi: 10.1007/s00170-019-03345-6.

[149] D. Novovic, D. K. Aspinwall, R. C. Dewes, P. Bowen, and B. Griffiths, “The effect of surface and subsurface condition on the fatigue life of Ti–25V–15Cr–2Al–0.2C %wt alloy,” *CIRP Ann Manuf Technol*, vol. 65, no. 1, pp. 523–528, 2016, doi: 10.1016/j.cirp.2016.04.074.

[150] D. Bacon and G. E. Dieter, *Mechanical Metallurgy*. McGraw-Hill Education, 1989.

[151] P. Ross, *Taguchi Techniques for Quality Engineering*, 2nd Edition. McGraw-Hill, 1988.

[152] British Standards Institution, (1986). ‘Statistical Terminology - Part 3: Glossary of Terms Relating to The Design of Experiments’, BS5532, Part3.

[153] D. Bhaduri *et al.*, “A study on ultrasonic assisted creep feed grinding of nickel-based superalloys,” in *Procedia CIRP*, Elsevier, 2012, pp. 359–364. doi: 10.1016/j.procir.2012.04.064.

[154] L. Tarasov, “How to Grinding Titanium,” *American Machinist*, vol. 96, no. 23. pp. 135–146, 1952.

[155] B. C. T Yang and M. C. Shaw, “The Grinding of Titanium Alloys,” 1955. [Online]. Available: http://asmedigitalcollection.asme.org/fluidsengineering/article-pdf/77/5/645/6894799/645_1.pdf

[156] D. Stewart and H. Soderstrom, “Residual Stress Versus Cutting Fluid Selection When Grinding High Temperature Alloys,” *Lubrication Engineering,* pp. 286–290, 1961.

[157] W. P. Koster and M. Field, “Effect of Machining Variables on The Surface and Structural Integrity of Titanium,” in *North American Metalworking Research Conference*, 1973, pp. 67–87.

[158] G. Sayutin and V. Nosenko, “A Study of Microchemical Changes in The Surface of Titanium Alloys During Grinding,” *Trenie I Iznos*, vol. 4, pp. 348–352, 1983.

[159] N. Larinov and G. Sayutin, “Study of Interaction of Materials Being Machined with Abrasive Tool in Grinding in Inert and Air Media,” *renie I Iznos.,* vol. 7, pp. 564–567, 1986.

[160] A. Sagarda, “Grinding Intractable Materials With Diamond And CBN Wheels,” *Machines & Tooling*, vol. XLV, pp. 43–44, 1974.

[161] N. Kumagai and K. Kamei, “Grinding of titanium with jet infusion of grinding fluid,” in *Proceeding 5’ international conference on titanium, titanium science and technology*, Munich, Germany, 1984, pp. 1015–1022.

[162] N. Kumagai, K. Kamei, and S. lnoue, “A study on grinding of titanium,” 1985.

[163] N. Kumagai, K. Kamei, and Y. Tanaka, “Effect of diamond wheel grain size on the grindinability of Ti-6Al-4V,” *Titanium 92 science and technology*, pp. 1617–1624, 1993.

[164] K. Kumar, “Superabrasive grinding of aerospace materials,” in *Diamond & CBN ultrahard materials symposium ’93*, Windsor, Canada, 1993, pp. 73–81.

[165] S. S. Silin, B. N. Leonov, V. A. Khrul’kov, A. v Lobanov, V. Poletaev, and E. B. Danchenko, “Special features of deep grinding of titanium aIloys,” *Soviet engineering research*, pp. 71–74, 1989.

[166] J. Campbell, “Comparison Of Reciprocating And Creep Feed Superabrasive Machining Of Titanium,” *SME, MR910215*. 1991.

[167] V. Nosenko, N. F. Larionov, N. Egorov, and M. P. Volkov, “Testing of abrasive wheels and coolants while deep grinding of titanium alloys,” *Soviet engineering research*, vol. 9, pp. 69–71, 1989.

[168] G. Guo, Z. Liu, Q. An, and M. Chen, “Experimental investigation on conventional grinding of Ti-6Al-4V using SiC abrasive,” *International Journal of Advanced Manufacturing Technology*, vol. 57, no. 1–4, pp. 135–142, Nov. 2011, doi: 10.1007/s00170-011-3272-z.

[169] A. V. de Mello, R. B. de Silva, Á. R. Machado, R. V. Gelamo, A. E. Diniz, and R. F. M. de Oliveira, “Surface Grinding of Ti-6Al-4V Alloy with SiC Abrasive Wheel at Various Cutting Conditions,” in *Procedia Manufacturing*, Elsevier B.V., 2017, pp. 590–600. doi: 10.1016/j.promfg.2017.07.057.

[170] A. Ahmed, D. Sarhan, W. P. Hong, and M. Sayuti, “Precision-Grinding-of-Titanium-Ti-6Al-4V-Alloy-Using-Nanolubrication,” *International Journal of Materials and Metallurgical Engineering*, vol. 10, no. No:3, 2016.

[171] X. Cui *et al.*, “Grindability of titanium alloy using cryogenic nanolubricant minimum quantity lubrication,” *J Manuf Process*, vol. 80, pp. 273–286, Aug. 2022, doi: 10.1016/j.jmapro.2022.06.003.

[172] J. Elanchezhian, M. Pradeep Kumar, and G. Manimaran, “Grinding titanium Ti-6Al-4V alloy with electroplated cubic boron nitride wheel under cryogenic cooling,” *Journal of Mechanical Science and Technology*, vol. 29, no. 11, pp. 4885–4890, Nov. 2015, doi: 10.1007/s12206-015-1036-7.

[173] Z. Shi and H. Attia, “High performance grinding of titanium alloys with electroplated diamond wheels,” in *Procedia CIRP*, Elsevier B.V., 2020, pp. 178–181. doi: 10.1016/j.procir.2020.11.008.

[174] A. Naskar, A. Choudhary, and S. Paul, “Wear mechanism in high-speed superabrasive grinding of titanium alloy and its effect on surface integrity,” *Wear*, vol. 462–463, Dec. 2020, doi: 10.1016/j.wear.2020.203475.

[175] B. Zhao, W. Ding, G. Xiao, J. Zhao, and Z. Li, “Self-sharpening property of porous metal-bonded aggregated cBN wheels during the grinding of Ti–6Al–4V alloys,” *Ceram Int*, vol. 48, no. 2, pp. 1715–1722, Jan. 2022, doi: 10.1016/j.ceramint.2021.09.250.

[176] Y. Seid Ahmed and L. W. H. González, “Ti6Al4V grinding using different lubrication modes for minimizing energy consumption,” *International Journal of Advanced Manufacturing Technology*, vol. 126, no. 5–6, pp. 2387–2405, May 2023, doi: 10.1007/s00170-023-11203-9.

[177] U. Teicher, K. Künanz, A. Ghosh, and A. B. Chattopadhyay, “Performance of diamond and CBN single-layered grinding wheels in grinding titanium,” *Materials and Manufacturing Processes*, vol. 23, no. 3, pp. 224–227, Mar. 2008, doi: 10.1080/10426910701860541.

[178] Y. Changyong, X. Jiuhua, D. Wenfeng, C. Zhenzhen, and F. Yucan, “Dimension accuracy and surface integrity of creep feed ground titanium alloy with monolayer brazed CBN shaped wheels,” *Chinese Journal of Aeronautics*, vol. 23, no. 5, pp. 585–590, Oct. 2010, doi: 10.1016/S1000-9361(09)60258-2.

[179] S. V. Nosenko, V. A. Nosenko, and A. A. Koryazhkin, “The effect of the operating speed and wheel characteristics on the surface quality at creep-feed grinding titanium alloys,” in *Solid State Phenomena*, Trans Tech Publications Ltd, 2018, pp. 369–374. doi: 10.4028/www.scientific.net/SSP.284.369.

[180] B. Zhao, Q. Huang, M. Zhang, W. Ding, and J. Xu, “Developing a novel porous aggregated cBN wheel and evaluating its grinding performance during machining Ti–6Al–4 V alloys,” *International Journal of Advanced Manufacturing Technology*, vol. 124, no. 7–8, pp. 2781–2790, Feb. 2023, doi: 10.1007/s00170-022-10706-1.

[181] T. Nolan, “Wet Surface Grinding Of NiAl, 809, 817 & TiAl,” *Industrial, Internal Evaluation Bulletin No. AD-91179*. 1991.

[182] Carborundum Abrasives GB Ltd, ‘Grinding Of XD Modified TiAl Alloys’, Personal communication, (1995), *Personal communication*.

[183] H. Zhang, A. Mantle, and M. Wise, “Investigation Of Subsurface Damage Of Gamma Titanium Aluminide After Creep Feed Grinding,” in *Procs. of the Eighth World Conference on Titanium*, 1995, pp. 497–503.

[184] R. Hood, D. K. Aspinwall, and W. Voice, “Creep feed grinding of a gamma titanium aluminide intermetallic alloy using SiC abrasives,” *J Mater Process Technol*, vol. 191, no. 1–3, pp. 210–214, Aug. 2007, doi: 10.1016/j.jmatprotec.2007.03.081.

[185] R. Hood, P. Cooper, D. K. Aspinwall, S. L. Soo, and D. S. Lee, “Creep feed grinding of γ-TiAl using single layer electroplated diamond superabrasive wheels,” *CIRP J Manuf Sci Technol*, vol. 11, pp. 36–44, Nov. 2015, doi: 10.1016/j.cirpj.2015.07.001.

[186] D. Bhaduri *et al.*, “Ultrasonic assisted creep feed grinding of gamma titanium aluminide using conventional and superabrasive wheels,” *CIRP Ann Manuf Technol*, vol. 66, no. 1, pp. 341–344, 2017, doi: 10.1016/j.cirp.2017.04.085.

[187] X. Xi, W. Ding, Z. Ww, and L. Anggei, “Performance evaluation of creep feed grinding of γ-TiAl intermetallics with electroplated diamond wheels,” *Chinese Journal of Aeronautics*, vol. 34, no. 6, pp. 100–109, Jun. 2021, doi: 10.1016/j.cja.2020.04.031.

[188] [Online]. Available: https://www.masterfluids.com/eu/en/data-sheet/di.php?pid=C270.

[189] J. R. Besse, (1987). Practical Creep Feed Grinding, SME Technical Paper, MR87-820.

[190] [Online]. Available: https://www.omega.co.uk/temperature/z/thermocoupleresponsetime.html.

[191] [Online]. Available: br.omega.com/omegaFiles/temperature/pdf/OB_OMEGABOND_AIR_SET.pdf.

[192] ANSI/ASME B46.1 - 2002 Surface Texture, Surface Roughness, Waviness and Lay, American Society of Mechanical Engineers, 2002.

[193] J. GUO, H. FU, B. PAN, and R. KANG, “Recent progress of residual stress measurement methods: A review,” *Chinese Journal of Aeronautics*, vol. 34, no. 2. Elsevier B.V., pp. 54–78, Feb. 01, 2021. doi: 10.1016/j.cja.2019.10.010.

[194] S. A. Bentley and D. K. Aspinwall, “The Identification of Significant Operating Parameters when Conventional Abrasive Creep Feed Grinding a Gamma Titanium Aluminide Intermetallic.”

[195] H. Dagnall, *Exploring Surface Texture*. Leicester, UK, 1986.

[196] T. R. Thomas, *Rough surfaces,* 2nd ed. Imperial College Press, London, 1999.

[197] H. B. Sharman, “Influence of sample size and relationships between the common surface texture parameters.”

[198] T. W. Hwang, C. J. Evans, E. P. Whitenton, and S. Malkin, “High Speed Grinding of Silicon Nitride With Electroplated Diamond Wheels, Part 1: Wear and Wheel Life,” 2000. [Online]. Available: http://asmedigitalcollection.asme.org/manufacturingscience/article-pdf/122/1/32/5812273/32_1.pdf

[199] T. W. Hwang, C. J. Evans, and S. Malkin, “Size effect for specific energy in grinding of silicon nitride.”

[200] W. B. Rowe, S. C. E. Black, B. Mills, H. S. Qi, and M. N. Morgan, “Experimental Investigation of Heat Transfer in Grinding.”

[201] D. K. Aspinwall, R. C. Dewes, J. M. Burrows, M. Bailey, S. L. Soo, M. Cook. The use of diamond and cubic boron nitride (CBN) mounted grinding points for the machining of nickel based superalloys. In: Proc of the INTERTECH 2003 Conference, Vancouver: August 2003. CD-ROM.

[202] S. A. Bentley, A. L. Mantle, and D. K. Aspinwall, “The effect of machining on the fatigue strength of a gamma titanium aluminide intertmetallic alloy.”

[203] T. Chen *et al.*, “On the residual stresses of turbine blade root of γ-TiAl intermetallic alloys induced by non-steady-state creep feed profile grinding,” *J Manuf Process*, vol. 82, pp. 800–817, Oct. 2022, doi: 10.1016/j.jmapro.2022.08.051.

[204] T. W. Hwang, C. J. Evans, and S. Malkin, “High Speed Grinding of Silicon Nitride With Electroplated Diamond Wheels, Part 2: Wheel Topography and Grinding Mechanisms,” 2000. [Online]. Available: http://asmedigitalcollection.asme.org/manufacturingscience/article-pdf/122/1/42/5810993/42_1.pdf

[205] R. Ohlsson, B. G. Ros6n, and J. Westberg, “The Interrelationship of 3D Surface Characterisation Techniques with Standardised 2D Techniques.”

[206] S. A. Niknam, R. Khettabi, and V. Songmene, “Machinability and Machining of Titanium Alloys: A Review,” 2014, pp. 1–30. doi: 10.1007/978-3-662-43902-9_1.

[207] W. Ding, L. Barbara, Y Zhu, Z Li, Y. C. Fu, S. Honghua and J. Xu, “Review on monolayer CBN superabrasive wheels for grinding metallic materials,” *Chinese Journal of Aeronautics*, vol. 30, no. 1. Chinese Journal of Aeronautics, pp. 109–134, Feb. 01, 2017. doi: 10.1016/j.cja.2016.07.003.

Appendix A: Assessments of the correlations between grinding inputs and outputs

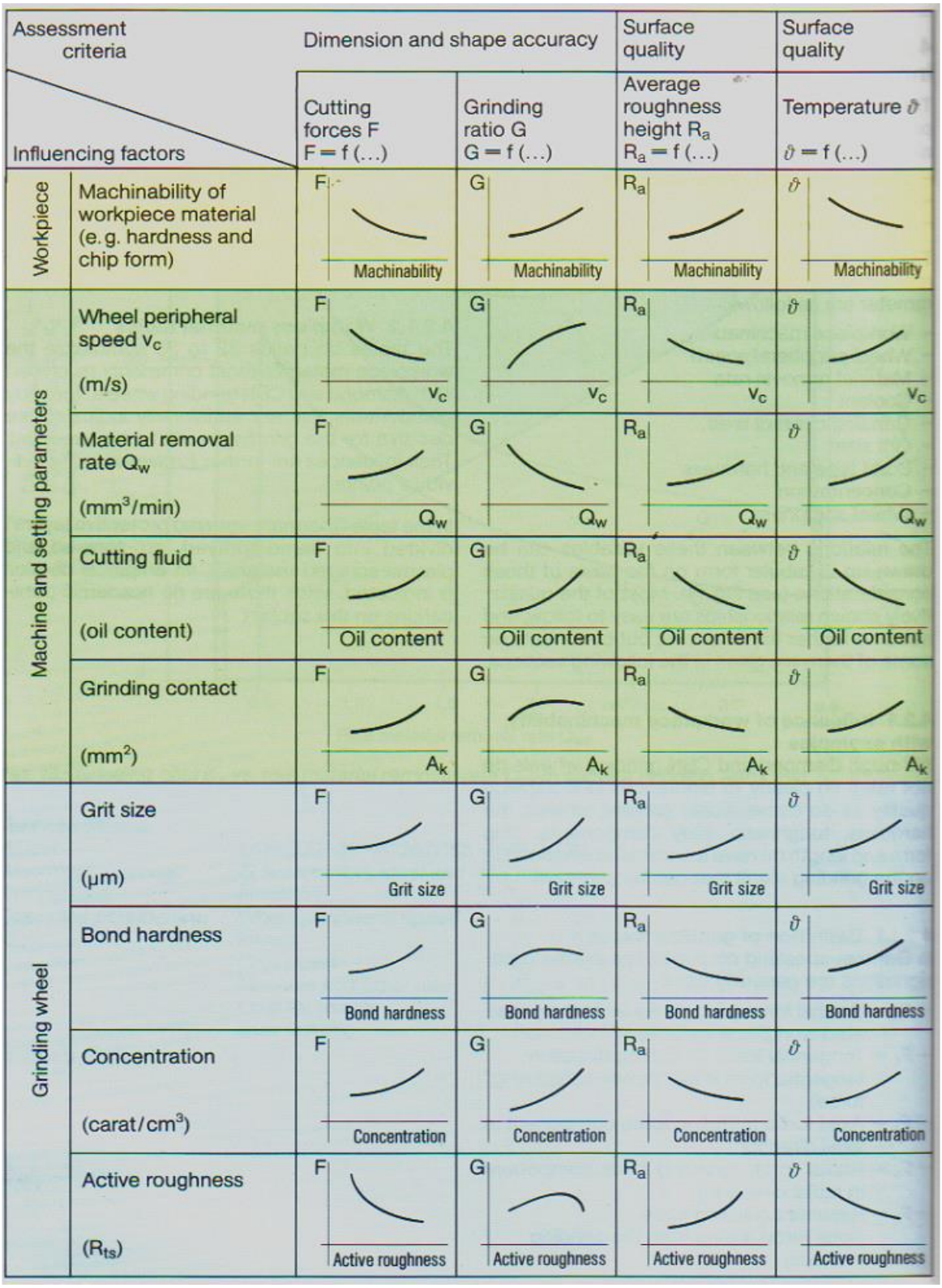


Figure A1: The influence of inputs characteristics on grinding outputs [7]

Appendix B: Grinding wheel standard coding systems

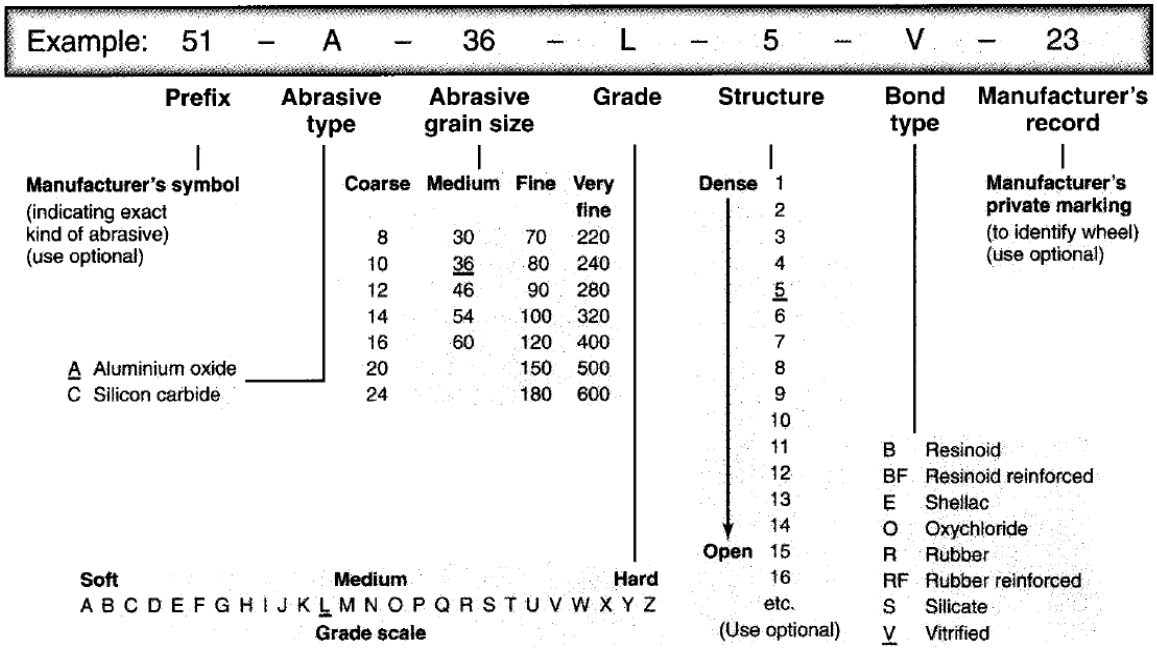


Figure B1: The standard coding system for conventional abrasive wheels [49]

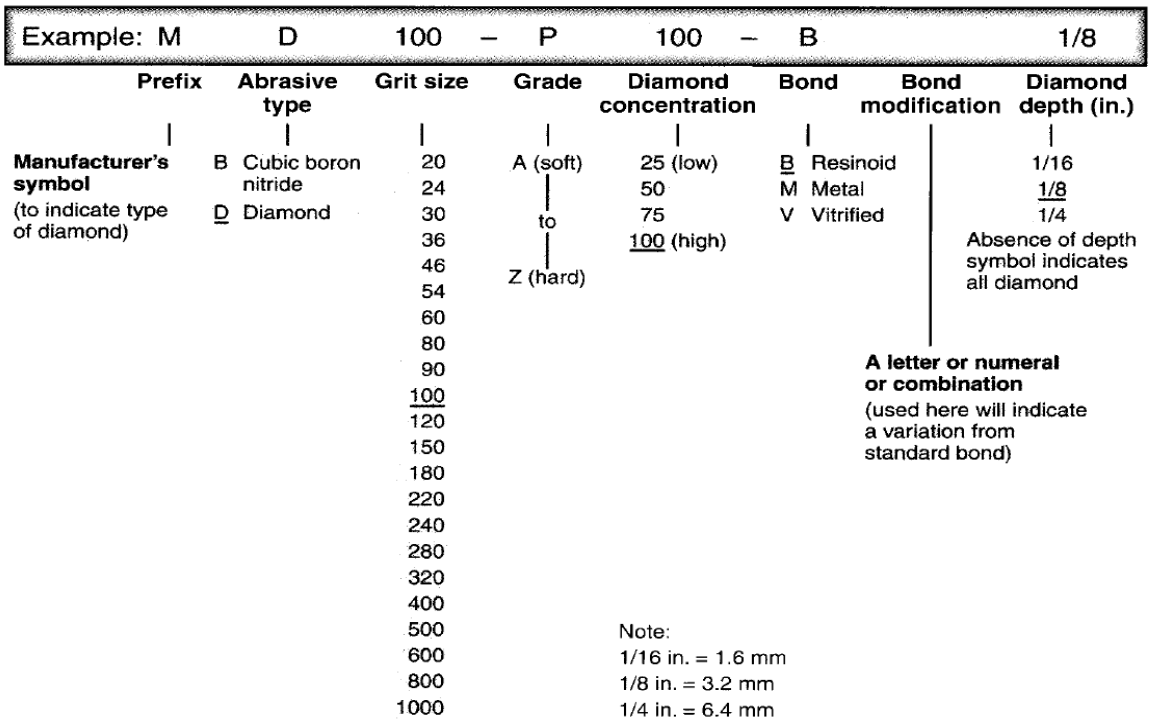


Figure B2: The standard coding system for super abrasive wheels [51]

Appendix C: Surface integrity evaluation techniques

Table C1: A list of techniques used to examine surface inhomogeneity [15], [133]

Metallurgical inhomogeneity	**Non-destructive techniques**			**Destructive** techniques
	Commonly employed	Specialised	Possible with further developments	
Macrocracks	Visual inspection Binocular inspection Magnetic particle Penetrant Eddy current Acid macroetch	Ultrasonic pulse echo Automatic optical scanning	Acoustic impact	Optical metallography
Microcracks	Binocular inspection High sensitivity fluorescent penetrant Magnetic particle	Ultrasonic pulse echo, surface waves and lambda waves	Radioactive gas penetrant High frequency ultrasonic Acoustic impact Surface electrical resistance	Optical metallography Scanning electron microscopy (SEM) Transmission electron microscopy (TEM)
Tears, laps and pits	Visual with etch Magnetic particle Eddy current Penetrant	Automatic optical scanning	Radioactive gas penetrant	Optical metallography SEM
Intergranular attack and selective etching		High sensitivity fluorescent penetrant		Macroetch Optical electron metallography TEM
Surface phase transformation (OTM, UTM, etc.)	Macroetch	X-ray diffraction Magnetic particle	Ultrasonic velocity Surface electrical resistance Eddy current	Optical metallography
Composition changes			Laser probe Mass spectrometry X-ray spectroscopy	Wet chemical analysis Electron microprobe
Surface hardness changes	Superficial hardness testing Ultrasonic hardness testing	Eddy current X-ray diffraction	Beta backscatter	Microhardness transverse
Redeposited and resolidified metal	Macroetch Visual inspection			Optical metallography
Recrystallisation and grain growth		Ultrasonic attenuation	Radioactive gas penetrant	Optical metallography
Plastic deformation	Superficial hardness testing	Eddy current Magnetic particle	Beta backscatter Radioactive gas penetrant Ultrasonic velocity	Optical metallography Microhardness transverse
Inclusions and voids	Ultrasonic pulse echo shear wave, surface wave and lambda wave Penetrant X-ray radiography Eddy current Magnetic particle	Gamma radiography Neutron radiography	Radioactive gas penetrant	Optical metallography
Residual stresses	X-ray diffraction	Ultrasonic velocity	Eddy current Electrochemical potential Ultrasonic attenuation Magneto-absorption	Parting-out Layer removal X-ray diffraction
Distortion	Visual inspection	Metrology		

Appendix D: OMEGA High temperature cement specification

High Temperature Air Set Cements



Applications

OMEGABOND® 300	OMEGABOND® 400	OMEGABOND® 500
Assembling	Coating	Coating
Sealing	Embedding	Dipping
Insulating	Insulating	Casting

Physical Properties†

	OMEGABOND 300	OMEGABOND 400	OMEGABOND 500
Type of Cement (1 or 2 Part)	**1 Part**	**1 Part**	**2 Part**
Coefficient of thermal expansion, in/in°F	6.2 x 10^{-6}	13.0 x 10^{-6}	10.93 x 10^{-6}
Color	Off white	Tan to gray	Off white
Compressive strength, psi	3900	3300	1500††
Dielectric constant	3.5 to 6.0	3.4 to 4.5	
Dielectric strength at 20°C (70°F), V/mil	12.5 to 51.0	12.5 to 51.0	
Dielectric strength at 400°C (750°F), V/mil	≤15.0	≤15.0	
Dielectric strength at 795°C (1475°F), V/mil	≤1.3	≤1.3	
Maximum service temperature, °C (°F)	980 (1800)	1425 (2600)	1205 (2200)
Modulus of rupture, psi	460		
Shear strength, psi	710	375	
Tensile strength, psi	410	325	1500
Volume resistivity at 20°C (70°F), Ω-cm	10^{5}-10^{9}	10^{5}-10^{9}	
Volume resistivity at 400°C (750°F), Ω-cm	10^{3}-10^{5}	10^{3}-10^{5}	
Volume resistivity at 795°C (1475°F), Ω-cm	10^{2}-10^{3}	10^{2}-10^{4}	
Density (wet), lbs/ft³			112
Density (dry), lbs/ft³			82
Flexural strength, psi			2000††
Modulus of elasticity, psi			3.6 x 10^{6}
Pot life, hr			1.0
Thermal conductivity, btu-in/ft²-hr-°F	4-6	11	
Mix ratio	1-part cement; just mix powder with water to a smooth, uniform consistency	1-part cement; just mix powder with water to a smooth, uniform consistency	2-part cement: just mix powder and binder; mix ratio for cast applications ranges from 1.87 to 2.0 parts powder to 1-part liquid binder by weight
Curing schedule	OMEGABOND 300® cures at room temperature by air drying in 18 to 24-hr, depending upon thickness and consistency; cure time can be accelerated by low temperature oven drying at 82°C (180°F); if the cement is to be exposed to elevated temperatures, cure for 18 to 24-hr at ambient temperature, then oven dry for 4-hr at 82°C (180°F) and for an additional 4-hr at 105°C (220°F), this helps to prevent spilling	OMEGABOND 400® cures at room temperature by air drying in 18 to 24-hr, depending upon thickness and consistency; cure time can be accelerated by low temperature oven drying at 82°C (180°F); if the cement is to be exposed to elevated temperatures, cure for 18 to 24-hr at ambient temperature, then oven dry for 4-hr at 82°C (180°F) and for an additional 4-hr at 105°C (220°F), this helps to prevent spilling	OMEGABOND 500® has a pot life of 1-hr after the powder and binder are mixed together; OB-500 reaches an initial air set after 4-hr at room temperature; a final set is only reached after oven baking at 55°C (130°F) for 4-hr; if the cement is to be used at temperatures above 100°C (212°F), OB-500 must under go an extended cure at 105°C (220°F) or above for 12 hours
Distinguishing characteristics and applications	Lower thermal conductivity and coefficient of thermal expansion	Higher thermal conductivity and coefficient of thermal expansion; high maximum temperature rating	Withstands short-term immersion in molten metal; used as a coating on expendable thermocouple tubes

† These physical properties were determined under laboratory conditions using applicable ASTM procedures. Actual field data may vary. Do not use physical properties data for specifications.

†† Strength at 1 day after curing at 105°C (220°F).

** Chemical set cements are also available. See OMEGABOND® 600, OMEGABOND® 700 and CC high temperature cement. These cements set or cure by an internal chemical action which does not require exposure to air. They can be used in thick applications (greater than ¼" thickness).*

*** Porous substrates may require dampening with thinning liquid before application of mixed cement. For OMEGABOND® 300 and OMEGABOND® 400 (1 part cements), order OMEGABOND® thinning liquid (8 fluid oz), **OB-TL**. For OMEGABOND® 500 (2 part cement), use OMEGABOND® 500 liquid to dampen porous substrates.*

F-24

Figure D1: Full description of used resin epoxy powder [191]

Appendix E: Grinding coolant specifications

TRIM® C270

High-performance Synthetic

Application Guidelines

- The harder you work this product the better the results will be.
- C270 is not recommended in machine tools that rely on the splash of the coolant to lubricate the mechanical portions of the machine tool, e.g. older screw machines, etc.
- C270 is not recommended on materials like magnesium or zirconium without special precautions.
- This product is a superior cleaning agent so it may "wash out" dirt and residues when a machine is first charged; a thorough cleaning of older machines is required when installing this product the first time.
- The minimum recommended concentration is 5% on cast iron and 4% on steel.
- Concentrations above 7.5% provide excellent corrosion inhibition, tool life, and sump life; however, the best concentration for your operation should be determined by on-site experience.
- For additional product application information, including performance optimisation, please contact your Master Fluid Solutions' Authorised Distributor at https://www.masterfluids.com/eu/en/distributors/index.php, your District Sales Manager, or call our Tech Line at +49 211 77 92 85 - 13.

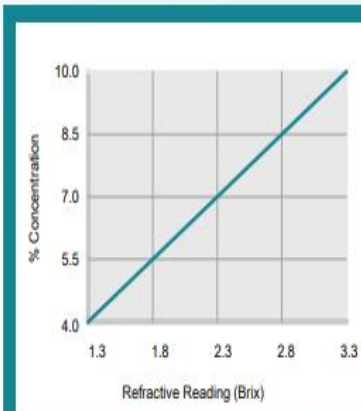
Physical Properties Typical Data

Colour (Concentrate)	Pale straw
Odour (Concentrate)	Mild Amine
Form (Concentrate)	Liquid
Flash Point (Concentrate) (ASTM D93-08)	> 100°C
pH (Typical Operating as Range)	8.8 - 9.4
Coolant Refractometer Factor	3.0
Digital Titration Factor	0.0189

Recommended Metalworking Concentrations

Light Duty	4.0% - 6.5%
Moderate Duty	6.5% - 8.5%
Heavy Duty	8.5% - 10.0%
Design Concentration Range	4.0% - 10.0%

Concentration by % Brix



% Concentration = Refractive Reading x Refractive Factor
Coolant Refractometer Factor % Brix = 3.0

Health and Safety

Request SDS

Figure E1: TRIM C270 specifications [188]

Appendix F: Additional experimental results

F1 Phase 1: Creep feed grinding of creep feed grinding of γ- titanium aluminide alloy (Ti-45Al-8Nb-0.2C)

a) Phase 1A: The influence of operating conditions on grinding performance when creep feed grinding with conventional silicon carbide wheel (SiC)

Table F1: ANOVA table for G-ratio (Phase 1A)

Source	DF	Seq SS	Contribution	Adj SS	Adj MS	F-Value	P-Value
Wheel speed	1	0.1653	0.38%	0.1653	0.1653	0.08	0.785
Depth of cut	1	33.8253	76.80%	33.8253	33.8253	17.36	0.014
Feed rate	1	2.2578	5.13%	2.2578	2.2578	1.16	0.342
Error	4	7.7938	17.70%	7.7938	1.9484	-	-
Total	7	44.0422	100.00%	-	-	-	-

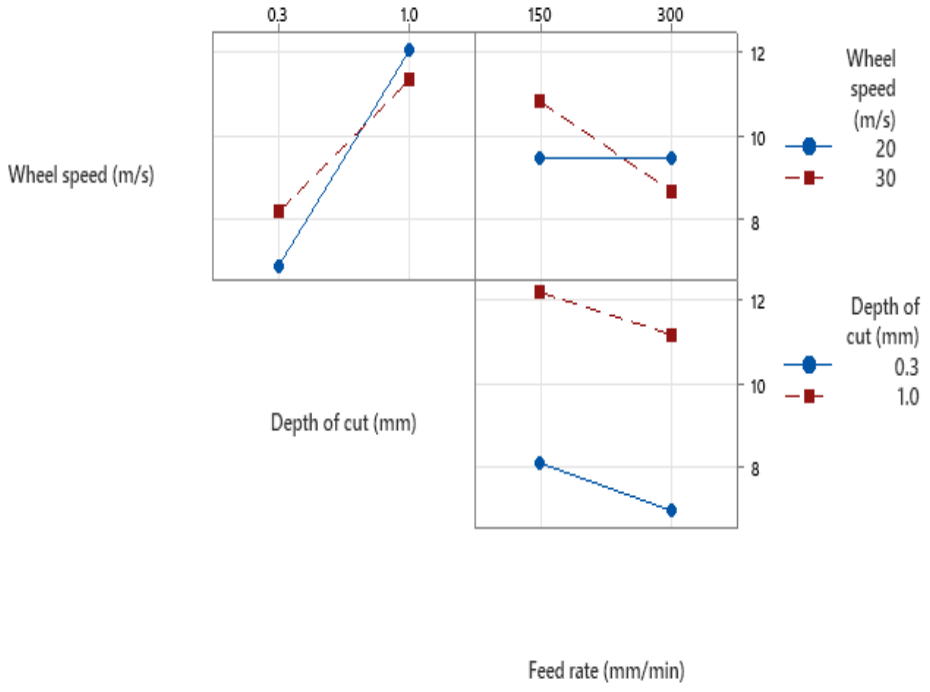


Figure F1: Interaction plot for G-ratio (Phase 1A)

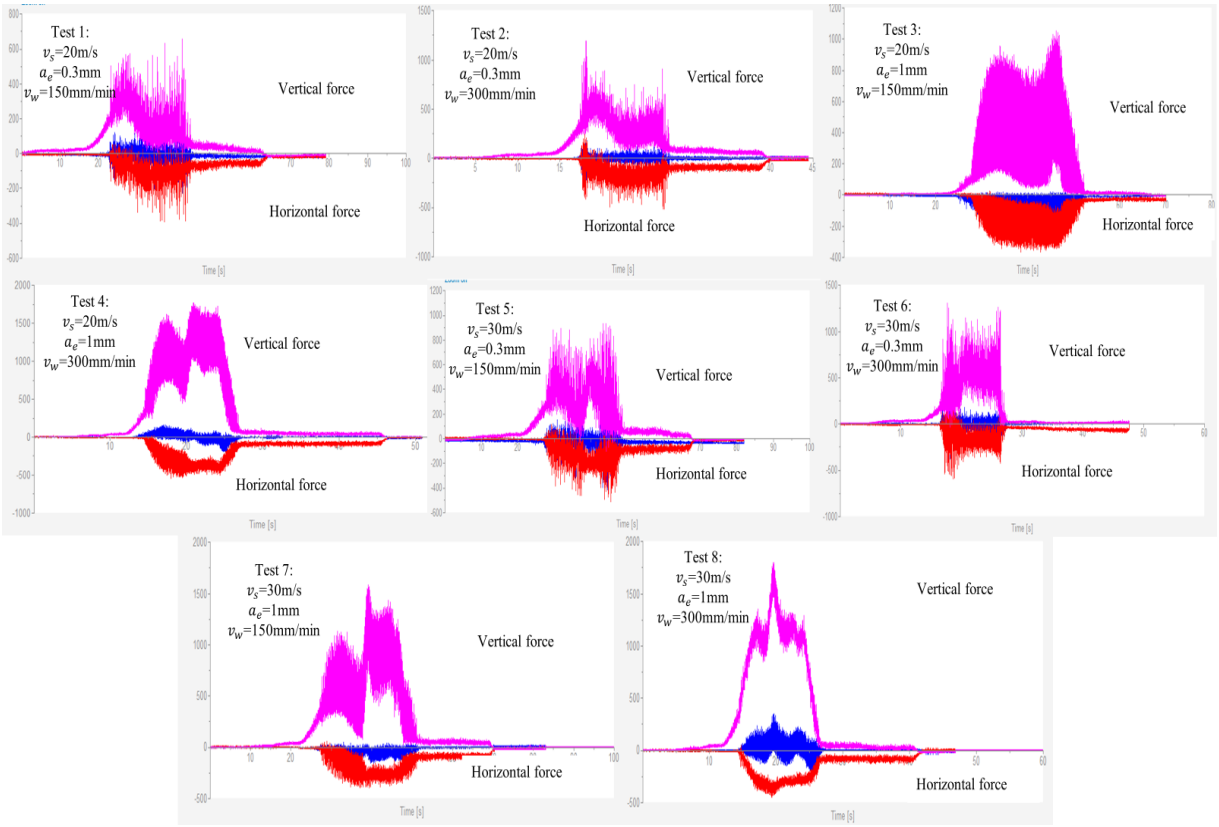


Figure F2: Grinding forces traces (Phase 1A)

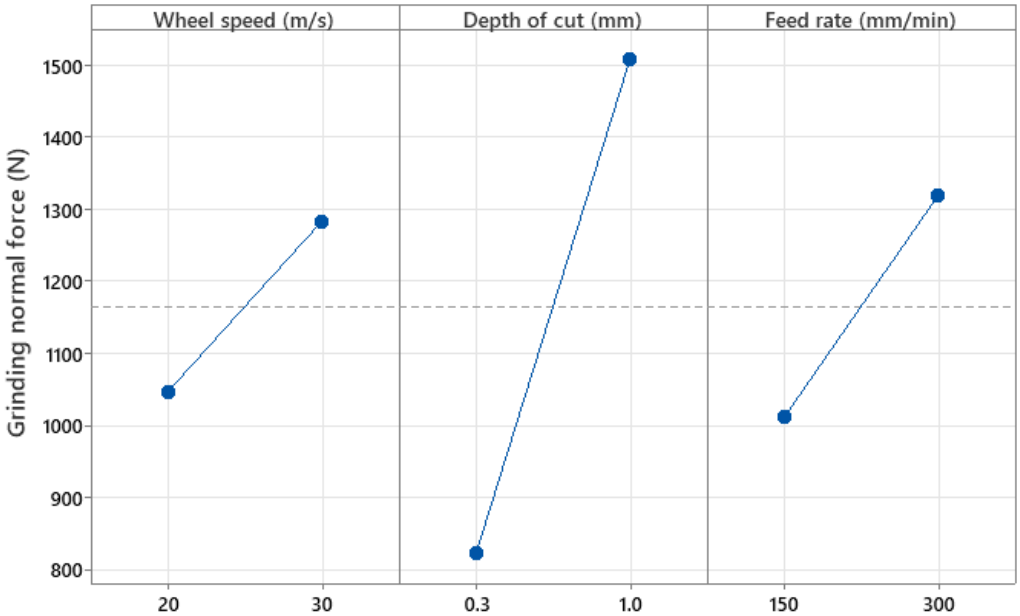


Figure F3: Main effect plot for normal forces (Phase 1A)

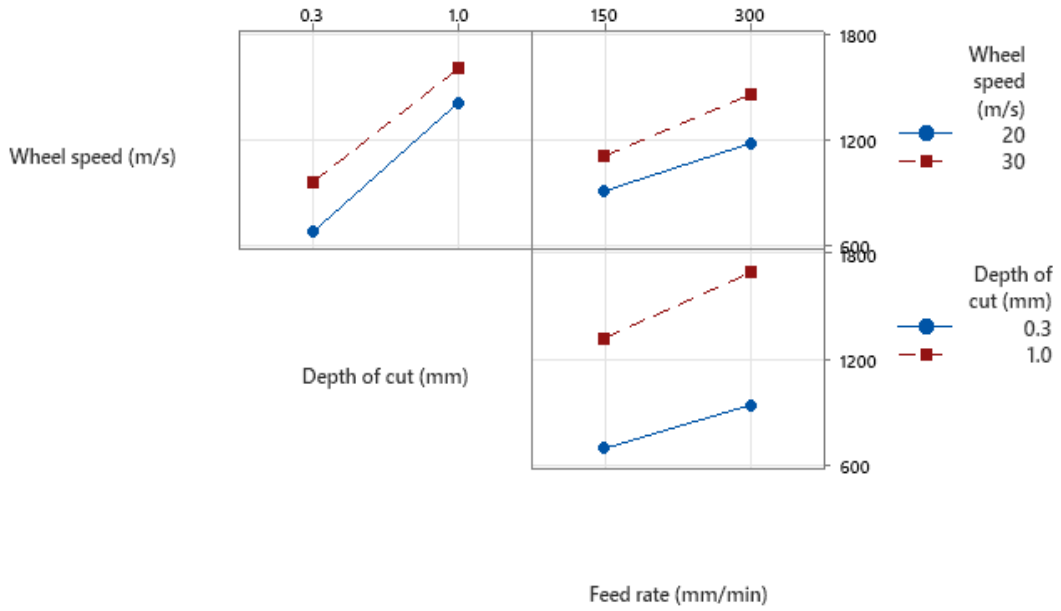


Figure F4: Interaction plot for normal forces (Phase 1A)

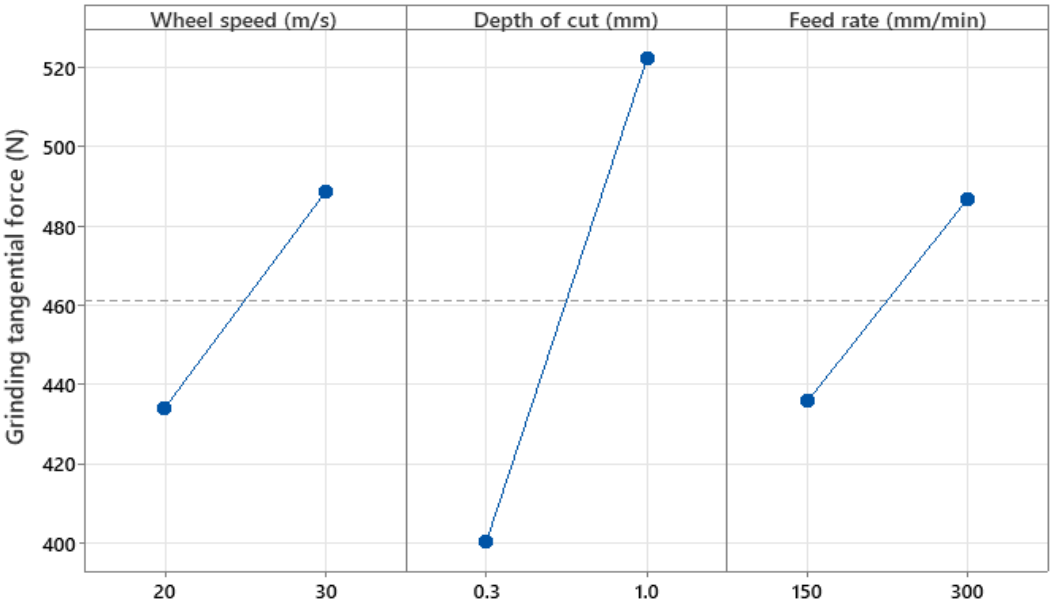


Figure F5: Main effect plot for tangential forces (Phase 1A)

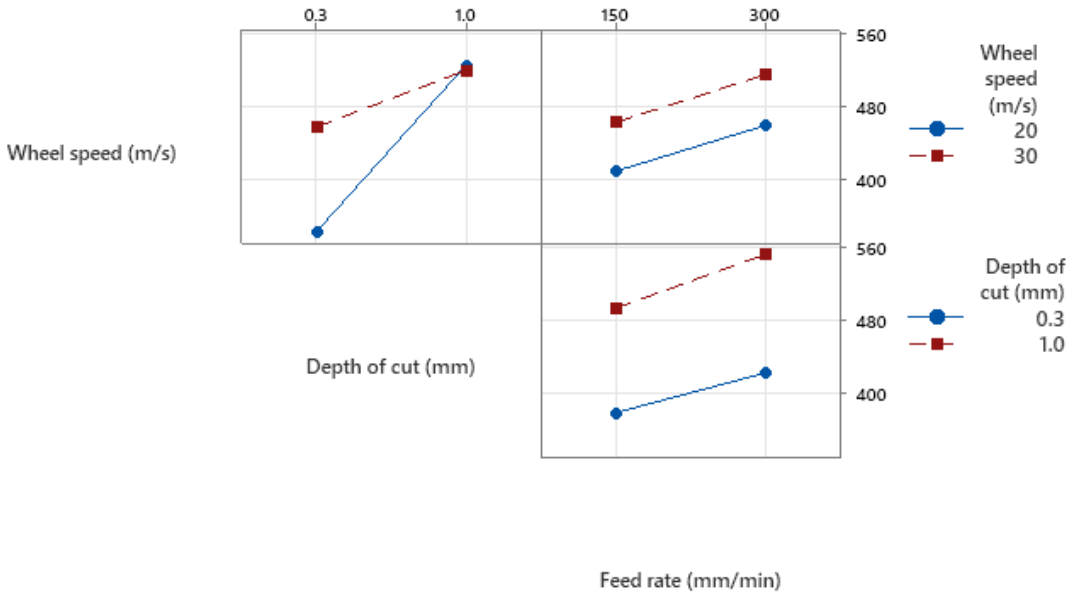


Figure F6: Interaction plot for tangential forces (Phase 1A)

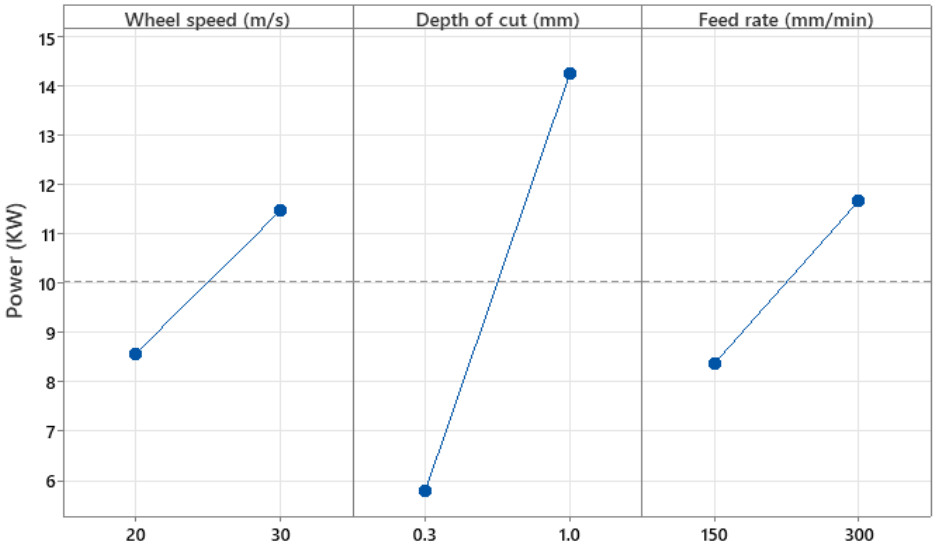


Figure F7: Main effect plot for power (Phase 1A)

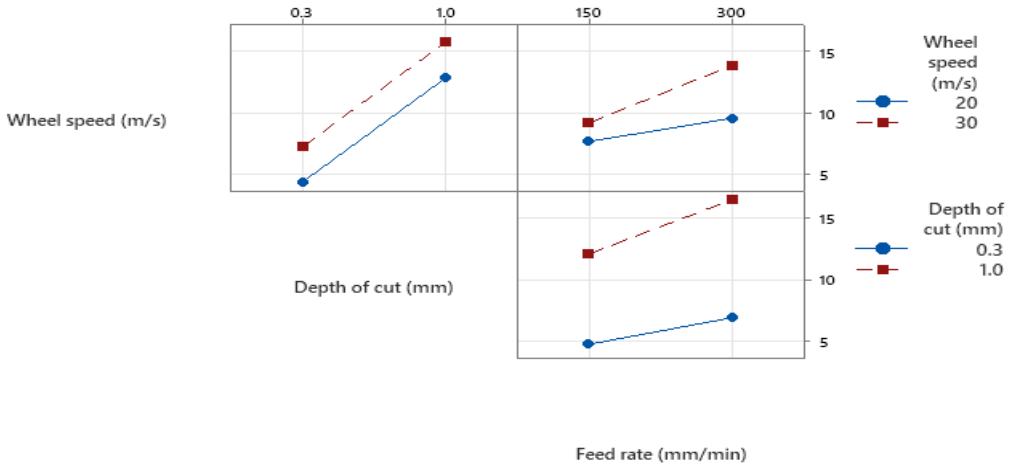


Figure F8: Interaction plot for power (Phase 1A)

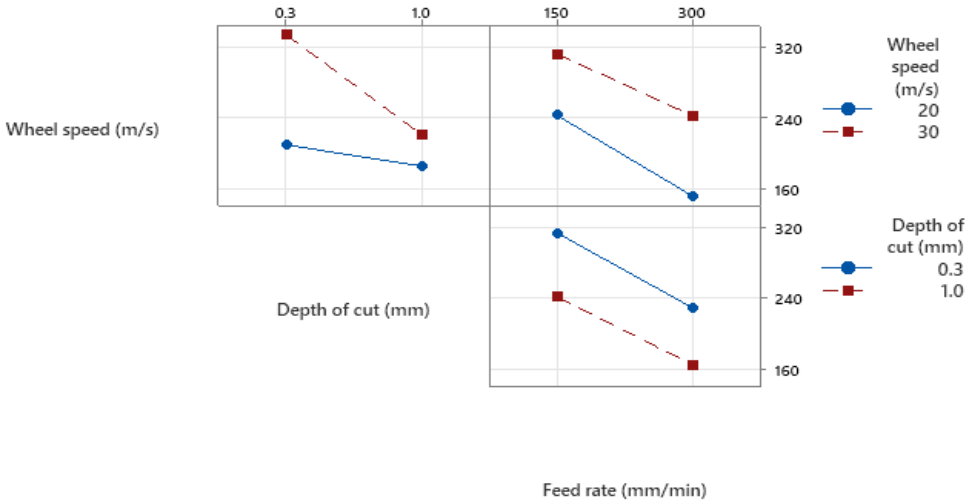


Figure F9: Interaction plot for specific energy (Phase 1A)

Table F2: ANOVA table for power (Phase 1A)

Source	DF	Seq SS	Contribution	Adj SS	Adj MS	F-Value	P-Value
Wheel speed (m/s)	1	16.820	8.91%	16.820	16.820	10.27	0.033
Depth of cut (mm)	1	143.651	76.08%	143.651	143.651	87.68	0.001
Feed rate (mm/min)	1	21.780	11.54%	21.780	21.780	13.29	0.022
Error	4	6.554	3.47%	6.554	1.638	-	-
Total	7	188.805	100.00%	-	-	-	-

Table F3: ANOVA table for specific energy (Phase 1A)

Source	DF	Seq SS	Contribution	Adj SS	Adj MS	F-Value	P-Value
Wheel speed (m/s)	1	12840	32.66%	12840	12840	12.23	0.025
Depth of cut (mm)	1	9350	23.79%	9350	9350	8.91	0.041
Feed rate (mm/min)	1	12920	32.87%	12920	12920	12.31	0.025
Error	4	4200	10.68%	4200	1050	-	-
Total	7	39310	100.00%	-	-	-	-

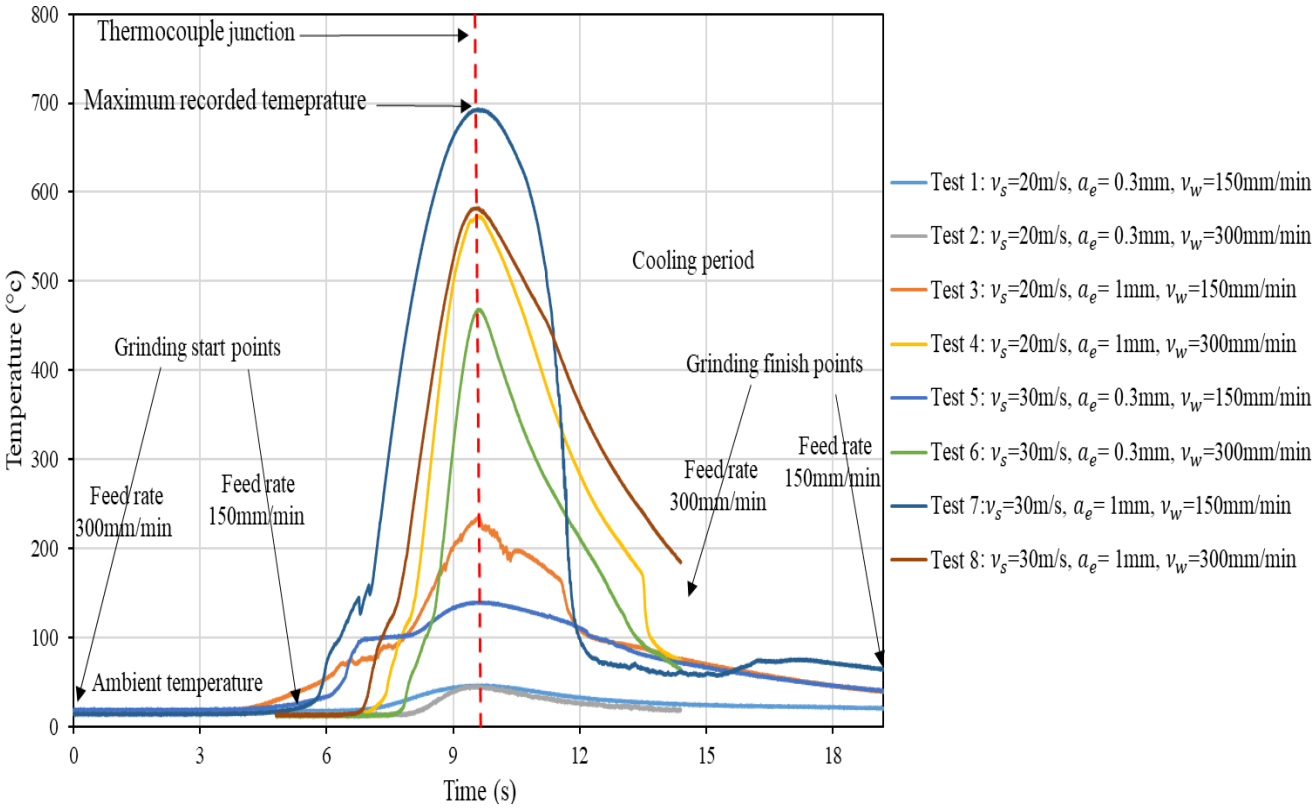


Figure F10: Grinding temperature traces (Phase 1A)

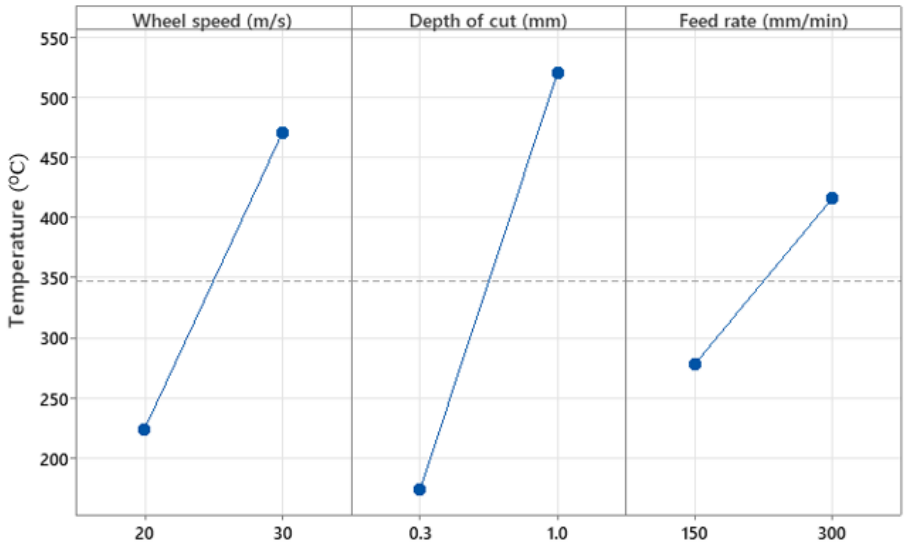


Figure F11: Main effect plot for temperature (Phase 1A)

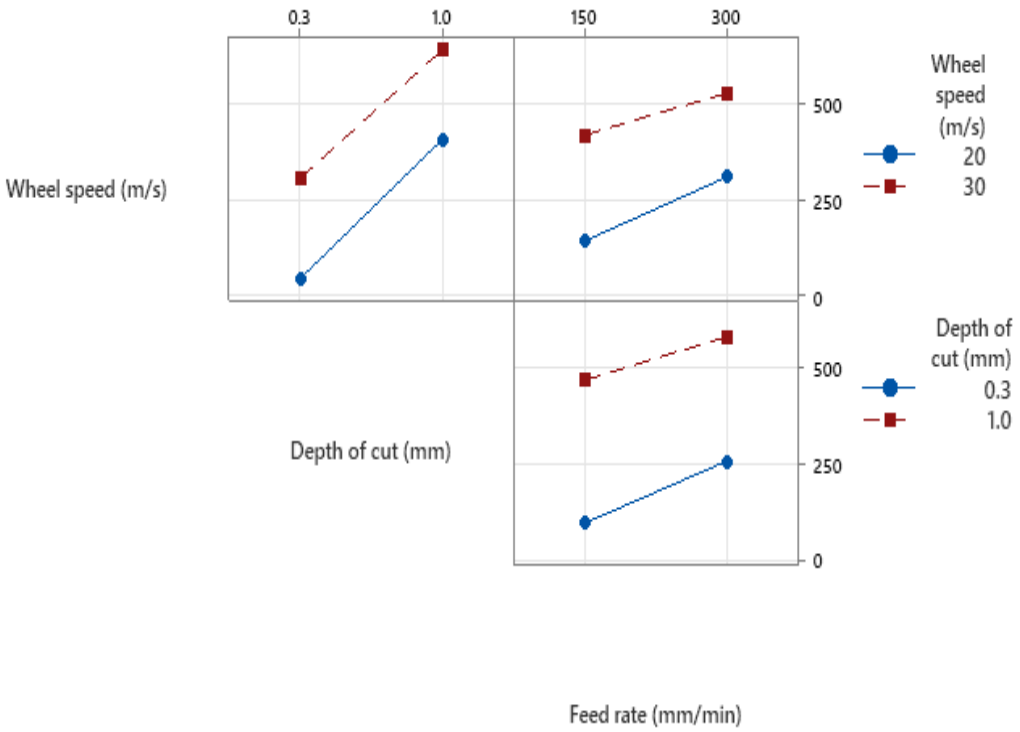


Figure F12: Interaction plot for temperature (Phase 1A)

Table F4: ANOVA table for temperature (Phase 1A)

Source	DF	Seq SS	Contribution	Adj SS	Adj MS	F-Value	P-Value
Wheel speed (m/s)	1	121525	25.35%	121525	121525	6.14	0.068
Depth of cut (mm)	1	240818	50.24%	240818	240818	12.16	0.025
Feed rate (mm/min)	1	37812	7.89%	37812	37812	1.91	0.239
Error	4	79219	16.53%	79219	19805	-	-
Total	7	479374	100.00%	-	-	-	-

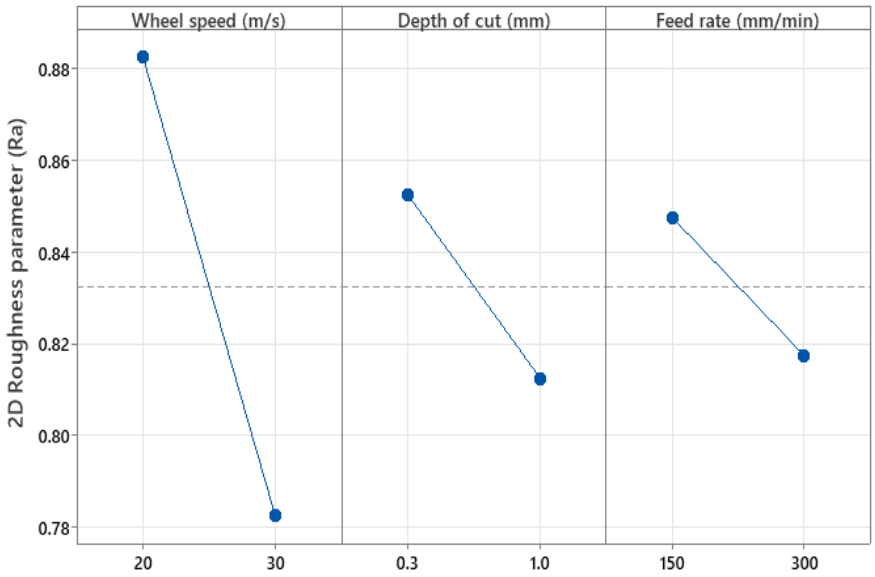


Figure F13: Main effect plot for 2D surface roughness parameter Ra (Phase 1A)

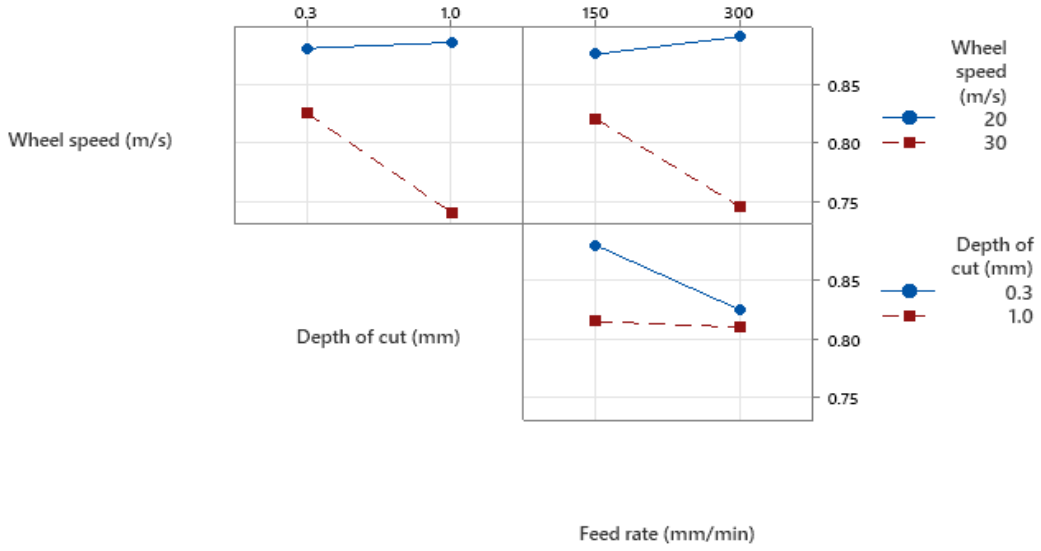


Figure F14: Interaction plot for 2D surface roughness parameter Ra (Phase 1A)

Table F5: ANOVA table for 2D surface roughness parameter Ra (Phase 1A)

Source	DF	Seq SS	Contribution	Adj SS	Adj MS	F-Value	P-Value
Wheel speed (m/s)	1	0.020000	50.83%	0.020000	0.020000	5.57	0.078
Depth of cut (mm)	1	0.003200	8.13%	0.003200	0.003200	0.89	0.398
Feed rate (mm/min)	1	0.001800	4.57%	0.001800	0.001800	0.50	0.518
Error	4	0.014350	36.47%	0.014350	0.003588	-	-
Total	7	0.039350	100.00%	-	-	-	-

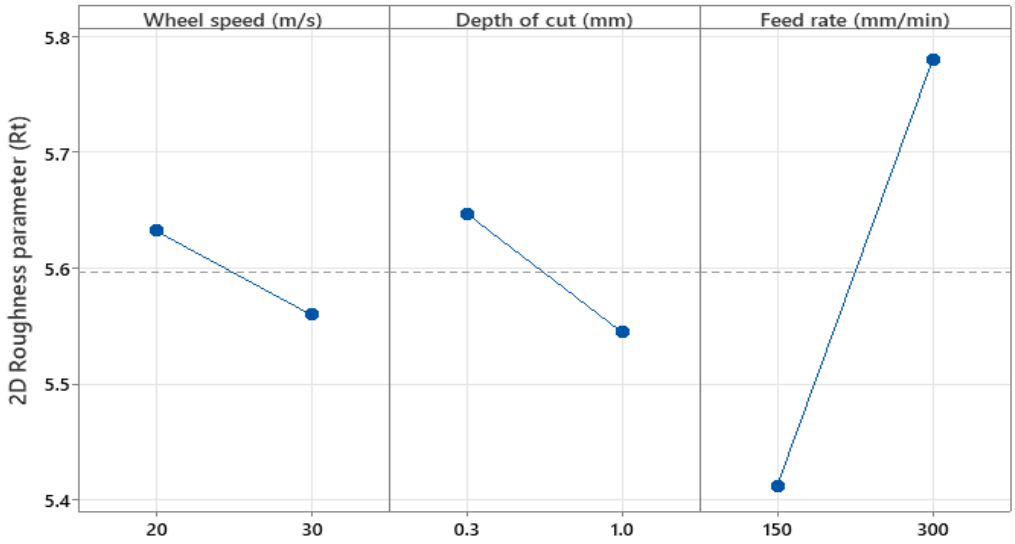


Figure F15: Main effect plot for 2D surface roughness parameter Rt (Phase 1A)

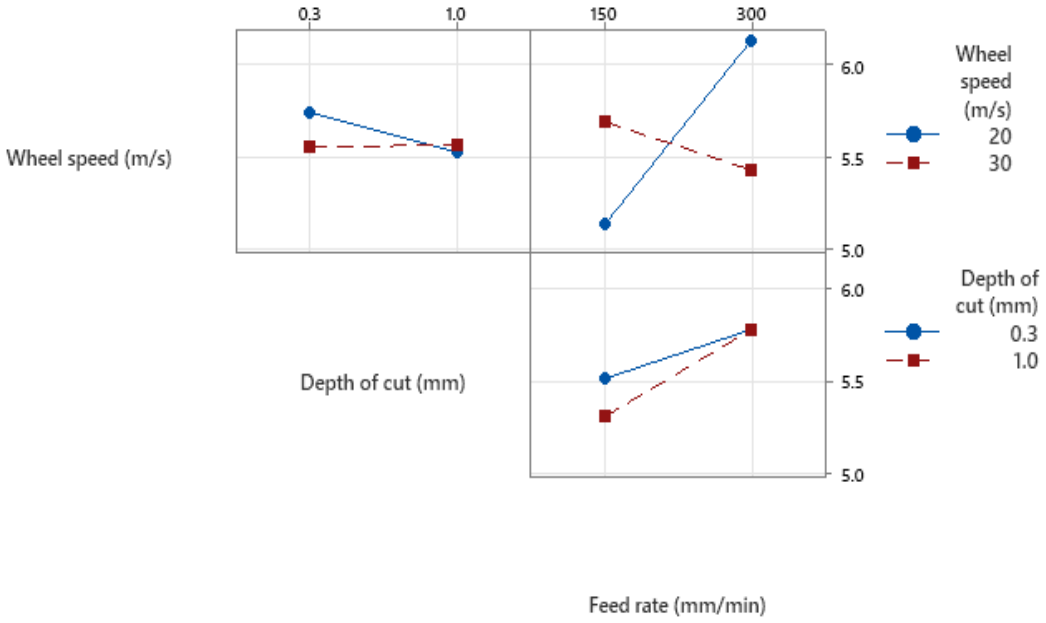


Figure F16: Interaction plot for 2D surface roughness parameter Rt (Phase 1A)

Table F6: ANOVA table for 2D surface roughness parameter Rt (Phase 1A)

Source	DF	Seq SS	Contribution	Adj SS	Adj MS	F-Value	P-Value
Wheel speed (m/s)	1	0.01051	0.52%	0.01051	0.01051	0.02	0.883
Depth of cut (mm)	1	0.02101	1.04%	0.02101	0.02101	0.05	0.836
Feed rate (mm/min)	1	0.27011	13.33%	0.27011	0.27011	0.63	0.473
Error	4	1.72495	85.12%	1.72495	0.43124	-	-
Total	7	2.02659	100.00%	-	-	-	-

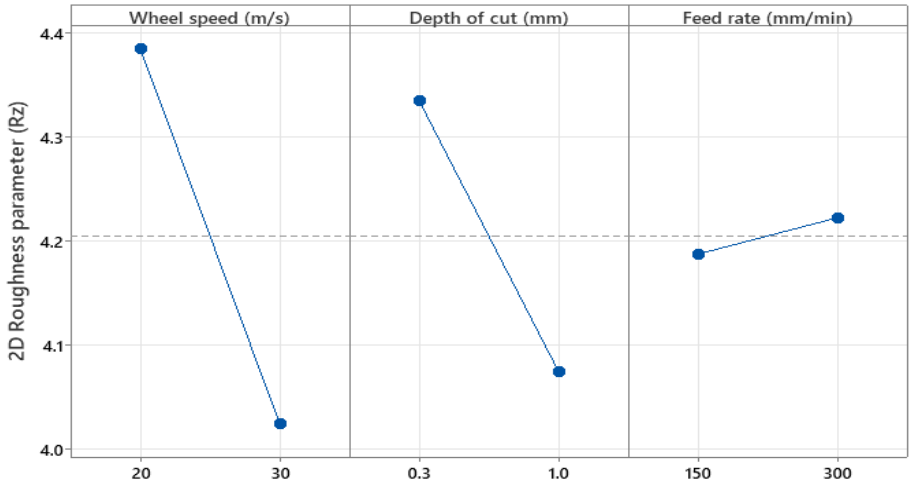


Figure F17: Main effect plot for 2D surface roughness parameter Rz (Phase 1A)

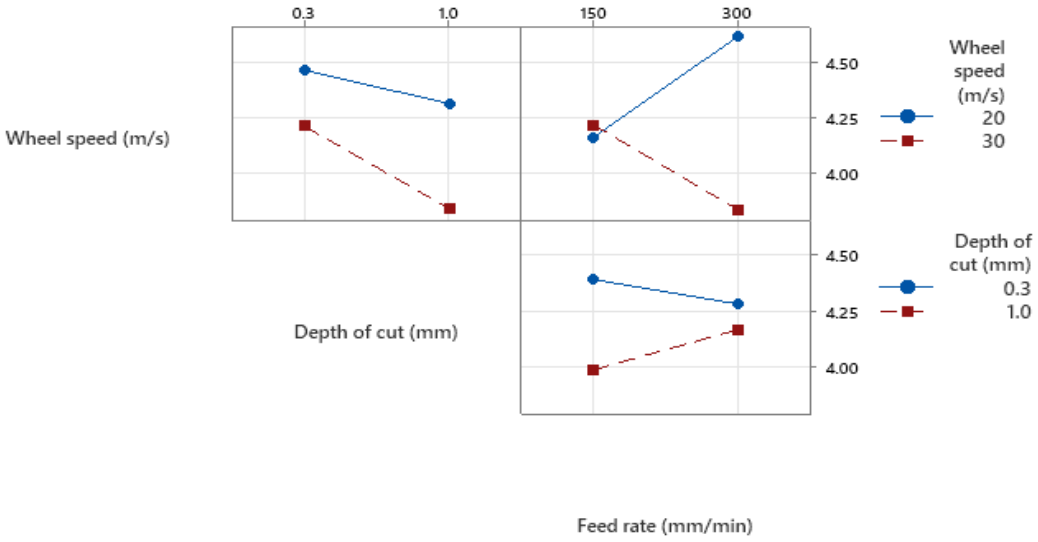


Figure F18: Interaction plot for 2D surface roughness parameter Rz (Phase 1A)

Table F7: ANOVA table for 2D surface roughness parameter Rz (Phase 1A)

Source	DF	Seq SS	Contribution	Adj SS	Adj MS	F-Value	P-Value
Wheel speed (m/s)	1	0.25920	19.37%	0.259200	0.259200	1.10	0.353
Depth of cut (mm)	1	0.13520	10.10%	0.135200	0.135200	0.57	0.491
Feed rate (mm/min)	1	0.00245	0.18%	0.002450	0.002450	0.01	0.924
Error	4	0.94115	70.34%	0.941150	0.235288	-	-
Total	7	1.33800	100.00%	-	-	-	-

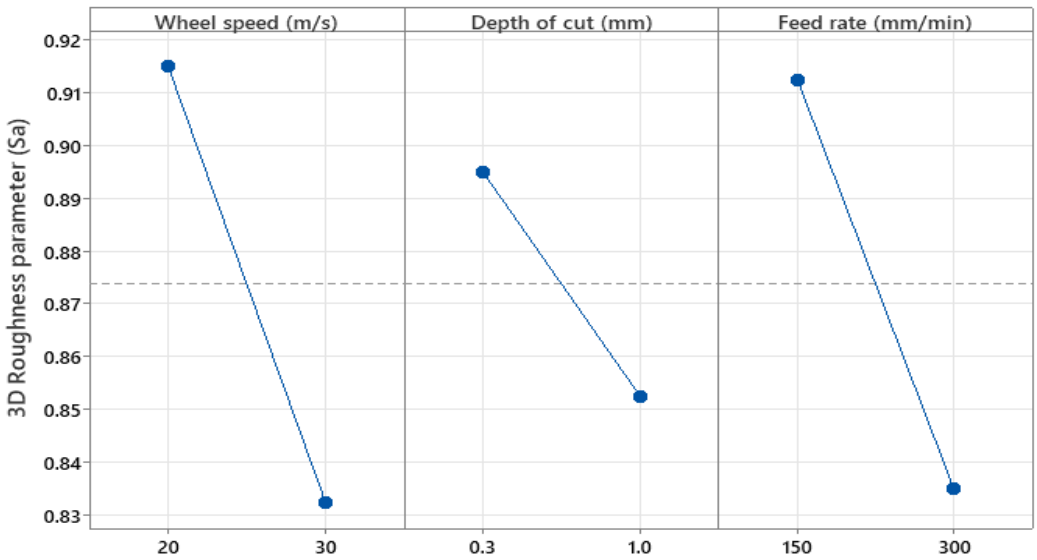


Figure F19: Main effect plot for 3D surface roughness parameter Sa (Phase 1A)

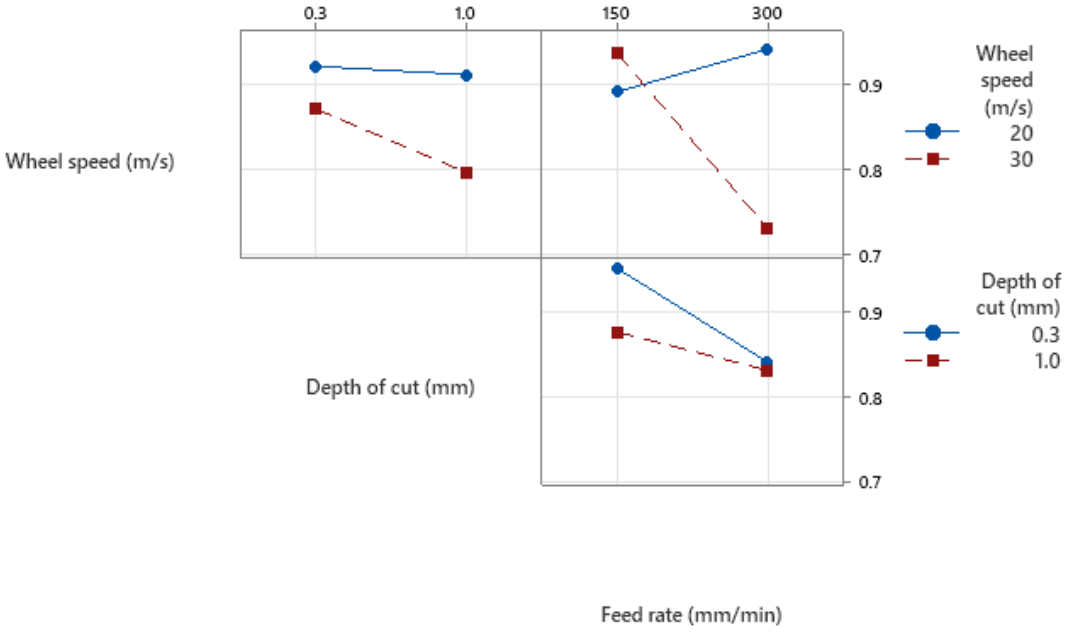


Figure F20: Interaction plot for 3D surface roughness parameter Sa (Phase 1A)

Table F8: ANOVA table for 3D surface roughness parameter Sa (Phase 1A)

Source	DF	Seq SS	Contribution	Adj SS	Adj MS	F-Value	P-Value
Wheel speed (m/s)	1	0.013613	15.65%	0.013613	0.013613	0.94	0.387
Depth of cut (mm)	1	0.003612	4.15%	0.003613	0.003613	0.25	0.643
Feed rate (mm/min)	1	0.012013	13.81%	0.012013	0.012013	0.83	0.413
Error	4	0.057750	66.39%	0.057750	0.014438	-	-
Total	7	0.086988	100.00%	-	-	-	-

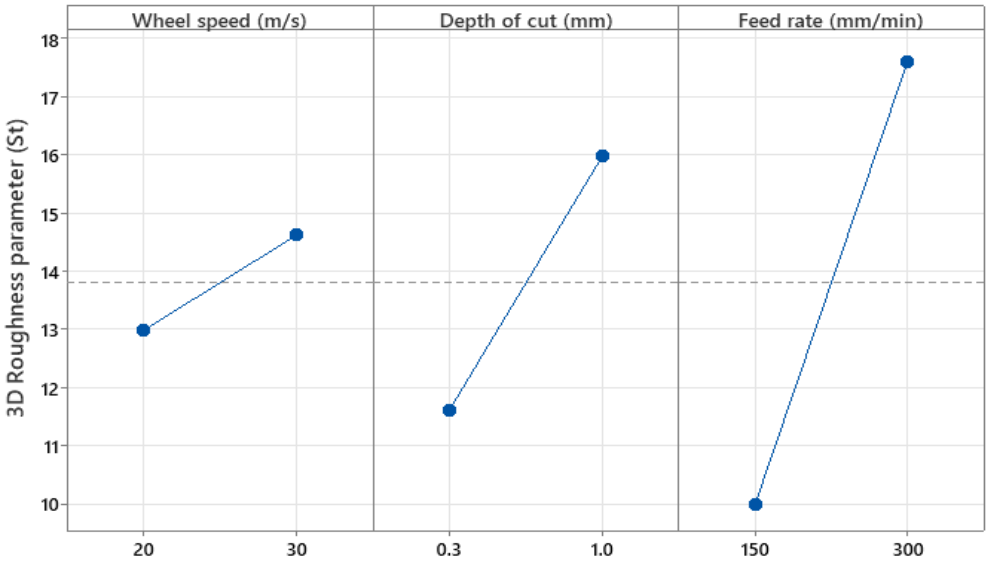


Figure F21: Main effect plot for 3D surface roughness parameter St (Phase 1A)

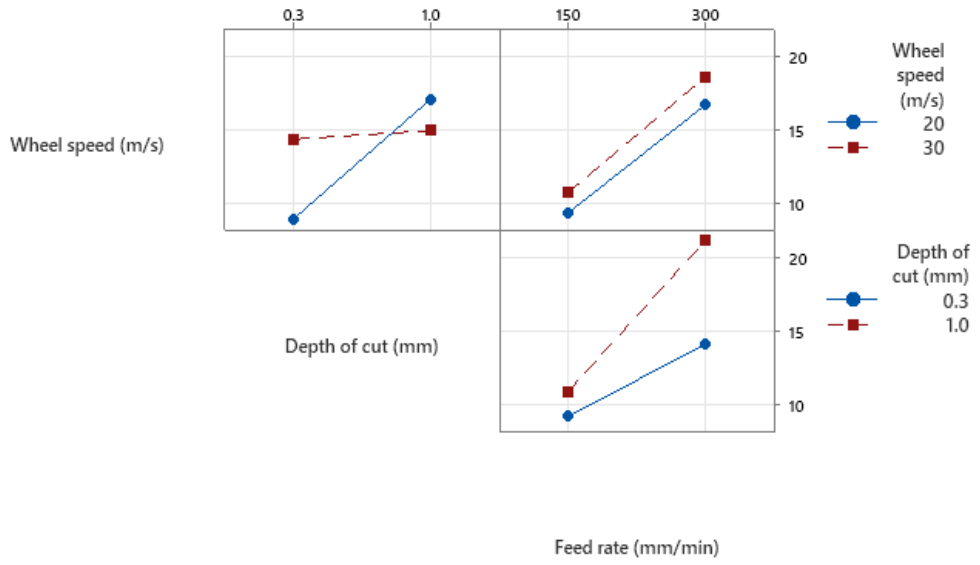


Figure F22: Interaction plot for 3D surface roughness parameter St (Phase 1A)

Table F9: ANOVA table for 3D surface roughness parameter St (Phase 1A)

Source	DF	Seq SS	Contribution	Adj SS	Adj MS	F-Value	P-Value
Wheel speed (m/s)	1	5.369	2.64%	5.369	5.369	0.48	0.526
Depth of cut (mm)	1	38.168	18.74%	38.168	38.168	3.42	0.138
Feed rate (mm/min)	1	115.474	56.70%	115.474	115.474	10.35	0.032
Error	4	44.643	21.92%	44.643	11.161	-	-
Total	7	203.655	100.00%	-	-	-	-

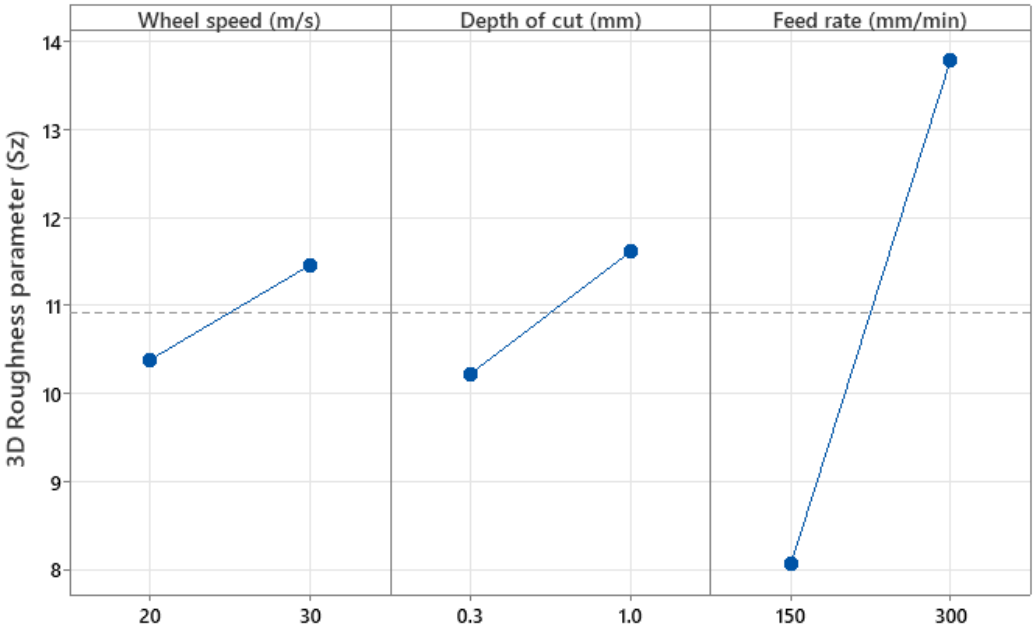


Figure F23: Main effect plot for 3D surface roughness parameter Sz (Phase 1A)

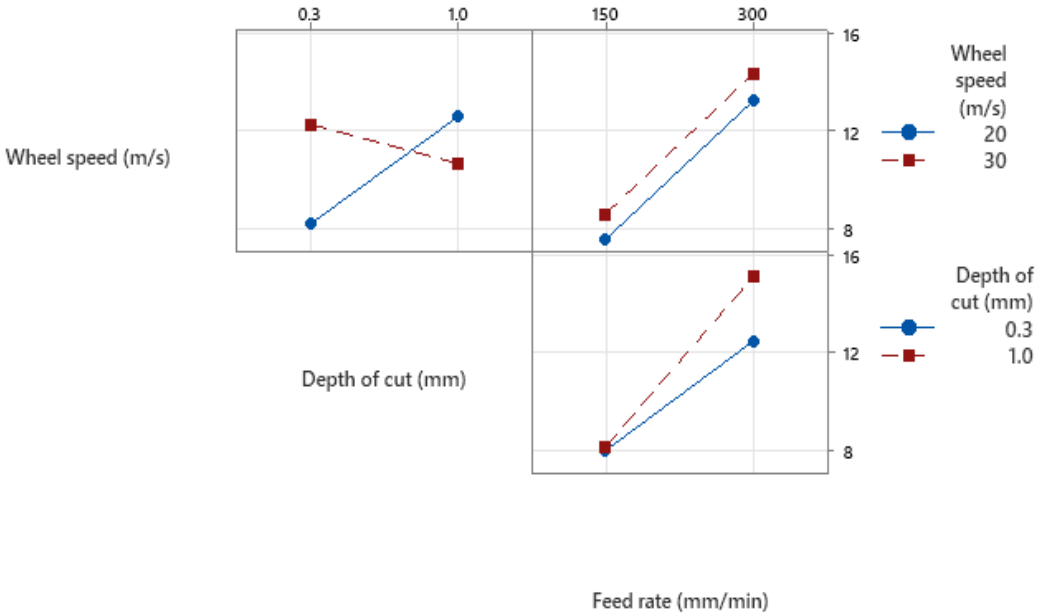


Figure F24: Interaction plot for 3D surface roughness parameter Sz (Phase 1A)

Table F10: ANOVA table for 3D surface roughness parameter Sz (Phase 1A)

Source	DF	Seq SS	Contribution	Adj SS	Adj MS	F-Value	P-Value
Wheel speed (m/s)	1	2.322	2.42%	2.322	2.322	0.38	0.569
Depth of cut (mm)	1	3.878	4.05%	3.878	3.878	0.64	0.469
Feed rate (mm/min)	1	65.380	68.23%	65.380	65.380	10.79	0.030
Error	4	24.241	25.30%	24.241	6.060	-	-
Total	7	95.820	100.00%	-	-	-	-

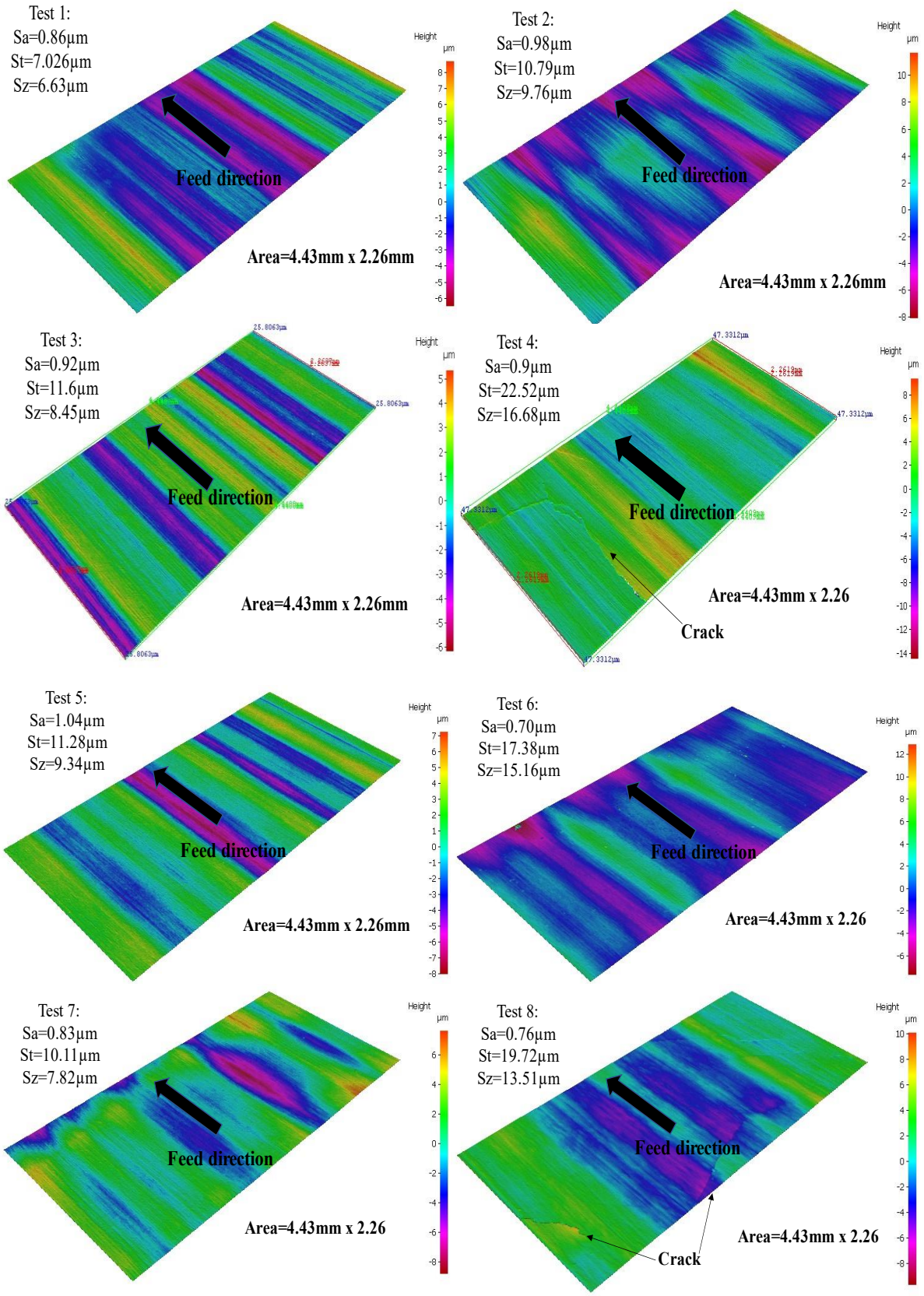


Figure F25: 3D topographies of ground surfaces, primary mapping not filtered (Phase 1A)

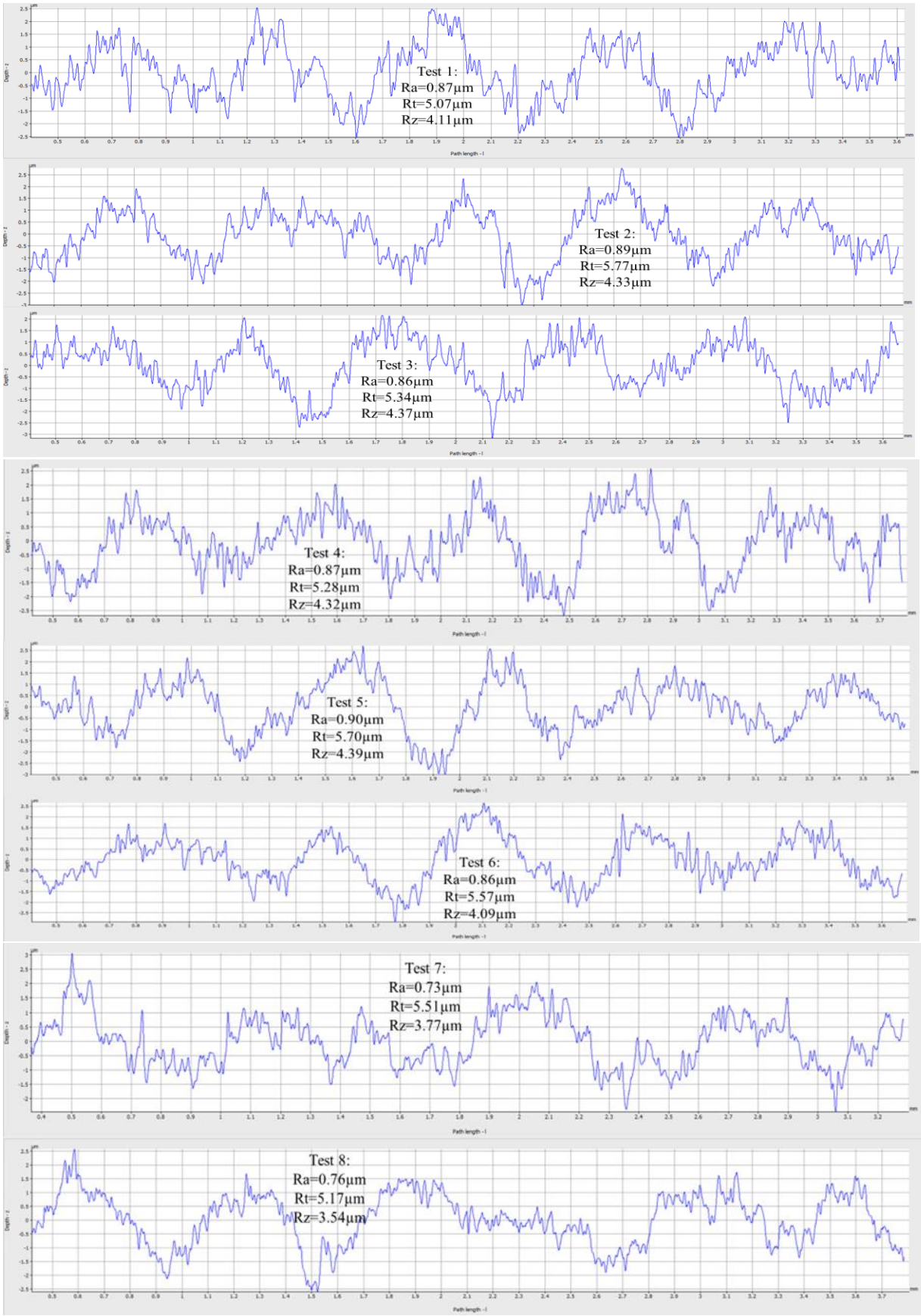


Figure F26: 2D topography traces – Roughness profiles (Phase 1A)

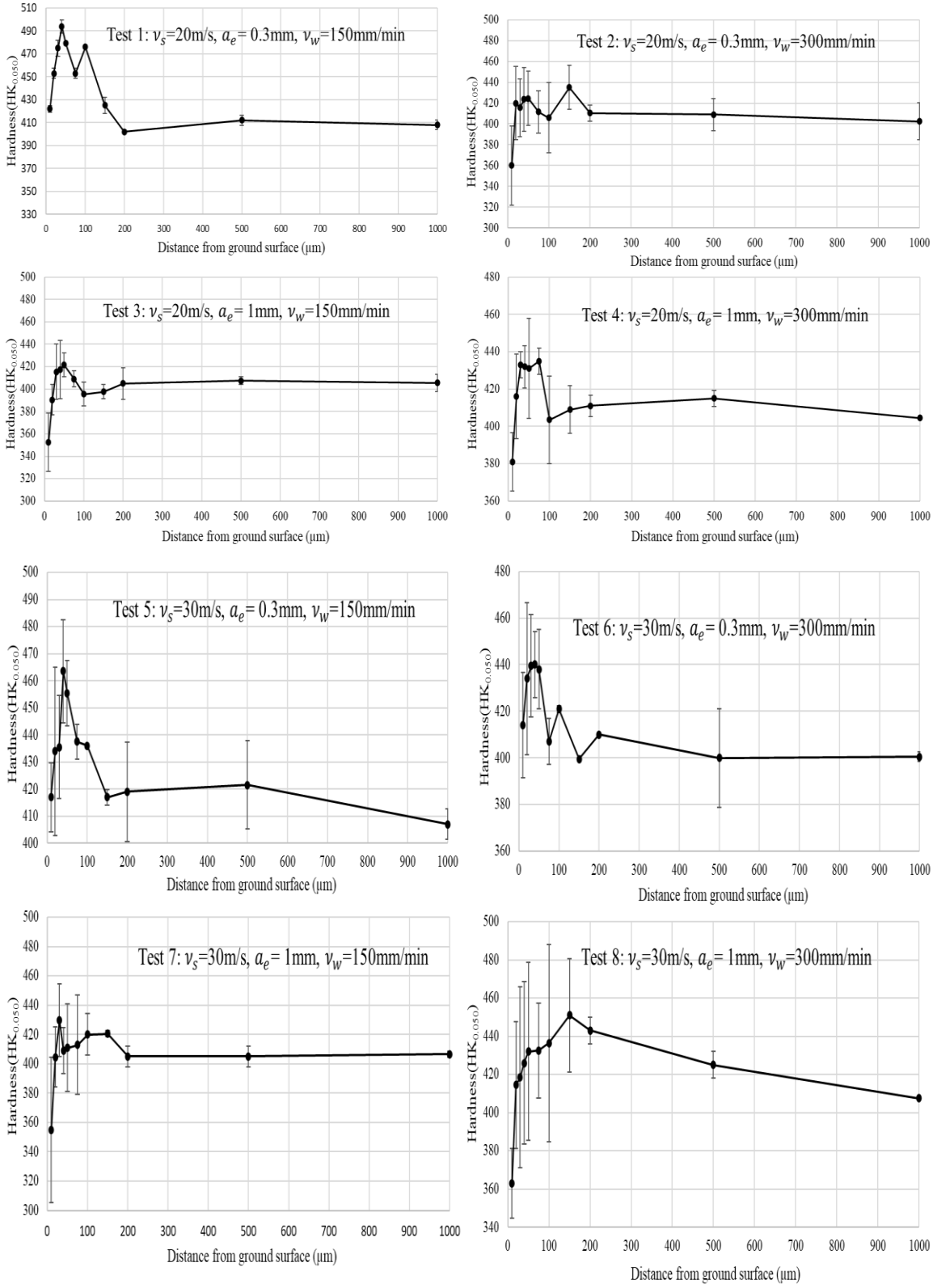


Figure F27: Individual microhardness profiles (Phase 1A)

b) Effect of operating conditions on grinding performance when creep feed grinding with super-abrasive diamond wheel and a comparison between two different wheel systems.

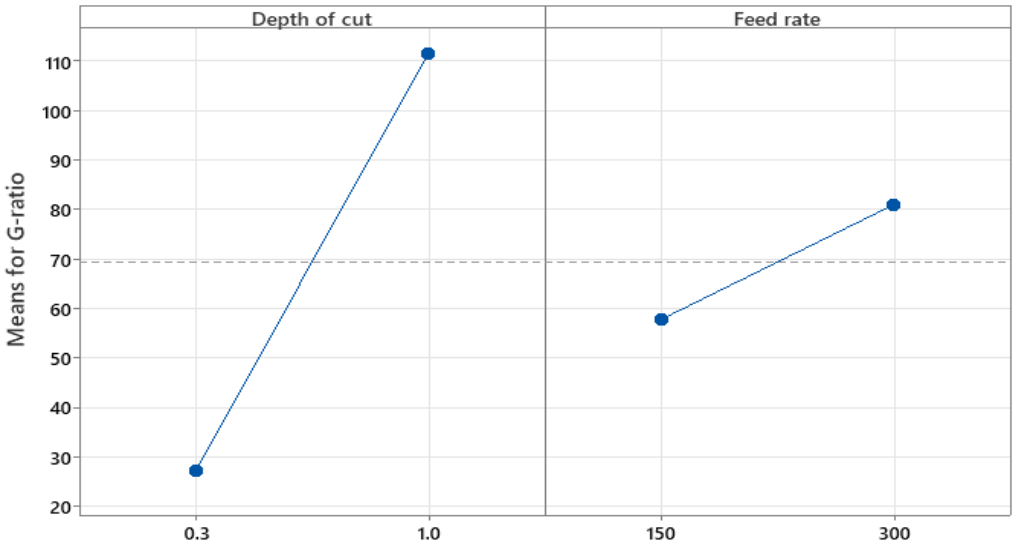


Figure F28: Main effect plot for G-ratio (Phase 1B)

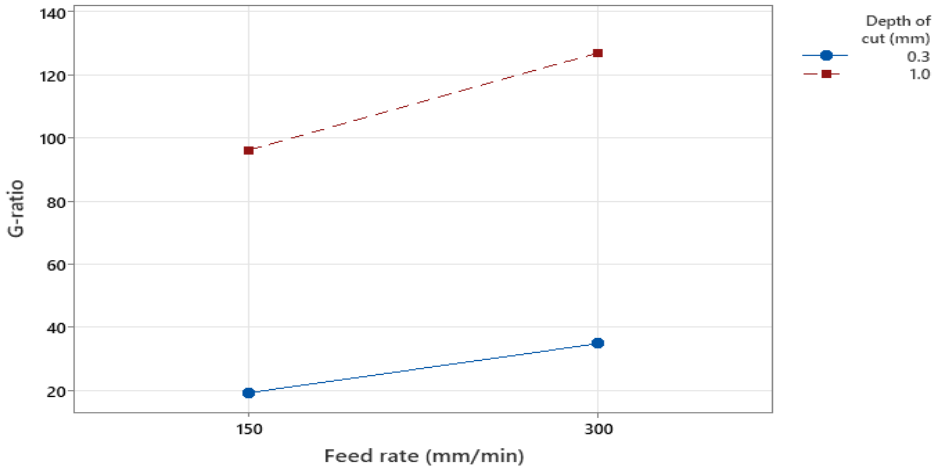


Figure F29: Interaction plot for G-ratio (Phase 1B)

Table F11: ANOVA table for G-ratio (Phase 1B)

Source	DF	Seq SS	Contribution	Adj SS	Adj MS	F-Value	P-Value
Depth of cut (mm)	1	7123.36	92.28%	7123.36	7123.36	123.33	0.057
Feed rate(mm/min)	1	538.24	6.97%	538.24	538.24	9.32	0.202
Error	1	57.76	0.75%	57.76	57.76	-	-
Total	3	7719.36	100.00%	-	-	-	-

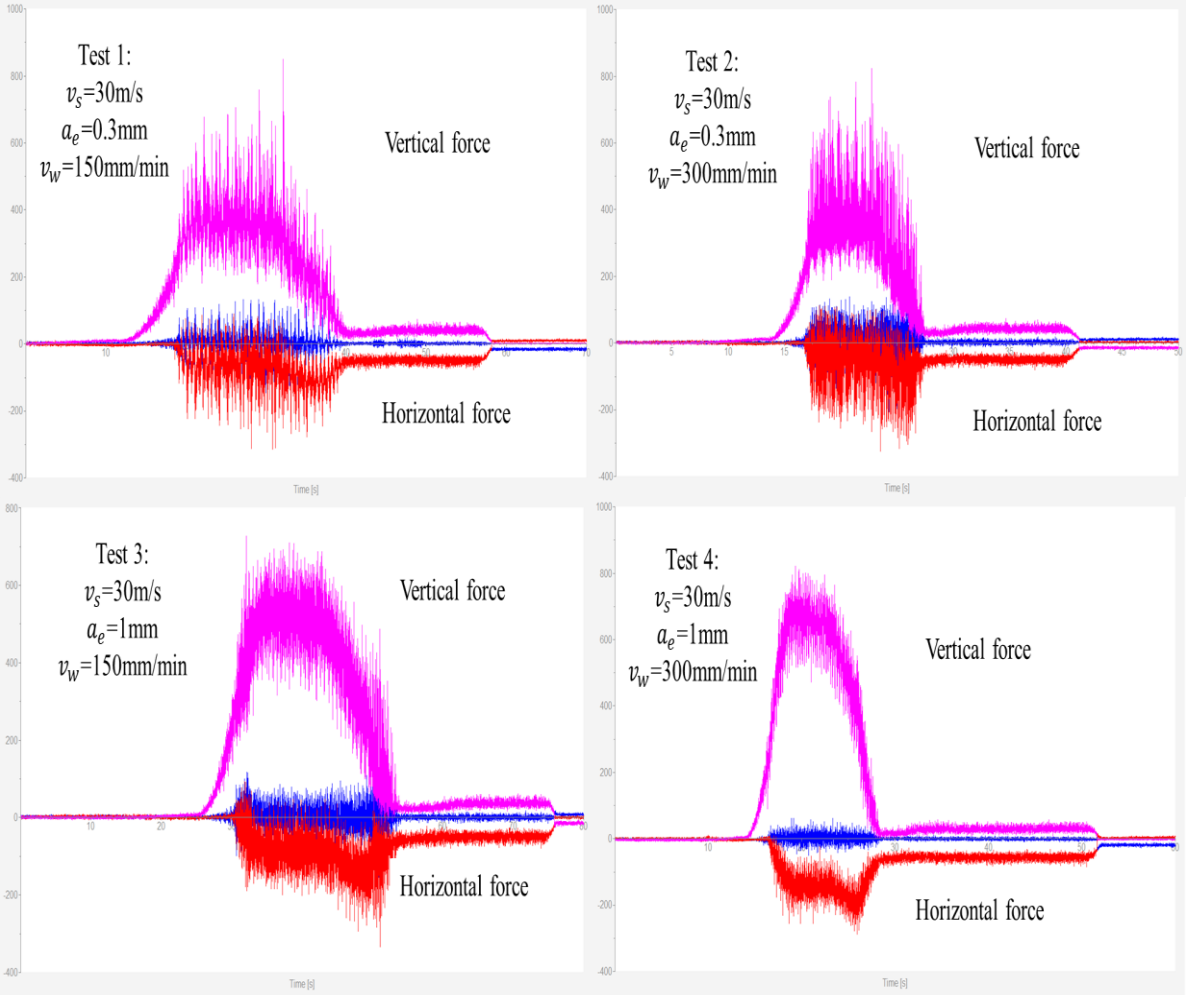


Figure F30: Grinding forces profiles (Phase 1B)

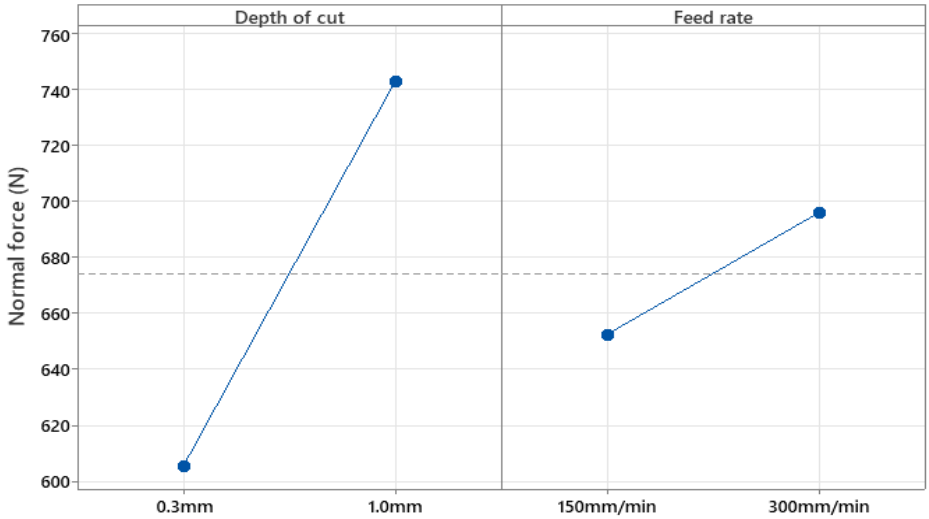


Figure F31: Main effect plot for normal force (Phase 1B)

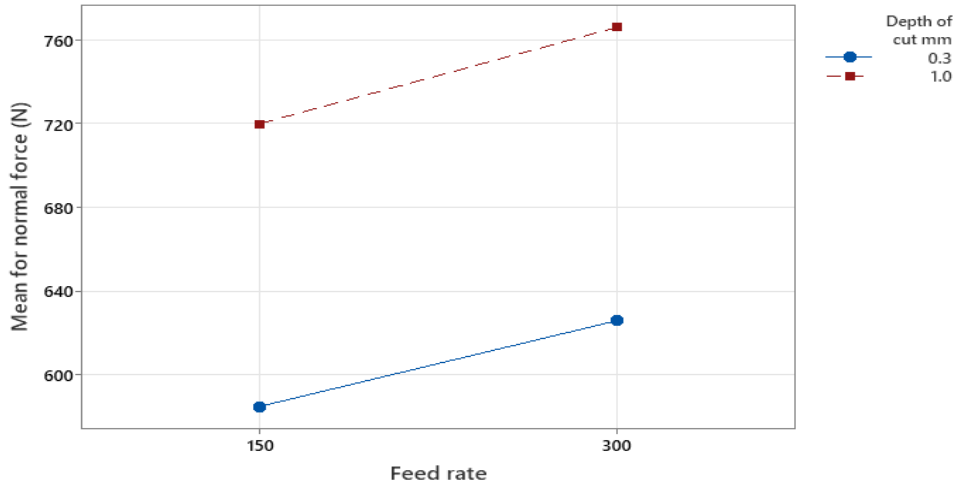


Figure F32: Interaction plot for normal force (Phase 1B)

Table F12: ANOVA table for normal force (Phase 1B)

Source	**DF**	**Seq SS**	**Contribution**	**Adj SS**	**Adj MS**	**F-Value**	**P-Value**
Depth of cut (mm)	1	18906.3	90.87%	18906.3	18906.3	3025.00	0.012
Feed rate (mm/min)	1	1892.3	9.10%	1892.3	1892.3	302.76	0.037
Error	1	6.3	0.03%	6.3	6.3	-	-
Total	3	20804.8	100.00%	-	-	-	-

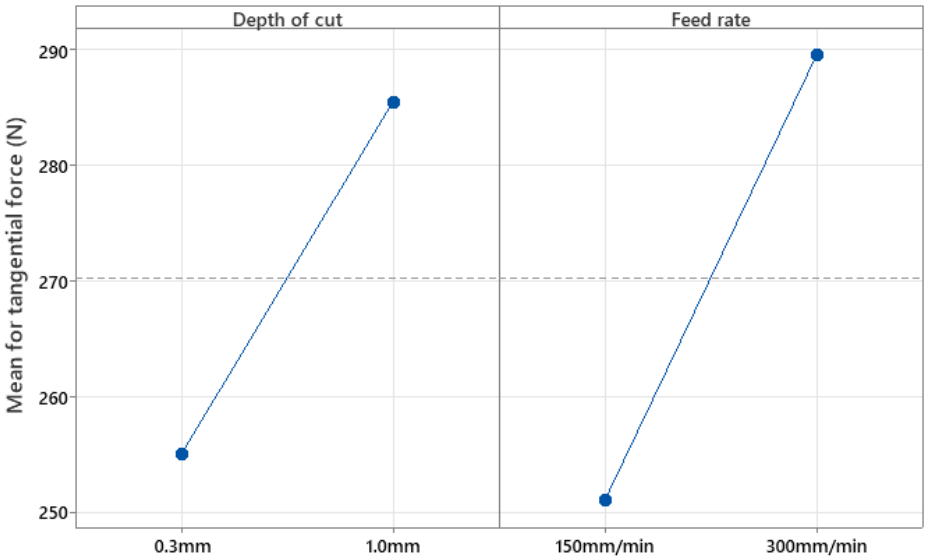


Figure F33: Main effect plot for tangential force (Phase 1B)

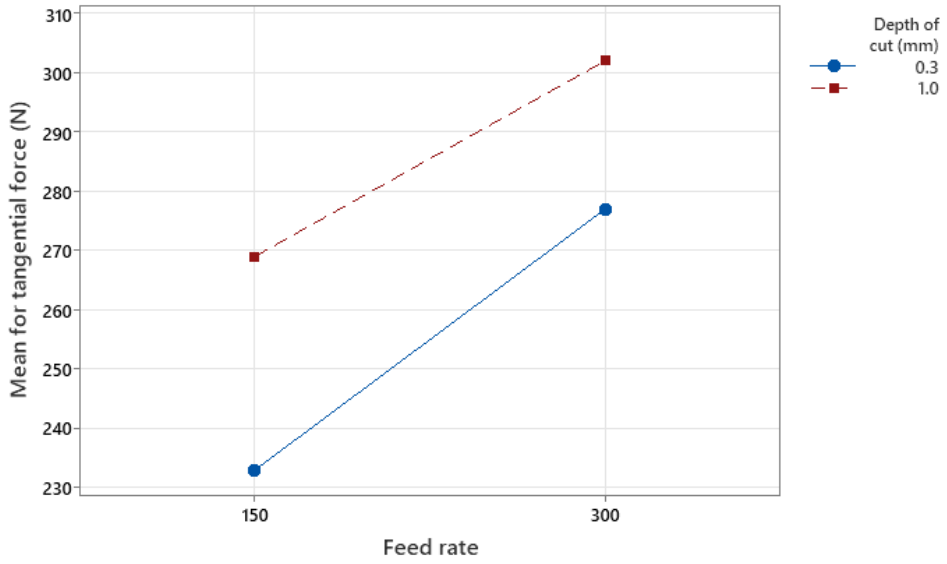


Figure F34: Interaction plot for tangential force (Phase 1B)

Table F13: ANOVA table for tangential force (Phase 1B)

Source	DF	Seq SS	Contribution	Adj SS	Adj MS	F-Value	P-Value
Depth of cut (mm)	1	42.5756	98.49%	42.5756	42.5756	70.89	0.075
Feed rate (mm/min)	1	0.0506	0.12%	0.0506	0.0506	0.08	0.820
Error	1	0.6006	1.39%	0.6006	0.6006	-	-
Total	3	43.2269	100.00%	-	-	-	-

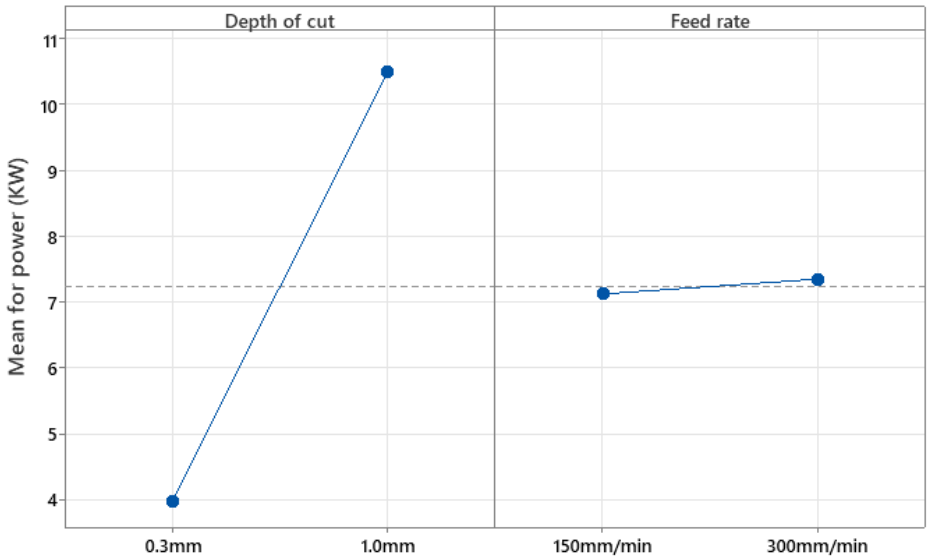


Figure F35: Main effect plot for power (Phase 1B)

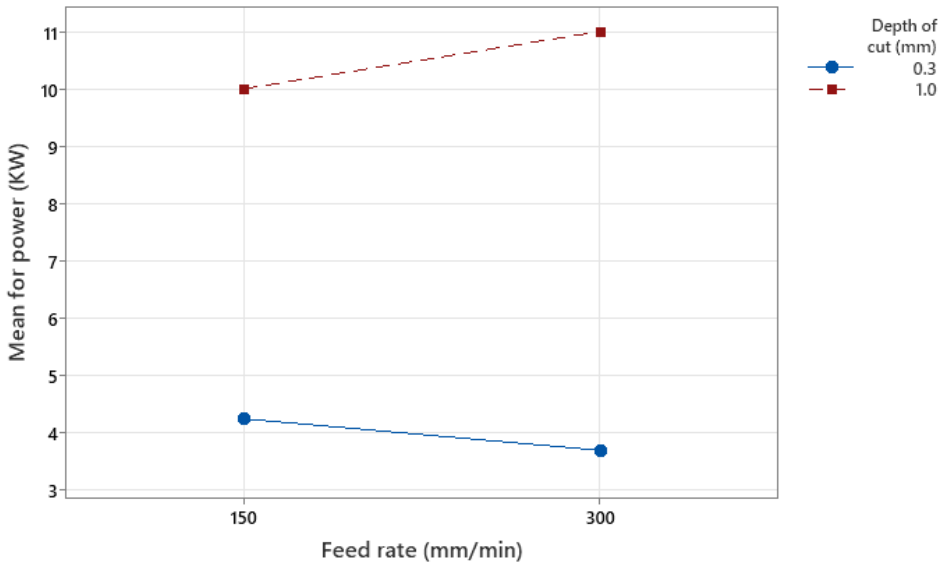


Figure F36: Interaction plot for power (Phase 1B)

Table F14: ANOVA table for power (Phase 1B)

Source	DF	Seq SS	Contribution	Adj SS	Adj MS	F-Value	P-Value
Depth of cut (mm)	1	930.25	38.08%	930.25	930.25	30.75	0.114
Feed rate (mm/min)	1	1482.25	60.68%	1482.25	1482.25	49.00	0.090
Error	1	30.25	1.24%	30.25	30.25	-	-
Total	3	2442.75	100.00%	-	-	-	-

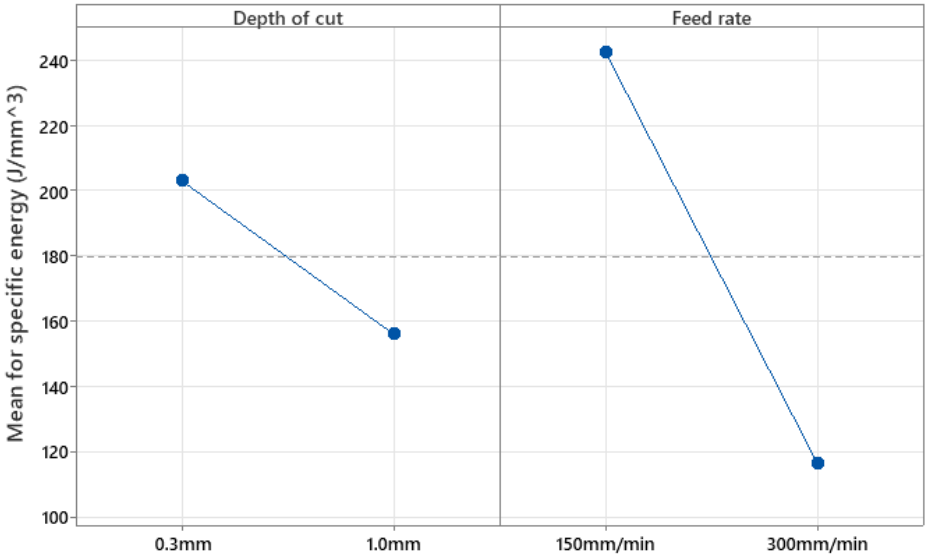


Figure F37: Main effect plot for specific energy (Phase 1B)

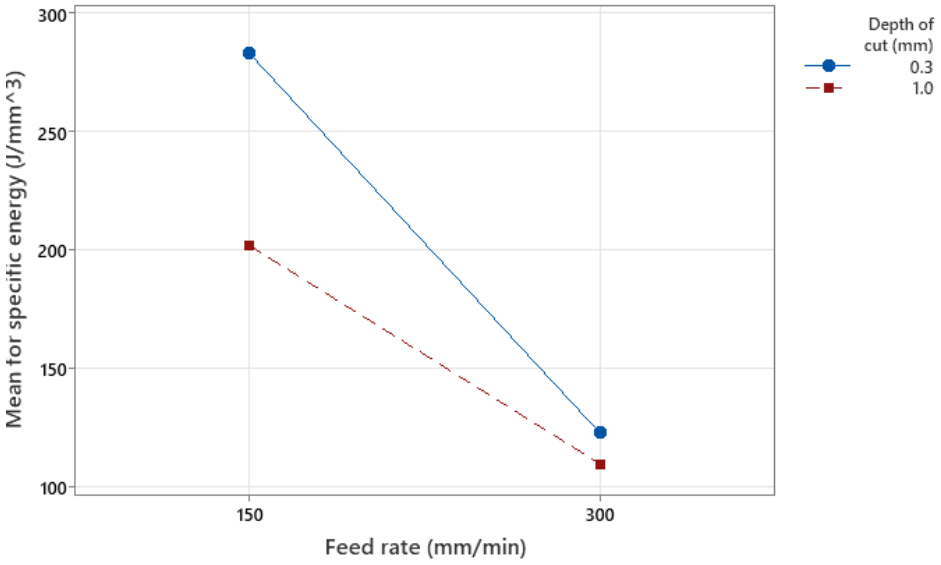


Figure F38: Interaction plot for specific energy (Phase 1B)

Table F15: ANOVA table for specific energy (Phase 1B)

Source	DF	Seq SS	Contribution	Adj SS	Adj MS	F-Value	P-Value
Depth of cut (mm)	1	2209	11.48%	2209	2209	1.91	0.399
Feed rate (mm/min)	1	15876	82.51%	15876	15876	13.73	0.168
Error	1	1156	6.01%	1156	1156	-	-
Total	3	19241	100.00%	-	-	-	-

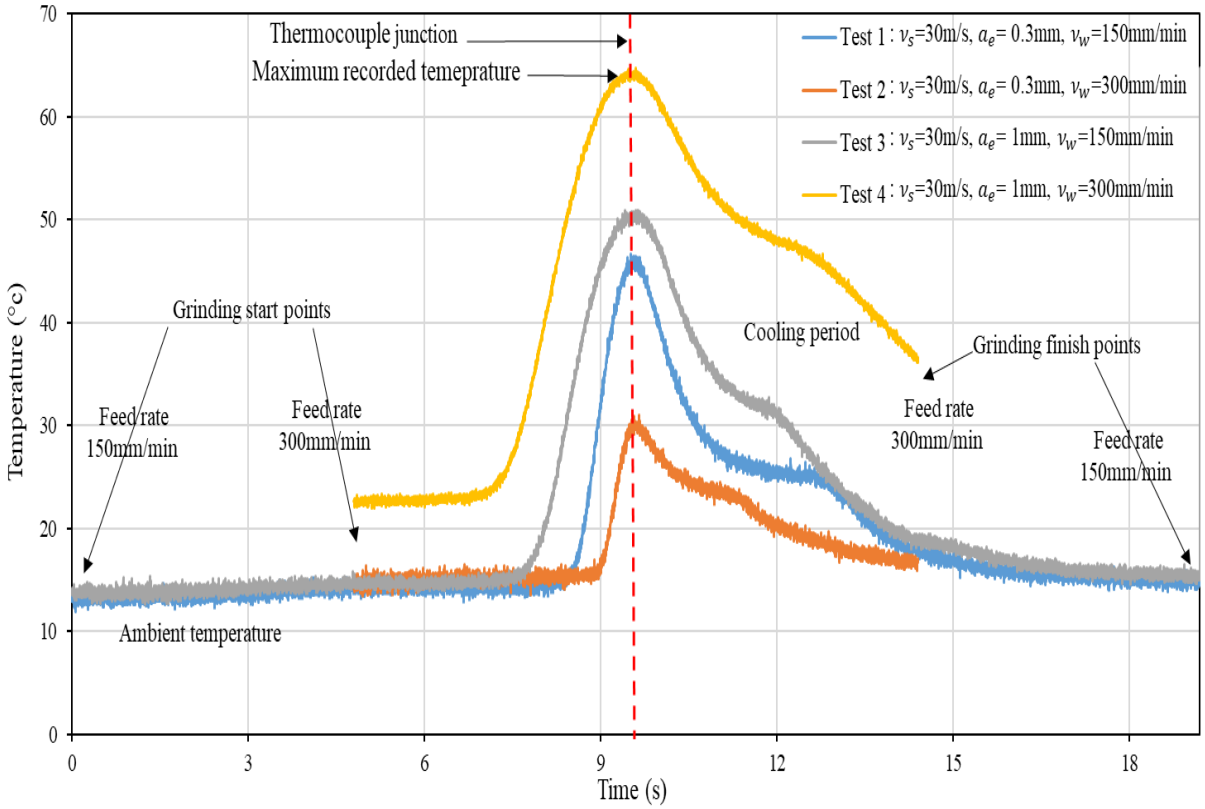


Figure F39: Grinding temperature traces (Phase 1B)

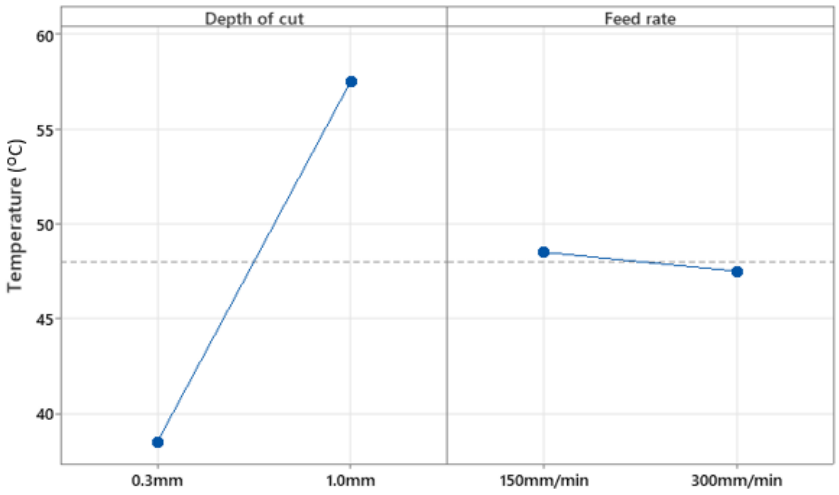


Figure F40: Main effect plot for temperature (Phase 1B)

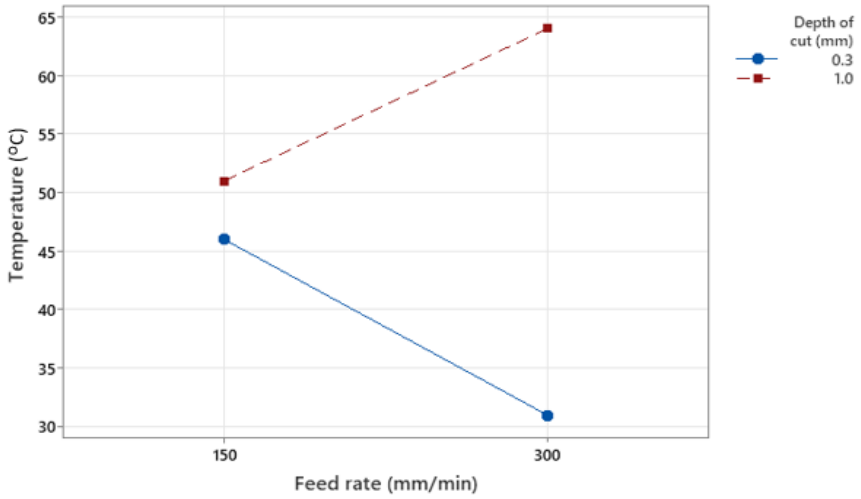


Figure F41: Interaction plot for temperature (Phase 1B)

Table F16: ANOVA table for temperature (Phase 1B)

Source	DF	Seq SS	Contribution	Adj SS	Adj MS	F-Value	P-Value
Depth of cut (mm)	1	361.000	64.70%	361.000	361.000	1.84	0.404
Feed rate (mm/min)	1	1.000	0.18%	1.000	1.000	0.01	0.955
Error	1	196.000	35.13%	196.000	196.000	-	-
Total	3	558.000	100.00%	-	-	-	-

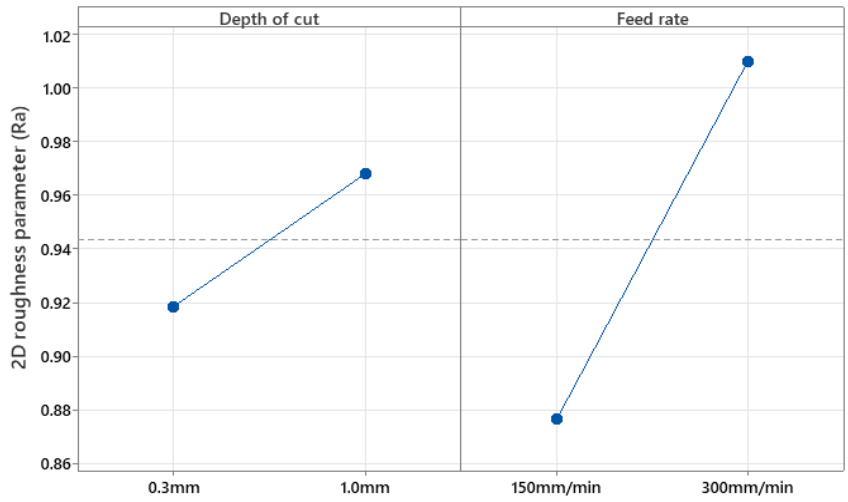


Figure F42: Main effect plot for 2D surface roughness parameter Ra (Phase 1B)

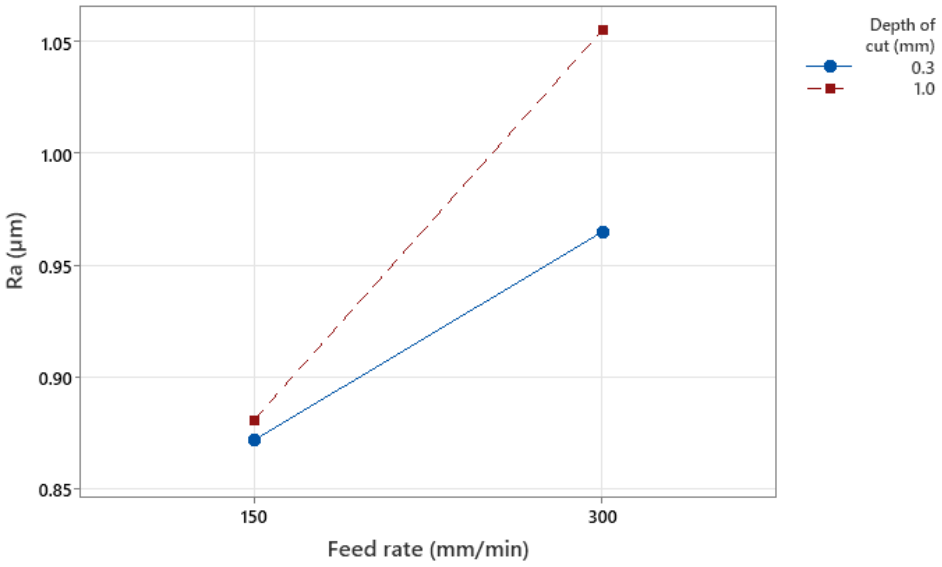


Figure F43: Interaction plot for 2D surface roughness parameter Ra (Phase 1B)

Table F17: ANOVA table for 2D surface roughness parameter Ra (Phase 1B)

Source	DF	Seq SS	Contribution	Adj SS	Adj MS	F-Value	P-Value
Depth of cut (mm)	1	0.002450	11.18%	0.002450	0.002450	1.49	0.437
Feed rate(mm/min)	1	0.017822	81.33%	0.017822	0.017822	10.87	0.188
Error	1	0.001640	7.49%	0.001640	0.001640	-	-
Total	3	0.021913	100.00%	-	-	-	-

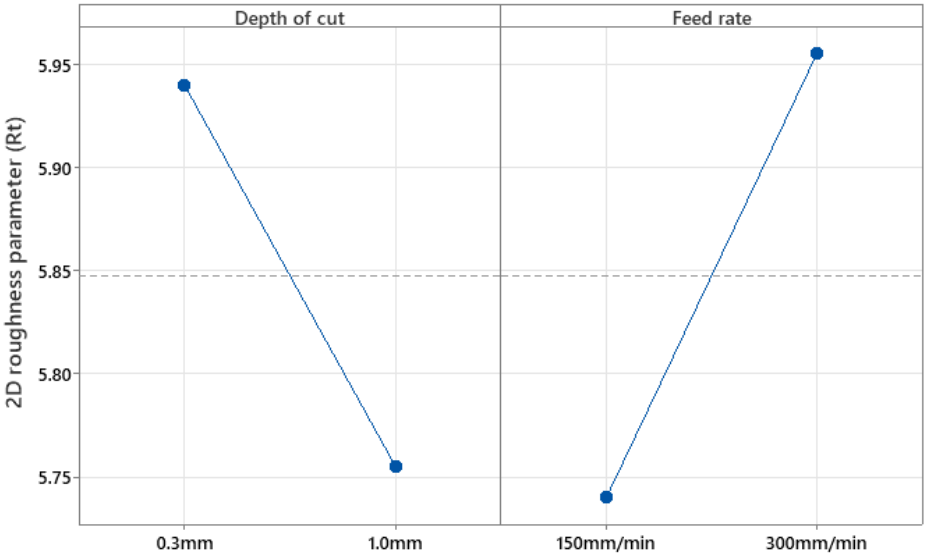


Figure F44: Main effect plot for 2D surface roughness parameter Rt (Phase 1B)

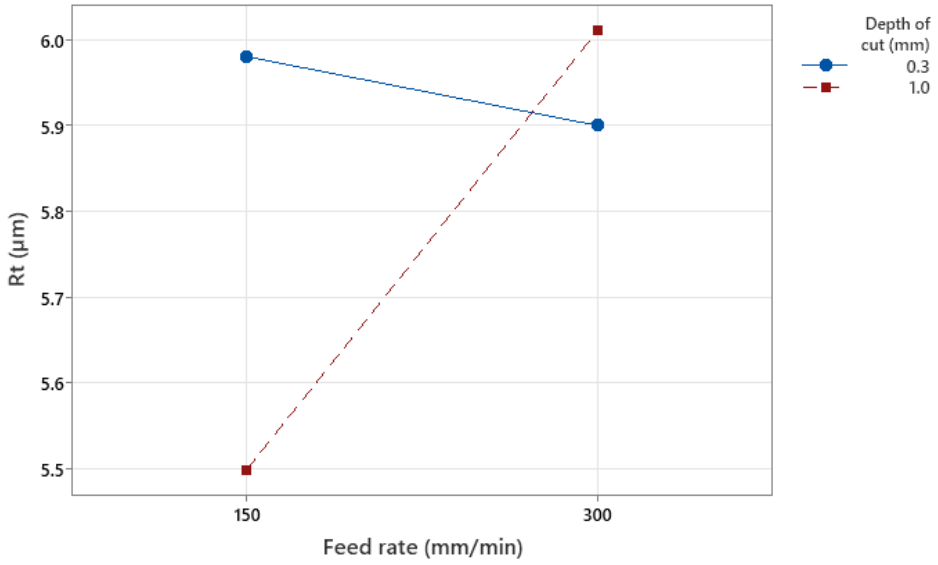


Figure F45: Interaction plot for 2D surface roughness parameter Rt (Phase 1B)

Table F18: ANOVA table for 2D surface roughness parameter Rt (Phase 1B)

Source	DF	Seq SS	Contribution	Adj SS	Adj MS	F-Value	P-Value
Depth of cut (mm)	1	0.03423	20.44%	0.03423	0.03423	0.39	0.643
Feed rate (mm/min	1	0.04622	27.60%	0.04622	0.04622	0.53	0.599
Error	1	0.08702	51.96%	0.08702	0.08702	-	-
Total	3	0.16748	100.00%	-	-	-	-

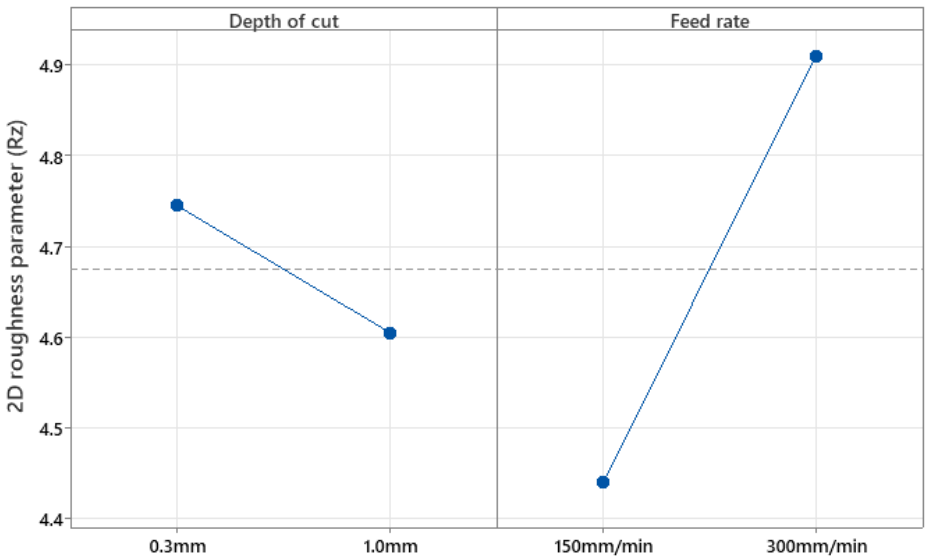


Figure F46: Main effect plot for 2D surface roughness parameter Rz (Phase 1B)

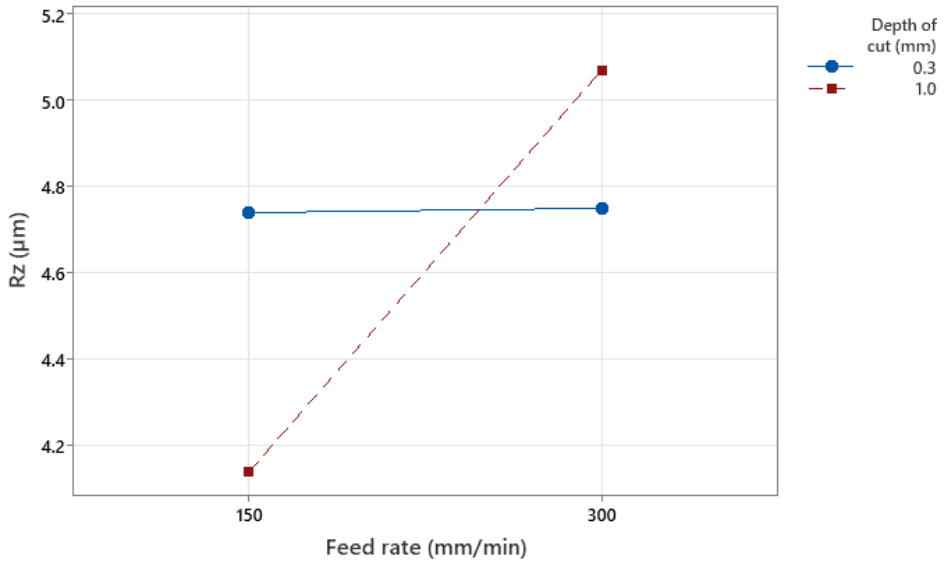


Figure F47: Interaction plot for 2D surface roughness parameter Rz (Phase 1B)

Table F19: ANOVA table for 2D surface roughness parameter Rz (Phase 1B)

Source	DF	Seq SS	Contribution	Adj SS	Adj MS	F-Value	P-Value
Depth of cut (mm)	1	0.01960	4.34%	0.01960	0.01960	0.09	0.812
Feed rate (mm/min)	1	0.22090	48.86%	0.22090	0.22090	1.04	0.493
Error	1	0.21160	46.80%	0.21160	0.21160	-	-
Total	3	0.45210	100.00%	-	-	-	-

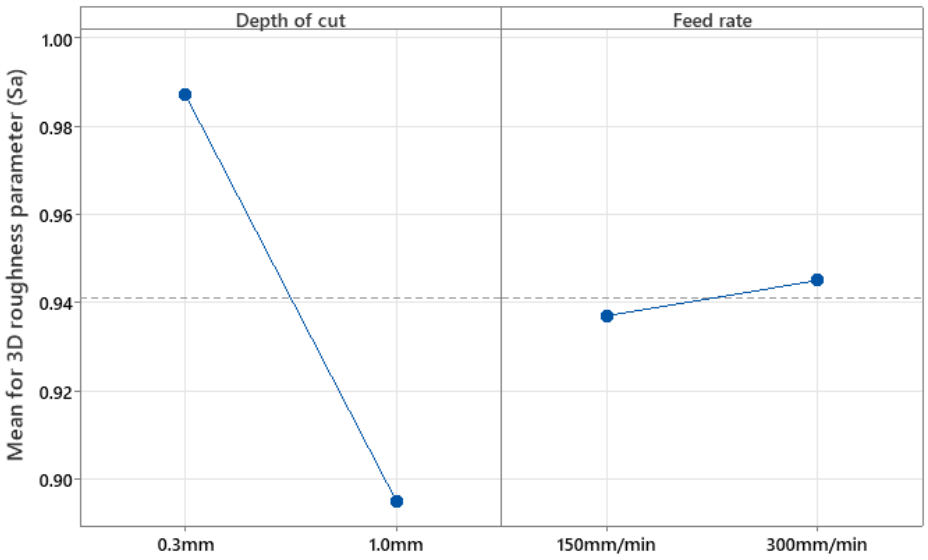


Figure F48: Main effect plot for 3D surface roughness parameter Sa (Phase 1B)

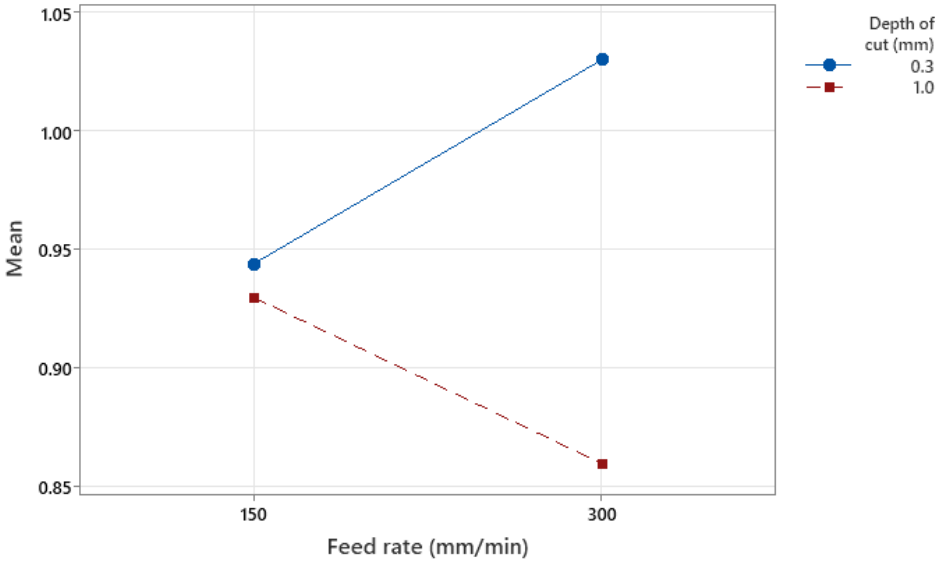


Figure F49: Interaction plot for 3D surface roughness parameter Sa (Phase 1B)

Table F20: ANOVA table for 3D surface roughness parameter Sa (Phase 1B)

Source	DF	Seq SS	Contribution	Adj SS	Adj MS	F-Value	P-Value
Depth of cut (mm)	1	0.008464	57.92%	0.008464	0.008464	1.39	0.448
Feed rate (mm/min)	1	0.000064	0.44%	0.000064	0.000064	0.01	0.935
Error	1	0.006084	41.64%	0.006084	0.006084	-	-
Total	3	0.014612	100.00%	-	-	-	-

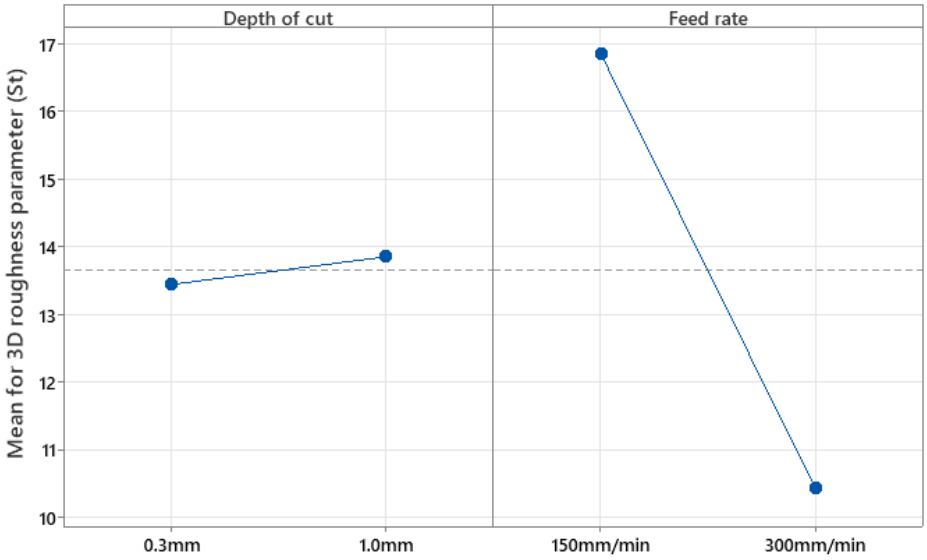


Figure F50: Main effect plot for 3D surface roughness parameter St (Phase 1B)

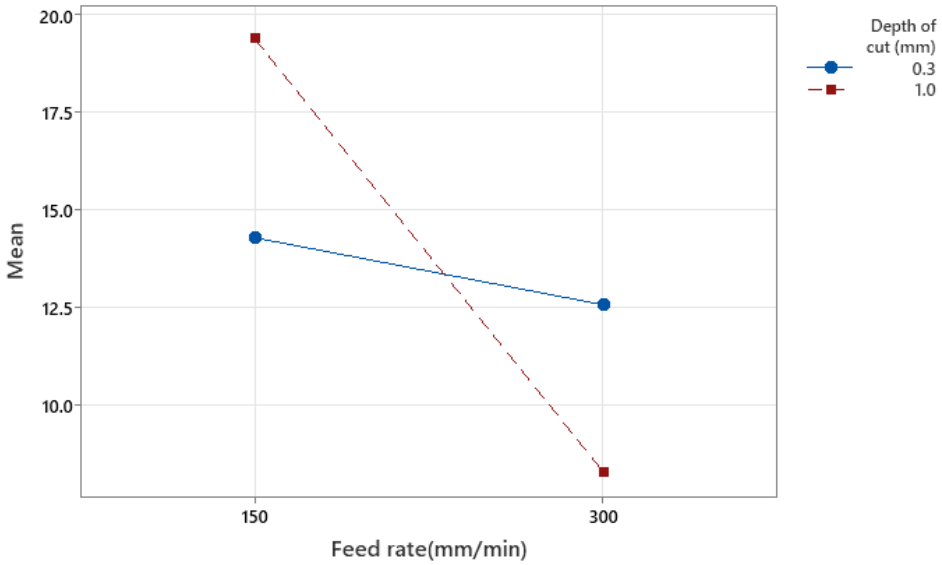


Figure F51: Interaction plot for 3D surface roughness parameter St (Phase 1B)

Table F21: ANOVA table for 3D surface roughness parameter St (Phase 1B)

Source	DF	Seq SS	Contribution	Adj SS	Adj MS	F-Value	P-Value
Depth of cut (mm)	1	0.1681	0.27%	0.1681	0.1681	0.01	0.944
Feed rate (mm/min)	1	41.0881	64.96%	41.0881	41.0881	1.87	0.402
Error	1	21.9961	34.78%	21.9961	21.9961	-	-
Total	3	63.2523	100.00%	-	-	-	-

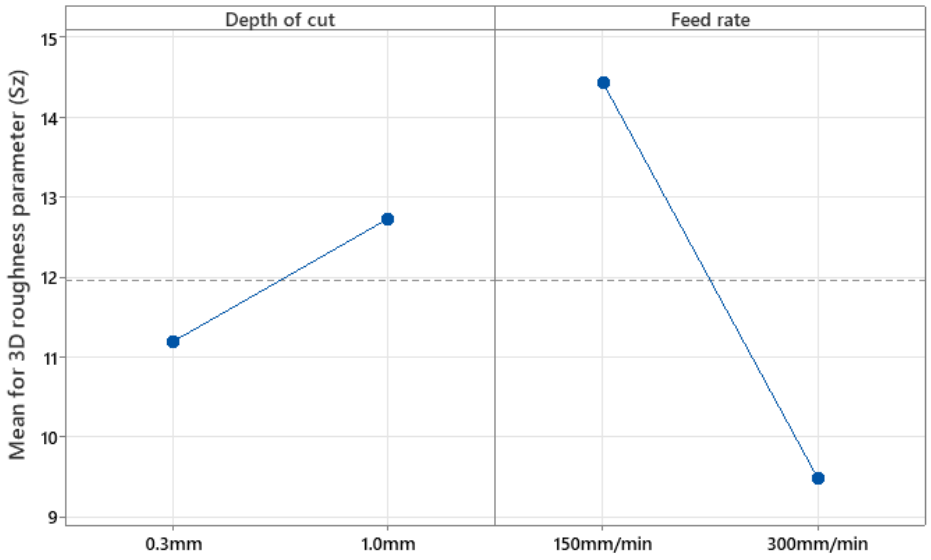


Figure F52: Main effect plot for 3D surface roughness parameter Sz (Phase 1B)

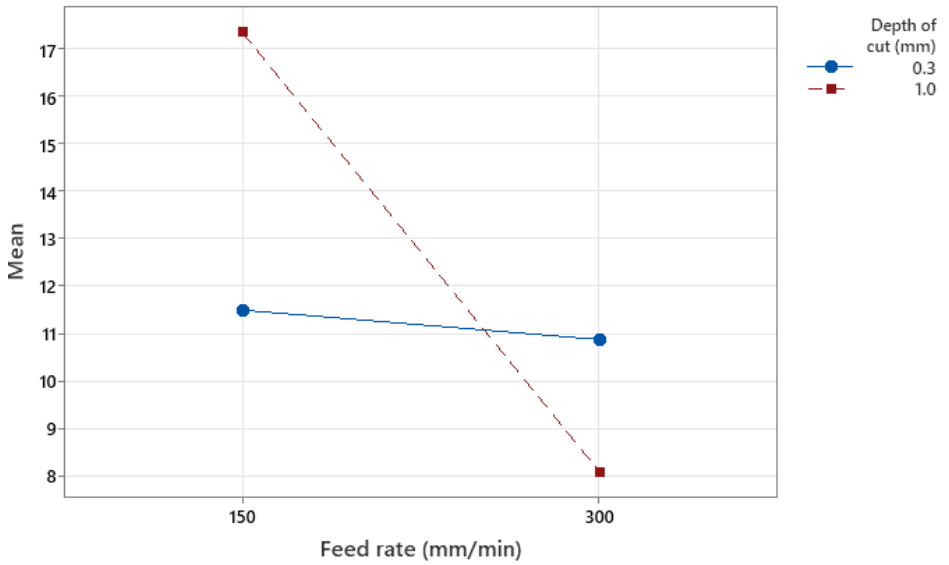


Figure F53: Interaction plot for 3D surface roughness parameter Sz (Phase 1B)

Table F22: ANOVA table for 3D surface roughness parameter Sz (Phase 1B)

Source	DF	Seq SS	Contribution	Adj SS	Adj MS	F-Value	P-Value
Depth of cut (mm)	1	2.356	5.20%	2.356	2.356	0.13	0.782
Feed rate (mm/min)	1	24.354	53.73%	24.354	24.354	1.31	0.457
Error	1	18.619	41.08%	18.619	18.619	-	-
Total	3	45.330	100.00%	-	-	-	-

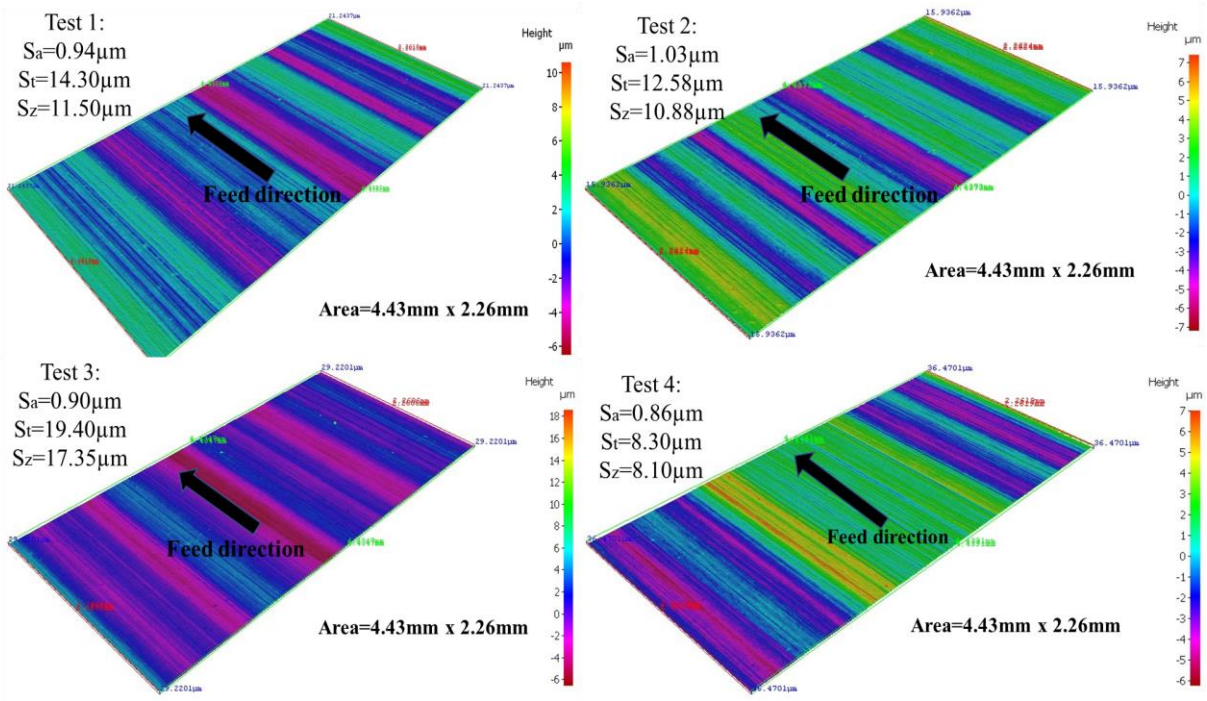


Figure F54: 3D topographies of ground surfaces, primary mapping not filtered (Phase 1B)

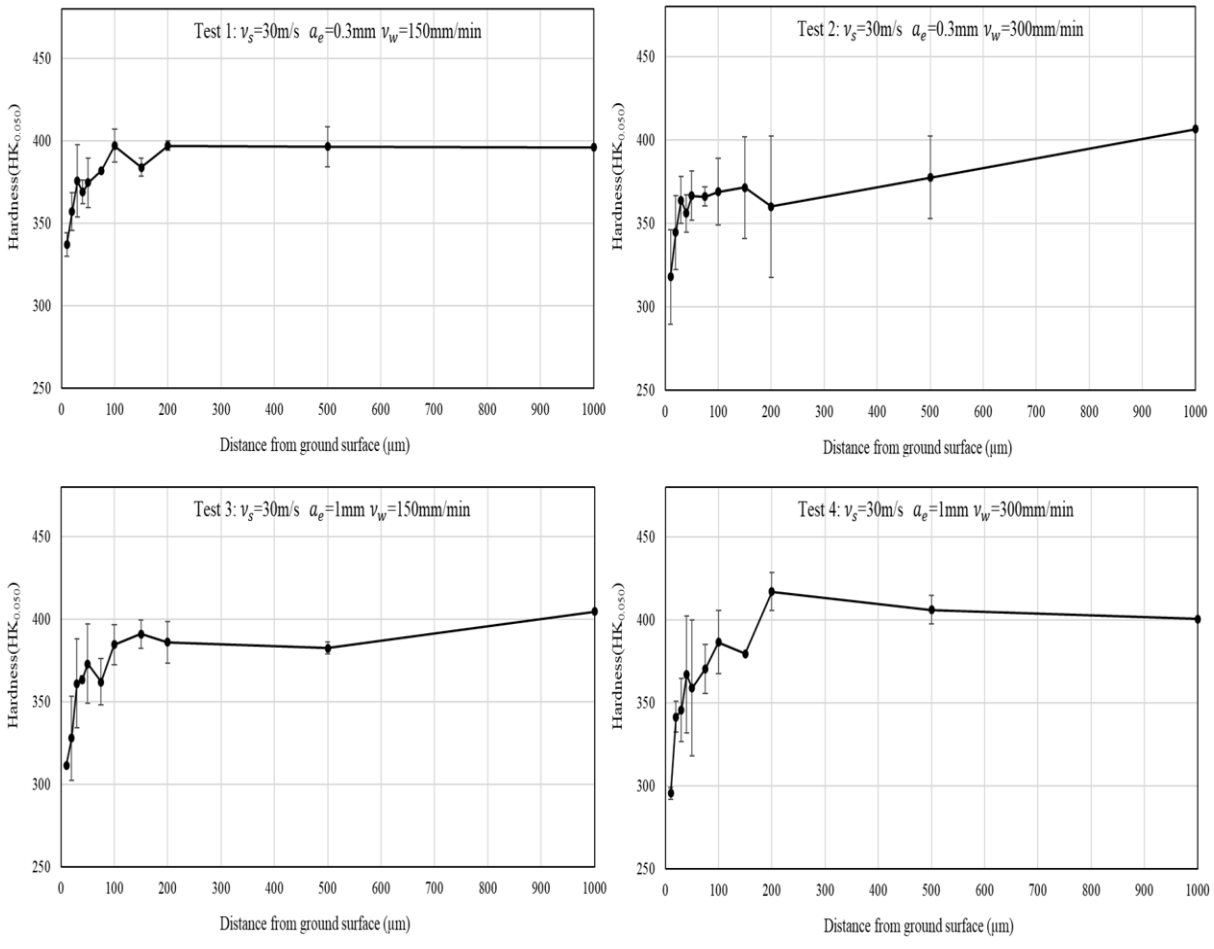


Figure F55: Individual microhardness profiles (Phase 1B)

F2 Phase 2: Creep feed grinding of burn resistant titanium alloy (Ti-25V-15Cr-2Al-0.2C)

a) Phase 2A: Assessment of significant operating parameters when creep feed grinding burn resistant titanium alloy (Ti-25V-15Cr-2Al-0.2C) with conventional silicon carbide wheel (SiC) and benchmark against γ-titanium aluminide alloy (Ti-45Al-8Nb-0.2C)

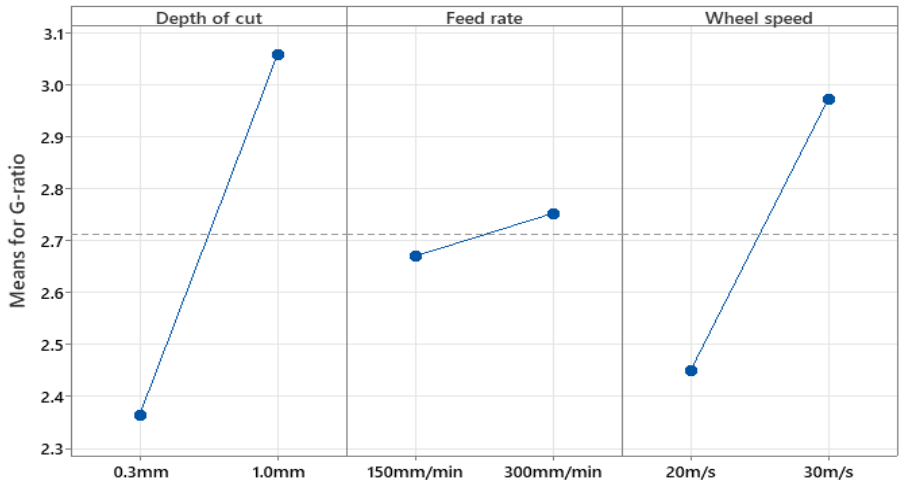


Figure F56: Main effect plot for G-ratio (Phase 2A)

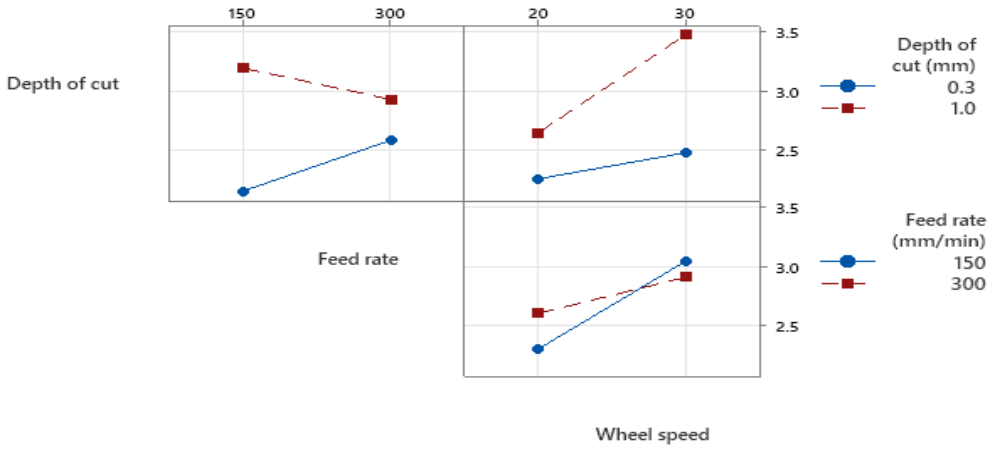


Figure F57: Interaction plot for G-ratio (Phase 2A)

Table F23: ANOVA table for G-ratio (Phase 2A)

Source	DF	Seq SS	Contribution	Adj SS	Adj MS	F-Value	P-Value
Wheel speed (m/s)	1	0.54601	25.60%	0.54601	0.54601	3.56	0.132
Depth of cut (mm)	1	0.95911	44.98%	0.95911	0.95911	6.25	0.067
Feed rate (mm/min)	1	0.01361	0.64%	0.01361	0.01361	0.09	0.781
Error	4	0.61375	28.78%	0.61375	0.15344	-	-
Total	7	2.13249	100.00%	-	-	-	-

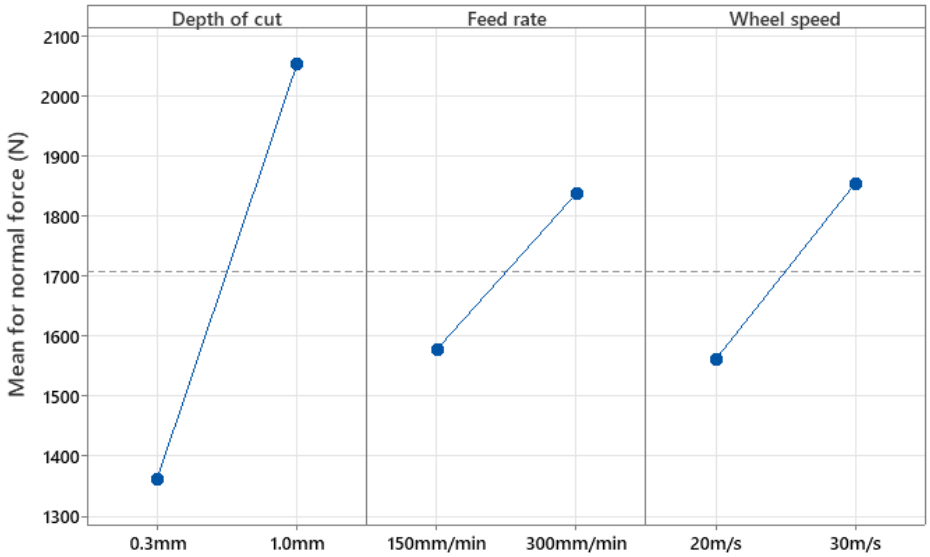


Figure F58: Main effect plot for normal force (Phase 2A)

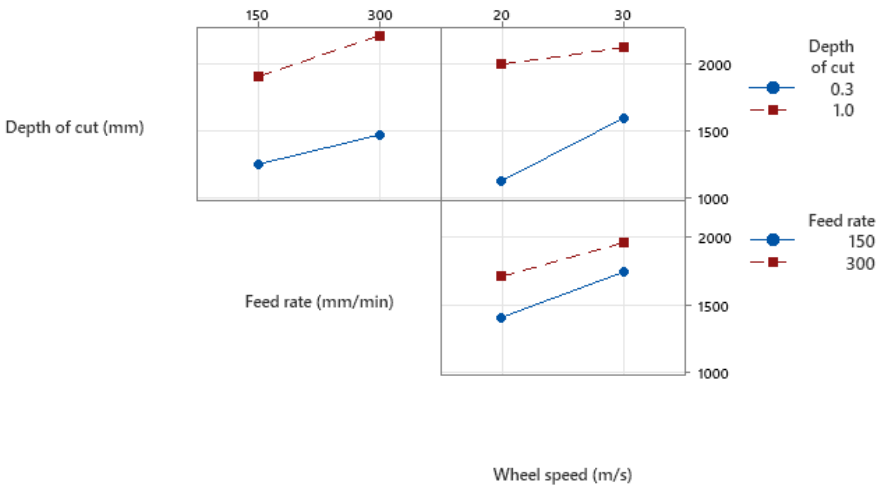


Figure F59: Interaction plot for normal force (Phase 2A)

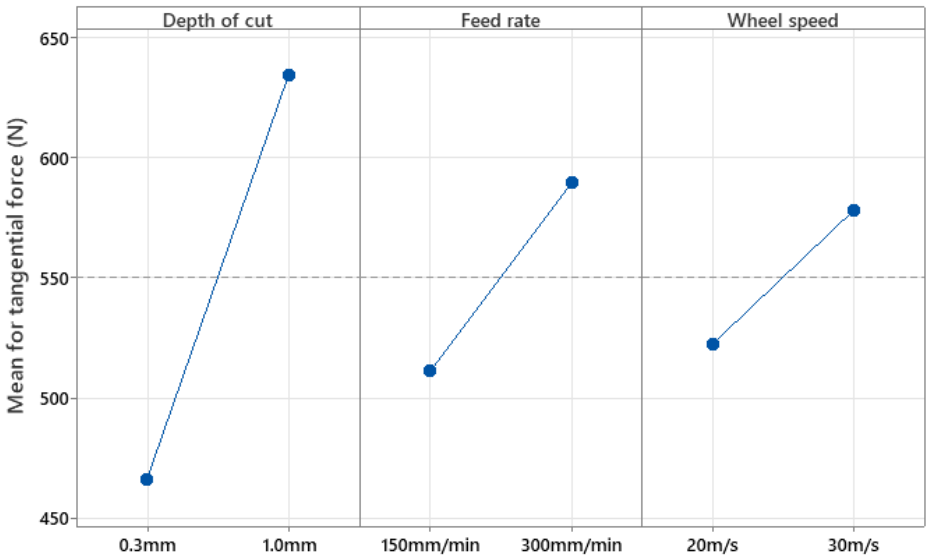


Figure F60: Main effect plot for tangential force (Phase 2A)

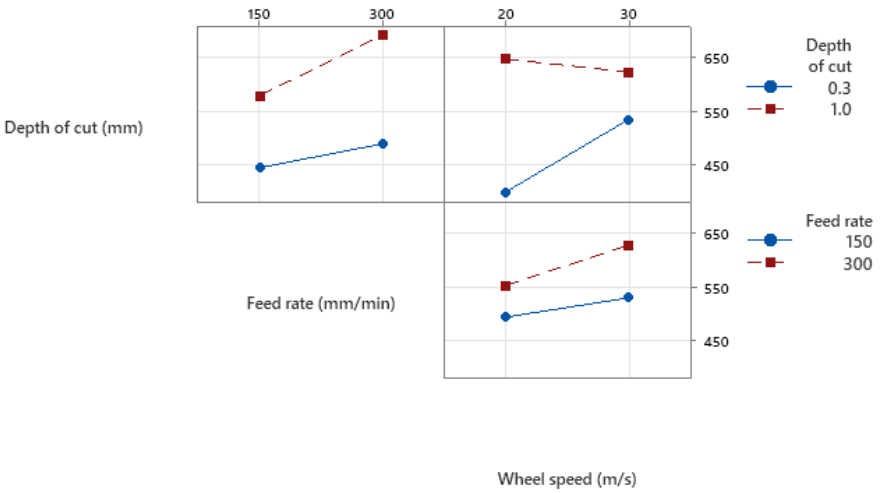


Figure F61: Interaction plot for tangential force (Phase 2A)

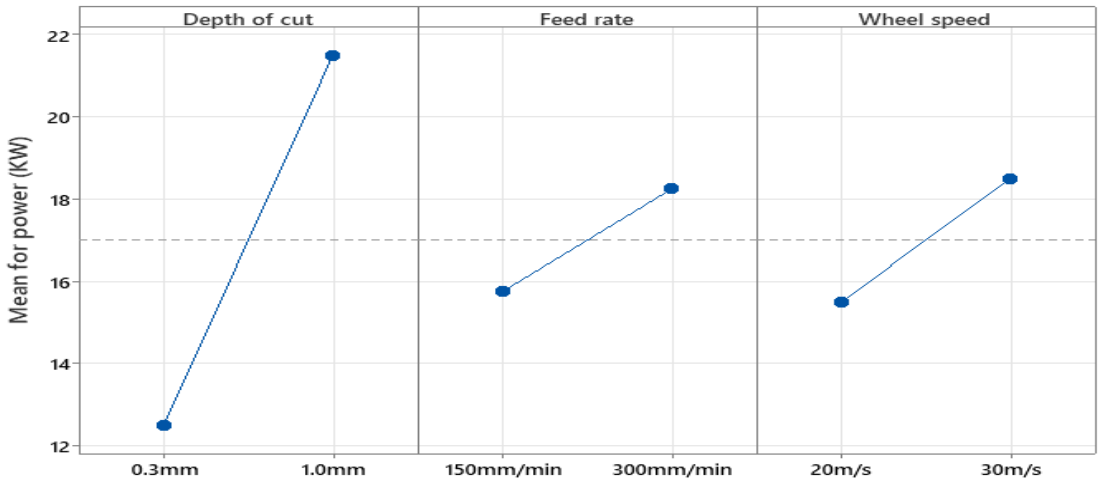


Figure F62: Main effect plot for power (Phase 2A)

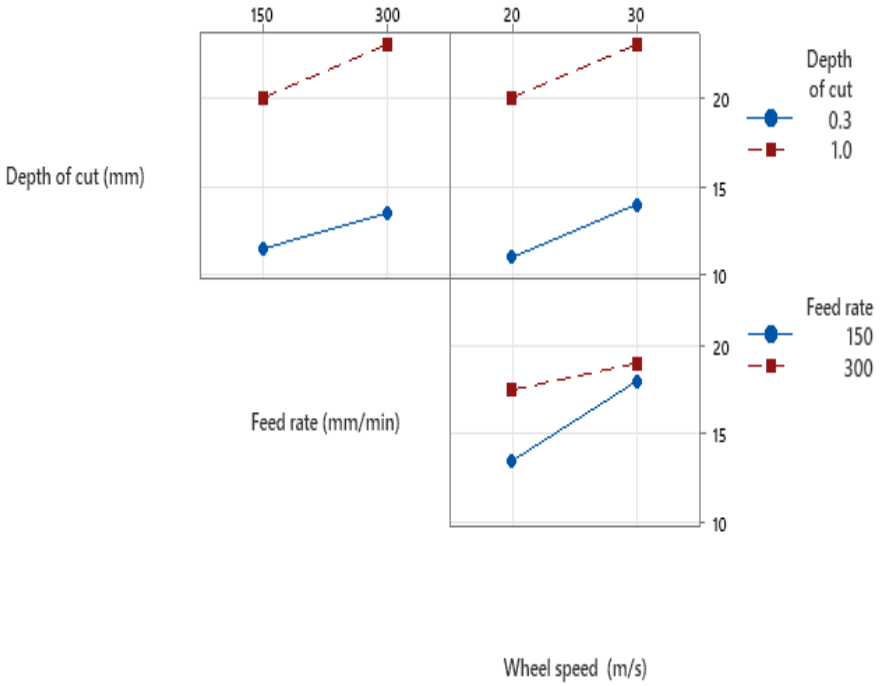


Figure F63: Interaction plot for power (Phase 2A)

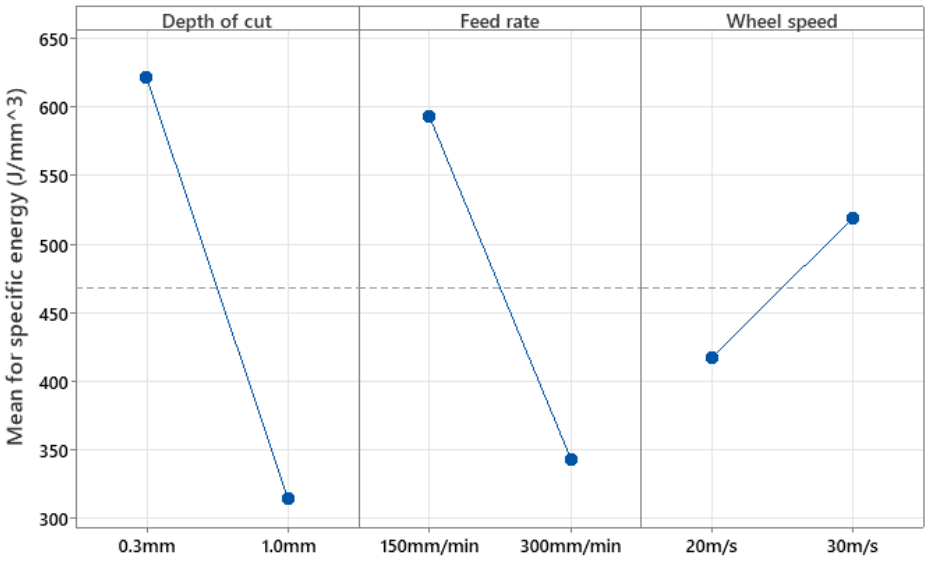


Figure F64: Main effect plot for specific energy (Phase 2A)

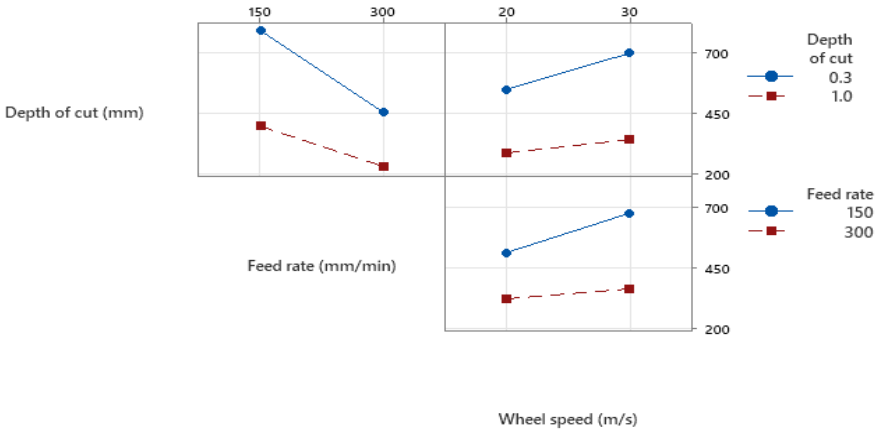


Figure F65: Interaction plot for specific energy (Phase 2A)

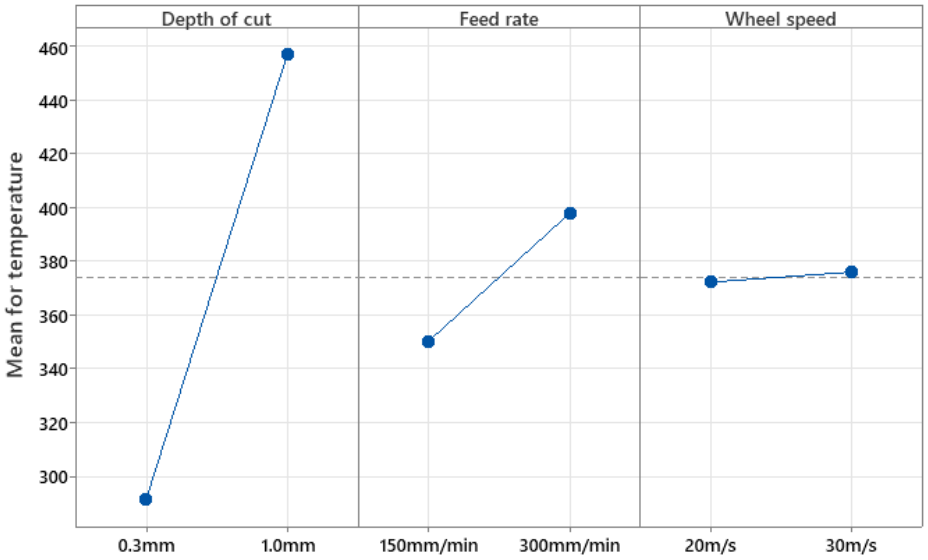


Figure F66: Main effect plot for temperature (Phase 2A)

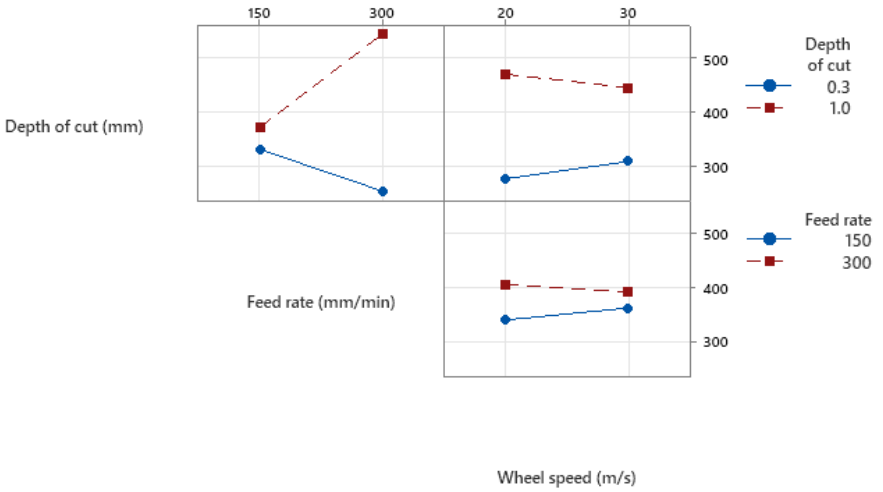


Figure F67: Interaction plot for temperature (Phase 2A)

Table F24: ANOVA table for temperature (Phase 2A)

Source	DF	Seq SS	Contribution	Adj SS	Adj MS	F-Value	P-Value
Wheel speed	1	15	0.01%	15.1	15.1	0.00	0.974
Depth of cut	1	50721	46.75%	50721.1	50721.1	3.91	0.119
Feed rate	1	5886	5.43%	5886.1	5886.1	0.45	0.537
Error	4	51867	47.81%	51866.5	12966.6	-	-
Total	7	108489	100.00%	-	-	-	-

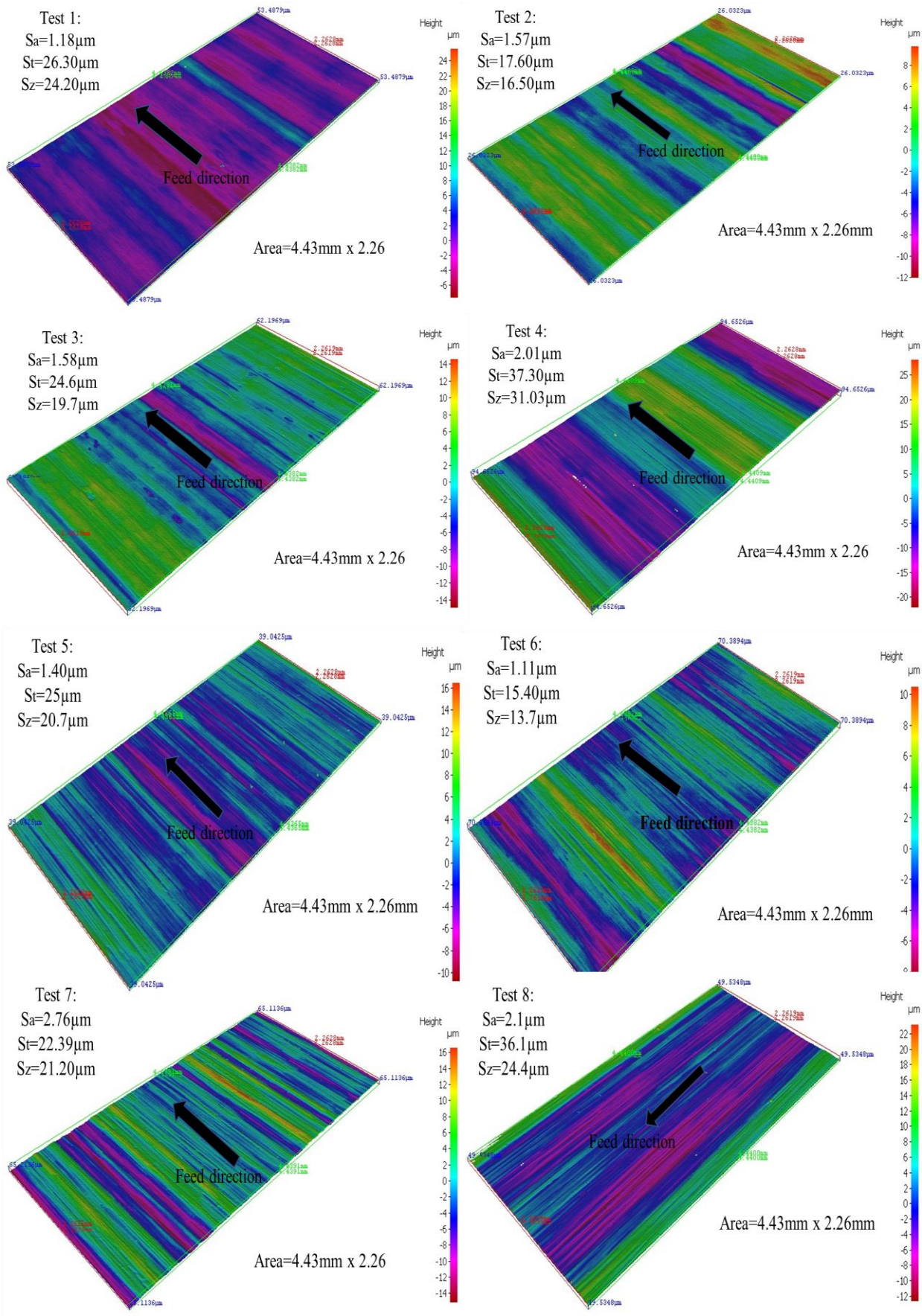


Figure F68: 3D topographies of ground surfaces, primary mapping not filtered (Phase 2A)

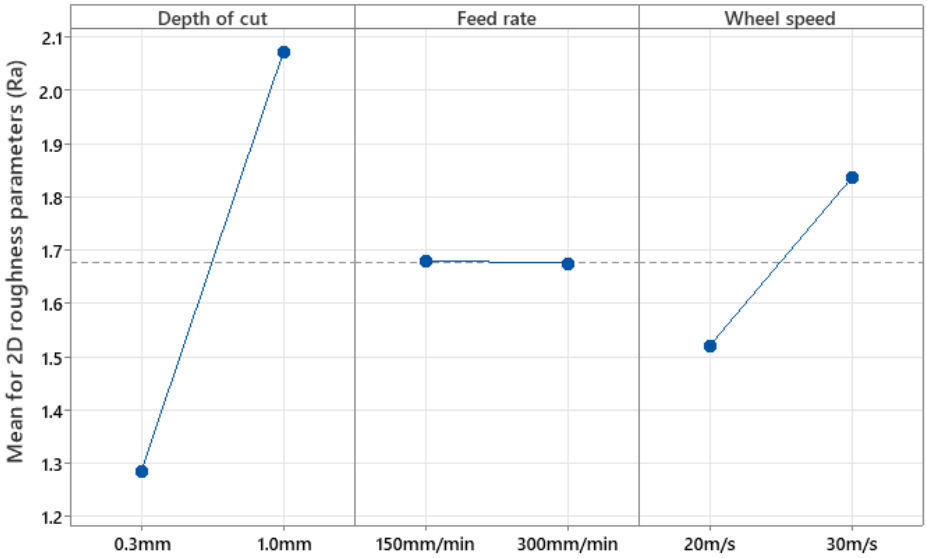


Figure F69: Main effect plot for 2D surface roughness parameter Ra in µm (Phase 2A)

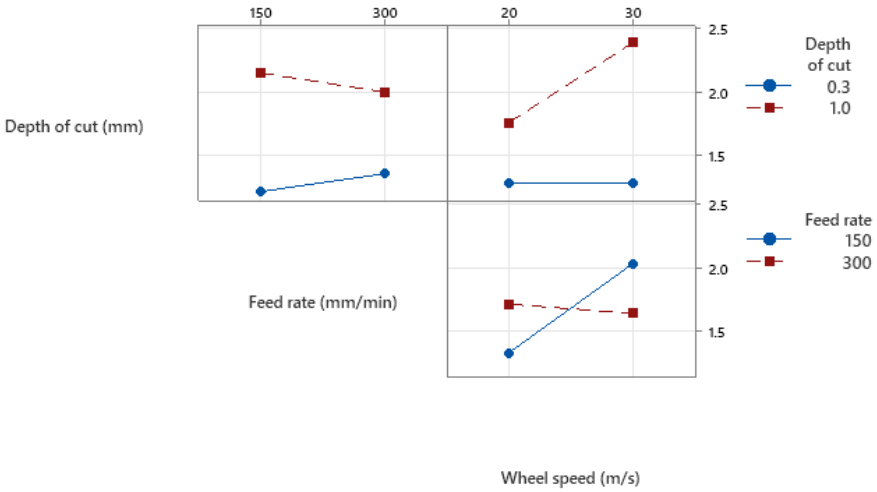


Figure F70: Interaction plot for 2D surface roughness parameter Ra (Phase 2A)

Table F25: ANOVA table for 2D surface roughness parameter Ra (Phase 2A)

Source	DF	Seq SS	Contribution	Adj SS	Adj MS	F-Value	P-Value
Wheel speed (m/s)	1	0.19845	9.71%	0.19845	0.19845	1.29	0.319
Depth of cut (mm)	1	1.23245	60.30%	1.23245	1.23245	8.04	0.047
Feed rate (mm/min)	1	0.00005	0.00%	0.00005	0.00005	0.00	0.986
Error	4	0.61300	29.99%	0.61300	0.15325	-	-
Total	7	2.04395	100.00%	-	-	-	-

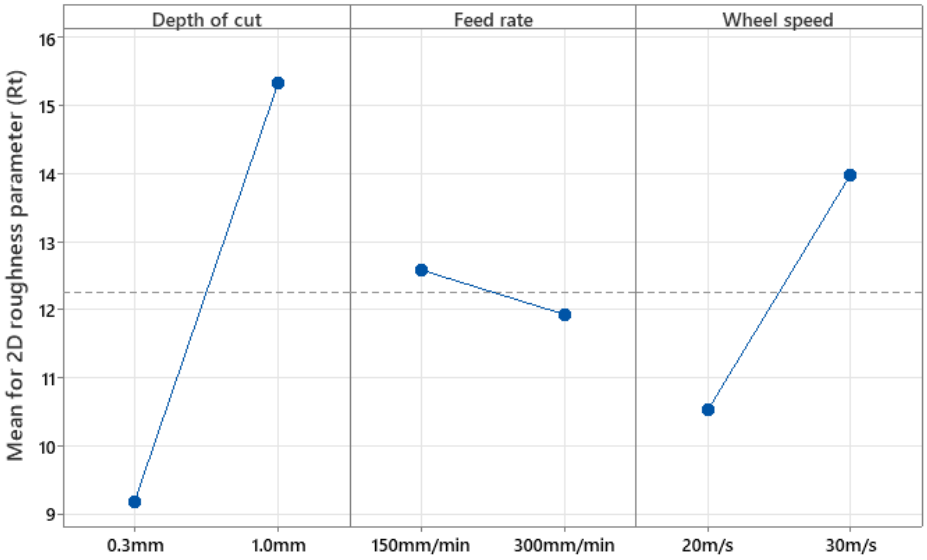


Figure F71: Main effect plot for 2D surface roughness parameter Rt in µm (Phase 2A)

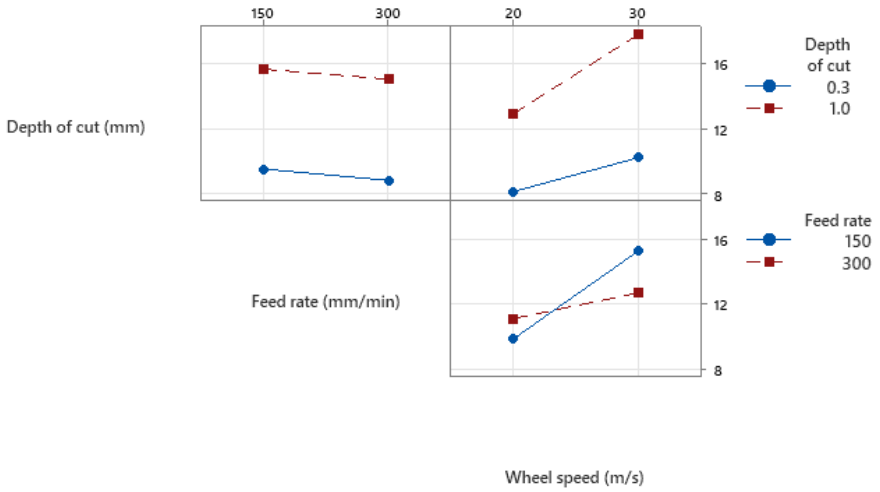


Figure F72: Interaction plot for 2D surface roughness parameter Rt (Phase 2A)

Table F26: ANOVA table for 2D surface roughness parameter Rt (Phase 2A)

Source	DF	Seq SS	Contribution	Adj SS	Adj MS	F-Value	P-Value
Wheel speed (m/s)	1	23.874	19.62%	23.8741	23.8741	4.41	0.104
Depth of cut (mm)	1	75.276	61.87%	75.2765	75.2765	13.90	0.020
Feed rate (mm/min)	1	0.858	0.71%	0.8581	0.8581	0.16	0.711
Error	4	21.658	17.80%	21.6580	5.4145	-	-
Total	7	121.667	100.00%	-	-	-	-

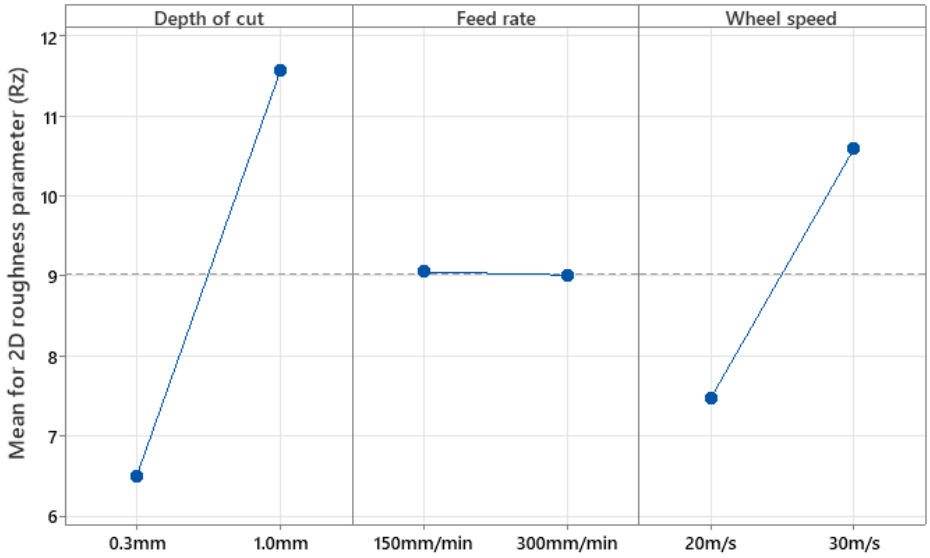


Figure F73: Main effect plot for 2D surface roughness parameter Rz in in µm (Phase 2A)

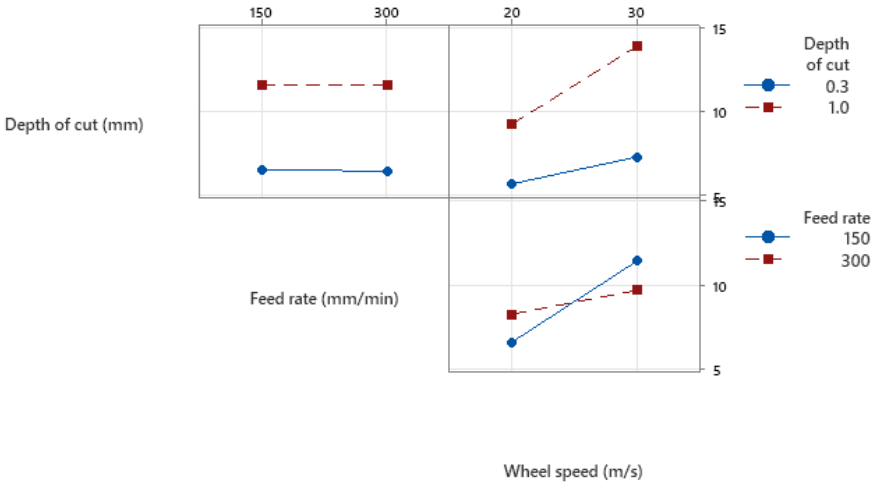


Figure F74: Interaction plot for 2D surface roughness parameter Rz (Phase 2A)

Table F27: ANOVA table for 2D surface roughness parameter Rz (Phase 2A)

Source	DF	Seq SS	Contribution	Adj SS	Adj MS	F-Value	P-Value
Wheel speed (m/s)	1	19.2821	23.33%	19.2821	19.2821	6.28	0.066
Depth of cut (mm)	1	51.1060	61.82%	51.1060	51.1060	16.66	0.015
Feed rate (mm/min)	1	0.0032	0.00%	0.0032	0.0032	0.00	0.976
Error	4	12.2725	14.85%	12.2725	3.0681	-	-
Total	7	82.6638	100.00%	-	-	-	-

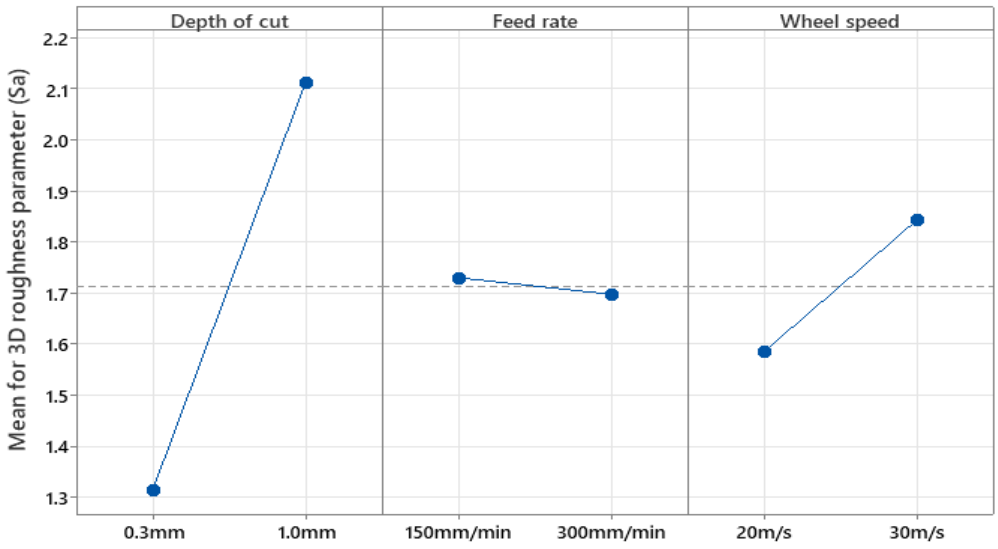


Figure F75: Main effect plot for 3D surface roughness parameter Sa in µm (Phase 2A)

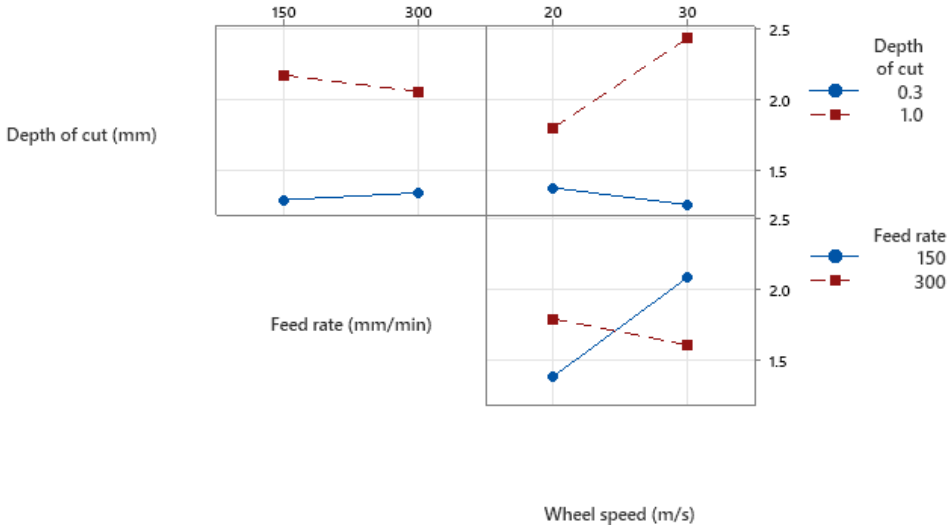


Figure F76: Interaction plot for 3D surface roughness parameter Sa (Phase 2A)

Table F28: ANOVA table for 3D surface roughness parameter Sa (Phase 2A)

Source	DF	Seq SS	Contribution	Adj SS	Adj MS	F-Value	P-Value
Wheel speed (m/s)	1	0.13261	6.26%	0.13261	0.13261	0.75	0.437
Depth of cut (mm)	1	1.27201	60.06%	1.27201	1.27201	7.15	0.056
Feed rate (mm/min)	1	0.00211	0.10%	0.00211	0.00211	0.01	0.918
Error	4	0.71125	33.58%	0.71125	0.17781	-	-
Total	7	2.11799	100.00%	-	-	-	-

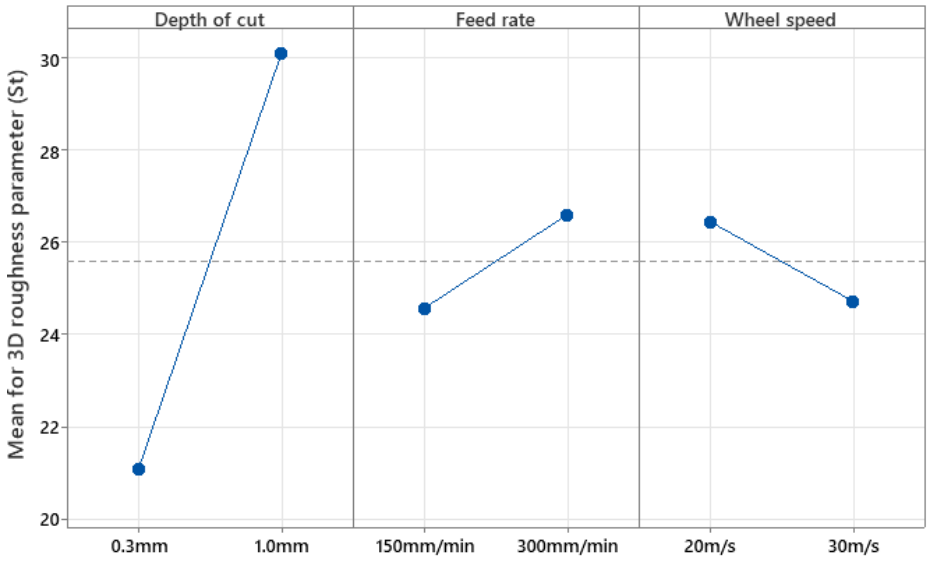


Figure F77: Main effect plot for 3D surface roughness parameter St in µm (Phase 2A)

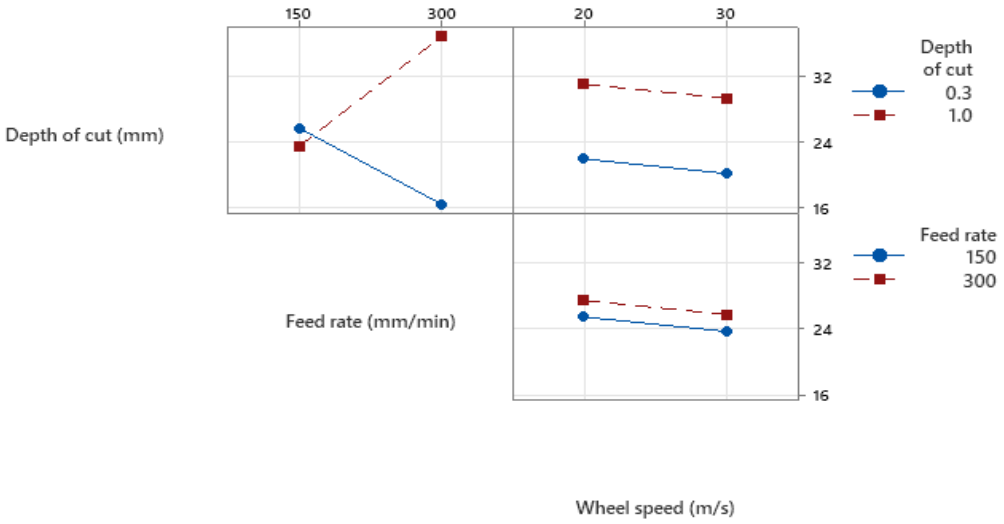


Figure F78: Interaction plot for 3D surface roughness parameter St (Phase 2A)

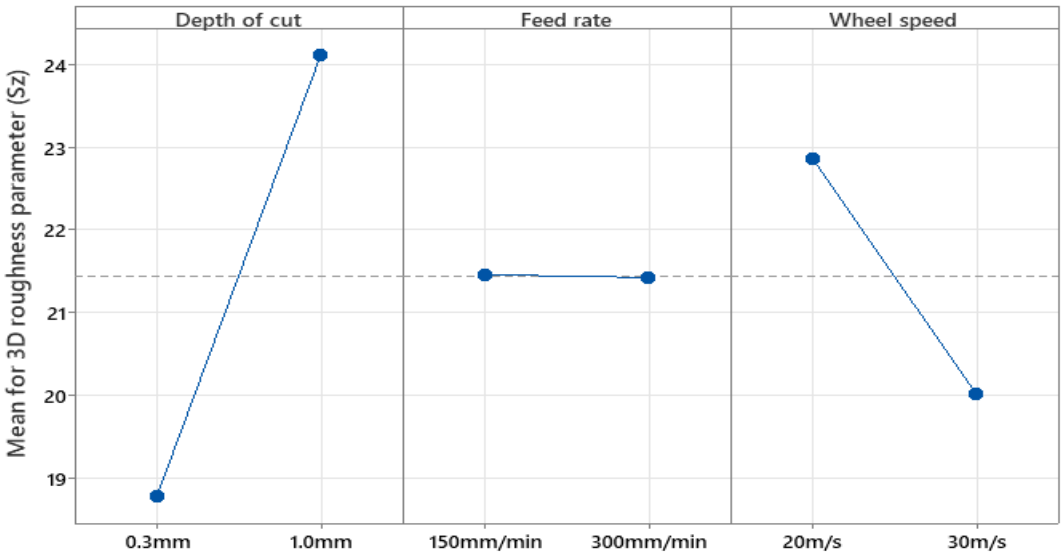


Figure F79: Main effect plot for 3D surface roughness parameter Sz in µm (Phase 2A)

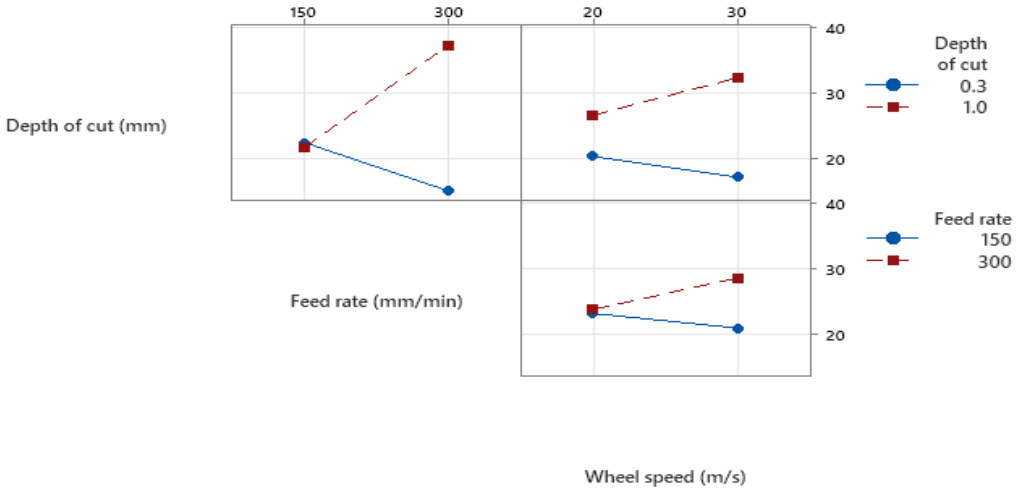


Figure F80: Interaction plot for 3D surface roughness parameter Sz (Phase 2A)

Table F29: ANOVA table for 3D surface roughness parameter Sz (Phase 2A)

Source	DF	Seq SS	Contribution	Adj SS	Adj MS	F-Value	P-Value
Wheel speed (m/s)	1	16.245	8.27%	16.245	16.245	1.70	0.416
Depth of cut (mm)	1	56.818	28.91%	56.818	56.818	5.95	0.248
Feed rate (mm/min)	1	0.002	0.00%	0.002	0.002	0.00	0.990
Wheel speed*Depth of cut	1	0.180	0.09%	0.180	0.180	0.02	0.913
Wheel speed*Feed rate	1	6.734	3.43%	6.734	6.734	0.71	0.555
Depth of cut*Feed rate	1	107.018	54.45%	107.018	107.018	11.21	0.185
Error	1	9.548	4.86%	9.548	9.548	-	-
Total	7	196.547	100.00%	-	-	-	-

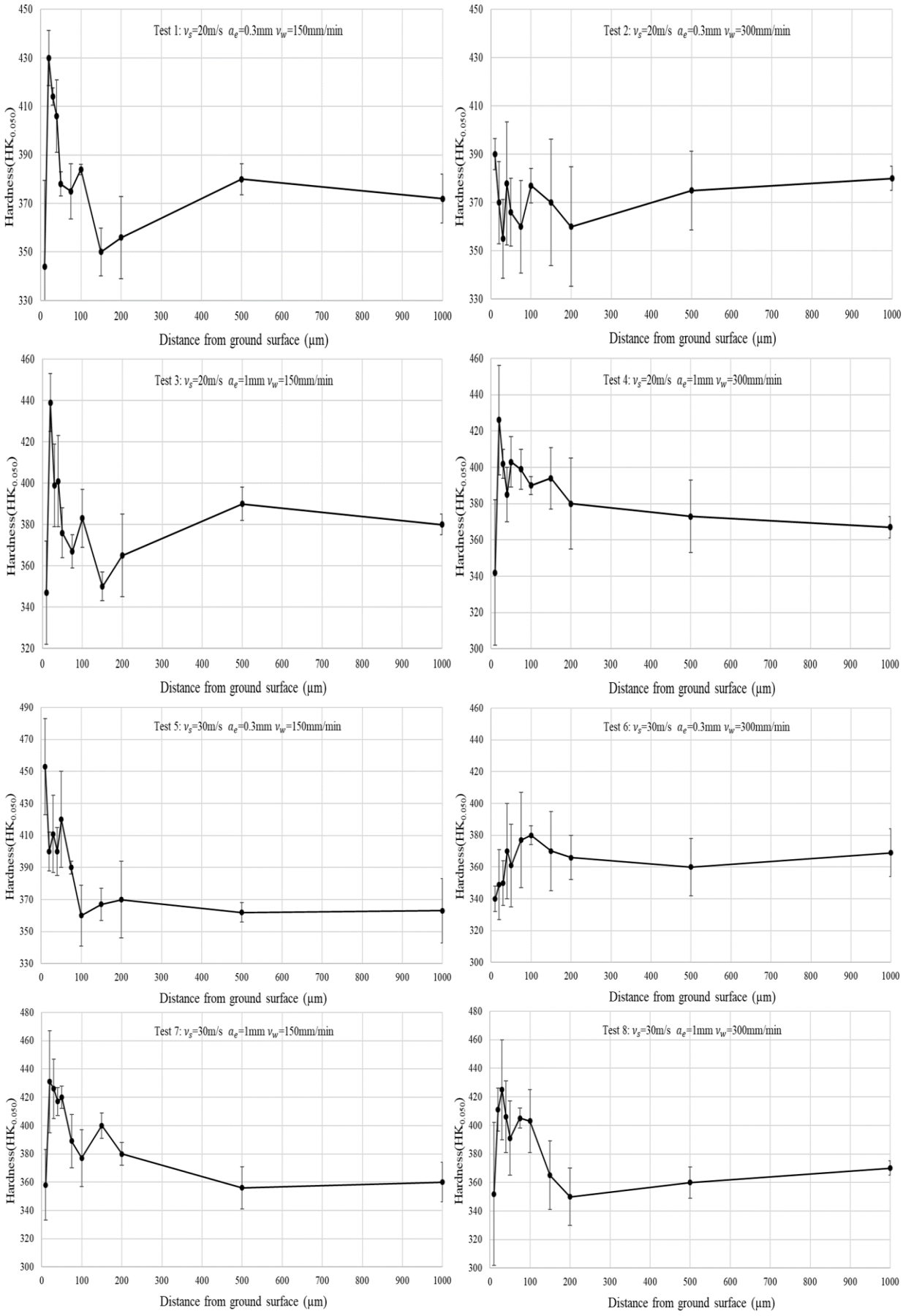


Figure F81: Individual microhardness profiles (Phase 2A)

b) Phase 2B: Assessment of grinding performance when creep feed grinding burn resistant titanium alloy (Ti-25V-15Cr-2Al-0.2C) with super-abrasive diamond wheel, and benchmark against γ-titanium aluminide alloy (Ti-45Al-8Nb-0.2C)

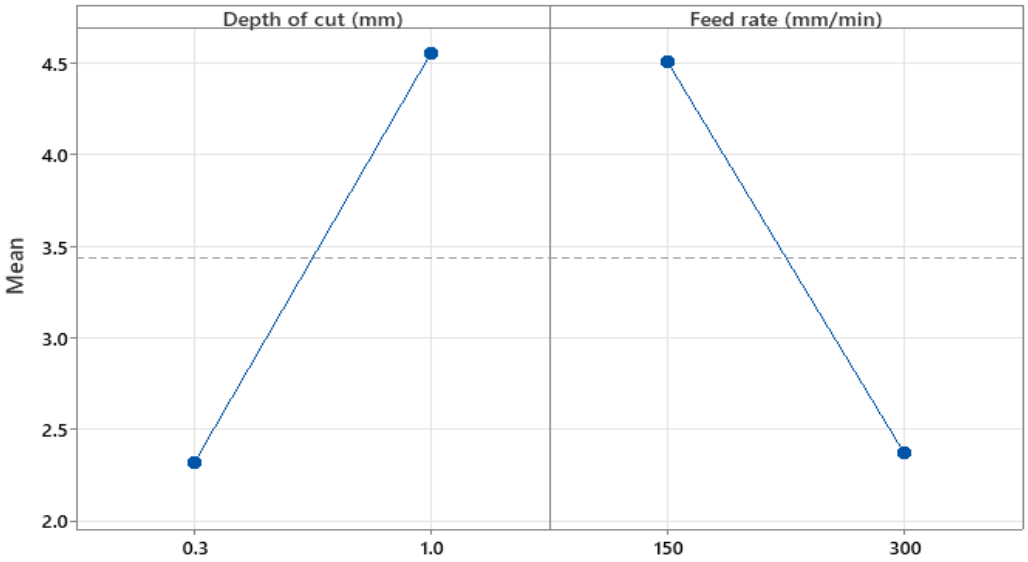


Figure F82: Main effect plot for G-ratio (Phase 2B)

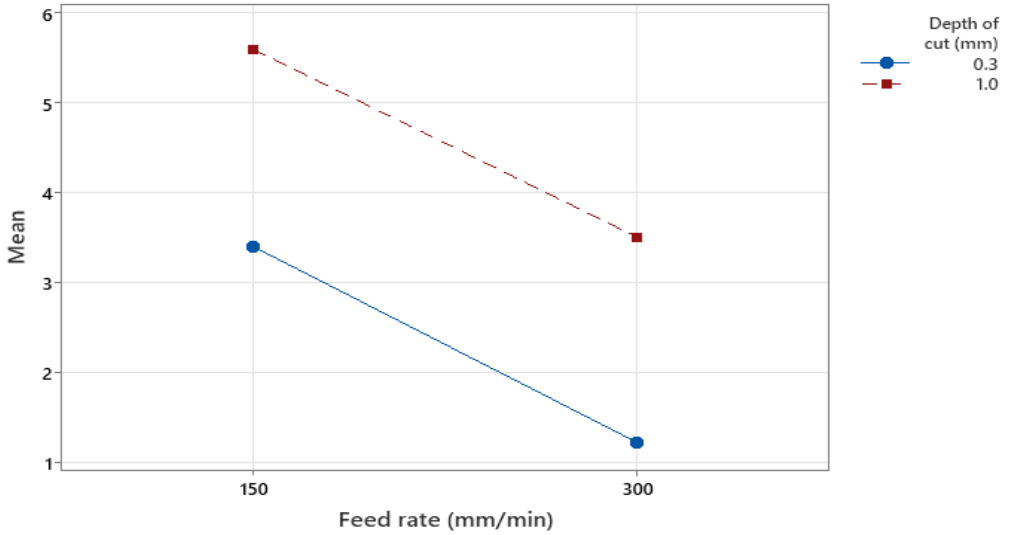


Figure F83: Interaction plot for G-ratio (Phase 2B)

Table F30: ANOVA table for G-ratio (Phase 2B)

Source	DF	Seq SS	Contribution	Adj SS	Adj MS	F-Value	P-Value
Depth of cut (mm)	1	4.99522	52.28%	4.99522	4.99522	2466.78	0.013
Feed rate (mm/min)	1	4.55823	47.70%	4.55823	4.55823	2250.98	0.013
Error	1	0.00203	0.02%	0.00203	0.00203	-	-
Total	3	9.55547	100.00%	-	-	-	-

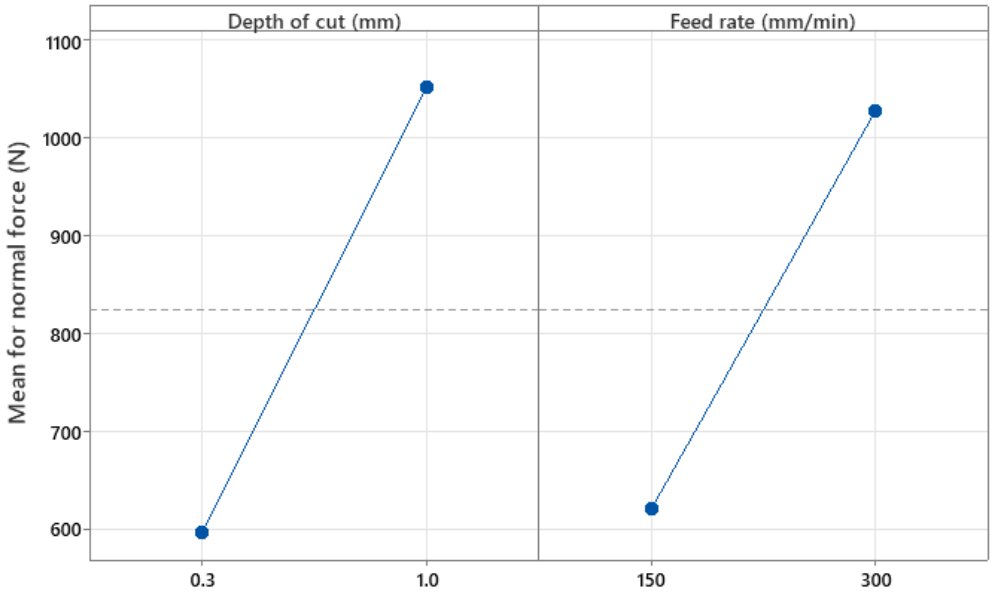


Figure F84: Main effect plot for normal force (Phase 2B)

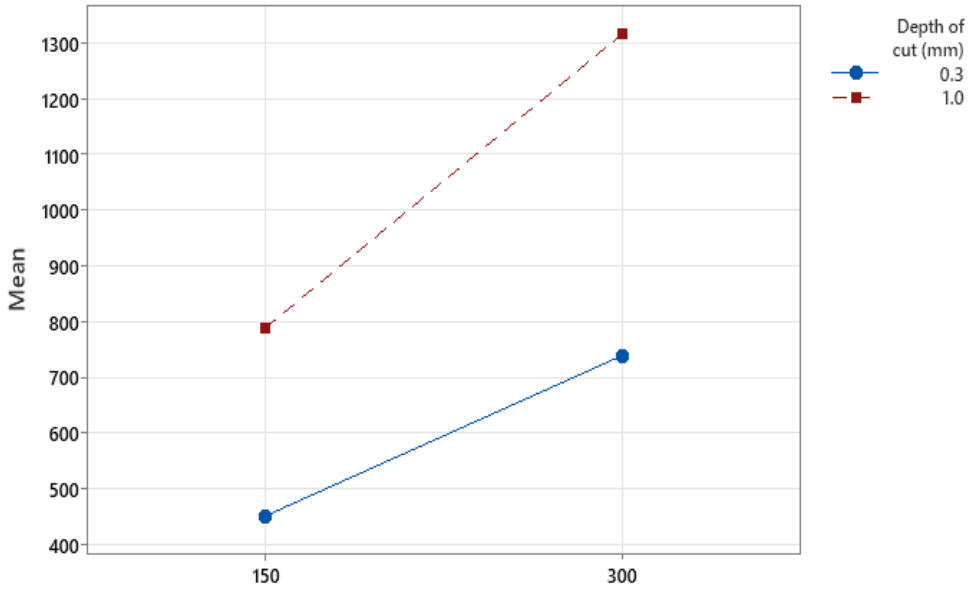


Figure F85: Interaction plot for normal force (Phase 2B)

Table F31: ANOVA table for normal force (Phase 2B)

Source	DF	Seq SS	Contribution	Adj SS	Adj MS	F-Value	P-Value
Depth of cut (mm)	1	208543	53.64%	208543	208543	14.56	0.163
Feed rate (mm/min)	1	165922	42.68%	165922	165922	11.59	0.182
Error	1	14320	3.68%	14320	14320	-	-
Total	3	388784	100.00%	-	-	-	-

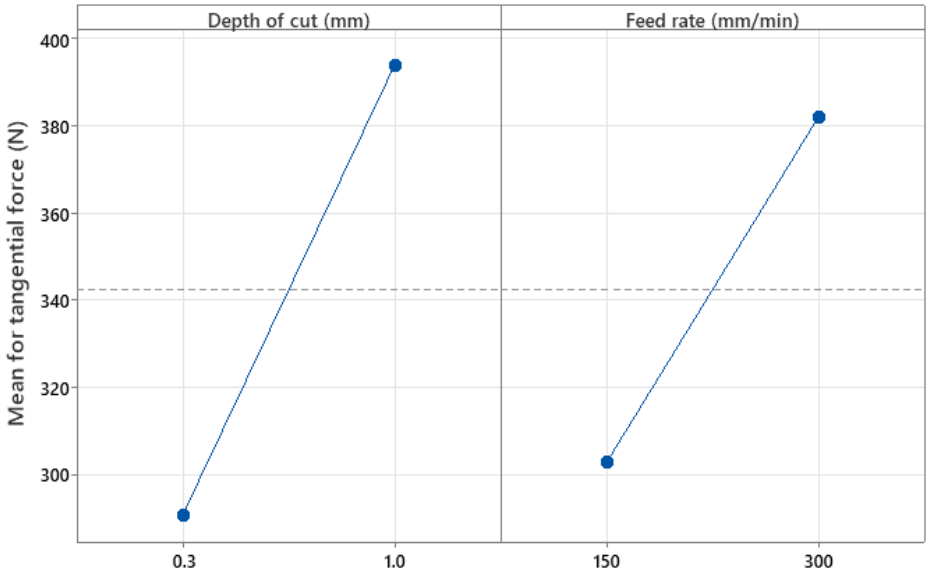


Figure F86: Main effect plot for tangential force (Phase 2B)

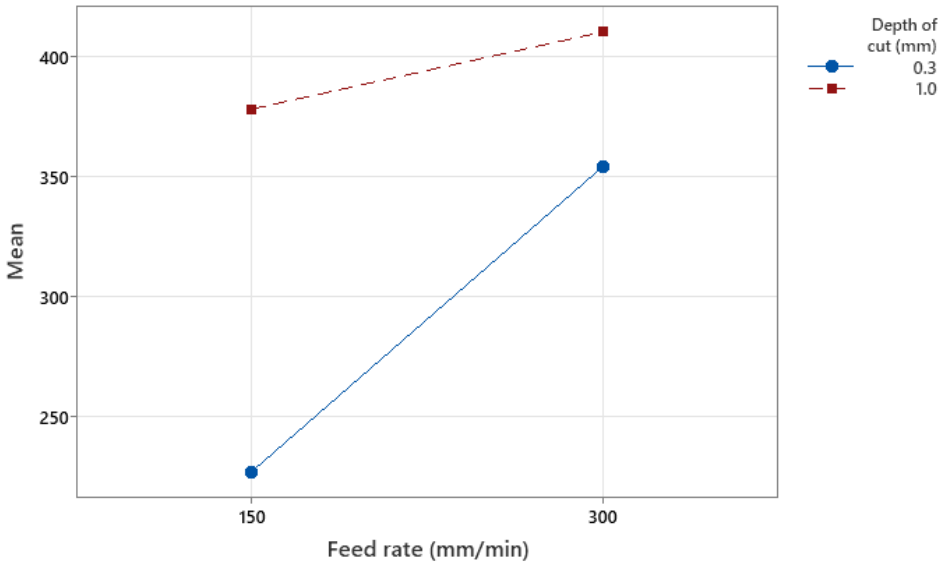


Figure F87: Interaction plot for tangential force (Phase 2B)

Table F32: ANOVA table for tangential force (Phase 2B)

Source	DF	Seq SS	Contribution	Adj SS	Adj MS	F-Value	P-Value
Depth of cut (mm)	1	10663	55.57%	10663	10663	4.77	0.273
Feed rate (mm/min)	1	6288	32.77%	6288	6288	2.81	0.342
Error	1	2237	11.66%	2237	2237	-	-
Total	3	19188	100.00%	-	-	-	-

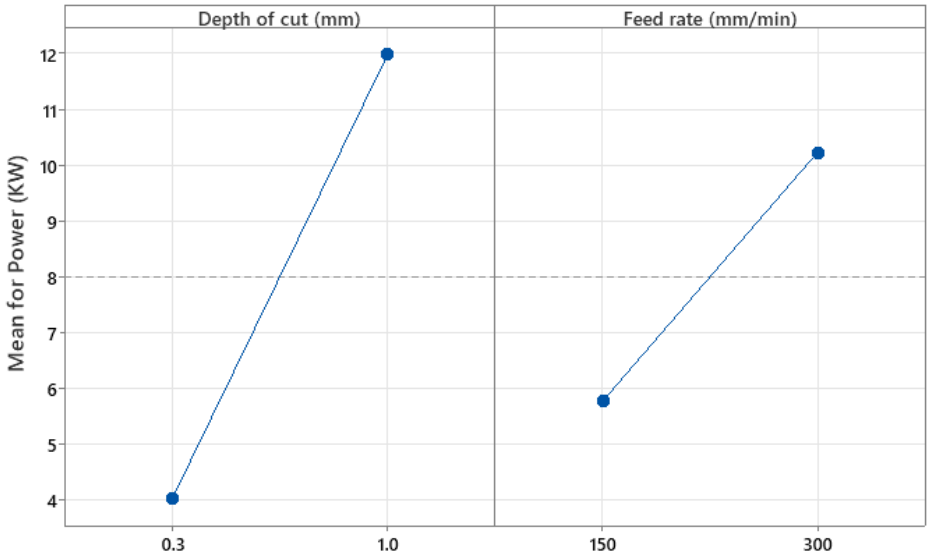


Figure F88: Main effect plot for grinding power (Phase 2B)

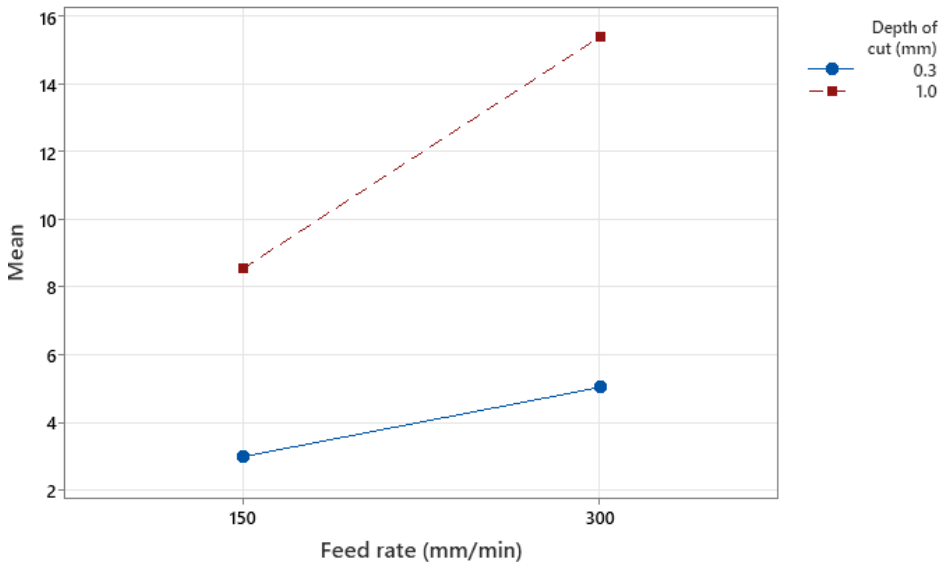


Figure F89: Interaction plot for grinding power (Phase 2B)

Table F33: ANOVA table for grinding power (Phase 2B)

Source	DF	Seq SS	Contribution	Adj SS	Adj MS	F-Value	P-Value
Depth of cut (mm)	1	63.203	71.20%	63.203	63.203	10.97	0.187
Feed rate (mm/min)	1	19.803	22.31%	19.803	19.803	3.44	0.315
Error	1	5.760	6.49%	5.760	5.760	-	-
Total	3	88.765	100.00%	-	-	-	-

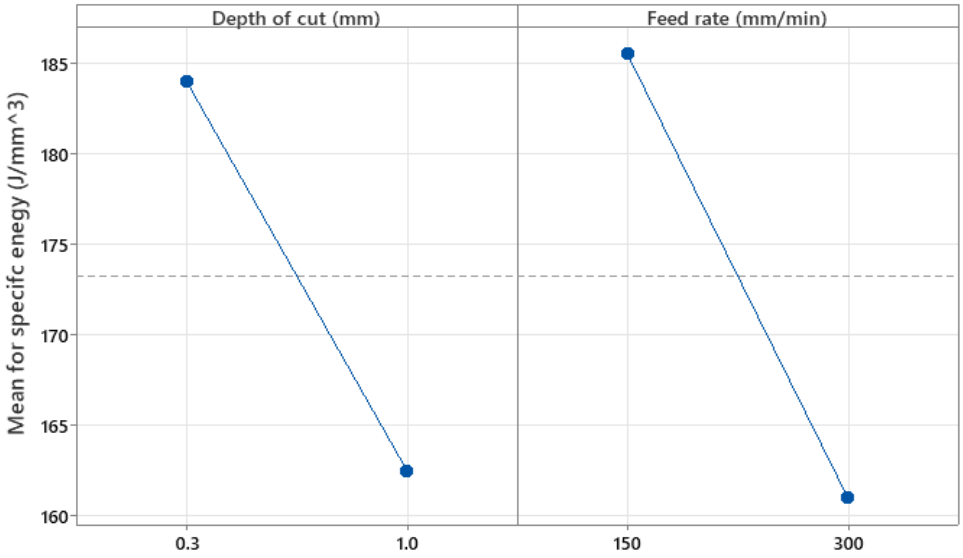


Figure F90: Main effect plot for specific energy (Phase 2B)

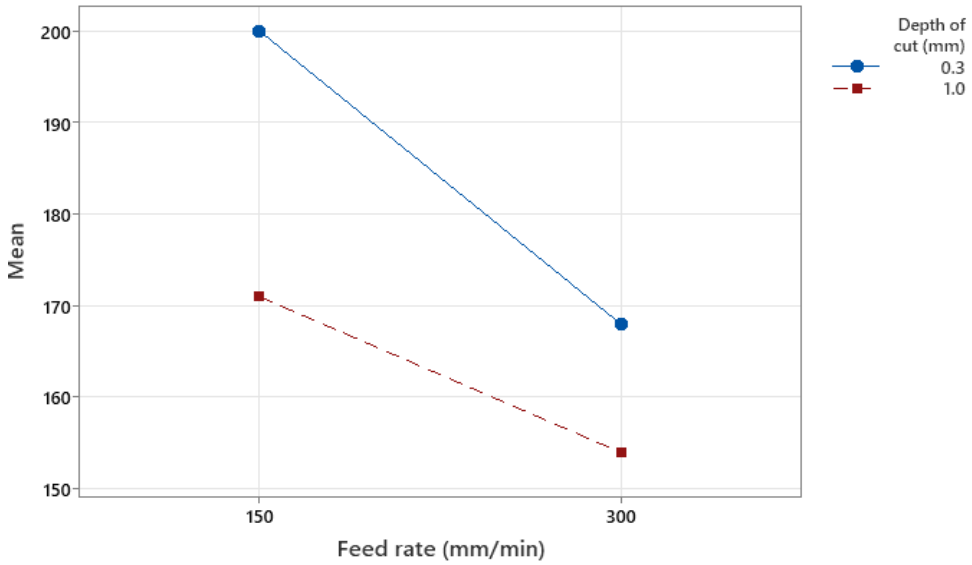


Figure F91: Interaction plot for specific energy (Phase 2B)

Table F34: ANOVA table for specific energy (Phase 2B)

Source	DF	Seq SS	Contribution	Adj SS	Adj MS	F-Value	P-Value
Depth of cut (mm)	1	462.25	41.32%	462.25	462.25	8.22	0.214
Feed rate (mm/min)	1	600.25	53.65%	600.25	600.25	10.67	0.189
Error	1	56.25	5.03%	56.25	56.25	-	-
Total	3	1118.75	100.00%	-	-	-	-

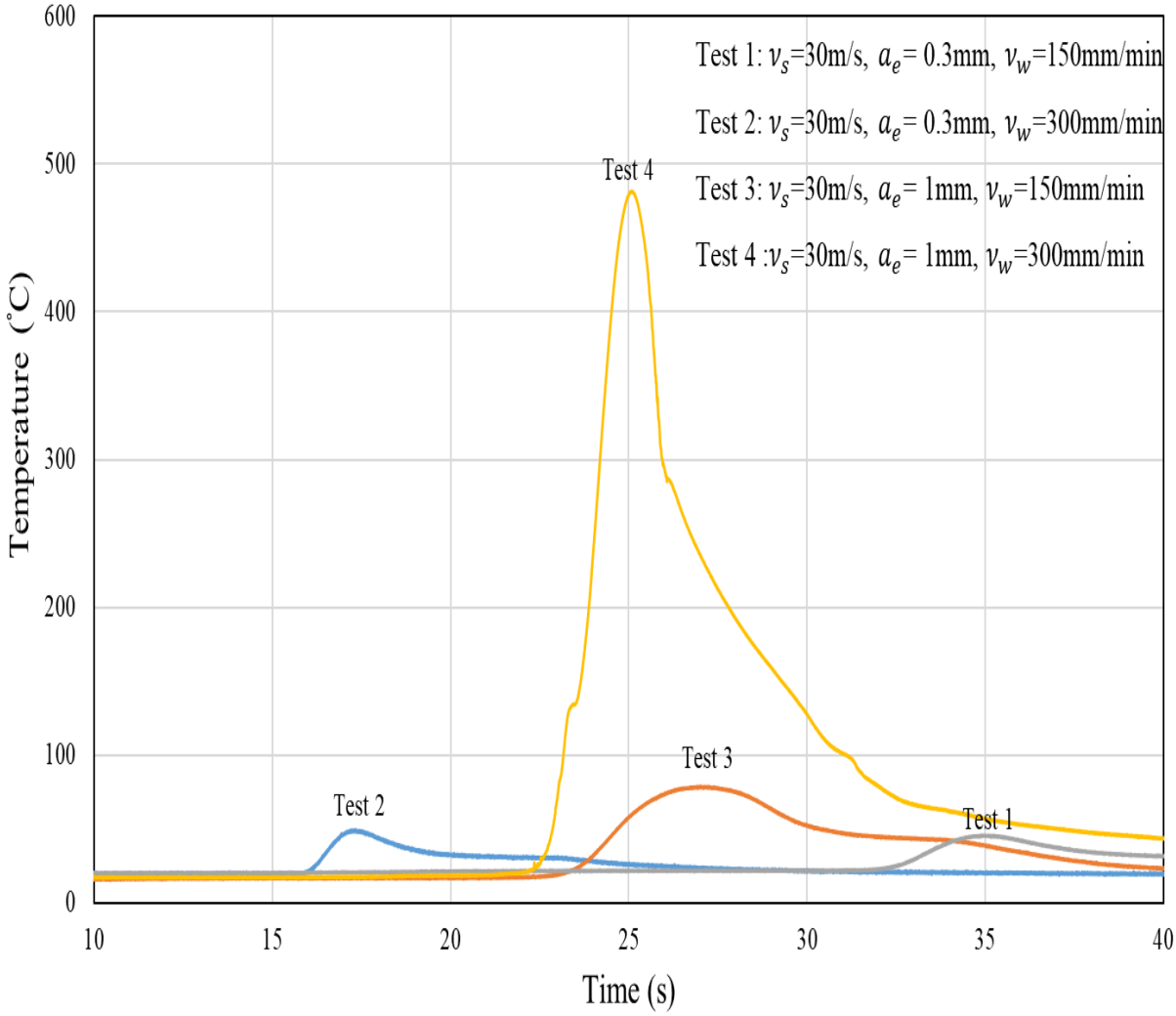


Figure F92: Grinding temperature traces (Phase 2B)

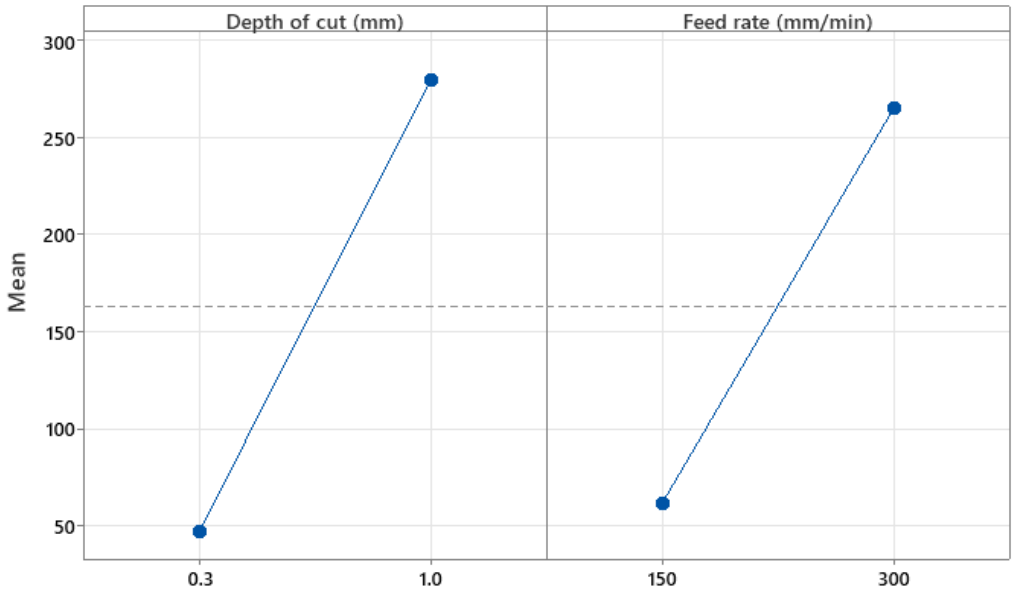


Figure F93: Main effect plot for grinding temperature (Phase 2B)

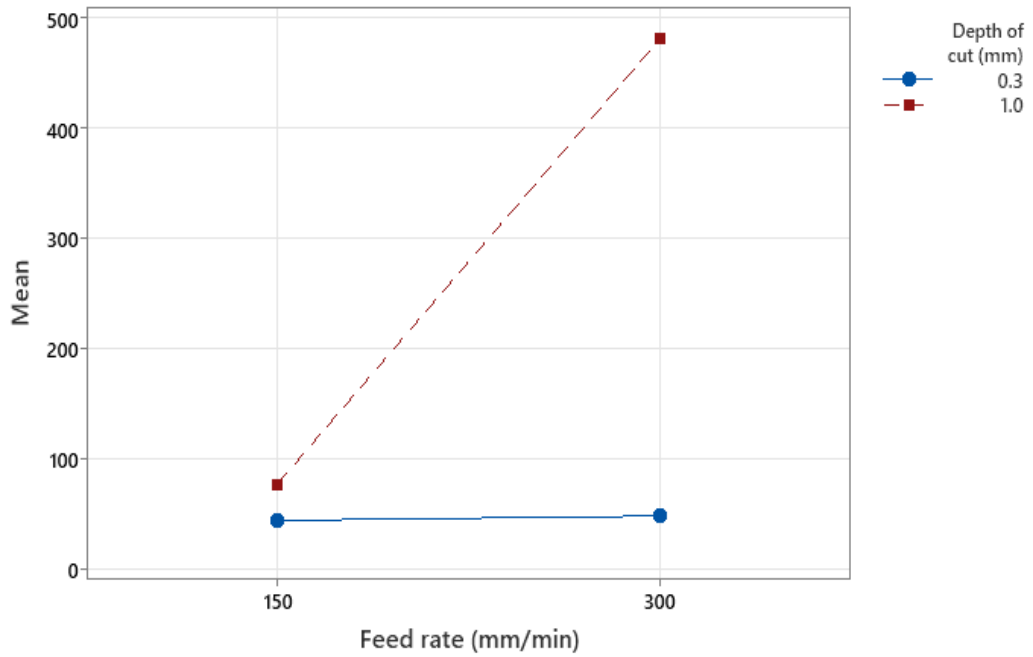


Figure F94: Interaction plot for grinding temperature (Phase 2B)

Table F35: ANOVA table for grinding temperature (Phase 2B)

Source	DF	Seq SS	Contribution	Adj SS	Adj MS	F-Value	P-Value
Depth of cut (mm)	1	54056	39.96%	54056	54056	1.36	0.451
Feed rate (mm/min)	1	41412	30.61%	41412	41412	1.04	0.494
Error	1	39800	29.42%	39800	39800	-	-
Total	3	135269	100.00%	-	-	-	-

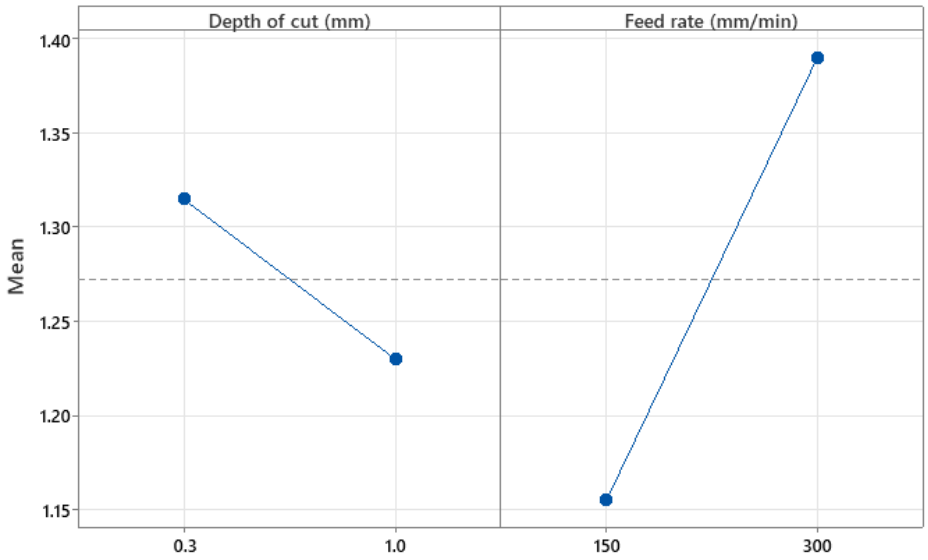


Figure F95: Main effect plot for 2D surface roughness parameter Ra in µm (Phase 2B)

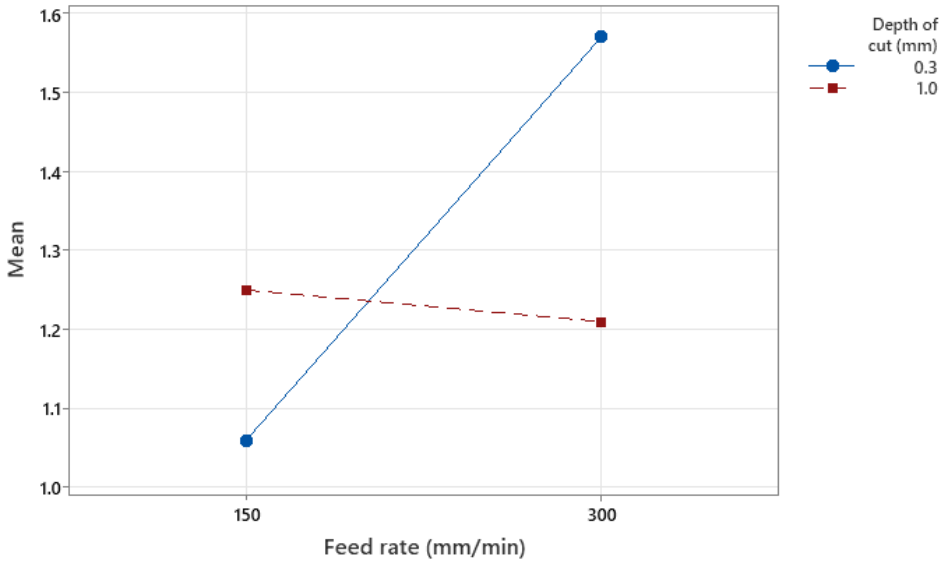


Figure F96: Interaction plot for 2D surface roughness parameter Ra in µm (Phase 2B)

Table F36: ANOVA table for 2D surface roughness parameter Ra (Phase 2B)

Source	DF	Seq SS	Contribution	Adj SS	Adj MS	F-Value	P-Value
Depth of cut (mm)	1	0.007225	5.23%	0.007225	0.007225	0.10	0.809
Feed rate (mm/min)	1	0.055225	40.00%	0.055225	0.055225	0.73	0.550
Error	1	0.075625	54.77%	0.075625	0.075625	-	-
Total	3	0.138075	100.00%	-	-	-	-

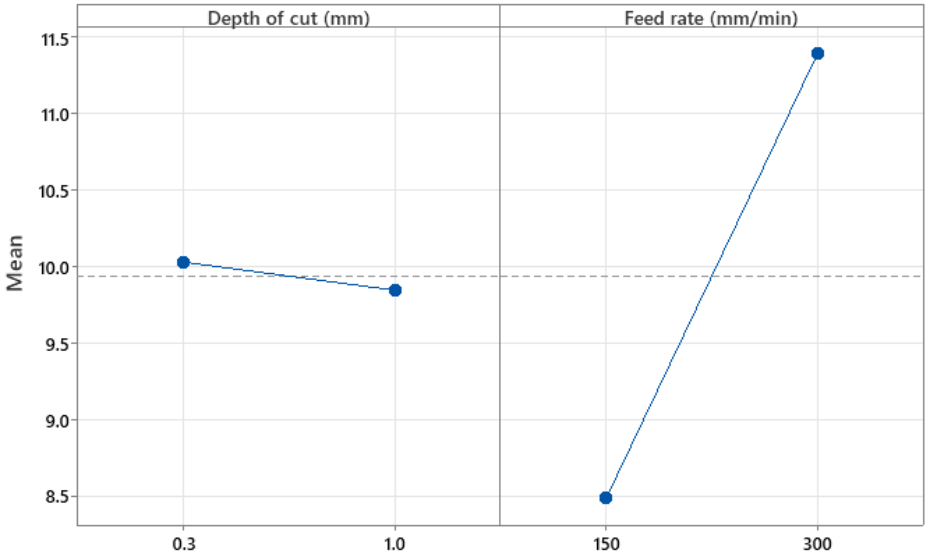


Figure F97: Main effect plot for 2D surface roughness parameter Rt in µm (Phase 2B)

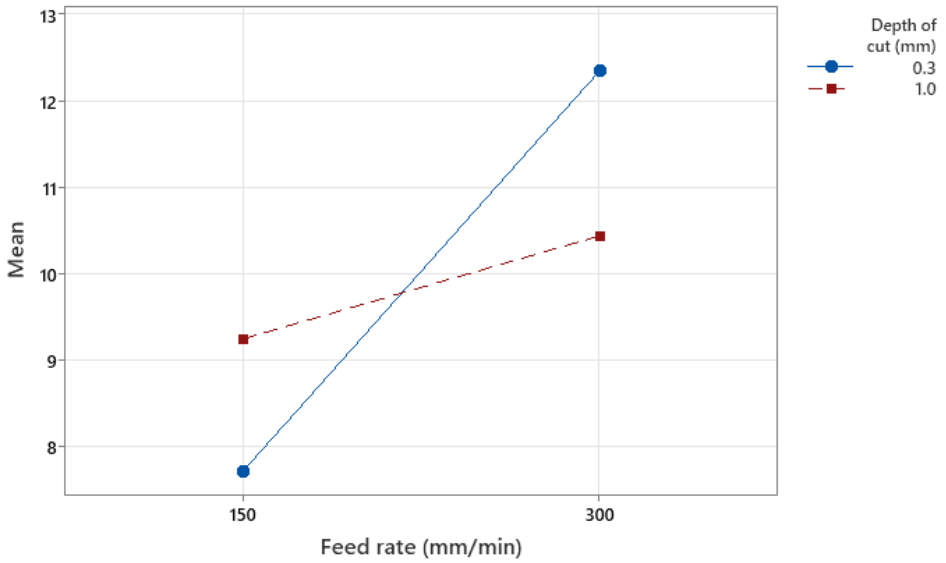


Figure F98: Interaction plot for 2D surface roughness parameter Rt in µm (Phase 2B)

Table F37: ANOVA table for 2D surface roughness parameter Rt (Phase 2B)

Source	DF	Seq SS	Contribution	Adj SS	Adj MS	F-Value	P-Value
Depth of cut (mm)	1	0.0342	0.30%	0.03422	0.03422	0.01	0.932
Feed rate (mm/min)	1	8.4390	73.93%	8.43903	8.43903	2.87	0.340
Error	1	2.9412	25.77%	2.94123	2.94123	-	-
Total	3	11.4145	100.00%	-	-	-	-

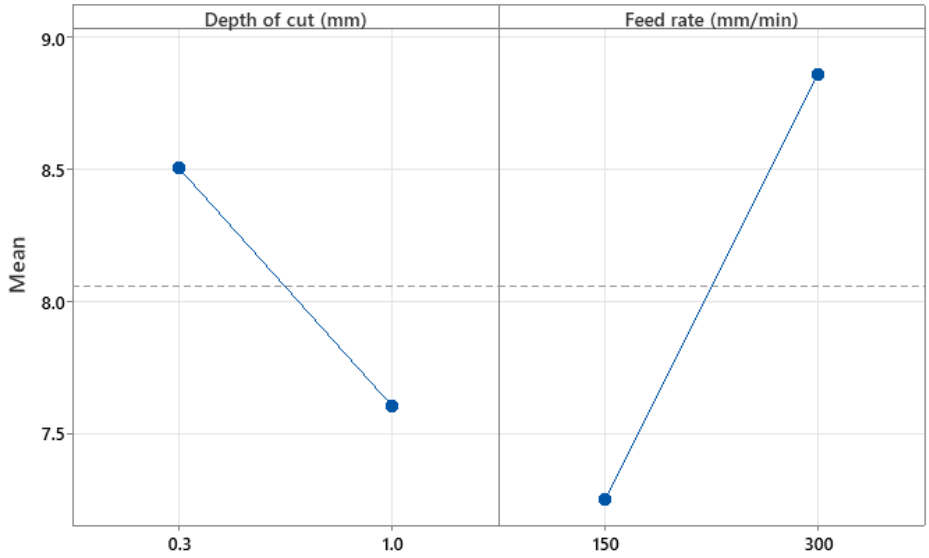


Figure F99: Main effect plot for 2D surface roughness parameter Rz in µm (Phase 2B)

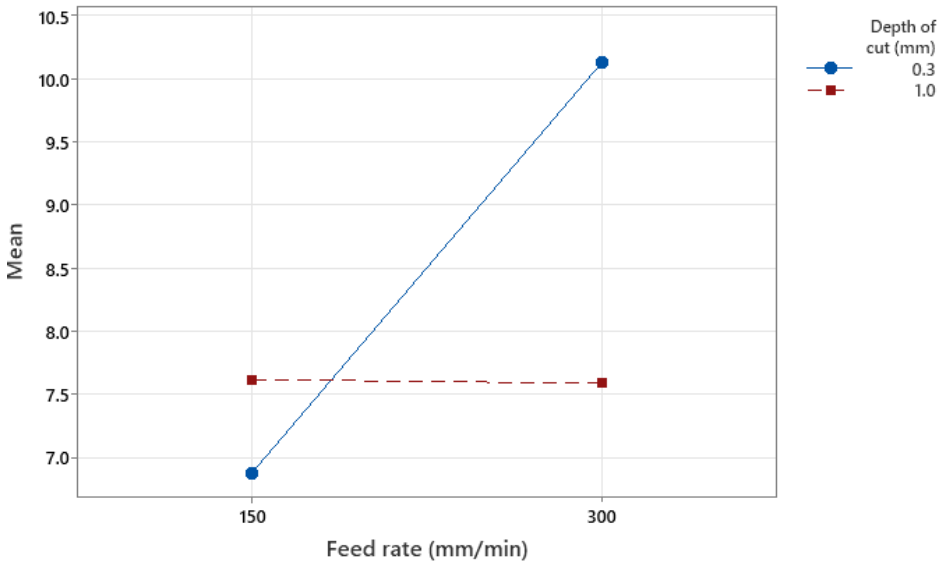


Figure F100: Interaction plot for 2D surface roughness parameter Rz in µm (Phase 2B)

Table F38: ANOVA table for 2D surface roughness parameter Rz (Phase 2B)

Source	DF	Seq SS	Contribution	Adj SS	Adj MS	F-Value	P-Value
Depth of cut (mm)	1	0.8100	13.30%	0.8100	0.8100	0.30	0.680
Feed rate (mm/min)	1	2.5921	42.55%	2.5921	2.5921	0.96	0.506
Error	1	2.6896	44.15%	2.6896	2.6896	-	-
Total	3	6.0917	100.00%	-	-	-	-

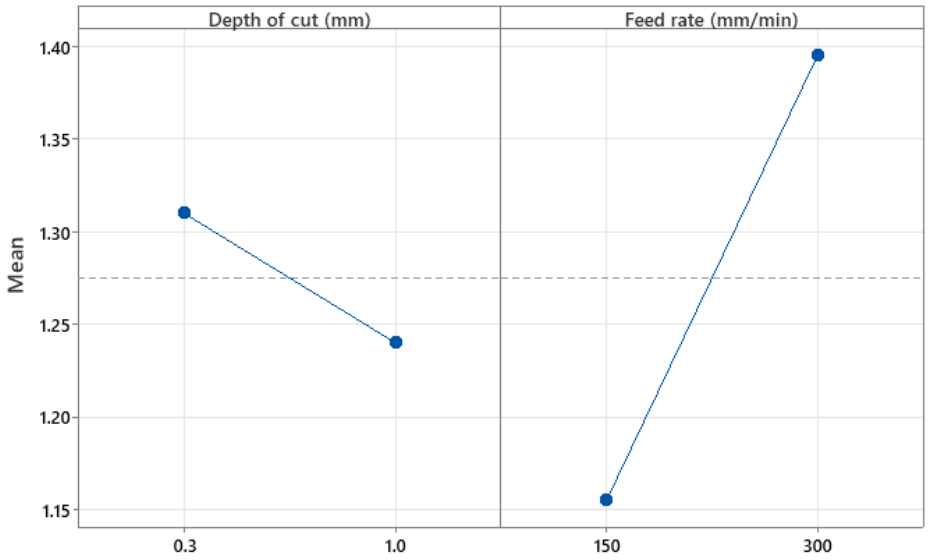


Figure F101: Main effect plot for 3D surface roughness parameter Sa in µm (Phase 2B)

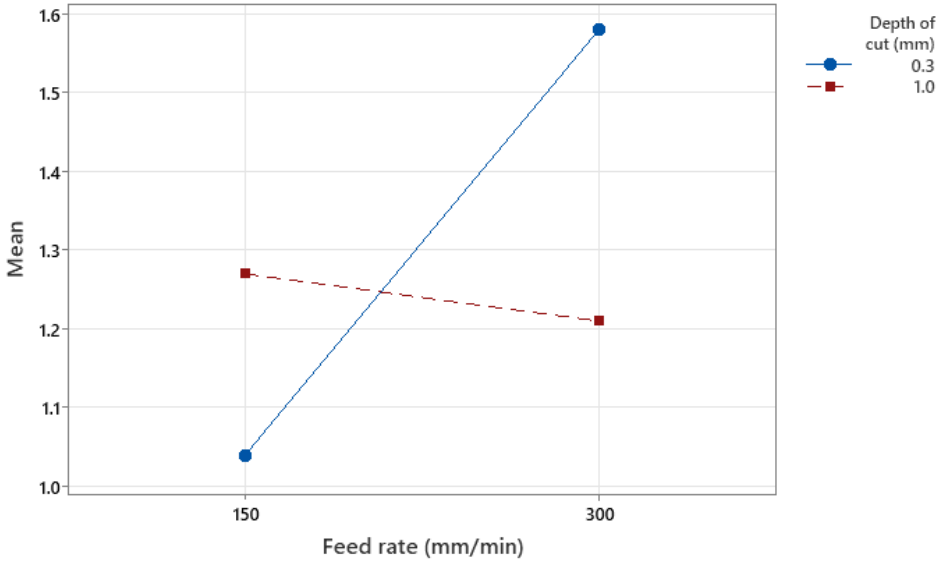


Figure F102: Interaction plot for 3D surface roughness parameter Sa in µm (Phase 2B)

Table F39: ANOVA table for 3D surface roughness parameter Sa (Phase 2B)

Source	DF	Seq SS	Contribution	Adj SS	Adj MS	F-Value	P-Value
Depth of cut (mm)	1	0.004900	3.21%	0.004900	0.004900	0.05	0.854
Feed rate (mm/min)	1	0.057600	37.77%	0.057600	0.057600	0.64	0.570
Error	1	0.090000	59.02%	0.090000	0.090000	-	-
Total	3	0.152500	100.00%	-	-	-	-

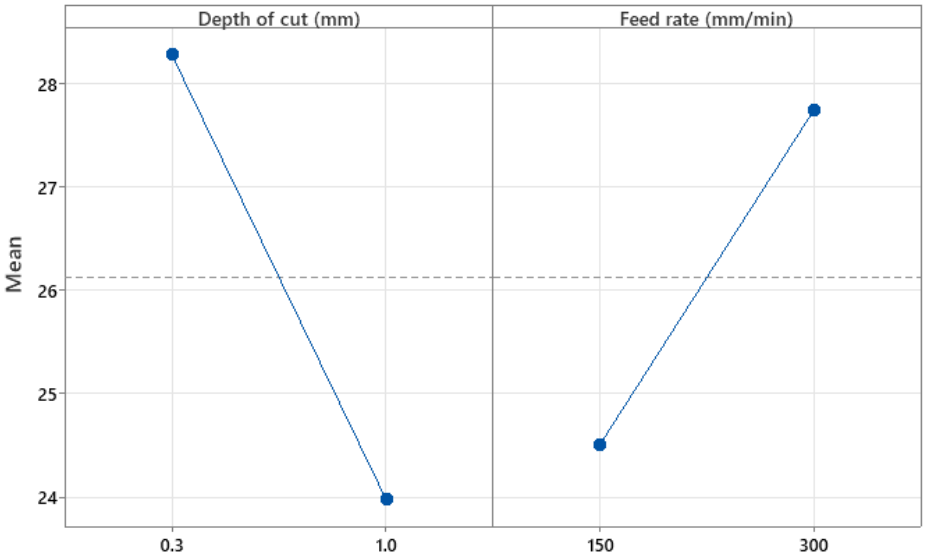


Figure F103: Main effect plot for 3D surface roughness parameter St in µm (Phase 2B)

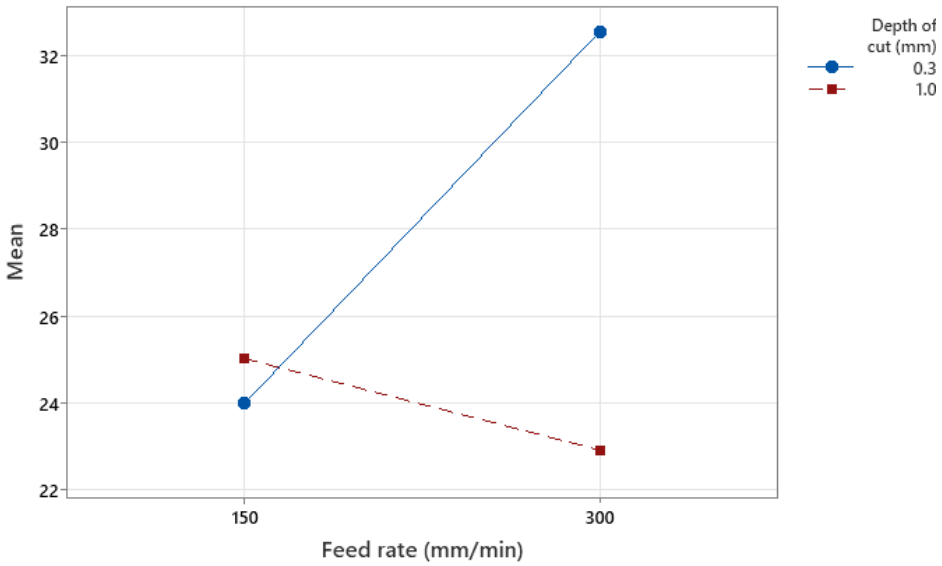


Figure F104: Interaction plot for 3D surface roughness parameter St in µm (Phase 2B)

Table F40: ANOVA table for 3D surface roughness parameter St (Phase 2B)

Source	DF	Seq SS	Contribution	Adj SS	Adj MS	F-Value	P-Value
Depth of cut (mm)	1	18.49	32.19%	18.49	18.49	0.65	0.568
Feed rate (mm/min)	1	10.43	18.16%	10.43	10.43	0.37	0.654
Error	1	28.52	49.65%	28.52	28.52	-	-
Total	3	57.44	100.00%	-	-	-	-

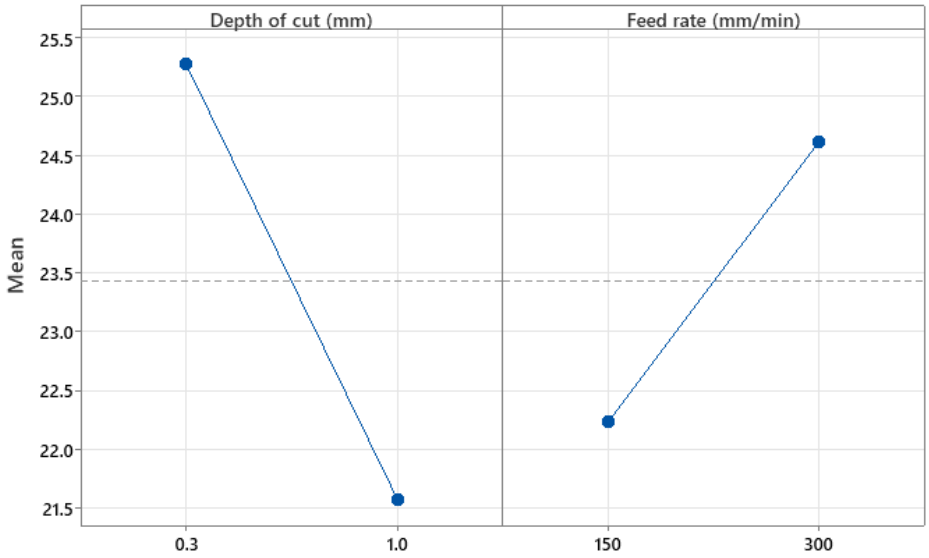


Figure F105: Main effect plot for 3D surface roughness parameter Sz in µm (Phase 2B)

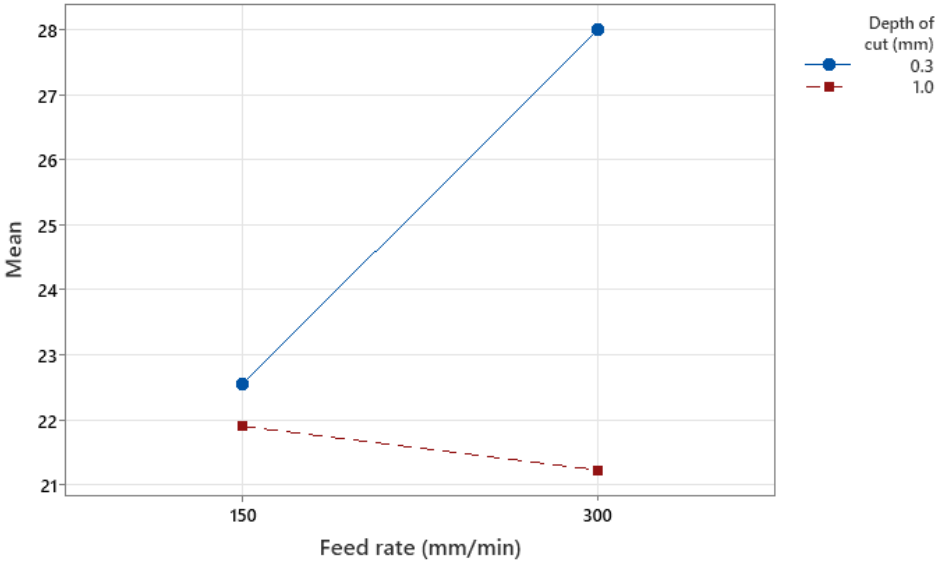


Figure F106: Interaction plot for 3D surface roughness parameter Sz in µm (Phase 2B)

Table F41: ANOVA table for 3D surface roughness parameter Sz (Phase 2B)

Source	DF	Seq SS	Contribution	Adj SS	Adj MS	F-Value	P-Value
Depth of cut (mm)	1	13.690	47.77%	13.690	13.690	1.47	0.439
Feed rate (mm/min)	1	5.664	19.77%	5.664	5.664	0.61	0.578
Error	1	9.303	32.46%	9.303	9.303	-	-
Total	3	28.657	100.00%	-	-	-	-

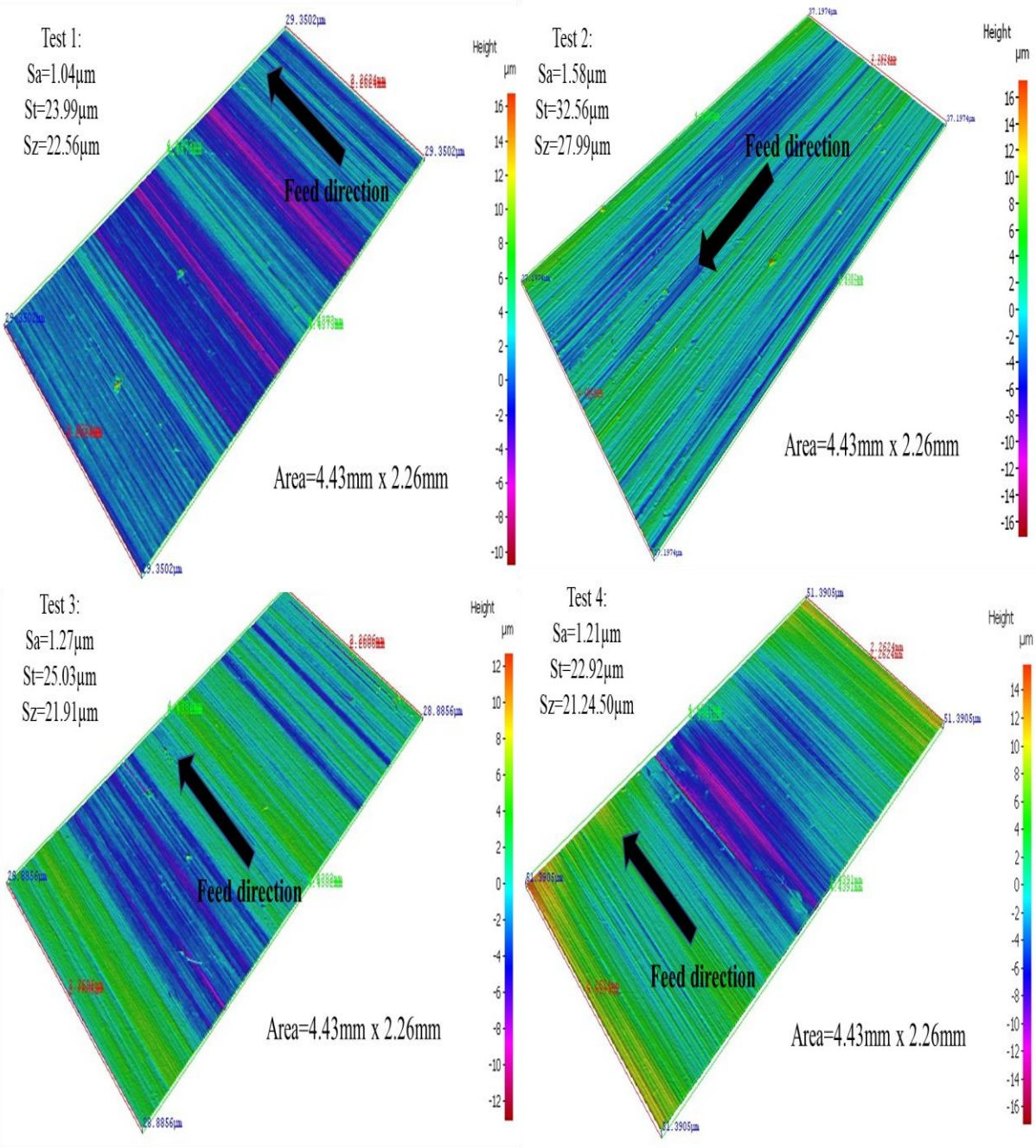


Figure F107: 3D topographies of ground surfaces, primary mapping not filtered (Phase 2B)

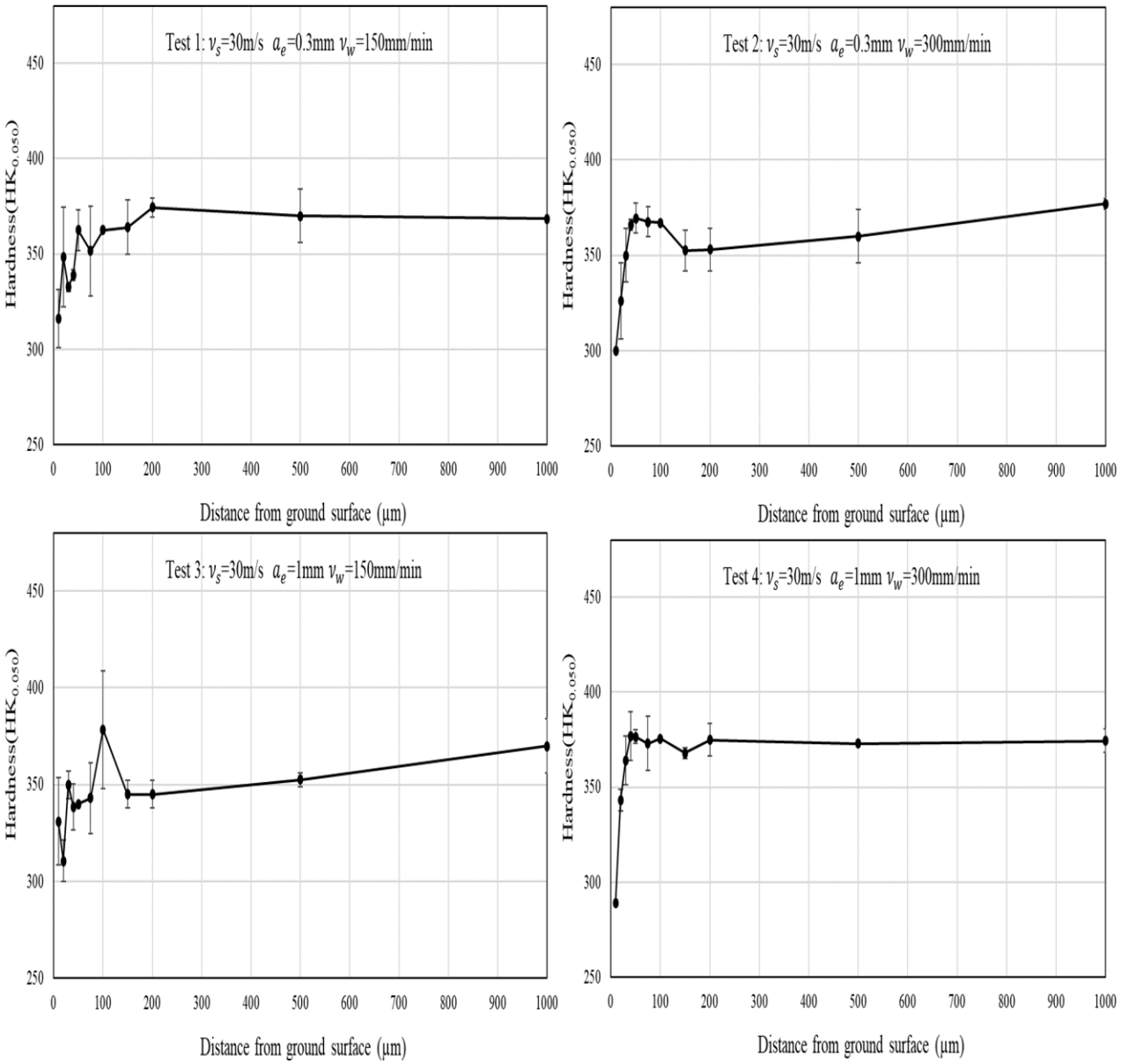


Figure F108: Individual microhardness profiles (Phase 2B)

F3 Phase 3: Creep feed grinding of conventional titanium alloy (Ti-6Al-4V)

b) Benchmarking the performance of conventional titanium alloy (Ti-6Al-4V) against γ-titanium aluminide alloy and burn resistant titanium alloy with diamond wheel

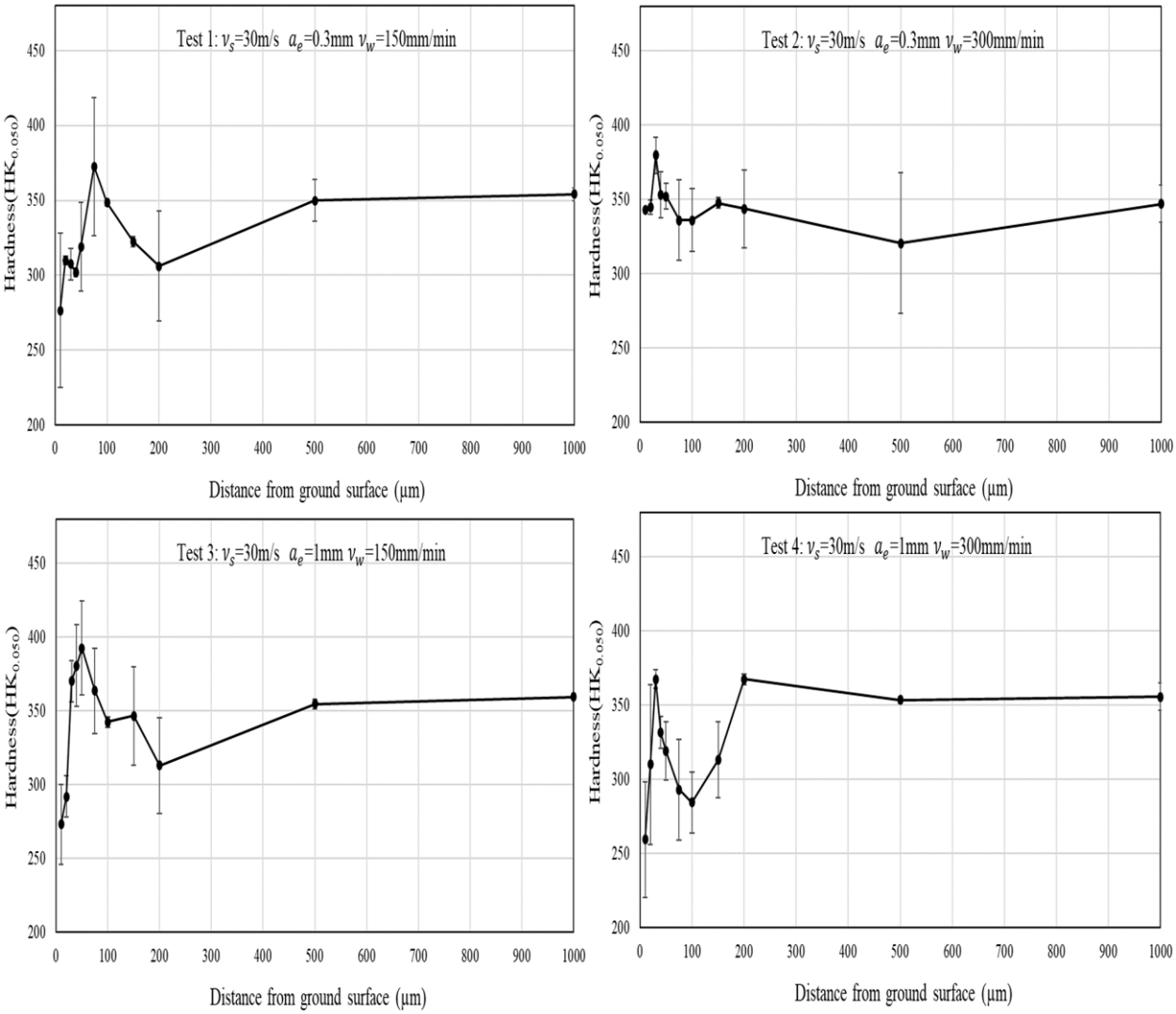


Figure F109: Individual microhardness profiles (Phase 3B)